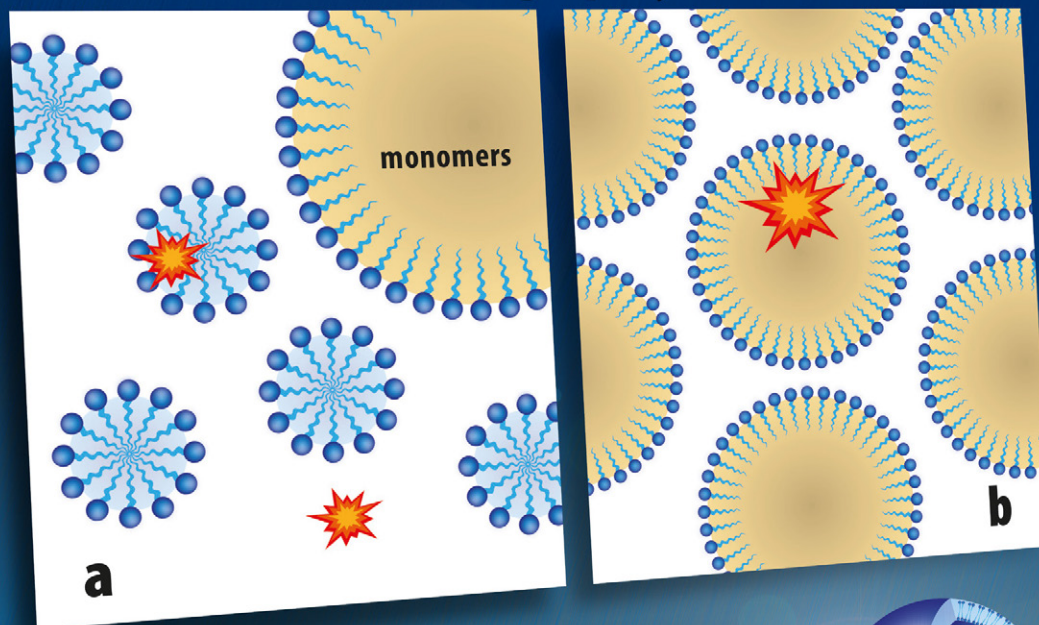




Acta Chimica Slo Acta Chimica Slo Slovenica Acta C

2

Particles through polymerization



69/2022

EDITOR-IN-CHIEF

KSENIJA KOGEJ

University of Ljubljana, Faculty of Chemistry and Chemical Technology, Večna pot 113, SI-1000 Ljubljana, Slovenija

E-mail: ACSi@fkk.uni-lj.si, Telephone: (+386)-1-479-8538

ASSOCIATE EDITORS

Alen Albreht, National Institute of Chemistry, Slovenia

Aleš Berlec, Jožef Stefan Institute, Slovenia

Janez Cerkovnik, University of Ljubljana, Slovenia

Mirela Dragomir, Jožef Stefan Institute, Slovenia

Ksenija Kogej, University of Ljubljana, Slovenia

Krištof Kranjc, University of Ljubljana, Slovenia

Matjaž Kristl, University of Maribor, Slovenia

Franc Perdih, University of Ljubljana, Slovenia

Aleš Ručigaj, University of Ljubljana, Slovenia

Helena Prosen, University of Ljubljana, Slovenia

Irena Vovk, National Institute of Chemistry, Slovenia

ADMINISTRATIVE ASSISTANT

Marjana Gantar Albreht, National Institute of Chemistry, Slovenia

EDITORIAL BOARD

Wolfgang Buchberger, Johannes Kepler University, Austria

Alojz Demšar, University of Ljubljana, Slovenia

Stanislav Gobec, University of Ljubljana, Slovenia

Marko Goličnik, University of Ljubljana, Slovenia

Günter Grampp, Graz University of Technology, Austria

Wojciech Grochala, University of Warsaw, Poland

Danijel Kikelj, University of Ljubljana

Janez Košmrlj, University of Ljubljana, Slovenia

Blaž Likozar, National Institute of Chemistry, Slovenia

Mahesh K. Lakshman, The City College and

The City University of New York, USA

Janez Mavri, National Institute of Chemistry, Slovenia

Friedrich Sreinc, University of Minnesota, USA

Walter Steiner, Graz University of Technology, Austria

Jurij Svete, University of Ljubljana, Slovenia

David Šarlah, University of Illinois at Urbana-Champaign, USA;

Università degli Studi di Pavia, Italy

Ivan Švancara, University of Pardubice, Czech Republic

Jiri Pinkas, Masaryk University Brno, Czech Republic

Gašper Tavčar, Jožef Stefan Institute, Slovenia

Ennio Zangrando, University of Trieste, Italy

ADVISORY EDITORIAL BOARD

Chairman

Branko Stanovnik, Slovenia

Members

Udo A. Th. Brinkman, The Netherlands

Attilio Cesaro, Italy

Vida Hudnik, Slovenia

Venc̃eslav Kaučič, Slovenia

Željko Knez, Slovenia

Radovan Komel, Slovenia

Stane Pejovnik, Slovenia

Anton Perdih, Slovenia

Slavko Pečar, Slovenia

Andrej Petrič, Slovenia

Boris Pihlar, Slovenia

Milan Randić, Des Moines, USA

Jože Škerjanc, Slovenia

Đurđa Vasić-Rački, Croatia

Marjan Veber, Slovenia

Gorazd Vesnaver, Slovenia

Jure Zupan, Slovenia

Boris Žemva, Slovenia

Majda Žigon, Slovenia

Acta Chimica Slovenica is indexed in: *Academic Search Complete*, *Central & Eastern European Academic Source*, *Chemical Abstracts Plus*, *Chemical Engineering Collection (India)*, *Chemistry Citation Index Expanded*, *Current Contents (Physical, Chemical and Earth Sciences)*, *Digitalna knjižnica Slovenije (dLib.si)*, *DOAJ*, *ISI Alerting Services*, *PubMed*, *Science Citation Index Expanded*, *SciFinder (CAS)*, *Scopus* and *Web of Science*. Impact factor for 2020 is IF = 1.735.



Articles in this journal are published under the Creative Commons Attribution 4.0 International License

Izdaja – Published by:

SLOVENSKO KEMIJSKO DRUŠTVO – SLOVENIAN CHEMICAL SOCIETY

Naslov redakcije in uprave – Address of the Editorial Board and Administration

Hajdrihova 19, SI-1000 Ljubljana, Slovenija

Tel.: (+386)-1-476-0252; Fax: (+386)-1-476-0300; E-mail: chem.soc@ki.si

Izdajanje sofinancirajo – Financially supported by:

National Institute of Chemistry, Ljubljana, Slovenia

Jožef Stefan Institute, Ljubljana, Slovenia

Faculty of Chemistry and Chemical Technology, University of Ljubljana, Slovenia

Faculty of Chemistry and Chemical Engineering, University of Maribor, Slovenia

University of Nova Gorica, Slovenia

Slovensko kemijsko društvo
Slovenian Chemical Society

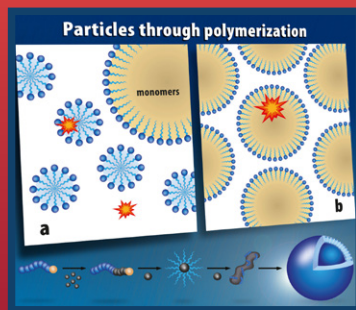


Acta Chimica Slovenica izhaja štirikrat letno v elektronski obliki na spletni strani <http://acta.chem-soc.si>. V primeru posvečenih številk izhaja revija tudi v tiskani obliki v omejenem številu izvodov.

Acta Chimica Slovenica appears quarterly in electronic form on the web site <http://acta.chem-soc.si>. In case of dedicated issues, a limited number of printed copies are issued as well.

Transakcijski račun: 02053-0013322846 Bank Account No.: SI56020530013322846-Nova Ljubljanska banka d. d., Trg republike 2, SI-1520 Ljubljana, Slovenia, SWIFT Code: LJBA SI 2X

Oblikovanje ovitka – Design cover: KULT, oblikovalski studio, Simon KAJTNA, s. p. Grafična priprava za tisk: OSITO, Laura Jankovič, s.p.

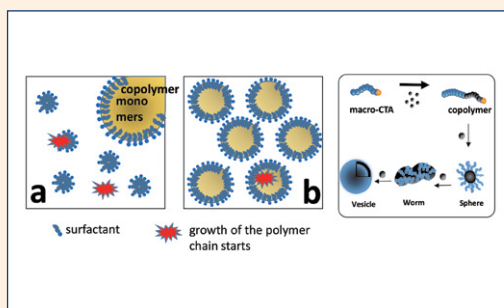


FEATURE ARTICLE

251–260 Review articles

Soft Poly(*N*-vinylcaprolactam) Based Aqueous Particles

Joonas Siirilä and Heikki Tenhu

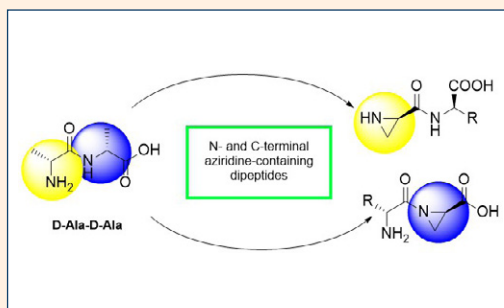


SCIENTIFIC PAPER

261–270 Organic chemistry

The Synthesis of (2*R*)-Aziridine-2-carboxylic Acid Containing Dipeptides

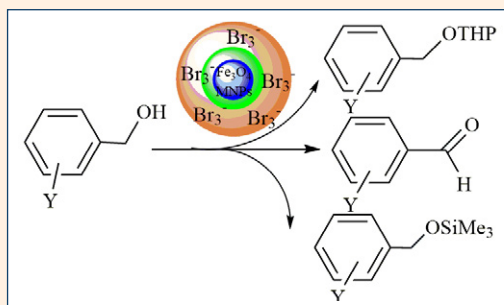
Samo Kuzmič, Martina Hrast and Rok Frlan



271–280 Organic chemistry

Magnetic Nanoparticles Linked to Pyridinium Hydrotribromide Groups as Catalysts for Selective Oxidation of Alcohols and Protection of Alcohols

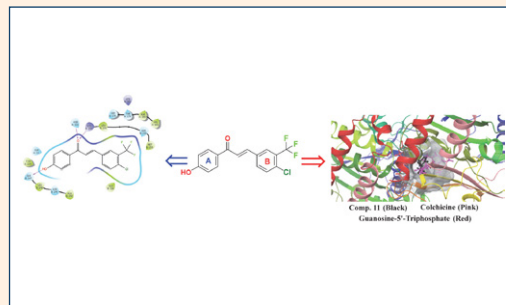
Sonia Tabari, Ali Reza Pourali and Ehsan Nazarzadeh Zare



281–292 General chemistry

(E)-1-(4-Hydroxyphenyl)-3-(substituted-phenyl)prop-2-en-1-ones: Synthesis, *In Vitro* Cytotoxic Activity and Molecular Docking Studies

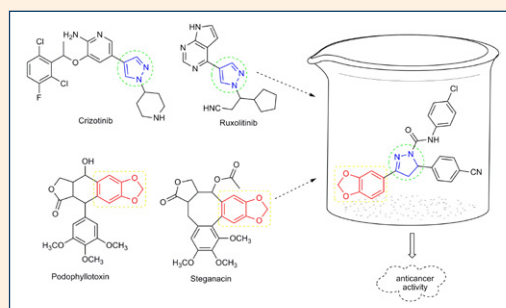
Lütfiye Sirka, Hacer Doğan, Mehmet Refik Bahar, Eray Çalışkan, Suat Tekin, Harun Uslu, Kenan Koran, Süleyman Sandal and Ahmet Orhan Görgülü



293–303 Organic chemistry

Design, Synthesis, *In Silico* ADMET Studies and Anticancer Activity of Some New Pyrazoline and Benzodioxole Derivatives

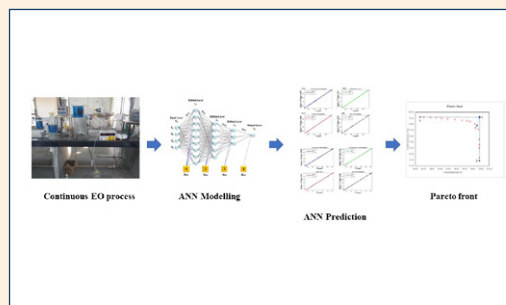
Fatih Tok, Ömer Erdoğan, Özge Çevik and Bedia Koçyiğit-Kaymakçioğlu



304–315 Chemical, biochemical and environmental engineering

Modelling and Multi-Objective Optimization of Continuous Indirect Electro-Oxidation Process for RTB21 Dye Wastewater Using ANN-GA Approach

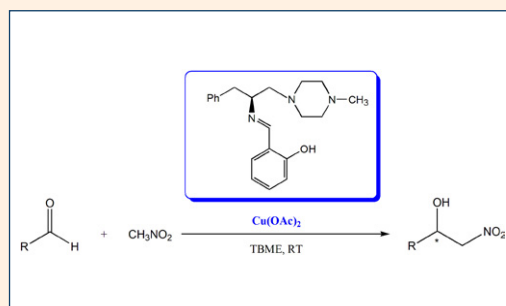
Naresh R Vaghela and Kaushik Nath



316–321 Organic chemistry

Enantioselective Henry Reaction Catalyzed by Chiral Piperazine Derivatives

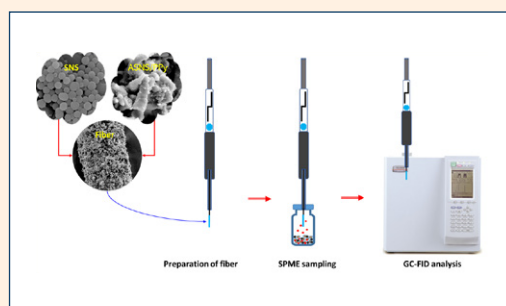
Leman Alkan



322–330 Analytical chemistry

In-Situ Intercalating of Silica Nanospheres into Polypyrrole During Its Electropolymerization to Prepare a Sorbent for Headspace Microextraction of Aldehydes in Edible Oils

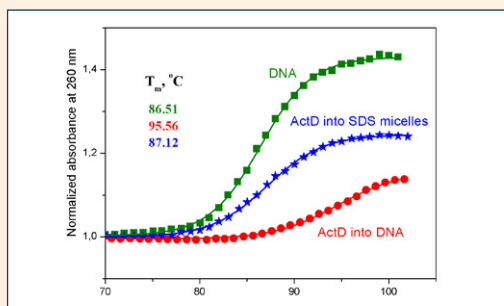
Amin Hamdi, Kolsoum Dalvand, Alireza Ghiasvand and Nahid Heidari



331–335 Physical chemistry

Effect of SDS Micelles on Actinomycin D – DNA Complexes

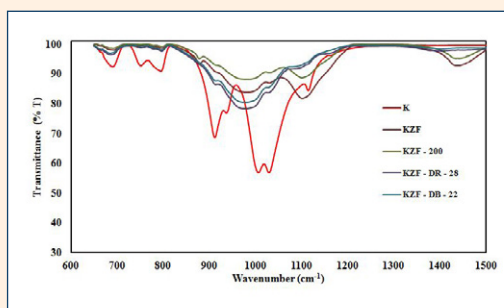
Ana Maria Toader, Izabella Dascalu and Mirela Enache



336–348 Chemical, biochemical and environmental engineering

Removal of Diazo Dye Direct Red 28 and Tetra Azo Dye Direct Black 22 Using Synthesized Magnetic Kaolin Supported Zinc Ferrite

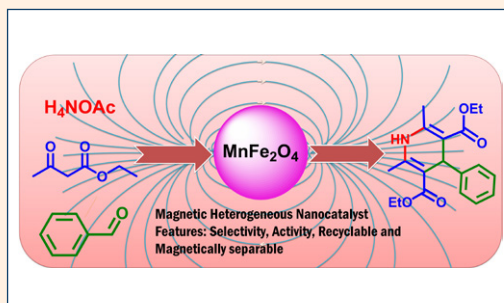
Serap Findik



349–358 Organic chemistry

Efficient One-Pot Synthesis of 1,4-Dihydropyridines Catalyzed by Magnetic MnFe_2O_4 Nanoparticles

Somayeh Moradi, Mohsen Moradian and Hossein Naeimi



359–370 Chemical education

Opportunities for Learning: Analysis of Czech Lower-Secondary Chemistry Textbook Tasks

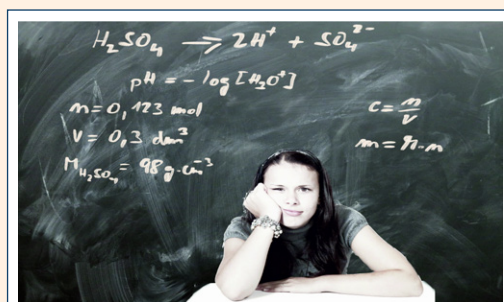
Karel Vojíř and Martin Rusek



371–377 Chemical education

To What Extent do Freshmen University Chemistry Students Master Chemistry Calculations?

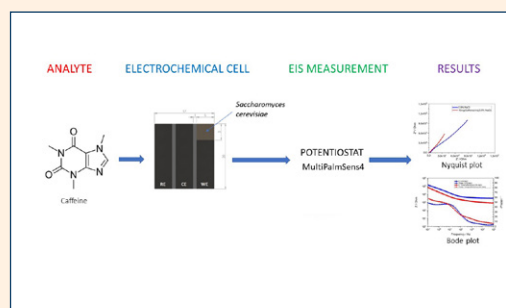
Martin Rusek, Karel Vojíř, Iveta Bártová, Marta Klečková, Vladimír Sirotek and Jitka Štrofová



378–384 Physical chemistry

The Use of Yeast *Saccharomyces Cerevisiae* as a Biorecognition element in the Development of a Model Impedimetric Biosensor for Caffeine Detection

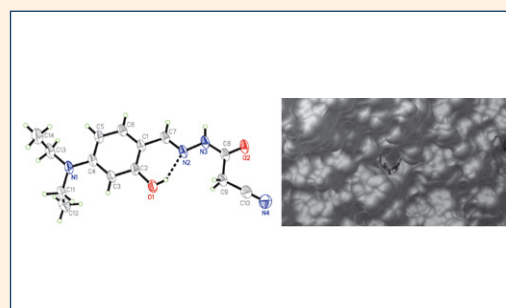
Zala Štukovnik, Regina Fuchs Godec and Urban Bren



385–392 Organic chemistry

Synthesis, Biological Evaluation, and Molecular Docking Studies of Hydrazones as Novel Xanthine Oxidase Inhibitors

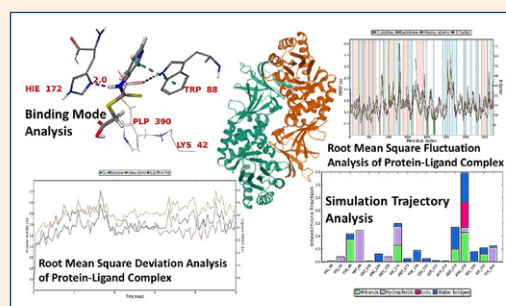
Ling-Wei Xue, Shi-Tong Li, Yong-Jun Han and Xiao-Qiang Luo



393–404 Chemical, biochemical and environmental engineering

Computational Molecular Modeling Studies of Some *Mycobacterium Tuberculosis* Alanine Racemase Inhibitors

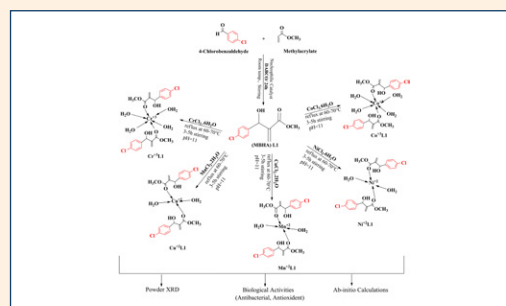
Unni Jayaram and Mohammed Afzal Azam



405–418 Inorganic chemistry

Synthesis, Characterization, Biological Activities and Ab-initio Study of Transition Metal Complexes of [Methyl 2-((4-chlorophenyl)(hydroxy)methyl) Acrylate]

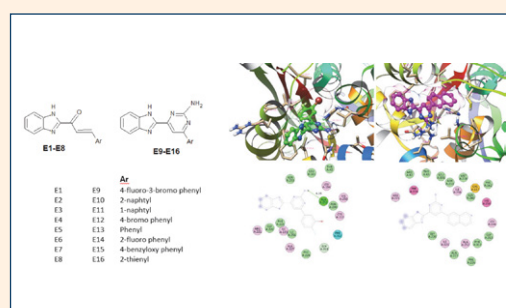
Shazia Ishfaq, Shazia Nisar, Saqib Ali, Sadaf Iqbal, Saima Imad, Samina Iqbal, Saeeda Bano, Syeda Kanwal Zahid, Nasreen Fatima and Muhammad Shahzaman



419–429 Organic chemistry

Novel Benzimidazole-Based Compounds as Antimicrobials: Synthesis, Molecular Docking, Molecular Dynamics and *in silico* ADME Profile Studies

Elif Yeşilçayır, İsmail Çelik, Hasan Tahsin Şen, Suna Sibel Gürpınar, Müjde Eryılmaz, Gülgün Ayhan-Kılıçgil



430–436 Chemical, biochemical and environmental engineering

Effects of Extraction Period on Bioactive Compounds Extracted from *Olea Europaea* (var. Domat) Leaves by Ultrasound-Assisted Extraction

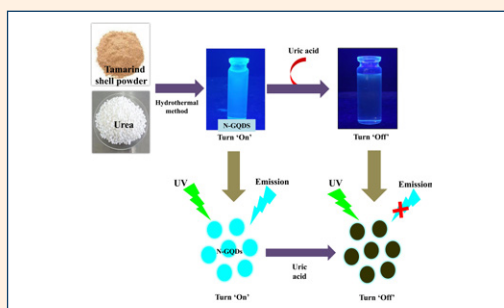
Dua Danjolli-Hashani and Şebnem Selen-Işbilir



437–447 Analytical chemistry

Design of “Turn-Off” Fluorescent Nanoprobe for Highly Sensitive Detection of Uric Acid using Green Synthesized Nitrogen-Doped Graphene Quantum Dots

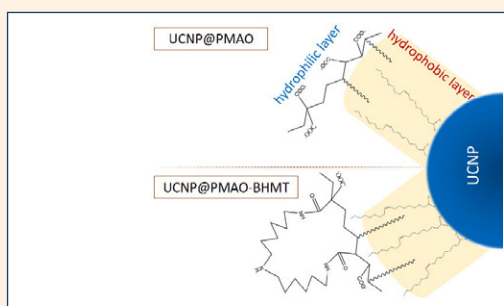
Sopan Nangare, Shweta Baviskar, Ashwini Patil and Pravin Patil



448–457 Materials science

Optimisation of Amphiphilic-Polymer Coatings for Improved Chemical Stability of NaYF₄-based Upconverting Nanoparticles

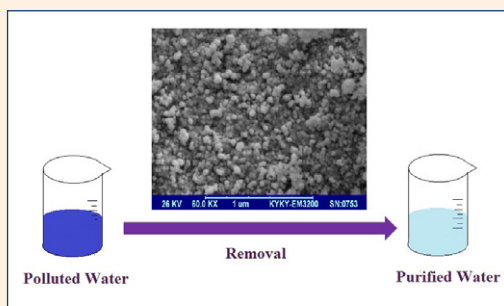
Tina Černič, Monika Koren, Boris Majaron, Maja Ponikvar-Svet and Darja Lisjak



458–465 Chemical, biochemical and environmental engineering

Adsorption Properties of Low-Cost Synthesized Nanozeolite L for Efficient Removal of Toxic Methylene Blue Dye from Aqueous Solution

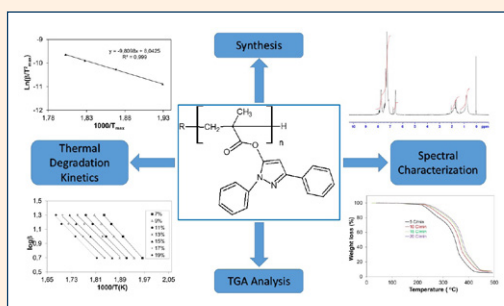
Neda Salek Gilani, Salma Ehsani Tilami and Seyed Naser Azizi



466–477 Materials science

Synthesis, Characterization and Thermal Degradation Kinetics of a New Pyrazole Derived Methacrylate Polymer, Poly(1,3-Diphenyl-1H-Pyrazol-5-Yl Methacrylate)

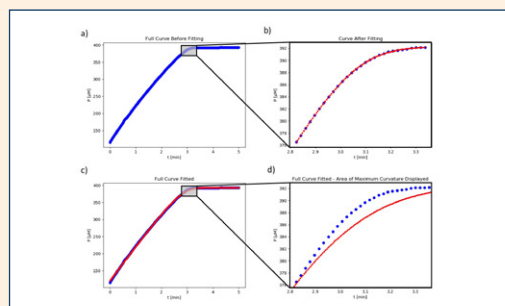
Adnan Kurt and Murat Koca



478–482 Biochemistry and molecular biology

iFIT: An Automated Web Tool for Determining Enzyme-kinetic Parameters Based on the High-curvature Region of Progress Curves

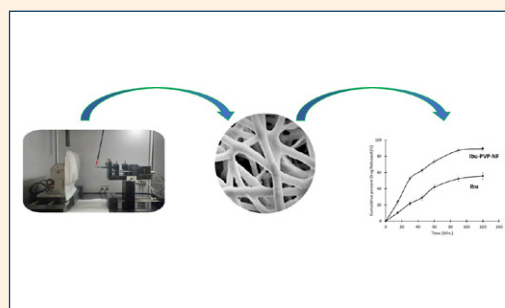
Boštjan Petrič, Marko Goličnik and Aljoša Bavec



483–488 Biomedical applications

Ibuprofen Loaded Electrospun Polymeric Nanofibers: A Strategy to Improve Oral Absorption

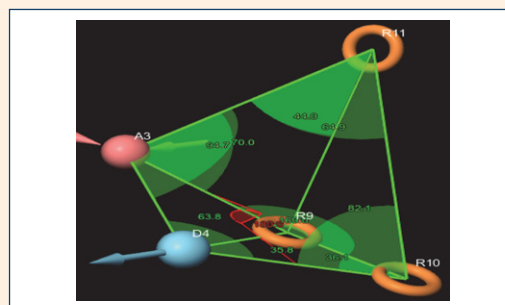
Dibya Sundar Panda, Nabil K. Alruwaili, Kalpana Swain and Satyanarayan Pattnaik



489–506 Chemical, biochemical and environmental engineering

Combined Pharmacophore Modeling, 3D-QSAR, Molecular Docking and Molecular Dynamics Study on Indolyl-aryl-sulfone Derivatives as New HIV1 Inhibitors

Mebarka Ouassaf, Faizan Abul Qais, Salah Belaidi, Mohamed Bakhouch, Ahmed Said Mohamed and Samir Chtita



Feature article

Soft Poly(*N*-vinylcaprolactam) Based Aqueous Particles

Joonas Siirilä and Heikki Tenhu

Department of Chemistry, University of Helsinki, Finland

* Corresponding author: E-mail: joonas.jukonen@helsinki.fi
heikki.tenhu@helsinki.fi

Received: 05-25-2022

Abstract

Soft nanoparticles are an important class of material with potential to be used as carriers of active compounds. Swollen, penetrable particles can act as a host for the active ingredients and provide stability, stimuli-responsiveness and recyclability for the guest. Thermoresponsive colloidal gel particles are especially attractive for such applications due to the extremely soft structure, size and responsiveness. Poly(*N*-vinylcaprolactam) (PNVCL) is a much studied, popular thermoresponsive polymer. The polymer has low toxicity and the phase transition temperature is close to body temperature. During the phase transition, the polymer becomes less soluble, the particle expels a large part of water and the particle collapses to a more compact form. The diffusion of material in and from the particles is largely affected by this transition. As the solubility of the polymer changes, so do the interactions with the loaded compound. This feature article focuses on the synthetic methods, properties and applications of soft PNVCL particles.

Keywords: Microgel; nanogel; synthesis; responsive; poly(*N*-vinyl caprolactam)

1. Introduction

There is a need for aqueous carriers of active compounds as a large portion of drugs is insoluble in water, a solvent which is the basis of biological fluids.¹ Especially for cancer drugs, there is a need to deliver the drug to target site in a way that suppresses the toxicity on healthy cells and also suppresses side-effects.^{2–4} In these applications the particles are used to mask the toxicity of the drug during the transport and to release it at a target site. Water is also an important environmentally benign solvent for chemical transformations, but many catalysts and reagents need to be stabilized in water either to increase their availability and reactivity or to protect them from degradation. Soft (deformable) nanoparticles may help in compatibilization of the reagents and catalysts and act as nanoreactors. The particles may also help in separation of the catalyst from the product. Typical catalysts include both enzymes⁵ and metal nanoparticles.^{6,7}

From the different options available; self-assemblies of amphiphilic polymers, mesoporous silica particles, latex particles and such, micro- and nanogel particles are unique due to their dualistic nature between a branched soluble polymer and a crosslinked dispersed insoluble polymer particle^{8–12} These, 1 nm to few μm sized polymer particles are robust, swollen with water and extremely soft / deform-

able. The deformability has been recognized as an important factor in determining the fate of carriers in human body as softer particles exhibit longer circulation times due to smaller response to the body immune system and due to being able to deform and pass through membranes.^{13–15}

Especially interesting soft nanoparticles are the stimuli responsive microgel particles as the responsiveness can be utilized to control the diffusion of material in and out from the particles¹⁶ and in separation of the particles from a dispersion. Stimuli can also be used to change the conformation of the polymers in the particle to reveal active binding sites.¹⁷ Responsiveness is typically caused by the changed solubility of the sub-chains of the particle in response to a stimulus. Typical stimuli include pH, light and temperature.

There are for example applications where the catalytic activity of a loaded catalyst is controlled by the swelling degree of the polymer particle.¹⁸ On the other hand, many microgel particles have also been reported to possess surface active properties and been used to stabilize emulsions.^{5,19–22} There is then a possibility to use these microgel particles as emulsifiers, which gives interesting possibilities when accompanied with a loaded catalyst for the catalysis at interphases.^{23–25}

Poly(*N*-vinyl caprolactam), PNVCL, is a popular polymer in general and also as a basis of responsive micro-

gel particles. The main reasons are the low toxicity, thermoresponsiveness at moderate temperatures and the compatibility with a great variety of polar and non-polar compounds. PNVCCL has been used in cosmetic products,²⁶ protein affinity columns,²⁷ and as a kinetic hydrate growth inhibitor in oil industry²⁸. The polymer is made via radical polymerization of *N*-vinylcaprolactam (NVCL; Figure 1). The monomer is synthesized from acetylene and caprolactam, which is a monomer mainly used for the synthesis of Nylon-6.²⁹ Recently, a company named Genomatica announced it had synthesized a precursor for caprolactam in a 1 metric ton scale by fermentation from renewable resource.³⁰ An excellent and comprehensive review exists about PNVCCL.³¹ Biomedical applications of the polymer are becoming increasingly important and have been the subject of two recent review articles.^{32,33}

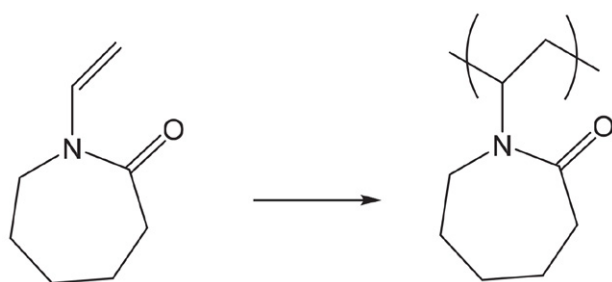


Figure 1. Synthesis of poly(*N*-vinyl caprolactam)

1. 1. Thermoresponsiveness

The phase transition temperature of PNVCCL depends on both the concentration and the molar mass of the polymer.³⁴ Increasing either of these will result in lowering the transition temperature. Similarly, added electrolytes or cosolvents will shift the transition temperature to a degree determined by the choice of the additive.^{27, 35–38} Commonly, the phase transition temperature is given as a cloud point, which is the temperature where a solution turns turbid as the polymer becomes less soluble and aggregates. Depending on the concentration the aggregation may result in monodisperse spherical aggregates referred to as mesoglobules or in a macroscopic phase separation.³⁸ Even though a single temperature value, i.e. the cloud point, is often used to describe the phase transition, high sensitivity DSC measurements and IR measurements have revealed that the phase transition process is gradual and happens within a relatively broad temperature range.^{39,40} According to the DSC measurements, the released heat per NVCL unit is in the range of 4–5 kJ/mol.³⁹ The transition has been studied using several methods. In a work by Speváček et al. NMR, IR and SAXS data combined with quantum chemical calculation elucidated the molecular basis of the transition.⁴¹ Below the transition temperature the polymer is well solvated due to extensive hydrogen

bonding. Every PNVCCL carbonyl binds on average two water hydrogens. During the phase transition the extent of this hydrogen bonding decreases, non-directly bound water is expelled and after the transition PNVCCL oxygen binds only one hydrogen. It is important to notice that the polymer is still hydrated, but to a lesser degree.

For a microgel particle, the phase transition temperature is often referred to as a volume phase transition temperature. The covalently crosslinked particles exhibit similar partial dehydration as the linear counterparts during heating, but instead of forming aggregates the particles shrink as water diffuses out from the gel network. Dynamic light scattering is the most utilized tool for analysing the transition. The degree of crosslinking is very important in determining the stability of the particles during heating. When the crosslinking degree is low, the microgels tend to aggregate similarly as the linear polymer.⁴² It is fascinating, how the prepacking to particles results in stability. Other tools used for analysing the transition are NMR, SANS, and DSC that directly monitor the transition. Various release tests analyse the effect of the transition on the loaded compounds; fluorescence probes and model drugs have been used in release analysis. There are also examples of responsive microgels with interacting moieties which allow temperature-switchable binding and release of proteins and bacteria.¹⁷

Copolymerization can be used to tailor the transition temperature of the PNVCCL containing copolymer.⁴³ Statistical copolymers of PNVCCL with a more hydrophobic comonomer, such as vinyl acetate exhibit lower phase transition temperature compared to the PNVCCL homopolymer with similar molecular weight. Vice versa, copolymers with a more hydrophilic comonomer, such as *N*-methyl-*N*-vinylacetamide, exhibit higher phase transition temperature compared to PNVCCL homopolymer. Distribution of repeating units in the copolymer has also a decisive role in determining the degree to which the incorporated comonomer affects the thermal behaviour. Therefore, it is possible to synthesize block copolymers with PNVCCL block and another thermoresponsive block, which exhibit two distinct phase transition temperatures, whereas a copolymer with more randomly distributed repeating units along the chain would exhibit only one transition.

In nano/microgels, the responsiveness is also often altered with comonomers, and comonomers are used to alter the stability of the dispersions.^{42–52} Acidic and basic comonomers affect the swelling degree depending on the pH.^{44,47,51,52} Crosslinking degree was already mentioned to have a huge impact on the gels. However, there are also several examples of gel particles with different sensitive cleavable crosslinkers, including pH, oxidation/reduction, enzymatically degradable and mechanoresponsive ones.^{42,48,55–57} The transformations induced by cleaving the crosslinks are generally not recoverable unlike the thermosensitivity derived from the responsive polymer.

1. 2. Utilization of the Thermoresponsiveness

During the thermal transition, interactions between the dispersing medium and the polymer PNVCCL change. This affects also the interactions between the polymer particle and the loaded content.^{45,49,58,59} The diffusion into and out of the particle is reduced above the phase transition temperature as the polymer collapses and forms a barrier.

Thermoresponsive nanoparticles, including PNVCCL particles, have been widely studied as drug delivery systems.^{45,48,49,51,58} The release from the particles is often diffusion controlled.¹⁶ The thermoresponsiveness is utilized to obtain a fast and efficient loading at lower temperatures and a sustained release at higher temperatures. The sustained release is important for the particle to reach its target prior to release. Specific interactions may be created by incorporating comonomers, often charged ones, to the particles. Acidic or basic units can provide a means for pH specific release.⁵³ Since the diffusion into and out of the particle depends on the swelling degree, accessibility and thus the activity of a loaded catalyst may be controlled with the swelling degree.^{18,60} Yang *et al.* have reported silver nanoparticle loaded poly(*N*-acryloylglycinamide) microgels with temperature on/off switchable catalytic activity. The reagents were able to reach the catalytic site only in the swollen state of the microgels. Similarly, functional groups in the gel structure may be available only in the collapsed state.¹⁷ Paul *et al.* have synthesized poly(*N*-isopropyl acrylamide) based microgels with a carbohydrate based comonomer. A protein *i.e.* lectin, and *E. coli* bacteria were shown to bind to the microgel particles at elevated temperatures, when the microgel was at the collapsed state and carbohydrate moieties were enriched on the particle outer layers.

Soft microgel particles have also been studied as stabilizers of emulsions, and in these cases the thermal collapse of the polymer changes the colloidal stability of the microgel and results in destabilization of the emulsion.^{5,19–21,23} There is potential in thermoresponsive soft nanoparticles in the above listed applications. However, so far the thermoresponsiveness of poly(*N*-vinylcaprolactam) has been utilized only in the loading and release of active ingredients, as far as authors are aware.

1. 3. Synthesis of Soft PNVCCL-Based Particles

Soft PNVCCL polymer particles can be synthesized from a preformed polymer using self-assembly or from the monomer by means of polymerization, either emulsion or precipitation polymerizations. Also, “from top to bottom” approach has been reported, where microgel particles were prepared by grinding a macro hydrogel down to microgels.

1. 4. Synthesis by Self-Assembly

PNVCCL homopolymer may form stable self-assembled aggregates in aqueous solutions upon heating above the thermal transition temperature under dilute condi-

tions. The particle size and size distribution depends on the molecular weight and concentration of the polymer and on the heating program.^{39,61,62} The self-assembled structures are stable for days, even months, and the self-assembly process can be used to capture material inside the particles. The particles are dynamic in their nature, stable against dilution, but disassemble by lowering the temperature. However, hydrogen bonding with phenols may be used to make the particles to withstand cooling.^{61,63} Similarly, PNVCCL-block copolymers can form assemblies upon heating and can be stabilized against heat induced disassembly.^{64,65}

In addition to thermoprecipitation, PNVCCL block copolymers form assemblies as any amphiphilic block copolymer. In these assemblies PNVCCL can be either one, the solvophobic or solvophilic block depending on the other block and on the conditions. PNVCCL-PEG copolymer particles have been formed for example both with thermoprecipitation⁶¹ and with solvent-exchange from DMF to H₂O (37 °C).⁶⁶ Additionally, PNVCCL block copolymers have been self-assembled using nanoprecipitation and by film-dehydration followed by membrane extrusion.⁶⁷

PNVCCL has also been assembled with silk fibroin using the layer-by-layer method to form multilayers on silica particles. Hydrophobic interactions and hydrogen bonding are responsible for the interactions between silk fibroin and PNVCCL.⁶⁸ The use of the self-assemblies of PNVCCL copolymers in biomedical applications has recently been reviewed.⁶⁹

2. Synthesis by the Means of Polymerization

2. 1. Precipitation Polymerization

Precipitation polymerization is a type of free radical polymerization that is used to make particles, especially colloidal gels. In the polymerization the monomer is soluble in the solvent, but the formed polymer is not and as a result, the polymer will precipitate during the polymerization. When synthesising a thermoresponsive polymer, the synthesis temperature is selected such that the formed polymer is insoluble. Surfactants are often used in the synthesis to guide the polymer to precipitate into well-defined, similar sized aggregates, which keep dispersed in the reaction mixture. When synthesizing colloidal gel particles, multiple polymerizable bonds containing comonomers *i.e.* crosslinkers, are used. Then the polymer particles/aggregates formed during the synthesis become permanent polymer networks that do not break even upon improving the solvent quality. Synthesis of colloidal PNVCCL hydrogels has been well studied and various comonomers have been incorporated to the particles during the polymerizations.^{44–52,70–77}

Typically, precipitation polymerizations have been performed as batch polymerizations, meaning that all

monomers are present from the start. In batch polymerizations, the reactivity difference between monomers can lead to a composition gradient in the particle structure as the more reactive monomer is incorporated first.^{52,71,72,75} For this reason, PNVCCL colloidal gels usually have a more crosslinked core and dangling chains on the surface, as the crosslinker, which is the more reactive monomer, has polymerized first.^{72,75} Continuous and semi-continuous addition of monomers can be used to control the spatial arrangement of the monomers in the gel particles. Imaz *et al.* and Willems *et al.* have reported synthesis of homogeneously crosslinked hydrogel particles with continued feed of the crosslinking monomer during the polymerization.^{52,72} Temperature ramp and continuous feed have also been used to synthesize large 1 to 5 μm sized particles.⁷⁸ Precipitation polymerization has also been performed without surfactants in an inject printer, where high shear forces and pressures have resulted in small stable particles (50 nm).⁷⁹ Precipitation polymerization in a continuous flow reactor has been reported as well.⁸⁰

Precipitation polymerization can also be used to polymerize a PNVCCL shell on a pre-existing particle or on a sacrificial template such as a dimethyldiethoxysilane droplet.⁸¹ Removal of the sacrificial template will produce particles with inner lumen, *i.e.* capsules.

2. 2. Emulsion Polymerization

Emulsion polymerization is "polymerization whereby monomer(s), initiator, dispersion medium, and possibly colloid stabilizer constitute initially an inhomogeneous system resulting in particles of colloidal dimensions containing the formed polymer", according to the IUPAC definition.⁸²

The typical precipitation polymerization of NVCL in water is sometimes referred to as an emulsion polymerization. However, in this text the term precipitation polymer-

ization is used for the aqueous polymerizations of NVCL, which are performed above the phase transition temperature of PNVCCL, and where the starting NVCL concentration (0.5–3 wt% monomer with respect to H_2O) is close to the solubility limit of NVCL. Most of the PNVCCL particle synthesis are precipitation polymerizations. The use of larger concentrations of NVCL has been reported to lead to colloidal instability and to the formation of coagulum during the polymerization.⁷²

In addition to precipitation polymerizations in water, PNVCCL particles have also been synthesized with miniemulsion^{83,84} and inverse miniemulsion polymerizations.^{85,86} In miniemulsion and in inverse miniemulsion polymerizations, the initial polymerization mixture consists of evenly sized droplets dispersed in a continuous phase, and these droplets act as the loci of the polymerization and in the end turn in to polymer particles (Figure 2).^{87,88} In contrast, in (macro)emulsion polymerization the picture is more complex. The starting mixture typically contains small surfactant micelles and large monomers droplets. There is a need for mass transportation from the monomer droplet to the growing particles during the polymerization. This can cause problems, including macro phase separation and formation of coagulum, when the formulation contains very solvophobic components with limited ability to migrate in the continuous phase. With these formulations, to avoid phase separation and instability, it is beneficial to choose the miniemulsion polymerization method, where transportation from monomer droplets to growing particles does not happen. Suitable conditions for miniemulsion are achieved by choosing correct surfactant and by using an intensive premixing process to create evenly sized small droplets before the polymerization. Additionally, the dispersed droplets often need to be stabilized against Ostwald ripening with a costabilizer, which is a compound that is very insoluble in the continuous phase, but soluble in the monomer phase.

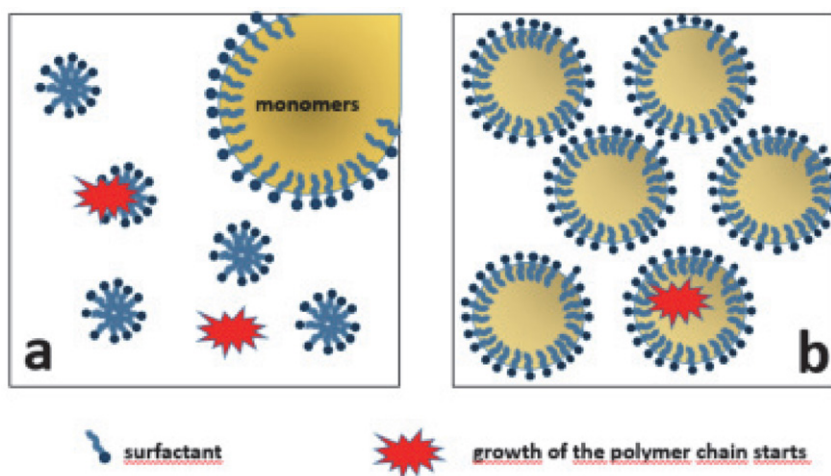


Figure 2. In emulsion polymerization (a) the polymer chains start to grow either in the surfactant micelles or in the continuous phase, whereas in miniemulsions (b) the chains grow in surfactant stabilized monomer droplets.

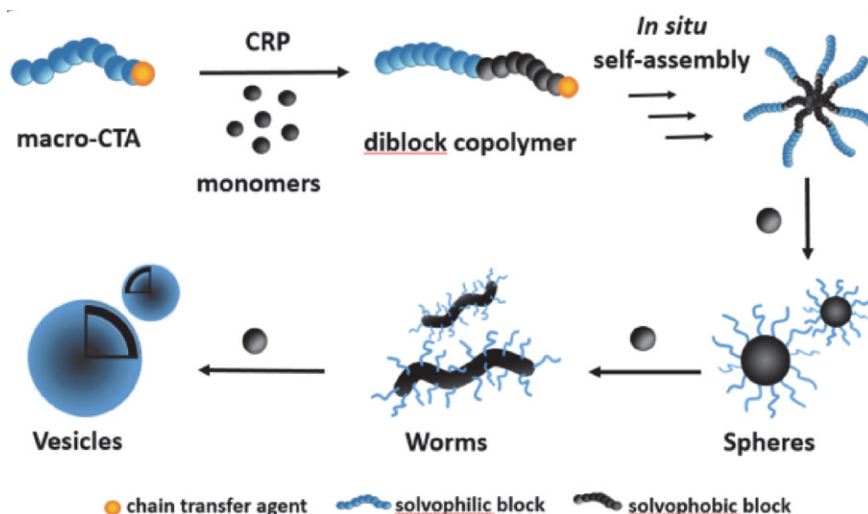


Figure 3. Polymerization induced self-assembly in water (drawn by Vikram Baddam)

In inverse miniemulsion polymerizations, the dispersed droplets consist of a polar solvent (usually water) and the monomer, and the continuous phase is non-polar. This method is suitable for the synthesis of water-soluble polymers. When the polymerization takes place in the droplet phase instead of the continuous water phase, polymer particles are formed instead of a macrogel. Effective incorporation of water-soluble compounds to the formed PNVCCL colloidal gel particles could be a reason to use this synthesis method.

In miniemulsion polymerization, the dispersed phase is organic and contains the monomer, and the continuous phase is aqueous. The method has been used for the synthesis of PNVCCL particles with high monomer concentrations (up to 16 wt% with respect to H₂O)^{83,84} and to synthesize PNVCCL particles with a water insoluble comonomer,⁸⁹ which can be difficult with precipitation polymerization. The miniemulsion polymerization often demands the use of an additional hydrophobe (costabilizer) such as hexadecane and possibly the use of a cosolvent for the formation of the dispersed phase. The additives can result in a need of extensive purification steps. There are however, reports of miniemulsion-like polymerization of NVCL without any cosolvent or costabilizers,^{89,90} with CTAB as the stabilizer and with starting NVLC concentration <1.4 wt% performed after homogenization with a microfluidizer (at least 1100 bars and 8 cycles). The polymerization conditions are almost identical to those used in the precipitation polymerizations, except for the homogenization process. NVCL is soluble in water at the used concentration, however relatively stable (at least for 250 min) monomer/surfactant droplets were observed with dynamic light scattering prior to addition of the initiator. This was because of the slowness of the dissolution of NVCL in water. This raises a question about the homogeneity of the starting situation in the precipitation polymerizations and on the correctness of the use of the term. In studies on the

precipitation polymerization of NVCL, the starting mixture has seldom been investigated to verify the homogeneity.

2. 3. Polymerization Induced Self-Assembly

Polymerization induced self-assembly (PISA) is a type of controlled polymerization, where a solvophilic polymer is chain extended with a solvophobic block (Figure 3).^{91,92} During the polymerization the growth of the solvophobic block causes the polymer to self-assemble. The polymerizations are most often reversible addition-fragmentation chain transfer (RAFT) polymerizations, where a solvophilic macromolecule with a chain transfer agent (CTA) as an end group, *i.e.* macromolecular CTA (macroCTA), is used to control the polymerization and as the soluble block in the forming copolymer. This is also a synthetic route to obtain polymer particles. These particles are not polymer networks but amphiphilic self-assemblies consisting of block copolymers with narrow molecular weight distributions. Usually, no surfactant is needed in addition to the soluble polymer whose chain is to be extended. Another appealing aspect of the polymerization is the possibility to obtain different well-defined morphologies by changing the block length ratio and concentration of the polymerization. Typically, high monomer concentrations (10 to 30 wt%) can and are used in the PISA polymerizations.

Recently, the first example of PISA of NVCL as the sole monomer was reported.⁶⁵ Prior work has shown how a partial utilization of the PISA concept can also be beneficial compared to the precipitation/emulsion free radical polymerizations. Etchenausia *et al.* have synthesized cationic hydrogel particles by polymerizing NVCL in water above the phase transition temperature of PNVCCL with crosslinker and a cationic macroCTA.⁹³ Using a crosslinker in a batch polymerization makes it unlikely to obtain a controlled po-

lymerization and hence the polymerization induced self-assembly. However, the synthetic approach proved to be suitable for the production of colloidal hydrogel particles at high monomer concentrations (up to 10 wt% in respect to mass of H₂O) compared to a free radical precipitation polymerization counterpart (no CTA, just surfactants). The macroCTA group reacted during polymerization and conferred unanticipated stability to the system against coagulation. The same group also performed aqueous PISA copolymerization of NVCL and vinylacetate with a PEG based macroCTA.⁹⁴ Control over molecular mass was limited and only few polymerizations were made, but the resultant material was interesting as the formed polymers resembled by composition Soluplus⁹⁵ (a commercial PNVCL containing polymer in clinical trials). No crosslinker was used as the hydrophobic comonomer prevented the dissolution of the formed assembly upon cooling if used in sufficiently high amounts (47 mol% of monomers in feed).

3. Comparison of the Synthesis Methods

Tabela 1. Various selected aspects of synthesis methods of PNVCL particles

Method	Concentration ^a	Suitable for	Surfactant ^b	REF.
Self-assembly	≤ 0.2 wt%	homo- and copolymers	not used	37,59,60,62,65,66
Precipitation polymerization	0.5–3 wt%	homo- and copolymers	0–8 wt%, or surfactant-type comonomer (2 – 50 wt%)	42–44, 46–50, 57,68–78,94
Miniemulsion polymerization	≤ 16 wt%	homo- and copolymers	0.4–2 wt% + possibly an additional costabilizer	81,82,87,88
Inverse miniemulsion polymerization	≤ 5 wt%	homo- and copolymers	100 wt%	84
PISA	1–30 wt%	copolymers	macroCTA	63,91,92

a) monomers with respect to the weight of solvents plus continuous phase

b) wt% given in respect to monomer weight

Various aspects of the different synthesis methods to obtain soft PNVCL nanoparticles are presented in Table 1, to allow convenient comparison between them.

4. Conclusions and Future

The PNVCL particles are widely utilized as active ingredient carriers and emulsion stabilizers. PNVCL provides a thermoresponsive matrix for hosting the guest. The polymer is ideal for this purpose due to its non-toxicity and compatibility with a broad variety of compounds. Solventphobicity is an efficient driving force in loading of the particles. The particles themselves can act as nanoreactors and the temperature-dependent conformation controls the accessibility of reagents inside the particles and diffusion of material into and from the particle. Together with the surface active properties, this offers opportunities for

interfacial reactions.

Current trend is to add functionality to the microgels for more specific tasks, and for more accurate delivery and release of the active ingredient. Similarly, more sophisticated architectures such as vesicular particles with drug loaded to the inner lumen surrounded by a membrane with temperature dependent permeability,⁶⁷ degradable crosslinks for triggered release,^{64,81} and core-shell particles with pH dependent accelerated release of proteins⁵³ are promising.

There is also a report of PNVCL gel particles showing antiviral activity against HIV-virus.⁷⁷ Additionally, soft particles may be found in future in various scavenging applications including temperature dependent interactions with bacteria¹⁷ or removing small amounts of oil from water²². New innovative applications keep appearing. As the synthesis methods develop and are getting industrially applicable, we see a great potential for soft PNVCL particles.

Acknowledgement

We thank Vikram Baddam for Figure 3.

5. References

- Merisko-Liversidge, E. M.; Liversidge, G. G. Drug nanoparticles: formulating poorly water-soluble compounds. *Toxicol. Pathol.* **2008**, *36*, 43–48. DOI:10.1177/0192623307310946
- Rosenblum, D.; Joshi, N.; Tao, W.; Karp, J. M.; Peer, D. Progress and challenges towards targeted delivery of cancer therapeutics. *Nat. Commun.* **2018**, *9*, 1410. DOI:10.1038/s41467-018-03705-y
- Shi, J.; Kantoff, P. W.; Wooster, R.; Farokhzad, O. C. Cancer nanomedicine: progress, challenges and opportunities. *Nat. Rev. Cancer* **2016**, *17*, 20. DOI:10.1038/nrc.2016.108
- Wilhelm, S.; Tavares, A. J.; Dai, Q.; Ohta, S.; Audet, J.; Dvorak, H. F.; Chan, W. C. W. Analysis of nanoparticle delivery to tumours. *Nat. Rev. Mater.* **2016**, *1*, 16014. DOI:10.1038/natrevmats.2016.14
- Jiang, H.; Liu, L.; Li, Y.; Yin, S.; Ngai, T. Inverse Pickering Emulsion Stabilized by Binary Particles with Contrasting Characteristics and Functionality for Interfacial Biocatalysis.

- ACS Appl. Mater. Interfaces* **2020**, *12*, 4989–4997.
DOI:10.1021/acsami.9b16117
6. Roa, R.; Stefano Angioletti-Uberti; Lu, Y.; Dzubiella, J.; Piazza, F.; Ballauff, M. Catalysis by Metallic Nanoparticles in Solution: Thermosensitive Microgels as Nanoreactors. *Zeitschrift für Physikalische Chemie* **2018**, *232*, 773–803.
DOI:10.1515/zpch-2017-1078
7. Shifrina, Z. B.; Matveeva, V. G.; Bronstein, L. M. Role of Polymer Structures in Catalysis by Transition Metal and Metal Oxide Nanoparticle Composites. *Chem. Rev.* **2020**, *120*, 1350–1396. DOI:10.1021/acs.chemrev.9b00137
8. Callejas-Fernández, J.; Estelrich, J.; Quesada-Pérez, M.; Forcada, J., Eds.; In *Soft nanoparticles for biomedical applications*; RSC nanoscience & nanotechnology; Royal Soc. of Chemistry: Cambridge, 2014; Vol. 34. DOI:10.1039/9781782625216
9. Pelaz, B.; Alexiou, C.; Alvarez-Puebla, R. A.; Alves, F.; Andrews, A. M.; Ashraf, S.; Balogh, L. P.; Ballerini, L.; Bestetti, A.; Brendel, C.; Bosi, S.; Carril, M.; Chan, W. C. W.; Chen, C.; Chen, X.; Chen, X.; Cheng, Z.; Cui, D.; Du, J.; Dullin, C.; Escudero, A.; Feliu, N.; Gao, M.; George, M.; Gogotsi, Y.; Grüneweller, A.; Gu, Z.; Halas, N. J.; Hampp, N.; Hartmann, R. K.; Hersam, M. C.; Hunziker, P.; Jian, J.; Jiang, X.; Jungebluth, P.; Kadhiresan, P.; Kataoka, K.; Khademhosseini, A.; Kopeček, J.; Kotov, N. A.; Krug, H. F.; Lee, D. S.; Lehr, C.; Leong, K. W.; Liang, X.; Ling Lim, M.; Liz-Marzán, L. M.; Ma, X.; Macchiarini, P.; Meng, H.; Möhwald, H.; Mulvaney, P.; Nel, A. E.; Nie, S.; Nordlander, P.; Okano, T.; Oliveira, J.; Park, T. H.; Penner, R. M.; Prato, M.; Puntès, V.; Rotello, V. M.; Samarakoon, A.; Schaak, R. E.; Shen, Y.; Sjöqvist, S.; Skirtach, A. G.; Soliman, M. G.; Stevens, M. M.; Sung, H.; Tang, B. Z.; Tietze, R.; Udugama, B. N.; VanEpps, J. S.; Weil, T.; Weiss, P. S.; Willner, I.; Wu, Y.; Yang, L.; Yue, Z.; Zhang, Q.; Zhang, Q.; Zhang, X.; Zhao, Y.; Zhou, X.; Parak, W. J. Diverse Applications of Nanomedicine. *ACS Nano* **2017**, *11*, 2313–2381.
DOI:10.1021/acs.nano.6b06040
10. Plamper, F. A.; Richtering, W. Functional Microgels and Microgel Systems. *Acc. Chem. Res.* **2017**, *50*, 131–140.
DOI:10.1021/acs.accounts.6b00544
11. Agrawal, G.; Agrawal, R. Functional Microgels: Recent Advances in Their Biomedical Applications. *Small* **2018**, *14*, e1801724-n/a. DOI:10.1002/smll.201801724
12. Karg, M.; Pich, A.; Hellweg, T.; Hoare, T.; Lyon, L. A.; Crasous, J. J.; Suzuki, D.; Gumerov, R. A.; Schneider, S.; Potemkin, I. I.; Richtering, W. Nanogels and microgels: From model colloids to applications, recent developments and future trends. *Langmuir* **2019**, *35*, 6231–6255.
DOI:10.1021/acs.langmuir.8b04304
13. Hui, Y.; Yi, X.; Hou, F.; Wibowo, D.; Zhang, F.; Zhao, D.; Gao, H.; Zhao, C. Role of Nanoparticle Mechanical Properties in Cancer Drug Delivery. *ACS nano* **2019**, *13*, 7410–7424.
DOI:10.1021/acs.nano.9b03924
14. Anselmo, A. C.; Zhang, M.; Kumar, S.; Vogus, D. R.; Mengatti, S.; Helgeson, M. E.; Mitragotri, S. Elasticity of Nanoparticles Influences Their Blood Circulation, Phagocytosis, Endocytosis, and Targeting. *ACS Nano* **2015**, *9*, 3169–3177.
DOI:10.1021/acs.nano.5b00147
15. Zhang, L.; Cao, Z.; Li, Y.; Ella-Menye, J.; Bai, T.; Jiang, S. Soft-zwitterionic Nanogels for Longer Circulation and Lower Splenic Accumulation. *ACS Nano* **2012**, *6*, 6681–6686.
DOI:10.1021/nn301159a
16. Klinger, D.; Landfester, K. Stimuli-responsive microgels for the loading and release of functional compounds: Fundamental concepts and applications. *Polymer* **2012**, *53*, 5209–5231.
DOI:10.1016/j.polymer.2012.08.053
17. Paul, T. J.; Rübél, S.; Hildebrandt, M.; Strzelczyk, A. K.; Spormann, C.; Lindhorst, T. K.; Schmidt, S. Thermosensitive Display of Carbohydrate Ligands on Microgels for Switchable Binding of Proteins and Bacteria. *ACS Appl. Mater. Interfaces* **2019**, *11*, 26674–26683. DOI:10.1021/acsami.9b08537
18. Yang, D.; Viitasuo, M.; Pooch, F.; Tenhu, H.; Hietala, S. Poly(N-acryloylglycinamide) microgels as nanocatalyst platform. *Polym. Chem.* **2018**, *9*, 517–524.
DOI:10.1039/C7PY01950E
19. Richtering, W. Responsive Emulsions Stabilized by Stimuli-Sensitive Microgels: Emulsions with Special Non-Pickering Properties. *Langmuir* **2012**, *28*, 17218–17229.
DOI:10.1021/la302331s
20. Li, Z.; Ngai, T. Microgel particles at the fluid–fluid interfaces. *Nanoscale* **2013**, *5*, 1399–1410. DOI:10.1039/c2nr33503d
21. Kwok, M.; Sun, G.; Ngai, T. Microgel Particles at Interfaces: Phenomena, Principles, and Opportunities in Food Sciences. *Langmuir* **2019**, *35*, 4205–4217.
DOI:10.1021/acs.langmuir.8b04009
22. Anakhov, M. V.; Gumerov, R. A.; Richtering, W.; Pich, A.; Potemkin, I. I. Scavenging One of the Liquids versus Emulsion Stabilization by Microgels in a Mixture of Two Immiscible Liquids. *ACS Macro Lett.* **2020**, *9*, 736–742.
DOI:10.1021/acsmacrolett.0c00191
23. Zhang, Y.; Zhang, H.; Liu, P.; Sun, H.; Li, B.; Wang, W. Programming Hydrogen Production via Controllable Emulsification/Demulsification in a Switchable Oil–Water System. *ACS Sustainable Chem. Eng.* **2019**, *7*, 7768–7776.
DOI:10.1021/acssuschemeng.8b06714
24. Jiang, H.; Liu, L.; Li, Y.; Yin, S.; Ngai, T. Inverse Pickering Emulsion Stabilized by Binary Particles with Contrasting Characteristics and Functionality for Interfacial Biocatalysis. *ACS Appl. Mater. Interfaces* **2020**, *12*, 4989–4997.
DOI:10.1021/acsami.9b16117
25. Wang, Y.; Zhu, L.; Zhang, H.; Huang, H.; Jiang, L. Formulation of pH and temperature dual-responsive Pickering emulsion stabilized by chitosan-based microgel for recyclable biocatalysis. *Carbohydrate Polymers* **2020**, *241*, 116373.
DOI:10.1016/j.carbpol.2020.116373
26. BASF Luviskol Plus. <https://www.carecreations.basf.com/product-formulations/products/products-detail/LUVISKOL%20PLUS/30054531> (accessed 29.11., 2019).
27. Liu, Z.; Wickramasinghe, S. R.; Qian, X. Ion-specificity in protein binding and recovery for the responsive hydrophobic poly(vinylcaprolactam) ligand. *RSC Advances* **2017**, *7*, 36351–36366. DOI:10.1039/C7RA06022J
28. Dirdal, E. G.; Kelland, M. A. Synthesis and Investigation of Polymers of 2-Methacrylamido-caprolactam as Kinetic Hy-

- drate Inhibitors. *Energy Fuels* **2020**, *34*, 6981–6990.
DOI:10.1021/acs.energyfuels.0c00929
29. Kirsh, Y. E. *Water soluble poly-N-vinylamides : synthesis and physicochemical properties*; Wiley: Chichester, 1998; , pp viii, 233 sivua.
30. Anonymousworlds-first-ton-of-renewable-nylon-intermediate. <https://www.genomatica.com/worlds-first-ton-of-renewable-nylon-intermediate/> (accessed 22.6., 2020).
DOI:10.1016/j.focat.2020.04.042
31. Cortez-Lemus, N. A.; Licea-Claverie, A. Poly(N-vinylcaprolactam), a comprehensive review on a thermoresponsive polymer becoming popular. *Prog. Polym. Sci.* **2016**, *53*, 1–51.
DOI:10.1016/j.progpolymsci.2015.08.001
32. Liu, J.; Debuigne, A.; Detrembleur, C.; Jérôme, C. Poly(N-vinylcaprolactam): A Thermoresponsive Macromolecule with Promising Future in Biomedical Field. *Adv. Healthcare Mater.* **2014**, *3*, 1941–1968. DOI:10.1002/adhm.201400371
33. Rao, K.M.; Rao, K.S.V.K.; Ha, C.-S. Stimuli Responsive Poly(Vinyl Caprolactam) Gels for Biomedical Applications. *Gels* **2016**, *2*, 6. DOI:10.3390/gels2010006
34. Meeussen, F.; Nies, E.; Berghmans, H.; Verbrugghe, S.; Goethals, E.; Du Prez, F. Phase behaviour of poly(N-vinyl caprolactam) in water. *Polymer* **2000**, *41*, 8597–8602.
DOI:10.1016/S0032-3861(00)00255-X
35. Maeda, Y.; Nakamura, T.; Ikeda, I. Hydration and Phase Behavior of Poly(N-vinylcaprolactam) and Poly(N-vinylpyrrolidone) in Water. *Macromolecules* **2002**, *35*, 217–222.
DOI:10.1021/ma011034+
36. Stokov, I. V.; Abramchuk, S. S.; Makhaeva, E. E. Salt and pH effect on thermoresponsive behavior of multiwalled carbon nanotube (MWCNT)/poly(N-vinylcaprolactam) dispersion. *Colloid Polym. Sci.* **2019**, *297*, 387–395.
DOI:10.1007/s00396-018-4424-6
37. Kirsh, Y. E.; Yanul, N. A.; Kalnins, K. K. Structural transformations and water associate interactions in poly-N-vinylcaprolactam–water system. *Eur. Polym. J.* **1999**, *35*, 305–316.
DOI:10.1016/S0014-3057(98)00114-1
38. Moghaddam, S. Z.; Thormann, E. The Hofmeister series: Specific ion effects in aqueous polymer solutions. *J. Colloid Interface Sci.* **2019**, *555*, 615–635. DOI:10.1016/j.jcis.2019.07.067
39. Laukkanen, A.; Valtola, L.; Winnik, F. M.; Tenhu, H. Formation of Colloidally Stable Phase Separated Poly(N-vinylcaprolactam) in Water: A Study by Dynamic Light Scattering, Microcalorimetry, and Pressure Perturbation Calorimetry. *Macromolecules* **2004**, *37*, 2268–2274.
DOI:10.1021/ma035124l
40. Sun, S.; Wu, P. Infrared Spectroscopic Insight into Hydration Behavior of Poly(N-vinylcaprolactam) in Water. *J. Phys. Chem. B.* **2011**, *115*, 11609–11618.
DOI:10.1021/jp2071056
41. Spěváček, J.; Dybal, J.; Starovoytova, L.; Zhigunov, A.; Sedláková, Z. Temperature-induced phase separation and hydration in poly(N-vinylcaprolactam) aqueous solutions: a study by NMR and IR spectroscopy, SAXS, and quantum-chemical calculations. *Soft Matter* **2012**, *8*, 611–6119.
DOI:10.1039/c2sm25432h
42. Aguirre, G.; Ramos, J.; Forcada, J. Synthesis of new enzymatically degradable thermo-responsive nanogels. *Soft Matter* **2013**, *9*, 261–270. DOI:10.1039/C2SM26753E
43. Kermagoret, A.; Fustin, C.; Bourguignon, M.; Detrembleur, C.; Jérôme, C.; Debuigne, A. One-pot controlled synthesis of double thermoresponsive N-vinylcaprolactam-based copolymers with tunable LCSTs. *Polym. Chem.* **2013**, *4*, 2575.
DOI:10.1039/c3py00134b
44. Laukkanen, A.; Hietala, S.; Maunu, S. L.; Tenhu, H. Poly(N-vinylcaprolactam) Microgel Particles Grafted with Amphiphilic Chains. *Macromolecules* **2000**, *33*, 8703–8708.
DOI:10.1021/ma000953h
45. Laukkanen, A.; Wiedmer, S. K.; Varjo, S.; Riekkola, M. -; Tenhu, H. Stability and thermosensitive properties of various poly (N-vinylcaprolactam) microgels. *Colloid Polym. Sci.* **2002**, *280*, 65–70. DOI:10.1007/s003960200009
46. Imaz, A.; Forcada, J. Synthesis strategies to incorporate acrylic acid into N-vinylcaprolactam-based microgels. *J. Polym. Sci. A Polym. Chem.* **2011**, *49*, 3218–3227.
DOI:10.1002/pola.24758
47. Pich, A.; Berger, S.; Ornatsky, O.; Baranov, V.; Winnik, M. A. The influence of PEG macromonomers on the size and properties of thermosensitive aqueous microgels. *Colloid Polym. Sci.* **2009**, *287*, 269–275. DOI:10.1007/s00396-008-1972-1
48. Wang, Y.; Nie, J.; Chang, B.; Sun, Y.; Yang, W. Poly(vinylcaprolactam)-Based Biodegradable Multiresponsive Microgels for Drug Delivery. *Biomacromolecules* **2013**, *14*, 3034–3046.
DOI:10.1021/bm401131w
49. Lou, S.; Gao, S.; Wang, W.; Zhang, M.; Zhang, Q.; Wang, C.; Li, C.; Kong, D. Temperature/pH dual responsive microgels of crosslinked poly(N-vinylcaprolactam-co-undecenoic acid) as biocompatible materials for controlled release of doxorubicin. *J Appl Polym Sci* **2014**, *131*, n/a.
DOI:10.1002/app.41146
50. Gonzalez-Ayon, M. A.; Cortez-Lemus, N. A.; Zizumbo-Lopez, A.; Licea-Claverie, A. Nanogels of Poly(N-Vinylcaprolactam) Core and Polyethyleneglycol Shell by Surfactant Free Emulsion Polymerization. *Soft Mater.* **2014**, *12*, 315–325.
DOI:10.1080/1539445X.2014.914537
51. González-Ayón, M. A.; Sañudo-Barajas, J. A.; Picos-Corrales, L. A.; Licea-Claverie, A. PNVCLE-PEGMA nanohydrogels with tailored transition temperature for controlled delivery of 5-fluorouracil. *J. Polym. Sci. Part A: Polym. Chem.* **2015**, *53*, 2662–2672. DOI:10.1002/pola.27766
52. Willems, C.; Pargen, S.; Balaceanu, A.; Keul, H.; Möller, M.; Pich, A. Stimuli responsive microgels decorated with oligoglycidol macromonomers: Synthesis, characterization and properties in aqueous solution. *Polymer* **2018**, *141*, 21–33.
DOI:10.1016/j.polymer.2018.02.047
53. Xu, W.; Rudov, A. A.; Schroeder, R.; Portnov, I. V.; Richtering, W.; Potemkin, I. I.; Pich, A. Distribution of Ionizable Groups in Polyampholyte Microgels Controls Interactions with Captured Proteins: From Blockade and “Levitation” to Accelerated Release. *Biomacromolecules* **2019**, *20*, 1578–1591.
DOI:10.1021/acs.biomac.8b01775
54. Chimisso, V.; Fodor, C.; Meier, W. Effect of Divalent Cation

- on Swelling Behavior of Anionic Microgels: Quantification and Dynamics of Ion Uptake and Release. *Langmuir* **2019**, *35*, 13413–13420. DOI:10.1021/acs.langmuir.9b02791
55. Izak-Nau, E.; Demco, D. E.; Braun, S.; Baumann, C.; Pich, A.; Göstl, R. Shear-Induced Structural and Functional Transformations of Poly(N-vinylcaprolactam) Microgels. *ACS Appl. Polym. Mater.* **2020**, *2*, 1682–1691. DOI:10.1021/acsapm.0c00111
56. Jung, S.; Schneider, S.; Plamper, F.; Pich, A. Responsive Supramolecular Microgels with Redox-Triggered Cleavable Crosslinks. *Macromolecules* **2020**, *53*, 1043–1053. DOI:10.1021/acs.macromol.9b01292
57. Kehren, D.; Lopez, C. M.; Theiler, S.; Keul, H.; Möller, M.; Pich, A. Multicompartment aqueous microgels with degradable hydrophobic domains. *Polymer* **2019**, *172*, 283–293. DOI:10.1016/j.polymer.2019.03.074
58. Madhusudana Rao, K.; Mallikarjuna, B.; Krishna Rao, K S V; Siraj, S.; Chowdoji Rao, K.; Subha, M. C. S. Novel thermo/pH sensitive nanogels composed from poly(N-vinylcaprolactam) for controlled release of an anticancer drug. *Colloids Surf. B* **2013**, *102*, 891–897. DOI:10.1016/j.colsurfb.2012.09.009
59. Siirilä, J.; Karesoja, M.; Pulkkinen, P.; Malho, J.; Tenhu, H. Soft poly(N-vinylcaprolactam) nanogels surface-decorated with AuNPs. Response to temperature, light, and RF-field. *Eur. Polym. J.* **2019**, *115*, 59–69. DOI:10.1016/j.eurpolymj.2019.03.010
60. Tan, K. H.; Xu, W.; Stefka, S.; Demco, D. E.; Kharandiuk, T.; Ivasiv, V.; Nebesnyi, R.; Petrovskii, V. S.; Potemkin, I. I.; Pich, A. Selenium-Modified Microgels as Bio-Inspired Oxidation Catalysts. *Angew. Chem. Int. Ed.* **2019**, *58*, 9791–9796. DOI:10.1002/anie.201901161
61. Laukkanen, A.; Valtola, L.; Winnik, F. M.; Tenhu, H. Thermosensitive graft copolymers of an amphiphilic macromonomer and N-vinylcaprolactam: synthesis and solution properties in dilute aqueous solutions below and above the LCST. *Polymer* **2005**, *46*, 7055–7065. DOI:10.1016/j.polymer.2005.05.100
62. Aseyev, V.; Hietala, S.; Laukkanen, A.; Nuopponen, M.; Confortini, O.; Du Prez, F. E.; Tenhu, H. Mesoglobules of thermoresponsive polymers in dilute aqueous solutions above the LCST. *Polymer* **2005**, *46*, 7118–7131. DOI:10.1016/j.polymer.2005.05.097
63. Vihola, H.; Laukkanen, A.; Tenhu, H.; Hirvonen, J. Drug release characteristics of physically cross-linked thermosensitive poly(N-vinylcaprolactam) hydrogel particles. *J. Pharm. Sci.* **2008**, *97*, 4783–4793. DOI:10.1002/jps.21348
64. Kozlovskaya, V.; Liu, F.; Xue, B.; Ahmad, F.; Alford, A.; Saeed, M.; Kharlampieva, E. Polyphenolic Polymersomes of Temperature-Sensitive Poly(N-vinylcaprolactam)-block-Poly(N-vinylpyrrolidone) for Anticancer Therapy. *Biomacromolecules* **2017**, *18*, 2552–2563. DOI:10.1021/acs.biomac.7b00687
65. Siirilä, J.; Häkkinen, S.; Tenhu, H. The emulsion polymerization induced self-assembly of a thermoresponsive polymer poly(N-vinylcaprolactam). *Polym. Chem.* **2019**, *10*, 766–775. DOI:10.1039/C8PY01421C
66. Mani, P.; Grailer, J. J.; Steeber, D. A.; Shaoqin, G. Thermosensitive Micelles Based on Folate-Conjugated Poly(N-vinylcaprolactam)-block-Poly(ethylene glycol) for Tumor-Targeted Drug Delivery. *Macromol. Biosci.* **2009**, *9*, 744–753. DOI:10.1002/mabi.200800366
67. Liu, F.; Kozlovskaya, V.; Medipelli, S.; Xue, B.; Ahmad, F.; Saeed, M.; Cropek, D.; Kharlampieva, E. Temperature-Sensitive Polymersomes for Controlled Delivery of Anticancer Drugs. *Chem. Mater.* **2015**, *27*, 7945–7956. DOI:10.1021/acs.chemmater.5b03048
68. Kozlovskaya, V.; Baggett, J.; Godin, B.; Liu, X.; Kharlampieva, E. Hydrogen-Bonded Multilayers of Silk Fibroin: From Coatings to Cell-Mimicking Shaped Microcontainers. *ACS Macro Lett.* **2012**, *1*, 384–387. DOI:10.1021/mz200118f
69. Kozlovskaya, V.; Kharlampieva, E. Self-Assemblies of Thermoresponsive Poly(N-vinylcaprolactam) Polymers for Applications in Biomedical Field. *ACS Appl. Polym. Mater.* **2020**, *2*, 26–39. DOI:10.1021/acsapm.9b00863
70. Vihola, H.; Laukkanen, A.; Hirvonen, J.; Tenhu, H. Binding and release of drugs into and from thermosensitive poly(N-vinyl caprolactam) nanoparticles. *Eur. J. Pharm. Sci.* **2002**, *16*, 69–74. DOI:10.1016/S0928-0987(02)00076-3
71. Häntzschel, N.; Zhang, F.; Eckert, F.; Pich, A.; Winnik, M. A. Poly(N-vinylcaprolactam-co-glycidyl methacrylate) Aqueous Microgels Labeled with Fluorescent LaF3:Eu Nanoparticles. *Langmuir* **2007**, *23*, 10793–10800. DOI:10.1021/la701691g
72. Imaz, A.; Forcada, J. N-vinylcaprolactam-based microgels: Synthesis and characterization. *J. Polym. Sci. A Polym. Chem.* **2008**, *46*, 2510–2524. DOI:10.1002/pola.22583
73. Imaz, A.; Forcada, J. N-vinylcaprolactam-based microgels: Effect of the concentration and type of cross-linker. *J. Polym. Sci. A Polym. Chem.* **2008**, *46*, 2766–2775. DOI:10.1002/pola.22609
74. Imaz, A.; Forcada, J. Optimized buffered polymerizations to produce N-vinylcaprolactam-based microgels. *Eur. Polym. J.* **2009**, *45*, 3164–3175. DOI:10.1016/j.eurpolymj.2009.08.003
75. Schneider, F.; Balaceanu, A.; Feoktystov, A.; Pipich, V.; Wu, Y.; Allgaier, J.; Pyckhout-Hintzen, W.; Pich, A.; Schneider, G. J. Monitoring the Internal Structure of Poly(N-vinylcaprolactam) Microgels with Variable Cross-Link Concentration. *Langmuir* **2014**, *30*, 15317–15326. DOI:10.1021/la503830w
76. Gau, E.; Mate, D. M.; Zou, Z.; Oppermann, A.; Töpel, A.; Jakob, F.; Wöll, D.; Schwaneberg, U.; Pich, A. Sortase-Mediated Surface Functionalization of Stimuli-Responsive Microgels. *Biomacromolecules* **2017**, *18*, 2789–2798. DOI:10.1021/acs.biomac.7b00720
77. Macchione, M. A.; Guerrero-Beltrán, C.; Rosso, A. P.; Euti, E. M.; Martinelli, M.; Strumia, M. C.; Muñoz-Fernández, M. Á. Poly(N-vinylcaprolactam) Nanogels with Antiviral Behavior against HIV-1 Infection. *Sci. Rep.* **2019**, *9*, 5732–10. DOI:10.1038/s41598-019-42150-9
78. Ksiazkiewicz, A. N.; Bering, L.; Jung, F.; Wolter, N. A.; Viell, J.; Mitsos, A.; Pich, A. Closing the 1–5 µm size gap: Temperature-programmed, fed-batch synthesis of µm-sized microgels. *Chemical Engineering Journal* **2020**, *379*, 122293. DOI:10.1016/j.cej.2019.122293
79. Kather, M.; Ritter, F.; Pich, A. Surfactant-free synthesis of ex-

- tremely small stimuli-responsive colloidal gels using a confined impinging jet reactor. *Chemical Engineering Journal* **2018**, *344*, 375–379. DOI:10.1016/j.cej.2018.03.082
80. QWolff, H. J. M.; Kather, M.; Breisig, H.; Richtering, W.; Pich, A.; Wessling, M. From Batch to Continuous Precipitation Polymerization of Thermoresponsive Microgels. *ACS Appl. Mater. Interfaces* **2018**, *10*, 24799–24806. DOI:10.1021/acsami.8b06920
81. Bian, S.; Zheng, J.; Tang, X.; Yi, D.; Wang, Y.; Yang, W. One-Pot Synthesis of Redox-Labile Polymer Capsules via Emulsion Droplet-Mediated Precipitation Polymerization. *Chem. Mater.* **2015**, *27*, 1262–1268. DOI:10.1021/cm5042315
82. Slomkowski S.; Alemán J., ; Gilbert R.; Heiss, M.; Horie K.; Jones R. G.; Kubisa P.; Meisel I.; Mormann W.; Stanisław P.; Stepto R. F. Terminology of polymers and polymerization processes in dispersed systems (IUPAC Recommendations 2011). *Pure Appl. Chem.* **2011**, *83*, 2229. DOI:10.1351/PAC-REC-10-06-03
83. Crespy, D.; Zuber, S.; Turshatov, A.; Landfester, K.; Popa, A. A straightforward synthesis of fluorescent and temperature-responsive nanogels. *J. Polym. Sci. A Polym. Chem.* **2012**, *50*, 1043–1048. DOI:10.1002/pola.25875
84. Petrizza, L.; Le Behec, M.; Decompte, E.; El Hadri, H.; Lacombe, S.; Save, M. Tuning photosensitized singlet oxygen production from microgels synthesized by polymerization in aqueous dispersed media. *Polym. Chem.* **2019**, *10*, 3170–3179. DOI:10.1039/C9PY00157C
85. Medeiros, S. F.; Santos, A. M.; Fessi, H.; Elaissari, A. Synthesis of biocompatible and thermally sensitive poly(N-vinylcaprolactam) nanogels via inverse miniemulsion polymerization: Effect of the surfactant concentration. *J. Polym. Sci. A Polym. Chem.* **2010**, *48*, 3932–3941. DOI:10.1002/pola.24165
86. Gao, F.; Mi, Y.; Wu, X.; Yao, J.; Qi, Q.; Cao, Z. Preparation of thermoresponsive poly(N-vinylcaprolactam-co-2-methoxyethyl acrylate) nanogels via inverse miniemulsion polymerization. *J. Appl. Polym. Sci.* **2019**, *136*, 48237. DOI:10.1002/app.48237
87. Schork, F.; Luo, Y.; Smulders, W.; Russum, J.; Butté, A.; Fontenot, K. In *Miniemulsion Polymerization*; Polymer Particles; Springer Berlin Heidelberg: Berlin, Heidelberg, 2005; Vol. 175, pp 129–255. DOI:10.1007/b100115
88. Landfester, K. Miniemulsion Polymerization and the Structure of Polymer and Hybrid Nanoparticles. *Angew. Chem., Int. Ed.* **2009**, *48*, 4488–4507. DOI:10.1002/anie.200900723
89. Gumerov, R. A.; Gau, E.; Xu, W.; Melle, A.; Filippov, S. A.; Sorokina, A. S.; Wolter, N. A.; Pich, A.; Potemkin, I. I. Amphiphilic PVCL/TBCHA microgels: From synthesis to characterization in a highly selective solvent. *J. Colloid Interface Sci.* **2020**, *564*, 344–356. DOI:10.1016/j.jcis.2019.12.123
90. Kehren, D.; Lopez, C. M.; Theiler, S.; Keul, H.; Möller, M.; Pich, A. Multicompartment aqueous microgels with degradable hydrophobic domains. *Polymer* **2019**, *172*, 283–293. DOI:10.1016/j.polymer.2019.03.074
91. Canning, S. L.; Smith, G. N.; Armes, S. P. A Critical Appraisal of RAFT-Mediated Polymerization-Induced Self-Assembly. *Macromolecules* **2016**, *49*, 1985–2001. DOI:10.1021/acs.macromol.5b02602
92. Khor, S. Y.; Quinn, J. F.; Whittaker, M. R.; Truong, N. P.; Davis, T. P. Controlling Nanomaterial Size and Shape for Biomedical Applications via Polymerization-Induced Self-Assembly. *Macromol. Rapid Commun.* **2019**, *40*, 1800438. DOI:10.1002/marc.201800438
93. Etchenausia, L.; Deniau, E.; Brûlet, A.; Forcada, J.; Save, M. Cationic Thermoresponsive Poly(Nvinylcaprolactam) Microgels Synthesized by Emulsion Polymerization Using a Reactive Cationic Macro-RAFT Agent. *Macromolecules* **2018**, *51*, 2551–2563. DOI:10.1021/acs.macromol.8b00155
94. Etchenausia, L.; Khoukh, A.; Deniau Lejeune, E.; Save, M. RAFT/MADIX emulsion copolymerization of vinyl acetate and N-vinylcaprolactam: towards waterborne physically crosslinked thermoresponsive particles. *Polym. Chem.* **2017**, *8*, 2244–2256. DOI:10.1039/C7PY00221A
95. BASF Soluplus. <https://pharmaceutical.basf.com/en/Drug-Formulation/Soluplus.html> (accessed 27.11., 2019).
96. Siirilä, J.; Hietala, S.; Ekholm, F. S.; Tenhu, H. Glucose and Maltose Surface-Functionalized Thermoresponsive Poly(N-Vinylcaprolactam) Nanogels. *Biomacromolecules* **2020**, *21*, 955–965. DOI:10.1021/acs.biomac.9b01596

Povzetek

Mehki nanodelci so pomembna vrsta materiala in se lahko uporabljajo kot nosilci aktivnih spojin. Nabrekli in prehodni delci lahko delujejo kot gostitelji za aktivne sestavine in zagotavljajo stabilnost, odzivnost na dražljaje in reciklabilnost za gosta. Termoodzivni koloidni gelski delci so še posebej privlačni za takšne aplikacije zaradi njihove izjemno mehke strukture, velikosti in odzivnosti. Poli(N-vinilkaprolaktam) (PNVCL) je veliko raziskan in priljubljen termoodzivni polimer. Ni (oz. je zelo malo) strupen, temperatura faznega prehoda pa je blizu telesne temperature. Med faznim prehodom postane polimer manj topen, PNVCL nanodelec izloči velik del vode in se skrči v bolj kompaktno obliko. Ta prehod v veliki meri vpliva na difuzijo materiala v delce in iz njih. Hkrati s topnostjo polimera se spreminjajo tudi interakcije z vgrajeno spojino. Ta članek se osredotoča na sintetične metode, lastnosti in aplikacije mehkih PNVCL delcev.



Except when otherwise noted, articles in this journal are published under the terms and conditions of the Creative Commons Attribution 4.0 International License

Scientific paper

The Synthesis of (2R)-Aziridine-2-carboxylic Acid Containing Dipeptides

Samo Kuzmič, Martina Hrast and Rok Frlan*

University of Ljubljana, Faculty of Pharmacy, The Chair of Pharmaceutical Chemistry,
Aškerčeva 7, 1000 Ljubljana, Slovenia

* Corresponding author: E-mail: rok.frlan@ffa.uni-lj.si;
Tel.: +386 1 4769 674; Fax: +386-1-4258031

Received: 03-05-2021

Abstract

Optimized conditions for the synthesis of fully deprotected (2R)-aziridine containing dipeptides are described. Preparation of fully protected N- and C- terminal aziridine containing dipeptides was found to be straightforward and high yielding for the majority of compounds, whereas their full deprotection was possible only for C-terminal analogs. Deprotection of N-terminal derivatives using standard procedures of peptide chemistry was found difficult providing only mixtures of unidentifiable products. The described molecules have potential as building blocks in synthetic chemistry, in the chemical biology arena, as covalent modifiers, and as biomarkers.

Keywords: Dipeptides; aziridines; biomarkers; warheads; antibacterial agents

1. Introduction

Small molecules that mimic the structures of bioactive peptides are an important synthetic tool in organic chemistry. A special interest has been given to the synthesis of conformationally restricted β -turn dipeptide mimetics, peptide bond isosteres and nonproteinogenic derivatives to obtain drug-like target molecules.^{1–3} A common strategy, that has been also widely applied, especially in the design of several protease inhibitors is to incorporate an electrophilic warhead that forms a covalent bond between amino acids in the active site and the inhibitor.^{4,5}

The importance of aziridine-2-carboxylic acid, as well as aziridine-containing peptides as useful intermediates in the synthesis of various amino acid and peptide derivatives, has been extensively recognized, both from a medicinal and a synthetic point of view.^{6–10} Furthermore, despite their reactivity aziridine-containing peptides and related compounds may be found in numerous bioactive compounds of natural origin, such as madurostatin A1¹¹ and miraziridine A¹² (Figure 1). In addition, this heterocyclic fragment has also been incorporated in numerous synthetic peptides as reactive electrophilic warheads to obtain promising irreversible inhibitors of different proteases, such as cathepsins,^{13,14} papain,¹⁵ aspartate proteases,¹⁶ HIV proteases¹⁷ and SARS-CoV main protease.¹⁸

Their unusual reactivity due to ring strain renders aziridine-2-carboxylic acid derivatives important for the preparation of amino acids,^{19–21} amino alcohols,^{22,23} peptides and other peptide-like compounds.^{17,24–33} In addition, they have also been used for labelling biomolecules with fluorine-18.^{34,35}

Consequently, the preparation of aziridine-containing dipeptides, which is a subject of this communication, is of great importance for medicinal as well as organic chemistry. There have been many reports in the literature describing their synthesis.^{36,37} Nonetheless, up to now, literature reports on the preparation of partially or fully deprotected dipeptide derivatives have been rare. To the best of our knowledge, there has been only one report by Korn³⁶ describing the synthesis of fully deprotected H-Azy-Leu-OH and only a couple of papers describing the synthesis of N-deprotected^{21,27,38,39} and C-deprotected dipeptides.^{34,36} Most of them suffer from low isolated yields following work-up and chromatography which reflects the inherent instability of these compounds. At the same time, it is known that aziridine-containing peptides possess the potential antifungal,^{16,40} antiviral¹⁸ antiprotozoal^{13,14} and cytostatic activity.^{13–15,41} Clearly, a more versatile approach to deprotected aziridine-containing dipeptides is desired, given their potential to serve as electrophiles in reactions with appropriate nucleophiles, as biomarkers and bioactive compounds.

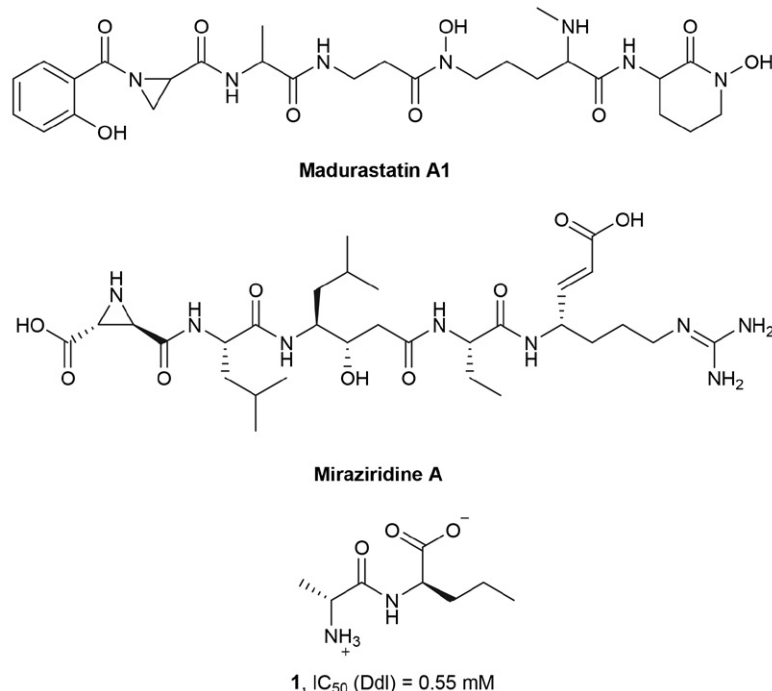


Figure 1. Natural products with aziridine ring and D-Ala:D-Ala ligase (Ddl) inhibitor 1.

During our ongoing study concerning the dipeptide D-Ala-D-Ala, we were interested in preparing its electrophilic aziridine-containing analogs with potential biological activity. D-Ala-D-Ala sequence is found in the stem termini of peptidoglycan side-chain pentapeptide and is recognized by multiple essential bacterial enzymes. Any molecule that could mimic its structure thus offers an attractive potential toward the development of new inhibitors or as a false substrate for any of those enzymes.⁴² Indeed, it was reported that dipeptides with D-Ala as a first amino acid inhibit bacterial enzyme D-Alanine:D-Alanine ligase (Ddl) in micromolar range (1, Figure 1).⁴³ (*R*)-aziridine-2-carboxylic acid was therefore chosen as a rigid surrogate of D-Ala because of its electrophilic character and close resemblance to D-Ala.

Herein, we report details of our efforts to develop a new approach to the preparation of a series of fully deprotected N-terminal aziridine containing dipeptides with general structure 2. In addition, an attempt on the synthesis of C-terminal aziridine containing dipeptides with general structure 3 is also reported (Figure 2).

The designed molecules are very attractive not only because of their biological potential but also because aziridines have become important building blocks in synthetic chemistry. Such small dipeptides have a potential as covalent modifiers and are therefore useful in the chemical biology arena with different applications including bioconjugation, activity-based protein profiling and target identification.^{6,8}

2. Experimental

2.1. General Methods

The reactions were monitored by TLC carried out on Merck silica gel (60 F254) by using UV light as a visualizing agent, KMnO₄ in water, phosphomolybdic acid in ethanol and ninhydrin in ethanol and heat as developing agents. Column chromatography was performed using Merck Silica Gel 60. Proton nuclear magnetic resonance spectra (¹H NMR) were obtained at 400 MHz on Bruker Avance III 400 spectrometers. Spectra were recorded in CDCl₃, MeOD and DMSO-d₆ solutions. Chemical shifts are reported in ppm, referenced to tetramethylsilane (TMS) as the external reference. Carbon-13 nuclear magnetic resonance spectra (¹³C NMR) were obtained at 100 MHz on Bruker 400 spectrometer. Chemical shifts are reported in ppm, referenced to the

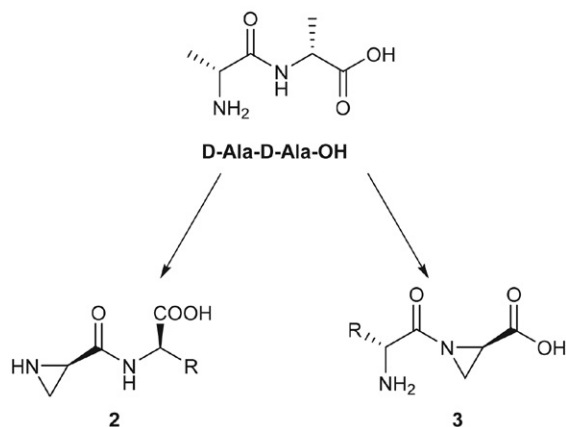


Figure 2. N- and C-terminal aziridine containing dipeptides.

solvent peak of CDCl_3 . Low-resolution mass spectra were obtained with a Shimadzu GC-MS-QP2010 mass spectrometer. High resolution mass spectra (HRMS) were recorded on Q Executive Plus LC-MS/MS system (Thermo Scientific). Melting points were found on the Cambridge instruments melting point apparatus and are corrected. Optical rotation was found with Perkin Elmer 1241MC polarimeter at wavelength 589,3 nm ($l = 10$ cm). Ethyl acetate and methanol were used as solvents. Infrared spectra were recorded on a Perkin-Elmer FTIR 1600 spectrometer. Melting points were determined using a Reichert hot-stage microscope and are corrected. HPLC analyses were performed on an HPLC Dionex UltiMate 3000 instrument with a UV-VIS detector. Three different analytical methods were used. Method 1: Column: Phenomenex Luna[®] 5 μm C18 100 \AA ; Injection volume: 10 μL ; Flow rate: 1,5 mL/min; Detection wavelengths: $\lambda = 210$ nm, 220 nm, 254 nm and 280 nm; Column temperature: 25 $^\circ\text{C}$; Mobile phase: 40% ACN in water to 100% ACN in 15 min. Method 2: Column: Supelco SUPELCOSIL[™] LC-1 HPLC; Injection volume: 1 μL ; Flow rate: 1 mL/min; Detection Wavelengths: $\lambda = 195$ nm, 210 nm, 220 nm and 254 nm; Column temperature: 25 $^\circ\text{C}$; Mobile phase: 5% ACN in 20 mM phosphate buffer (pH = 2.10) to 60% ACN in 20 min. Method 3: Column: Agilent ZORBAX Extend-C18; Injection volume: 5 μL ; Flow rate: 1 mL/min; Detection wavelengths $\lambda = 210$ nm, 220 nm, 254 nm and 280 nm; Column temperature 25 $^\circ\text{C}$; Mobile phase: 40% ACN in water to 100% ACN in 20 min.

2. 2. Synthesis and Characterization

(R)-3-hydroxy-1-methoxy-1-oxopropan-2-aminium chloride (4).

To a solution of D-serine (20.00 g, 190.3 mmol, 1.00 equiv.) in 500 mL MeOH, SOCl_2 (24.90 mL, 342.6 mmol, 1.80 equiv.) was added at 0 $^\circ\text{C}$. The reaction mixture was stirred at 80 $^\circ\text{C}$ for 2 h and stirred at room temperature for an additional 20 h. The solution was concentrated under reduced pressure and diethyl ether (250 mL) was added to remove the excess of HCl. The solvent was evaporated under reduced pressure yielding 28.95 g (97.8%) of compound **2** as white crystals. mp 178.1–179.0 $^\circ\text{C}$ (lit. 175–176 $^\circ\text{C}^{44}$). R_f 0.11 (CH_2Cl_2 :MeOH = 7:1 + 3% Et_3N).

Methyl trityl-D-serinate (5)

To a cooled solution of **4** (29.27 g, 188.1 mmol, 1.00 equiv.) and Et_3N (55.10 mL, 396.1 mmol, 2.11 equiv.) in CH_2Cl_2 (500 mL), trityl chloride (52.45 g, 188.1 mmol, 1.00 equiv.) was added and the mixture was stirred for 2 hours at 0 $^\circ\text{C}$. The reaction mixture was washed with 10% citric acid solution (3×150 mL) and brine (150 mL). The organic phase was dried over anhydrous Na_2SO_4 , the drying agent was filtered off and the solvent was evaporated under reduced pressure. The product was purified via flash column chromatography (hexane:EtOAc = 2:1) to obtain 55.70 g (81.9%) of **5** as white solid. mp 158.8–161.5 $^\circ\text{C}$ (lit.

152–154 $^\circ\text{C}^{45}$). R_f 0.27 (hexane:EtOAc = 2:1). ^1H NMR (400 MHz, CDCl_3): δ 2.29 (dd, J 6.2 Hz, 6.0 Hz, 1H, OH), 2.97 (bs, 1H, NH), 3.30 (s, 3H, CH_3), 3.50–3.61 (m, 2H, CH_2 and CH), 3.65–3.75 (m, 1H, CH_2), 7.16–7.32 (m, 9H, CPh_3), 7.43–7.51 (m, 6H, CPh_3) ppm.

Methyl (R)-1-tritylaziridine-2-carboxylate (6)

To a cooled solution of **5** (5.01 g, 13.9 mmol, 1.00 equiv.) and Et_3N (4.25 mL, 30.5 mmol, 2.20 equiv.) in anhydrous THF (40 mL), methanesulfonyl chloride (1.08 mL, 14.0 mmol, 1.01 equiv.) was added dropwise. Reaction mixture was stirred for 30 minutes at room temperature. The temperature was then raised to 65 $^\circ\text{C}$ (reflux temperature) and reaction mixture was refluxed for 48 hours. The solvent was evaporated under reduced pressure, the solid residue was dissolved in EtOAc (40 mL) and washed with 10% citric acid solution (3×10 mL), saturated NaHCO_3 solution (3×10 mL) and brine (1×10 mL). The organic phase was dried over anhydrous Na_2SO_4 , the drying agent was filtered off and the solvent was evaporated under reduced pressure. The product was purified via flash column chromatography (hexane:EtOAc = 4:1) to yield 3.42 g (71.9%) **6** as white crystals. mp 122.0–123.0 $^\circ\text{C}$ (lit. 122–123 $^\circ\text{C}^{46}$). R_f 0.36 (Hexane:EtOAc = 4:1). ^1H NMR (400 MHz, CDCl_3): δ 1.41 (dd, J 6.3 Hz, 1.7 Hz, 1H, CH_2), 1.89 (dd, J 6.3 Hz, 2.7 Hz, 1H, CH), 2.26 (dd, J 2.7 Hz, 1.7 Hz, 1H, CH_2), 3.76 (s, 3H, CH_3), 7.19–7.31 (m, 9H, CPh_3), 7.47–7.52 (m, 6H, CPh_3) ppm. IR (ATR): $\bar{\nu}$ 3705, 3467, 2973, 1742, 1596, 1489, 1445, 1394, 1328, 1234, 1181, 1011, 893, 843, 756, 697 cm^{-1} .

Potassium (R)-1-tritylaziridine-2-carboxylate (7, $\text{C}_{22}\text{H}_{18}\text{KNO}_2$)

To a cooled solution of **6** (5.78 g, 16.8 mmol, 1.00 equiv.) in THF (17 mL), 1M solution of KOH was added (16.84 mL, 16.84 mmol, 1.00 equiv.). Reaction mixture was stirred at room temperature for 24 hours. The solvent was removed under reduces pressure to obtain 6.15 g (99.4%) of **7** as lightly yellow solid. Reaction product was stable in salt form, but unstable in acid form. Yield: 99.4. mp Thermal $T_{\text{dec}} > 250.0$ $^\circ\text{C}$. R_f 0.30 (hexane:EtOAc = 1:1 + 0.3% CH_3COOH). ^1H NMR (400 MHz, CDCl_3): δ 1.80–1.88 (m, 2H, CH_2), 3.71–3.78 (m, 1H, CH), 7.18–7.33 (m, 15H, CPh_3) ppm. ^{13}C NMR (100 MHz, CDCl_3): δ 28.82, 34.95, 74.28, 126.67–128.36 (signals overlap), 129.51, 144.32, 178.15 ppm. MS m/z (relative intensity): 327.7 ($[\text{M}-\text{H}]^-$, 100%). HRMS-ESI: $[\text{M}-\text{H}]^-$ calcd for $\text{C}_{22}\text{H}_{18}\text{NO}_2$, 328.1343. found, 328.1341. IR (ATR): $\bar{\nu}$ 3366, 3060, 2972, 2167, 1960, 1580, 1488, 1423, 1325, 1217, 1155, 1057, 1013, 900, 847, 750, 699 cm^{-1} . $[\alpha]_{\text{D}}^{20} +184.0$ (c 0.31, EtOAc).

2. 3. General Procedure for Coupling reactions (Procedure A, Compounds 8a–8e)

To a cooled solution of compound **7** (1.00 equiv.) and protected D-amino acid (1.00–1.10 equiv.) in 50 mL dichloromethane, HOBT (1.10 equiv.), NMM (3.00 equiv.)

and EDC (1.10 equiv.) were added at 0 °C. The reaction mixture was stirred at room temperature for 24 h. The mixture was washed with 10% citric acid solution (3 × 50 mL), saturated NaHCO₃ solution (3 × 50 mL) and brine (1 × 50 mL). The organic phase was dried over anhydrous Na₂SO₄, the drying agent was filtered off and the solvent was evaporated under reduced pressure.

Methyl ((R)-1-tritylaziridine-2-carbonyl)-D-alaninate (**8a**)

The compound was synthesized according to the general procedure A. The product was purified via flash column chromatography. Initial mobile phase was CH₂Cl₂:hexane = 2:1, which was gradually replaced by hexane:EtOAc = 1:1. Yield: 1.198 g (53.1%) of **8a** as white crystals. Mp 161.0–165.2 °C. *R*_f: 0.48 (hexane:EtOAc = 1:1). ¹H NMR (400 MHz, CDCl₃): δ 1.44–1.51 (m, 4H, CHCH₃ and aziridine CH₂), 1.98–2.02 (m, 2H, aziridine CH and aziridine CH₂), 3.81 (s, 3H, OCH₃), 4.69 (qd, *J* 7.5 Hz, 7.2 Hz, 1H, NHCHCH₃), 7.20–7.34 (m, 10H, CPh₃ and CONH), 7.41–7.48 (m, 6H, CPh₃) ppm. ¹³C NMR (100 MHz, CDCl₃): δ 18.79, 30.12, 34.17, 47.61, 52.79, 74.82, 127.34, 128.00, 129.60, 143.45, 170.74, 173.46 ppm. MS (ESI⁺): *m/z* = 436.85 ([M+Na]⁺, 100%). HRMS-ESI (*m/z*): [M+H]⁺ calcd for C₂₆H₂₇N₂O₃, 415.2016. found, 415.2017. IR (ATR): $\bar{\nu}$ 3705, 3293, 2972, 2869, 1746, 1645, 1532, 1491, 1448, 1359, 1276, 1206, 1165, 1056, 1009, 956, 905, 857, 771, 747, 703 cm⁻¹. HPLC: Method 1: *t*_r: 6.25 min (95.1% at 220 nm). [α]_D²⁰ +132.1 (c 0.33, EtOAc).

Methyl (R)-3-(1-tritylaziridine-2-carboxamido)propionate (**8b**, C₂₆H₂₆N₂O₃)

The compound was synthesized according to the general procedure A. The product was purified via flash column chromatography (hexane:EtOAc = 2:1), which was gradually replaced by hexane:EtOAc = 1:1. Yield: 1.24 g (62.9%) of **8b** as white crystals. mp 65.0–67.0 °C. *R*_f: 0.32 (hexane:EtOAc = 1:1). ¹H NMR (400 MHz, CDCl₃): δ 1.45 (dd, *J* 6.6 Hz, 0.7 Hz, 1H, aziridine CH₂), 1.96 (dd, *J* 2.7 Hz, 0.7 Hz, 1H, aziridine CH₂), 1.99 (dd, *J* 6.6 Hz, 2.7 Hz, 1H, aziridine CH), 2.57–2.71 (m, 2H, CH₂COO), 3.44–3.55 (m, 1H, NHCH₂), 3.65–3.79 (m, 4H, NHCH₂ and OCH₃), 7.20–7.30 (m, 9H, CPh₃), 7.33 (dd, *J* 6.2 Hz, 6.2 Hz, 1H, CONH), 7.38–7.44 (m, 6H, CPh₃) ppm. ¹³C NMR (100 MHz, CDCl₃): δ 29.94, 34.15, 34.29, 34.61, 52.10, 74.73, 127.30, 127.91, 129.48, 143.47, 171.12, 172.99 ppm. MS (*m/z* relative intensity): 436.7 ([M+Na]⁺, 100%). *m/z* = 412.5 ([M-H]⁻, 100%). HRMS-ESI (*m/z*): [M+H]⁺ calcd for C₂₆H₂₇N₂O₃, 415.2016. found, 415.2014. IR (ATR): $\bar{\nu}$ 3706, 3333, 2949, 1733, 1663, 1522, 1442, 1365, 1256, 1180, 1059, 1009, 901, 858, 749, 702 cm⁻¹. HPLC: Method 1: *t*_r: 5.69 min (99.4% at 220 nm). [α]_D²⁰ +109.4 (c 0.33, EtOAc).

Methyl ((R)-1-tritylaziridine-2-carbonyl)-D-phenylalaninate (**8c**)

The compound was synthesized according to the general procedure A. The product was purified via flash

column chromatography (hexane:EtOAc = 2:1), yielding 1.480 g (62.8%) of **8c** as white crystals. mp 120.5–122.0 °C. *R*_f: 0.23 (hexane:EtOAc = 2:1). ¹H NMR (400 MHz, CDCl₃): δ 1.37 (dd, *J* 6.7 Hz, 0.7 Hz, 1H, aziridine CH₂), 1.69 (dd, *J* 2.7 Hz, 0.7 Hz, 1H, aziridine CH₂), 1.95 (dd, *J* 6.7 Hz, 2.7 Hz, 1H, aziridine CH), 3.18 (dd, *J* 13.9 Hz, 6.2 Hz, 1H, CH₂Ph), 3.21 (dd, *J* 13.9 Hz, 6.0 Hz, 1H, CH₂Ph), 3.80 (s, 3H, OCH₃), 4.93 (ddd, *J* 8.7 Hz, 6.2 Hz, 6.0 Hz, 1H, CH₂Ph), 7.15–7.39 (m, 21H, CPh₃, Ph and CONH) ppm. ¹³C NMR (100 MHz, CDCl₃): δ 30.04, 33.99, 38.06, 52.08, 52.66, 74.64, 127.25, 127.50, 127.90 (signals overlap), 128.91, 129.46, 135.98, 143.35, 170.54, 171.99 ppm. MS (*m/z* relative intensity): 488.6 ([M-H]⁻, 100%). HRMS-ESI (*m/z*): [M+H]⁺ calcd for C₃₂H₃₁N₂O₃, 491.2329. found, 491.2326. IR (ATR): $\bar{\nu}$ 3709, 3360, 3281, 2974, 2037, 1743, 1679, 1596, 1501, 1446, 1356, 1277, 1197, 1164, 1129, 1057, 1009, 903, 858, 808, 748, 703 cm⁻¹. HPLC: Method 1: *t*_r: 7.69 min (99.5% at 220 nm). [α]_D²⁰ +74.9 (c 0.31, EtOAc).

Methyl ((R)-1-tritylaziridine-2-carbonyl)-D-valinate (**8d**)

The compound was synthesized according to the general procedure B. The product was purified via flash column chromatography (hexane:EtOAc = 4:1), yielding 1.17 g (64.7%) of **8d** as white crystals. mp 111.0–113.0 °C. *R*_f: 0.34 (hexane:EtOAc = 3:1). ¹H NMR (400 MHz, CDCl₃): δ 0.97 (d, *J* 6.8 Hz, 3H, CH(CH₃)₂), 0.98 (d, *J* 6.8 Hz, 3H, CH(CH₃)₂), 1.51 (dd, *J* 6.2 Hz, 1.0 Hz, 1H, aziridine CH₂), 1.99–2.03 (m, 2H, aziridine CH₂ and aziridine CH), 2.25 (qqd, *J* 6.8 Hz, 6.8 Hz, 5.0 Hz, 1H, CH(CH₃)₂), 3.81 (s, 3H, COOCH₃), 4.59 (dd, *J* 9.3 Hz, 5.0 Hz, 1H, CHCOO), 7.21–7.32 (m, 9H, CPh₃), 7.34 (d, *J* 9.3 Hz, 1H, CONH), 7.42–7.47 (m, 6H, CPh₃) ppm. ¹³C NMR (100 MHz, CDCl₃): δ 17.95, 19.39, 30.33, 31.50, 34.28, 52.45, 56.53, 74.77, 127.32, 127.99, 129.54, 143.44, 170.93, 172.39 ppm. MS (*m/z* relative intensity): 440.6 ([M-H]⁻, 100%). HRMS-ESI (*m/z*): [M+H]⁺ calcd for C₂₉H₃₃N₂O₃, 457.2486. found, 457.2486. IR (ATR): $\bar{\nu}$ 3273, 2965, 1742, 1649, 1554, 1490, 1444, 1314, 1264, 1210, 1150, 1011, 902, 749, 701, 634 cm⁻¹. HPLC: Method 1: *t*_r: 7.32 min (100.0% at 220 nm). [α]_D²⁰ +145.0 (c 0.32, EtOAc).

Dimethyl ((R)-1-tritylaziridine-2-carbonyl)-D-glutamate (**8e**)

The compound was synthesized according to the general procedure A. The product was purified via flash column chromatography (hexane:EtOAc = 2:1), yielding 0.555 g (23.9%) of **8e** as white crystals. mp 151.5–152.5 °C. *R*_f: 0.23 (hexane:EtOAc = 2:1). ¹H NMR (400 MHz, CDCl₃): δ 1.49 (dd, *J* 6.0 Hz, 1.5 Hz, 1H, aziridine CH₂), 1.96–2.00 (m, 2H, aziridine CH₂ and aziridine CH), 2.05–2.16 (m, 1H, CH₂COO), 2.23–2.34 (m, 1H, CH₂COO), 2.36–2.54 (m, 2H, CH₂), 3.67 (s, 3H, OCH₃), 3.82 (s, 3H, OCH₃), 4.68 (ddd, *J* 8.3 Hz, 8.3 Hz, 5.1 Hz, 1H, CHCOO), 7.21–7.32 (m, 9H, CPh₃), 7.44–7.50 (m, 7H, CPh₃ and CONH) ppm. ¹³C NMR (100 MHz, CDCl₃): δ 27.30, 30.05, 30.37, 34.13, 51.44, 52.13, 52.82, 74.84,

127.29, 127.95, 129.59, 143.44, 171.33, 172.23, 173.59 ppm. MS m/z (relative intensity): 508.7 ($[M+Na]^+$, 80%). m/z = 484.5 ($[M-H]^-$, 70%). HRMS-ESI (m/z): $[M+H]^+$ calcd for $C_{29}H_{31}N_2O_5$, 487.2227, found, 487.2228. IR (ATR): $\bar{\nu}$ 3696, 3362, 3059, 2956, 2068, 1977, 1738, 1670, 1596, 1509, 1441, 1373, 1344, 1312, 1205, 1181, 1129, 1098, 1065, 1013, 904, 869, 820, 768, 747, 705 cm^{-1} . HPLC: Method 1: t_r : 6.33 min (99.9% at 220 nm). $[\alpha]_D^{20} +119.4$ (c 0.32, EtOAc).

2. 4. General Procedure for Removal of Trityl Protection Group (Procedure B, Compounds 9a-9e)

To a cooled solution of the starting compound (**8a-8e**, 1.00 equiv.) and triethylsilane (1.75 equiv.) in 30 mL dichloromethane, trifluoroacetic acid (3.50 equiv.) was added drop-wise at 0 °C and stirred for another 30 min on ice bath. After the completion of the reaction (monitored by TLC), the solvent was evaporated under reduced pressure and the solid residue was washed with 25 mL diethyl ether and water (25 mL). $NaHCO_3$ was added to the aqueous phase to give a solution with a pH = 10. To further reduce solubility of the product, NaCl was added and the aqueous phase was washed with ethyl acetate (6 × 25 mL). The collected organic phases were washed with brine (1 × 50 mL) and dried over anhydrous Na_2SO_4 . The drying agent was filtered off and the solvent was evaporated under reduced pressure.

Methyl ((R)-aziridine-2-carbonyl)-D-alaninate (**9a**, $C_7H_{12}N_2O_3$)

The compound was synthesized according to the general procedure B. Yield: 0.140 mg (52.7%) as white crystals. mp 99.5–102.3 °C. R_f : 0.45 (CH_2Cl_2 :MeOH = 9:1 + 3% Et_3N). 1H NMR (400 MHz, MeOD): δ 1.39 (d, $I = 7.3$ Hz, 3H, $CHCH_3$), 1.79–1.86 (m, 2H, aziridine CH_2), 2.55 (dd, J 5.7 Hz, 3.2 Hz, 1H, aziridine CH), 3.70 (s, 3H, OCH_3), 4.44 (q, J 7.3 Hz, 1H, $CHCH_3$) ppm. ^{13}C NMR (100 MHz, MeOD): δ 17.65, 26.28, 30.42, 52.95, 172.73, 174.55 ppm, one signal covered by solvent. MS m/z (relative intensity): 171,3 ($[M-H]^-$, 50%). HRMS-ESI (m/z): $[M+H]^+$ calcd for $C_7H_{12}N_2O_3$, 172.0848. found, 173.0920. IR (ATR): $\bar{\nu}$ 3701, 3286, 3196, 2973, 1732, 1665, 1560, 1451, 1405, 1374, 1344, 1211, 1137, 1058, 1011, 932, 826, 713 cm^{-1} . HPLC: Method 2: t_r : 4.29 min (94.6% at 195 nm). $[\alpha]_D^{20} +32.9$ (c 0.33, MeOH).

Methyl (R)-3-(aziridine-2-carboxamido)propanoate (**9b**)

The compound was synthesized according to the general procedure B. The product was purified via flash column chromatography using Al_2O_3 (CH_2Cl_2 :MeOH = 20:1), yielding 0.173 g (43.6%) of **9b** as white crystals. mp 93.8–95.8 °C. R_f : 0.26 (CH_2Cl_2 :MeOH = 9:1 + 3% Et_3N). 1H NMR (400 MHz, $CDCl_3$): δ 1.70–2.00 (m, 2H, aziridine CH_A / CH_B), 2.46 (bs, 1H, aziridine CH), 2.56 (t, J 6.1 Hz, 2H, CH_2COO), 3.49–3.60 (m, 2H, $NHCH_2CH_2$), 3.71 (s, 3H,

OCH_3), 7.09 (bs, 1H, CONH) ppm. ^{13}C NMR (100 MHz, $CDCl_3$): δ 26.33, 30.34, 33.80, 34.98, 51.87, 171.11, 172.77 ppm. HRMS-ESI (m/z): $[M+H]^+$ calcd for $C_7H_{12}N_2O_3$, 172.0848. found, 173.0924. IR (ATR): $\bar{\nu}$ 3704, 3272, 3212, 2958, 2841, 1723, 1657, 1577, 1440, 1407, 1371, 1295, 1266, 1227, 1195, 1172, 1112, 1056, 1017, 978, 909, 884, 841, 740 cm^{-1} . HPLC: Method 2: t_r : 4.23 min (97.6% at 210 nm). $[\alpha]_D^{20} +32.9$ (c 0.33, MeOH).

Methyl ((R)-aziridine-2-carbonyl)-D-phenylalaninate (**9c**, $C_{13}H_{16}N_2O_3$)

The compound was synthesized according to the general procedure B. The product was purified via flash column chromatography (CH_2Cl_2 :MeOH = 20:1), yielding 0.450 g (67.9%) of **9c** as white crystals. mp 95.7–98.2 °C. R_f : 0.24 (CH_2Cl_2 :MeOH = 20:1). 1H NMR (400 MHz, MeOD): δ 1.82 (bs, 2H, aziridine CH_2), 2.53 (dd, J 5.5 Hz, 3.2 Hz, 1H, aziridine CH), 3.01 (dd, J 13.8 Hz, 8.8 Hz, 1H, CH_2Ph), 3.20 (dd, J 13.8 Hz, 5.6 Hz, 1H, CH_2Ph), 3.71 (s, 3H, OCH_3), 4.73 (dd, J 8.8 Hz, 5.6 Hz, 1H, $CHCH_2Ph$), 7.19–7.34 (m, 5H, Ph) ppm. ^{13}C NMR (100 MHz, MeOD): δ 26.18, 30.24, 38.45, 52.77, 55.31, 127.98, 129.54, 130.23, 137.98, 172.72, 173.17 ppm. MS m/z (relative intensity): 271,24 ($[M+Na]^+$, 100%). HRMS-ESI (m/z): $[M+H]^+$ calcd for $C_{13}H_{16}N_2O_3$, 248.1161. found, 249.1230. IR (ATR): $\bar{\nu}$ = 3703, 3208, 2945, 1736, 1661, 1543, 1446, 1401, 1362, 1219, 1164, 1110, 1055, 1012, 954, 914, 827, 699 cm^{-1} . HPLC: Method 2: t_r : 14.84 min (99.3% at 210 nm). $[\alpha]_D^{20} +18.7$ (c 0.31, MeOH).

Methyl ((R)-aziridine-2-carbonyl)-D-valinate (**9d**)

The compound was synthesized according to the general procedure C, yielding 0.365 mg (75.5%) of **9d**. mp 93.5–94.8 °C. R_f : 0.42 (CH_2Cl_2 :MeOH = 9:1 + 3% Et_3N). 1H NMR (400 MHz, MeOD): δ 0.96 (d, J 6.9 Hz, 3H, $CH(CH_3)_2$), 0.96 (d, J 6.9 Hz, 3H, $CH(CH_3)_2$), 1.85 (bs, 2H, aziridine CH_2), 2.16 (qqd, J 6.9 Hz, 6.9 Hz, 5.9 Hz, 1H, $CH(CH_3)_2$), 2.66 (dd, J 5.4 Hz, 3.1 Hz, 1H, aziridine CH), 3.72 (s, 3H, $COOCH_3$), 4.37 (d, J 5.9 Hz, 1H, $CH-COOCH_3$) ppm. ^{13}C NMR (100 MHz, MeOD): δ 18.53, 19.57, 26.37, 30.33, 32.00, 52.67, 59.53, 173.17, 173.44 ppm. HRMS-ESI (m/z): $[M-H]^-$ calcd for $C_9H_{16}N_2O_3$, 200.1161. found, 199.1081. IR (ATR): $\bar{\nu}$ 3704, 3278, 3202, 2967, 1731, 1666, 1558, 1463, 1439, 1391, 1346, 1318, 1285, 1235, 1203, 1160, 1069, 1005, 940, 891, 840, 822, 722 cm^{-1} . HPLC: Method 2: t_r : 6.98 min (95.0% at 195 nm). $[\alpha]_D^{20} +114.7$ (c = 0.34, MeOH).

Dimethyl ((R)-aziridine-2-carbonyl)-D-glutamate (**9e**, $C_{10}H_{16}N_2O_5$)

The compound was synthesized according to the general procedure B. The product was purified via flash column chromatography using Al_2O_3 (CH_2Cl_2 :MeOH = 50:1), which was gradually replaced by CH_2Cl_2 :MeOH = 20:1, yielding 0.124 g (48.9%) of **9d** as colourless viscous oil. R_f : 0.38 (CH_2Cl_2 :MeOH = 9:1). 1H NMR (400 MHz,

CDCl₃): δ 1.84 (bs, 1H, aziridine CH₂), 1.88–2.07 (m, 2H, aziridine CH₂ and CH₂COO), 2.16–2.28 (m, 1H, CH₂COO), 2.31–2.48 (m, 2H, CH₂), 2.54 (bs, 1H, aziridine CH), 3.69 (s, 3H, OCH₃), 3.76 (s, 3H, OCH₃), 4.58–4.68 (m, 1H, CHCO), 7.16 (d, *J* 8.0 Hz, 1H, CONH) ppm. ¹³C NMR (100 MHz, CDCl₃): δ 26.73, 27.35, 30.13, 30.38, 51.64, 52.00, 52.69, 171.27, 172.13, 173.25 ppm. HRMS-ESI (*m/z*): [M+H]⁺ calcd for C₁₀H₁₆N₂O₅, 244.1059. found, 245.1131. IR (ATR): $\bar{\nu}$ 3704, 3668, 2970, 2868, 1736, 1657, 1535, 1437, 1341, 1215, 1170, 1056, 1011, 833 cm⁻¹. HPLC: Method 2: t_r: 5.66 min (96.6% at 210 nm). [α]_D²⁰ +54.0 (c 0.25, MeOH).

2. 5. General Procedure for Removal of Methyl protection group (procedure C, compounds 2a–2e)

To a cooled solution of **8a–8e** (1.00 equiv.) in MeOH (20 mL), 0.1 M LiOH solution (5.00 equiv.) was added drop-wise at 0 °C. After the completion of the reaction (monitored by TLC), the pH of the reaction mixture was adjusted to pH=7 with a 0.1 M HCl solution and the solvent was evaporated under reduced pressure.

((R)-aziridine-2-carbonyl)-D-alanine (2a)

The compound was synthesized according to the general procedure C. The product was purified via flash column chromatography (EtOAc:MeOH:H₂O = 4:2:1), yielding 0.080 g (98%) of **2a** as lightly yellow crystals. mp thermal T_{dec} > 250 °C. R_f: 0.26 (EtOAc:MeOH:H₂O = 4:2:1). ¹H NMR (400 MHz, MeOD): δ 1.36 (d, *J* 7.1 Hz, 3H, CHCH₃), 1.78–1.87 (m, 2H, aziridine CH₂), 2.58 (dd, *J* 5.8 Hz, 3.2 Hz, 1H, aziridine CH), 4.24 (q, *J* 7.1 Hz, 1H, CHCH₃) ppm. ¹³C NMR (100 MHz, MeOD): δ 19.48, 26.17, 30.85, 52.26, 171.82, 179.66 ppm. HRMS-ESI (*m/z*): [M+H]⁺ calcd for C₆H₁₀N₂O₃:158.0691. found, 159.0764. IR (ATR): $\bar{\nu}$ 3659, 3324, 3100, 2970, 2872, 1643, 1606, 1562, 1457, 1405, 1365, 1319, 1269, 1236, 1167, 1104, 1054, 1017, 981, 942, 919, 868, 837, 756, 685 cm⁻¹. HPLC: Method 2: t_r: 3.46 min (95.1% at 195 nm). [α]_D²⁰ +66.7 (c 0.33, MeOH).

(R)-3-(aziridine-2-carboxamido)propanoic acid (2b, C₆H₁₀N₂O₃)

The compound was synthesized according to the general procedure C. The product was purified via flash column chromatography (EtOAc:MeOH:H₂O = 4:2:1), yielding 0.096 g (65%) **2b** as white crystals. mp thermal T_{dec} > 250 °C. R_f: 0.24 (EtOAc:MeOH:H₂O = 4:2:1). ¹H NMR (400 MHz, D₂O): δ 1.83 (d, *J* 3.1 Hz, 1H, aziridine CH₂), 1.87 (d, *J* 6.0 Hz, 1H, aziridine CH₂), 2.36 (t, *J* 6.9 Hz, 2H, CH₂COO), 2.56 (dd, *J* 6.0 Hz, 3.1 Hz, 1H, aziridine CH), 3.39 (t, *J* 6.9 Hz, 2H, NHCH₂) ppm. ¹³C NMR (100 MHz, D₂O): δ 24.82, 29.59, 33.32, 53.91, 172.50, 180.15 ppm. HRMS-ESI (*m/z*): [M+H]⁺ calcd for C₆H₁₀N₂O₃, 158.0691. found, 159.0764. IR (ATR): $\bar{\nu}$ 3702,

3659, 3258, 3086, 2975, 2871, 1646, 1556, 1404, 1312, 1259, 1162, 1126, 1061, 1016, 908, 832, 622 cm⁻¹. [α]_D²⁰ +143.6 (c 0.30, MeOH).

((R)-aziridine-2-carbonyl)-D-phenylalanine (2c)

The compound was synthesized according to the general procedure C. The product was purified via flash column chromatography (EtOAc:MeOH:H₂O = 4:1:1), yielding 0.163 g (71.4%) of **2c** as white crystals. mp thermal T_{dec} > 180 °C. R_f: 0.37 (EtOAc:MeOH:H₂O = 4:2:1). ¹H NMR (400 MHz, D₂O): δ 1.75 (bs, 2H, aziridine CH_ACH_B), 2.52 (bs, 1H, aziridine CH), 2.91 (dd, *J* 14.0 Hz, 8.8 Hz, 1H, CH₂Ph), 3.18 (dd, *J* 14.0 Hz, 4.9 Hz, 1H, CH₂Ph), 4.45 (dd, *J* 8.8 Hz, 4.9 Hz, 1H, CHCOO), 7.21–7.36 (m, 5H, Ph) ppm. ¹³C NMR (100 MHz, MeOH): δ 25.05, 29.48, 38.63, 54.38, 126.89, 128.61, 129.30, 137.59, 172.08, 178.00 ppm. HRMS-ESI: [M-H]⁻ calc for C₁₂H₁₄N₂O₃, 234.1004. found, 233.0928. IR (ATR): $\bar{\nu}$ 3371, 2976, 2117, 2005, 1595, 1418, 1273, 1162, 1106, 1056, 923, 696 cm⁻¹. HPLC: Method 2: t_r: 7.22 min (86.5% at 210 nm). [α]_D²⁰ +25.7 (c 0.30, MeOH).

((R)-aziridine-2-carbonyl)-D-valine (2d, C₉H₁₆N₂O₃)

The compound was synthesized according to the general procedure C. The product was purified via flash column chromatography (EtOAc:MeOH:H₂O = 4:2:1), yielding 0.109 g (63.7%) of **2e**. mp thermal T_{dec} > 220 °C. R_f: 0.31 (EtOAc:MeOH:H₂O = 4:2:1). ¹H NMR (400 MHz, D₂O): δ 0.87 (d, *J* 7.0 Hz, 3H, CH(CH₃)₂), 0.90 (d, *J* 7.0 Hz, 3H, CH(CH₃)₂), 1.84 (d, *J* 3.4 Hz, 1H, aziridine CH₂), 1.90 (d, *J* 5.9 Hz, 1H, aziridine CH₂), 2.10 (qqd, *J* 7.0 Hz, 7.0 Hz, 5.6 Hz, 1H, CH(CH₃)₂), 2.68 (dd, *J* 5.9 Hz, 3.4 Hz, 1H, aziridine CH), 4.06 (d, *J* 5.6 Hz, 1H, CHCOO) ppm. ¹³C NMR (100 MHz, MeOD): δ 18.36, 20.33, 26.30, 30.89, 32.67, 61.76, 172.45, 178.40 ppm. HRMS-ESI: [M-H]⁻ calc for C₈H₁₃N₂O₃, 185.0932. found, 185.0933. IR (ATR): $\bar{\nu}$ 3707, 3666, 3288, 2970, 2871, 1644, 1590, 1546, 1424, 1235, 1162, 1057, 1011, 939, 915, 835, 752, 669 cm⁻¹. HPLC: Method 2: t_r: 4.11 min (85.4% at 210 nm). [α]_D²⁰ +52.6 (c 0.33, MeOH).

Benzyl aziridine-2-carboxylate (10)

To a cooled solution of **7** (15.01 g, 40.84 mmol, 1.00 equiv.) in acetonitrile (400 mL) benzyl bromide (4.85 mL, 40.8 mmol, 1 equiv.) was added. After stirring at room temperature for 3 h, solvent was evaporated under reduced pressure. The oily residue was dissolved in CH₂Cl₂ (200 mL), and washed with water (200 mL), and brine (150 mL). The organic phase was dried over anhydrous Na₂SO₄, the drying agent was filtered off and the solvent was evaporated under reduced pressure to obtain 14.34 g (83.4%) viscous oil, which was used for further reaction without additional purification. The trityl group was removed following the standard procedure B, yielding 0.697 g (83.9%) of **10** as colourless oil. R_f: 0.32 (hexane:EtOAc = 1:2 + 3% Et₃N). ¹H NMR (400 MHz, CDCl₃): δ 1.89 (dd, *J* 5.5 Hz, 1.4 Hz, 1H, CH₂), 2.04 (dd, *J* 2.9 Hz, 1.4 Hz, 1H, CH₂), 2.58

(dd, J 5.5 Hz, 2.9 Hz, 1H, CH), 5.18 (d, J 12.3 Hz, 1H, CH₂Ph), 5.22 (d, J 12.3 Hz, 1H, CH₂Ph), 7.32–7.42 (m, 5H, Ph) ppm. IR (ATR): $\bar{\nu}$ 3285, 3229, 3065, 3037, 1725, 1564, 1456, 1402, 1360, 1187, 1113, 1007, 970, 871, 825, 744, 697 cm⁻¹. ¹H NMR spectra was found to be identical to the ones described in ref.¹⁹

Benzyl (R)-1-((tert-butoxycarbonyl)-D-alanyl)aziridine-2-carboxylate (11)

The compound was synthesized according to the general procedure A. The product was purified via flash column chromatography (hexane:EtOAc = 3:1), yielding 0.471 g (25.7%) of **11** as viscous oil. R_f : 0.23 (MF: hexane:EtOAc = 3:1). ¹H NMR (400 MHz, CDCl₃): δ 1.42 (s, 9H, C(CH₃)₃), 1.45 (d, J 7.1 Hz, 3H, CHCH₃), 2.63 (dd, J 3.1 Hz, 1.9 Hz, 1H, aziridine CH₂), 2.72 (dd, J 5.8 Hz, 1.9 Hz, 1H, aziridine CH₂), 3.28 (dd, J 5.8 Hz, 3.1 Hz, 1H, aziridine CH), 4.30 (qd, J 7.1 Hz, 7.1 Hz, 1H, CHCH₃), 5.01 (d, J 7.1 Hz, 1H, CONH), 5.20 (s, 2H, CH₂Ph), 7.32–7.42 (m, 5H, Ph) ppm. ¹³C NMR (100 MHz, MeOD): δ 18.98, 28.42, 30.96, 34.45, 51.30, 67.71, 80.02, 128.65, 128.73, 128.78 (overlapping of signals), 135.06, 155.33, 168.31, 184.23 ppm. HRMS-ESI (m/z): [M+H]⁺ calcd for C₁₈H₂₄N₂O₅, 348.1685. found, 349.1753. IR (ATR): $\bar{\nu}$ 3354, 3177, 3036, 1972, 2935, 2878, 1681, 1497, 1452, 1367, 1324, 1273, 1248, 1168, 1063, 1018, 944, 913, 854, 750, 699 cm⁻¹. HPLC: Method 3. t_r : 6.64 min (95.1% at 220 nm). [α]_D²⁰ +84.4 (c = 0.27, EtOAc).

Benzyl (R)-1-(((benzyloxy)carbonyl)-D-phenylalanyl)aziridine-2-carboxylate (13)

The compound was synthesized according to the general procedure B. The product was purified via flash column chromatography (hexane:EtOAc = 3:1), yielding 1.67 g (92.4%) **11** as viscous oil. R_f : 0.62 (hexane:EtOAc = 1:1). ¹H NMR (400 MHz, CDCl₃): δ 2.57–2.63 (m, 2H, aziridine CH₂), 3.05–3.15 (m, 2H, CH₂Ph and aziridine CH), 3.25 (dd, J 14.0 Hz, 5.8 Hz, 1H, CH₂Ph), 4.55–4.63 (m, 1H, CH), 5.0 (d, J 12.3 Hz, 1H, OCH₂Ph), 5.06 (d, J 12.3 Hz, 1H, OCH₂Ph), 5.17 (s, 2H, OCH₂Ph), 5.23 (d, J 8.1 Hz, 1H, OCONH), 7.12–7.42 (m, 15H, 3 × Ph) ppm. ¹³C NMR (100 MHz, MeOD): δ 31.68, 35.63, 38.98, 58.87, 67.65, 68.65, 127.87, 128.75, 129.04, 129.57, 129.61, 129.76 (overlapping of 3 signals), 130.52, 136.95, 138.32, 138.70, 158.37, 169.74, 183.98 ppm. MS m/z (relative intensity): 480.6 ([M+Na]⁺, 100%). HRMS-ESI: [M-H]⁺ calcd for C₂₇H₂₆N₂O₅, 458.1842. found, 457.1773. IR (ATR): $\bar{\nu}$ 3328, 3062, 3033, 2952, 1699, 1505, 1452, 1375, 1248, 1191, 1077, 1047, 1027, 910, 747, 696 cm⁻¹. HPLC: Method 3. t_r : 9.24 min (70.5% at 210 nm). [α]_D²⁰ +45.6 (c = 0.43, EtOAc).

3. Results and Discussion

There are two common strategies concerning the synthesis of aziridine containing peptides. The first strate-

gy starts from a partially protected serine dipeptides followed by cyclization. This approach is reportedly less efficient because several various by-products are formed in the cyclization step.^{27,28,37,39,47} The second more efficient strategy, which starts from the aziridine-2-carboxylic acid, was therefore used.^{34,39,48}

The synthesis of N-terminal aziridine containing dipeptides **2a-e** was straightforward and high yielding. It started with the introduction of a trityl protective group onto D-Ser-OMe (**4**)⁴⁹ in 82% yield followed by cyclization using methanesulfonyl chloride^{50,51} to obtain the aziridine **6** in 72% yield. Next, the screening of different bases (NaOH, LiOH, KOH) and solvents (THF, CH₃CN and EtOH) for the subsequent saponification was performed. 1M KOH in THF was found to be the most optimal in terms of yield (99%) and purity of the final carboxylate **7**. Our attempts to neutralize **7** with diluted HCl or acetic acid were not successful because of its decomposition upon neutralization. Potassium salt was therefore used in the coupling reactions between (*R*)-aziridine-2-carboxylate **7** and different amino acids to obtain the aziridine containing dipeptide products **8a-e** in 24–65% yield.³⁹ Acidolytic treatment of **8** following the literature reported procedures^{37,39} using CF₃COOH in CH₂Cl₂/MeOH or CH₂Cl₂ generated a mixture of degradation products and was therefore unsatisfactory for the synthesis of larger amounts of final products. The analysis of reaction mixtures by NMR confirmed that the products were present in very small quantities, which we were unable to purify. Difficulties in removing trityl as well as Boc protective group from aziridine peptides using CF₃COOH, formic acid or HCl have been previously reported.^{1,7,36} Instead, optimization of reaction conditions following different reaction procedures demonstrated that the addition of Et₃SiH to the reaction mixture was essential for the successful reaction.⁵² Hence, reductive deprotection of N-tritylaziridines **8** and basification with triethylamine prior to isolation was successfully applied to obtain deprotected aziridines **9a-e** in 31–98% yield. Finally, basic hydrolysis with LiOH in a mixture of MeOH and H₂O yielded compounds **2a-d** in 31–98% yield. A reaction with Glu derivative **9e** yielded **2e** as confirmed by MS and NMR analysis. However, a product was unstable on silica or Al₂O₃ and purification was therefore not possible. The majority of compounds were stable for up to 3 weeks if stored under argon and in the fridge. However, after prolonged storage, significant decomposition was observed, which is in agreement with literature data. It is not uncommon that many aziridine derivatives exhibit sequence-dependent instability in both reaction and purification steps, as well as on storage. This is caused by self-protonation to generate a reactive aziridinium species that subsequently decompose (Figure 3).^{31,53,54}

The synthesis of compounds with general structure **3** was started from benzyl protected (*R*)-aziridine-2-carboxylic acid **10** which was then coupled with Boc-D-Ala and

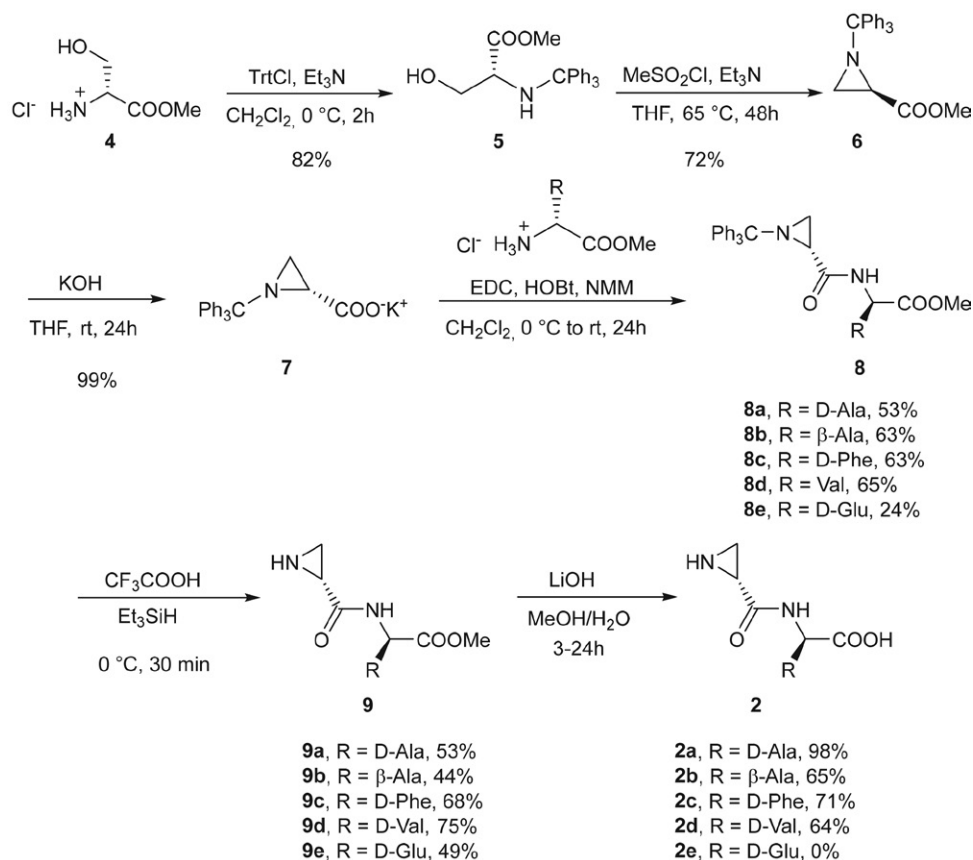


Figure 3. Synthesis of aziridine containing dipeptides.

Cbz-D-Phe to obtain *tert*-butoxycarbonyl and benzyloxycarbonyl protected dipeptides **11** and **13** in 26% and 32% yields, respectively. N-acylated aziridine derivatives have major issues with stability due to acylation and subsequent lower electronic density of the aziridine ring.²⁵ It was therefore expected that the removal of a protective group could potentially yield unstable compounds if free NH₂ group was present. Boc and Cbz protective groups were therefore chosen because they are easy to remove to hypothetical products **12** and **14** that have NH₂ groups in the form of a HCl salt or as a zwitterion, respectively. However, the deprotection of Boc to obtain **12** using CF₃COOH or

HCl in anhydrous THF or diethyl ether did not provide us with the final product and only a mixture of unidentifiable compounds could be isolated. NMR analysis indicated that the opening of the aziridine ring could be the cause. Interestingly, NMR analysis also indicated that the opening of the aziridine ring is favoured compared to the removal of Boc protective group at concentrations of HCl below 0.1 M. Deprotection under neutral conditions using catalytic hydrogenation was next applied to remove both benzyl protective groups from **13** and to yield **14** in "zwitterionic" form. However, a mixture of unidentifiable products was obtained, again (Figure 4).

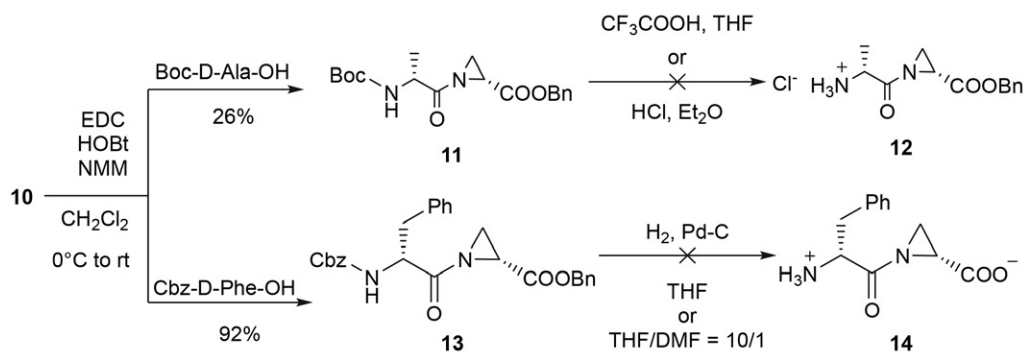


Figure 4. Study on the preparation of **12** and **14**.

4. Conclusions

In conclusion, fully deprotected aziridine-containing dipeptides can be easily synthesized from trityl protected aziridine-carboxylic acid. In most cases, the deprotection of the trityl group from the aziridine ring and final hydrolysis proceeds smoothly in moderate to high yields. However, significant decomposition of deprotected dipeptides was observed after 3 weeks even if stored under argon in the fridge. The synthesis of derivatives with aziridine-2-carboxylic acid in place of a second amino acid in the dipeptide sequence was not possible due to the instability of the acylated aziridine ring in the presence of a free amino group.

Acknowledgement

This research was funded by Slovenian Research Agency (ARRS, research core funding no. P1-566 0208).

Author Contribution

All authors contributed to the study conception and design. Material preparation, data collection and analysis were performed by Samo Kuzmič and Rok Frlan. The first draft of the manuscript was written by Rok Frlan and all authors commented on previous versions of the manuscript. All authors read and approved the final manuscript. The authors declare no competing financial interest.

5. References

1. A. Burger, in: E. Jucker (Ed.): *Isosterism and bioisosterism in drug design*, in *Progress in Drug Research*, Birkhäuser, Basel, **1991**, pp. 287–371. DOI:10.1007/978-3-0348-7139-6_7
2. Peptidomimetic, in: G. Detlev, R. Klaus (Eds.): *Encyclopedic Reference of Genomics and Proteomics in Molecular Medicine*, Springer, Berlin, Heidelberg, **2006**, pp. 1377–1378. DOI:10.1007/3-540-29623-9_8175
3. J. Vagner, H. Qu, V. J. Hraby, *Curr. Opin. Chem. Biol.* **2008**, *12*, 292–296. DOI:10.1016/j.cbpa.2008.03.009
4. R. A. Bauer, *Drug Discov. Today* **2015**, *20*, 1061–1073. DOI:10.1016/j.drudis.2015.05.005
5. R. Mah, J. R. Thomas, C. M. Shafer, *Bioorg. Med. Chem. Lett.* **2014**, *24*, 33–39. DOI:10.1016/j.bmcl.2013.10.003
6. F. M. D. Ismail, D. O. Levitsky, V. M. Dembitsky, *Eur. J. Med. Chem.* **2009**, *44*, 3373–3387. DOI:10.1016/j.ejmech.2009.05.013
7. K. Okawa, K. Nakajima, *Biopolymers* **1981**, *20*, 1811–1821. DOI:10.1002/bip.1981.360200906
8. S. G. Singh, *Mini-Rev. Med. Chem.* **2016**, *16*, 892–904. DOI:10.2174/1389557515666150709122244
9. R. R. Gupta, M. Kumar, V. Gupta, in: *Three-Membered Heterocycles*, in *Heterocyclic Chemistry*, Springer, Berlin, Heidelberg, **1998**, pp. 275–355. DOI:10.1007/978-3-642-72276-9_6
10. L. Gate, K. D. Tew, in: B. R. Minev (Ed.): *Alkylating Agents, in Cancer Management in Man: Chemotherapy, Biological Therapy, Hyperthermia and Supporting Measures*, Springer, Netherlands, **2011**, pp. 61–85. DOI:10.1007/978-90-481-9704-0_4
11. A. R. Tyler, H. Mosaei, S. Morton, P. G. Waddell, C. Wills, W. McFarlane, J. Gray, M. Goodfellow, J. Errington, N. Allenby, N. Zenkin, M. J. Hall, *J. Nat. Prod.* **2017**, *80*, 1558–1562. DOI:10.1021/acs.jnatprod.7b00082
12. H. Konno, K. Kubo, H. Makabe, E. Toshiro, N. Hinoda, K. Nosaka, K. Akaji, *Tetrahedron* **2007**, *63*, 9502–9513. DOI:10.1016/j.tet.2007.06.082
13. P. Fey, R. Chartomatsidou, W. Kiefer, J. C. Mottram, C. Kersten, T. Schirmeister, *Eur. J. Med. Chem.* **2018**, *156*, 587–597. DOI:10.1016/j.ejmech.2018.07.012
14. R. Vicik, K. Baumann, J. Ziebuhr, T. Schirmeister, *ChemMedChem* **2006**, *1*, 1126–1141. DOI:10.1002/cmdc.200600106
15. T. Schirmeister, *Arch. Pharm.* **1996**, *329*, 239–244. DOI:10.1002/ardp.19963290504
16. B. Degel, P. Staib, S. Rohrer, J. Scheiber, E. Martina, C. Büchold, K. Baumann, J. Morschhäuser, T. Schirmeister, *ChemMedChem* **2008**, *3*, 302–315. DOI:10.1002/cmdc.200700101
17. B. Saha, J. P. Nandy, S. Shukla, I. Siddiqui, J. Iqbal, *J. Org. Chem.* **2002**, *67*, 7858–7860. DOI:10.1021/jo0109826
18. E. Martina, N. Stiefl, B. Degel, F. Schulz, A. Breuning, M. Schiller, R. Vicik, K. Baumann, J. Ziebuhr, T. Schirmeister, *Bioorg. Med. Chem. Lett.* **2005**, *15*, 5365–5369. DOI:10.1016/j.bmcl.2005.09.012
19. D. R. Latypova, L. I. Vlasova, N. Z. Baibulatova, A. N. Lobov, L. V. Spirikhin, V. A. Dokichev, *Chem. Heterocycl. Compd.* **2008**, *44*, 996–1002. DOI:10.1007/s10593-008-0146-x
20. K. J. M. Beresford, N. J. Church, D. W. Young, *Org. Biomol. Chem.* **2006**, *4*, 2888–2897. DOI:10.1039/B605026N
21. D. A. Ryan, D. Y. Gin, *J. Am. Chem. Soc.* **2008**, vol. 130, p. 15228. DOI:10.1021/ja804589j
22. D. M. Hodgson, B. Štefane, T. J. Miles, J. Witherington, *Chem. Commun.* **2004**, 2234–2235. DOI:10.1039/B409486G
23. Y.-Q. Zhang, F. Bohle, R. Bleith, G. Schnakenburg, S. Grimme, A. Gansäuer, *Angew. Chem. Int. Ed.* **2018**, *57*, 13528–13532. DOI:10.1002/anie.201808034
24. K. Bajaj, D. S. Agarwal, R. Sakhuja, G. G. Pillai, *Org. Biomol. Chem.* **2018**, *16*, 4311–4319. DOI:10.1039/C8OB00676H
25. A. P. Spork, T. J. Donohoe, *Org. Biomol. Chem.* **2015**, *13*, 8545–8549. DOI:10.1039/C5OB00856E
26. S. Armaroli, G. Cardillo, L. Gentilucci, M. Gianotti, A. A. Tolomelli, *Org. Lett.* **2000**, *2*, 1105–1107. DOI:10.1021/ol005659o
27. N. D. Ide, D. P. Galonić, W. A. Donk, D. Y. Gin, *Synlett* **2005**, 2011–2014. DOI:10.1055/s-2005-871972
28. R. S. Schwab, P. H. Schneider, *Tetrahedron* **2012**, *68*, 10449–10455. DOI:10.1016/j.tet.2012.08.082
29. M. M. Joullié, S. Berritt, E. Hamel, *Tetrahedron Lett.* **2011**, *52*, 2136–2139. DOI:10.1016/j.tetlet.2010.11.165
30. F. B. Dyer, C. -M. Park, R. Joseph, P. Garner, *J. Am. Chem. Soc.* **2011**, *133*, 20033–20035. DOI:10.1021/ja207133t

31. C. J. White, A. K. Yudin, *Org. Lett.* **2012**, *14*, 2898–2901. DOI:10.1021/ol301178r
32. C. J. White, J. L. Hickey, C. C. G. Scully, A. K. Yudin, *J. Am. Chem. Soc.* **2014**, *136*, 3728–3731. DOI:10.1021/ja412256f
33. T. M. Vishwanatha, N. Narendra, V. V. Sureshbabu, *Tetrahedron Lett.* **2011**, *52*, 5620–5624. DOI:10.1016/j.tetlet.2011.08.090
34. U. Roehn, J. Becaud, L. Mu, A. Srinivasan, T. Stellfeld, A. Fitzner, K. Graham, L. Dinkelborg, A. P. Schubiger, S. M. Ametamey, *J. Fluor. Chem.* **2009**, *130*, 902–912. DOI:10.1016/j.jfluchem.2009.07.003
35. B. Schweitzer-Chaput, M. Keita, T. Milcent, S. Ongeri, B. Crousse, *Tetrahedron* **2012**, *68*, 7028–7034. DOI:10.1016/j.tet.2012.06.093
36. A. Korn, S. Rudolph-Böhner, L. Moroder, *Tetrahedron* **1994**, *50*, 1717–1730. DOI:10.1016/S0040-4020(01)80847-4
37. D. P. Galonić, N. D. Ide, W. A. Donk, D. Y. Gin, *J. Am. Chem. Soc.* **2005**, *127*, 7359–7369. DOI:10.1021/ja050304r
38. S. Sun, I. Tirota, N. Zia, C. A. Hutton, *Aust. J. Chem.* **2014**, *67*, 411–415. DOI:10.1071/CH13464
39. F. Polyak, T. Dorofeeva, R. Sturkovich, Y. Goldberg, *Synth. Commun.* **1991**, *21*, 239–248. DOI:10.1080/00397919108020818
40. C. Sheng, W. Zhang, *Curr. Med. Chem.* **2011**, *18*, 733–766. DOI:10.2174/092986711794480113
41. T. Schirmeister, *J. Med. Chem.* **1999**, *42*, 560–572. DOI:10.1021/jm981061z
42. E. Kuru, A. Radkov, X. Meng, A. Egan, L. Alvarez, A. Dowson, G. Booher, E. Breukink, D. I. Roper, F. Cava, W. Vollmer, Y. Brun, M. S. VanNieuwenhze, *ACS Chem. Biol.* **2019**, *14*, 2745–2756. DOI:10.1021/acscchembio.9b00664
43. J. N. Sangshetti, S. S. Joshi, R. H. Patil, M. G. Moloney, D. B. Shinde, *Curr. Pharm. Des.* **2017**, *23*, 3164–3196. DOI:10.2174/1381612823666170214115048
44. B. T. Zeng, Z. G. Zhao, X. L. Liu, Y. Shi, *Chin. Chem. Lett.* **2008**, *19*, 33–36. DOI:10.1016/j.cclet.2007.10.051
45. D. Foley, M. Pieri, R. Pettecrew, R. Price, S. Miles, H. K. Lam, P. Bailey, D. Meredith, *Org. Biomol. Chem.* **2009**, *7*, 3652–3656. DOI:10.1039/b909221h
46. Y. -C. Wu, J. Zhu, *Org. Lett.* **2009**, *11*, 5558–5561. DOI:10.1021/ol9024919
47. D. A. Ryan, D. Y. Gin, *J. Am. Chem. Soc.* **2008**, *130*, 15228–15229. DOI:10.1021/ja804589j
48. C. Lambert, H. Viehe, *Tetrahedron Lett.* **1985**, *26*, 4439–4442. DOI:10.1016/S0040-4039(00)88924-8
49. K. D. Park, J. P. Stables, R. Liu, H. Kohn, *Org. Biomol. Chem.* **2010**, *8*, 2803–2813. DOI:10.1039/c000987c
50. K. O'Brien, K. O. Proinsias, F. Kelleher, *Tetrahedron* **2014**, *70*, 5082–5092. DOI:10.1016/j.tet.2014.06.011
51. K. Koteva, A. M. King, A. Capretta, G.D. Wright, *Angew. Chem.-Int. Ed.* **2016**, *55*, 2210–2212. DOI:10.1002/anie.201510057
52. E. Vedejs, A. Klapars, D. L. Warner, A. H. Weiss, *J. Org. Chem.* **2001**, *66*, 7542–7546. DOI:10.1021/jo0106243
53. C. Palomo, J. M. Aizpurua, E. Balentova, A. Jimenez, J. Oyarbide, R. M. Fratila, J. I. Miranda, *Org. Lett.* **2007**, *9*, 101–104. DOI:10.1021/ol0626241
54. S. N. Filigheddu, M. Taddei, *Tetrahedron Lett.* **1998**, *39*, 3857–3860. DOI:10.1016/S0040-4039(98)00632-7

Povzetek

V prispevku so opisani optimizirani pogoji za sintezo dipeptidov, ki vsebujejo popolnoma odščiten (2R)-aziridin. Priprava popolnoma zaščitenih N- in C- terminalnih dipeptidov, ki vsebujejo aziridin, je enostavna in poteka z visokim izkoristkom za večino spojin, medtem ko je njihova popolna odščita možna le za C-terminalne analoge. Odstranjevanje zaščite z N-terminalnih derivatov z uporabo standardnih postopkov peptidne kemije se je izkazalo kot težko, saj vodi do mešanice nedoločljivih produktov. Opisane molekule imajo velik potencial kot gradniki v sintezni kemiji, na področju kemijske biologije, kot kovalentni modifikatorji in kot biomarkerji.



Except when otherwise noted, articles in this journal are published under the terms and conditions of the Creative Commons Attribution 4.0 International License

Scientific paper

Magnetic Nanoparticles Linked to Pyridinium Hydrotribromide Groups as Catalysts for Selective Oxidation of Alcohols and Protection of Alcohols

Sonia Tabari, Ali Reza Pourali* and Ehsan Nazarzadeh Zare

School of Chemistry, Damghan University, Damghan 36715-364, Iran

* Corresponding author: E-mail: pourali@du.ac.ir

+982335220095; Fax: +982335220095. ORCID: 0000-0002-8918-1818

Received: 02-18-2021

Abstract

In this research, a novel magnetic nanocatalyst based on iron oxide nanoparticles linked with pyridinium hydrotribromide ($\text{Fe}_3\text{O}_4@ \text{PyHBr}_3$) was synthesized in three steps. In the first step, 3-(aminopropyl)triethoxysilane (APTES) was reacted with 4-(bromomethyl)pyridine hydrobromide. In the second step, the product obtained in the first step was reacted with iron oxide nanoparticles. In the last step, a grinding reaction was carried out with KBr and HIO_4 in a mortar. The $\text{Fe}_3\text{O}_4@ \text{PyHBr}_3$ nanocatalyst was characterized by FT-IR, CHN, XRD, SEM, TGA and VSM analysis. The magnetic nanocatalyst was used as a catalyst for the selective oxidation of alcohols to aldehydes and ketones using 30% H_2O_2 as oxidant in a short time and with high yields. Moreover, no overoxidation of the alcohols was observed. The nanocatalyst was efficiently recycled in five consecutive cycles without significant loss of its catalytic activity. Moreover, trimethylsilylation and tetrahydropyranlation of alcohols were carried out in the presence of this nanocatalyst.

Keywords: Magnetic nanoparticles; pyridinium hydrotribromide; oxidation of alcohols; tetrahydropyranlation; trimethylsilylation

1. Introduction

Organic tribromides are widely used as selective bromination reagents for various organic functionalities.^{1–6} In addition, they are also used as efficient catalysts for the oxidation of some organic substrates such as alcohols,⁷ aldehydes,⁸ and sulfides,^{9,10} trimethylsilylation^{11,12} or tetrahydropyranlation¹³ of alcohols, α -thiocyanation¹⁴ or thioacetalization¹⁵ of ketones, and the synthesis of heterocyclic rings.¹⁶ Typical organic tribromides include tetrabutylammonium tribromide (TBATB),^{2,9} pyridinium hydrotribromide (PyHTB),^{4–6,14} benzyltrimethylammonium tribromide (BTMATB),⁷ 2-carboxyethyltriphenylphosphonium tribromide (CTPTB)¹¹ and benzyltriphenylphosphonium tribromide.^{13,15} These reagents have attracted considerable attention in organic synthesis and have proven to be leaders over liquid bromine such as N-bromosuccinimide (NBS), Br_2/HBr and other conventional bromination reagents due to their ease of use, mildness, efficiency and selectivity. They are stable and crystalline

solids that can release a stoichiometric amount of bromine. Other advantages include their recoverability and reusability when used as catalysts.

In recent years, much attention has been paid to Br_3^- immobilized on polymers,^{1,17} magnetic nanoparticles (MNP)^{16,18–23} and other solid supports.²⁴ The organic tribromide immobilized on magnetic nanoparticles can be easily separated from the reaction mixture using an external magnet without the need for filtration or other workup processes. The use of magnetic nanoparticles (MNP) as a catalyst support enables efficient recovery of the catalyst. This can solve the problems associated with nanoparticle separation.^{25,26} Although several immobilized tribromides have been synthesized, in most cases their preparation involves the use of liquid Br_2 and/or HBr ,^{16,21–24} which leads to an environmental problem.

Numerous improved methods for the synthesis of organic tribromides have been described in the literature and are considered to be environmentally friendly. These improved methods use an oxidation system for the oxida-

tion of organic bromide to organic tribromides, such as $(\text{NH}_4)_2\text{S}_2\text{O}_8/\text{H}^+$,⁷ NaOCl/H^+ ,¹⁰ KMnO_4/H^+ ,¹¹ H_5IO_6 ,¹² oxone[®],¹⁵ MCPBA,³ H_2MoO_4 or $\text{V}_2\text{O}_5/\text{H}_2\text{O}_2$,²⁷ and CAN.²⁸ Despite the introduction of these oxidation methods in the literature, many of the recently reported methods for the synthesis of magnetic nanoparticles (MNP)^{16,21–23} or polymer-assisted^{1,17} bromine sources involve liquid Br_2 and/or HBr , which continues to cause environmental problems. Therefore, the development of newer strategies that do not require the use of molecular bromine or metals and strong mineral acids remains a challenge for the synthesis of immobilized organic tribromides, especially nanoparticle-based magnetic catalysts.

In this work, we reported a novel method for the synthesis of pyridinium hydrotribromide on magnetic Fe_3O_4 nanoparticles (MNPs) by oxidation of immobilized organic bromide to tribromide using periodic acid (H_5IO_6) as a cheap, nontoxic, efficient, and easy-to-use oxidant. $\text{Fe}_3\text{O}_4@$ PyHBr₃ was used as a catalyst for the selective oxidation of alcohols to aldehydes and ketones using 30% H_2O_2 . In addition, trimethylsilylation and tetrahydropyranlation of alcohols were carried out in the presence of this catalyst.

2. Experimental Section

2.1. Instrumentation, Analysis and Raw Materials

All products were known and characterized by comparing their physical data with those of known samples or by their spectral data. Infrared spectra (IR) were recorded on the KBr matrix using a Perkin Elmer RXI spectrometer. Nuclear magnetic resonance (NMR) spectra were recorded in $\text{DMSO}-d_6$ or CDCl_3 using tetramethylsilane (TMS) as an internal standard with a Bruker Avance DRX spectrometer. Thermogravimetric analysis (TGA) was performed using a Bahr Thermo analyze STA 503 instrument. XRD patterns were recorded using a Bruker D8-Advance diffractometer. Elemental analysis was performed using a Costech Elemental Combustion System CHNS-O (ECS 4010). Field emission scanning electron microscopy (FESEM) was performed using a MIRA3 TESCAN instrument. A Lakeshore 7400 vibratory magnetometer (VSM) was used to characterize magnetic properties at room temperature.

2.2. Preparation of the Fe_3O_4 Magnetic Nanoparticles (Fe_3O_4 MNP)

Fe_3O_4 -MNP were prepared according to the method described in the literature.²⁹ Typically, $\text{FeCl}_3 \cdot 6\text{H}_2\text{O}$ (5.406 g, 20 mmol) and $\text{FeCl}_2 \cdot 4\text{H}_2\text{O}$ (1.988 g, 10 mmol) were dissolved in distilled water (75 mL) in a three-neck flask (250 mL) under an inert atmosphere. Then NaOH solution (10 M, 10 mL) was added with vigorous mechanical stirring until the pH of the solution was increased to

11. The temperature of the mixture was raised to 80 °C. The mixture was kept in an ultrasonic bath for 1 hour. The black precipitate was separated with a magnet, washed with double-distilled water to neutrality, then washed with ethanol (2 × 20 mL) and dried at 60 °C in a vacuum oven.

2.3. Synthesis of $\text{Fe}_3\text{O}_4@$ PyHBr₃ MNP

(3-Aminopropyl)triethoxysilane (APTES) (1.771 g, 8 mmol) was dissolved in CHCl_3 (10 mL) and then 4-(bromomethyl) pyridine hydrobromide (2.024 g, 8 mmol) was added to the solution. The mixture was heated under reflux for 24 hours. Then the solvent was evaporated and the product (APTES-MPyHBr) was dried. Then magnetic Fe_3O_4 nanoparticles (1.2 g) were added to APTES-MPyHBr (2 g) in toluene (10 mL) and the mixture was heated for 12 hours under N_2 atmosphere under reflux conditions. The magnetic $\text{Fe}_3\text{O}_4@$ PyHBr nanoparticles were isolated with a magnet, washed with CH_2Cl_2 (3 × 20 mL), and dried at 60 °C in a vacuum oven.

Analytical data for $\text{Fe}_3\text{O}_4@$ PyHBr: C, 18.65; H, 3.02; N, 4.86%.

A mixture of $\text{Fe}_3\text{O}_4@$ PyHBr (3 g), KBr (1.27 g, 10.67 mmol), and HIO_4 (2.70 g, 14.07 mmol) were ground in a mortar for 30 min at room temperature. The color of the mixture was changed from orange to dark brown. The $\text{Fe}_3\text{O}_4@$ PyHBr₃ MNPs were washed with H_2O (3 × 15 mL) and then with ethanol (3 × 15 mL) and dried at 60 °C in a vacuum oven. Analytical data for $\text{Fe}_3\text{O}_4@$ PyHBr₃: C, 12.96; H, 1.67; N, 3.65%.

2.4. Typical Procedures

2.4.1. Oxidation of 4-nitrobenzyl Alcohol

Magnetic nanocatalyst $\text{Fe}_3\text{O}_4@$ PyHBr₃ (0.070 g, 0.091 mmol) was added to a mixture of 4-nitrobenzyl alcohol (0.153 g, 1 mmol) and H_2O (1 mL), followed by the addition of hydrogen peroxide (30%, 0.45 mL, 4 mmol), and the resulting mixture was heated to 50 °C. The progress of the reaction was monitored by TLC using n-hexane-ethyl acetate (7:3) as eluent. After completion of the reaction (75 min), the catalyst was separated using a magnet. Then the reaction mixture was extracted with diethyl ether (3 × 5 mL). The organic layer was dried over anhydrous magnesium sulfate and evaporated under reduced pressure to give 4-nitrobenzaldehyde (0.128 g, 0.85 mmol); mp: 104–106 °C.

FT-IR (KBr, cm^{-1}): ν 3107 (w), 3066 (w), 2956(s), 2926 (s), 2854 (s), 1706 (s), 1608 (s), 1544 (s), 1454 (s), 1378 (s), 1360 (s), 1346 (s), 1197 (s), 852 (s), 818 (s), 740 (s).

¹HNMR ($\text{DMSO}-d_6$, ppm): δ 8.12–8.17 (m, 2H), 8.39–8.42 (m, 2H), 10.15 (s, 1H).

2.4.2. Trimethylsilylation of Benzyl Alcohol

The magnetic $\text{Fe}_3\text{O}_4@$ PyHBr₃ nanocatalyst (0.070 g, 0.091 mmol) was added to a mixture of benzyl alcohol

(0.108 g, 1 mmol) and HMDS (0.113 g, 0.7 mmol) in CH_2Cl_2 (5 mL), and the resulting mixture was mechanically stirred at room temperature. The progress of the reaction was monitored by TLC using n-hexane-ethyl acetate (7:3) as eluent. After completion of the reaction (10 min), the catalyst was separated using a magnet. Then the reaction mixture was extracted with diethyl ether (3×5 mL). The organic layer was dried over anhydrous magnesium sulfate and evaporated under reduced pressure to give benzyl trimethylsilyl ether (0.166 g, 0.92 mmol).

Colorless liquid; b.p. 93 °C.

FT-IR (KBr, cm^{-1}): ν 2957, 1250, 1094, 727.

^1H NMR (CDCl_3 , ppm): δ 0.18 (s, 9H), 4.29 (s, 2H), 7.26–7.40 (m, 5H); ^{13}C NMR (CDCl_3) δ : 0.09, 70.7, 127.1, 127.3, 129.0, 145.7.

2. 4. 3. Tetrahydropyranylation of 4-chlorobenzyl Alcohol

The magnetic nanocatalyst $\text{Fe}_3\text{O}_4@ \text{PyHBr}_3$ (0.070 g, 0.091 mmol) was added to a mixture of 4-chlorobenzyl alcohol (0.143 g, 1 mmol) and DHP (0.126 g, 1.5 mmol) in CH_3CN (5 mL), and the resulting mixture was mechanically stirred at room temperature. The progress of the reaction was monitored by TLC using n-hexane-ethyl acetate (7:3) as eluent. After completion of the reaction (3 h), the catalyst was separated using a magnet. Then the reaction mixture was extracted with diethyl ether (3×5 mL). The organic layer was dried over anhydrous magne-

sium sulfate and evaporated under reduced pressure to afford 4-chlorobenzyl tetrahydropyranyl ether (0.213 g, 0.94 mmol).

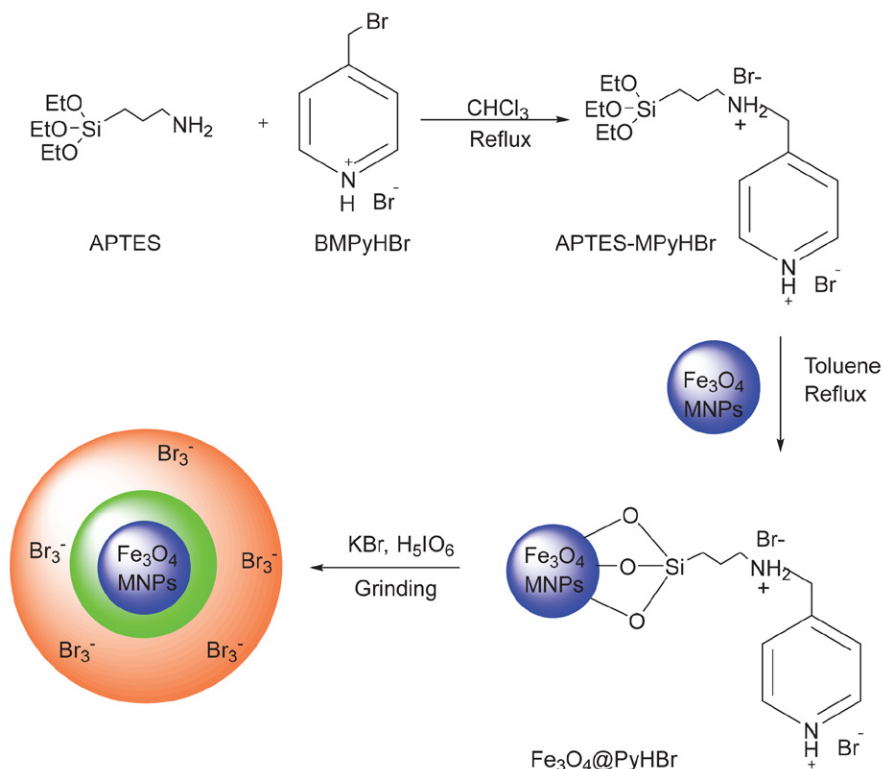
FT-IR (KBr, cm^{-1}): ν 3070 (w), 2944(s), 2871 (s), 1442 (m), 1343 (m), 1128 (s), 1029 (s), 754 (s).

^1H NMR (CDCl_3 , ppm): δ 1.57–1.60 (m, 2H), 1.64–1.65 (m, 2H), 1.66–1.78 (m, 2H), 3.56–3.60 (m, 1H), 3.91–3.96 (m, 1H), 4.50–4.52 (d, 1H), 4.72–4.74 (t, 1H), 4.77–4.80 (d, 1H), 7.30–7.36 (m, 4H).

3. Results and Discussion

The synthesis of Fe_3O_4 MNP linked to pyridinium hydrotribromide ($\text{Fe}_3\text{O}_4@ \text{PyHBr}_3$) was carried out in three steps. In the first step, APTES-MPyHBr was synthesized by the reaction of 3-(aminopropyl)triethoxysilane (APTES) with 4-(bromomethyl)pyridine hydrobromide (MPyHBr) in CHCl_3 under reflux conditions. In the second step, APTES-MPyHBr was reacted with Fe_3O_4 magnetic nanoparticles to obtain the $\text{Fe}_3\text{O}_4@ \text{PyHBr}$ magnetic nanoparticles. In the last step, the mixture of $\text{Fe}_3\text{O}_4@ \text{PyHBr}$, KBr and HIO_4 was ground in a mortar to obtain the magnetic $\text{Fe}_3\text{O}_4@ \text{PyHBr}_3$ nanoparticles (Scheme 1).

$\text{Fe}_3\text{O}_4@ \text{PyHBr}_3$ was characterized by FT-IR, CHN, XRD, SEM, TGA and VSM analysis. The FT-IR spectra confirmed the preparation of the magnetic nanocatalyst at each step (Figure 1). The FTIR spectrum of $\text{Fe}_3\text{O}_4@ \text{PyHBr}_3$ nanoparticles (Figure 2) showed two sharp absorption



Scheme 1. Synthesis of magnetic $\text{Fe}_3\text{O}_4@ \text{PyHBr}_3$ nanoparticles.

bands at 2927 cm^{-1} and 1222 cm^{-1} , which are related to stretching and bending vibrations of CH_2 groups, respectively. The broad absorption bands at 1045 cm^{-1} and 1115 cm^{-1} are related to the stretching vibrations of the Si-O bonds. The absorption band at 3421 cm^{-1} is due to the N-H group overlaid by the hydroxyl group (Fe^3O_4 has a OH-rich surface). In addition, the absorption band at 585 cm^{-1} is due to the stretching vibration of the Fe-O bond in Fe_3O_4 .

The elemental analysis results (CHN) showed that the carbon, hydrogen and nitrogen contents of $\text{Fe}_3\text{O}_4@\text{PyHBr}_3$ were 12.96, 1.67 and 3.65 (wt%), respectively, corresponding to a loading of 1.3 mmol of nitrogen groups (Br_3^- content) per gram of catalyst. The analytical results of CHN showed that the carbon, hydrogen and nitrogen contents of $\text{Fe}_3\text{O}_4@\text{PyHBr}$ (monobromide) were 18.65, 3.02 and 4.86 (wt%), respectively. Comparing the total weight percentages of carbon, hydrogen and nitrogen in $\text{Fe}_3\text{O}_4@\text{PyHBr}$ and $\text{Fe}_3\text{O}_4@\text{PyHBr}_3$, the ratio is 1.45, which is very close to 1.36, calculated from the chemical formula of the organic segment of these compounds.

X-ray powder diffraction (XRD) analysis was performed to characterize the crystalline structure of $\text{Fe}_3\text{O}_4@\text{PyHBr}_3$. The XRD pattern of $\text{Fe}_3\text{O}_4@\text{PyHBr}_3$ showed a semi-crystalline nature compared to the XRD pattern of Fe_3O_4 (not shown here).²⁶

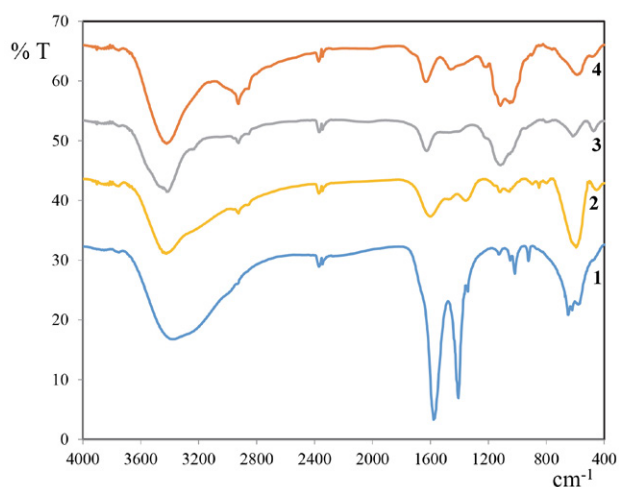


Figure 1. FT-IR spectrum of Fe_3O_4 MNPs (1); $\text{Fe}_3\text{O}_4@\text{PyHBr}$ MNPs (2); $\text{Fe}_3\text{O}_4@\text{PyHBr}_3$ MNPs (3); APTES-MPYHBr (4).

The image of the magnetic $\text{Fe}_3\text{O}_4@\text{PyHBr}_3$ nanoparticles in the field emission scanning electron microscope (FESEM) shows a spherical structure with a particle size in the range of 35–40 nm (Figure 4).

The magnetic properties of Fe_3O_4 and $\text{Fe}_3\text{O}_4@\text{PyHBr}_3$ were studied using a vibrating sample magnetometer (VSM) at room temperature. The saturation magnetization of $\text{Fe}_3\text{O}_4@\text{PyHBr}_3\text{-MNP}$ was about 50 emu g^{-1} , which was

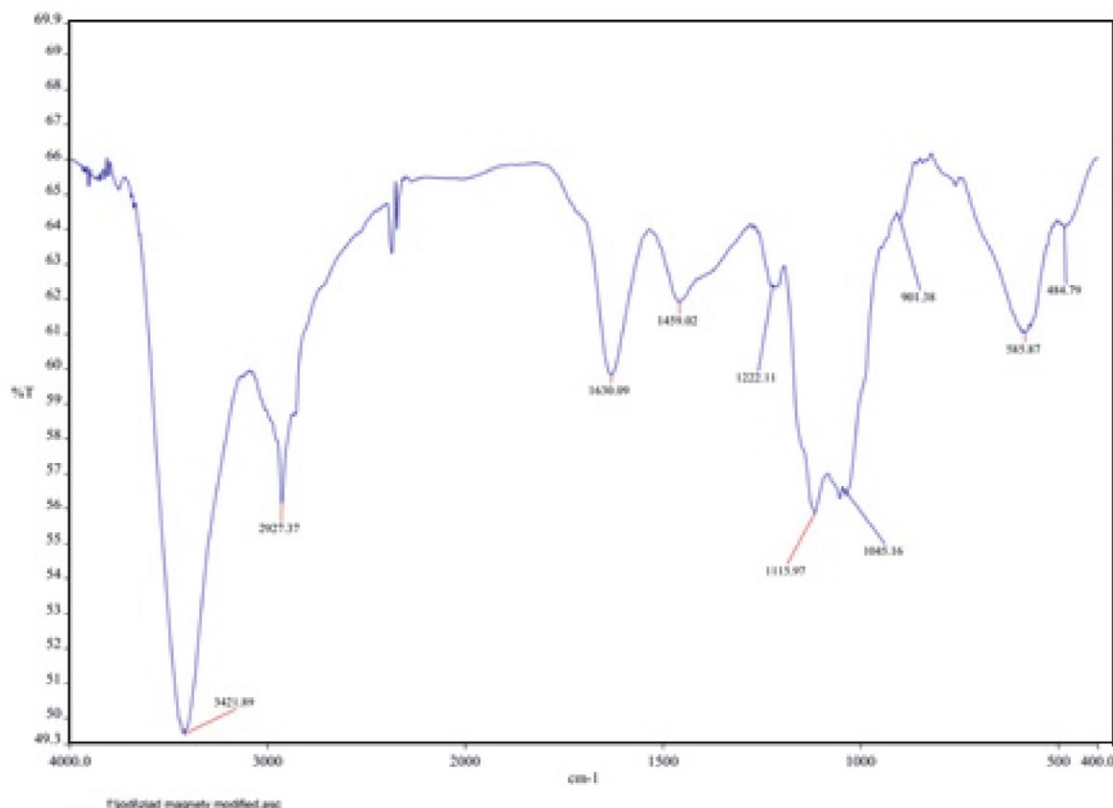


Figure 2. FT-IR spectrum of $\text{Fe}_3\text{O}_4@\text{PyHBr}_3$ MNP (KBr).

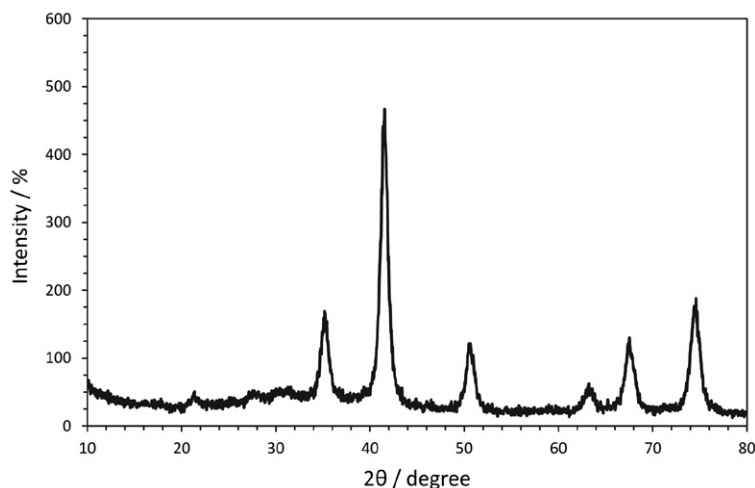


Figure 3. XRD pattern of $\text{Fe}_3\text{O}_4@ \text{PyHBr}_3$ MNP.

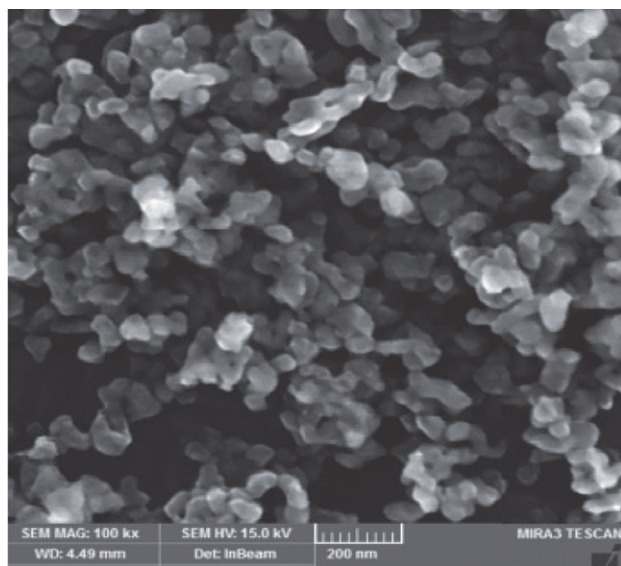


Figure 4. Field emission scanning electron microscopy (FESEM) micrograph of $\text{Fe}_3\text{O}_4@ \text{PyHBr}_3$ MNP.

lower than that of pure Fe_3O_4 -MNP (74 emu g^{-1}) (not shown here). The decrease in the measured saturation magnetization was due to the presence of organics around Fe_3O_4 .

The thermal stability of the Fe_3O_4 MNPs and $\text{Fe}_3\text{O}_4@ \text{PyHBr}_3$ MNPs was also investigated. Comparison of the respective thermograms showed that no significant weight loss was observed for the Fe_3O_4 thermogram (Figure 5, black thermogram). On the other hand, the thermograms of $\text{Fe}_3\text{O}_4@ \text{PyHBr}_3$ showed three weight loss steps of about 15 % in the range of 200–600 °C, which could be attributed to the evaporation of residues trapped in the samples and the removal of the organic content.

The oxidation of alcohol is one of the most important reactions in the synthesis of organic compounds.^{30–38} Some of these reactions occur under difficult conditions, such as high temperatures, the use of unfavorable solvents, and the use of toxic oxidizing agents, including transition metal compounds that produce harmful by-products. Usually, compounds such as chromic acid, di-

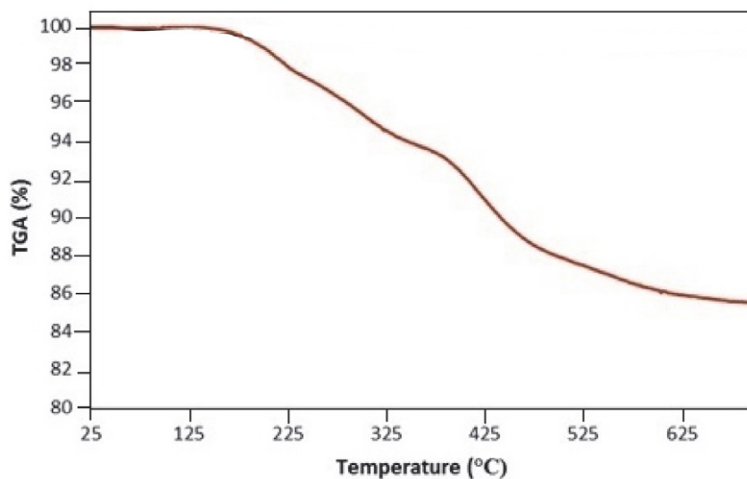
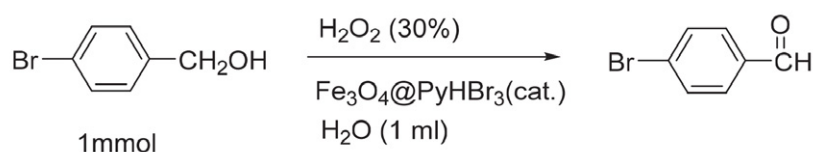


Figure 5. Thermograms of pure Fe_3O_4 MNPs (black) and $\text{Fe}_3\text{O}_4@ \text{PyHBr}_3$ MNPs (red).

chromate/ H^+ , PCC, PDC are used to oxidize alcohols.³⁴ Due to the limitations of existing methods, efforts are being made to perform environmentally friendly reactions. The goal of these efforts is to catalytically oxidize alcohols using low-cost green oxidants such as air, oxygen, and hydrogen peroxide, and using heterogeneous (solid) catalysts and harmless and environmentally friendly solvents. Hydrogen peroxide (H_2O_2) is an attractive oxidant for liquid-phase reactions.^{34–38} This water-soluble oxidant is safe, inexpensive, and has a high oxygen content that does not require a buffer. In addition, it is considered a green and environmentally friendly oxidant because it releases water as a byproduct. After the synthesis of pyridinium hydrotribromide on Fe_3O_4 MNP, we investigated the effectiveness of $Fe_3O_4@PyHBr_3$ MNP as a catalyst in the oxidation of benzyl alcohols with 30% hydrogen peroxide. To optimize the reaction conditions, the oxidation of 4-bromobenzyl alcohol with different amounts of 30% hydrogen peroxide, different amounts of $Fe_3O_4@PyHBr_3$ catalyst and different reaction temperatures were investigated (Scheme 2).



Scheme 2. Oxidation of 4-bromobenzyl alcohol by hydrogen peroxide in the presence of $Fe_3O_4@PyHBr_3$.

To determine the optimum amount of hydrogen peroxide, the reaction of 4-bromobenzyl alcohol (1 mmol) in various molar ratios of H_2O_2 to alcohol was studied in the presence of 0.020 g catalyst at 50 °C in H_2O (1 mL)

Table 1. Optimization of the oxidation of 4-bromobenzyl alcohol by 30% H_2O_2 .^a

Entry	$\frac{H_2O_2}{\text{alcohol}}$ Molar ratio	Catalyst (g)	T (°C)	Reaction time (min)	Conversion (%)
1	1	0.02	50	120	30
2	2	0.02	50	120	45
3	3	0.02	50	90	50
4	4	0.02	50	60	60
5	4	0.04	50	45	80
6	4	0.07	50	20	100
7	4	0.07	25	60	65
8	4	0.07	70	20	90
9	4	0.08	50	18	100
10	3	0.07	50	40	80
11	4	0.23 ^b	50	40	96
12	4	–	50	240	5

^a The reaction was performed using 4-bromobenzyl alcohol (1 mmol) in H_2O (1 mL). ^b Fe_3O_4 MNP were used as a catalyst.

(Table 1, entries 1–4). According to the results, it was found that the reaction had a higher conversion (60 %) and a shorter time (60 minutes) when 4 mmol of H_2O_2 was used, but this time additional amounts of catalyst were used to increase the conversion (Table 1, entries 5–6 and 9). The results show that increasing the amount of catalyst leads to an increase in conversion. The effects of reaction temperature were also studied (Table 1, entries 6–8). At 25 °C and 70 °C, the conversions were 65 % and 90 %, respectively.

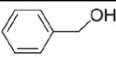
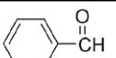
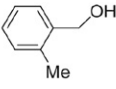
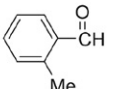
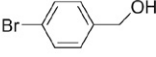
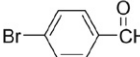
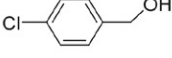
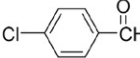
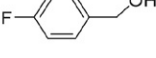
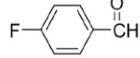
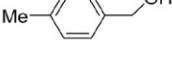
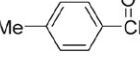
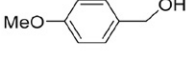
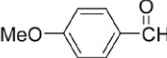
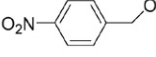
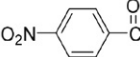
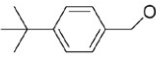
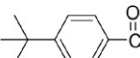
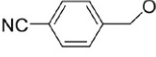
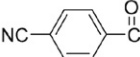
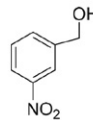
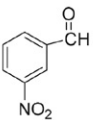
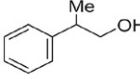
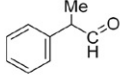
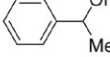
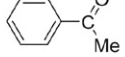
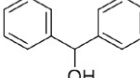
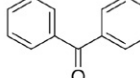
The reaction was also carried out with Fe_3O_4 (0.23 g), and it was found that the reaction time was longer than that of the $Fe_3O_4@PyHBr_3$ catalyst (Table 1, entry 11). When the reaction was carried out without catalyst, the desired product was produced after 4 hours with a very low conversion (Table 1, entry 12).

According to the results in Table 1, the optimum conditions for this reaction are 4 mmol 30% hydrogen peroxide as oxidant, 0.070 g (9.1 mol%) $Fe_3O_4@PyHBr_3$ as catalyst at 50 °C (Table 1, entry 6). Under these optimum conditions, 4-bromobenzaldehyde was obtained in 20 min

with an excellent conversion rate of 100 %. The reaction of benzyl alcohol and other benzyl alcohols with electron donor and electron acceptor substituents was carried out under these optimum conditions, and the results are shown in Table 2. Benzyl alcohols with electron donor group (Table 2, entries 2, 6, 7, 9) were oxidized in shorter time than alcohols with strong electron acceptor group (Table 2, entries 8, 10, 11). The secondary benzyl alcohols (entries 13 and 14) were also oxidized to the corresponding ketones. The study showed that the oxidation time of the non-benzyl alcohol 2-phenyl-1-propanol was longer than that of the benzyl alcohols (Table 2, entry 12). Moreover, no additional oxidation to the carboxylic acid was observed for the primary alcohols, which is one reason for the mildness and selectivity of the present method.

After the reaction was completed, the catalyst was separated with a magnet. To evaluate the performance of $Fe_3O_4@PyHBr_3$ catalyst after recovery, the catalyst used in each reaction was separated with a magnet and reused in the next reaction after rinsing with CH_2Cl_2 (3×5 ml). The catalyst recovery results for the oxidation of 4-bromobenzyl alcohol showed that the catalyst could be used for up to 5 cycles without significantly reducing the reaction yield (Table 3).

Table 2. Fe₃O₄@PyHBr₃ MNP catalyze the oxidation of alcohols to carbonyl compounds.^a

Entry	Substrate	Product	Reaction Time (min.)	yield ^b (%)
1			20	88
2			10	95
3			20	95
4			30	93
5			35	90
6			25	98
7			15	90
8			75	85
9			18	86
10			60	97
11			60	88
12			80	91
13			35	94
14			10	95

^a Reaction conditions: substrate (1 mmol), Fe₃O₄@PyHBr₃ MNP (0.07 g, 9.1 molar%), aqueous hydrogen peroxide (4 mmol, 30%), H₂O (1 mL), at 50 °C. ^b Isolated yields.

Table 3. Recyclability of Fe₃O₄@PyHBr₃ catalyst.

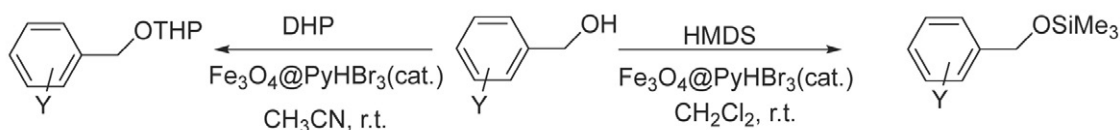
Run	1	2	3	4	5
Yield (%)	95	90	88	85	80
Time (min)	20	20	20	20	20

The efficiency of this catalyst can also be illustrated by comparing the results obtained in this study for the oxidation of benzyl alcohol with those published in the literature. For this purpose, several recent methods are given in Table 4 along with the temperature, reaction time, and yield.

Table 4. Comparison of the present method with other methods reported for the oxidation of benzyl alcohol.

Reagents	Reaction time (min)	Temperature (°C)	Yield%
PVP-Br ₃	70	r.t.	94 ¹⁷
Silica-supported *DABCO-Br ₃	60	80	95 ²⁴
H ₂ O ₂ (1.1 eq), {[K.18-Crown-6]Br ₃ } _n	30	80	81 ³⁶
H ₂ O ₂ (3 eq), **DBDMH (0/5 eq)	120	60	85 ³⁷
H ₂ O ₂ (1.3eq), MgFe ₂ O ₄ MNPs	55	60	88 ³⁸
H ₂ O ₂ , K ₈ [BW ₁₁ O ₃₉ H] ₁₃ H ₂ O	360	90	98 ³⁴
H ₂ O ₂ , VHPW/MCM-41/NH ₂	480	80	97 ³⁵
H ₂ O ₂ , Fe ₃ O ₄ @PyHBr ₃	20	50	88 ^{this work}

*DABCO = 1,4-diazabicyclo[2.2.2]octane **DBDMH = 1,3-Dibromo-5,5-dimethylhydantoin

**Scheme 3.** Trimethylsilylation and tetrahydropyranylation of benzyl alcohols in the presence of Fe₃O₄@PyHBr₃

Trimethylsilylation and tetrahydropyranylation of benzyl alcohols were studied in the presence of Fe₃O₄@PyHBr₃ (Scheme 3). According to the optimum conditions obtained for 4-bromobenzyl alcohol, trimethylsilylation of various alcohols was carried out with Fe₃O₄@PyHBr₃ (0.07 g, 9.1 mol%), HMDS (0.7 mmol) in CH₂Cl₂ (5 mL) at room temperature (Scheme 3, Table 5). Tetrahydropyranylation of alcohols was also carried out with Fe₃O₄@PyHBr₃ (0.07 g, 9.1 mol%), DHP (1.5 mmol) in CH₃CN (5 mL) at room temperature (Scheme 3, Table 5).

These results show that for all types of benzyl alcohols with electron donor and electron acceptor substituents, the corresponding trimethylsilyl ethers were obtained in short time and in excellent yield. The reaction times are shorter for benzyl alcohols with electron donor substituents than for benzyl alcohols with strong electron acceptor substituents.

These results showed that the corresponding tetrahydropyranyl ethers were obtained in high yields for primary benzyl alcohols with electron acceptor or electron donor substitutions. However, the reaction times were shorter for benzyl alcohols with electron donor substitutions.

4. Conclusions

In summary, the magnetic Fe₃O₄@PyHBr₃ nanocatalyst was prepared and characterized by FTIR, CHN, TGA, XRD, FE-SEM and VSM analyzes. The efficiency of this magnetic nanocatalyst in the oxidation reaction of alcohols to aldehydes and ketones was investigated. The results showed that Fe₃O₄@PyHBr₃ was very effective as a catalyst

in the oxidation of alcohols using H₂O₂ as a green oxidant. This method has some advantages, such as very mild reaction conditions, easy separation and reusability of the catalyst, very short reaction times, high yields, and the use of H₂O as a green solvent. No additional oxidation to the carboxylic acid was observed for the primary alcohols, which is one reason for the mildness and selectivity of the present method. The use of this magnetic catalyst in the reactions of trimethylsilylation and tetrahydropyranylation of alcohols was also studied, and it was found to have many advantages, such as easy separation of the catalyst, good yields, and mild reaction conditions.

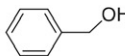
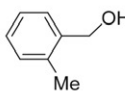
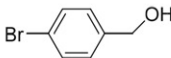
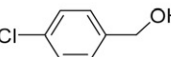
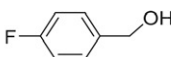
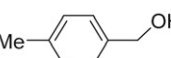
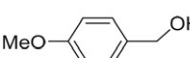
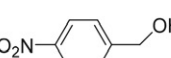
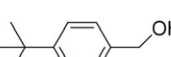
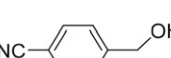
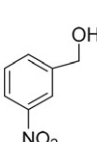
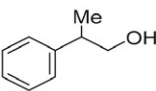
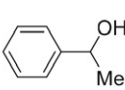
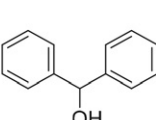
Acknowledgment

The authors gratefully acknowledge financial support for this work from Damghan University.

5. References

- B. Han, Z. Zheng, D. Zheng, L. Zhang, P. Cui, J. Shi, C. Li, *Synth. Commun.* **2019**, *49*, 2512–2520. DOI:10.1080/00397911.2019.1631348
- S. Gao, T. K. Bethel, T. Kakeshpour, G. E. Hubbell, J. E. Jackson, J. J. Tepe, *J. Org. Chem.* **2018**, *83*, 9250–9255. DOI:10.1021/acs.joc.8b01251
- R. R. Dey, B. Paul, S. S. Dhar, *Synth. Commun.* **2015**, *45*, 714–726. DOI:10.1080/00397911.2014.979509
- D. Bliman, M. Pettersson, M. Bood, M. Grötl, *Tetrahedron Lett.* **2014**, *55*, 2929–2931. DOI:10.1016/j.tetlet.2014.03.084
- M. Simurdiak, O. Olukoga, K. Hedberg, *J. Chem. Edu.* **2016**, *93*, 322–325. DOI:10.1021/acs.jchemed.5b00283

Table 5. Fe₃O₄@PyHBr₃ MNP-catalyzed trimethylsilylation and tetrahydropyranylation of alcohols.

Entry	Substrate	Trimethylsilylation ^a		Tetrahydropyranylation ^b	
		Time (min)	Yield ^c (%)	Time (min)	Yield ^c (%)
1		10	92	120	86
2		12	85	150	80
3		10	95	120	96
4		20	88	180	94
5		25	96	200	87
6		10	94	120	92
7		8	96	90	98
8		45	80	245	80
9		10	88	100	95
10		30	80	175	90
11		35	86	210	75
12		20	80	240	70
13		50	82	240	70
14		30	89	150	85

^a Reaction conditions: substrate (1 mmol), Fe₃O₄@ PyHBr₃ (0.07 g, 9.1 molar%), HMDS (0.7 mmol), CH₂Cl₂ (5 mL), at room temperature. ^b Reaction conditions: substrate (1 mmol), Fe₃O₄@ PyHBr₃ (0.07 g, 9.1 molar%), DHP (1.5 mmol), CH₃CN (5 mL), at room temperature. ^c Isolated yield.

6. S.-H. Yang, *Synlett* **2009**, 8, 1351–1352.

DOI:10.1055/s-0029-1216645

7. M. Dey, S. S. Dhar, M. Kalita, *Synth. Commun.* **2013**, 43, 1734–1742.

DOI:10.1080/00397911.2012.666694

8. J. K. Joseph, S. L. Jain, B. Sain, *Catal. Commun.* **2007**, 8, 83–87.

DOI:10.1016/j.catcom.2006.05.035

9. P. Gogoi, S. Hazarika, P. Barrman, *RSC Adv.*, **2015**, 5, 38044–38047.

DOI:10.1039/C5RA04573H

10. M. Dey, R. R. Dey, S. S. Dhar, *Chem. Lett.* **2014**, *43*, 631–633. DOI:10.1246/cl.131192
11. M. Dey, S. S. Dhar, *Green Chem. Lett. Rev.* **2012**, *5*, 639–642. DOI: DOI:10.1080/17518253.2012.692820
12. R. R. Dey, B. Paul, S. S. Dhar, S. Bhattacharjee, *Chem. Lett.* **2014**, *43*, 1545–1547. DOI:10.1246/cl.140564
13. A. R. Hajipour, S. A. Pourmousavi, A. E. Ruoho, *Synth. Commun.* **2005**, *35*, 2889–2894. DOI:10.1080/00397910500297297
14. L. Wu, X. Yang, *Phosphorus, Sulfur Silicon Relat. Elem.* **2012**, *187*, 748–753. DOI:10.1080/10426507.2011.616561
15. A. R. Hajipour, S. A. Pourmousavi, A. E. Ruoho, *Phosphorus, Sulfur Silicon Relat. Elem.* **2007**, *182*, 921–937. DOI:10.1080/1042650601088739
16. A. Kharazmi, R. Ghorbani-Vaghei, S. Alavinia, *ChemistrySelect* **2020**, *5*, 1424–1430. DOI:10.1002/slct.201904697
17. A. Ghorbani-Choghamarani, M. Nikoorazm, B. Tahmasbi, M. Norouzi, *J. Saudi Chem. Soc.* **2017**, *21*, 408–414. DOI:10.1016/j.jscs.2015.08.002
18. N. E. Sodan, A. Hol, O. Caylak, L. Elci, *Acta Chim. Slov.* **2020**, *67*, 375–385. DOI:10.17344/acsi.2018.4636
19. O. Arjmand, M. Ardjmand, A. M. Amani, M. H. Eikani, *Acta Chim. Slov.* **2020**, *67*, 496–506. DOI:10.17344/acsi.2019.5513
20. K. Vasic, Z. Knez, S. Kumar, J. K. Pandey, M. Leitgeb, *Acta Chim. Slov.* **2020**, *67*, 1172–1179. DOI:10.17344/acsi.2020.6065
21. M. Ghobadi, P. Pourmoghaddam Qhazvini, M. Eslami, M. Kazemi, *Synth. Commun.* **2021**, *51*, 325–350. DOI:10.1080/00397911.2020.1829646
22. L. Shiri, M. Kazemi, *Phosphorus, Sulfur Silicon Relat. Elem.*, **2017**, *192*, 1171–1176. DOI:10.1080/10426507.2017.1347654
23. A. Rostami, Y. Navasi, D. Moradi, A. Ghorbani-Choghamarani, *Catal. Commun.* **2014**, *43*, 16–20. DOI:10.1016/j.catcom.2013.08.025
24. F. Matloubi Moghaddam, N. Masoud, B. Koushki Foroushani, S. Saryazdi, N. Ghonouei, E. Daemi, *Sci. Iran., Trans. C: Chem. Chem. Eng.* **2013**, *20*, 598–602. DOI:10.1016/j.scient.2013.02.015
25. M. Ghobadi, M. Kargar Razi, R. Javahershenas, M. Kazemi, *Synth. Commun.* **2021**, *51*, 647–669. DOI:10.1080/00397911.2020.1819328
26. J. Govan, Y. K. Gun'ko, *Nanomaterials*, **2014**, *4*, 222–241. DOI:10.3390/nano4020222
27. U. Bora, M. K. Chaudhuri, D. Dey, S. S. Dhar, *Pure Appl. Chem.* **2001**, *73*, 93–102. DOI:10.1351/pac200173010093
28. R. Borah, A. J. Thakur, *Synth. Commun.* **2007**, *37*, 933–939. DOI:10.1080/00397910601163794
29. Z. Zarnegar, J. Safari, *J. Mol. Struct.*, **2014**, *1072*, 53–60. DOI:10.1016/j.molstruc.2014.04.023
30. Q. L. Luo, W. H. Nan, Y. Li, X. Chen, *ARKIVOC* **2014**, (iv), 350–361. DOI:10.3998/ark.5550190.p008.707
31. A. R. Pourali, M. Tabaeen, S. M. R. Nazifi, *Chin. Chem. Lett.* **2012**, *23*, 21–24. DOI:10.1016/j.ccl.2011.07.022
32. S. Bahrami-Nasab, A. Pourali, *Curr. Chem. Lett.* **2014**, *3*, 43–48. DOI:10.5267/j.ccl.2013.10.004
33. M. A. Zolfigol, A. R. Pourali, S. Sajjadifar, S. Farahmand, *Curr. Catal.* **2013**, *8*, 151–158. DOI:10.2174/2211544711302020009
34. X. Dong, D. Wang, K. Li, Y. Zhen, H. Hu, G. Xue, *Mater. Res. Bull.* **2014**, *57*, 210–220. DOI:10.1016/j.materresbull.2014.05.041
35. W. Zhao, Y. Zhang, B. Ma, Y. Yong Ding, W. Qiu, *Catal. Commun.* **2010**, *11*, 527–531. DOI:10.1016/j.catcom.2009.12.010
36. M. Rasouli, M. A. Zolfigol, M. H. Moslemin, G. Chehardoli, *Green Chem. Lett. Rev.* **2017**, *10*, 117–120. DOI:10.1080/17518253.2017.1306614
37. J. Lee, J. C. Lee, *Lett. Org. Chem.* **2018**, *15*, 895–898. DOI:10.2174/1570178615666180613080548
38. F. Sadri, A. Ramazani, H. Ahankar, S. Taghavi Fardood, P. Azimzadeh Asiabi, M. Khoobi, S. Woo Joo, N. Dayyani, *J. Nanostruct.* **2016**, *6*, 264–272. DOI: 10.22052/JNS.2016.41621

Povzetek

V raziskavi je bil v treh korakih sintetiziran nov magnetni nanokatalizator na osnovi nanodelcev železovega oksida, povezanih s piridinijevim hidrottribromidom ($\text{Fe}_3\text{O}_4@\text{PyHBr}_3$). V prvi stopnji so 3-(aminopropil)trietoksisilan (APTES) reagirali s 4-(bromometil)piridin hidrobromidom. V drugem koraku pa so produkt prve stopnje reagirali z nanodelci železovega oksida. V zadnjem koraku so izvedli reakcijo s pomočjo mletja s KBr in HIO_4 v mlinu, in nanokatalizator $\text{Fe}_3\text{O}_4@\text{PyHBr}_3$ okarakterizirali s FT-IR, CHN, XRD, SEM, TGA in VSM analizo. Magnetni nanokatalizator je bil uporabljen kot katalizator za selektivno oksidacijo alkoholov v aldehide in ketone z uporabo 30 % H_2O_2 kot oksidanta. Reakcija je potekla v kratkem času in z visokimi izkoristki, poleg tega pa niso opazili nadaljnje oksidacije alkoholov. Magnetni nanokatalizator so učinkovito reciklirali v petih zaporednih ciklih brez pomembnejše izgube katalitične aktivnosti. Prav tako so z njim uspešno izvedli trimetilsililiranje in tetrahidropiranilizacijo alkoholov.



Except when otherwise noted, articles in this journal are published under the terms and conditions of the Creative Commons Attribution 4.0 International License

Scientific paper

(E)-1-(4-Hydroxyphenyl)-3-(substituted-phenyl) prop-2-en-1-ones: Synthesis, *In Vitro* Cytotoxic Activity and Molecular Docking Studies

Lütfiye Sirka,¹ Hacer Doğan,¹ Mehmet Refik Bahar,² Eray Çalışkan,³ Suat Tekin,⁴ Harun Uslu,⁵ Kenan Koran,^{1,*} Süleyman Sandal⁴ and Ahmet Orhan Görgülü⁶

¹ Firat University, Faculty of Science, Department of Chemistry, 23119, Elazığ, Turkey

² Osmaniye Korkut Ata University, Faculty of Health Sciences, Department of Nutrition and Dietetics, 80010, Osmaniye, Turkey

³ Bingol University, Faculty of Science, Department of Chemistry, 12000, Bingol, Turkey

⁴ Inonu University, Faculty of Medicine, Department of Physiology, 44280, Malatya, Turkey

⁵ Firat University, Vocational School of Health Services, Department of Anesthesiology, 23600, Elazığ, Turkey

⁶ Marmara University, Faculty of Arts and Sciences, Department of Chemistry, 34722, Istanbul, Turkey

* Corresponding author: E-mail: kkoran@firat.edu.tr

Received: 07-29-2021

Abstract

A series of chalcone compounds (2–11) were designed and synthesized to determine their cytotoxic effects. The structures of 2–11 were fully characterized by their physical and spectral data. The *in vitro* cytotoxic effects of 2–11 were evaluated against human ovarian cancer (A2780), breast cancer (MCF-7) and prostate cancer (PC-3 and LNCaP) cell lines. The activity potentials of compounds were further evaluated through molecular docking studies with AutoDock4 and Vina softwares. All the compounds (except compound 5) showed significant cytotoxic effects at high doses in all cancer cell lines. Among all the compounds studied, one compound i.e. compound 2 demonstrated dose-dependent activity, particularly against A2780/LNCaP cancer cell lines. The most effective compounds 8, 9, 10 and 11 reduced the cell viability of A2780, MCF-7, PC-3 and LNCaP cells by 50–98%, while other compounds 2, 4 and 7 reduced the cell viability of A2780 cells by 70–90% at concentrations of 50 and 100 μ M.

Keywords: Chalcone; cytotoxic; A2780; MTT assay; molecular docking

1. Introduction

The chalcones or phenyl styryl ketones are unsaturated ketones, containing the reactive keto-ethylenic group. Chalcone is an important chemo type that has attracted great research interest for decades due to the abundant natural chalcone-based compounds, the easy synthesis and derivatization, and most importantly, the diverse biological activities of various chalcone-based compounds.^{1–6} The well documented biological activities of chalcones include anti-HIV,⁷ antibacterial,⁸ anti-cancer and antioxidant,^{9–11} antituberculosis agents,¹² anti-prolif-

erative,¹³ antiplatelet,^{14,15} and antimalarial.^{16,17} Numerous studies have attempted to elucidate the mechanisms of action and target interactions responsible for these biological activities.^{18–20} Additionally, these compounds have applications in a variety of areas including nonlinear optical materials,^{21,22} dye sensitized solar cell,^{23,24} and optoelectronic and fluorescence materials.^{25–27}

There are several methods available for the synthesis of chalcones. The Claisen–Schmidt condensation reaction, one of the most widely used chalcone synthesis methods, was used in the synthesis of compounds in this article by using sodium/potassium hydroxide.^{28–36} The base-cata-

lysed other method of chalcone synthesis include Claisen–Schmidt reaction.³⁷ The acid catalyzed methods that have been used to synthesize chalcones includes Friedel–Crafts acylation,³⁸ silica-sulfuric acid,³⁹ dry HCl,^{40, 41} boron trifluoride-diethyletherate (BF₃·Et₂O),⁴² Aldol condensation,⁴³ Suzuki coupling reaction,⁴⁴ Julia–Kocienski olefination⁴⁵ and Wittig reaction.⁴⁶ Among these the direct aldol condensation and Claisen–Schmidt condensation still occupy prominent position.

In addition to the wide potential applications of chalcone derivatives, their ability to be easily isolated from natural plants as well as their synthetic accessibility with many synthesis procedures, as mentioned above, increased the studies on these compounds.

Herein, we have synthesized a series of chalcone derivatives in order to evaluate their cytotoxic effects against four human cancer cell lines namely ovarian (A2780), prostate (PC-3 and LNCaP), and breast (MCF-7). For this reason, the synthesis of target compounds was achieved by the condensation of *para*-hydroxyacetophenone with benzaldehyde using sodium hydroxide as a condensing agent. These compounds **2–11** were confirmed by using mass (MALDI-TOF-MS), FT-IR, elemental analysis, ¹H, ¹³C-APT NMR spectroscopy.

Disruption of the microtubules can lead to apoptosis induction as it has vital importance to the continuation of the cell cycle. Therefore, the literature emphasizes that tubulin inhibitors can be used as effective anticancer drugs.^{47,48} Binding site for colchicine is well determined in the tubule.⁴⁹ Potential tubulin inhibition effects with synthesized molecules were determined by tubulin–colchicine complex. The interactions of compounds with the tubulin–colchicine complex were put forth via molecular docking studies. And their possible anti-cancer properties were investigated against A2780, MCF-7, PC-3 and LNCaP cell lines by using MTT assay method.^{50–53} Our results indicate that these compounds displayed strong cytotoxic activity on these cell lines.

2. Experimental

2.1. Synthesis

All aldehydes and solvents used in the present study were provided by Sigma-Aldrich and Merck. ¹H and ¹³C-APT NMR spectra, infrared analysis and microanalysis were acquired using a Bruker DPX-400 MHz spectrometer, a Perkin Elmer FT-IR spectrometer and a LECO 932 CHNS-O apparatus, respectively. A Bruker microflex LT MALDI-TOF MS spectrometer was used to obtain mass spectra. In cell culture studies, the human prostate (PC-3 and LNCaP), breast (MCF-7), and ovarian cancer cell lines were provided by ATCC (the American Type Culture Collection), new-born calf serum and Dulbecco's modified Eagle's medium (DMEM) were provided by Hyclone (Waltham, MA, USA); and penicillin, trypsin, streptomycin.

Nuve MN-120 as biological safety cabinet, Panasonic as CO₂ Incubator, BioTEK spectrophotometer as microplate reader, Inverted Microscope SOIF-XDS for maintenance and control of cells and Nuve for Sterilization were used.

2.1.1. General Synthesis Method of (*E*)-1-(4-Hydroxyphenyl)-3-(substituted-phenyl)prop-2-en-1-one Compounds

Appropriate *para*-hydroxyacetophenone (1.00 equiv.) was placed in a round bottom flask with ethanol (50 mL) and 60% sodium hydroxide (25 mL). After 30 min, aldehyde (1.015 equiv.) was added to the reaction mixture. The solution was let to stir overnight. The mixture was then poured into an ice/water mixture. Concentrated HCl was added until the solution reached an acidic pH (until about pH 6). Upon addition of the acid a precipitate formed. The precipitate was filtered and washed with plenty of water to pH neutral. The product was recrystallized in ethanol.

(*E*)-1-(4-Hydroxyphenyl)-3-(3-methoxyphenyl)prop-2-en-1-one (**2**)

Yield: 92%; yellow solid; MALDI-MS: *m/z* calcd: 254.29; found: 255.58 [M+H]⁺. FT-IR (KBr) ν_{\max} (cm⁻¹): 3294 ν_{OH} , 3000 and 3018 $\nu_{\text{Ar-CH}}$, 2829, 2903 and 2965 $\nu_{\text{Aliphatic-CH}}$, 1652 $\nu_{\text{C=O}}$, 1512, 1573, 1594 and 1606 $\nu_{\text{C=C}}$. ¹H NMR (DMSO-*d*₆) δ 3.84 (3H, s, H¹⁷ (-OCH₃)), 6.91–6.93 (2H, d, *J* = 8.8 Hz, Ar-H^{3,5}), 7.01–7.04 (1H, d, Ar-H¹⁴), 7.35–7.39 (1H, t, Ar-H¹⁵), 7.42–7.43 (1H, d, Ar-H¹²), 7.47–7.48 (1H, d, Ar-H¹⁶), 7.65–7.69 (1H, d, *J* = 15.6 Hz, H⁹ (-CH=)), 7.91–7.95 (1H, d, *J* = 15.6 Hz, H¹⁰ (=CH-)), 8.09–8.11 (2H, d, *J* = 8.8 Hz, Ar-H^{2,6}), 10.43 (1H, s, H⁷ (Ph-OH)). ¹³C-APT NMR (DMSO-*d*₆) δ 55.75 (C¹⁷ (-OCH₃)), 113.64 (Ar-C¹⁴), 115.85 (Ar-C^{3,5}), 116.90 (Ar-C¹²), 122.01 (Ar-C¹⁶), 122.80 (C⁹ (-CH=)), 129.55 (Ar-C¹), 130.37 (Ar-C¹⁵), 131.73 (Ar-C^{2,6}), 136.77 (Ar-C¹¹), 143.21 (C¹⁰ (=CH-)), 160.11 (Ar-C¹³), 162.71 (Ar-C⁴), 187.59 (C⁸ (-C=O)). Anal. Calcd for C₁₆H₁₄O₃: C, 75.58; H, 5.55. Found: C, 75.69; H, 5.49%.

(*E*)-1-(4-Hydroxyphenyl)-3-(2,4-dimethoxyphenyl)prop-2-en-1-one (**3**)

Yield: 83%; yellow solid; MALDI-MS: *m/z* calcd: 284.31; found: 284.48. FT-IR (KBr) ν_{\max} (cm⁻¹): 3144 ν_{OH} , 3005 and 3013 $\nu_{\text{Ar-CH}}$, 2835 and 2934 $\nu_{\text{Aliphatic-CH}}$, 1645 $\nu_{\text{C=O}}$, 1506, 1541, 1569, 1590 and 1600 $\nu_{\text{C=C}}$. ¹H NMR (DMSO-*d*₆) δ 3.85 (3H, s, H¹⁸ (-OCH₃)), 3.91 (3H, s, H¹⁷ (-OCH₃)), 6.64–6.65 (2H, m, Ar-H¹³, H¹⁵), 6.89–6.91 (2H, d, *J* = 8.4 Hz, Ar-H^{3,5}), 7.72–7.76 (1H, d, *J* = 15.6 Hz, H⁹ (-CH=)), 7.89–7.91 (1H, d, *J* = 8.8 Hz, Ar-H¹⁶), 7.93–7.97 (1H, d, *J* = 15.6 Hz, H¹⁰ (=CH-)), 8.02–8.05 (2H, d, *J* = 8.4 Hz, Ar-H^{2,6}), 10.36 (1H, s, H⁷ (Ph-OH)). ¹³C-APT NMR (DMSO-*d*₆) δ 55.98 (C¹⁸ (-OCH₃)), 56.26 (C¹⁷ (-OCH₃)), 98.74 (Ar-C¹³), 106.70 (Ar-C¹⁵), 115.77 (Ar-C^{3,5}), 116.55

(Ar-C¹¹), 119.55 (C⁹ (-CH=)), 129.96 (Ar-C¹), 130.35 (Ar-C¹⁶), 131.37 (Ar-C^{2,6}), 137.93 (C¹⁰ (=CH-)), 160.22 (Ar-C¹⁴), 162.35 (Ar-C¹²), 163.28 (Ar-C⁴), 187.65 (C⁸ (-C=O)). Anal. Calcd for C₁₇H₁₆O₄: C, 71.82; H, 5.67. Found: C, 71.89; H, 5.72%.

(E)-1-(4-Hydroxyphenyl)-3-(3,4-dimethoxyphenyl) prop-2-en-1-one (4)

Yield: 77%; yellow solid; MALDI-MS: *m/z* calcd: 284.31; found: 285.38 [M+H]⁺. FT-IR (KBr) ν_{\max} (cm⁻¹): 3112 ν_{OH} , 3026 and 3071 $\nu_{\text{Ar-CH}}$, 2835 and 2956 $\nu_{\text{Aliphatic-CH}}$, 1641 $\nu_{\text{C=O}}$, 1506, 1541, 1581, 1591 and 1608 $\nu_{\text{C=C}}$. ¹H NMR (DMSO-*d*₆) δ 3.83 (3H, s, H¹⁸ (-OCH₃)), 3.88 (3H, s, H¹⁷ (-OCH₃)), 6.91–6.93 (2H, d, *J* = 8.8 Hz, Ar-H^{3,5}), 7.01–7.03 (1H, d, *J* = 8.4 Hz, Ar-H¹⁶), 7.35–7.38 (1H, d, *J* = 9.6 Hz, Ar-H¹⁵), 7.53 (1H, s, Ar-H¹²), 7.64–7.68 (1H, d, *J* = 15.6 Hz, H⁹ (-CH=)), 7.79–7.83 (1H, d, *J* = 15.6 Hz, H¹⁰ (=CH-)), 8.08–8.10 (2H, d, *J* = 8.4 Hz, Ar-H^{2,6}), 10.39 (1H, s, H⁷ (Ph-OH)). ¹³C-APT NMR (DMSO-*d*₆) δ 56.05 (C¹⁷ (-OCH₃)), 56.20 (C¹⁸ (-OCH₃)), 111.09 (Ar-C¹²), 112.02 (Ar-C¹⁵), 120.13 (C⁹ (-CH=)), 124.10 (Ar-C¹⁶), 128.20 (Ar-C¹¹), 129.83 (Ar-C¹), 131.54 (Ar-C^{2,6}), 143.68 (C¹⁰ (=CH-)), 149.49 (Ar-C¹³), 151.50 (Ar-C¹⁴), 162.49 (Ar-C⁴), 187.52 (C⁸ (-C=O)). Anal. Calcd for C₁₇H₁₆O₄: C, 71.82; H, 5.67. Found: C, 71.89; H, 5.72%.

(E)-1-(4-Hydroxyphenyl)-3-(2,3,4-trimethoxyphenyl) prop-2-en-1-one (5)

Yield: 79%; yellow solid; MALDI-MS: *m/z* calcd: 314.34; found: 315.42 [M+H]⁺. FT-IR (KBr) ν_{\max} (cm⁻¹): 3392 ν_{OH} , 3005 and 3050 $\nu_{\text{Ar-CH}}$, 2830 and 2938 $\nu_{\text{Aliphatic-CH}}$, 1657 $\nu_{\text{C=O}}$, 1530, 1580, and 1606 $\nu_{\text{C=C}}$. ¹H NMR (DMSO-*d*₆) δ 3.79 (3H, s, H¹⁸ (-OCH₃)), 3.87 (3H, s, H¹⁹ (-OCH₃)), 3.89 (3H, s, H¹⁷ (-OCH₃)), 6.90–6.94 (3H, m, Ar-H^{3,5}), 7.75–7.80 (2H, m, H⁹ (-CH=), Ar-H¹⁶), 7.75–7.88 (1H, d, *J* = 15.6 Hz, H¹⁰ (=CH-)), 8.03–8.05 (2H, d, *J* = 8 Hz, Ar-H^{2,6}), 10.37 (1H, s, H⁷ (Ph-OH)). ¹³C-APT NMR (DMSO-*d*₆) δ 56.51 (C¹⁹ (-OCH₃)), 60.94 (C¹⁸ (-OCH₃)), 61.98 (C¹⁷ (-OCH₃)), 108.90 (Ar-C¹⁵), 115.82 (Ar-C^{3,5}), 120.91 (C⁹ (-CH=)), 121.65 (Ar-C¹¹), 123.73 (Ar-C¹⁶), 129.76 (Ar-C¹), 131.50 (Ar-C^{2,6}), 137.58 (C¹⁰ (=CH-)), 142.21 (Ar-C¹³), 153.42 (Ar-C¹²), 155.96 (Ar-C¹⁴), 162.52 (Ar-C⁴), 187.57 (C⁸ (-C=O)). Anal. Calcd for C₁₈H₁₈O₅: C, 68.78; H, 5.77. Found: C, 68.71; H, 5.71%.

(E)-1-(4-Hydroxyphenyl)-3-(2,4,5-trimethoxyphenyl) prop-2-en-1-one (6)

Yield: 72%; yellow solid; MALDI-MS: *m/z* calcd: 314.34; found: 314.48. FT-IR (KBr) ν_{\max} (cm⁻¹): 3307 ν_{OH} , 3028 and 3067 $\nu_{\text{Ar-CH}}$, 2827 and 2929 $\nu_{\text{Aliphatic-CH}}$, 1639 $\nu_{\text{C=O}}$, 1505, 1544, 1583, and 1613 $\nu_{\text{C=C}}$. ¹H NMR (DMSO-*d*₆) δ 3.83 (3H, s, H¹⁸ (-OCH₃)), 3.88 (3H, s, H¹⁹ (-OCH₃)), 3.91 (3H, s, H¹⁷ (-OCH₃)), 6.76 (1H, s, H¹³), 6.90–6.92 (2H, d, *J* = 8.4 Hz, Ar-H^{3,5}), 7.50 (1H, s, H¹⁶), 7.71–7.75 (1H, d, *J* = 15.6 Hz, H⁹ (-CH=)), 7.98–8.02 (1H, d, *J* = 15.6 Hz, H¹⁰ (=CH-)), 8.04–8.06 (2H, d, *J* = 8.4 Hz,

Ar-H^{2,6}), 10.29 (1H, s, H⁷ (Ph-OH)). ¹³C-APT NMR (DMSO-*d*₆) δ 56.33 (C¹⁷ (-OCH₃)), 56.94 (C¹⁸ (-OCH₃)), 56.96 (C¹⁹ (-OCH₃)), 98.28 (Ar-C¹³), 111.73 (Ar-C¹⁶), 115.16 (Ar-C¹¹), 115.74 (Ar-C^{3,5}), 119.49 (C⁹ (-CH=)), 130.09 (Ar-C¹), 131.38 (Ar-C^{2,6}), 137.73 (C¹⁰ (=CH-)), 143.65 (Ar-C¹²), 153.07 (Ar-C¹⁵), 154.53 (Ar-C¹⁴), 162.32 (Ar-C⁴), 187.69 (C⁸ (-C=O)). Anal. Calcd for C₁₈H₁₈O₅: C, 68.78; H, 5.77. Found: C, 68.83; H, 5.82%.

(E)-1-(4-Hydroxyphenyl)-3-(1,1'-biphenyl)prop-2-en-1-one (7)

Yield: 65%; yellow solid; MALDI-MS: *m/z* calcd: 300.36; found: 300.54. FT-IR (KBr) ν_{\max} (cm⁻¹): 3162 ν_{OH} , 3026 and 3059 $\nu_{\text{Ar-CH}}$, 2824 and 2960 $\nu_{\text{Aliphatic-CH}}$, 1652 $\nu_{\text{C=O}}$, 1515, 1553, 1595, and 1609 $\nu_{\text{C=C}}$. ¹H NMR (DMSO-*d*₆) δ 6.91–6.94 (2H, d, *J* = 8.8 Hz, Ar-H^{3,5}), 7.41–7.43 (1H, t, H²⁰), 7.49–7.51 (2H, t, H^{19,21}), 7.72–7.79 (5H, m, H⁹ (-CH=), Ar-H^{12,16}, Ar-H^{18,22}), 7.94–7.98 (3H, m, H¹⁰ (=CH-), Ar-H^{13,15}), 8.09–8.11 (2H, d, *J* = 8.4 Hz, Ar-H^{2,6}), 10.41 (1H, s, H⁷ (Ph-OH)). ¹³C-APT NMR (DMSO-*d*₆) δ 115.88 (Ar-C^{3,5}), 122.54 (C⁹ (-CH=)), 127.20 (C²⁰), 127.53 (Ar-C^{12,16}), 128.43 (Ar-C^{13,15}), 129.43 (Ar-C^{18,22}), 129.61 (Ar-C¹), 129.87 (Ar-C^{19,21}), 131.69 (Ar-C^{2,6}), 134.53 (Ar-C¹¹), 139.75 (Ar-C¹⁴), 142.27 (Ar-C¹⁷), 142.70 (C¹⁰ (=CH-)), 162.75 (Ar-C⁴), 187.55 (C⁸ (-C=O)). Anal. Calcd for C₂₁H₁₆O₂: C, 83.98; H, 5.37. Found: C, 84.05; H, 5.42%.

(E)-1-(4-Hydroxyphenyl)-3-(3,5-difluorophenyl)prop-2-en-1-one (8)

Yield: 66%; yellow solid; MALDI-MS: *m/z* calcd: 260.24; found: 261.31 [M+H]⁺. FT-IR (KBr) ν_{\max} (cm⁻¹): 3223 ν_{OH} , 3026 and 3100 $\nu_{\text{Ar-CH}}$, 2829 and 2972 $\nu_{\text{Aliphatic-CH}}$, 1657 $\nu_{\text{C=O}}$, 1516, 1593, and 1613 $\nu_{\text{C=C}}$. ¹H NMR (DMSO-*d*₆) δ 6.91–6.93 (2H, d, *J* = 8.8 Hz, Ar-H^{3,5}), 7.29–7.34 (1H, Ar-H¹⁴), 7.63–7.67 (1H, d, *J* = 15.6 Hz, H⁹ (-CH=)), 7.70–7.72 (2H, m, Ar-H¹², Ar-H¹⁶), 8.03–8.06 (1H, d, *J* = 15.6 Hz, H¹⁰ (=CH-)), 8.11–8.13 (2H, d, *J* = 8.4 Hz, Ar-H^{2,6}), 10.49 (1H, s, H⁷ (Ph-OH)). ¹³C-APT NMR (DMSO-*d*₆) δ 105.80 (Ar-C¹⁴), 112.02 (Ar-C¹²), 112.21 (Ar-C¹⁶), 115.86 (Ar-C^{3,5}), 125.25 (C⁹ (-CH=)), 129.25 (Ar-C¹), 131.93 (Ar-C^{2,6}), 139.22 (Ar-C¹¹), 140.58 (C¹⁰ (=CH-)), 161.96 (Ar-C¹⁵), 162.96 (Ar-C⁴), 164.40 (Ar-C¹³), 187.30 (C⁸ (-C=O)). Anal. Calcd for C₁₅H₁₀F₂O₂: C, 69.23; H, 3.87. Found: C, 69.29; H, 3.92%.

(E)-1-(4-Hydroxyphenyl)-3-(2-fluoro-4-chlorophenyl) prop-2-en-1-one (9)

Yield: 58%; yellow solid; MALDI-MS: *m/z* calcd: 276.69; found: 276.98. FT-IR (KBr) ν_{\max} (cm⁻¹): 3270 ν_{OH} , 3026 and 3067 $\nu_{\text{Ar-CH}}$, 2865 and 2943 $\nu_{\text{Aliphatic-CH}}$, 1647 $\nu_{\text{C=O}}$, 1514, 1572, 1595 and 1605 $\nu_{\text{C=C}}$. ¹H NMR (DMSO-*d*₆) δ 6.91–6.93 (2H, d, *J* = 8.8 Hz, Ar-H^{3,5}), 7.40–7.42 (1H, d, *J* = 9.6 Hz, Ar-H¹⁵), 7.55–7.57 (1H, d, *J* = 10.4 Hz, Ar-H¹⁶), 7.70–7.74 (1H, d, *J* = 15.6 Hz, H⁹ (-CH=)), 7.95–7.99 (1H, d, *J* = 15.6 Hz, H¹⁰ (=CH-)), 8.06–8.08 (2H, d, *J* = 8 Hz, Ar-H^{2,6}), 8.15 (1H, s, Ar-H¹³), 10.46 (1H, s, H⁷ (Ph-

OH)). ^{13}C -APT NMR (DMSO- d_6) δ 115.95 (Ar-C 3,5), 117.32 (Ar-C 13), 122.11 (Ar-C 11), 125.02 (Ar-C 15), 125.80 (C 9 (-CH=)), 129.19 (Ar-C 1), 130.65 (Ar-C 16), 131.83 (Ar-C 2,6), 133.10 (C 10 (=CH-)), 136.03 (Ar-C 14), 159.78 (Ar-C 12), 162.98 (Ar-C 4), 187.16 (C 8 (-C=O)). Anal. Calcd for C $_{15}$ H $_{10}$ ClFO $_2$: C, 65.11; H, 3.64. Found: C, 65.17; H, 3.69%.

(E)-1-(4-Hydroxyphenyl)-3-(3-(trifluoromethyl)phenyl)prop-2-en-1-one (10)

Yield: 69%; yellow solid; MALDI-MS: m/z calcd: 292.26; found: 293.19 [M+H] $^+$. FT-IR (KBr) ν_{max} (cm $^{-1}$): 3330 ν_{OH} , 3013 and 3067 $\nu_{\text{Ar-CH}}$, 2882 and 2981 $\nu_{\text{Aliphatic-CH}}$, 1646 $\nu_{\text{C=O}}$, 1514, 1557, 1597 and 1606 $\nu_{\text{C=C}}$. ^1H NMR (DMSO- d_6) δ 6.92–6.94 (2H, d, J = 8.8 Hz, Ar-H 3,5), 7.67–7.71 (1H, t, Ar-H 15), 7.75–7.79 (1H, d, J = 15.6 Hz, H 9 (-CH=)), 7.77 (1H, s, Ar-H 16), 8.09–8.18 (4H, m, Ar-H 2,6 , H 10 (=CH-)), Ar-H 14), 8.33 (1H, s, Ar-H 12), 10.46 (1H, s, H 7 (Ph-OH)). ^{13}C -APT NMR (DMSO- d_6) δ = 115.88 (Ar-C 3,5), 124.51 (Ar-C 12), 125.40 (C 9 (-CH=)), 126.90 (Ar-C 14), 129.35 (Ar-C 1), 130.10 (Ar-C 17), 130.38 (Ar-C 15), 130.42 (Ar-C 13), 131.91 (Ar-C 2,6), 133.28 (Ar-C 16), 136.55 (Ar-C 11), 141.39 (C 10 (=CH-)), 162.90 (Ar-C 4), 187.43 (C 8 (-C=O)). Anal. Calcd for C $_{16}$ H $_{11}$ F $_3$ O $_2$: C, 65.76; H, 3.79. Found: C, 65.83; H, 3.75%.

(E)-1-(4-Hydroxyphenyl)-3-(3-(trifluoromethyl)-4-chlorophenyl)prop-2-en-1-one (11)

Yield: 73%; yellow solid; MALDI-MS: m/z calcd: 326.70; found: 327.73 [M+H] $^+$. FT-IR (KBr) ν_{max} (cm $^{-1}$): 3315 ν_{OH} , 3029, 3060 and 3076 $\nu_{\text{Ar-CH}}$, 2837 and 2961 $\nu_{\text{Aliphatic-CH}}$, 1647 $\nu_{\text{C=O}}$, 1515, 1553, 1595 and 1603 $\nu_{\text{C=C}}$. ^1H NMR (DMSO- d_6) δ 6.91–6.93 (2H, d, J = 8.8 Hz, Ar-H 3,5), 7.74–7.78 (1H, d, J = 15.6 Hz, H 9 (-CH=)), 7.81–7.83 (1H, d, J = 8.4 Hz, Ar-H 15), 8.10–8.14 (1H, d, J = 15.6 Hz, H 10 (=CH-)), 8.12–8.14 (2H, d, J = 8.4 Hz, Ar-H 2,6), 8.21–8.23 (2H, d, J = 8.4 Hz, Ar-H 16), 8.39 (1H, s, Ar-H 12), 10.52 (1H, s, H 7 (Ph-OH)). ^{13}C -APT NMR (DMSO- d_6) δ 115.88 (Ar-C 3,5), 124.17 (Ar-C 17), 125.10 (C 9 (-CH=)), 127.53 (Ar-C 13), 128.33 (Ar-C 15), 129.29 (Ar-C 1), 131.93 (Ar-C 2,6), 132.17 (Ar-C 14), 132.58 (Ar-C 16), 134.30 (Ar-C 12), 135.24 (Ar-C 11), 140.30 (C 10 (=CH-)), 162.93 (Ar-C 4), 187.35 (C 8 (-C=O)). Anal. Calcd for C $_{16}$ H $_{11}$ F $_3$ O $_2$: C, 58.82; H, 3.09. Found: C, 58.93; H, 3.14%.

2. 2. In Vitro Cytotoxic Activity

Changes in cell viability of compounds at concentrations such as 1, 5, 25, 50 and 100 μM were determined by MTT analysis. This method is based on the principle of MTT dye breaking down the tetrazolium ring, and in the first stage, MTT is actively absorbed into living cells and the reaction is catalyzed by mitochondrial succinate dehydrogenase. Finally, it is reduced to the blue-violet water-insoluble form. Formazan formation, a marker of cell viability, occurs only in living cells with active mitochondria. The value determined spectrophotometrically is related to

the number of live cells. 0.5 mg/mL MTT working solution in sterile PBS was prepared from the stock MTT solution and added to 96 well plates. The optical densities of the cells in the plates were kept in the incubator for 3 hours and then scanned at the 550 nm wavelength with ELISA device (Synergy HT USA). The average of the absorbance values obtained from the control wells was accepted as 100% live cells. The absorbance values obtained from the solvent and agent and wells were proportional to the control absorbance value and were considered as percent viability.^{50–53}

In this study, human prostate cancer (PC-3, LNCaP), human breast cancer (MCF-7) and human ovarian cancer cell lines (A2780) were selected as cell types. Feeding of all cells was done using RPMI-1640 medium (prepared by adding 10% FCS, 100 U/mL penicillin and 0.1 mg/mL streptomycin) in 25 cm 2 culture flasks. The cells of the medium were kept twice at 37 $^\circ\text{C}$ in the carbon dioxide (5% CO $_2$) incubator and the medium was changed twice a week. When cells were combined, they were removed from the flasks using trypsin-EDTA solution and transferred to 96-well plates and used for 3-(4,5-dimethylthiazole-2-yl) diphenyltetrazolium bromide (MTT) analysis. Relative cell viability (%) was expressed as a percentage relative to untreated control cells. Each value represents an average of 10 measurements. All cellular results were obtained against negative control cells.^{51–53}

In cell culture experiments, solutions of the compounds in dimethyl sulfoxide (DMSO) were used. In the comparison of the obtained results for this reason, the effects of the substances against DMSO were determined by statistical analysis. The same amounts of solvent (DMSO) were added to the wells containing the concentrations of the tested compounds at 1, 5, 25, 50 and 100 μM and were incubated in a CO $_2$ incubator (Panasonic, Japan) for 24 hours at 37 $^\circ\text{C}$. After incubations, viability of the cells was determined using 0.4% trypan blue in a hemocytometer.

IBM SPSS Statistics 22.0 (Windows) package program was used for statistical analysis. Conformity to normal distribution was evaluated with the Shapiro Wilk test. Comparison of quantitative variables between groups was measured by Kruskal Wallis H test. When significant statistical differences between the groups were determined, multiple comparisons between the groups were made with the Bonferroni-corrected Mann Whitney U test. Data were presented as mean \pm standard deviation. $p < 0.05$ value was considered statistically significant. LogIC $_{50}$ values were calculated by using Graphpad prism 6 program in computer environment according to the obtained MTT results.

2. 3. Molecular Docking Studies

Ligands were energy-minimized using ChemOffice on Windows 10 operating system. Grid box points as size

of 60-60-60 Å³ and a regular space of 0.375 Å were determined by centering on colchicine. “Tubulin-colchicine complex” pdb file (PDB ID: 4O2B) was get (<https://www.rcsb.org/>) and was modified using the Maestro.⁵⁴ Lamarckian Genetic Algorithm was preferred and standard settings used for all compounds. Docking scores were obtained using both AutoDock 4.2 software,⁵⁵ and AutoDock Vina software.⁵⁶ To validate the Autodock program, the co-crystallized ligand (PDB ID: LOC) was redocked on the target and RMSD value of 0.42 was found for tubulin-colchicine complex.

3. Results and Discussion

3.1. Synthesis

In this work, 1-(4-hydroxyphenyl)-3-(3-substituted-phenyl)prop-2-en-1-one compounds **2–11** were prepared by the interaction of *para*-hydroxyacetophenone (**1**) with substitute aldehydes (3-methoxy, 2,4-dimethoxy, 3,4-dimethoxy, 2,3,4-trimethoxy, 2,4,5-trimethoxy, 4-phenyl, 3,5-difluoro, 4-chloro-2-fluoro, 3-(trifluoromethyl) phenyl, 4-chloro-3-(trifluoromethyl) benzaldehyde) in the presence of ethanol and aqueous NaOH at room temperature.²⁸ The structures of compounds **2–11** were determined by MS, FT-IR, microanalysis, and 1D (¹H and ¹³C-APT) NMR spectroscopic methods. The synthetic pathway of **2–11** and their numbering for ¹H and ¹³C-APT NMR characterizations is shown in Scheme 1.

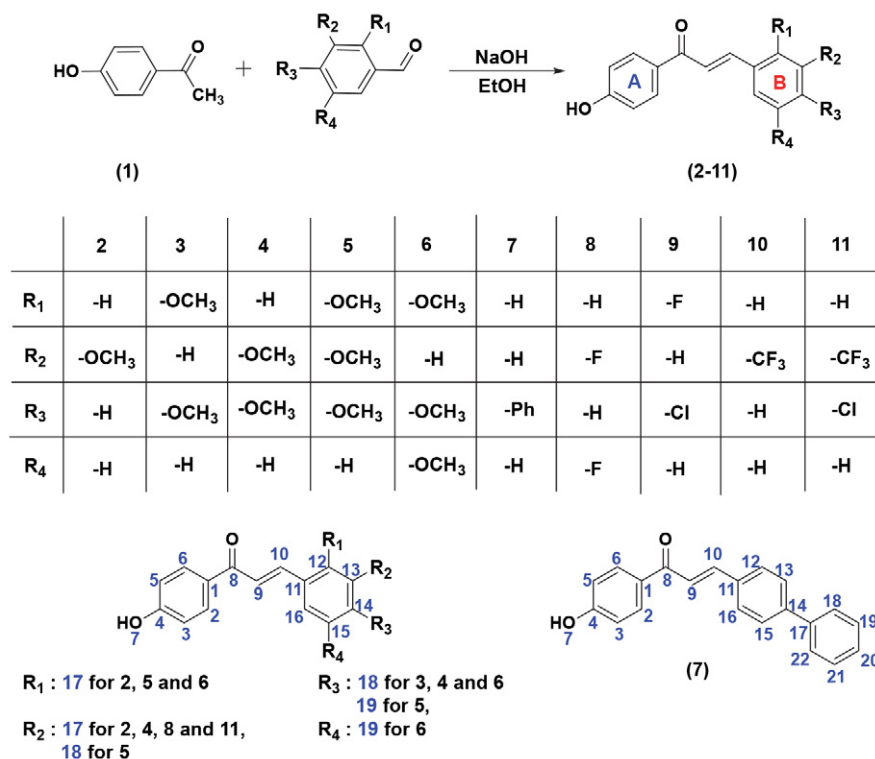
The compounds have only primary, tertiary and quaternary (–CH, –CH₃ and –C) carbon atoms in their structure. Therefore, ¹³C-APT NMR analyzes were performed. These carbons provided easier assignment of NMR spectra.

When the proton and carbon NMR spectra of **2–11** are investigated, the methoxy proton and carbon peaks (H/C) of compounds containing methoxy as side groups have been observed at 3.84 / 55.75 ppm for **2** (number 17 proton and carbon peaks); 3.91 / 56.26 and 3.85 / 55.98 for **3**; 3.88 / 56.05 and 3.83 / 56.20 for **4** (number 17 and 18 proton and carbon peaks, respectively); 3.89 / 61.98, 3.79 / 60.94 and 3.87 / 56.51 for **5**; and 3.91 / 56.33, 3.83 / 56.94 and 3.88 / 56.94 for **6** (number 17, 18 and 19 proton and carbon peaks, respectively).

The carbonyl stretching vibrations, carbonyl protons and carbonyl carbon peaks of the starting compound aldehydes were not observed in the FT-IR, ¹H and ¹³C-APT NMR spectra of the synthesized compounds **2–11**, respectively. The carbon numbers and the integration of proton signals in the NMR spectra of **2–11** support the structures of synthesized compounds. The ¹H and ¹³C-APT NMR spectra of compound **2** are given as examples in Figure 1. The spectra of other compounds are given in Figures S1–30 in the Supplementary Information file.

3.2. In Vitro Cytotoxic Activity

The chalcone compounds contain two phenyl rings shown as A and B in the scaffold (see Scheme 1). By chang-



Scheme 1. Synthetic pathway of **2–11** and their numbering for ¹H and ¹³C-APT NMR characterizations

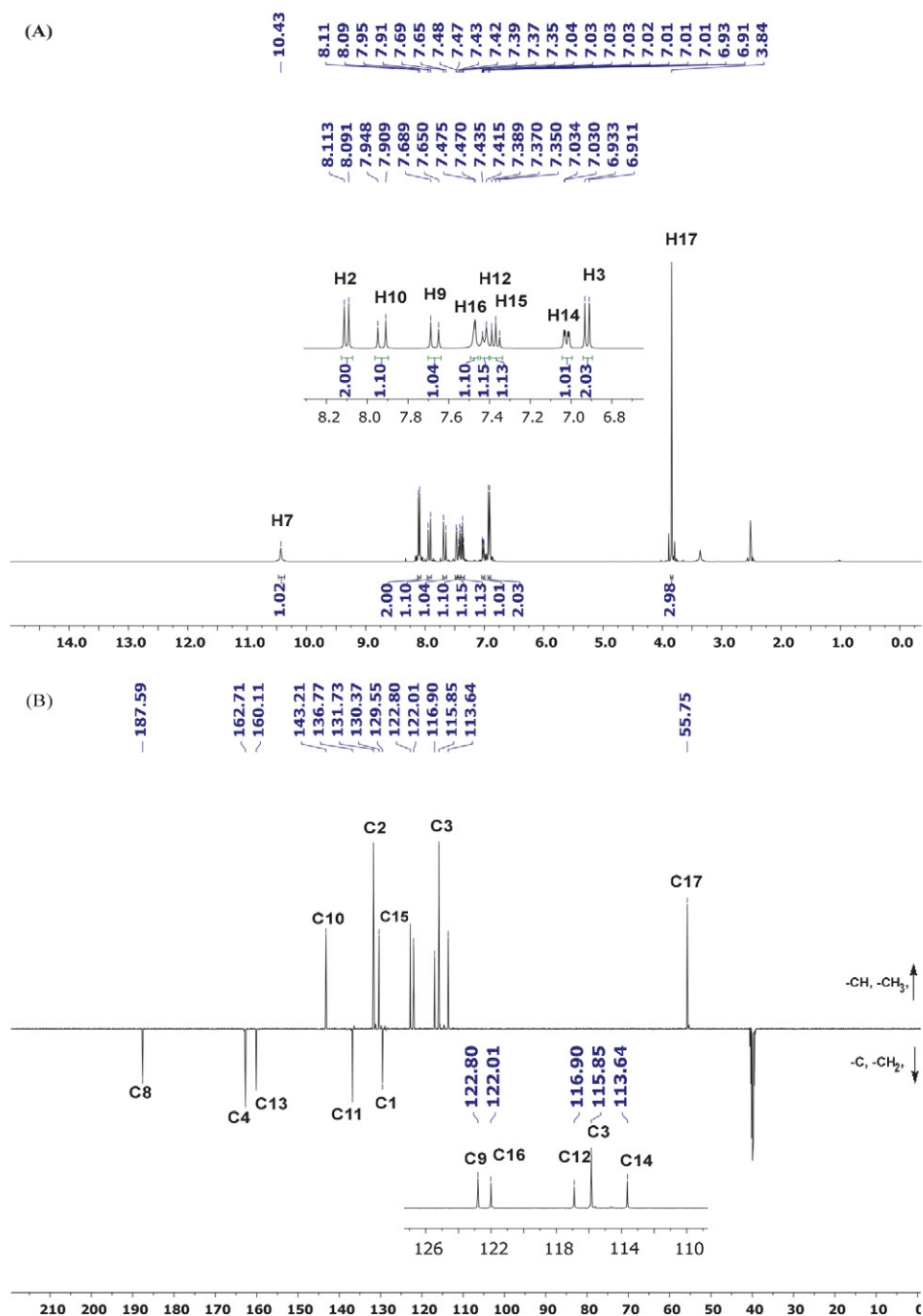


Figure 1. (A) ^1H NMR spectrum and (B) ^{13}C -APT NMR spectrum of 2 (DMSO- d_6)

ing the side groups on the phenyl rings of these compounds, biologically active molecules with different effects are formed. Numerous pure chalcones isolated from different plants have been approved for clinical studies in the treatment of cancer, viral and cardiovascular disorders. For example, the methochalcone compound containing methoxy group in the 2 and 4 positions of ring A and in the 4 positions of ring B has been approved for clinical use as a choleric and diuretic agent. Similarly, some chalcone derivatives have been clinically tested and approved to

show various biological activities, including anti-ulcer/mucoprotective activity (sofalkonin), vascular protection (hesperidin methyl-chalcone), anti-microbial activity (isobavachalcone), anti-cancer effect (flavokawain A), inflammatory action (cardamonin) and anti-diabetes-acting compound (4-hydroxyderricin) can be given as examples.^{18–20} Each of these compounds has different side groups in rings A and B. This causes different biological activity. Therefore, in this study, a series of chalcone compounds with various groups in the side chains were syn-

thesized and their cytotoxic effects on different cancer cells were investigated. For this purpose, compounds having the -OH functional group in ring A and different side groups in ring B were synthesized.

Changes in cell viability rates of compounds 2–11 against A2780, LNCaP, PC-3 and MCF-7 cell lines are presented in Tables 1 and 2.

When the cytotoxic effects of the compounds 2–6 with the methoxy group(s) at different positions of the ring B against A2780 cells were examined, it was found that the compound 2 caused a significant decrease in cell viability in a dose-dependent manner ($p < 0.05$). In other compounds, cytotoxic effects were observed only for 25, 50 and 100 μM concentrations ($p < 0.05$). When the structure-activity relationship between the compound 2 with one methoxy group and the compounds 3, 4, 5 and 6 with two or three methoxy groups was examined, different cytotoxic effects were observed at different concentrations. Compound 2 exhibited cytotoxic effect at all concentrations. However, other compounds with more than one methoxy group did not show this effect. Despite these results, compounds carrying more than one methoxy group caused significant reductions at high concentrations. In particular, the effect of the compound 4 on cell viability is noteworthy.

In terms of IC_{50} values, it is seen that the compound 2 has an IC_{50} value of 10 μM , and the compound 4 has an IC_{50} value of 12.61 μM .

When the cytotoxic effects of these compounds in LNCaP cancer cell lines were examined, it was found that compound 2 decreased cell viability in the cell line depending on the dose ($p < 0.05$). Other compounds containing the methoxy group also had an effect at only 25, 50 and 100 μM concentrations ($p < 0.05$). Compound 4 caused decreases in cell viability at only 100 μM concentrations ($p < 0.05$). Although it causes a significant decrease at this concentration, its cytotoxic effect does not seem to be as strong as in A2780 cells. Especially for compound 2, which acts on dose-dependent reduction of cell viability against A2780 and LNCaP cell lines, the IC_{50} value is 10.9 μM against A2780 cell lines, while this value is 1.823 μM against LNCaP cell lines. Considering the results, compound 2 seems to have a better effect against A2780 cell lines than LNCaP cell lines.

When the cytotoxic effects of these compounds on PC-3 and MCF-7 cancer cell lines were examined, it was observed that especially the compound 2 did not produce a cytotoxic effect in both cell lines. A similar situation was observed for the compound 5. Compound 6 showed an effect at only 100 μM concentrations in both cells ($p < 0.05$). These compounds, which contain the methoxy group, appear to have very different effects in different cells. Overall, the results show that methoxy-containing compounds 2–6 are more effective against A2780 and LNCaP cells ($p < 0.05$).

Table 1. Cell viability (in %) of compounds 2–11 against human cancer cell lines ($p^* < 0.05$).

		A2780 Human Cancer Cell Lines					
	Control	Solvent	1 μM	5 μM	25 μM	50 μM	100 μM
2	100 \pm 9.67	91.25 \pm 8.16	61.82 \pm 8.12*	51.25 \pm 5.58*	44.80 \pm 9.21*	30.18 \pm 6.94*	23.74 \pm 4.11*
3	100 \pm 9.67	91.25 \pm 8.16	109.5 \pm 12.31	100.9 \pm 13.09	66.66 \pm 6.29*	64.64 \pm 7.02*	47.49 \pm 5.16*
4	100 \pm 9.67	91.25 \pm 8.16	92.18 \pm 8.06	77.25 \pm 10.05	37.64 \pm 6.68*	10.77 \pm 2.06*	6.54 \pm 2.19*
5	100 \pm 9.67	91.25 \pm 8.16	97.22 \pm 8.65	85.48 \pm 7.77	68.95 \pm 6.09*	68.88 \pm 8.01*	14.42 \pm 2.26*
6	100 \pm 9.67	91.25 \pm 8.16	199.5 \pm 9.31	90.58 \pm 8.1	65.33 \pm 5.27*	66.34 \pm 6.3*	30.26 \pm 5.36*
7	100 \pm 9.67	91.25 \pm 8.16	81.56 \pm 10.17	66.07 \pm 8.72*	11.35 \pm 2.36*	13.98 \pm 3.24*	11.64 \pm 4.41*
8	100 \pm 9.67	91.25 \pm 8.16	85.62 \pm 7.16	96.10 \pm 11.29	6.78 \pm 2.03*	4.74 \pm 1.41*	4.60 \pm 1.12*
9	100 \pm 9.67	91.25 \pm 8.16	102.6 \pm 13.28	60.41 \pm 10.25*	4.75 \pm 2.02*	3.23 \pm 1.26*	2.45 \pm 0.96*
10	100 \pm 9.67	91.25 \pm 8.16	103.8 \pm 14.06	101.0 \pm 11.64	26.38 \pm 4.11*	6.91 \pm 3.09*	4.67 \pm 1.01*
11	100 \pm 9.67	91.25 \pm 8.16	104.1 \pm 10.21	97.87 \pm 12.17	5.70 \pm 3.06*	4.51 \pm 2.41*	4.14 \pm 2.13*
		MCF-7 Human Breast Cancer Cell Lines					
	Control	Solvent	1 μM	5 μM	25 μM	50 μM	100 μM
2	100 \pm 8.76	94.22 \pm 7.87	106.6 \pm 9.75	105.1 \pm 14.21	97.2 \pm 11.12	105.2 \pm 10.11	93.97 \pm 13.91
3	100 \pm 8.76	94.22 \pm 7.87	103.5 \pm 9.51	84.89 \pm 8.74	84.76 \pm 11.41	81.64 \pm 6.43*	67.24 \pm 7.79*
4	100 \pm 8.76	94.22 \pm 7.87	103.3 \pm 11.5	98.59 \pm 13.54	86.02 \pm 13.41	28.45 \pm 6.97*	29.17 \pm 9.98*
5	100 \pm 8.76	94.22 \pm 7.87	118.3 \pm 17.7	109.0 \pm 15.62	105.8 \pm 14.5	106.7 \pm 17.9	107.3 \pm 12.4
6	100 \pm 8.76	94.22 \pm 7.87	10.75 \pm 11.37	99.77 \pm 10.23	78.81 \pm 9.40	83.88 \pm 12.84	29.04 \pm 5.42*
7	100 \pm 8.76	94.22 \pm 7.87	99.66 \pm 13.68	102.9 \pm 14.81	102.0 \pm 17.9	93.00 \pm 9.72	37.22 \pm 6.38*
8	100 \pm 8.76	94.22 \pm 7.87	93.04 \pm 12.31	66.94 \pm 10.23*	16.26 \pm 4.81*	11.15 \pm 2.37*	11.34 \pm 3.46*
9	100 \pm 8.76	94.22 \pm 7.87	96.83 \pm 12.56	103.4 \pm 16.66	21.15 \pm 5.67*	11.37 \pm 3.06*	12.11 \pm 4.21*
10	100 \pm 8.76	94.22 \pm 7.87	92.46 \pm 9.99	70.47 \pm 5.25*	21.93 \pm 3.30*	23.42 \pm 4.81*	23.69 \pm 2.46*
11	100 \pm 8.76	94.22 \pm 7.87	105.6 \pm 14.5	106.2 \pm 15.88	31.97 \pm 5.64*	21.74 \pm 3.77*	21.25 \pm 4.27*

μM : Micromolar.

Table 2. Cell Viability (in %) of compounds 2–11 against cancer cell lines ($p^* < 0.05$).

LNCaP Human Prostate Cancer Cell Lines							
	Control	Solvent	1 μ M	5 μ M	25 μ M	50 μ M	100 μ M
2	100 \pm 8.99	93.17 \pm 10.12	42.86 \pm 5.21*	38.13 \pm 3.26*	34.88 \pm 6.78*	24.44 \pm 4.12*	20.21 \pm 3.96*
3	100 \pm 8.99	93.17 \pm 10.12	103.8 \pm 14.4	92.66 \pm 13.29	59.60 \pm 9.87*	47.28 \pm 8.86*	38.22 \pm 9.16*
4	100 \pm 8.99	93.17 \pm 10.12	96.94 \pm 9.26	99.02 \pm 11.23	78.82 \pm 10.87	70.03 \pm 14.69	58.95 \pm 8.26*
5	100 \pm 8.99	93.17 \pm 10.12	77.79 \pm 10.86	74.92 \pm 12.22	51.56 \pm 8.26*	45.94 \pm 9.13*	39.18 \pm 7.75*
6	100 \pm 8.99	93.17 \pm 10.12	81.98 \pm 10.34	86.62 \pm 11.2	54.5 \pm 8.7*	46.21 \pm 8.6*	38.12 \pm 9.6*
7	100 \pm 8.99	93.17 \pm 10.12	95.72 \pm 14.26	90.69 \pm 12.25	90.82 \pm 13.23	99.67 \pm 10.51	61.55 \pm 8.29*
8	100 \pm 8.99	93.17 \pm 10.12	86.25 \pm 9.12	85.55 \pm 8.26	55.74 \pm 9.41*	48.52 \pm 7.26*	39.05 \pm 7.29*
9	100 \pm 8.99	93.17 \pm 10.12	96.00 \pm 9.26	97.42 \pm 13.41	52.40 \pm 8.24*	51.00 \pm 9.12*	41.92 \pm 7.66*
10	100 \pm 8.99	93.17 \pm 10.12	91.28 \pm 8.21	83.96 \pm 9.22	51.78 \pm 7.42*	10.14 \pm 2.45*	11.52 \pm 3.11*
11	100 \pm 8.99	93.17 \pm 10.12	88.21 \pm 9.77	80.90 \pm 9.29	62.67 \pm 7.39*	14.78 \pm 2.88*	10.78 \pm 3.21*
PC-3 Human Prostate Cancer Cell Lines							
	Control	Solvent	1 μ M	5 μ M	25 μ M	50 μ M	100 μ M
2	100 \pm 9.13	92.36 \pm 8.13	110.2 \pm 13.97	103.3 \pm 13.2	96.57 \pm 11.2	108.8 \pm 15.2	90.97 \pm 9.96
3	100 \pm 9.13	92.36 \pm 8.13	101.26 \pm 7.34	110.7 \pm 12.7	76.93 \pm 8.96	70.95 \pm 9.34*	5.67 \pm 1.22*
4	100 \pm 9.13	92.36 \pm 8.13	99.53 \pm 10.41	98.96 \pm 8.41	67.72 \pm 7.34*	62.73 \pm 6.13*	23.98 \pm 3.81*
5	100 \pm 9.13	92.36 \pm 8.13	103.5 \pm 12.32	95.55 \pm 13.21	99.24 \pm 8.99	93.53 \pm 14.22	92.23 \pm 7.49
6	100 \pm 9.13	92.36 \pm 8.13	102.6 \pm 7.14	109.6 \pm 11.5	79.94 \pm 8.86	85.96 \pm 8.33	5.67 \pm 1.22*
7	100 \pm 9.13	92.36 \pm 8.13	112.4 \pm 10.85	85.97 \pm 9.34	89.10 \pm 8.45	80.97 \pm 7.78	11.14 \pm 2.39*
8	100 \pm 9.13	92.36 \pm 8.13	88.59 \pm 9.29	91.12 \pm 11.29	55.90 \pm 8.21*	7.98 \pm 1.14*	3.61 \pm 1.22*
9	100 \pm 9.13	92.36 \pm 8.13	70.11 \pm 8.28*	65.34 \pm 7.92*	64.46 \pm 9.12*	2.68 \pm 0.78*	1.81 \pm 0.84*
10	100 \pm 9.13	92.36 \pm 8.13	82.71 \pm 9.21	80.33 \pm 8.93	38.16 \pm 6.23*	1.90 \pm 0.37*	1.73 \pm 0.22*
11	100 \pm 9.13	92.36 \pm 8.13	92.08 \pm 10.12	87.54 \pm 11.98	72.65 \pm 9.93	1.85 \pm 0.42*	1.65 \pm 0.34*

 μ M: Micromolar.

Although compound 7 significantly reduced cell viability at 5, 25, 50 and 100 μ M concentrations in A2780 cell lines, it caused significant reductions in cell viability at only 100 μ M concentration in other cell lines ($p < 0.05$). The IC_{50} value of the compound 7 against A2780 cell lines is 6.898 μ M. In terms of structure-activity relationship, the fact that the compound contains a phenyl ring at the *para*

position caused a significant decrease in cell viability. The $\log IC_{50}/IC_{50}$ values of the compounds are given in Table 3. When the cytotoxic activities of the compounds 8, 9, 10 and 11, which contain -F, -Cl, -CF₃ groups separately or together, were observed against four cell lines, there was a significant decrease in cell viability, especially at concentrations of 50 and 100 μ M ($p < 0.05$). In particular, these

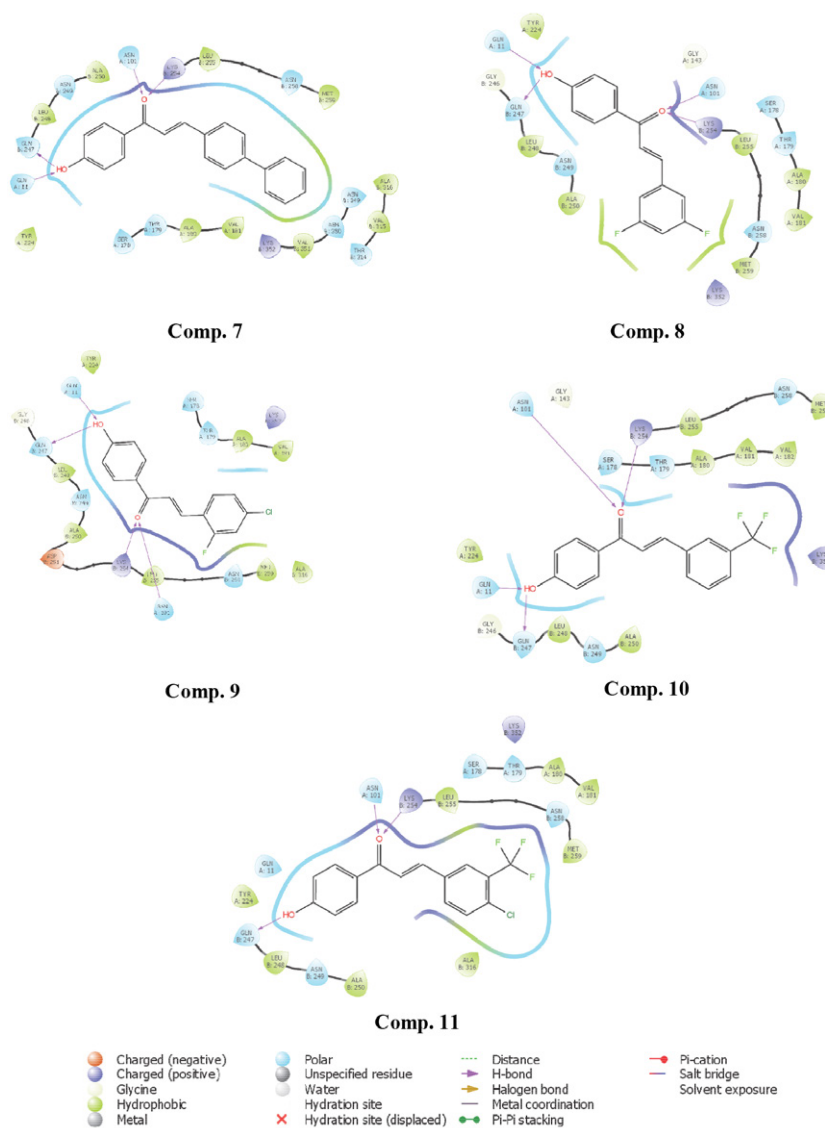
Table 3. The $\log IC_{50}/IC_{50}$ (50% inhibition-causing concentration) values (μ M) of compounds 2–11 against A2780, LNCaP, PC-3 and MCF-7 cancer cell lines

Comp.	A2780 $\log IC_{50} / IC_{50}$ (μ M)	LNCaP $\log IC_{50} / IC_{50}$ (μ M)	PC-3 $\log IC_{50} / IC_{50}$ (μ M)	MCF-7 $\log IC_{50} / IC_{50}$ (μ M)
2	1.037 / 10.9	0.2607 / 1.823	–	3.537 / 3445
3	1.911 / 81.4	1.674 / 47.24	1.763 / 57.88	2.285 / 192.9
4	1.101 / 12.61	2.097 / 125.1	1.747 / 55.91	1.67 / 46.78
5	1.712 / 51.53	1.548 + / 35.35	2.1066 / 27.616	–
6	1.818 / 65.71	1.605 / 40.29	1.853 / 71.36	1.935 / 86.12
7	0.8387 / 6.898	2.403 / 253	1.866 / 73.52	2.18 / 151.2
8	0.9888 / 9.746	1.635 / 43.19	1.259 / 18.16	0.9071 / 8.075
9	0.7853 / 6.1	1.684 / 48.34	1.112 / 12.93	1.164 / 14.57
10	1.153 / 14.24	1.242 / 17.47	1.049 / 11.18	1.062 / 11.54
11	1.027 / 10.64	1.3198 / 20.84	1.312 / 20.49	1.32 / 20.9
Paclitaxel	0.7516 / 5.645	–	–	–
Tamoxifen	–	–	–	1.308 / 20.33
Docetaxel	–	0.7792 / 6.014	1.229 / 16.95	–

 μ M: Micromolar.

Table 4. Molecular docking binding scores of some compounds, within the tubulin-colchicine complex (PDB ID: 4O2B) active site. Residues participating in H-bonds with the compounds are shown.

Comp.	Auto dock Result			Docking Score	Vina Result Docking Score
	Residues participating H-bonds Receptor		Estimated Inhibition Constant, Ki		
	A Chain	B Chain			
2	Gln11, Asn101	Gln247, Lys254	1.91 μ M	-7.80	-8.4
3	Gln11	Gln247, Lys254	1.96 μ M	-7.79	-8.2
4	Gln11, Asn101	Gln247, Lys254	1.77 μ M	-7.85	-8.2
5	Gln11, Asn101	Gln247, Lys254	1.25 μ M	-8.05	-8.4
6	Gln11, Asn101	Gln247, Lys254	1.07 μ M	-8.15	-8.2
7	Gln11, Asn101	Gln247, Lys254	22.01 μ M	-10.45	-8.9
8	Gln11, Asn101	Gln247, Lys254	3.48 μ M	-7.45	-8.5
9	Gln11, Asn101	Gln247, Lys254	1.16 μ M	-8.10	-8.3
10	Gln11, Asn101	Gln247, Lys254	2.25 μ M	-7.70	-9.3
11	Gln11	Gln247, Lys254	1.25 μ M	-8.05	-9.7

nM: nanomolar, μ M: micromolar**Figure 2.** 2D interaction diagram for compounds 7–11 at the tubulin binding cavity.

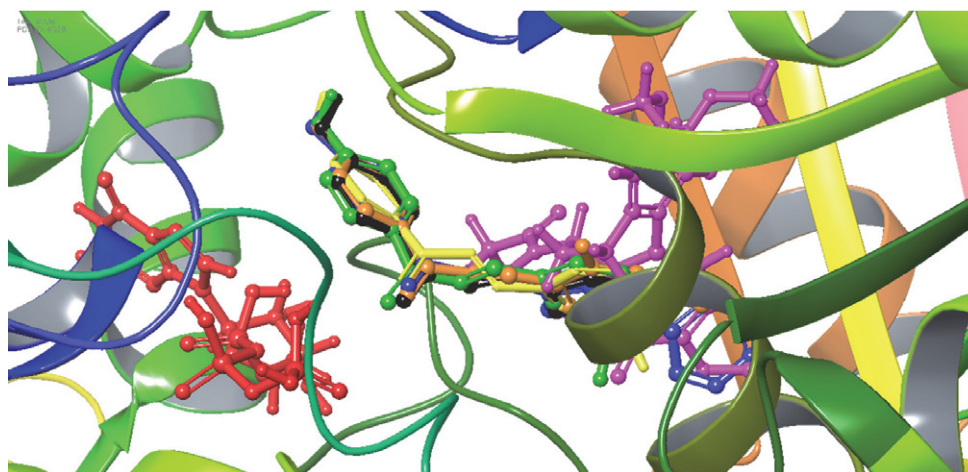


Figure 3. Compounds **7** (blue), **8** (yellow), **9** (orange), **10** (green), and **11** (black), colchicine (pink) and guanosine-5'-triphosphate (red) are present in the tubulin-colchicine complex binding cavity.

compounds were found to have strong cytotoxic effects ($p < 0.05$) against A2780 and PC-3 cell lines.

According to the results, especially against the A2780 and LNCaP cell lines, the compounds **2–7** with electron releasing groups (methoxy / phenyl) in the phenyl ring showed strong cytotoxic effect ($p < 0.05$). Compounds **8–11** containing electron withdrawing groups in the phenyl ring were found to have strong cytotoxic effects against four cell lines at different doses ($p < 0.05$).

3. 3. Molecular Docking Studies

According to the X-ray crystallographic structure of tubulin-colchicine complex (PDB ID: 4O2B), main binding site has been determined around small molecules such as colchicine (ligand ID: LOC) and guanosine-5'-triphosphate (ligand ID: GTP) in receptor (<https://www.rcsb.org/>). It has been declared that colchicine interacts with active site in tubulin as the binding site. It has been previously established that colchicine interacts with Ser178A, Thr179A, Ala180A, Val181A, Cys241B, Leu242B, Leu248B, Ala250B, Asp251B, Lys254B, Leu255B, Asn258B, Met259B, Thr314B, Val315B, Ala316B, Ile318B, Asn350B, Lys352B, Ile378B residues (<https://www.ebi.ac.uk/pdbe/>). The formation of hydrogen bonds between the hydroxyl group in the phenol ring of all compounds by Gln11A and Gln247B showed binding to the gorge. The Lys254B has a position in the active site to interact with carbonyl of compounds by establishing a hydrogen bond (Table 4).

Docking studies were performed for all compounds and interaction modes for compounds **7**, **8**, **9**, **10** and **11** with enzyme active sites were determined (Figure 2). The binding types and residues were produced showed by Maestro software (Maestro, Schrödinger, LLC, New York, NY, 2020). These compounds binding modes were similar as with colchicine (Figure 3). The results of molecular

docking studies were exhibited to be relevant for the results of the *in vitro* activity studies.

4. Conclusion

All the compounds (except compound **5**) showed significant cytotoxic effects at high doses in all cancer cell lines. Among all the compounds studied, one compound i.e. compound **2** demonstrated dose-dependent activity, particularly against A2780/LNCaP cancer cell lines. The most effective compounds **8**, **9**, **10** and **11** reduced the cell viability of A2780, MCF-7, PC-3 and LNCaP cells by 50–98%, while other compounds **2**, **4** and **7** reduced the cell viability of A2780 cells by 70–90% at concentrations of 50 and 100 μM . The results indicate that these compounds have high cytotoxic effect against these human cancer cell lines. Molecular docking studies exhibited the interaction mode of all compounds with tubulin including hydrophobic interactions and hydrogen bonds. Chalcone analogues continue to show hope as an anticancer agent through tubulin inhibition, suggesting that this aspect should be improved. Thus, the next aim of the future study will be to determine activities against various human cancer cell lines and non-tumorigenic epithelial cell lines. *In vivo* experiments will be carried out by selecting those that show significant activity among these compounds.

Acknowledgements.

The researchers are grateful to The Scientific and Technological Research Council of Turkey for financial support of this work (Project no: 116Z758).

Conflict of Interest

Authors declare no conflict of interest

5. References

- J. Higgs, C. Wasowski, A. Marcos, M. Jukic, C. H. Pavan, S. Gobec, F. D. Pinto, N. Coletti, M. Marder, *Heliyon* **2019**, *5*, 1–35. DOI:10.1016/j.heliyon.2019.e01376
- Z. Nowakowska, *Eur. J. Med. Chem.* **2007**, *42*, 125–137. DOI:10.1016/j.ejmech.2006.09.019
- F. de Campos-Buzzi, P. Padaratz, A. V. Meira, R. Correa, R. J. Nunes, V. Cechinel-Filho, *Molecules* **2007**, *12*, 896–906. DOI:10.3390/12040896
- Z.-P. Liu, C.-D. Gong, L.-Y. Xie, X.-L. Du, Y. Li, J. Qin, *Acta Chim. Slov.* **2019**, *66*, 421–426. DOI:10.17344/acsi.2018.4887
- F. Tok, B. Koçyiğit-Kaymakçioğlu, *Acta Chim. Slov.* **2020**, *67*, 1139–1147. DOI:10.17344/acsi.2020.6028
- A. Srinivas, M. Sunitha, P. Karthik, K. V. Reddy, *Acta Chim. Slov.* **2017**, *64*, 1030–1041. DOI:10.17344/acsi.2017.3805
- L. Mishra, R. Sinha, H. Itokawa, K. F. Bastow, Y. Tachibana, Y. Nakanishi, N. Kilgore, K. H. Lee, *Bioorg. Med. Chem.* **2001**, *9*, 1667–1671. DOI:10.1016/S0968-0896(01)00074-8
- M. V. Kaveri, R. Prabhakaran, R. Karvembu, K. Natarajan, *Spectrochim. Acta A Mol. Biomol. Spectrosc.* **2005**, *61*, 2915–2918. DOI:10.1016/j.saa.2004.11.001
- F. Hayat, E. Moseley, A. Salahuddin, R. L. Van Zyl, A. Azam, *Eur. J. Med. Chem.* **2011**, *46*, 1897–1905. DOI:10.1016/j.ejmech.2011.02.004
- L. Xie, X. Zhai, C. Liu, P. Li, Y. Li, G. Guo, P. Gong, *Arch. Pharm.* **2011**, *344*, 639–647. DOI:10.1002/ardp.201000391
- S. Shenvi, K. Kumar, K. S. Hatti, K. Rijesh, L. Diwakar, G. C. Reddy, *Eur. J. Med. Chem.* **2013**, *62*, 435–442. DOI:10.1016/j.ejmech.2013.01.018
- Y.-M. Lin, Y. Zhou, M. T. Flavin, L.-M. Zhou, W. Nie, F.-C. Chen, *Bioorg. Med. Chem.* **2002**, *10*, 2795–2802. DOI:10.1016/S0968-0896(02)00094-9
- D. J. Fu, S. Y. Zhang, Y. C. Liu, L. Zhang, J. J. Liu, J. Song, R. H. Zhao, F. Li, H. H. Sun, H. M. Liu, Y. B. Zhang, *Bioorg. Med. Chem. Lett.* **2016**, *26*, 3918–3922. DOI:10.1016/j.bmcl.2016.07.012
- L. M. Zhao, H. S. Jin, L. P. Sun, H. R. Piao, Z. S. Quan, *Bioorg. Med. Chem. Lett.* **2005**, *15*, 5027–5029. DOI:10.1016/j.bmcl.2005.08.039
- A. E. Maatougui, M. Yáñez, A. Crespo, N. Fraiz, A. Coelho, E. Raviña, R. Laguna, E. Cano, M. I. Loza, J. Brea, H. Gutiérrez de Terán, E. Sotelo, *Chemistryselect* **2017**, *2*, 4920–4933. DOI:10.1002/slct.201700243
- M. Liu, P. Wilairat, S. L. Croft, A. L.-C. Tan, M.-L. Go, *Bioorg. Med. Chem.* **2003**, *11*, 2729–2738. DOI:10.1016/S0968-0896(03)00233-5
- C. E. Gutteridge, J. V. Vo, C. B. Tillett, J. A. Vigilante, J. R. Dettmer, S. L. Patterson, K. A. Werbovetz, J. Capers, D. A. Nichols, A. K. Bhattacharjee, L. Gerena, *Med. Chem. (Sharjah (United Arab Emirates))* **2007**, *3*, 115–119. DOI:10.2174/157340607780059530
- D. I. Batovska, I. T. Todorova, *Curr. Clin. Pharmacol.* **2010**, *5*, 1–29. DOI:10.2174/157488410790410579
- N. K. Sahu, S. S. Balbhadra, J. Choudhary, D. V. Kohli, *Curr. Med. Chem.* **2012**, *19*, 209–225. DOI:10.2174/092986712803414132
- P. Singh, A. Anand, V. Kumar, *Eur. J. Med. Chem.* **2014**, *85*, 758–777. DOI:10.1016/j.ejmech.2014.08.033
- J. M. F. Custodio, W. F. Vaz, E. C. M. Faria, M. M. Anjos, C. E. M. Campos, G. R. Oliveira, F. T. Martins, C. C. da Silva, C. Valverde, F. A. P. Osório, B. Baseia, H. B. Napolitano, *J. Mol. Struct.* **2020**, *1201*, 127131. DOI:10.1016/j.molstruc.2019.127131
- S. Omar, M. Shkir, M. Ajmal Khan, Z. Ahmad, S. AlFaify, *Optik* **2020**, *204*, 164172. DOI:10.1016/j.ijleo.2020.164172
- T. P. Phan, K. Y. Teo, Z.-Q. Liu, J.-K. Tsai, M. G. Tay, *Chemical Data Collections* **2019**, *22*, 100256. DOI:10.1016/j.cdc.2019.100256
- M. M. Makhlof, A. S. Radwan, B. Ghazal, *Appl. Surf. Sci.* **2018**, *452*, 337–351. DOI:10.1016/j.apsusc.2018.05.007
- J. M. F. Custodio, J. J. A. Guimarães-Neto, R. Awad, J. E. Queiroz, G. M. V. Verde, M. Mottin, B. J. Neves, C. H. Andrade, G. L. B. Aquino, C. Valverde, F. A. P. Osório, B. Baseia, H. B. Napolitano, *Arab. J. Chem.* **2020**, *13*, 3362–3371. DOI:10.1016/j.arabjc.2018.11.010
- H. Hegde, R. K. Sinha, S. D. Kulkarni, N. S. Shetty, *J. Photochem. Photobiol. A: Chemistry* **2020**, *389*, 112222. DOI:10.1016/j.jphotochem.2019.112222
- J. Prabhu, K. Velmurugan, A. Raman, N. Duraipandy, M. S. Kiran, S. Easwaramoorthi, R. Nandhakumar, *Sensors and Actuators B: Chemical* **2017**, *238*, 306–317. DOI:10.1016/j.snb.2016.07.018
- A. J. H. Brian S. Furniss, Peter W.G. Smith, Austin R. Tatchell, Book Vogel's Textbook of Practical Organic Chemistry, Longman Scientific Technical, John Wiley Sons, Inc., New York, **1989**.
- W. S. Murphy, S. Wattanasin, *J. Chem. Soc., Perkin Trans. 1* **1980**, 1567–1577. DOI:10.1039/p19800001567
- F. Chimenti, A. Bolasco, F. Manna, D. Secci, P. Chimenti, O. Befani, P. Turini, V. Giovannini, B. Mondovi, R. Cirilli, F. La Torre, *J. Med. Chem.* **2004**, *47*, 2071–2074. DOI:10.1021/jm031042b
- M. Satyanarayana, P. Tiwari, B. K. Tripathi, A. K. Srivastava, R. Pratap, *Bioorg. Med. Chem.* **2004**, *12*, 883–889. DOI:10.1016/j.bmc.2003.12.026
- S. T. K. V.N. Ingle, U.G. Upadhyay, *Indian J. Chem. Sec. B.* **2005**, *44*, 801–805.
- K. K. Hsu, T. S. Wu, J. Y. Ski, *J. Chin. Chem. Soc.* **1972**, *19*, 45–48. DOI:10.1002/jccs.197200006
- G. Bist, N. T. Pun, T. B. Magar, A. Shrestha, H. J. Oh, A. Khakurel, P. H. Park, E. S. Lee, *Bioorg. Med. Chem. Lett.* **2017**, *27*, 1205–1209. DOI:10.1016/j.bmcl.2017.01.061
- F. Tok, B. Koçyiğit-Kaymakçioğlu, *Acta Chim. Slov.* **2020**, *67*, 1139–1147. DOI:10.17344/acsi.2020.6028
- H. Doğan, M. R. Bahar, E. Çalışkan, S. Tekin, H. Uslu, F. Akman, K. Koran, S. Sandal, A. O. Görgülü, *J. Biomol. Struct. Dyn.* **2020**, 1–15. DOI:10.1080/07391102.2020.1846621

37. J. B. Daskiewicz, G. Comte, D. Barron, A. Di Pietro, F. Thomasson, *Tetrahedron Lett.* **1999**, *40*, 7095–7098. DOI:10.1016/S0040-4039(99)01461-6
38. N. O. Calloway, L. D. Green, *J. Am. Chem. Soc.* **1937**, *59*, 809–811. DOI:10.1021/ja01284a011
39. G. Thirunarayanan. G. Vanangamudi, *Arhivoc* **2006**, *2006*, 58–64. DOI:10.3998/ark.5550190.0007.c07
40. T. Széll, I. Sohár, *Can. J. Chem.* **1969**, *47*, 1254–1258. DOI:10.1139/v69-207
41. G. Y. Sipos, F. Sirokman, *Nature* **1964**, *202*, 489–489. DOI:10.1038/202489a0
42. T. Narender, K. Papi Reddy, *Tetrahedron Lett.* **2007**, *48*, 3177–3180. DOI:10.1016/j.tetlet.2007.03.054
43. Z. Ze, D. Ya-Wei, W. Guan-Wu, *Chem. Lett.* **2003**, *32*, 966–967. DOI:10.1246/cl.2003.966
44. S. Eddarir, N. Cotellet, Y. Bakkour, C. Rolando, *Tetrahedron Lett.* **2003**, *44*, 5359–5363. DOI:10.1016/S0040-4039(03)01140-7
45. A. Kumar, S. Sharma, V. D. Tripathi, S. Srivastava, *Tetrahedron* **2010**, *66*, 9445–9449. DOI:10.1016/j.tet.2010.09.089
46. T. Maegawa, R. Mizui, M. Urasaki, K. Fujimura, A. Nakamura, Y. Miki, *ACS Omega* **2018**, *3*, 5375–5381. DOI:10.1021/acsomega.8b00594
47. R. O. Carlson, *Expert Opin. Investig. Drugs* **2008**, *17*, 707–722. DOI:10.1517/13543784.17.5.707
48. S. Sengupta, S. A. Thomas, *Expert Rev. Anticancer Ther.* **2006**, *6*, 1433–1447. DOI:10.1586/14737140.6.10.1433
49. A. E. Prota, F. Danel, F. Bachmann, K. Bargsten, R. M. Buey, J. Pohlmann, S. Reinelt, H. Lane, M. O. Steinmetz, *J. Mol. Biol.* **2014**, *426*, 1848–1860. DOI:10.1016/j.jmb.2014.02.005
50. N. K. Singh, S. B. Singh, *Synthesis and Reactivity in Inorganic and Metal-Organic Chemistry* **2002**, *32*, 25–47. DOI:10.1081/SIM-120013144
51. A. O. Görgülü, K. Koran, F. Özen, S. Tekin, S. Sandal, *J. Mol. Struct.* **2015**, *1087*, 1–10. DOI:10.1016/j.molstruc.2015.01.033
52. S. Keser, F. Keser, O. Kaygili, S. Tekin, I. Turkoglu, E. Demir, S. Turkoglu, M. Karatepe, S. Sandal, S. Kirbag, *Anal. Chem. Lett.* **2017**, *7*, 344–355. DOI:10.1080/22297928.2017.1329664
53. T. R. Mosmann, H. Cherwinski, M. W. Bond, M. A. Giedlin, R. L. Coffman, *J. Immunol. (Baltimore, Md.)* **1986**, *136*, 2348–2357.
54. Maestro, New York, NY, Schrödinger LLC, 2020.
55. G. M. Morris, R. Huey, W. Lindstrom, M. F. Sanner, R. K. Belew, D. S. Goodsell, A. J. Olson, *J. Comput. Chem.* **2009**, *30*, 2785–2791. DOI:10.1002/jcc.21256
56. O. Trott, A. J. Olson, *J. Comput. Chem.* **2010**, *31*, 455–461.

Povzetek

Načrtovali in izvedli smo sintezo serije halkonskih spojin (2–11) z namenom, da določimo njihove citotoksične učinke. Strukture 2–11 smo karakterizirali s pomočjo fizikalnih in spektroskopskih podatkov. Citotoksični učinek spojin 2–11 smo *in vitro* določali na človeških rakastih celičnih linijah raka jajčnika (A2780), raka dojke (MCF-7) in raka prostate (PC-3 ter LNCaP). Potencialne aktivnosti spojin smo še dodatno raziskali s pomočjo študij molekulskega sidranja s programoma AutoDock4 in Vina. Vse spojine (z izjemo spojine 5) so pri visokih odmerkih pokazale opazne citotoksične učinke proti vsem rakastim celičnim linijam. Izmed vseh preiskovanih spojin, je spojina 2 izkazala aktivnost, odvisno od koncentracije, še posebej proti A2780/LNCaP rakastim celičnim linijam. Najbolj učinkovite spojine 8, 9, 10 in 11 so zmanjšale sposobnost preživetja celic pri A2780, MCF-7, PC-3 ter LNCaP celičnih linijah za 50–98%; spojine 2, 4 in 7 pa so zmanjšale sposobnost preživetja celic pri A2780 celični liniji za 70–90% pri koncentracijah 50 in 100 μM .



Except when otherwise noted, articles in this journal are published under the terms and conditions of the Creative Commons Attribution 4.0 International License

Scientific paper

Design, Synthesis, *In Silico* ADMET Studies and Anticancer Activity of Some New Pyrazoline and Benzodioxole Derivatives

Fatih Tok,^{1,*} Ömer Erdoğan,² Özge Çevik²
and Bedia Koçyiğit-Kaymakçioğlu¹

¹ Department of Pharmaceutical Chemistry, Faculty of Pharmacy, Marmara University, Istanbul, Turkey

² Department of Biochemistry, School of Medicine, Aydin Adnan Menderes University,

* Corresponding author: E-mail: fatih.tok@marmara.edu.tr
Tel: +90-216-7775200.

Received: 09-02-2021

Abstract

A new series of 2-pyrazoline derivatives starting from substituted benzodioxole chalcones were designed and synthesized. IR and ¹H NMR spectral data and elemental analysis were used to characterize the structures of the synthesized compounds. The cytotoxic activities on HeLa, MCF-7 cancer cell lines and NIH-3T3 for these compounds were tested by using MTT assay. Among the synthesized compounds **2d**, **2j**, **3j** and **3n** against MCF-7 cells, and **3c** against HeLa exhibited significant cytotoxic activity with IC₅₀ between 10.08 and 27.63 μM. Compound **3f** showed the most potent anticancer activity against both cancer cells with good selectivity (IC₅₀ = 11.53 μM on HeLa with SI = 81.75 and IC₅₀ = 11.37 μM on MCF-7 with SI = 82.90). Furthermore, *in silico* ADMET analyses were performed and the drug-likeness properties of the compounds were investigated.

Keywords: Pyrazoline; carboxamide; anticancer activity; breast cancer; cervical cancer.

1. Introduction

Pyrazolines are electron rich nitrogen heterocycles that are appropriate for the discovery of bioactive molecules.¹ Pyrazolines occur naturally in animal and plant cells, in the form of vitamins, pigments and alkaloids.² These heterocyclic compounds are known to exhibit good pharmacological and biological activities such as antimicrobial, antiinflammatory, analgesic, anti-depressant and anticancer.^{3–7}

Heterocyclic anticancer agents bearing nitrogen-nitrogen (*N–N*) bonds, such as crizotinib, ruxolitinib, axitinib, encorafenib and ibrutinib, have been approved by the FDA in the last decades.⁸ Podophyllotoxin and steganacin bearing benzo[*d*][1,3]dioxol moiety are natural bioactive molecules with very strong cytotoxic activity. Some adverse effects related to complex pharmacokinetics including unpredictable drug-drug interactions can appear because of the therapeutics of combining multiple drugs. It is an important strategy for drug discovery that constructing a single molecule modulates multiple targets simulta-

neously.^{9,10} Therefore, we designed two series of pyrazoline derivatives containing benzo[*d*][1,3]dioxol moiety by the molecular assembly principle (Figure 1).

Herein we report the synthesis of 2-pyrazolines starting from 1-(benzo[*d*][1,3]dioxol-5-yl)ethanone and further evaluated their anticancer activities on HeLa (human cervical adenocarcinoma), MCF7 (human breast adenocarcinoma) cancer cells. NIH-3T3 mouse embryonic fibroblast cell lines were also used to determine the tumor selectivity of the synthesized compounds.

2. Experimental

2. 1. Chemistry

All chemicals were obtained from Sigma-Aldrich or Merck Chemical Company and used without further purification. The reaction processes and the purity of compounds were monitored by thin layer chromatography using a UV lamp. Melting points were determined on a Kleinfeld SMP II apparatus and are uncorrected. The IR

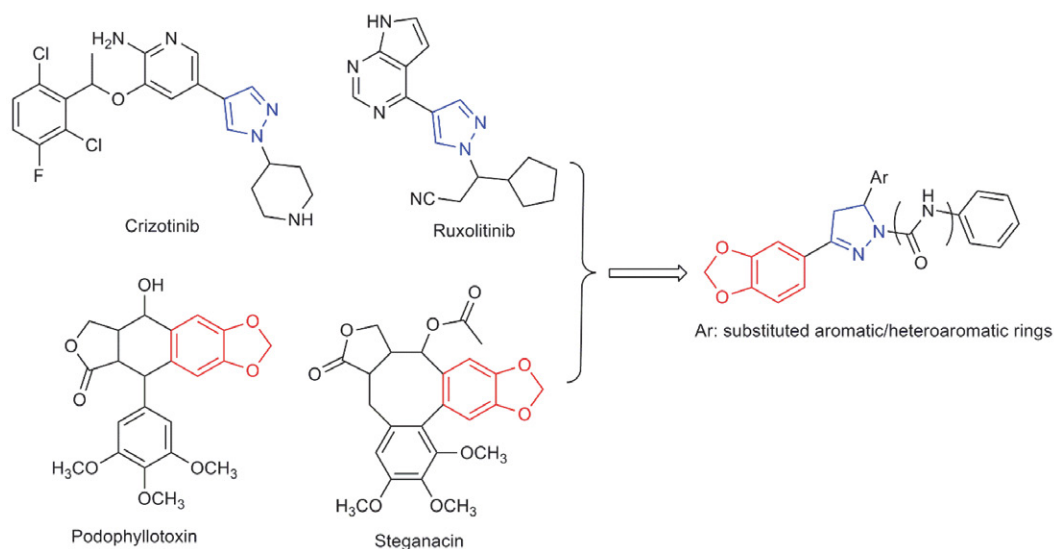


Figure 1. Design strategy of the target compounds

spectra were recorded using a Shimadzu FTIR 8400S spectrometry. ^1H NMR spectra were taken on a Bruker (400 MHz) spectrometer. Elemental analysis was performed on Leco CHNS-932 analyzer.

General Procedure for the Preparation of Chalcone Derivatives 1a–1o

1-(Benzo[*d*][1,3]dioxol-5-yl)ethanone (1 mmol, 0.164 g) and corresponding aromatic aldehyde (1 mmol) were dissolved in 20 mL methanol. A solution of sodium hydroxide (50%, 3 mL) was added to the reaction mixture. The mixture was stirred on magnetic stirrer for 8 h. The precipitated product was filtered, washed with water and recrystallized from methanol.¹¹

General Procedure for Preparation of Pyrazoline Derivatives 2a–2o

Chalcone derivatives (1 mmol) and phenylhydrazine hydrochloride (1 mmol, 0.145 g) was dissolved in 25 mL ethanol. Catalytic quantity of acetic acid (1.5 mL) was added to the reaction mixture. The mixture was refluxed for 8 h. The mixture was cooled, the precipitated product was filtered, washed with water and recrystallized from ethanol.¹²

3-(Benzo[*d*][1,3]dioxol-5-yl)-1,5-diphenyl-4,5-dihydro-1H-pyrazole (2a)

Yield: 280 mg (82%) of white powder; m.p. 172.8–173.2 °C. IR (ν_{max} , cm^{-1}): 3028 (=C-H), 2914 (C-H), 1593 (C=N), 1249 (C-O), 1033 (C-N); ^1H NMR (400 MHz, $\text{DMSO-}d_6$): δ 3.03 (dd, $J_{\text{ax}} = 6.5$ Hz, $J_{\text{ab}} = 17.4$ Hz, 1H, Ha), 3.84 (dd, $J_{\text{bx}} = 12.2$ Hz, $J_{\text{ab}} = 17.5$ Hz, 1H, Hb), 5.40 (dd, $J_{\text{ax}} = 6.4$ Hz, $J_{\text{bx}} = 12.1$ Hz, 1H, Hx), 6.04 (s, 2H, O-CH₂-O), 6.65–7.36 (m, 13H, Ar-H). Anal. Calcd for $\text{C}_{22}\text{H}_{18}\text{N}_2\text{O}_2$: C, 77.17; H, 5.30; N, 8.18. Found: C, 77.07; H, 5.32; N, 8.15%.

3-(Benzo[*d*][1,3]dioxol-5-yl)-5-(4-fluorophenyl)-1-phenyl-4,5-dihydro-1H-pyrazole (2b)

Yield: 288 mg (80%) of white powder; m.p. 138.1–138.3 °C. IR (ν_{max} , cm^{-1}): 3066 (=C-H), 2891 (C-H), 1591 (C=N), 1211 (C-O), 1037 (C-N); ^1H NMR (400 MHz, $\text{DMSO-}d_6$): δ 3.03 (dd, $J_{\text{ax}} = 6.3$ Hz, $J_{\text{ab}} = 17.5$ Hz, 1H, Ha), 3.83 (dd, $J_{\text{bx}} = 12.1$ Hz, $J_{\text{ab}} = 17.5$ Hz, 1H, Hb), 5.44 (dd, $J_{\text{ax}} = 6.3$ Hz, $J_{\text{bx}} = 12.0$ Hz, 1H, Hx), 6.05 (s, 2H, O-CH₂-O), 6.68–7.31 (m, 12H, Ar-H). Anal. Calcd for $\text{C}_{22}\text{H}_{17}\text{FN}_2\text{O}_2$: C, 73.32; H, 4.75; N, 7.77. Found: C, 73.20; H, 4.77; N, 7.80%.

3-(Benzo[*d*][1,3]dioxol-5-yl)-5-(4-bromophenyl)-1-phenyl-4,5-dihydro-1H-pyrazole (2c)

Yield: 341 mg (81%) of white crystals; m.p. 164.5–164.8 °C. IR (ν_{max} , cm^{-1}): 3082 (=C-H), 2885 (C-H), 1595 (C=N), 1211 (C-O), 1033 (C-N); ^1H NMR (400 MHz, $\text{DMSO-}d_6$): δ 3.04 (dd, $J_{\text{ax}} = 6.3$ Hz, $J_{\text{ab}} = 17.4$ Hz, 1H, Ha), 3.83 (dd, $J_{\text{bx}} = 12.2$ Hz, $J_{\text{ab}} = 17.5$ Hz, 1H, Hb), 5.42 (dd, $J_{\text{ax}} = 6.3$ Hz, $J_{\text{bx}} = 12.1$ Hz, 1H, Hx), 6.05 (s, 2H, O-CH₂-O), 6.68–7.51 (m, 12H, Ar-H). Anal. Calcd for $\text{C}_{22}\text{H}_{17}\text{BrN}_2\text{O}_2$: C, 62.72; H, 4.07; N, 6.65. Found: C, 62.81; H, 4.08; N, 6.61%.

3-(Benzo[*d*][1,3]dioxol-5-yl)-5-(4-nitrophenyl)-1-phenyl-4,5-dihydro-1H-pyrazole (2d)

Yield: 325 mg (84%) of yellow powder; m.p. 110.2–110.5 °C. IR (ν_{max} , cm^{-1}): 3078 (=C-H), 2881 (C-H), 1595 (C=N), 1213 (C-O), 1033 (C-N); ^1H NMR (400 MHz, $\text{DMSO-}d_6$): δ 3.10 (dd, $J_{\text{ax}} = 6.3$ Hz, $J_{\text{ab}} = 17.5$ Hz, 1H, Ha), 3.90 (dd, $J_{\text{bx}} = 12.3$ Hz, $J_{\text{ab}} = 17.5$ Hz, 1H, Hb), 5.61 (dd, $J_{\text{ax}} = 6.3$ Hz, $J_{\text{bx}} = 12.3$ Hz, 1H, Hx), 6.05 (s, 2H, O-CH₂-O), 6.70–8.20 (m, 12H, Ar-H). Anal. Calcd for $\text{C}_{22}\text{H}_{17}\text{N}_3\text{O}_4$: C, 68.21; H, 4.42; N, 10.85. Found: C, 68.04; H, 4.41; N, 10.89%.

3-(Benzo[d][1,3]dioxol-5-yl)-1-phenyl-5-*para*-tolyl-4,5-dihydro-1H-pyrazole (2e)

Yield: 278 mg (78%) of white powder; m.p. 146.4–146.6 °C. IR (ν_{\max} , cm^{-1}): 3022 (=C-H), 2901 (C-H), 1595 (C=N), 1215 (C-O), 1035 (C-N); ^1H NMR (400 MHz, DMSO- d_6): δ 2.23 (s, 3H, CH₃), 3.00 (dd, $J_{\text{ax}} = 6.4$ Hz, $J_{\text{ab}} = 17.4$ Hz, 1H, Ha), 3.81 (dd, $J_{\text{bx}} = 12.2$ Hz, $J_{\text{ab}} = 17.4$ Hz, 1H, Hb), 5.35 (dd, $J_{\text{ax}} = 6.4$ Hz, $J_{\text{bx}} = 12.1$ Hz, 1H, Hx), 6.04 (s, 2H, O-CH₂-O), 6.66–7.35 (m, 12H, Ar-H). Anal. Calcd for C₂₃H₂₀N₂O₂: C, 77.51; H, 5.66; N, 7.86. Found: C, 77.39; H, 5.68; N, 7.85%.

4-(3-(Benzo[d][1,3]dioxol-5-yl)-1-phenyl-4,5-dihydro-1H-pyrazol-5-yl)benzotrile (2f)

Yield: 290 mg (79%) of white crystals; m.p. 135.9–136.3 °C. IR (ν_{\max} , cm^{-1}): 3053 (=C-H), 2901 (C-H), 1593 (C=N), 1217 (C-O), 1033 (C-N); ^1H NMR (400 MHz, DMSO- d_6): δ 3.08 (dd, $J_{\text{ax}} = 6.3$ Hz, $J_{\text{ab}} = 17.5$ Hz, 1H, Ha), 3.87 (dd, $J_{\text{bx}} = 12.3$ Hz, $J_{\text{ab}} = 17.5$ Hz, 1H, Hb), 5.55 (dd, $J_{\text{ax}} = 6.2$ Hz, $J_{\text{bx}} = 12.1$ Hz, 1H, Hx), 6.05 (s, 2H, O-CH₂-O), 6.70–7.80 (m, 12H, Ar-H). Anal. Calcd for C₂₃H₁₇N₃O₂: C, 75.19; H, 4.66; N, 11.44. Found: C, 75.11; H, 4.66; N, 11.46%.

3-(Benzo[d][1,3]dioxol-5-yl)-5-(2,6-dimethylphenyl)-1-phenyl-4,5-dihydro-1H-pyrazole (2g)

Yield: 296 mg (80%) of white powder; m.p. 117.8–118.0 °C. IR (ν_{\max} , cm^{-1}): 3037 (=C-H), 2881 (C-H), 1597 (C=N), 1213 (C-O), 1037 (C-N); ^1H NMR (400 MHz, DMSO- d_6): δ 2.03 (s, 3H, CH₃), 2.24 (s, 3H, CH₃), 3.01 (dd, $J_{\text{ax}} = 6.3$ Hz, $J_{\text{ab}} = 17.4$ Hz, 1H, Ha), 3.91 (dd, $J_{\text{bx}} = 12.1$ Hz, $J_{\text{ab}} = 17.4$ Hz, 1H, Hb), 5.56 (dd, $J_{\text{ax}} = 6.3$ Hz, $J_{\text{bx}} = 12.0$ Hz, 1H, Hx), 6.05 (s, 2H, O-CH₂-O), 6.66–7.36 (m, 11H, Ar-H). Anal. Calcd for C₂₄H₂₂N₂O₂: C, 77.81; H, 5.99; N, 7.56. Found: C, 77.90; H, 5.96; N, 7.59%.

3-(Benzo[d][1,3]dioxol-5-yl)-1-phenyl-5-*ortho*-tolyl-4,5-dihydro-1H-pyrazole (2h)

Yield: 303 mg (85%) of white powder; m.p. 163.9–164.2 °C. IR (ν_{\max} , cm^{-1}): 3066 (=C-H), 2881 (C-H), 1597 (C=N), 1203 (C-O), 1033 (C-N); ^1H NMR (400 MHz, DMSO- d_6): δ 2.24 (s, 3H, CH₃), 2.92 (dd, $J_{\text{ax}} = 6.6$ Hz, $J_{\text{ab}} = 17.4$ Hz, 1H, Ha), 3.96 (dd, $J_{\text{bx}} = 12.3$ Hz, $J_{\text{ab}} = 17.4$ Hz, 1H, Hb), 5.50 (dd, $J_{\text{ax}} = 6.6$ Hz, $J_{\text{bx}} = 12.3$ Hz, 1H, Hx), 6.05 (s, 2H, O-CH₂-O), 6.68–7.36 (m, 12H, Ar-H). Anal. Calcd for C₂₃H₂₀N₂O₂: C, 77.51; H, 5.66; N, 7.86. Found: C, 77.59; H, 5.66; N, 7.88%.

3-(Benzo[d][1,3]dioxol-5-yl)-1-phenyl-5-*meta*-tolyl-4,5-dihydro-1H-pyrazole (2i)

Yield: 310 mg (87%) of white powder; m.p. 148.8–149.2 °C. IR (ν_{\max} , cm^{-1}): 3061 (=C-H), 2893 (C-H), 1595 (C=N), 1211 (C-O), 1033 (C-N); ^1H NMR (400 MHz, DMSO- d_6): δ 2.24 (s, 3H, CH₃), 3.01 (dd, $J_{\text{ax}} = 6.3$ Hz, $J_{\text{ab}} = 17.5$ Hz, 1H, Ha), 3.83 (dd, $J_{\text{bx}} = 12.1$ Hz, $J_{\text{ab}} = 17.5$ Hz, 1H, Hb), 5.33 (dd, $J_{\text{ax}} = 6.3$ Hz, $J_{\text{bx}} = 12.0$ Hz, 1H, Hx),

6.05 (s, 2H, O-CH₂-O), 6.67–7.31 (m, 12H, Ar-H). Anal. Calcd for C₂₃H₂₀N₂O₂: C, 77.51; H, 5.66; N, 7.86. Found: C, 77.61; H, 5.64; N, 7.89%.

4-(3-(Benzo[d][1,3]dioxol-5-yl)-1-phenyl-4,5-dihydro-1H-pyrazol-5-yl)pyridine (2j)

Yield: 268 mg (78%) of gray powder; m.p. 108.2–108.3 °C. IR (ν_{\max} , cm^{-1}): 3030 (=C-H), 2881 (C-H), 1597 (C=N), 1242 (C-O), 1033 (C-N); ^1H NMR (400 MHz, DMSO- d_6): δ 3.06 (dd, $J_{\text{ax}} = 6.4$ Hz, $J_{\text{ab}} = 17.4$ Hz, 1H, Ha), 3.82 (dd, $J_{\text{bx}} = 12.1$ Hz, $J_{\text{ab}} = 17.4$ Hz, 1H, Hb), 5.43 (dd, $J_{\text{ax}} = 6.4$ Hz, $J_{\text{bx}} = 12.1$ Hz, 1H, Hx), 6.08 (s, 2H, O-CH₂-O), 6.52–7.62 (m, 12H, Ar-H). Anal. Calcd for C₂₁H₁₇N₃O₂: C, 73.45; H, 4.99; N, 12.24. Found: C, 73.32; H, 5.01; N, 12.23%.

3-(Benzo[d][1,3]dioxol-5-yl)-1-phenyl-5-(thiophen-2-yl)-4,5-dihydro-1H-pyrazole (2k)

Yield: 271 mg (78%) of red powder; m.p. 152.7–153.0 °C. IR (ν_{\max} , cm^{-1}): 3074 (=C-H), 2893 (C-H), 1595 (C=N), 1201 (C-O), 1031 (C-N); ^1H NMR (400 MHz, DMSO- d_6): δ 3.21 (dd, $J_{\text{ax}} = 5.9$ Hz, $J_{\text{ab}} = 17.3$ Hz, 1H, Ha), 3.81 (dd, $J_{\text{bx}} = 11.6$ Hz, $J_{\text{ab}} = 17.3$ Hz, 1H, Hb), 5.75 (dd, $J_{\text{ax}} = 5.9$ Hz, $J_{\text{bx}} = 11.6$ Hz, 1H, Hx), 6.06 (s, 2H, O-CH₂-O), 6.72–7.36 (m, 11H, Ar-H). Anal. Calcd for C₂₀H₁₆N₂O₂S: C, 68.94; H, 4.63; N, 8.04. Found: C, 68.85; H, 4.65; N, 8.08%.

3-(Benzo[d][1,3]dioxol-5-yl)-5-(furan-2-yl)-1-phenyl-4,5-dihydro-1H-pyrazole (2l)

Yield: 272 mg (82%) of brown powder; m.p. 120.1–120.5 °C. IR (ν_{\max} , cm^{-1}): 3078 (=C-H), 2908 (C-H), 1595 (C=N), 1211 (C-O), 1033 (C-N); ^1H NMR (400 MHz, DMSO- d_6): δ 3.28 (dd, $J_{\text{ax}} = 6.0$ Hz, $J_{\text{ab}} = 17.3$ Hz, 1H, Ha), 3.70 (dd, $J_{\text{bx}} = 12.1$ Hz, $J_{\text{ab}} = 17.3$ Hz, 1H, Hb), 5.53 (dd, $J_{\text{ax}} = 6.0$ Hz, $J_{\text{bx}} = 12.2$ Hz, 1H, Hx), 6.05 (s, 2H, O-CH₂-O), 6.38–7.54 (m, 11H, Ar-H). Anal. Calcd for C₂₀H₁₆N₂O₃: C, 72.28; H, 4.85; N, 8.43. Found: C, 72.41; H, 4.88; N, 8.38%.

3-(Benzo[d][1,3]dioxol-5-yl)-5-(5-bromothiophen-2-yl)-1-phenyl-4,5-dihydro-1H-pyrazole (2m)

Yield: 376 mg (88%) of gray powder; m.p. 143.0–143.4 °C. IR (ν_{\max} , cm^{-1}): 3039 (=C-H), 2908 (C-H), 1595 (C=N), 1215 (C-O), 1035 (C-N); ^1H NMR (400 MHz, DMSO- d_6): δ 3.01 (dd, $J_{\text{ax}} = 6.4$ Hz, $J_{\text{ab}} = 17.4$ Hz, 1H, Ha), 3.82 (dd, $J_{\text{bx}} = 12.1$ Hz, $J_{\text{ab}} = 17.4$ Hz, 1H, Hb), 5.36 (dd, $J_{\text{ax}} = 6.4$ Hz, $J_{\text{bx}} = 12.1$ Hz, 1H, Hx), 6.06 (s, 2H, O-CH₂-O), 6.67–7.36 (m, 10H, Ar-H). Anal. Calcd for C₂₀H₁₅BrN₂O₂S: C, 56.21; H, 3.54; N, 6.56. Found: C, 56.08; H, 3.53; N, 6.59%.

3-(Benzo[d][1,3]dioxol-5-yl)-1-phenyl-5-(4-(trifluoromethyl)phenyl)-4,5-dihydro-1H-pyrazole (2n)

Yield: 328 mg (80%) of white powder; m.p. 146.4–146.6 °C. IR (ν_{\max} , cm^{-1}): 3078 (=C-H), 2887 (C-H), 1597 (C=N), 1213 (C-O), 1033 (C-N); ^1H NMR (400 MHz,

DMSO- d_6): δ 3.10 (dd, $J_{ax} = 5.9$ Hz, $J_{ab} = 17.3$ Hz, 1H, Ha), 3.88 (dd, $J_{bx} = 11.6$ Hz, $J_{ab} = 17.3$ Hz, 1H, Hb), 5.57 (dd, $J_{ax} = 5.9$ Hz, $J_{bx} = 11.6$ Hz, 1H, Hx), 6.06 (s, 2H, O-CH₂-O), 6.70–7.71 (m, 12H, Ar-H). Anal. Calcd for C₂₃H₁₇F₃N₂O₂: C, 67.31; H, 4.18; N, 6.83. Found: C, 67.15; H, 4.17; N, 6.79%.

3-(Benzo[d][1,3]dioxol-5-yl)-5-(3-chlorophenyl)-1-phenyl-4,5-dihydro-1H-pyrazole (2o)

Yield: 320 mg (85%) of white crystals; m.p. 131.0–131.3 °C. IR (ν_{\max} , cm⁻¹): 3072 (=C-H), 2908 (C-H), 1593 (C=N), 1213 (C-O), 1035 (C-N); ¹H NMR (400 MHz, DMSO- d_6): δ 3.11 (dd, $J_{ax} = 6.3$ Hz, $J_{ab} = 17.5$ Hz, 1H, Ha), 3.92 (dd, $J_{bx} = 12.1$ Hz, $J_{ab} = 17.5$ Hz, 1H, Hb), 5.48 (dd, $J_{ax} = 6.2$ Hz, $J_{bx} = 12.1$ Hz, 1H, Hx), 6.08 (s, 2H, O-CH₂-O), 6.58–7.68 (m, 12H, Ar-H). Anal. Calcd for C₂₂H₁₇ClN₂O₂: C, 70.12; H, 4.55; N, 7.43. Found: C, 70.21; H, 4.57; N, 7.42%.

General Procedure for Preparation of Pyrazoline Derivatives 3a–3o

Firstly, the synthesis of *N*-(4-chlorophenyl)hydrazinecarboxamide was carried out. Hydrazine monohydrate (1 mmol, 48.5 μ L) was added dropwise to 4-chlorophenylisocyanate (1 mmol, 128.0 μ L) in 15 mL diethyl ether. The mixture was stirred for 1 h. The white precipitated product was filtered, dried.¹³

Chalcone derivatives (1 mmol) and *N*-(4-chlorophenyl)hydrazinecarboxamide (1 mmol) was dissolved in 20 mL ethanol, and then a solution of sodium hydroxide (20%, 1 mL) was added to the reaction mixture. The mixture was refluxed for 10 h. The mixture was cooled, the precipitated product was filtered, washed with water and recrystallized from ethanol.¹³

3-(Benzo[d][1,3]dioxol-5-yl)-*N*-(4-chlorophenyl)-5-phenyl-4,5-dihydro-1H-pyrazole-1-carboxamide (3a)

Yield: 328 mg (78%) of white powder; m.p. 139.1–139.3 °C. IR (ν_{\max} , cm⁻¹): 3290 (N-H), 3078 (=C-H), 2989, 2901 (C-H), 1666 (C=O), 1631 (C=N), 1222 (C-O), 1033 (C-N); ¹H NMR (400 MHz, DMSO- d_6): δ 3.13 (dd, $J_{ax} = 5.2$ Hz, $J_{ab} = 17.8$ Hz, 1H, Ha), 3.81 (dd, $J_{bx} = 11.7$ Hz, $J_{ab} = 17.8$ Hz, 1H, Hb), 5.51 (dd, $J_{ax} = 5.2$ Hz, $J_{bx} = 11.7$ Hz, 1H, Hx), 6.08 (s, 2H, O-CH₂-O), 6.90–7.97 (m, 12H, Ar-H), 9.14 (s, 1H, NH). Anal. Calcd for C₂₃H₁₈ClN₃O₃: C, 65.79; H, 4.32; N, 10.01. Found: C, 65.89; H, 4.35; N, 9.95%.

3-(Benzo[d][1,3]dioxol-5-yl)-*N*-(4-chlorophenyl)-5-(4-fluorophenyl)-4,5-dihydro-1H-pyrazole-1-carboxamide (3b)

Yield: 350 mg (80%) of white powder; m.p. 134.4–134.5 °C. IR (ν_{\max} , cm⁻¹): 3292 (N-H), 3066 (=C-H), 2987, 2885 (C-H), 1666 (C=O), 1633 (C=N), 1228 (C-O), 1033 (C-N); ¹H NMR (400 MHz, DMSO- d_6): δ 3.15 (dd, $J_{ax} = 5.3$ Hz, $J_{ab} = 17.9$ Hz, 1H, Ha), 3.85 (dd, $J_{bx} = 11.6$ Hz, $J_{ab} = 17.9$ Hz, 1H, Hb), 5.52 (dd, $J_{ax} = 5.2$ Hz, $J_{bx} = 11.7$ Hz, 1H, Hx), 6.14 (s, 2H, O-CH₂-O), 7.04–7.94 (m, 11H, Ar-H), 9.16 (s, 1H, NH). Anal. Calcd for C₂₃H₁₇ClFN₃O₃: C, 63.09; H, 3.91; N, 9.60. Found: C, 63.00; H, 3.90; N, 9.65%.

Yield: 424 mg (85%) of white powder; m.p. 123.7–123.9 °C. IR (ν_{\max} , cm⁻¹): 3290 (N-H), 3072 (=C-H), 2974, 2989 (C-H), 1666 (C=O), 1633 (C=N), 1222 (C-O), 1033 (C-N); ¹H NMR (400 MHz, DMSO- d_6): δ 3.14 (dd, $J_{ax} = 5.5$ Hz, $J_{ab} = 17.9$ Hz, 1H, Ha), 3.80 (dd, $J_{bx} = 11.6$ Hz, $J_{ab} = 17.9$ Hz, 1H, Hb), 5.49 (dd, $J_{ax} = 5.3$ Hz, $J_{bx} = 11.7$ Hz, 1H, Hx), 6.02 (s, 2H, O-CH₂-O), 7.07–7.85 (m, 11H, Ar-H), 9.06 (s, 1H, NH). Anal. Calcd for C₂₃H₁₇BrClN₃O₃: C, 55.39; H, 3.44; N, 8.42. Found: C, 55.55; H, 3.41; N, 8.45%.

3-(Benzo[d][1,3]dioxol-5-yl)-5-(4-bromophenyl)-*N*-(4-chlorophenyl)-4,5-dihydro-1H-pyrazole-1-carboxamide (3c)

Yield: 400 mg (86%) of yellow powder; m.p. 128.8–129.0 °C. IR (ν_{\max} , cm⁻¹): 3290 (N-H), 3078 (=C-H), 2989, 2912 (C-H), 1666 (C=O), 1631 (C=N), 1230 (C-O), 1033 (C-N); ¹H NMR (400 MHz, DMSO- d_6): δ 3.14 (dd, $J_{ax} = 5.2$ Hz, $J_{ab} = 18.0$ Hz, 1H, Ha), 3.81 (dd, $J_{bx} = 11.9$ Hz, $J_{ab} = 18.0$ Hz, 1H, Hb), 5.51 (dd, $J_{ax} = 5.2$ Hz, $J_{bx} = 11.9$ Hz, 1H, Hx), 6.10 (s, 2H, O-CH₂-O), 7.10–7.77 (m, 11H, Ar-H), 9.06 (s, 1H, NH). Anal. Calcd for C₂₃H₁₇ClN₄O₃: C, 59.43; H, 3.69; N, 12.05. Found: C, 59.60; H, 3.73; N, 12.12%.

3-(Benzo[d][1,3]dioxol-5-yl)-*N*-(4-chlorophenyl)-5-(4-nitrophenyl)-4,5-dihydro-1H-pyrazole-1-carboxamide (3d)

Yield: 356 mg (82%) of white powder; m.p. 161.9–162.3 °C. IR (ν_{\max} , cm⁻¹): 3292 (N-H), 3078 (=C-H), 2987, 2887 (C-H), 1666 (C=O), 1631 (C=N), 1228 (C-O), 1033 (C-N); ¹H NMR (400 MHz, DMSO- d_6): δ 2.30 (s, 3H, CH₃), 3.07 (dd, $J_{ax} = 5.3$ Hz, $J_{ab} = 17.9$ Hz, 1H, Ha), 3.78 (dd, $J_{bx} = 11.9$ Hz, $J_{ab} = 17.9$ Hz, 1H, Hb), 5.43 (dd, $J_{ax} = 5.3$ Hz, $J_{bx} = 11.9$ Hz, 1H, Hx), 6.07 (s, 2H, O-CH₂-O), 7.05–7.65 (m, 11H, Ar-H), 9.00 (s, 1H, NH). Anal. Calcd for C₂₄H₂₀ClN₃O₃: C, 66.44; H, 4.65; N, 9.68. Found: C, 66.29; H, 4.62; N, 9.73%.

3-(Benzo[d][1,3]dioxol-5-yl)-*N*-(4-chlorophenyl)-5-*para*-tolyl-4,5-dihydro-1H-pyrazole-1-carboxamide (3e)

Yield: 312 mg (70%) of gray powder; m.p. 188.1–188.5 °C. IR (ν_{\max} , cm⁻¹): 3292 (N-H), 3084 (=C-H), 2918, 2848 (C-H), 1666 (C=O), 1631 (C=N), 1230 (C-O), 1033 (C-N); ¹H NMR (400 MHz, DMSO- d_6): δ 3.11 (dd, $J_{ax} = 5.6$ Hz, $J_{ab} = 17.9$ Hz, 1H, Ha), 3.78 (dd, $J_{bx} = 12.0$ Hz, $J_{ab} = 17.9$ Hz, 1H, Hb), 5.48 (dd, $J_{ax} = 5.5$ Hz, $J_{bx} = 12.0$ Hz, 1H, Hx), 6.09 (s, 2H, O-CH₂-O), 6.98–7.85 (m, 11H, Ar-H), 9.02 (s, 1H, NH). Anal. Calcd for C₂₄H₁₇ClN₄O₃: C, 64.80; H, 3.85; N, 12.59. Found: C, 64.65; H, 3.88; N, 12.56%.

3-(Benzo[d][1,3]dioxol-5-yl)-*N*-(4-chlorophenyl)-5-(4-cyanophenyl)-4,5-dihydro-1H-pyrazole-1-carboxamide (3f)

Yield: 312 mg (70%) of gray powder; m.p. 188.1–188.5 °C. IR (ν_{\max} , cm⁻¹): 3292 (N-H), 3084 (=C-H), 2918, 2848 (C-H), 1666 (C=O), 1631 (C=N), 1230 (C-O), 1033 (C-N); ¹H NMR (400 MHz, DMSO- d_6): δ 3.11 (dd, $J_{ax} = 5.6$ Hz, $J_{ab} = 17.9$ Hz, 1H, Ha), 3.78 (dd, $J_{bx} = 12.0$ Hz, $J_{ab} = 17.9$ Hz, 1H, Hb), 5.48 (dd, $J_{ax} = 5.5$ Hz, $J_{bx} = 12.0$ Hz, 1H, Hx), 6.09 (s, 2H, O-CH₂-O), 6.98–7.85 (m, 11H, Ar-H), 9.02 (s, 1H, NH). Anal. Calcd for C₂₄H₁₇ClN₄O₃: C, 64.80; H, 3.85; N, 12.59. Found: C, 64.65; H, 3.88; N, 12.56%.

3-(Benzo[d][1,3]dioxol-5-yl)-N-(4-chlorophenyl)-5-(2,6-dimethylphenyl)-4,5-dihydro-1H-pyrazole-1-carboxamide (3g)

Yield: 323 mg (72%) of white powder; m.p. 155.1–155.5 °C. IR (ν_{\max} , cm^{-1}): 3290 (N-H), 3066 (=C-H), 2987, 2918, 2848 (C-H), 1672 (C=O), 1631 (C=N), 1220 (C-O), 1033 (C-N); ^1H NMR (400 MHz, DMSO- d_6): δ 2.08 (s, 3H, CH₃), 2.34 (s, 3H, CH₃), 3.04 (dd, $J_{\text{ax}} = 5.9$ Hz, $J_{\text{ab}} = 17.3$ Hz, 1H, Ha), 3.81 (dd, $J_{\text{bx}} = 11.6$ Hz, $J_{\text{ab}} = 17.3$ Hz, 1H, Hb), 5.85 (dd, $J_{\text{ax}} = 5.9$ Hz, $J_{\text{bx}} = 11.6$ Hz, 1H, Hx), 6.10 (s, 2H, O-CH₂-O), 7.00–7.70 (m, 10H, Ar-H), 9.12 (s, 1H, NH). Anal. Calcd for C₂₅H₂₂ClN₃O₃: C, 67.04; H, 4.95; N, 9.38. Found: C, 66.91; H, 4.99; N, 9.45%.

3-(Benzo[d][1,3]dioxol-5-yl)-N-(4-chlorophenyl)-5-ortho-tolyl-4,5-dihydro-1H-pyrazole-1-carboxamide (3h)

Yield: 343 mg (79%) of white powder; m.p. 129.8–130.1 °C. IR (ν_{\max} , cm^{-1}): 3367 (N-H), 3095 (=C-H), 2982, 2881 (C-H), 1667 (C=O), 1631 (C=N), 1220 (C-O), 1033 (C-N); ^1H NMR (400 MHz, DMSO- d_6): δ 2.34 (s, 3H, CH₃), 2.99 (dd, $J_{\text{ax}} = 5.5$ Hz, $J_{\text{ab}} = 17.8$ Hz, 1H, Ha), 3.87 (dd, $J_{\text{bx}} = 12.0$ Hz, $J_{\text{ab}} = 17.8$ Hz, 1H, Hb), 5.63 (dd, $J_{\text{ax}} = 5.5$ Hz, $J_{\text{bx}} = 12.0$ Hz, 1H, Hx), 6.12 (s, 2H, O-CH₂-O), 7.00–7.67 (m, 11H, Ar-H), 9.20 (s, 1H, NH). Anal. Calcd for C₂₄H₂₀ClN₃O₃: C, 66.44; H, 4.65; N, 9.68. Found: C, 66.57; H, 4.64; N, 9.72%.

3-(Benzo[d][1,3]dioxol-5-yl)-N-(4-chlorophenyl)-5-meta-tolyl-4,5-dihydro-1H-pyrazole-1-carboxamide (3i)

Yield: 339 mg (78%) of white powder; m.p. 159.8–160.2 °C. IR (ν_{\max} , cm^{-1}): 3292 (N-H), 3093 (=C-H), 2989, 2901 (C-H), 1689 (C=O), 1633 (C=N), 1220 (C-O), 1033 (C-N); ^1H NMR (400 MHz, DMSO- d_6): δ 2.24 (s, 3H, CH₃), 3.10 (dd, $J_{\text{ax}} = 5.9$ Hz, $J_{\text{ab}} = 17.6$ Hz, 1H, Ha), 3.80 (dd, $J_{\text{bx}} = 11.6$ Hz, $J_{\text{ab}} = 17.6$ Hz, 1H, Hb), 5.45 (dd, $J_{\text{ax}} = 5.9$ Hz, $J_{\text{bx}} = 11.6$ Hz, 1H, Hx), 6.08 (s, 2H, O-CH₂-O), 6.76–7.96 (m, 11H, Ar-H), 9.18 (s, 1H, NH). Anal. Calcd for C₂₄H₂₀ClN₃O₃: C, 66.44; H, 4.65; N, 9.68. Found: C, 66.31; H, 4.61; N, 9.73%.

3-(Benzo[d][1,3]dioxol-5-yl)-N-(4-chlorophenyl)-5-(pyridin-4-yl)-4,5-dihydro-1H-pyrazole-1-carboxamide (3j)

Yield: 337 mg (80%) of gray powder; m.p. 134.4–134.6 °C. IR (ν_{\max} , cm^{-1}): 3290 (N-H), 3005 (=C-H), 2918, 2848 (C-H), 1672 (C=O), 1631 (C=N), 1220 (C-O), 1033 (C-N); ^1H NMR (400 MHz, DMSO- d_6): δ 3.11 (dd, $J_{\text{ax}} = 5.6$ Hz, $J_{\text{ab}} = 17.9$ Hz, 1H, Ha), 3.81 (dd, $J_{\text{bx}} = 12.0$ Hz, $J_{\text{ab}} = 17.9$ Hz, 1H, Hb), 5.48 (dd, $J_{\text{ax}} = 5.5$ Hz, $J_{\text{bx}} = 11.9$ Hz, 1H, Hx), 6.08 (s, 2H, O-CH₂-O), 6.96–7.87 (m, 11H, Ar-H), 9.16 (s, 1H, NH). Anal. Calcd for C₂₂H₁₇ClN₄O₃: C, 62.79; H, 4.07; N, 13.31. Found: C, 62.93; H, 4.11; N, 13.37%.

3-(Benzo[d][1,3]dioxol-5-yl)-N-(4-chlorophenyl)-5-(thiophen-2-yl)-4,5-dihydro-1H-pyrazole-1-carboxamide (3k)

Yield: 320 mg (75%) of yellow powder; m.p. 158.7–159.0 °C. IR (ν_{\max} , cm^{-1}): 3296 (N-H), 3093 (=C-H), 2974,

2901 (C-H), 1689 (C=O), 1631 (C=N), 1228 (C-O), 1033 (C-N); ^1H NMR (400 MHz, DMSO- d_6): δ 3.30 (dd, $J_{\text{ax}} = 4.7$ Hz, $J_{\text{ab}} = 18.0$ Hz, 1H, Ha), 3.79 (dd, $J_{\text{bx}} = 11.6$ Hz, $J_{\text{ab}} = 18.0$ Hz, 1H, Hb), 5.84 (dd, $J_{\text{ax}} = 4.7$ Hz, $J_{\text{bx}} = 11.6$ Hz, 1H, Hx), 6.08 (s, 2H, O-CH₂-O), 7.06–7.65 (m, 10H, Ar-H), 9.08 (s, 1H, NH). Anal. Calcd for C₂₁H₁₆ClN₃O₃S: C, 59.22; H, 3.79; N, 9.87. Found: C, 59.05; H, 3.75; N, 9.93%.

3-(Benzo[d][1,3]dioxol-5-yl)-N-(4-chlorophenyl)-5-(furan-2-yl)-4,5-dihydro-1H-pyrazole-1-carboxamide (3l)

Yield: 332 mg (81%) of brown powder; m.p. 175.5–175.9 °C. IR (ν_{\max} , cm^{-1}): 3294 (N-H), 3080 (=C-H), 2980, 2901 (C-H), 1680 (C=O), 1631 (C=N), 1219 (C-O), 1033 (C-N); ^1H NMR (400 MHz, DMSO- d_6): δ 3.30 (dd, $J_{\text{ax}} = 5.2$ Hz, $J_{\text{ab}} = 17.3$ Hz, 1H, Ha), 3.68 (dd, $J_{\text{bx}} = 11.9$ Hz, $J_{\text{ab}} = 17.3$ Hz, 1H, Hb), 5.60 (dd, $J_{\text{ax}} = 5.2$ Hz, $J_{\text{bx}} = 11.9$ Hz, 1H, Hx), 6.11 (s, 2H, O-CH₂-O), 7.01–7.83 (m, 10H, Ar-H), 9.10 (s, 1H, NH). Anal. Calcd for C₂₁H₁₆ClN₃O₄: C, 61.54; H, 3.94; N, 10.25. Found: C, 61.68; H, 3.96; N, 10.28%.

3-(Benzo[d][1,3]dioxol-5-yl)-5-(5-bromothiophen-2-yl)-N-(4-chlorophenyl)-4,5-dihydro-1H-pyrazole-1-carboxamide (3m)

Yield: 404 mg (80%) of gray powder; m.p. 108.9–109.1 °C. IR (ν_{\max} , cm^{-1}): 3288 (N-H), 3086 (=C-H), 2989, 2918 (C-H), 1681 (C=O), 1631 (C=N), 1220 (C-O), 1033 (C-N); ^1H NMR (400 MHz, DMSO- d_6): δ 3.26 (dd, $J_{\text{ax}} = 5.0$ Hz, $J_{\text{ab}} = 17.9$ Hz, 1H, Ha), 3.77 (dd, $J_{\text{bx}} = 11.5$ Hz, $J_{\text{ab}} = 17.9$ Hz, 1H, Hb), 5.73 (dd, $J_{\text{ax}} = 5.0$ Hz, $J_{\text{bx}} = 11.4$ Hz, 1H, Hx), 6.09 (s, 2H, O-CH₂-O), 6.99–7.78 (m, 9H, Ar-H), 9.09 (s, 1H, NH). Anal. Calcd for C₂₁H₁₅BrClN₃O₃S: C, 49.97; H, 3.00; N, 8.32. Found: C, 50.11; H, 3.02; N, 8.35%.

3-(Benzo[d][1,3]dioxol-5-yl)-N-(4-chlorophenyl)-5-(4-(trifluoromethyl)phenyl)-4,5-dihydro-1H-pyrazole-1-carboxamide (3n)

Yield: 366 mg (75%) of white powder; m.p. 110.6–110.9 °C. IR (ν_{\max} , cm^{-1}): 3290 (N-H), 3093 (=C-H), 2980, 2866 (C-H), 1670 (C=O), 1631 (C=N), 1222 (C-O), 1033 (C-N); ^1H NMR (400 MHz, DMSO- d_6): δ 3.16 (dd, $J_{\text{ax}} = 5.7$ Hz, $J_{\text{ab}} = 17.7$ Hz, 1H, Ha), 3.84 (dd, $J_{\text{bx}} = 11.6$ Hz, $J_{\text{ab}} = 17.7$ Hz, 1H, Hb), 5.64 (dd, $J_{\text{ax}} = 5.7$ Hz, $J_{\text{bx}} = 11.6$ Hz, 1H, Hx), 6.11 (s, 2H, O-CH₂-O), 7.02–7.85 (m, 11H, Ar-H), 9.17 (s, 1H, NH). Anal. Calcd for C₂₄H₁₇ClF₃N₃O₃: C, 59.09; H, 3.51; N, 8.61. Found: C, 59.27; H, 3.54; N, 8.65%.

3-(Benzo[d][1,3]dioxol-5-yl)-5-(3-chlorophenyl)-N-(4-chlorophenyl)-4,5-dihydro-1H-pyrazole-1-carboxamide (3o)

Yield: 327 mg (72%) of white powder; m.p. 168.3–168.5 °C. IR (ν_{\max} , cm^{-1}): 3292 (N-H), 3093 (=C-H), 2914, 2947 (C-H), 1687 (C=O), 1631 (C=N), 1228 (C-O), 1033 (C-N); ^1H NMR (400 MHz, DMSO- d_6): δ 3.12 (dd, $J_{\text{ax}} = 5.5$ Hz, $J_{\text{ab}} = 17.9$ Hz, 1H, Ha), 3.78 (dd, $J_{\text{bx}} = 11.8$ Hz, $J_{\text{ab}} = 17.9$ Hz, 1H, Hb), 5.49 (dd, $J_{\text{ax}} = 5.4$ Hz, $J_{\text{bx}} = 11.8$ Hz, 1H, Hx), 6.06 (s, 2H, O-CH₂-O), 6.99–7.86 (m,

11H, Ar-H), 9.10 (s, 1H, NH). Anal. Calcd for $C_{23}H_{17}Cl_2N_3O_3$: C, 60.81; H, 3.77; N, 9.25. Found: C, 60.93; H, 3.75; N, 9.28%.

2. 2. Anticancer Activity

HeLa (human cervical adenocarcinoma), MCF-7 (human breast adenocarcinoma) and NIH-3T3 (mouse embryonic fibroblast) cell lines were used for MTT assay.¹⁴ Cells were cultured in DMEM medium supplemented with 10% fetal bovine serum (FBS), 100 U/mL penicillin and 100 μ g/mL streptomycin and 2 mM L-glutamine. The cultures were incubated at 37 °C in a humidified atmosphere with 5% CO₂. Briefly, cells were seeded into a 96-well plate at a density of 1×10^4 cells/well in the 100 μ L medium. After incubating the cells for 24 h, the dilutions of compounds at different doses (0.1–1000 μ M) were added and incubated for 24h. After that, the culture medium was discarded and the wells were washed with PBS twice, followed by the addition of 10 μ L MTT dye (0.5 mg/mL) into each well in the 100 μ L medium. The cells were incubated for another 4 h at 37 °C. After removing all the culture medium, 100 μ L DMSO was added per well. The percentage of cell viability was measured on ELISA reader (Biotek Co., USA) at wavelength of 570 nm. The IC₅₀ values of compounds on the HeLa, MCF-7 and NIH-3T3 cells were calculated using GraphPad Prism 7. The images of cells treatment of compound were also assessed by inverted microscope (Zeiss Axiovert). All experiments were repeated multiple times.

2. 3. Colony Formation Assay

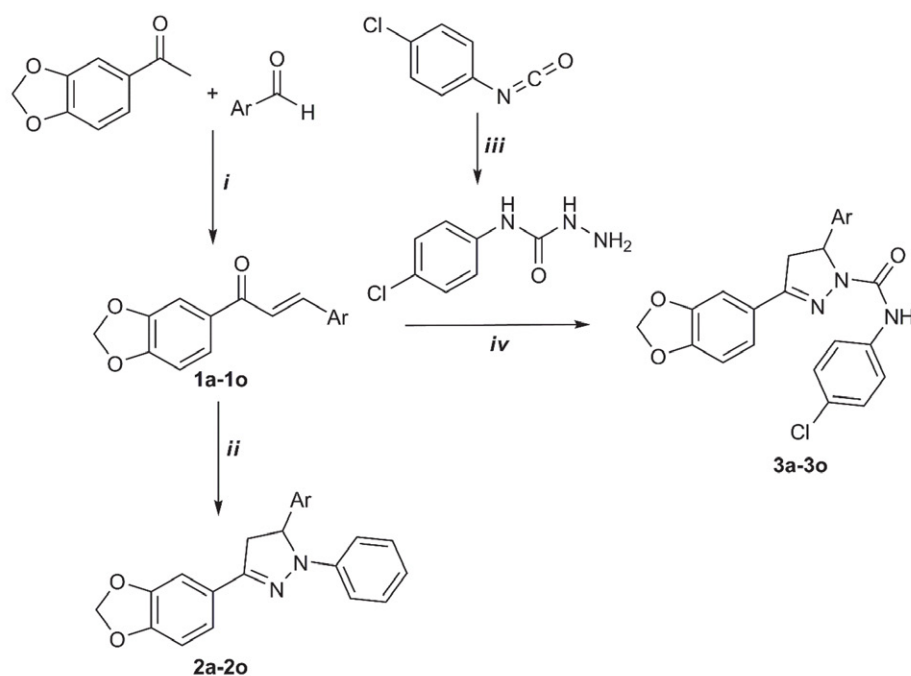
MCF-7 and HeLa cells were seeded in to 12-well plates at a density of 1000 cells/well in the 800 μ L medium. After incubating the cells for 24 h, the at IC₅₀ values of compound (μ M) were added and incubated for 24 h. After treatment, the medium containing compounds was removed and replaced with pure medium. Medium was changed every 3 days for 10 days until visible colonies were formed. The medium was aspirated from wells and cells were washed three times with PBS. Then, colonies were simultaneously fixed with 500 μ L of fixing reagent (methanol/acetic acid = 3/1) and incubated at room temperature for 5 min. Then, cells were stained with 0.5% crystal violet solution and incubated at room temperature. The plate was washed with ddH₂O. The stained cells were examined with invert microscope (Zeiss Axiovert, Germany) and imaging system.¹⁵

2. 4. In Silico ADMET Analysis

The ADMET parameters, pharmacokinetic properties and violations of drug-likeness of all synthesized compounds were investigated with the SwissADME webserver (<http://www.swissadme.ch/>).

2. 5. Statistical Analysis

In this study, data were collected from 3 different biological replicates and the results were plotted as mean \pm



Scheme 1. The synthesis pathway of the target compounds: (i) methanol, NaOH; (ii) ethanol, acetic acid; (iii) hydrazine monohydrate, ether; (iv) ethanol, NaOH.

SD. One-way ANOVA was used as statistical analysis by GraphPad Prism 7. P-value <0.05 was considered statistically significant.

3. Result and Discussion

3. 1. Chemistry

The synthesis of new pyrazoline derivatives was carried out by the methods outlined in Scheme 1. The cyclization of chalcones with phenylhydrazine hydrochloride in acidic media gave the 2-pyrazoline compounds (**2a–2o**). The cyclization of chalcones with semicarbazide in basic media gave the 2-pyrazoline-1-carboxamide compounds (**3a–3o**). The structures of these pyrazolines were elucidated by using IR and ¹H NMR spectral methods besides elemental analysis.

The IR spectra of compounds **2a–2o** and **3a–3o** showed C=N intense absorption bands in the range of 1591–1597 cm⁻¹ and 1631–1633 cm⁻¹, respectively. The IR spectra of compounds **3a–3o** demonstrated intense ab-

sorption bands in the range of 3288–3367 cm⁻¹ due to the N–H bond and 1666–1689 cm⁻¹ due to the C=O bond. In the ¹H NMR spectrum, the finding of three double doublet peaks belonging to the Ha, Hb and Hx protons indicated the synthesis of the pyrazoline ring successfully. The Ha and Hb methylene protons of the pyrazoline ring in position 4 appeared as double doublet signals at 2.92–3.30 ppm and 3.68–3.96 ppm, respectively. The methine proton of Hx resonated as double doublet signals at 5.33–5.85 ppm. Furthermore, compound **3a–3o** revealed the singlet signal assigned to NH proton of carboxamide moiety at 9.00–9.20 ppm. The methylene protons belonging to 1,3-benzodioxole ring gave a singlet peak at 6.02–6.14 ppm. The elemental analysis also supported these structures.

3. 2. Biological Activity

The anticancer activity of synthesized pyrazoline derivatives was evaluated on HeLa (human cervical adenocarcinoma), MCF-7 (human breast adenocarcinoma) and NIH-3T3 (mouse embryonic fibroblast) cell lines using

Table 1. The IC₅₀ values of synthesized pyrazoline derivatives

Compounds	IC ₅₀ (μM)			Selectivity Index (SI)*	
	HeLa	MCF-7	NIH-3T3	NIH-3T3/HeLa	NIH-3T3/MCF-7
2a	128.24 ± 20.16	109.65 ± 6.68	ND	9.87	11.54
2b	93.88 ± 14.02	ND	684.13 ± 14.20	7.29	ND
2c	103.91 ± 2.65	113.19 ± 11.02	594.89 ± 31.08	5.73	5.26
2d	289.24 ± 24.28	27.63 ± 3.51	899.52 ± 3.65	3.11	32.56
2e	75.15 ± 22.14	269.19 ± 2.69	212.12 ± 16.21	2.82	0.79
2f	82.35 ± 14.62	186.39 ± 12.66	724.93 ± 5.22	8.80	3.89
2g	168.42 ± 6.31	ND	533.436 ± 3.68	3.17	ND
2h	81.02 ± 2.44	74.75 ± 12.55	290.13 ± 14.03	3.58	3.88
2i	158.31 ± 13.70	255.61 ± 22.08	152.08 ± 8.25	0.96	0.59
2j	108.84 ± 3.11	14.30 ± 1.10	528.71 ± 6.69	4.86	36.97
2k	97.54 ± 6.63	83.07 ± 3.08	495.38 ± 18.09	5.08	5.96
2l	111.58 ± 4.12	181.76 ± 6.24	985.04 ± 10.85	8.83	5.42
2m	188.75 ± 2.25	221.12 ± 19.30	181.74 ± 14.03	0.96	0.82
2n	79.18 ± 12.37	54.07 ± 6.36	ND	ND	ND
2o	50.02 ± 3.48	340.56 ± 17.10	908.74 ± 7.49	18.17	2.67
3a	75.26 ± 13.50	ND	232.78 ± 21.01	3.09	ND
3b	93.49 ± 2.84	114.05 ± 6.66	476.97 ± 13.14	5.10	4.18
3c	13.74 ± 1.33	24.49 ± 3.81	381.21 ± 3.86	27.74	15.57
3d	120.22 ± 10.07	78.85 ± 5.64	665.01 ± 18.29	5.53	8.43
3e	81.15 ± 2.66	37.75 ± 3.37	615.61 ± 11.94	7.59	16.31
3f	11.53 ± 3.09	11.37 ± 1.08	942.61 ± 18.38	81.75	82.90
3g	533.14 ± 18.13	117.45 ± 6.54	233.74 ± 10.93	0.44	1.99
3h	123.09 ± 8.07	ND	556.01 ± 14.22	4.52	ND
3i	111.84 ± 6.53	108.14 ± 12.07	279.01 ± 19.38	2.49	2.58
3j	422.80 ± 2.49	10.08 ± 1.04	693.45 ± 9.21	1.64	68.79
3k	137.21 ± 15.08	516.56 ± 3.98	130.76 ± 3.45	0.95	0.25
3l	ND	122.29 ± 11.82	560.43 ± 3.70	ND	4.58
3m	115.53 ± 5.74	369.25 ± 22.47	605.59 ± 17.93	5.24	1.64
3n	ND	13.67 ± 2.65	968.15 ± 21.80	ND	70.82
3o	ND	41.53 ± 6.12	252.15 ± 15.54	ND	6.07

* ND: not determined

MTT assay. The IC_{50} values of all compounds are given in Table 1. Compound **2d** bearing 4-nitrophenyl and compound **2j** bearing pyridine ring from phenylpyrazoline derivatives (**2a–2o**) and compound **3j** bearing pyridine and **3n** bearing 4-trifluoromethylphenyl ring showed the highest cytotoxicity activity the MCF-7 cancer cell lines. On the other hand, compound **3c** bearing 4-bromophenyl ring from pyrazoline carboxamide derivatives (**3a–3o**) demonstrated the highest cytotoxicity activity on HeLa cancer cell lines. Among all pyrazoline derivatives, compound **3f** exhibited the most potent cytotoxic activity on both two cancer cells.

Additionally, selectivity index (SI) IC_{50} for NIH-3T3 cell line/ IC_{50} for HeLa and MCF-7 cell line was calculated for the evaluation of cytotoxic effects of molecules against both normal and cancer cells. Most of the compounds displayed low cytotoxicity against normal cells and especially, it was determined that the selectivity indices of compounds **2d**, **2j**, **3c**, **3f**, **3j**, **3n** showing the highest cytotoxic activity were quite high. The most selective compound **3f** had SI 81.75 for HeLa, and 82.90 for MCF-7 cell line.

After the MTT results, the images taken under the microscope of the compounds with antiproliferative effect are presented in Figure 2. When the synthesized compounds were compared with the control group in MCF-7 cells, their interaction with each other decreased and their growth was found to be slowed down when treated with compounds **2d**, **2j**, **3f**, **3j** and **3n**. Although cancer cells are

cells that grow close to each other and proliferate rapidly, the synthesized compounds at IC_{50} reduced high-growing cancer cells such as MCF7 and HeLa. In HeLa cells, it was shown that reduced cell interactions and growth was observed when treated with compounds **3c** and **3f** in comparison to the control group.

Cancer cells can survive when they migrate from their region to other regions by forming a colony on their own. Colony formation assay measurement is an important method to measure the effect of cancer cells on growth alone and is used to determine the effects of drugs on circulating cancer cells. The effect of newly synthesized compounds on the colony formation potential is shown in Figure 3 with MCF-7 and HeLa cells. Compared with the control group MCF-7 cells, it was shown that compounds **2d**, **2j**, **3f**, **3j** and **3n** reduced colony formation in cells and reduced the potential for colony formation. In HeLa cells, when compared to the control group, it was observed with the microscope that compounds **3c** and **3f** reduced the colony formation of the cells.

3. 3. *In Silico* ADMET Results

Oral bioavailability is an important factor in order to develop new drug candidates targeted for oral use. It is possible for drug candidates to succeed in phase studies with good lipophilicity, water solubility, physicochemical and pharmacokinetics properties.¹⁶ Therefore, we evaluat-

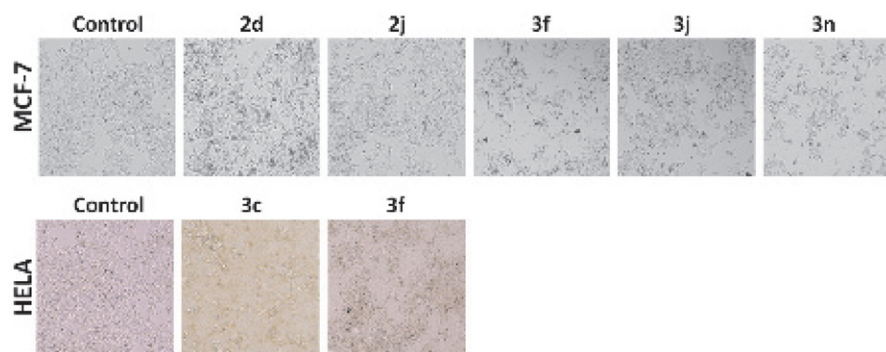


Figure 2. The images of cells treatment with IC_{50} values of synthesized pyrazoline derivatives in MCF-7 cells and HeLa cells

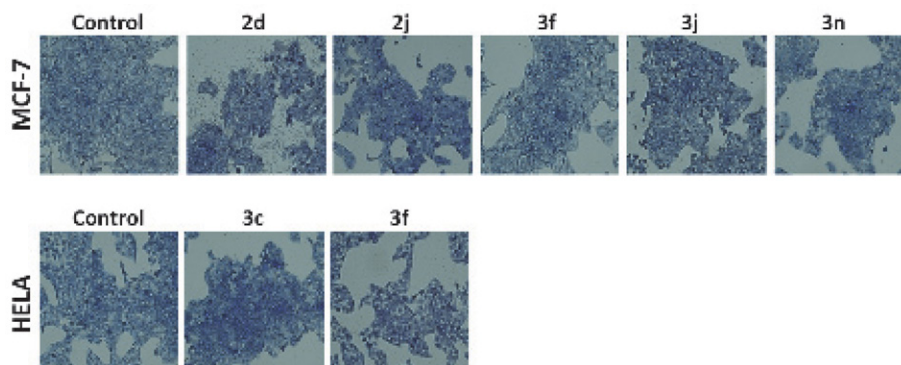


Figure 3. The colony formation images of MCF-7 cells and HeLa cells.

Table 2. Lipinski and Veber Parameters of the synthesized compounds.

Comp	Physicochemical Properties						Lipophilicity			Druglikeness			Water Solubility		Pharmacokinetics		
	MW	Fsp3	RB	HBA	HBD	MR	tPSA	clogP	Lipinski	Ghose	Veber	Egan	Muegge	ESOL	Class	GI absorption	F
2a	342.39	0.14	3	3	0	108.32	34.06	4.07	✓	✓	✓	✓	✓	-5.33	Moderately	High	0.55
2b	360.38	0.14	3	4	0	108.28	34.06	4.38	✓	✓	✓	✓	✓	-5.48	Moderately	High	0.55
2c	421.29	0.14	3	3	0	116.02	34.06	4.70	✓	✓	✓	1	✓	-6.23	Poorly	High	0.55
2d	387.39	0.14	4	5	0	117.15	79.88	3.65	✓	✓	✓	✓	✓	-5.37	Moderately	High	0.55
2e	356.42	0.17	3	3	0	113.29	34.06	4.39	✓	✓	✓	1	✓	-5.62	Moderately	High	0.55
2f	367.40	0.13	3	4	0	113.04	57.85	3.85	✓	✓	✓	✓	✓	-5.26	Moderately	High	0.55
2g	370.44	0.21	3	3	0	118.26	34.06	4.70	✓	✓	✓	1	✓	-5.92	Moderately	High	0.55
2h	356.42	0.17	3	3	0	113.29	34.06	4.39	✓	✓	✓	1	✓	-5.62	Moderately	High	0.55
2i	356.42	0.17	3	3	0	113.29	34.06	4.41	✓	✓	✓	1	✓	-5.62	Moderately	High	0.55
2j	343.38	0.14	3	4	0	106.12	46.95	3.32	✓	✓	✓	✓	✓	-4.66	Moderately	High	0.55
2k	348.42	0.15	3	3	0	106.20	62.30	4.06	✓	✓	✓	✓	✓	-5.17	Moderately	High	0.55
2l	332.35	0.15	3	4	0	100.59	47.20	3.39	✓	✓	✓	✓	✓	-4.69	Moderately	High	0.55
2m	427.31	0.15	3	3	0	113.90	62.30	4.75	✓	✓	✓	1	✓	-6.29	Poorly	High	0.55
2n	410.39	0.17	4	6	0	113.33	34.06	5.09	✓	✓	✓	1	✓	-6.17	Moderately	High	0.55
2o	376.84	0.14	3	3	0	113.33	34.06	4.59	✓	✓	✓	1	✓	-5.91	Moderately	High	0.55
3a	419.86	0.13	5	4	1	122.51	63.16	4.07	✓	✓	✓	✓	✓	-5.41	Moderately	High	0.55
3b	437.85	0.13	5	5	1	122.47	63.16	4.51	✓	✓	✓	✓	✓	-5.57	Moderately	High	0.55
3c	498.76	0.13	5	4	1	130.21	63.16	4.81	✓	1	✓	✓	✓	-6.32	Poorly	High	0.55
3d	464.86	0.13	6	6	1	131.33	108.98	3.52	✓	✓	✓	✓	✓	-5.48	Moderately	High	0.55
3e	433.89	0.17	5	4	1	127.48	63.16	4.53	✓	✓	✓	✓	✓	-5.71	Moderately	High	0.55
3f	444.87	0.12	5	5	1	127.23	86.95	3.99	✓	✓	✓	✓	✓	-5.36	Moderately	High	0.55
3g	447.91	0.20	5	4	1	132.44	63.16	4.73	✓	1	✓	1	✓	-6.02	Poorly	High	0.55
3h	433.89	0.17	5	4	1	127.48	63.16	4.41	✓	✓	✓	✓	✓	-5.71	Moderately	High	0.55
3i	433.89	0.17	5	4	1	127.48	63.16	4.53	✓	✓	✓	✓	✓	-5.71	Moderately	High	0.55
3j	420.85	0.14	5	5	1	120.31	76.05	3.33	✓	✓	✓	✓	✓	-4.74	Moderately	High	0.55
3k	425.89	0.14	5	4	1	120.39	91.40	4.10	✓	✓	✓	✓	✓	-5.26	Moderately	High	0.55
3l	409.82	0.14	5	5	1	114.78	76.30	3.42	✓	✓	✓	✓	✓	-4.77	Moderately	High	0.55
3m	504.78	0.14	5	4	1	128.09	91.40	4.86	2	1	✓	1	✓	-6.38	Poorly	High	0.17
3n	487.86	0.17	6	7	1	127.51	63.16	5.12	✓	2	✓	1	✓	-6.27	Poorly	High	0.55
3o	454.31	0.13	5	4	1	127.52	63.16	4.73	✓	✓	✓	1	✓	-6.01	Poorly	High	0.55

Molecular weight: MW, topological polar surface area: tPSA, Molar Refractivity: MR, fraction of sp³ carbon atoms: Fsp₃, HBD: hydrogen bonds donor, HBA: hydrogen bond acceptor, RB: rotatable bonds, LogP values: indicator of Lipophilicity, ESOL: aqueous solubility parameter, Log Kp: skin permeation, F: Bioavailability Score.

ed the druglikeness properties such as Lipinski, Ghose, Veber, Egan and Muegge filters of all synthesized compounds. The results showed that the majority of all compounds did not violate these filters. Aqueous solubility plays a critical role for drug's bioavailability. Therefore, ESOL (Log S) values of all compounds were calculated and the solubility of all compounds was determined to be moderate, except for compounds **2c**, **2m**, **3c**, **3g**, **3m**, **3n** and **3o**. In addition, the GI absorptions of all compounds was determined to be high. The bioavailability score of compounds was found to be ideal.¹⁷ Among these compounds **3f**, showing the best anticancer activity, possesses good drug score values. Compound **3f** did not appear to violate any of the rules described here (Table 2).

The BOILED-Egg server getting from swissadme program gives pharmacokinetic properties (such as gastrointestinal absorption, brain access and P-glycoprotein) of molecules by calculating with partition constant (log P) and topological polar surface area (TPSA). The yellow area (BBB) shows molecules that easily permeate through the blood-brain barrier, the white region (HIA) demonstrates molecules that easily permeate through the gastrointestinal membranes, while the gray area presents molecules having low absorption. Based on this BOILED-Egg server, all synthesized molecules permeate through either the blood-brain barrier or the gastrointestinal membranes. None of the molecules are in the low absorption region (Figure 4). In addition, PGP⁺ identifies the molecules to be effluated from the central nervous system by the P-glycoprotein. PGP⁻ also identifies the molecules that are non-substrate of the P-glycoprotein. Among these com-

pounds **3f**, showing the best anticancer activity, permeates through the gastrointestinal membranes easily and is non-substrate of the P-glycoprotein according to Figure 4.

4. Conclusion

In the present study, a number of new molecules contained two pharmacodynamic groups (2-pyrazoline and benzo[d][1,3]dioxol) inducing significant synergistic lethality of cancer cells were designed and synthesized. These pyrazolines were assessed for anticancer activity on HeLa, MCF-7 cancer cell lines and NIH-3T3 normal cell lines. The results demonstrated that compounds **2d**, **2j**, **3c**, **3j** and **3n** exhibited higher activity than the other substituted pyrazoline derivatives. Notably, compound **3f** was identified as the most potent cytotoxic molecule in this study with IC₅₀ values of 11.53 μM on HeLa and 11.37 μM on MCF-7. In silico ADMET analysis and drug-likeness displayed that compound **3f** has good pharmacokinetic characteristics and absorption-solubility properties. Therefore, compound **3f** can be a lead compound for the development of novel anticancer agents in drug discovery.

Acknowledgements

This research was partly presented at the 13th International Symposium on Pharmaceutical Sciences, June 22–25, 2021, Ankara, Turkey.

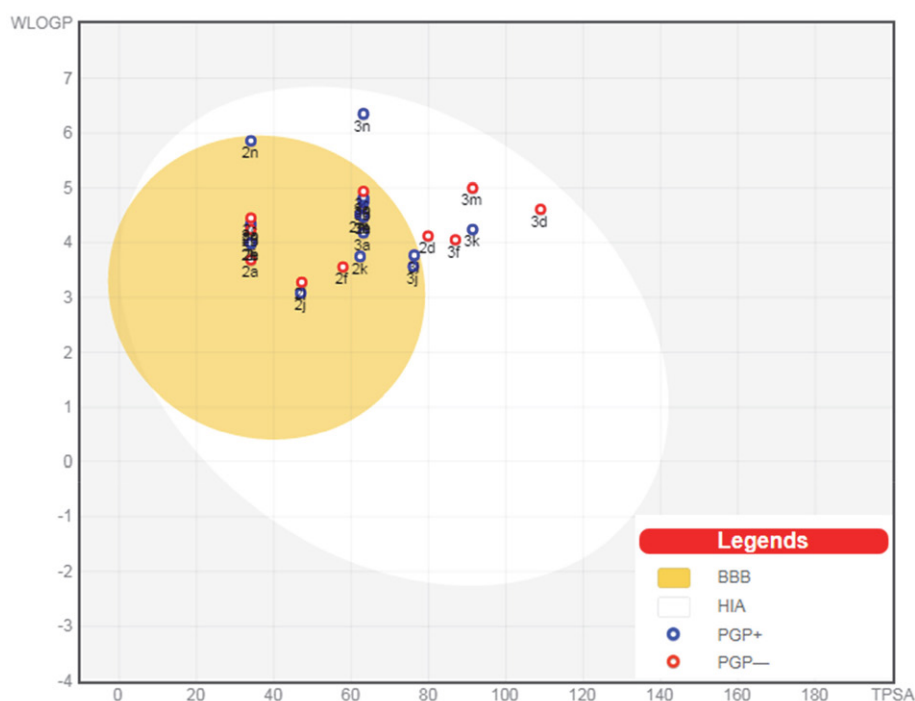


Figure 4. The BOILED-Egg predictive models of all compounds

Supporting Information

Contains copies of IR and ^1H NMR spectra of synthesized compounds (**2a–2o** and **3a–3o**).

5. References

1. S. C. Karad, V. B. Purohit, P. Thakor, V. R. Thakkar, D. K. Raval, *Eur. J. Med Chem.* **2016**, *112*, 270–279. DOI:10.1016/j.ejmech.2016.02.016
2. M. Yusuf, P. Jain, *Arab. J. Chem.* **2014**, *7*, 553–596. DOI:10.1016/j.arabjc.2011.09.013
3. F. Hayat, A. Salahuddin, S. Umar, A. Azam, *Eur. J. Med Chem.* **2010**, *45*, 4669–4675. DOI:10.1016/j.ejmech.2010.07.028
4. A. Özdemir, M. D. Altıntop, Z. A. Kaplancıklı, Ö. D. Can, Ü. Demir Özkay, G. Turan-Zitouni, *Molecules*, **2015**, *20*, 2668–2684. DOI:10.3390/molecules20022668
5. S. Y. Jadhav, S. P. Shirame, S. D. Kulkarni, S. B. Patil, S. K. Palsale, R. B. Bhosale, *Bioorg. Med. Chem. Lett.* **2013**, *23*, 2575–2578. DOI:10.1016/j.bmcl.2013.02.105
6. Z. A. Kaplancıklı, G. Turan-Zitouni, A. Özdemir, Ö. D. Can, P. Chevallet, *Eur. J. Med Chem.* **2009**, *44*, 2606–2610. DOI:10.1016/j.ejmech.2008.09.002
7. Y. Song, S. Feng, J. Feng, J. Dong, K. Yang, Z. Liu, X. Qiao, *Eur. J. Med Chem.* **2020**, *200*, 1–13. DOI:10.1016/j.ejmech.2020.112459
8. D. Matiadis, M. Sagnou, *Int. J. Mol. Sci.* **2020**, *21*, 1–38. DOI:10.3390/ijms21155507
9. Z. Yuan, S. Chen, Q. Sun, N. Wang, D. Li, S. Miao, C. Gao, Y. Chen, C. Tan, Y. Jiang, *Bioorg. Med. Chem.* **2017**, *25*, 4100–4109. DOI:10.1016/j.bmc.2017.05.058
10. S. Li, X. Li, T. Zhang, J. Zhu, W. Xue, X. Qian, F. Meng, *Bioorg. Chem.* **2020**, *96*, 1–14. DOI:10.1016/j.bioorg.2020.103575
11. N. Beyhan, B. Koçyiğit-Kaymakçioğlu, S. Gümrü, F. Arıcıoğlu, *Arab. J. Chem.* **2017**, *10*, 2073–2081. DOI:10.1016/j.arabjc.2013.07.037
12. A. Ahmad, A. Husain, S. A. Khan, M. Mujeeb, A. Bhandari, *J. Saudi Chem. Soc.* **2016**, *20*, 577–584. DOI:10.1016/j.jscs.2014.12.004
13. B. Koçyiğit-Kaymakçioğlu, N. Beyhan, N. Tabanca, A. Ali, D. E. Wedge, S. O. Duke, U. R. Bernier, I. A. Khan, *Med. Chem. Res.* **2015**, *24*, 1–13. DOI:10.1007/s00044-015-1415-8
14. F. Tok, B. İ. Abas, Ö. Çevik, B. Koçyiğit-Kaymakçioğlu, *Bioorg. Chem.* **2020**, *102*, 1–10. DOI:10.1016/j.bioorg.2020.104063
15. Ö. Çevik, F. A. Turut, H. Acidereli, Ş. Yıldırım, *Turk. J. Biochem.* **2019**, *44*, 47–54. DOI:10.1515/tjb-2017-0355
16. F. Tok, B. Koçyiğit-Kaymakçioğlu, *Acta Chim. Slov.* **2020**, *67*, 1139–1147. DOI:10.17344/acsi.2020.6028
17. Daina, O. Michielin, V. Zoete, *Sci. Rep.* **2017**, *42717*, 1–13. DOI:10.1038/srep42717

Povzetek

Načrtovali in izvedli smo sintezo nove serije 2-pirazolinskih derivatov. Kot izhodne spojine smo uporabili substituirane benzodioksol halkone. IR in ^1H NMR spektroskopija ter elementne analize so bile uporabljene za karakterizacijo strukture pripravljenih spojin. Citotoksične aktivnosti na HeLa in MCF-7 rakaste celične linije ter na NIH-3T3 celice smo za sintetizirane spojine določili s pomočjo MTT metode. Med pripravljenimi spojinami so izkazale opazno citotoksično aktivnost (z IC_{50} vrednostmi v intervalu 10.08 do 27.63 μM) spojine **2d**, **2j**, **3j** in **3n** proti MCF-7 celicam ter **3c** proti HeLa celicam. Spojina **3f** je izkazala močno protirakavo učinkovitost na obe celični liniji z dobrimi vrednostmi selektivnosti ($\text{IC}_{50} = 11.53 \mu\text{M}$ za HeLa s SI = 81.75 ter $\text{IC}_{50} = 11.37 \mu\text{M}$ za MCF-7 s SI = 82.90). Dodatno smo z *in silico* ADMET analizo ugotovili sposobnost pripravljenih spojin, da bi delovale kot uspešne učinkovine.



Except when otherwise noted, articles in this journal are published under the terms and conditions of the Creative Commons Attribution 4.0 International License

Scientific paper

Modelling and Multi-Objective Optimization of Continuous Indirect Electro-Oxidation Process for RTB21 Dye Wastewater Using ANN-GA Approach

Naresh R Vaghela¹ and Kaushik Nath²

¹ Department of Chemical Engineering, Government Engineering College (Affiliated to Gujarat Technological University, Ahmedabad), Bharuch- 392002, Gujarat, India

² Department of Chemical Engineering, G H Patel College of Engineering & Technology, Vallabh Vidyanagar- 388120, Gujarat, India

* Corresponding author: E-mail: email.drkaushiknath2013@gmail.com

Received: 09-14-2021

Abstract

A continuous indirect electro-oxidation (EO) process was developed using graphite electrode to investigate the treatability of reactive turquoise blue RTB21 dye wastewater under specific operating conditions of initial pH, current density, hydraulic retention time (HRT), and electrolyte (NaCl) concentration. The experiments were performed in accordance with the central composite design (CCD), and the findings were used to create a model utilizing artificial neural networks (ANNs). According to the predicted findings of the ANN model, the MSE values for colour and COD removal efficiencies were estimated to be 0.748 and 0.870, respectively, while the R^2 values were 0.9999 and 0.9998, respectively. The Multi-objective optimization using genetic algorithm (MOGA) over the ANN model maximizes the multiple responses: colour and COD removal efficiency (%). The MOGA generates a non-dominated Pareto front, which provides an insight into the process's optimum operating conditions.

Keywords: Multi-objective optimization, Artificial neural network, Genetic algorithm, wastewater, reactive turquoise blue 21

1. Introduction

Clean water and sanitation is one of the major agenda of the United Nation's sustainable development initiative. According to the UN's world water development report 2021, around 2 billion individuals live under water stress conditions, and by 2030, the world would face a water deficit of 40%.¹ The quantity of wastewater generated worldwide has increased exponentially due to the rise in population and rapid industrial and technological development over the last few decades. India generates approximately 64,000 tonnes of dyes annually, of which 7,040 tonnes are dumped directly into the environment. These dyestuffs are widely used by textiles, paper and pulp, leather, and many other industries, but unfortunately, their impact on health and the environment are poorly evaluated.² Despite numerous Physico-chemical techniques for dye wastewater treatment, most of these systems appear to be marred by low practical efficiency or an inadequate benefit-cost ratio. Several traditional, as well as novel strategies, have been proposed in the literature to treat dye wastewater. These

include adsorption by activated carbon,³ chemical coagulation,⁴ photodegradation under UV light irradiation,⁵ hydrodynamic cavitation,⁶ sonochemical degradations,⁷ ozonation,⁸ electrocoagulation,⁹ Fenton like processes,¹⁰ membrane filtration,¹¹ electrochemical methods,¹²⁻¹⁴ and many more.

A primary drawback with many of these dye removal techniques is that they cannot remove all types of dyes from the wastewater. Adsorption is a highly successful technique for treating dye-containing effluent, but adsorbent regeneration is an expensive process. Prolonged treatment time and post-treatment solid disposal are limitations of the adsorption process.¹⁵ Chemical coagulation can bring high removal efficiency and a high quantity of wastewater but relatively high processing costs.¹⁶ Fenton-like techniques generate a substantial amount of sludge and are thus impractical for completely degrading dye molecules. Almost all types of dyes may be separated from wastewater using the membrane process. There is no sludge development, and footprint requirement is

also low. However, the cost of the membrane and associated equipment and the fouling issue during operation are drawbacks of the membrane process.¹⁷ While biological treatment could be cost-competitive, it is less effective to deal with refractory organic wastes.¹⁶ As a result, finding an effective and environmentally acceptable treatment technique with high removal efficiency and low cost is essential for completely removing dye molecules from industrial wastewater.

Electrochemical techniques, such as anodic oxidation or indirect electrochemical oxidation (EO), have garnered significant interest in industrial wastewater treatment.¹⁸ Electrochemical techniques offer enormous promise for wastewater treatment due to their wide range of environmental compatibility, increased process efficiency, and cost-effectiveness. However, several process factors, such as initial pH, current density, electrolyte concentration, process time, etc., impact electrochemical processes. Thus, optimizing process parameters is crucial from a process performance, economic, and scale-up perspective.¹⁹

Typically, modelling and optimization of electrochemical processes have been described using the conventional one-variable-at-a-time approach (OVAT). However, OVAT ideas suffer from several drawbacks, including the inability to show the interactive effect of process factors, being time demanding, and economically costly.²⁰ Artificial intelligence (AI) has gained immense attention to overcome such limitations and emerged as an encouraging tool for modelling and process optimization. AI tools, such as ANN, GA, fuzzy logic, and machine learning have been widely considered for modeling and optimizing wastewater treatment processes.²¹ ANN, inspired by biological neuron phenomena of the human brain, was a computational modelling technique used for non-linear problems and to predict the output values for given input parameters from their training values.²² GA optimization tool can be used to more precisely optimized the ANN model. GA is a search heuristic algorithm inspired by Charles Darwin's

principle of natural evolution on the concept of "survival of the fittest". The GA approach is used to search for a global optimum solution with the ANN model as a fitness function.²³

Single-objective optimization of the electrochemical process using the ANN-GA approach has been fairly reported in the literature. However, optimization problems involve multiple objectives, which require simultaneously to optimize: maximize or minimize. Many attempts have so far been made for multi-objective optimization of the electrocoagulation process for wastewater. However, to the best of our knowledge, the literature has not reported ANN modeling accompanied by multi-objective optimization using GA of continuous EO process for dye wastewater. In this work, our primary objective of research is to develop two distinctive ANN models for the prediction of colour removal efficiency and COD removal efficiency for continuous EO process to degrade reactive turquoise blue 21 (RTB21) dye wastewater. Finally, ANN models are simultaneously optimized using the GA approach to maximize both the objectives: colour removal efficiency and COD removal efficiency.

2. Materials and Method

2.1. Chemicals and Materials

M/s Snehal Dye Chem Ltd, Ankleshwar, Gujarat, India, supplied the model RTB21 dye. All other chemicals used during experiments were of analytical grade. De-ionized water (DI) with 1 $\mu\text{S}/\text{cm}$ conductivity was used to perform all experiments. Graphite electrode plates (10×10×0.2 cm) used in the EO process were procured from M/s Prime Industries, Maharashtra, India.

2.2. Electrochemical experiments

The continuous flow EO reactor was constructed from an acrylic sheet with three sections, as shown in Fig.1, with

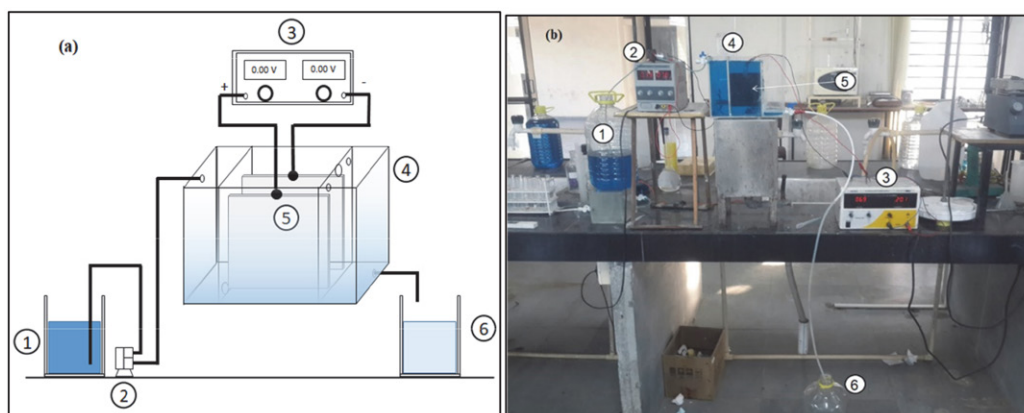


Fig. 1. (a) A conceptual schematic diagram of Continuous EO experimental setup, (b) Actual Experimental setup of continuous EO process: (1) RTB21 Wastewater Reservoir, (2) Peristaltic Pump, (3) DC Power Supply, (4) Electrochemical Cell, (5) Graphite Electrodes, and (6) Receiving cell

a working volume of 1.5 L. The two graphite electrode plates were connected vertically with a gap of 10 mm, connected in monopolar mode to a DC power supply (Make: SIGMA, 0–30 V 0–5 A). A mini peristaltic pump (GOSO Technology, Model: AB 11, 7.5 W) was used to pump the simulated wastewater into the top of the first section of the EO reactor from the reservoir. The wastewater from the first section passed to the second section through holes provided at the bottom of the first section, flowed upward through the layers of the electrodes, and drained out at the third section from the top of the reactor. After experiencing the specified EO process time, the effluent samples of the continuous EO process were collected. To change the pH of the solution, dilute solutions of H₂SO₄ and NaOH were used. NaCl was added to the solution as an electrolyte to adjust the conductivity.

The colour removal efficiency of the sample collected at various time intervals was calculated using Eq. 1.²⁴

$$\text{Colour removal efficiency (\%)} = \left(1 - \frac{A}{A_0}\right) \times 100 \quad (1)$$

Where A_0 and A are the light absorbance of a sample before and after the electrochemical process, respectively, measured using a UV/VIS spectrophotometer (Model CL 335).

$$\text{COD removal efficiency (\%)} = \left(1 - \frac{C}{C_0}\right) \times 100 \quad (2)$$

Where C_0 and C are the COD of a sample before and after the electrochemical process, respectively, measured using the open reflux method following standard meth-

odologies (APHA. American Public Health Association 2005).

2.3. Experimental design

Central composite design (CCD) was used for the design of experiments (DOE). Four process variables: ini-

Table 1. Experiment range and levels of Independent variable used as per CCD.

Variables	Levels				
	-2(α)	-1	0	+1	+2(α)
Initial pH	3	5	7	9	11
CD (A/m ²)	100	150	200	250	300
HRT (min)	50	75	100	125	150
NaCl Conc. (g/L)	1	1.5	2	2.5	3

tial pH (3–11), Current density (100–300 A/m²), Hydraulic retention time (HRT) (50–150 min), Electrolyte NaCl concentration (1–3 g/L), with five levels used for the design of experiments as shown in Table 1.

A total of 31 experiments as per Table 2 design were performed, and colour removal efficiency and COD removal efficiency were calculated. To avoid systemic bias, the runs were carried out in a randomized manner. Colour removal and COD removal efficiencies were considered to be response 1 and response 2, respectively. These were obtained for the experiments performed and are presented in Table 2.

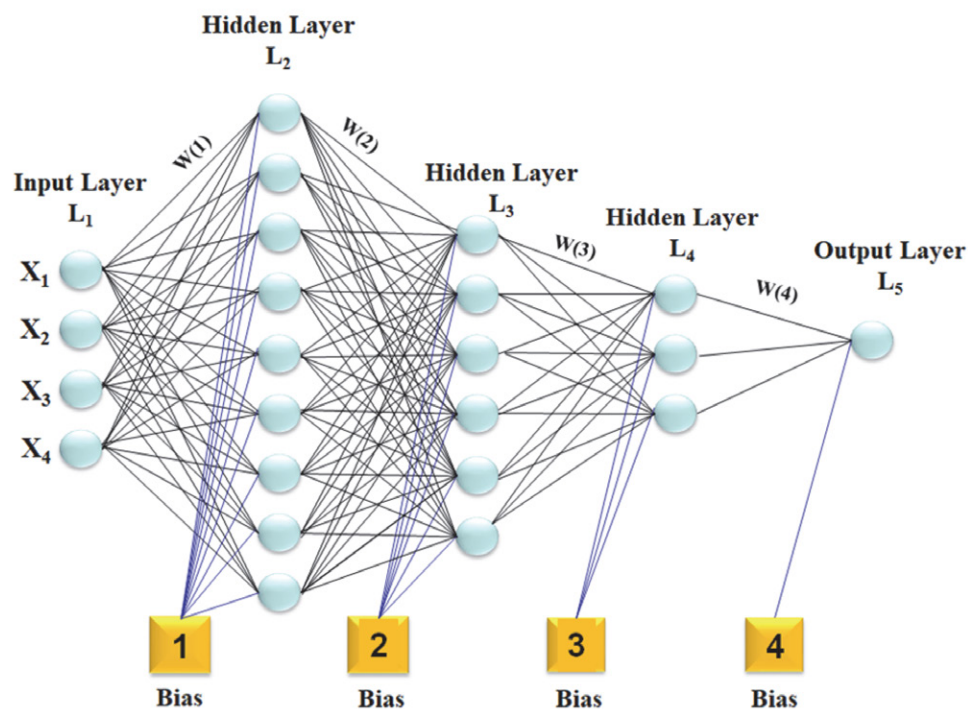


Fig. 2. Optimized architecture of ANN network for EO process.

Table 2. CCD design with observed and predicted responses.

Exp. Run	Parameters (Actual value)				Response 1 Colour removal (%)		Response 2 COD removal (%)	
	pH	Current density	HRT	NaCl Conc.	Expt.	ANN Predicted	Expt.	ANN Predicted
1	3	200	100	2.0	21.12	21.12	12.78	11.99
w`2	5	150	75	1.5	14.20	14.25334	9.60	9.69
3	5	150	75	2.5	45.02	45.02	21.21	21.53
4	5	150	125	1.5	33.89	33.89	25.55	26.33
5	5	150	125	2.5	65.32	65.31208	40.22	39.71
6	5	250	75	1.5	24.79	24.79	15.50	16.24
7	5	250	75	2.5	48.22	48.22	32.30	32.41
8	5	250	125	1.5	77.01	76.86996	44.50	44.24
9	5	250	125	2.5	99.20	99.2	60.12	61.95
10	7	100	100	2.0	44.32	44.32	21.30	20.75
11	7	200	50	2.0	8.26	8.26	6.40	5.75
12	7	200	100	1.0	43.43	43.43	32.23	31.58
13	7	200	100	2.0	96.11	95.64333	58.23	58.65
14	7	200	100	2.0	95.15	95.64333	59.03	58.65
15	7	200	100	2.0	96.28	95.64333	59.34	58.65
16	7	200	100	2.0	95.92	95.64333	58.51	58.65
17	7	200	100	2.0	95.10	95.64333	58.11	58.65
18	7	200	100	2.0	95.50	95.64333	59.20	58.65
19	7	200	100	2.0	95.00	95.64333	58.11	58.65
20	7	200	100	3.0	97.00	97	62.00	61.13
21	7	200	150	2.0	78.12	78.12	52.80	51.93
22	7	300	100	2.0	89.22	89.22	50.50	49.54
23	9	150	75	1.5	9.40	9.4	5.90	5.97
24	9	150	75	2.5	38.88	38.88	17.10	17.82
25	9	150	125	1.5	28.23	28.23	22.34	22.61
26	9	150	125	2.5	56.20	56.2	35.11	36.00
27	9	250	75	1.5	19.99	19.25079	12.12	12.52
28	9	250	75	2.5	40.87	40.64716	28.33	28.69
29	9	250	125	1.5	70.05	70.05	39.80	40.53
30	9	250	125	2.5	91.10	90.93601	58.70	58.23
31	11	200	100	2.0	8.10	8.1	5.30	4.57

2. 4. ANN Model

ANN models were created for both the responses to measure the performance of the EO reactor to treat the RTB21 model dye wastewater. The artificial neural network (ANN) is a soft computation tool inspired by biological neurons in the brain.²⁵ In recent years, the ANN has been employed as an efficient and versatile approach in various applications.²⁶ In ANN, there are three layers: the input layer, one or more hidden layers, and the output layer shown in Fig. 2.

An ANN's structure is made of processing components referred to as neurons (nodes). Weights and biases are used to connect each layer of neurons.²⁷ The weighted sum of each neuron's inputs are passed through the activation function to produce the output.²⁸ Feed-forward Levenberg-Marquardt Back-Propagation (LM-BP) algorithms were used for learning. ANN models were developed for both responses to evaluate the EO reactor's performance in treating the RTB21 model dye wastewater. The mean square error (MSE) was utilized for training the ANN.

70% of the data were used to train the neural network. After training, the remaining data were used in an equivalent proportion for validation and testing. More data were allocated for the training, which resulted in an improved model with a shorter processing time.

The testing offered an unbiased evaluation of the network's performance, whereas the validation evaluated the network's generalization, which was terminated when no further progress was detected.²⁹ The ANN models can be used as a fitness function for a GA used for multi-objective EO process optimization.

2. .5 GA Model

GA is a well-known robust AI technique for solving global search optimization problems.³⁰ The GA algorithm is based on Darwin's evolutionary theory. The 'gamultiobj' function in MATLAB (R2020b) was used to generate the Pareto front of colour removal efficiency and COD removal efficiency using GA and the direct search toolbox. The 'gamultiobj' function in MATLAB

employs a controlled elitist GA, which is a variation of NSGA-II.³¹

Initially, a random population of individuals called chromosomes is randomly generated within the lower and upper limits of decision variables, and the optimization process starts. Three genetic algorithm rules are used to produce the populations of the future generation: selection, crossover, and mutation. To generate the next generation, the best population was chosen based on fitness level function. The fitness value indicates an individual's merits for evaluation.²⁸ Crossover, also known as recombination, is the process through which two populations' genetic information is combined to generate new offspring. Then, random changes in the individual population are performed during the mutation process to preserve and add diversity. When the fitness value of a population does not improve over subsequent generations, the population eventually achieves the optimal solution.³²

2. 6. ANN-GA

Typically, when we deal with more than one objective, they are often conflicting with each other. Therefore, objectives are simultaneously optimized using a multi-objective optimization algorithm; mathematically equally good solutions known as non-dominated or Pareto frontier are selected as the optimum designs.³³ ANN-MOGA has been applied for predicting optimum conditions of colour removal efficiency and COD removal efficiency. The ANN models were used as a fitness function for MOGA. An ANN function named myANN1 and myANN2 was trained using the experimental data for Colour removal efficiency and COD removal efficiency, respectively.

Then, using MATLAB (R2020b) and the myANN1 and myANN2 function, a multi-objective function code was developed. Finally, the MOGA program was run to generate Pareto optimal solutions by setting all input variables' upper and lower limits.

3. Results and Discussion

3. 1. Experimental Results

In a batch electrochemical cell, the indirect electrochemical oxidation method was carried out to treat the RTB21 wastewater. The experimental results obtained from the batch process were then used to build a continuous process, and colour removal efficiency and COD removal efficiency were measured. Based on the batch process results, the initial pH, current density, and NaCl concentration range were fixed for the continuous process. It was possible to determine the influence of hydraulic retention time (HRT) on the colour removal and COD removal efficiency by altering the HRT values from 25 to 200 min, as shown in Fig. 3.

The other parameters, such as pH, current density, and NaCl concentration, were kept constant at 7, 200 A/m² and 2 g/L, respectively. HRT was found to have a beneficial influence on the EO process by increasing the response time. As per the DOE set, continuous EO process experiments were performed, and colour removal efficiency and COD removal efficiency were calculated, as shown in Table 2. By raising the HRT, adequate time for process reaction could be provided; hence, the colour removal efficiency (%) and the COD removal efficiency (%) improved. The synergistic effect of increased HRT can be attributed

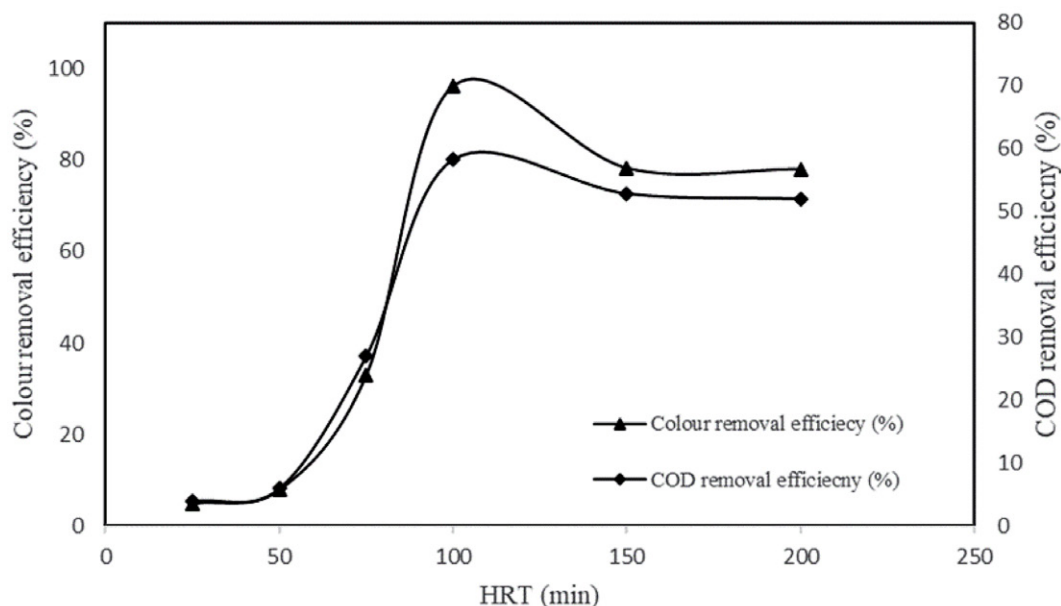


Fig. 3. Effect of HRT (min) on Colour removal efficiency (%) and COD removal efficiency (%) at 7 pH, 200 A/m²CD, and 2 g/L NaCl concentration.

to the generation of more oxidants for pollutant degradation.³⁴ With the enhancement of HRT more than 100 min, degradation efficiency declines because of unsuitable side reactions.³⁵ The highest colour removal efficiency (%) and COD removal efficiency (%) achieved were 96.11% and 58.23% at 100 HRT (min), pH of 7, 200 A/m², and 2 g/L NaCl concentration.

3. 2. Prediction with ANN

The primary objective of the ANN is to predict the colour removal efficiency and COD removal efficiency for DOE data sets. The present research used a feed-for-

ward LM-BP ANN with a tangent sigmoid transfer function (tansig) at a hidden layer. At each iteration, the ANN learns by testing and validating the predictability against the remaining data and deciding its absolute accuracy based on the overall correlation coefficient. It is always critical to pick a sufficient number of neurons in the hidden layer to properly well train the network. However, the larger the hidden layer's number of neurons, the longer it takes to process the data and learn the noise.³⁶ Therefore, a solid network is required to determine an accurate ANN architecture to obtain accurate predictions, and this step was developed through trial and error.³⁷ This was done to achieve the minimum possible deviation between predic-

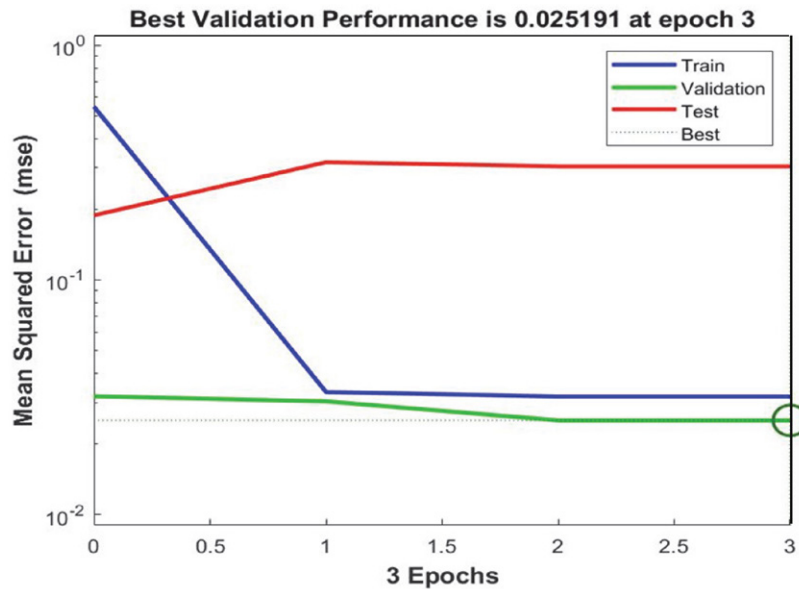


Fig. 4. Performance of ANN for colour removal efficiency

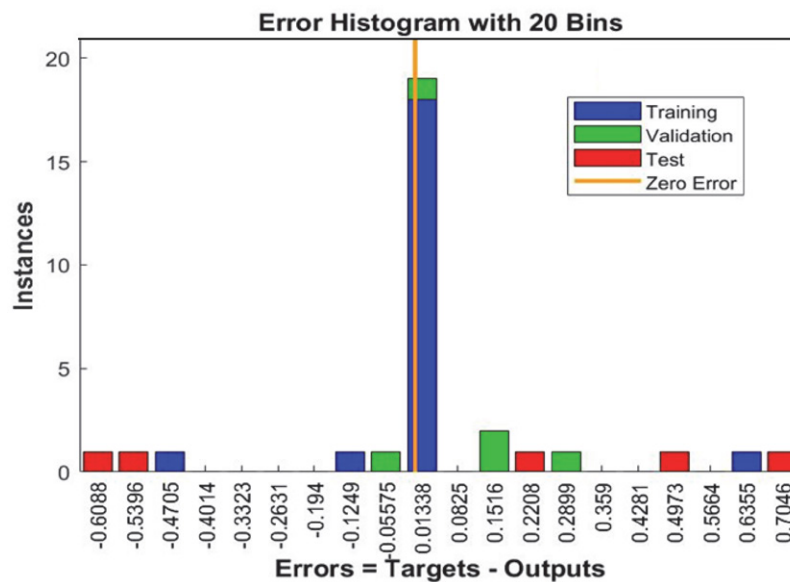


Fig. 5. Error histogram with 20 bins for the training, validation, and testing of ANN for colour removal efficiency prediction.

tions and experimental results and limit the potential of over-fitting the model to the data. Numerous topologies were tested to obtain the optimal ANNs network based on the most miniature Mean Square Error (MSE) and largest Correlation coefficient (R) values. The best ANN network was a back-propagation with 4-9-6-3-1 neurons. The inputs consist of pH, CD, HRT, NaCl concentration, and output consists of colour removal efficiency and COD removal efficiency.

MSE is a statistic that represents the average of the squares of the errors, the magnitude by which the value indicated by the model varies from the quantity to be observed; when MSE reaches zero, it indicates that our model's error reduces. The R is calculated by dividing the coefficient of determination (R^2) by its square root function, which determines the relationship between outputs and targets. The R-value of 0 and 1 indicates a random relationship and close relationship, respectively.

For the colour removal efficiency, the optimum network performance was reached at an epoch of 3. Fig. 4 shows the performance of the ANN for colour removal efficiency prediction during training, validation, and testing and the mean squared error (MSE) of the network.

As shown in Fig. 4, the error started at a high value during training, validation, and testing but gradually reduced as the number of epochs increased. The training was terminated at epoch 3 to prevent overfitting the data sets, and the best validation performance was achieved at epoch 3, with a mean square error of 0.025191.

As the error histogram of the colour removal efficiency (Fig. 5) shows, most of the errors fall between -0.6066 and 0.7046 . The zero error is in a vertical line parallel to the ordinate with 19 instances during training.

The values of regression coefficient of correlation between the experimentally obtained colour removal and the ANN predicted colour removal during training, validation, and testing are 0.99998, 1, and 0.999993 (Fig. 6 (a,b,c)), respectively. The regression coefficient of the network (training, testing, and validation) was 0.99996 (Fig. 6 (d)).

For the COD removal efficiency, the optimum network performance was reached at an epoch of 2. Fig. 7 shows the performance of the ANN for COD removal efficiency prediction during training, validation, and testing and the mean squared error (MSE) of the network. As Fig. 7 shows, the best validation performance occurred at epoch 2, with a 0.01971 MSE value.

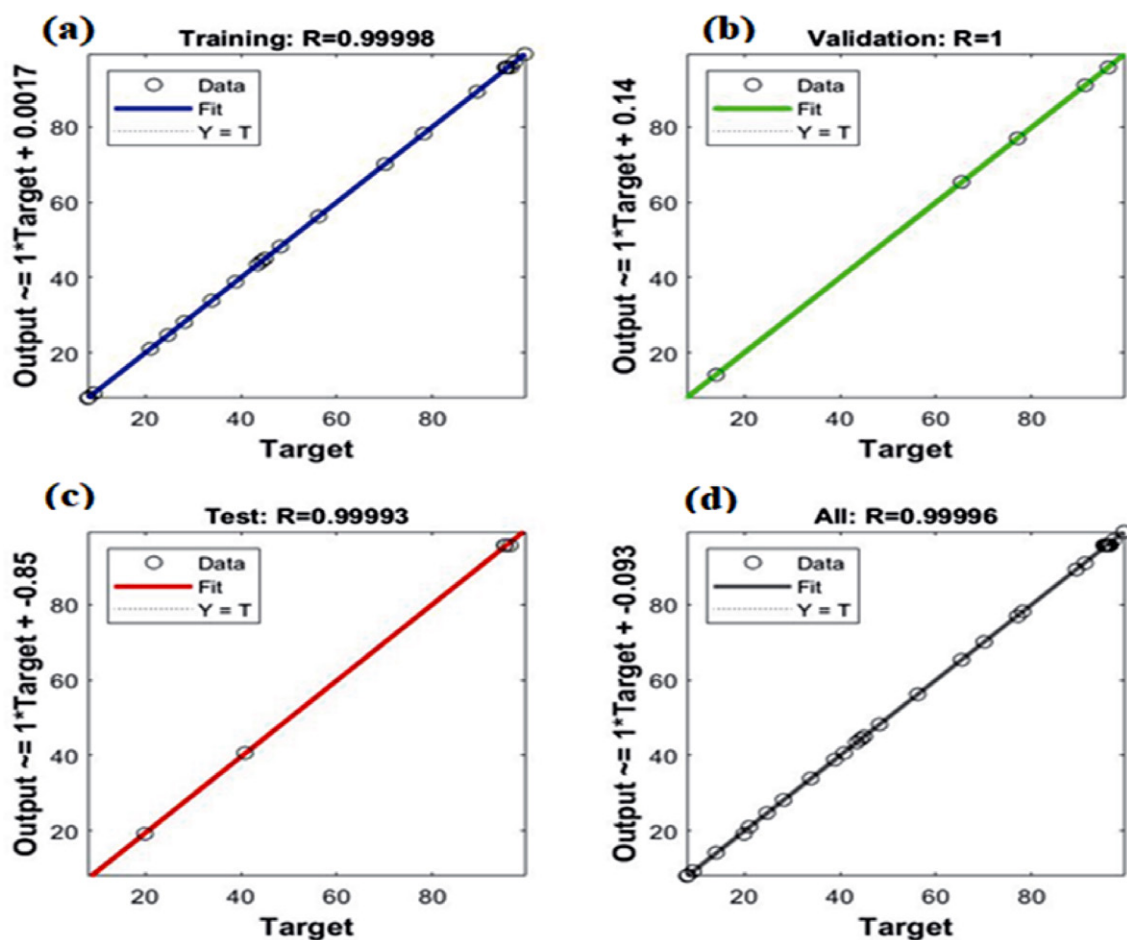


Fig. 6. ANN predictions of colour removal efficiency versus experimental data

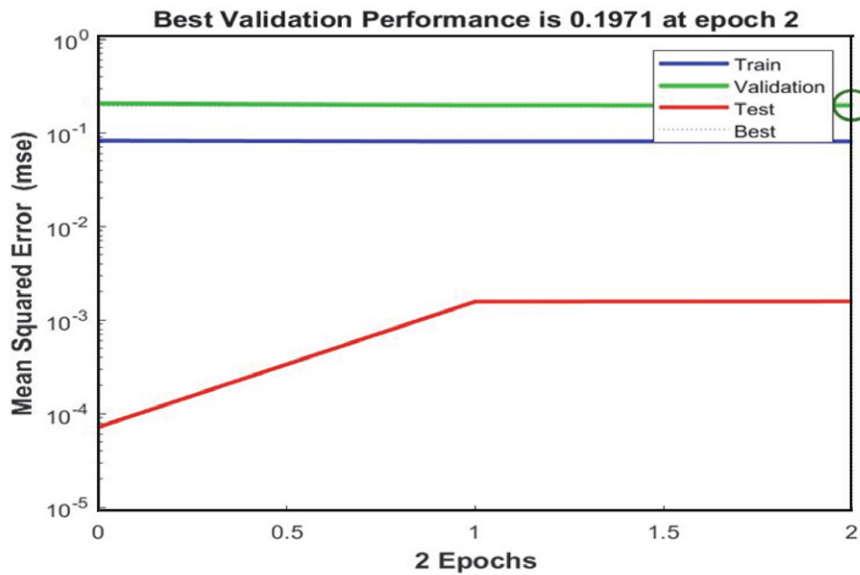


Fig. 7. Performance of ANN for COD removal efficiency.

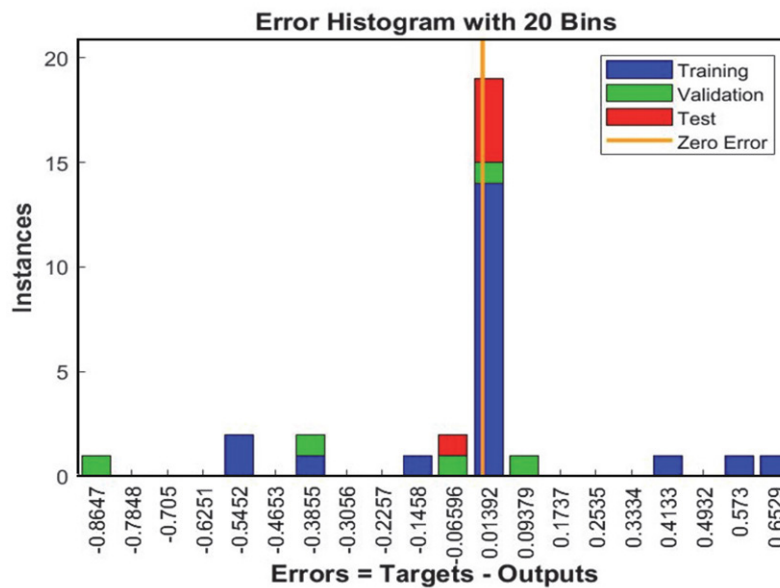


Fig. 8. Error histogram with 20 bins for the training, validation, and testing of ANN for COD removal efficiency prediction.

Fig. 8 shows the error histogram of the ANN for COD removal efficiency. As the error histogram shows, most of the errors fall between -0.8647 and 0.6529 . The zero error is in a vertical line parallel to the ordinate with 19 instances during training.

The regression coefficient of correlation between the experimentally obtained COD removal efficiency and the ANN predicted COD removal efficiency during training, validation, and testing is shown in Fig. 9 (a,b,c) with values of 0.9999, 0.99987, and 1, respectively. The regression coefficient of the network (training, testing, and validation) was 0.99989, as shown in Fig. 9 (d).

3. 3. ANN-GA Process Result

The well-trained ANNs MATLAB functions were used as the fitness function, and the MOGA function is used to optimize all responses simultaneously using the “gamultiobj” algorithm. Fig. 10 depicts the conceptual model of the technique designed for multi-objective optimization of a continuous EO process for RTB21 dye wastewater treatment using ANN and MOGA.

The upper and lower bounds are set in accordance with DOE data. To generate the Pareto front, the population size, and scattered crossover rate was set to 50 and

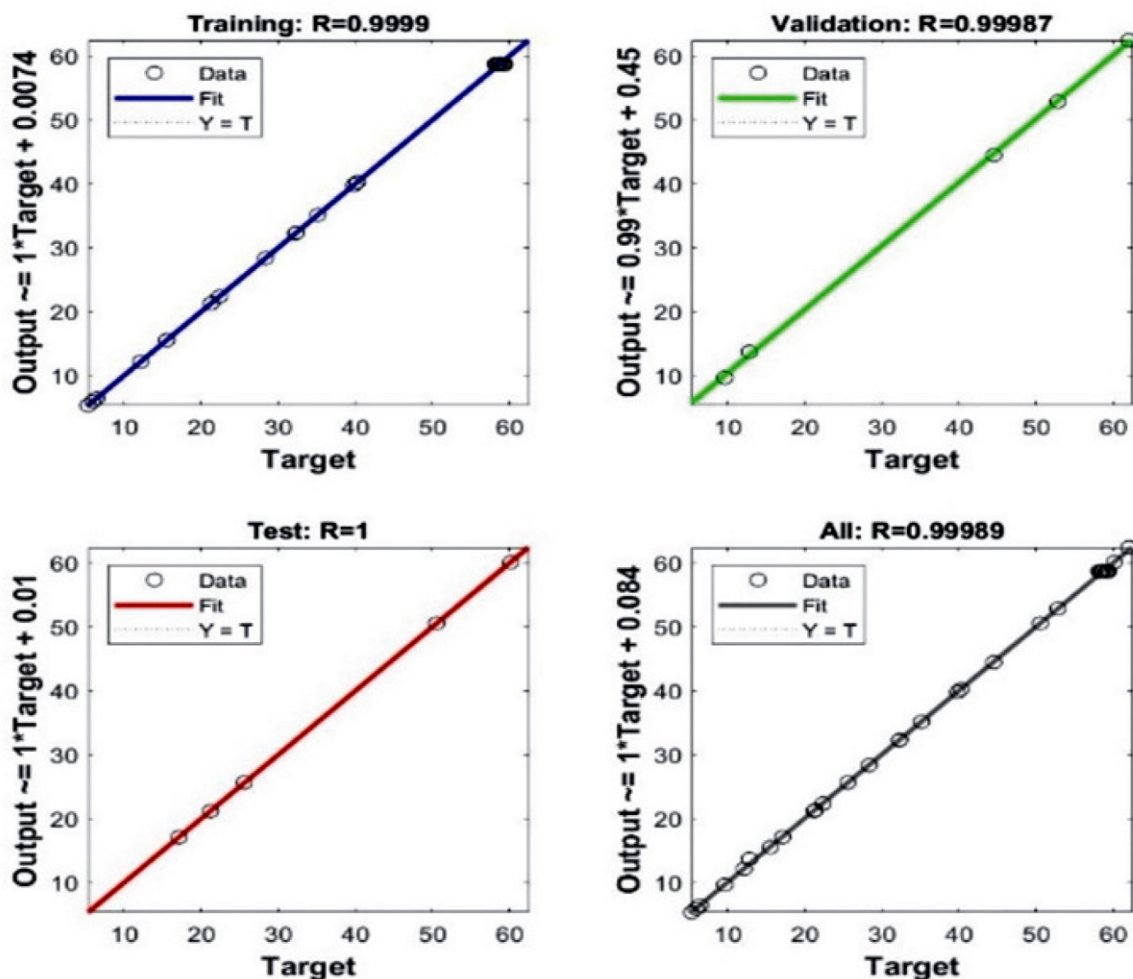


Fig. 9. ANN predictions of colour removal efficiency versus experimental data.

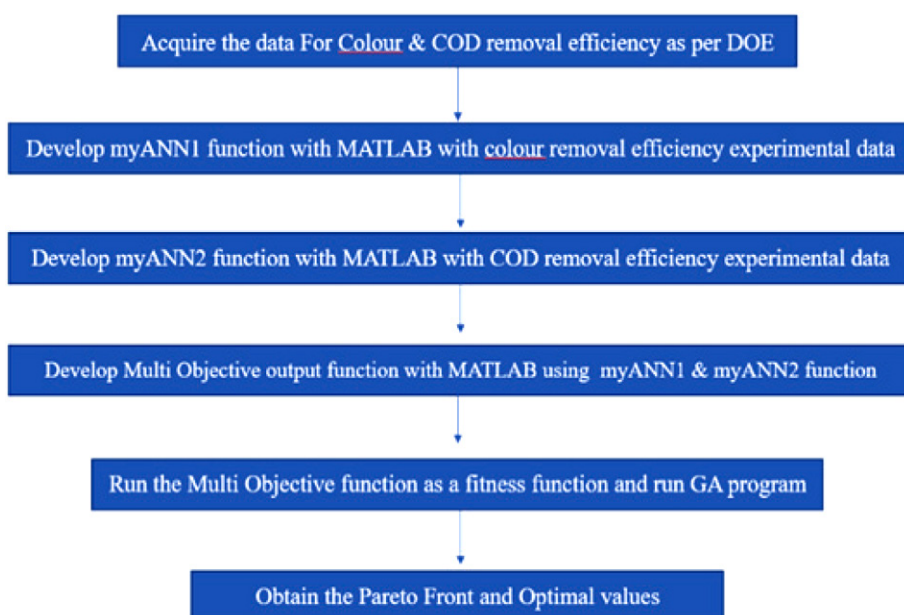


Fig. 10. Conceptual model of ANN-MOGA.

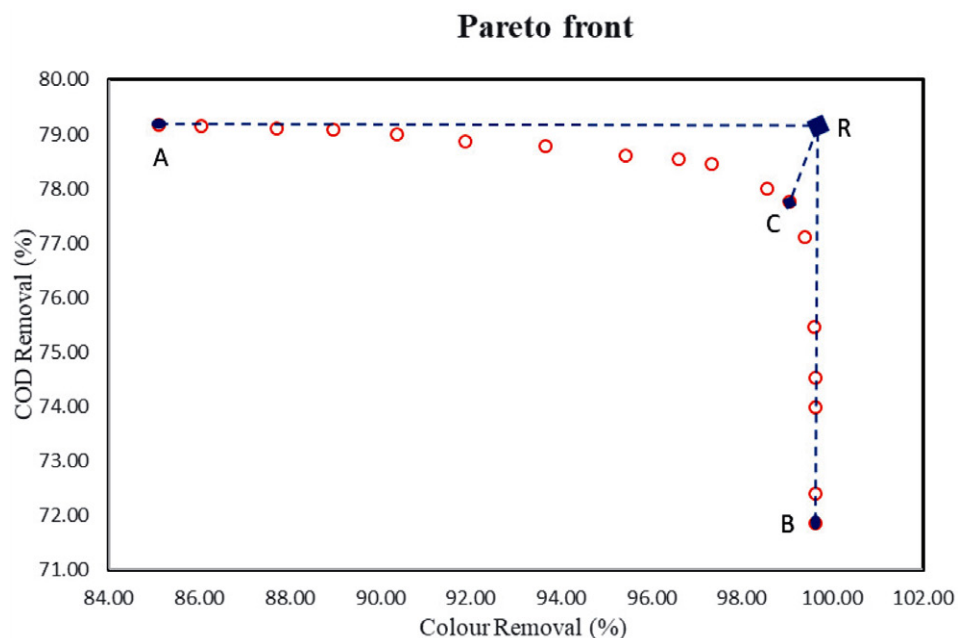


Fig. 11. Pareto front of solutions obtained from multi-objective optimization of colour removal efficiency and COD removal efficiency.

Table 3. Pareto front results.

Sr No.	pH	CD	HRT	NaCl Conc.	Colour removal efficiency	COD removal efficiency
1	8.787827	299.5076	138.5276	2.996047	99.61891	73.9798
2	6.363786	298.0398	140.3197	2.081875	85.10173	79.17201
3	6.449391	298.1739	140.1821	2.235604	91.86767	78.88044
4	6.974005	299.1398	138.9455	2.56925	99.39556	77.10913
5	9.185247	299.9831	138.2816	2.999956	99.62148	71.86423
6	6.363786	298.0085	140.3197	2.107265	86.02775	79.16041
7	6.428636	299.3274	140.3134	2.171365	88.94894	79.08443
8	6.711324	298.9897	139.8307	2.345993	96.60149	78.53708
9	7.927858	298.8051	138.4173	2.989545	99.61496	74.53391
10	8.10627	299.6478	139.1243	2.908942	99.60828	75.46253
11	6.847544	298.2432	140.1611	2.494421	99.04663	77.75342
12	6.579091	298.9179	139.9584	2.312797	95.42957	78.61332
13	6.45257	298.1872	140.203	2.146821	87.71312	79.09912
14	6.79187	298.932	139.2222	2.43517	98.55288	77.99996
15	6.92752	298.8918	139.8317	2.372651	97.32729	78.46639
16	6.593751	298.7015	140.2943	2.202841	90.35593	79.00198
17	9.091421	299.5083	138.4265	2.996635	99.62033	72.40382
18	6.534363	298.0117	140.3169	2.274754	93.64972	78.79096

0.8, respectively. The Pareto front, as a result of MOO, is depicted in Fig. 11. Table 3 contains the input values for both responses in accordance with Pareto solutions.

The multi-objective optimization solution of colour removal efficiency and COD removal efficiency has no unique solution but a mathematically equally good solution known as non-dominated or Pareto optimal solutions. As can be observed colour removal efficiency increases from 85.10% to 99.62% at the cost of decrease-

ing COD removal efficiency from 79.17% to 72.40%. As shown from this Fig. 10, the Pareto front provides all possible Colour removal efficiency and COD removal efficiency choices. The utopia point C (99.05, 77.75) is selected such that it has the minimum Euclidean distance from the reference point R. The reference point is a point corresponding to maximum values of colour removal efficiency point B (99.62, 72.40) and COD removal efficiency point A (85.10, 79.17).

Table 4. Statistical Parameters of well-trained ANN models for colour removal efficiency and COD removal efficiency.

Statistical Parameters	MSE	RMSE	MAE	MPE (%)	Chi Square statistics (χ^2)	R ²
Colour removal efficiency	0.0748	0.2735	0.1462	0.2737	0.0478	0.9999
COD removal efficiency	0.0870	0.2949	0.1569	0.1398	0.0919	0.9998

3. 4. Confirmatory Experiments

The results of the well-trained ANNs model were checked with their predicted capability in terms of standard statistical performance parameters such as mean square error (MSE), root mean square error (RMSE), mean absolute error (MAE), model predictive error (MPE) (%), Chi-Square statistics (χ^2), and R². A chi-square test is a statistical test used to compare experimental results with predicted results. The value of χ^2 is close to zero, and the R² value close to one displays the well-trained ANN models. Statistical parameters of well-trained ANN models for colour and COD removal efficiencies are presented in Table 4.

Optimized parameters (pH: 6.85, CD: 298.24 A/m², HRT: 140.16 min, NaCl concentration: 2.49 g/L) generated by the ANN-MOGA model for achieving maximizing Colour removal efficiency (%) and COD removal efficiency (%) simultaneously were validated by performing confirmatory experiments. The confirmatory experiment was carried out at the predicted optimal condition for model validation in triplicate, and average values are shown in Table 5.

Table 5. Comparative results of optimized and confirmatory experiments for model validation.

Process Parameters	ANN-MOGA	
	Optimized Value	Experimental Value
pH	6.85	6.9
CD	298.24	299
HRT	140.16	141
NaCl Conc.	2.49	2.5
Colour removal efficiency (%)	99.05	98.82
COD removal efficiency (%)	77.75	77.60

A perusal of Table 5 indicates close agreements between optimized and experimental values. The percentage variation between experimental and simulated results was determined in the $\sim\pm 1\%$ error range. This suggested that the models' prediction capacity was satisfactory. Hence, the adequacy of ANN-MOGA models on predicting the Colour removal efficiency (%) and COD removal efficiency (%) was validated.

4. Conclusion

The ANN approach was successfully used to forecast all responses for continuous EO processes in accordance

with an input parameter such as pH, current density, hydraulic retention time, and NaCl concentration. To build ANN models, the feed-forward LM-BP training algorithm was used. The well-trained ANN models had three hidden layers with 9-6-3 neurons in the hidden layers. For colour removal efficiency and COD removal efficiency, the MSE values were 0.748, 0.870, and the R² values were 0.9999, 0.9998, respectively. The ANN modelling technique could offer several advantages, including speed, dependability, fault tolerance, resilience, universal application, and usability, making it an intriguing choice for modelling complicated systems such as wastewater treatment.

The use of a genetic algorithm to perform multi-objective optimization of the ANN model resulted in a set of Pareto optimum points. The solutions to the Pareto front points could be utilised as a guideline for designing a continuous EO for the RTB21 dye wastewater process. The ANN-MOGA approach was utilised to estimate the best process variable values for maximum colour removal efficiency and COD removal efficiency, which resulted in the generation of the Convex nature Pareto front. The utopia point (99.05, 77.75) was selected such that it had the minimum euclidean distance from the reference point R. In essence, data obtained in the present study could be useful for possible scale-up of the electro-oxidation process for similar types of reactive dyes.

5. Reference

1. United Nations, *VALUING WATER (2021): The United Nations World Water Development Report 2021*. Vol 9781849773; 2021. DOI:10.4324/9781849773355
2. P. V. Nidheesh, M. Zhou, M. A. Oturan, *Chemosphere*, **2018**, 197, 210–227. DOI:10.1016/j.chemosphere.2017.12.195
3. J. Saini, V. K. Garg, R. K. Gupta, N. Kataria, *J Environ Chem Eng*, **2017**, 5(1), 884–892. DOI:10.1016/j.jece.2017.01.012
4. E. Yuksel, E. Gurbulak, E. Murat, *Environ Sci Technol*, **2014**, 33(2), 482–489. DOI:10.1002/ep
5. Q. Wang, G. Yun, Y. Bai, et al., *Appl Surf Sci*, **2014**, 313, 537–544. DOI:10.1016/j.apsusc.2014.06.018
6. M. Sivakumar, A. B. Pandit, *Ultrason Sonochem*, **2002**, 9(3), 123–131. DOI:10.1016/S1350-4177(01)00122-5
7. Y. L. Pang, S. Bhatia, A. Z. Abdullah, *Sep Purif Technol*, **2011**, 77(3), 331–338. DOI:10.1016/j.seppur.2010.12.023
8. HJ Hsing, P. C. Chiang, E. E. Chang, M. Y. Chen, *J Hazard Mater*, **2007**, 141(1), 8–16. DOI:10.1016/j.jhazmat.2006.05.122

9. A. I. Adeogun, R. B. Balakrishnan, *Appl Water Sci*, **2017**, *7*(4), 1711–1723. DOI:10.1007/s13201-015-0337-4
10. X. Xue, K. Hanna, N. Deng, *J Hazard Mater*, **2009**, *166*(1), 407–414. DOI:10.1016/j.jhazmat.2008.11.089
11. S. Sachdeva, A. Kumar, *J Memb Sci*, **2009**, *329*(1-2), 2–10. DOI:10.1016/j.memsci.2008.10.050
12. P. V. Nidheesh, R. Gandhimathi, *Clean – Soil, Air, Water*, **2014**, *42*(6), 779–784. DOI:10.1002/clen.201300093
13. H. Xu, S. Qi, Y. Li, Y. Zhao, *Environ Sci Pollut Res*, **2013**, *20*, 5764–5772. DOI:10.1007/s11356-013-1578-0
14. N. R. Vaghela, K. Nath, *J Sci Ind Res*, **2019**, *78*(09), 624–628.
15. N. Daneshvar, M. A. Behnajady, M. K. A. Mohammadi, M.S.S. Dorraji, *Desalination*, **2008**, *230*(1-3), 16–26. DOI:10.1016/j.desal.2007.11.012
16. S. Farhadi, B. Aminzadeh, A. Torabian, V. Khatibikamal, M. Alizadeh Fard, *J Hazard Mater*, **2012**, *219*–220, 35–42. DOI:10.1016/j.jhazmat.2012.03.013
17. V. Khandegar, A. K. Saroha, *J Environ Manage*, **2013**, *128*(September), 949–963. DOI:10.1016/j.jenvman.2013.06.043
18. N. Nordin, S. F. M. Amir, M. R. Yusop, M.R. Othman, *Acta Chim Slov*, **2015**, *62*(3), 642–651. DOI:10.17344/acsi.2014.1264
19. Y. Sewsynker-Sukai, F. Faloye, E. B. G. Kana, *Biotechnol Bio-technol Equip*, **2017**, *31*(2), 221–235. DOI:10.1080/13102818.2016.1269616
20. H. S. M. Yahya, T. Abbas, N. A. S. Amin, *Int J Hydrogen Energy*, **2020**. DOI:10.1016/j.ijhydene.2020.05.033
21. M. Bayat Varkeshi, K. Godini, M. ParsiMehr, M. Vafae, *Avicenna J Environ Heal Eng*, **2019**, *6*(2), 92–99. DOI:10.34172/ajehe.2019.12
22. M. Fan, T. Li, J. Hu, et al., *Materials (Basel)*, **2017**, *10*(5). DOI:10.3390/ma10050544
23. M. R. Samarghandi, A. Dargahi, A. Shabanloo, H. Z. Nasab, Y. Vaziri, A. Ansari, *Arab J Chem*, **2020**, *13*(8), 6847–6864. DOI:10.1016/j.arabjc.2020.06.038
24. N. R. Vaghela, K. Nath, *SN Appl Sci*, **2020**, *2*(11). DOI:10.1007/s42452-020-03719-6
25. SN Sahu, Published online 2012.
26. N. Semache, F. Benamia, B. Kerouaz, et al., *Acta Chim Slov*, **2021**, *68*(3), 575–586. DOI:10.17344/acsi.2020.6401
27. S. Podunavac-Kuzmanović, L. Jevrić, J. Švarc-Gajić, et al., *Acta Chim Slov*, **2015**, *62*(1), 190–195. DOI:10.17344/acsi.2014.888
28. S. Azadi, A. Karimi-Jashni, S. Javadpour, *Process Saf Environ Prot*, **2018**, *117*, 267–277. DOI:10.1016/j.psep.2018.03.038
29. CE Onu, J. T. Nwabanne, P. E. Ohale, C. O. Asadu, *South African J Chem Eng*, **2021**, *36*(January 2021), 24–42. DOI:10.1016/j.sajce.2020.12.003
30. H. Kumar, V. Kumar, *Chem Eng Process – Process Intensif*, **2019**, *144*, 107649. DOI:10.1016/j.cep.2019.107649
31. K. Deb, In: *Multi-Objective Evolutionary Optimisation for Product Design and Manufacturing*, **2011**. DOI:10.1007/978-0-85729-652-8
32. F. Mohammadi, M. R. Samaei, A. Azhdarpoor, H. Teiri, A. Badeenezhad, S. Rostami, *Chemosphere*, **2019**, *237*, 124486. DOI:10.1016/j.chemosphere.2019.124486
33. QQ. Feng, L. Liu, X. Zhou, *Int J Adv Manuf Technol*, **2020**, *106*(1-2), 559–575. DOI:10.1007/s00170-019-04488-2
34. M. Gotsi, N. Kalogerakis, E. Psillakis, P. Samaras, D. Mantzavinos, *Water Res*, **2005**, *39*(17), 4177–4187. DOI:10.1016/j.watres.2005.07.037
35. A. R. Rahmani, K. Godini, D. Nematollahi, G. Azarian, S. Maleki, *Korean J Chem Eng*, **2016**, *33*(2), 532–538. DOI:10.1007/s11814-015-0175-y
36. M. Rakshit, P. P. Srivastav, *J Food Process Preserv*, **2021**, *45*(1), 1–14. DOI:10.1111/jfpp.15078
37. A. Picos, J. M. Peralta-Hernández, *Water Sci Technol*, **2018**, *78*(4), 925–935. DOI:10.2166/wst.2018.370

Povzetek

Razvili smo kontinuirni posredni proces elektrooksidacije (EO) z uporabo grafitne electrode, s katerim smo preučili možnosti odstranjevanja barvila turkizno modro RTB21 in odpadnih voda: Pri tem smo optimirali začetno pH vrednost, gostoto električnega toka, zadrževalni čas (HRT) in koncentracijo elektrolita (NaCl). Poskusi so bili izvedeni v skladu s središčnim sestavljenim načrtom (ang. CCD), rezultati pa so bili uporabljeni za učenje modela na osnovi umetnih nevronske mreže (ang. ANN). Glede na predvidene ugotovitve modela ANN so bile MSE vrednosti za učinkovitost odstranjevanja barve in KPK ocenjene na 0.748 oziroma 0.870, vrednosti R2 pa na 0.9999 oziroma 0.9998. Večkriterijska optimizacija z genetskimi algoritmi (MOGA) uporabljena po ANN modelu je odatno optimizirala učinkovitost odstranjevanja barvo in zmanjševanja KPK. MOGA pada nedominantno (Pareto) fronto, ki omogočajo vpogled v optimalne pogoje delovanja procesa.



Except when otherwise noted, articles in this journal are published under the terms and conditions of the Creative Commons Attribution 4.0 International License

Scientific paper

Enantioselective Henry Reaction Catalyzed by Chiral Piperazine Derivatives

Leman Alkan*

Department of Chemistry, Faculty of Science, Ege University, Izmir, 35100 Turkey

* Corresponding author: E-mail: alkanleman@gmail.com

Tel: +90 232 388 82 64

Received: 09-15-2021

Abstract

A series of novel tridentate Schiff bases is synthesized from piperazine-amine and substituted salicylaldehydes, and characterized by spectroscopic methods. These chiral ligands were used to catalyze the addition of nitromethane to various aldehydes in the presence of Cu(II) ions under ambient conditions in good yields (98%) and high enantioselectivities (9:91 *er*).

Keywords: Piperazine; Schiff base; chiral catalyst; enantioselective Henry reaction

1. Introduction

The catalytic asymmetric Henry (nitroaldol) reaction is a very efficient and atom economic method for stereoselective C–C bond formation. The resulting chiral products of this reaction, β -hydroxynitroalkanes, contain two functional groups (hydroxyl and nitro groups) and can be easily transformed into many valuable building blocks in asymmetric organic synthesis. The asymmetric Henry reaction has also been applied to the synthesis of bioactive natural products and pharmaceutical agents.^{1–7} Since the Shibasaki group reported the first catalytic asymmetric Henry reaction,⁸ a great deal of effort has been devoted to the development of various metal-containing catalysts.^{9–13} In particular, Cu(II) complexes of various tridentate ligands have recently been used as chiral catalysts with good enantioselectivity.^{14–18}

The piperazine skeleton is a unique structure often found in biologically active compounds. Piperazine based compounds are found in antihistamines, antibiotics, antidepressant and anticancer drugs. Their metal complexes are also successfully used as catalyst in different organic reactions.¹⁹ Transition metal complexes of amine ligands containing piperazine moiety are very stable form. However, there isn't any report that tridentate Schiff base ligands derived from piperazine are used as catalyst in the asymmetric Henry reaction.

In our previous publications we reported the synthesis and catalytic activity of copper(II) complexes of triden-

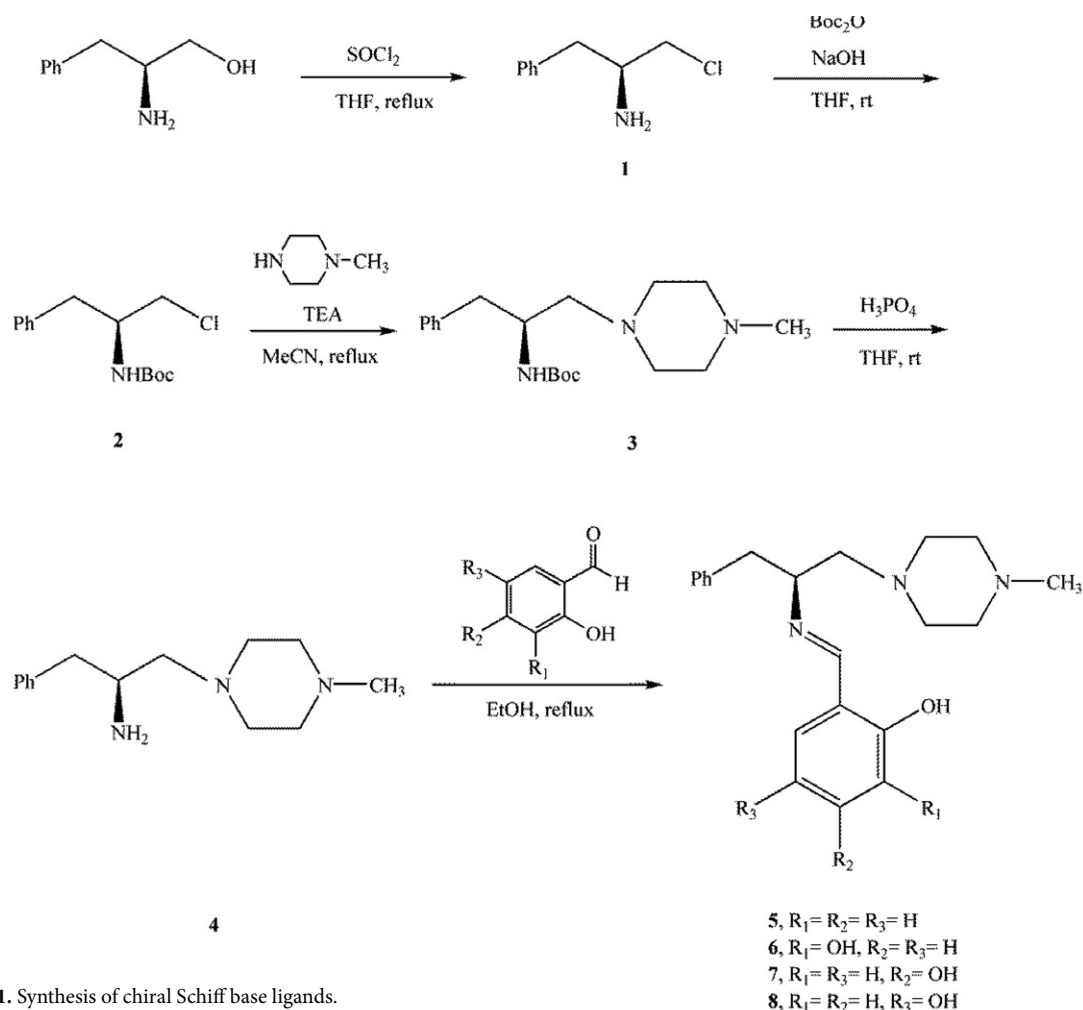
tate Schiff base ligands derived from amino acids.^{20–21} Herein, we report novel chiral tridentate Schiff bases which can be readily synthesized from piperazine-amine and can be used as catalysts in enantioselective Henry reactions under mild conditions. We thought that the N group in the ring, which is not coordinated to the metal, will increase the enantioselectivity due to the bifunctional capability of the piperazine derivatives.

2. Results and Discussion

For the purpose of creating structurally different chiral tridentate Schiff bases, (S)-1-(4-methylpiperazin-1-yl)-3-phenylpropan-2-amine **4** was reacted with a variety of 2-hydroxybenzaldehydes. Our preparative routes to the piperazine-amine involved protection of amino alcohol derivative followed by addition of piperazine ring and deprotection of Boc group as can be seen in Scheme 1. Subsequent reaction with different aldehydes afforded the desired chiral Schiff base ligands **5–8** in high yields.

Initial studies were focused on the effect of these ligands **5–8** on the asymmetric Henry reaction by carrying out reactions between 2-chlorobenzaldehyde as a model substrate and nitromethane in the presence of Cu(OAc)₂·n-H₂O. The results are summarized in Table 1.

The first experimental results showed that substituents in aromatic ring of the ligand had a significant effect on the enantioselectivity. Ligand **5** was expressly superior



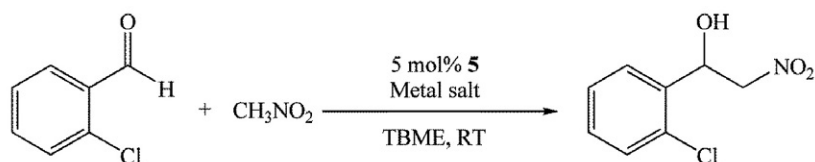
Scheme 1. Synthesis of chiral Schiff base ligands.

Table 1. Reaction of 2-chlorobenzaldehyde: screening of ligands and solvent effect

Entry	Ligand	Solvent	Time (h)	Yield ^a (%)	<i>er</i> ^{b,c}
1	5	TBME	48	98	9:91
2	5	<i>i</i> -PrOH	48	73	20:80
3	5	THF	48	49	41:59
4	6	TBME	48	84	10:90
5	6	<i>i</i> -PrOH	48	67	14:86
6	6	THF	48	38	39:61
7	7	TBME	48	60	22:78
8	7	<i>i</i> -PrOH	48	49	24:76
9	7	THF	48	45	24:76
10	8	TBME	48	n.d.	–
11	8	<i>i</i> -PrOH	48	50	15:75
12	8	THF	48	42	28:72

^a Isolated yields after column chromatography; ^b enantiomeric ratio (*er*) determined by HPLC analysis using a Chiralcel OD-H column; ^c the absolute configuration of the major product was assigned as *S* by comparison with the literature values;^{22–24} n.d.: not determined.

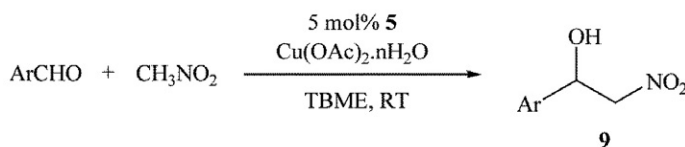
Table 2. Optimization of the reaction conditions



Entry	Metal Salt	Temp. (°C)	Time (h)	Yield ^a (%)	<i>er</i> ^{b,c}
1	Copper(II) benzoate	RT	48	75	9:91
2	Copper(II) formate	RT	48	n. d.	–
3	Copper(II) acetate	RT	48	98	9:91
4	Copper(II) acetate	0	48	52	27:73
5 ^d	Copper(II) acetate	RT	48	74	42:58

^a Isolated yields after column chromatography; ^b enantiomeric ratio (*er*) determined by HPLC analysis using a Chiralcel OD-H column; ^c the absolute configuration of the major product was assigned as *S* by comparison with the literature values;^{22–24} ^d with 10 mol% ligand and Cu(OAc)₂ loading; n.d.: not determined.

Table 3. Substrate scope



Entry	ArCHO	Product	Time (h)	Yield ^a	<i>er</i> ^b	Config. ^c
1	2-Chlorobenzaldehyde	9a	48	98	9:91	<i>S</i>
2	2-Bromobenzaldehyde	9b	48	83	15:85	<i>S</i>
3	2-Methoxybenzaldehyde	9c	48	89	10:90	<i>S</i>
4	3-Nitrobenzaldehyde	9d	48	71	51:49	<i>S</i>
5	Benzaldehyde	9e	96	92	21:79	<i>S</i>
6	4-Methylbenzaldehyde	9f	120	85	35:65	<i>S</i>
7	4-Ethylbenzaldehyde	9g	120	60	24:76	n. d.
8	4-Methoxybenzaldehyde	9h	120	68	64:36	<i>R</i>
9	4-Chlorobenzaldehyde	9i	48	88	13:87	<i>S</i>

^a Isolated yields after column chromatography; ^b enantiomeric ratio (*er*) determined by HPLC analysis using a Chiralcel OD-H column; ^c the absolute configuration of the major product was assigned by comparison with the literature values;^{22–24} n.d.: not determined.

among the other ligands **6–8** in terms of *er* values. Next, *tert*-butyl methyl ether was found to be the best solvent for enantioselective nitroaldol reaction. The best results were observed when substrate was stirred for 48 h in the presence of 5 mol% **5** and Cu(OAc)₂·nH₂O at room temperature in TBME (Table 1, entry 1).

After the selection of the ligand for the catalyst system and the solvent, the reaction parameters, including copper salt, temperature and catalyst loading, were optimised. As can be seen from Table 2, surprisingly, when the reaction was performed using copper(II) formate, product formation was not observed (entry 2). However, when copper(II) benzoate and copper(II) acetate were used in the reaction, high *er* values were observed (entries 1, 3). These results show that carboxylate counter ion in copper salt is very effective in the copper(II) catalysed enantioselective Henry reaction. Afterward, the catalyst loadings were tested (entries 3, 5) and 5 mol% was found to afford

the best results. In addition, room temperature is an optimal reaction temperature (entries 3, 4).

Finally, with the optimised conditions, the scope of the substrate was investigated using a variety of aromatic aldehydes (Table 3). Moderate to good enantiomeric ratio and yield of the desired β-hydroxynitroalkanes were obtained. The data clearly showed that the substrates with *ortho*-substituent (entries 1–3) gave seriously higher enantioselectivities than other. These increases in enantioselectivity are possibly due to the geometry of the substrate having a great and important role in the mechanism.

3. Experimental

All chemicals were purchased from Merck, Sigma-Aldrich, Alfa Aesar, or Fluka and were used without any purification. Silica gel F₂₅₄ (Merck 5554) precoated

plates were used for thin layer chromatography. For column chromatography, silica gel 60 (Merck 7743) was used. IR spectra were recorded using a Perkin Elmer 100 FTIR spectrometer. ^1H NMR and ^{13}C NMR spectra were obtained by using a 400 MHz Varian NMR spectrometer at ambient temperature. Optical rotations were determined using a Rudolph Research Analytical AUTOPOL I automatic polarimeter. HPLC analysis was carried out on Agilent Technologies 1200 series with chiral stationary phase column (Chiralcel OD-H). Elemental analyses were performed on a Leco CHNS-932 elemental analyzer. High resolution mass spectra (HRMS) were measured on a Waters Synapt G1 mass spectrometer using ESI-TOF ionization. Compound **2** was prepared according to the literature method.²⁵

Preparation of (S)-tert-butyl (1-benzyl-2-chloroethyl) carbamate (2). SOCl_2 (0.3 mL, 4 mmol) was added dropwise to a solution of (S)-2-amino-3-phenyl-1-propanol (150 mg, 1 mmol) in THF (10 mL) at 0 °C and the resulting solution was refluxed for 12 h. Then the solvent was evaporated in vacuo and the residue **1** was used without purification. To a solution of **1** and NaOH (88 mg, 2.2 mmol) in THF (10 mL) was added di-tert-butyl dicarbonate (Boc_2O) (240 mg, 1.1 mmol). The reaction mixture was stirred at room temperature for 24 h. Evaporation of the solvent gave a residue that was purified with column chromatography (1:8 ethyl acetate:hexane) to give the title compound as light yellow crystals. Yield 94%, mp 83–84 °C. IR (KBr) ν 3339, 2978, 1691, 1528, 1169 cm^{-1} . ^1H NMR (400 MHz, CDCl_3) δ 7.33–7.24 (m, 5H), 4.80 (br s, 1H), 4.12 (br s, 1H), 3.63–3.47 (dd, $J = 3.6, 11.2$ Hz, 2H), 2.93–2.85 (m, 2H), 1.43 (s, 9H). ^{13}C NMR (400 MHz, CDCl_3) δ 154.98, 137.01, 129.16, 128.58, 126.82, 79.76, 51.90, 46.88, 37.77, 28.32. Anal. Calcd for $\text{C}_{14}\text{H}_{20}\text{ClNO}_2$: C, 62.33; H, 7.47; N, 5.19. Found: C, 61.40; H, 7.17; N, 5.13.

Preparation of (S)-tert-butyl [1-(4-methylpiperazin-1-yl)-3-phenylpropan-2-yl]carbamate (3). To a solution of **2** (50 mg, 0.185 mmol) in acetonitrile under nitrogen atmosphere was added triethylamine (0.078 mL, 0.555 mmol) and 1-methylpiperazine (185.3 mg, 1.85 mmol). The reaction mixture was refluxed for 12 h. After completion of the reaction (as monitored by TLC), the solvent was evaporated in vacuo. The residue was purified with column chromatography (1:1 ethyl acetate:hexane) to give the title compound as an off-white solid. Yield 86%, mp 125–127 °C. IR (KBr) ν 3385, 2944, 1681, 1508, 1166 cm^{-1} . ^1H NMR (400 MHz, CDCl_3) δ 7.29–7.16 (m, 5H), 4.58 (br s, 1H), 3.92 (br s, 1H), 2.85 (d, $J = 6$ Hz, 2H), 2.41–2.26 (m, 10H), 2.24 (s, 3H), 1.42 (s, 9H). ^{13}C NMR (400 MHz, CDCl_3) δ 155.54, 137.77, 129.65, 128.21, 126.22, 79.06, 60.44, 55.13, 53.28, 48.54, 45.99, 28.40. Anal. Calcd for $\text{C}_{19}\text{H}_{31}\text{N}_3\text{O}_2$: C, 68.43; H, 9.37; N, 12.60. Found: C, 66.42; H, 8.92; N, 12.74.

Preparation of (S)-1-(4-methylpiperazin-1-yl)-3-phenylpropan-2-amine (4). The compound **3** (100 mg, 0.3 mmol) was dissolved in 3 mL THF and 3 mL 85% H_3PO_4 was added dropwise to the solution. The reaction was stirred overnight at room temperature. To terminate the reaction, 5 mL distilled water was added and the reaction mixture was neutralized with saturated NaOH. The solution was extracted with ethyl acetate. The organic phase was dried using Na_2SO_4 and evaporated in vacuo. The residue was purified with column chromatography (1:1 methanol:ethyl acetate) to give the title compound as a yellow oil. Yield 95%. IR (NaCl) ν 3362, 2800, 1601 cm^{-1} . ^1H NMR (400 MHz, CDCl_3) δ 7.31–7.19 (m, 5H), 3.22–3.15 (m, 1H), 2.74–2.71 (dd, $J = 4.8, 13.6$ Hz, 1H), 2.50–2.29 (m, 11H), 2.27 (s, 3H). ^{13}C NMR (400 MHz, CDCl_3) δ 139.18, 129.22, 128.38, 126.23, 64.71, 55.21, 53.42, 49.22, 45.91, 42.07.

General Procedure for The Preparation of Chiral Schiff Bases 5–8

A solution of **4** (1 mmol) and the appropriate aldehyde (1 mmol) in 10 mL ethanol was refluxed until the aldehyde has been consumed. The solvent was evaporated in vacuo and crude product was purified with flash chromatography.

2-((E)-{[(1S)-1-Benzyl-2-(4-methylpiperazin-1-yl)ethyl]imino}methyl)phenol (5). Yellow crystals, yield 96%, mp 88–90 °C, $[\alpha]_D^{19} -120$ (c 0.25, CH_3OH). IR (KBr) ν 3213, 2796, 1630, 1581 cm^{-1} . ^1H NMR (400 MHz, CDCl_3) δ 8.04 (s, 1H), 7.28–7.13 (m, 7H), 6.82 (d, $J = 8$ Hz, 1H), 6.77 (t, $J = 7.6$ Hz, 1H), 3.71–3.64 (m, 1H), 3.07–3.02 (dd, $J = 4, 16$ Hz, 1H), 2.84–2.79 (dd, $J = 8, 12$ Hz, 1H), 2.65–2.62 (dd, $J = 4, 8$ Hz, 2H), 2.55–2.34 (m, 8H), 2.23 (s, 3H). ^{13}C NMR (400 MHz, CDCl_3) δ 165.22, 162.38, 138.17, 132.29, 131.42, 129.30, 128.85, 127.90, 125.95, 118.32, 117.79, 116.74, 67.67, 62.61, 54.20, 52.54, 44.76, 40.41. HRMS ESI-TOF (m/z): $[\text{M} + \text{H}]^+$ calcd for $\text{C}_{21}\text{H}_{28}\text{N}_3\text{O}$: 338.2232. Found: 338.2229. HPLC (hexane:*i*-PrOH (95:15), wavelength: 267 nm, flow rate: 1.0 mL/min): $t_r = 10.627$ min.

3-((E)-{[(1S)-1-Benzyl-2-(4-methylpiperazin-1-yl)ethyl]imino}methyl)benzene-1,2-diol (6). Yellow solid, yield 87%, mp 101–102 °C, $[\alpha]_D^{19} -102$ (c 0.26, CH_3OH). IR (KBr) ν 3439, 2808, 1632, 1540 cm^{-1} . ^1H NMR (400 MHz, CDCl_3) δ 8.00 (s, 1H), 7.24–7.14 (m, 5H), 6.83–6.81 (dd, $J = 1.6, 7.6$ Hz, 1H), 6.65–6.63 (dd, $J = 1.6, 8$ Hz, 1H), 6.57 (t, $J = 8$ Hz, 1H), 3.75–3.68 (m, 1H), 3.07–3.03 (dd, $J = 4, 12$ Hz, 1H), 2.86–2.80 (dd, $J = 8, 12$ Hz, 1H), 2.65–2.62 (dd, $J = 2.8, 5.2$ Hz, 2H), 2.56–2.37 (m, 8H), 2.23 (s, 3H). ^{13}C NMR (400 MHz, CDCl_3) δ 165.43, 153.26, 146.04, 138.02, 129.32, 128.00, 126.06, 122.14, 117.55, 117.04, 116.94, 66.87, 62.53, 54.45, 52.69, 44.54, 40.24. HRMS ESI-TOF (m/z): $[\text{M} + \text{H}]^+$ calcd for $\text{C}_{21}\text{H}_{28}\text{N}_3\text{O}_2$: 354.2182. Found: 354.2177. HPLC (hex-

ane:*i*-PrOH (95:15), wavelength: 267 nm, flow rate: 1.0 mL/min): $t_r = 15.218$ min.

4-((*E*)-{[(1*S*)-1-Benzyl-2-(4-methylpiperazin-1-yl)ethyl]imino}methyl)benzene-1,3-diol (7). Pale yellow solid, yield 92%, mp 112–114 °C, $[\alpha]_D^{20} = -104$ (*c* 0.25, CH₃OH). IR (KBr) ν 3384, 2811, 1624, 1601 cm⁻¹. ¹H NMR (400 MHz, CDCl₃) δ 7.80 (s, 1H), 7.29–7.15 (m, 6H), 6.92 (d, *J* = 12 Hz, 1H), 6.11 (d, *J* = 8 Hz, 1H), 3.80–3.75 (m, 1H), 3.06–3.01 (dd, *J* = 8, 16 Hz, 1H), 2.88–2.82 (dd, *J* = 8, 12 Hz, 1H), 2.64–2.54 (m, 10H), 2.31 (s, 3H). ¹³C NMR (400 MHz, CDCl₃) δ 174.16, 162.85, 137.45, 134.61, 129.20, 128.11, 126.23, 109.91, 107.82, 62.62, 61.82, 54.53, 52.64, 44.54, 39.53. HRMS ESI-TOF (*m/z*): [M + H]⁺ calcd for C₂₁H₂₈N₃O₂: 354.2182. Found: 354.2165. HPLC (hexane:*i*-PrOH (95:15), wavelength: 267 nm, flow rate: 1.0 mL/min): $t_r = 15.302$ min.

2-((*E*)-{[(1*S*)-1-Benzyl-2-(4-methylpiperazin-1-yl)ethyl]imino}methyl)benzene-1,4-diol (8). Light brown solid, yield 79%, mp 142–144 °C, $[\alpha]_D^{20} = -112$ (*c* 0.25, CH₃OH). IR (KBr) ν : 3193, 2810, 1636, 1591 cm⁻¹. ¹H NMR (400 MHz, CDCl₃) δ 7.94 (s, 1H), 7.24–7.13 (m, 5H), 6.78–6.75 (dd, *J* = 4, 8 Hz, 1H), 6.69 (d, *J* = 8 Hz, 1H), 6.58 (d, *J* = 4 Hz, 1H), 3.66–3.60 (m, 1H), 3.05–3.01 (dd, *J* = 4, 12 Hz, 1H), 2.82–2.76 (dd, *J* = 8, 12 Hz, 1H), 2.65–2.62 (dd, *J* = 2.8, 5.2 Hz, 2H), 2.60–2.44 (m, 8H), 2.30 s (3H). ¹³C NMR (400 MHz, CDCl₃) δ 164.91, 154.20, 149.03, 138.35, 129.37, 128.99, 127.90, 125.93, 119.65, 118.49, 116.74, 116.23, 68.52, 62.88, 54.41, 54.13, 52.74, 44.54, 40.60, 40.31. HRMS ESI-TOF (*m/z*): [M + H]⁺ calcd for C₂₁H₂₈N₃O₂: 354.2182. Found: 354.2180. HPLC (hexane:*i*-PrOH (95:15), wavelength: 267 nm, flow rate: 1.0 mL/min): $t_r = 17.391$ min.

General Procedure for the Asymmetric Henry Reaction

The chiral Schiff base ligand **5–8** (0.01 mmol) and Cu(OAc)₂ · nH₂O (0.01 mmol) were allowed to stir in 2 mL of solvent at room temperature for 2 h. A color of solution change from light green to dark green was observed during this time. Subsequently, the appropriate aldehyde (0.2 mmol) and nitromethane (2 mmol) were added into the solution. The reaction mixture was stirred until most of the aldehyde has been consumed. The volatile components were evaporated in vacuo and the crude product was purified with column chromatography (1:5 ethyl acetate:hexane) to give the desired β -hydroxynitroalkane. Enantiomeric ratio (*er*) was determined by using HPLC with Chiracel OD-H column.

(S)-1-(2-Chlorophenyl)-2-nitroethanol (9a).²² Colorless oil, yield 98%. HPLC conditions: hexane:*i*-PrOH (93:7), wavelength: 267 nm, flow rate: 0.8 mL/min, $t_{minor} = 14.3$ min, $t_{major} = 14.8$ min, 9:91 *er*.

(S)-1-(2-Bromophenyl)-2-nitroethanol (9b).²² Colorless oil, yield 83%. HPLC conditions: hexane:*i*-PrOH (85:15),

wavelength: 267 nm, flow rate: 1.0 mL/min, $t_{minor} = 9.2$ min, $t_{major} = 9.7$ min, 15:85 *er*.

(S)-1-(2-Methoxyphenyl)-2-nitroethanol (9c).²² Yellow oil, yield 89%. HPLC conditions: hexane:*i*-PrOH (90:10), wavelength: 267 nm, flow rate: 1.0 mL/min, $t_{minor} = 11.8$ min, $t_{major} = 12.7$ min, 10:90 *er*.

(S)-1-(3-Nitrophenyl)-2-nitroethanol (9d).²⁴ Yellow oil, yield 71%. HPLC conditions: hexane:*i*-PrOH (90:10), wavelength: 267 nm, flow rate: 1.0 mL/min, $t_{major} = 28.2$ min, $t_{minor} = 31.0$ min, 51:49 *er*.

(S)-1-Phenyl-2-nitroethanol (9e).²³ Yellow oil, yield 92%. HPLC conditions: hexane:*i*-PrOH (90:10), wavelength: 267 nm, flow rate: 1.0 mL/min, $t_{minor} = 14.1$ min, $t_{major} = 15.1$ min, 21:79 *er*.

(S)-1-(4-Methylphenyl)-2-nitroethanol (9f).²² Yellow crystals, yield 85%. HPLC conditions: hexane:*i*-PrOH (90:10), wavelength: 267 nm, flow rate: 1.0 mL/min, $t_{minor} = 12.9$ min, $t_{major} = 15.4$ min, 35:65 *er*.

(S)-1-(4-Ethylphenyl)-2-nitroethanol (9g).²² Yellow oil, yield 60%. HPLC conditions: hexane:*i*-PrOH (90:10), wavelength: 267 nm, flow rate: 1.0 mL/min, $t_{minor} = 11.6$ min, $t_{major} = 14.2$ min, 24:76 *er*.

(R)-1-(4-Methoxyphenyl)-2-nitroethanol (9h).²² Yellow oil, yield 68%. HPLC conditions: hexane:*i*-PrOH (90:10), wavelength: 267 nm, flow rate: 1.0 mL/min, $t_{major} = 19.9$ min, $t_{minor} = 24.3$ min, 64:36 *er*.

(S)-1-(4-Chlorophenyl)-2-nitroethanol (9i).²² Colorless oil, yield 88%. HPLC conditions: hexane:*i*-PrOH (90:10), wavelength: 267 nm, flow rate: 1.0 mL/min, $t_{minor} = 14.0$ min, $t_{major} = 16.7$ min, 13:87 *er*.

4. Conclusions

Four novel tridentate Schiff bases have been prepared from a chiral (*S*)-2-amino-3-phenyl-1-propanol, which can be used in the asymmetric Henry reaction. Compared with other catalytic systems, the advantages of our method are mild reaction conditions, low loading of the catalyst (5 mol %) necessary, no need for additives and without any precautions against the presence of air and moisture needed.

Acknowledgments

This study was financially supported by Ege University Scientific Research Projects Coordination Unit (Grant number: 18 FEN 045). I thank Prof. Stephen T. Astley for helpful discussions concerning about this manuscript.

Supplementary Data

¹H and ¹³C NMR spectra of compounds 2–8 and HPLC chromatograms of compounds 5–8.

5. References

1. F. A. Luzzio, *Tetrahedron*, **2001**, *57*, 915–945. DOI: 10.1016/S0040-4020(00)00965-0
2. J. Boruwa, N. Gogoi, P. P. Saikia, N. C. Barua, *Tetrahedron: Asymmetry*, **2006**, *17*, 3315–3326. DOI: 10.1016/j.tetasy.2006.12.005
3. M. R. I. Kureshy, A. Das, N. U. H. Khan, S. H. R. Abdiu, H. C. Bajaj, *ACS Catal.*, **2011**, *1*, 1529–1535. DOI: 10.1021/cs2004467
4. L. Liu, S. L. Zhang, F. Xue, G. S. Lou, H. Y. Zhang, S. C. Ma, W. H. Duan, W. Wang, *Chem. Eur. J.*, **2011**, *17*, 7791–7795. DOI: 10.1002/chem.201101025
5. Z. L. Guo, Y. Q. Deng, S. Zhong, G. Lu, *Tetrahedron: Asymmetry*, **2011**, *22*, 1395–1399. DOI: 10.1016/j.tetasy.2011.08.008
6. D. Uraguchi, S. Nakamura, T. Ooi, *Angew. Chem. Int. Ed.*, **2010**, *49*, 7562–7565. DOI: 10.1002/anie.201004072
7. B. M. Trost, V. S. C. Yeh, H. Ito, N. Bremeyer, *Org. Lett.*, **2002**, *4*, 2621–2623. DOI: 10.1021/ol020077n
8. H. Sasai, T. Suzuki, S. Arai, T. Arai, M. Shibasaki, *J. Am. Chem. Soc.*, **1992**, *114*, 4418–4420. DOI: 10.1021/ja00037a068
9. D. A. Evans, D. Seidel, M. Rueping, H. W. Lam, T. Shaw, C. W. Downey, *J. Am. Chem. Soc.*, **2003**, *125*, 112692–112693. DOI: 10.1021/ja0373871
10. K. Kodama, K. Sugawara, T. Hirose, *Chem. Eur. J.*, **2011**, *17*, 13584–13592. DOI: 10.1002/chem.201102136
11. F. Liu, S. Ma, Z. Tian, H. Wu, L. Wu, X. Xu, Y. Huang, Y. Wang, *Tetrahedron: Asymmetry*, **2013**, *24*, 736–743. DOI: 10.1016/j.tetasy.2013.05.009
12. F. Liu, S. Gou, L. Li, *Appl. Organometal. Chem.*, **2014**, *28*, 186–193. DOI: 10.1002/aoc.3107
13. M. N. Kopylovich, T. C. O. MacLeod, K. T. Mahmudov, M. F. C. Guedes da Silva, A. J. L. Pombeiro, *Dalton Trans.*, **2011**, *40*, 5352–5361. DOI: 10.1039/C0DT01457E
14. K. Xu, G. Lai, Z. Zha, S. Pan, H. Chen, Z. Wang, *Chem. Eur. J.*, **2012**, *18*, 12357–12362. DOI: 10.1002/chem.201201775
15. G. Lai, S. Wang, Z. Wang, *Tetrahedron: Asymmetry*, **2008**, *19*, 1813–1819. DOI: 10.1016/j.tetasy.2008.06.036
16. D. Xu, Q. Sun, Z. Quan, W. Sun, X. Wang, *Tetrahedron: Asymmetry*, **2017**, *28*, 954–963. DOI: 10.1016/j.tetasy.2017.05.013
17. Y. Shi, Y. Li, J. Sun, Q. Lai, C. Wei, Z. Gong, Q. Gu, Z. Song, *Appl. Organometal. Chem.*, **2015**, *29*, 661–667. DOI: 10.1002/aoc.3347
18. G. Qiang, T. Shen, X. Zhou, X. An, Q. Song, *Chirality*, **2014**, *26*, 780–783. DOI: 10.1002/chir.22369
19. R. Kant, S. Maji, *Dalton Trans.*, **2021**, *50*, 785–800. DOI: 10.1039/D0DT03569F
20. A. Akıncı, D. B. Celepci, L. Karadeniz, N. Korkmaz, M. Aygün, S. T. Astley, *Appl. Organometal. Chem.*, **2017**, *31*, 3831–3837. DOI: 10.1002/aoc.3831
21. L. Alkan, S. T. Astley, *Karalimas Fen ve Mühendislik Dergisi*, **2018**, *8*, 151–155.
22. G. Blay, E. Climent, I. Fernandez, V. Hernandez-Olmos, J. R. Pedro, *Tetrahedron: Asymmetry*, **2007**, *18*, 1603–1612. DOI: 10.1016/j.tetasy.2007.06.023
23. Q. T. Nguyen, J. H. Jeong, *Polyhedron*, **2006**, *25*, 1787–1790. DOI: 10.1016/j.poly.2005.11.028
24. J. Boruwa, N. Gogoi, P. P. Saika, N. C. Barua, *Tetrahedron: Asymmetry*, **2006**, *17*, 3315–3326. DOI: 10.1016/j.tetasy.2006.12.005
25. A. Roy, L. A. Reddy, N. Dwivedi, J. Naram, R. Swapna, G. C. Malakondaiah, M. Ravikumar, D. Bhalerao, T. B. Pratap, P. P. Reddy, A. Bhattacharya, R. Bandichhor, *Tetrahedron Lett.*, **2011**, *52*, 6968–6970. DOI: 10.1016/j.tetlet.2011.10.087

Povzetek

Iz piperazin-aminov in substituiranih salicilaldehidov smo sintetizirali novo serijo tridentatnih Schiffovih baz ter jih karakterizirali s spektroskopskimi metodami. Tako pripravljene kiralne ligande smo uporabili kot katalizatorje za adicijo nitrometana na različne aldehide, ki smo jo izvedli ob dodatku Cu(II) ionov pri sobnih pogojih, produkte pa smo pripravili z dobrimi izkoristki (98 %) in visokimi enantioselektivnostmi (9:1 er).



Except when otherwise noted, articles in this journal are published under the terms and conditions of the Creative Commons Attribution 4.0 International License

Scientific paper

***In-Situ* Intercalating of Silica Nanospheres into Polypyrrole During Its Electropolymerization to Prepare a Sorbent for Headspace Microextraction of Aldehydes in Edible Oils**

Amin Hamdi, Kolsoum Dalvand*, Alireza Ghiasvand* and Nahid Heidari*Department of Chemistry, Lorestan University, Khoramabad, Iran*** Corresponding author: E-mail: kolsoomdalvand@gmail.com, a_ghiasvand@yahoo.com**Tel-Fax: +98 66 33120612, +98 66 33120612**Received: 09-29-2021*

Abstract

The quality of edible oils is significantly affected by autoxidation of lipids, which alters their flavor and nutritional quality through production of toxic materials like aldehydes (an important class of oil deterioration markers). Herein, an amino-silica nanospheres/polypyrrole (ASNS/PPy) nanocomposite sorbent was synthesized and used as the fiber coating for headspace solid-phase microextraction (HS-SPME) of aldehydes in edible oils, followed by gas chromatography (GC) separation and determination. Amino-silica nanoparticles were prepared by an amended Stöber method and composited with polypyrrole during its electropolymerization on the surface of a platinized stainless-steel fiber. The synergy between *in-situ* electropolymerization and rough surface of the platinized metal substrate created a durable fiber coating with unique uniformity, cohesiveness, and adsorption properties. The synthesized nanocomposite was characterized using Fourier transform infrared spectroscopy and scanning electron microscopy techniques. The performance of the prepared fiber was optimized by investigating the affecting variables including extraction temperature and time, stirring rate, and desorption conditions. The obtained limits of detection for hexanal and heptanal in sunflower oil were 0.005–0.009 $\mu\text{g mL}^{-1}$. The prepared fiber exhibited excellent repeatability and reproducibility with the intra-fiber and inter-fiber relative standard deviations in the ranges of 3.9–8.8% and 7.3–15.1%, respectively. The proposed HS-SPME-GC strategy was successfully applied for the analysis of aldehydes in commercial edible oil samples.

Keywords: Amino-silica nanospheres; polypyrrole nanocomposite; headspace solid-phase microextraction; edible oil; aldehydes.

1. Introduction

Researchers have recently paid more attention to edible oils because of their importance in human health and nutrition. The quality of edible oils depends on their origin, processing, and oxidation state. The main edible oil components are saturated and unsaturated fatty acids.¹ Oxidation is the main reason for the instability of edible oils and causes a change in chemical and nutritional properties of oils. Oxygen in the air causes unsaturated fatty acids of edible oil to undergo non-enzymatic self-oxidation, leading to the production of peroxides.^{2,3} Aldehydes are an important class of lipid oxidation products, well-known for their health risks. They are a major cause of unpleasant odor of rancid oil. Therefore, quantification of aldehydes (as chemical markers) in edible oils is of great

importance for quality control purpose. There is a wide range of saturated and unsaturated aldehydes and ketones in oxidized edible oils, however, short chain aldehydes like hexanal and heptanal are more abundant. Therefore, these compounds are the most used biomarkers for the quality control of edible oils, due to their higher concentrations in oxidized edible oils. Despite huge advances in chemical analysis, sample pretreatment of edible oils for oxidation stability studies is still mostly performed using classical extraction methods like solvent extraction and Soxhlet which are tedious, time-consuming, and expensive. Moreover, these methods usually use toxic organic solvents and reactive chemical compounds which can expose operators and/or samples to hazardous materials.⁴ Accordingly, development and application of novel and green methods for chemical analysis of edible oils is now a necessity.

Solid-phase microextraction (SPME) is a green solvent-free sample pretreatment technique, demonstrated to be a promising method for the sampling of organic compounds in food, biological, and environmental samples.⁵ SPME can be easily coupled with different chromatographic techniques, automated, and portabilized. The most widely used mode of SPME is headspace (HS), which extracts analytes from the upper atmosphere of the sample, without direct contact with the sample matrix. HS-SPME is the best choice for the sampling of volatile and semi-volatile organic compounds. That is why HS-SPME has been widely used for the sampling of odors, flavors, and fragrances in food samples.^{1,6} Extensive efforts have been devoted to expanding applicability and improve performance of SPME, particularly by preparation of new sorbents using nanomaterials. Compared to the commercial sorbents, nanomaterial-based sorbents benefit from higher porosity, larger surface-to-volume ratio, better thermal and chemical stability, more selectivity, and higher extraction efficiency.⁵ Among these, silica nanoparticles have received more attention due to their abundance, cheapness, various available surface modification methods, high porosity and adsorption power, and non-toxicity.^{7–9} To improve the extraction efficiency and selectivity, silica nanoparticles have been composited with different materials like TiO₂,¹⁰ graphene oxide (GO),¹¹ Fe₃O₄,¹² and conductive polymers.¹³ Among conductive polymers, polypyrrole (PPy) and its derivatives have attracted much consideration in SPME techniques due to their significant advantages including non-toxicity, low-cost, thermal stability, and particularly simple synthesis routes.¹⁴ As a unique and promising feature in the preparation of SPME sorbents, thin layers of PPy with controllable properties can be coated on conductive surfaces like stainless-steel through *in-situ* electropolymerization during electrophoretic deposition (EPD) from different aqueous or organic solutions.¹⁵ For this reason, different composites of PPy like graphene/polypyrrole,^{16,17} magnetite nanoparticles/polypyrrole,¹⁸ multiwalled carbon nanotubes/polypyrrole,¹⁹ functionalized graphene and ionic liquid co-doped polypyrrole,²⁰ and iron oxide/silica/polypyrrole²¹ have been successfully employed for the preparation of SPME fibers. The efficiency of PPy composites (e.g., polypyrrole/graphene oxide) for the extraction of aldehydes in edible oil has been previously demonstrated through a reduced-pressure fiber-in-needle technique.²²

In this research, amino-silica nanospheres (ASNS) were synthesized and composited with PPy during its *in-situ* electropolymerization on the surface of a stainless-steel fiber. The ASNS/PPy coated fiber was applied for the HS-SPME sampling of aldehydes (hexanal and heptanal) in edible oils. The analytes were quantified using gas chromatography-flame ionization detection (GC-FID), without derivatization. To the best of our knowledge ASNS/PPy has not been previously reported as a SPME fiber coating.

2. Materials and Methods

2.1. Chemicals

Analytical reagent grade aldehydes were obtained from Merck (Darmstadt, Germany). Stock standard solutions (1000 mg L⁻¹) of hexanal (Hex) and heptanal (Hep) were prepared in methanol and stored at 4 °C. Working standard solutions were prepared by dilution of the stock solution in double distilled water, on a daily basis. Pyrrole (> 99%) was provided by Fluka (Buchs, Switzerland). Pyrrole was redistilled and stored in a dark bottle under nitrogen atmosphere in a refrigerator before each use. Tetraethyl orthosilicate (TEOS, 98%), succinic anhydride, *N,N*-dimethylformamide (DMF) and, *N,N*-dicyclohexylcarbodiimide (DCC) were purchased from Merck. Analytical grade potassium hexachloroplatinate(IV) (K₂PtCl₆), ethanol, methanol, NaNO₃, NaOH, LiClO₄, concentrated hydrochloric acid (HCl), and aqueous ammonia (NH₃,aq) solutions were purchased from Merck.

2.2. Gas Chromatographic Analysis

A Shimadzu GC-2010 Plus AF gas chromatograph (Shimadzu, Kyoto, Japan), equipped with a split/splitless injector (SPL-2010 Plus) and a flame ionization detector (FID-2010 Plus), was used for the gas chromatographic separations and determinations. It used GC solution software (version 2.4) and a BP-5 fused-silica capillary column (30 m × 0.25 mm × 0.25 μm). Ultra-high purity nitrogen was used as the carrier gas with a constant flow rate of 1 mL min⁻¹. All SPME injections were performed in splitless mode. The initial column temperature was set at 60 °C and then increased to 100 °C at a rate of 4 °C min⁻¹. Finally, it was ramped to 280 °C at a rate of 70 °C min⁻¹. The GC detector and injector were maintained at 300 and 280 °C, respectively. Hydrogen and zero-air were used as the FID gases at flow rates of 30 and 300 mL min⁻¹. Nitrogen was used as the make-up gas with a flow rate of 30 mL min⁻¹. Fourier transform infrared (FT-IR) spectra were obtained in the transmittance mode, by a Shimadzu FT-IR 8400 spectrometer. Scanning electron microscopy (SEM) micrographs were recorded using a CM120 Vega field-emission scanning electron microscope (TESCAN, Brno, Czech Republic), to investigate the surface morphology of the nanocomposite.

2.3. Preparation of ASNS/PPy Coated SPME Fiber

Silica nanospheres was prepared through hydrolysis of TEOS according to an amended version of Stober's method.⁹ For synthesis of ASNS, 20 mg of silica nanospheres was dispersed in 20 mL of DMF in an ultrasonic bath. Then, 20 mL of succinic anhydride solution (0.1 M) was added dropwise, and the suspension stirred for 24 h. Finally, the precipitate was centrifuged, rinsed with DMF, and dried in a vacuum oven at 60 °C for 4 h.

To create a porous, high surface area and robust fiber substrate, the surface of stainless-steel fiber (4 cm length and 0.075 mm i.d.) was platinized based on an EPD method.²³ Then, the fiber was coated by ASNS/PPy nanocomposite *via* intercalating of ASNS in PPy during electropolymerization of pyrrole, using a two-electrode electrochemical system. To this end, 0.08 g ASNS was dispersed in 10 mL pyrrole solution (containing 0.1 M LiClO₄). The platinized fiber was connected to the anode and a normal stainless-steel wire was connected to the cathode of a DC power supply and immersed into the suspension. The distance between the electrodes was 2.0 cm and a 1.0 V DC voltage applied to the electrodes for 20 min. Then, the fiber was removed from the electrochemical cell and rinsed with water and ethanol and dried. Before the first use the fiber was preconditioned under nitrogen atmosphere for 30 min at 280 °C.

2. 4. HS-SPME Sampling of Aldehydes in Edible Oils

Using a blank sample matrix (model matrix) is essential to optimize an extraction method in a reliable way. This fact is more serious for the analysis of complex sample matrices like edible oils. In this research, a liquid oil sample was used as the model matrix, after being processed to remove its aldehyde content. For this purpose, 500 mL of sample oil was poured into a 1000-mL vacuum container and subjected to vacuum for 20 min at 25 °C along with continuous stirring. Under the vacuum, aldehyde contents were removed from the oil matrix, resulting in a model matrix without aldehydes. It was stored at 4 °C in a fridge under nitrogen atmosphere to prevent further oxidation and production of aldehydes. The absence of aldehydes in the model sample was checked by using GC analysis. To optimize the parameters affecting the extraction efficiency, 3 mL of model sample was transferred to a 10 mL SPME vial and spiked with known concentrations of the analytes. Then, the vial was capped, and the sample was homogenized by sonication for 2 min. After that, the extraction vial was placed into a water bath on a hotplate-magnetic stirrer at 50 ° and stirred at 750 rpm. The ASNS/PPy fiber was mounted on a handmade fiber holder and exposed to the headspace of the sample for 15 min. Finally, the fiber was retracted and immediately injected into the GC injection port for thermal desorption of the extracted analytes at 280 ° for 1 min.

3. Results and Discussion

Regardless of the physicochemical stability of the coating and fiber substrate, a serious problem in commercial and homemade SPME fibers is weak adhesion between the coating and the fiber substrate. Hence, the coating is easily stripped or exfoliated from the substrate after expo-

sure to high temperature, organic solvents, and/or mechanical tension. Two complementing strategies have been suggested to address this problem, the first chemical bonding of the coating to the substrate²⁴ and the second roughening the surface of the substrate.²⁵ Fortunately, to prepare industrial protective and anticorrosion coatings for stainless-steel extensive studies have been done and deep knowledge developed.²⁶ For example, Vasconcelos *et al.*²⁷ prepared a very highly thermally stable and substantially corrosion resistant coating for stainless-steel using silica thin-films through a sol-gel technique. Accordingly, in this research, the surface of the stainless-steel fiber was platinized to create a rough and increased surface area substrate. The effectiveness of this method has been well proven in our previous studies.^{9,23,28} This research tried to fabricate a very durable SPME fiber by electrodeposition of ASNS/PPy on the rough surface of platinized stainless-steel fiber.

3. 1. Characterization of ASNS/PPy Nanocomposite

To characterize the chemical bonds in the structure of SNS, ASNS, and ASNS/PPy, their FT-IR spectra were recorded (Fig. 1). The absorption peak at 1099 cm⁻¹ (indicating O-Si-O bond) and the peaks appearing at 802.33 and 470.60 cm⁻¹ (correspond to the symmetric stretching and rocking vibrations of Si-O-Si, respectively) show the polymeric structure of silica. The presence of N-H bond in the ASNS structure can be clearly inferred from the vibrational peak 1635 cm⁻¹. While ASNS/PPy nanocomposite characteristic peaks can be seen at 1099 cm⁻¹ (O-Si-O bond), 1554 cm⁻¹ (N-H and C-N bonds), 1635 cm⁻¹ (N-H bond), 1658 cm⁻¹ (C=O bond), 2927 cm⁻¹ (C-H bond), and 3417 cm⁻¹ (O-H bond).²⁹

SEM micrographs of ASNS and ASNS/PPy nanocomposite were recorded to evaluate their morphological surface features, as depicted in Fig. 2. The spherical configuration of the silica nanospheres and their particle size uniformity are obvious in Fig. 2a. Additionally, conical pillars of PPy can be clearly observed in Fig. 2b and 2c. These conical pillar structures can be considered as the grown (thickened) forms of PPy nanowires, as has been shown previously.³⁰ Mechanical strength of the coating was tested by scraping the fiber coating using a knife to simulate its possible damage by the edge of the protecting needle during the injection/withdraw cycles.³¹ It was found that the ASNS/PPy coating was difficult to be scraped using a knife. The thermal stability of the fiber was demonstrated by performing up to 90 extractions, each followed by a thermal desorption step in the GC injector at 280 °C. To evaluate the stability of the ASNS/PPy coated fiber against organic solvents, it was directly immersed in ethanol, acetone, acetonitrile, hexane, and methanol for 30 min. Then, the fiber was rinsed with water and conditioned in GC injector for 10 min at 250 °C to

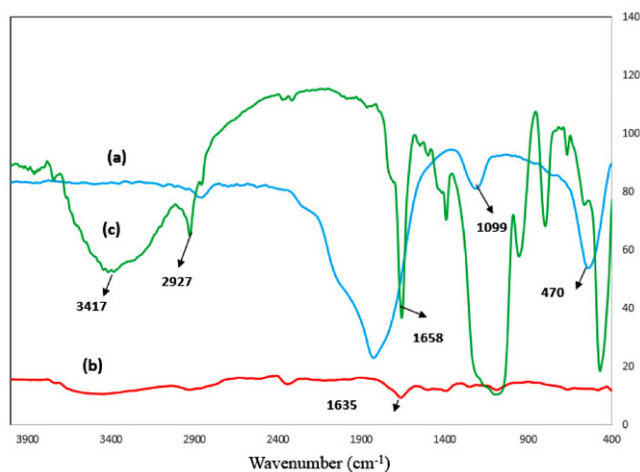


Fig. 1. FT-IR spectra of SNS (a), ASNS (b), and ASNS/PPy nanocomposite (c).

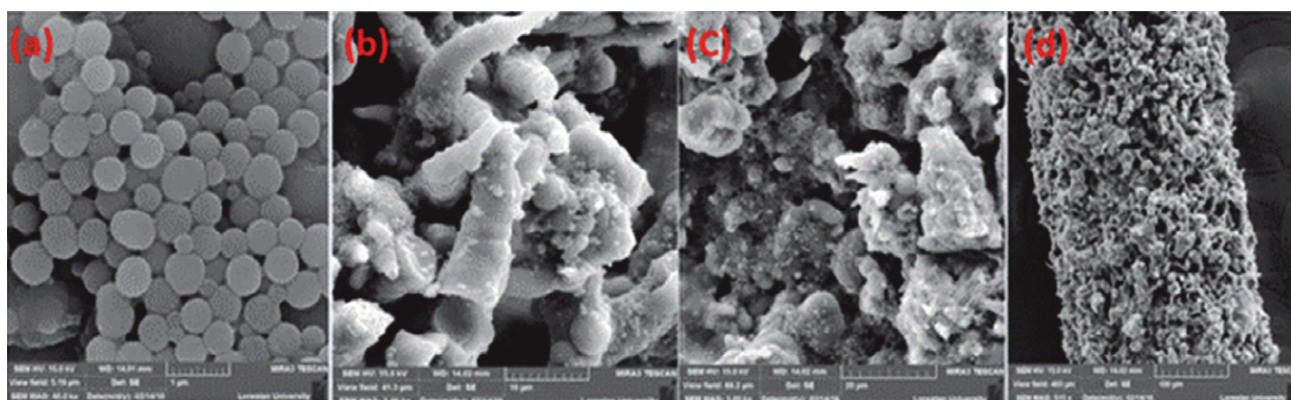


Fig. 2. SEM micrographs of (a) SNS, (b and c) ASNS/PPy nanocomposite at different magnifications, and (d) the ASNS/PPy coated stainless-steel fiber.

remove any possible solvent residues, before extracting the analytes. The results demonstrated that the fiber was resistant to organic solvents and the extraction efficiency didn't change significantly (< 5%).

3. 2. Optimization of the Extraction Conditions

To achieve the highest extraction efficiency, the important influential variables including desorption time, desorption temperature, sampling temperature, sampling time, and stirring rate were optimized. To ensure the complete transfer of the extracted analytes from the fiber to the chromatographic column and acquire accurate results, desorption conditions must be optimized first. Accordingly, desorption temperature and desorption time were investigated in the ranges of 200–300 °C and 1–4 min, respectively. The highest peak areas were observed at desorption temperatures more than 280 °C and at desorption time of 1 min, with the minimum carryover effect (< 5%). Therefore, 280 °C and 1 min were selected as the optimal desorption conditions for further investigations.

3. 2. 1. Effect of Sampling Temperature

Extraction temperature is one of the main influential parameters affecting the equilibration of analytes between the headspace and fiber coating, and consequently on the extraction efficiency, particularly for volatile analytes like short-chain aldehydes. Higher temperatures improve the release of analyte from the sample matrix and increase their concentrations in the headspace, leading to an increase in the extraction amounts. Simultaneously, temperature of the fiber coating also rises and reduces the analyte trapping, due to the exothermic effect of adsorption process. For this reason, HS-SPME sampling temperature needs to be optimized carefully.³² Therefore, sampling temperature was evaluated over the range of 40–90 °C. As can be seen from the results (Fig. 3a), the peak areas of the analytes increased by raising sample temperature. This fact can be explained by the formation of more aldehydes by raising the sample temperature (due to increased lipid oxidation), as substantiated in previous investigations.²² Therefore, it was better to select a temperature from the most stable part of the graph (Fig. 3a), with minimal fluctuations of response with temperature change. Therefore,

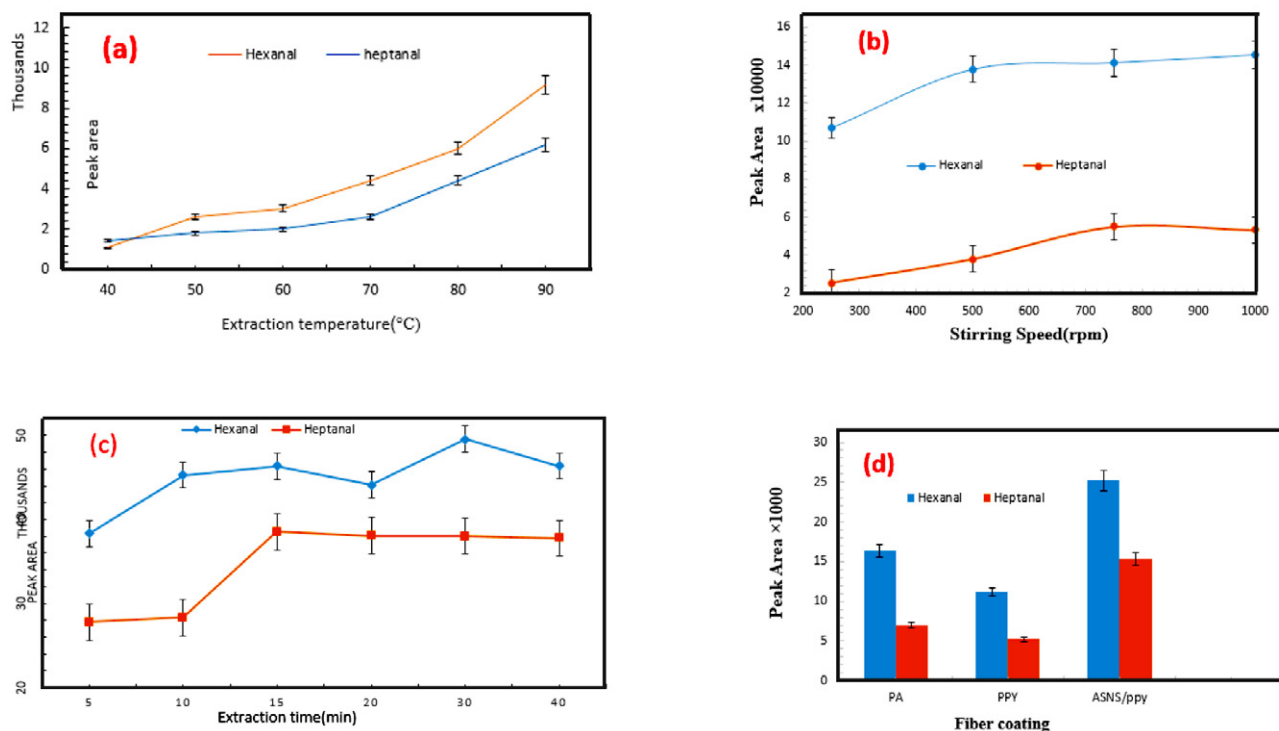


Fig. 3. Dependence of the extraction efficiency of the developed HS-SPME method on sample temperature (a), stirring speed (b), and extraction time (c). Comparison of the ASNS/PPy coated fiber with commercial polyacrylate fiber and a homemade PPy fiber (d), under the optimized conditions (extraction time, 20 min; stirring rate, 600 rpm; desorption temperature: 280 °C; and desorption time, 1 min; repeated three times).

50 °C was chosen as the optimal HS-SPME sampling temperature.

3. 2. 2. Effect of Sample Stirring Speed

Increasing the stirring speed in HS-SPME improves the mass transfer and increases concentration of analytes in the sample headspace. Furthermore, the time required to achieve thermodynamic equilibrium is reduced. To evaluate this effect, stirring speed was varied over the range of 200–1000 rpm and GC-FID peak areas of the analytes were recorded. The results depicted in Fig. 3b show that the peak areas for both analytes increase with raising the stirring speed up to 750 rpm and then remain nearly constant. So, 750 rpm was chosen as the optimal stirring speed for further studies.

3. 2. 3. Effect of Sampling Time

To achieve the highest extraction efficiency, the extraction time was examined in the range of 5–40 min. As

shown in Fig. 3c, peak areas of both analytes increased by prolonging the extraction time up to 15 min and then remained constant. Thus, 15 min was chosen as the extraction time for further experiments.

3. 3. Analytical Performance

To evaluate the quantitative analytical figures of merit of the developed method, its linear dynamic ranges (LDRs), limits of detection (LODs), and relative standard deviations (RSDs) for the extraction of Hex and Hep from edible oil samples were investigated, under the optimized conditions. The calibration graphs were linear over the range of 0.03–20 $\mu\text{g mL}^{-1}$ for hexane and 0.05–25 $\mu\text{g mL}^{-1}$ for heptanal, with linear regression coefficients greater than 0.998. The LODs correspond to the analyte amounts for which the signal-to-noise ratio was equal to 3, and were found to be 0.005 for hexanal and 0.009 $\mu\text{g mL}^{-1}$ for heptanal. The precision was assessed by obtaining the RSDs including repeatability (intra-fiber) and reproduc-

Table 1. Analytical figures of merit of the HS-SPME-GC procedure for the sampling and quantification of hexanal and heptanal in edible oil.

Analyte	Equation	R ²	LDR ($\mu\text{g mL}^{-1}$)	LOD ($\mu\text{g mL}^{-1}$)	RSD% (n = 6)	
					Intra-fiber	Inter-fiber
Hexanal	$y = 1139.4x + 5807.1$	0.9989	0.03–20	0.005	3.9	7.3
Heptanal	$y = 209.09x + 1586.2$	0.9982	0.05–25	0.009	8.8	15.1

ibility (inter-fiber), which varied between 3.9–8.8% and 7.3–15.1%, respectively (Table 1). A single fiber was used for more than 90 extractions (extraction/desorption cycles) without significant change (< 5%) in its extraction efficiency.

To evaluate reliability and applicability of the ASNS/PPy coated fiber, it was compared with a commercial PA coated fiber and a homemade PPy coated fiber, under the optimized conditions (Fig. 3d). The results demonstrated that the ASNS/PPy fiber was remarkably more efficient than the tested fibers for the extraction of the aldehydes in edible oils.

3. 4. Comparison of the Proposed Method with Similar Reported Procedures

To further indicate the supremacy of the proposed microextraction strategy, its significant features were compared with some of the similar reported microextraction methods.^{22,33–36} As can be seen in Table 2, the proposed procedure shows wider linear ranges and acceptable RSDs, compared to most of the listed procedures. Additionally, the LODs are lower than most of the reported methods, even compared to the method that used a MS detector.³⁶ However, its LODs and LDRs are not comparable with the

reduced-pressure fiber-in-needle method (RP-FIN) technique, which has used a low-pressure dynamic microextraction strategy.²² Anyhow, the proposed method uses a low-cost and durable fiber and instrumentation (GC-FID), without any derivatization methods.

3. 5. Determination of Hexanal and Heptanal in Edible Oils

To test the applicability of the developed method, it was applied for the determination of hexanal and heptanal in three commercial sunflower oil samples of different brands, produced at different dates. Samples 1, 2, and 3 had been produced 35, 36, and 4 months before the analysis time, respectively. The samples had been stored unopened at the same conditions. To ensure the reliability of the HS-SPME-GC-FID strategy, each sample was also spiked with 1 $\mu\text{g mL}^{-1}$ of the analytes and subjected to the analysis, three times. As shown by the results in Table 3, acceptable recoveries and RSDs were obtained, indicating that the developed method can be successfully applied for the quantification of aldehydes and study of oxidative stability of edible oils. Fig. 4 shows a typical GC-FID chromatogram of a sunflower oil, analyzed by the developed HS-SPME-GC-FID method.

Table 2. Comparison of the developed HS-SPME-GC procedure with some similar microextraction procedures for the analysis of aldehydes in edible oils.

Method	Extraction phase	LDR ($\mu\text{g mL}^{-1}$)	LOD (ng mL^{-1})	Intra-fiber RSD (%)	Inter-fiber RSD (%)	Matrix	Ref.
USABE-GC-FID ^a	Triton X-114 in CHCl_3	0.05–20	20–150	2–4	–	Heated soybean, sunflower, and olive oils	35
HS-SPME-GC-FID	PDMS/CAR	0.05–10	5–10	8.9	–	Peanut, soybean, and olive oils	36
HS-SPME-GC-FID	DVB/CAR/PDMS	–	160–350	4.02–8.53	–	Sunflower and rapeseed oils	37
SPME-GC-MS	PDMS/PEG	0.02–1	6–15	8.9–11.2	9.3–16.2	Sunflower oil	38
RP-FIN-GC-FID ^b	PPY/GO	0.0007–50	1–8	5.9–9.0	–	Corn, sunflower, soybean, olive, canola, and sesame oils	24
HS-SPME-GC-FID	ASNS/PPy	0.03–25	5–9	3.9–8.8	7.3–15.1	Sunflower oil	This work

^a Ultrasound-assisted back extraction reverse micelles method coupled with GC-FID. ^b Reduced-pressure fiber-in-needle coupled with GC-FID.

Table 3. HS-SPME-GC-FID sampling and determination of hexanal and heptanal in commercial edible oil samples using the ASNS/PPy coated fiber.

Edible oil	Added ($\mu\text{g mL}^{-1}$)	Found ($\mu\text{g mL}^{-1}$)		Recovery (%)	
		Hexanal	Heptanal	Hexanal	Heptanal
Sample# 1	0	0.67	1.79	–	–
	1	1.58	2.73	90	93
Sample# 2	0	9.34	8.99	–	–
	1	10.28	9.87	94.5	88.5
Sample# 3	0	0.56	0.09	–	–
	1	1.43	0.93	86.8	84.2

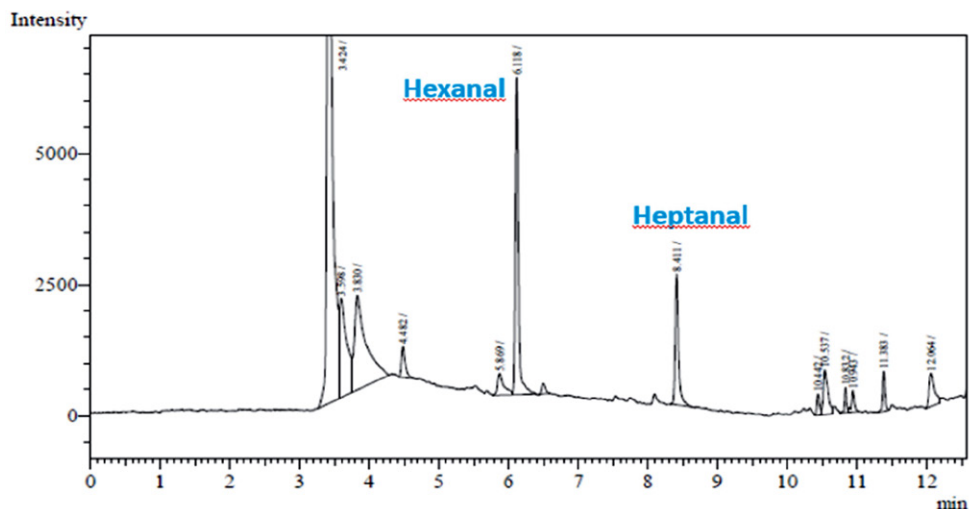


Fig. 4. A GC-FID chromatogram of a sunflower edible oil sample after HS-SPME sampling using an ASNS/PPy coated fiber.

4. Conclusions

Amino-functionalized silica nanospheres/polypyrrole (ASNS/PPy) composite was synthesized, characterized, and employed to prepare a SPME fiber. First ASNS was synthesized *via* a green sol-gel procedure. They were then dispersed into a pyrrole solution, in a two-electrode electrochemical cell, and coated on the surface of a platinumized stainless-steel fiber, during electropolymerization of polypyrrole. By combining the features of a platinumized metallic surface and an *in-situ* electropolymerization, a highly porous and durable SPME fiber was obtained. The sorption efficiency and durability of the fiber was confirmed by successful extraction of aldehydes from edible oil samples. The results demonstrated that the developed fiber and methodology can be effectively applied for the sampling and trapping of volatile and semi-volatile analytes in food, biological, and environmental samples.

5. References

1. S. Jiang, Y. Xie, M. Li, Y. Guo, Y. Cheng, H. Qian and W. Yao, Evaluation on the oxidative stability of edible oil by electron spin resonance spectroscopy, *Food Chem.* **2020**, *309*, 125714. DOI:10.1016/j.foodchem.2019.125714
2. K. Hu, Z. Huyan, S. Ding, Y. Dong and X. Yu, Investigation on food packaging polymers: Effects on vegetable oil oxidation, *Food Chem.* **2020**, *315*, 126299. DOI:10.1016/j.foodchem.2020.126299
3. Y. Jiang, M. Su, T. Yu, S. Du, L. Liao, H. Wang, Y. Wu and H. Liu, Quantitative determination of peroxide value of edible oil by algorithm-assisted liquid interfacial surface enhanced Raman spectroscopy, *Food Chem.* **2021**, *344*, 128709. DOI:10.1016/j.foodchem.2020.128709
4. J.-F. Liu, B.-F. Yuan and Y.-Q. Feng, Determination of hexanal and heptanal in human urine using magnetic solid phase extraction coupled with in-situ derivatization by high performance liquid chromatography, *Talanta* **2015**, *136*, 54–59. DOI:10.1016/j.talanta.2015.01.003
5. V. Jalili, A. Barkhordari and A. Ghiasvand, A comprehensive look at solid-phase microextraction technique: A review of reviews, *Microchem. J* **2020**, *152*, 104319. DOI:10.1016/j.microc.2019.104319
6. A. R. Ghiasvand, L. Setkova and J. Pawliszyn, Determination of flavour profile in Iranian fragrant rice samples using cold-fibre SPME–GC–TOF–MS, *Flav. Frag. J.* **2007**, *22*, 377–391. DOI:10.1002/ffj.1809
7. F. Harati, A. Ghiasvand, K. Dalvand and P. R. Haddad, Fused-silica capillary internally modified with nanostructured octadecyl silica for dynamic in-tube solid-phase microextraction of polycyclic aromatic hydrocarbons from aqueous media, *Microchem. J* **2020**, *155*, 104672. DOI:10.1016/j.microc.2020.104672
8. E. Akbari, A. Ghiasvand and K. Dalvand, Nanostructured octadecylsilica chemically coated stainless-steel fiber for vacuum-assisted HS-SPME sampling of PAHs in soil, *Microchem. J* **2020**, *158*, 105201. DOI:10.1016/j.microc.2020.105201
9. N. Heidari, A. Ghiasvand and S. Abdolhosseini, Amino-silica/graphene oxide nanocomposite coated cotton as an efficient sorbent for needle trap device, *Anal. Chim. Acta* **2017**, *975*, 11–19. DOI:10.1016/j.aca.2017.04.031
10. Z. Es'haghi and E. Esmaili-Shahri, Sol-gel-derived magnetic SiO₂/TiO₂ nanocomposite reinforced hollow fiber-solid phase microextraction for enrichment of non-steroidal anti-inflammatory drugs from human hair prior to high performance liquid chromatography, *J. Chromatogr. B* **2014**, *973*, 142–151. DOI:10.1016/j.jchromb.2014.09.030
11. K. Molaei, H. Bagheri, A. A. Asgharinezhad, H. Ebrahimzadeh and M. Shamsipur, SiO₂-coated magnetic graphene oxide modified with polypyrrole–polythiophene: A novel and efficient nanocomposite for solid phase extraction of trace amounts of heavy metals, *Talanta* **2017**, *167*, 607–616. DOI:10.1016/j.talanta.2017.02.066

12. E. Esmaeili-Shahri and Z. Es'haghi, Superparamagnetic Fe₃O₄@SiO₂ core-shell composite nanoparticles for the mixed hemimicelle solid-phase extraction of benzodiazepines from hair and wastewater samples before high-performance liquid chromatography analysis, *J. Sep. Sci.* **2015**, *38*, 4095–4104. DOI:10.1002/jssc.201500743
13. D. Chen, S. Ma, X. Zhang, X. Wang, M. Gao, J. Li and H. Wang, Enhanced extraction of organophosphorus pesticides from fruit juices using magnetic effervescent tablets composed of the NiFe₂O₄@SiO₂@PANI-IL nanocomposites, *RSC Adv.*, *11*, 1668–1678. DOI:10.1039/D0RA09100F
14. W. Fang, X. Jiang, H. Luo and J. Geng, Synthesis of graphene/SiO₂@polypyrrole nanocomposites and their application for Cr(VI) removal in aqueous solution, *Chemosphere* **2018**, *197*, 594–602. DOI:10.1016/j.chemosphere.2017.12.163
15. J. Wu, W. M. Mullett and J. Pawliszyn, Electrochemically controlled solid-phase microextraction based on conductive polypyrrole films, *Anal. Chem.* **2002**, *74*, 4855–4859. DOI:10.1021/ac025595q
16. J. Zou, X. Song, J. Ji, W. Xu, J. Chen, Y. Jiang, Y. Wang and X. Chen, Polypyrrole/graphene composite-coated fiber for the solid-phase microextraction of phenols, *J Sep Sci* **2011**, *34*, 2765–2772. DOI:10.1002/jssc.201100303
17. C. Zhang, Z. Zhang and G. Li, Preparation of sulfonated graphene/polypyrrole solid-phase microextraction coating by in situ electrochemical polymerization for analysis of trace terpenes, *J. Chromatogr. A* **2014**, *1346*, 8–15. DOI:10.1016/j.chroma.2014.04.043
18. H. Zhao, M. Huang, J. Wu, L. Wang and H. He, Preparation of Fe₃O₄@PPy magnetic nanoparticles as solid-phase extraction sorbents for preconcentration and separation of phthalic acid esters in water by gas chromatography–mass spectrometry, *J. Chromatogr. B* **2016**, *1011*, 33–44. DOI:10.1016/j.jchromb.2015.12.041
19. L. Chen, W. Chen, C. Ma, D. Du and X. Chen, Electropolymerized multiwalled carbon nanotubes/polypyrrole fiber for solid-phase microextraction and its applications in the determination of pyrethroids, *Talanta* **2011**, *84*, 104–108. DOI:10.1016/j.talanta.2010.12.027
20. J. Du, F. Zhao and B. Zeng, Preparation of functionalized graphene and ionic liquid co-doped polypyrrole solid phase microextraction coating for the detection of benzoates preservatives, *Talanta* **2021**, *228*, 122231. DOI:10.1016/j.talanta.2021.122231
21. A. Ghiasvand, N. Heidari and S. Abdolhosseini, Iron oxide/silica/polypyrrole nanocomposite sorbent for the comparison study of direct-immersion and headspace solid-phase microextraction of aldehyde biomarkers in human urine, *J. Pharm. Biomed. Anal.* **2018**, *159*, 37–44. DOI:10.1016/j.jpba.2018.06.052
22. A. Ghiasvand, M. Behfar and F. Yazdankhah, Reduced-pressure fiber-in-needle sampling of aldehydes for room temperature assessment of edible oils' oxidative stability, *Chromatographia* **2019**, *82*, 1405–1414. DOI:10.1007/s10337-019-03752-7
23. A. Ghiasvand, S. Dowlatshah, N. Nouraei, N. Heidari and F. Yazdankhah, A solid-phase microextraction platinized stainless steel fiber coated with a multiwalled carbon nanotube-polyaniline nanocomposite film for the extraction of thymol and carvacrol in medicinal plants and honey, *J. Chromatogr. A* **2015**, *1406*, 87–93. DOI:10.1016/j.chroma.2015.06.052
24. Z. Feng, C. Huang, Y. Guo, P. Tong and L. Zhang, Chemical bonding of oxygenated carbon nitride nanosheets onto stainless steel fiber for solid-phase microextraction of phthalic acid esters, *Anal. Chim. Acta* **2019**, *1084*, 43–52. DOI:10.1016/j.aca.2019.08.015
25. C. Liu, X. Zhang, L. Li, J. Cui, Y.-e. Shi, L. Wang and J. Zhan, Silver nanoparticle aggregates on metal fibers for solid phase microextraction–surface enhanced Raman spectroscopy detection of polycyclic aromatic hydrocarbons, *Analyst* **2015**, *140*, 4668–4675. DOI:10.1039/C5AN00590F
26. M. Aparicio, A. Jitianu, G. Rodriguez, A. Degnah, K. Al-Marzoki, J. Mosa and L. C. Klein, Corrosion protection of AISI 304 stainless steel with melting gel coatings, *Electrochim. Acta* **2016**, *202*, 325–332. DOI:10.1016/j.electacta.2015.12.142
27. D. C. L. Vasconcelos, J. A. N. Carvalho, M. Mantel and W. L. Vasconcelos, Corrosion resistance of stainless steel coated with sol-gel silica, *J. Non-Cryst. Solids* **2000**, *273*, 135–139. DOI:10.1016/S0022-3093(00)00155-1
28. S. Abdolhosseini, A. Ghiasvand and N. Heidari, A high area, porous and resistant platinized stainless steel fiber coated by nanostructured polypyrrole for direct HS-SPME of nicotine in biological samples prior to GC-FID quantification, *J. Chromatogr. B* **2017**, *1061-1062*, 5–10. DOI:10.1016/j.jchromb.2017.06.042
29. L. Zhang, Y. Xiong, E. Ou, Z. Chen, Y. Xiong and W. Xu, Preparation and properties of nylon 6/carboxylic silica nanocomposites via in situ polymerization, *J. Appl. Polym. Sci.* **2011**, *122*, 1316–1324. DOI:10.1002/app.33967
30. C. Yang, S. Zhang and C. Guan, Polypyrrole nanowires coated with a hollow shell for enhanced electrochemical performance, *Mater. Res. Bull.* **2018**, *100*, 116–119. DOI:10.1016/j.materresbull.2017.12.015
31. C. Wen, M. Li, W. Li, Z. Li, W. Duan, Y. Li, J. Zhou, X. Li and J. Zeng, Graphene deposited onto aligned zinc oxide nanorods as an efficient coating for headspace solid-phase microextraction of gasoline fractions from oil samples, *J. Chromatogr. A* **2017**, *1530*, 45–50. DOI:10.1016/j.chroma.2017.11.016
32. K. Dalvand and A. Ghiasvand, Simultaneous analysis of PAHs and BTEX in soil by a needle trap device coupled with GC-FID and using response surface methodology involving Box-Behnken design, *Anal. Chim. Acta* **2019**, *1083*, 119–129. DOI:10.1016/j.aca.2019.07.063
33. Z. Ramezani, R. Mirzajani and F. Kardani, A novel ultrasound-assisted back extraction reverse micelles method coupled with gas chromatography–flame ionization detection for determination of aldehydes in heated edibles oils, *Food Chem.* **2015**, *188*, 30–36. DOI:10.1016/j.foodchem.2015.04.112
34. C. Ma, J. Ji, C. Tan, D. Chen, F. Luo, Y. Wang and X. Chen, Headspace solid-phase microextraction coupled to gas chromatography for the analysis of aldehydes in edible oils, *Talanta* **2014**, *120*, 94–99. DOI:10.1016/j.talanta.2013.11.021

35. J. Gromadzka and W. Wardencki, Static headspace sampling and solid-phase microextraction for assessment of edible oils stability, *Chromatographia* **2010**, *71*, 81–86. DOI:10.1365/s10337-010-1516-y
36. F. Hasanli, S. Mohammadiazar, M. Bahmaei and A. A. M. Sharif, Coating of sol-gel film on silver nanodendrite as a novel solid-phase microextraction fiber for determination of volatile aldehydes in edible oils, *Food Anal. Methods* **2018**, *11*, 2149–2157. DOI:10.1007/s12161-018-1189-y

Povzetek

Na kakovost jedilnih olj znatno vpliva avtooksidacija lipidov, ki spremeni njihov okus in prehransko kakovost zaradi nastanka strupenih snovi, kot so aldehidi (pomemben razred označevalcev razkroja olja). V našem primeru smo sintetizirali nanokompozitni sorbent: nanokroglice iz amino-silicijevega dioksida/polipirola (ASNS/PPy), ki smo ga uporabili kot prevleko za vlakno za mikroekstrakcijo na trdno fazo iz nadprostora (HS-SPME) aldehydov iz jedilnih olj, sledila pa je ločba in določitev s plinsko kromatografijo (GC). Nanodelci iz amino-silicijevega dioksida so bili pripravljene po prirejeni Stöberjevi metodi in skupaj s polipirolom z elektropolimerizacijo deponirani na površino platiniziranega vlakna iz nerjavečega jekla. Sinergija med *in-situ* elektropolimerizacijo ter grobo površino platiniziranega kovinskega substrata je ustvarila odporno prevleko vlakna z edinstveno enakomernim nanosom, kohezivnostjo in adsorpcijskimi lastnostmi. Sintetizirani nanokompozit smo okarakterizirali z infrardečo spektroskopijo s Fourierjevo transformacijo ter z vrstično elektronsko mikroskopijo. Učinkovitost pripravljenega vlakna smo optimizirali s spreminjanjem pogojev, kot so temperatura in čas ekstrakcije, hitrost mešanja in pogoji desorpcije. Dosežene meje zaznave za heksanal in heptanal v sončničnem olju so bile 0,005–0,009 $\mu\text{g mL}^{-1}$. Pripravljeno vlakno je imelo odlično ponovljivost in obnovljivost z relativnimi standardnimi odmiki 3,9–8,8 % za eno vlakno ter 7,3–15,1 % med vlakni. Predlagano HS-SPME-GC metodo smo uspešno uporabili za analizo aldehydov v komercialnih vzorcih jedilnih olj.



Scientific paper

Effect of SDS Micelles on Actinomycin D – DNA Complexes

Ana Maria Toader, Izabella Dascalu and Mirela Enache*

Institute of Physical Chemistry Ilie Murgulescu, Romanian Academy, Splaiul Independentei 202, Bucharest 060021, Romania

* Corresponding author: E-mail: enachemir@yahoo.com

Received: 10-06-2021

Abstract

DNA thermal denaturation was evaluated as a measure of the effect of antitumor drug actinomycin D on the stability of the double helix and also the effect of SDS micelles on actinomycin D – DNA complexes. The results indicated that the melting temperature of DNA was dependent on drug concentration, increasing with actinomycin D concentration. High thermal stabilization (about 10 °C) of the DNA helix after the association with actinomycin D clearly demonstrates the intercalative binding mode. The presence of SDS micelles leads to the release of intercalated actinomycin D molecules from DNA double helix and their further relocation in surfactant micelles. These results highlighted that the drug release can be controlled in time and by varying the concentration and nature of surfactant.

Keywords: Actinomycin D, DNA, micelles, thermal denaturation

1. Introduction

Actinomycin D (ActD) is a chromopeptide anticancer drug used for the treatment of pediatric rhabdomyosarcoma and Wilms' tumor as a component of VAC (vincristine, actinomycin D, cyclophosphamide) therapy.¹ Structurally, actinomycin D contains a 2-aminophenoxazin-3-one chromophore and two identical cyclic pentapeptide lactones (Fig. 1). Actinomycin D exerts the anticancer activity by tight binding to DNA which determines the inhibition of transcription elongation by blocking RNA polymerase.^{2,3} The interaction of actinomycin D with DNA in terms of binding mode and sequence specificity was extensively investigated using different experimental techniques.^{4–8} The actinomycin D-DNA complex is made by intercalation of planar phenoxazine ring between 5'GpC3' sequence and strong hydrogen bonds are formed in the minor groove between the guanine 2-amino groups and the carbonyl oxygen atoms of the L-threonine residues of the pentapeptides chains.^{4,5} Additional stabilization of this complex are acquired from hydrophobic interactions between groups on the pentapeptides and sugar residues and from other specific hydrogen bonding and atom–atom intermolecular interactions.^{6,9} Actinomycin D also binds to some DNA sequences that do not contain G–C sites^{10,11} and to single stranded DNA.^{12,13}

Stopped-flow kinetic studies indicate that the binding of actinomycin D to DNA is characterized by five rate constants with three slow processes.^{14,15} As these slow processes are absent in the binding of actinomine (a peptide-lacking analog of actinomycin D) to DNA, the slow

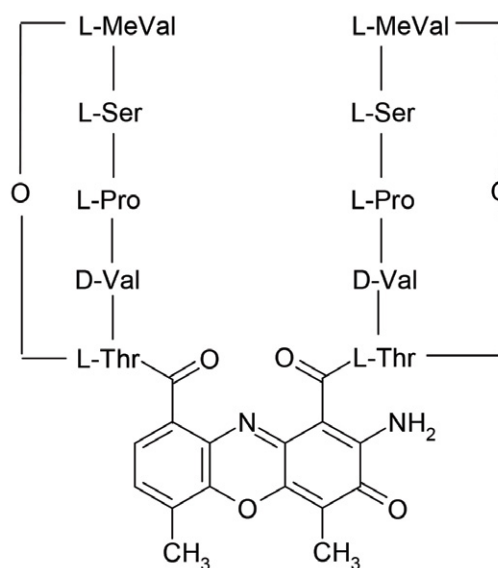


Figure 1. Molecular structure of actinomycin D (ActD).

kinetics of interaction of actinomycin D with DNA was explained by conformational changes in the peptide chains of actinomycin D during the accommodation of molecules into double helix of DNA.¹⁴ Also, SDS induced actinomycin D dissociation from DNA presents multiexponential decay, with the slowest rate of 1500 seconds.¹⁶

In the present work, the thermal denaturation profile of DNA is used to evaluate the effect of anticancer drug actinomycin D on the stability of the DNA double helix. These results together with our previous research can provide information about the nature and the strength of interaction between actinomycin D and DNA. Moreover, the effect of SDS micelles on actinomycin D – DNA complexes is investigated taking into account that micelle-induced sequestration can be applied as a simple method for the removal of drug molecules from DNA.¹⁷

2. Materials and Methods

2.1. Materials

Actinomycin D (ActD), deoxyribonucleic acid (DNA) sodium salt from calf thymus and sodium dodecyl sulphate (SDS) were purchased from Sigma-Aldrich. The concentration of the prepared DNA stock solutions was determined by measuring the absorbance at 260 nm using the molar absorbance coefficient, $\epsilon = 6600 \text{ M}^{-1} \text{ cm}^{-1}$ (in nucleotide concentration). All the sample solutions were prepared in 0.1 M phosphate buffer, pH 7.4. All chemicals used were of analytical grade or higher and were used without further purification. The concentration of actinomycin D was determined spectrophotometrically using the molar absorption coefficient at 440 nm, $\epsilon = 24400 \text{ M}^{-1} \text{ cm}^{-1}$.

2.2. Thermal Denaturation Experiments

Thermal denaturation experiments were performed in stoppered quartz cuvettes on a Jasco V-550 UV-VIS spectrophotometer equipped with a Jasco ETC-505T cell-temperature controller. The temperature of DNA solutions alone and in the presence of actinomycin D at ratios (R) of [ActD]/[DNA]: 0.05, 0.1, 0.2, 0.5 and 1.00 was increased gradually from 25 to 103 °C at a speed of 1 °C/min and the absorbance at 260 nm was read automatically. The melting temperature (T_m) of DNA in the absence and the presence of actinomycin D was determined using the second derivative method in the frame of Melting Temperature Calculation Program provided by the spectrophotometer. All measurements of T_m were repeated three times and the data presented are the average values.

The hyperchromicity (%H) of DNA was calculated in the absence and presence of the different concentrations of actinomycin D at 260 nm using the equation (1):¹⁸

$$\%H = \frac{A_U - A_L}{A_L} \times 100 \quad (1)$$

where A_U and A_L are the absorbance of the upper baseline and the absorbance of the lower baseline respectively.

3. Results and Discussion

The DNA helix is a fairly stable structure due to hydrogen bonds between base-pairs and base stacking interactions. Thermal DNA denaturation or DNA melting is the process of the dissociation of double helix of DNA into two single strands by the breaking of hydrogen bonds between the bases when temperature is raised. The thermal behavior of DNA in the presence of different ligand molecules can give information about the nature and the strength of the interaction of ligands with DNA. In general, the intercalation binding stabilize the DNA double helix leading to a significant rise in T_m by about 5–8 °C, while in the case of non-intercalative interaction (groove binding or electrostatic binding at the DNA surface), a small change in the T_m is observed.^{19,20}

The experimental melting curves of DNA upon addition of actinomycin D within the concentration range $0 < R < 1$, where $R = [\text{ActD}]/[\text{DNA}]$ ratios are presented in Fig. 2. The parameters of the helix-to-coil transition (the melting temperature (T_m), the melting shift (ΔT_m – the difference between the melting temperatures of actinomycin D – DNA complexes and DNA alone) and the hyperchromicity (%H)) are reported in Table 1 and Fig. 2. In the present work, the melting temperature of DNA is about 86.51 °C under our experimental conditions. The addition of actinomycin D to DNA solution results in an increase in the T_m of DNA with the increasing R ratio. The high positive ΔT_m values (Fig.3) indicate the stabilization of double helix of DNA by intercalation mode of binding of actinomycin D drug. The value of $\Delta T_m \sim 10$ °C is in the range of the values corresponding to other intercalative anticancer drugs, such as mitoxantrone, doxorubicin, daunomy-

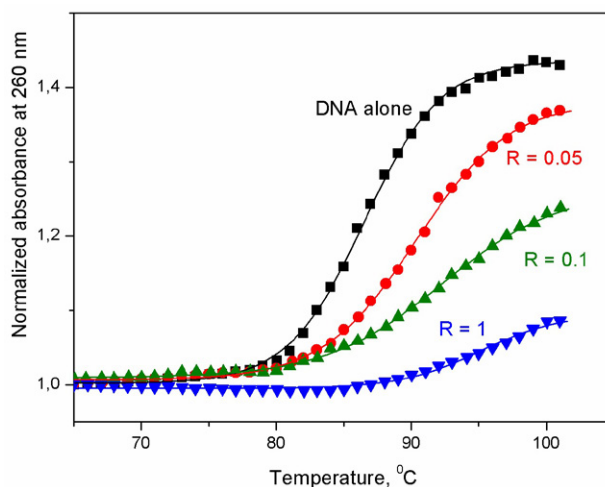


Figure 2. Thermal melting profile of DNA alone and in the presence of actinomycin D at different molar ratio ($R = [\text{ActD}]/[\text{DNA}]$).

cin.^{21,22} In addition, it can also see that the maximum value of ΔT_m is reached at $R = 1$. However, the magnitude of ΔT_m in the range of $R = 0.2 - 1$ does not differ significantly.

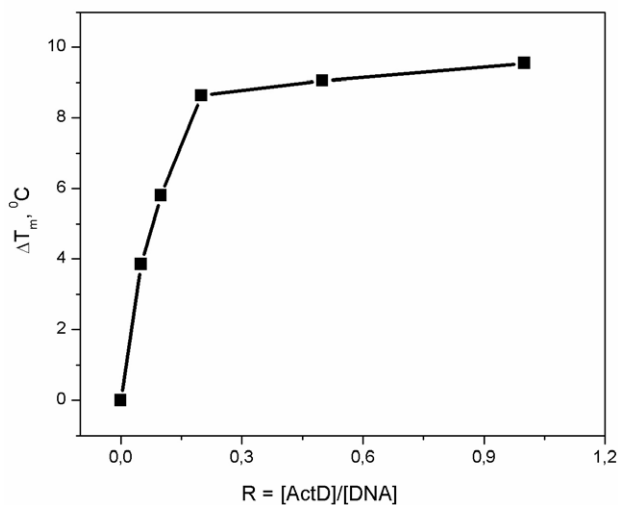


Figure 3. The melting shift ΔT_m at different molar ratios, $R = [\text{ActD}]/[\text{DNA}]$.

Table 1. DNA melting temperature (T_m) and the hyperchromicity (%H) at different molar ratios ($R = [\text{ActD}]/[\text{DNA}]$).

$R = [\text{ActD}]/[\text{DNA}]$	T_m (°C) ^a	%H
DNA alone	86.5±0.3	53.3
0.05	90.4±0.4	42.4
0.1	92.3±0.2	24.3
0.2	95.1±0.2	18.6
0.5	95.6±0.1	13.0
1	96.1±0.3	7.87

^a All values are the average ± standard deviation of three experiments.

Also, in Fig. 2 a decrease of the hyperchromicity (%H) is observed. In the absence of the drug, the hyperchromicity of DNA calculated using the equation (1) is about 53.3% (Table 1). As the concentration of actinomycin D increases (R ratio increases), the hyperchromicity of DNA significantly decreases. These results suggest that the dissociation of double helix in the DNA solutions containing actinomycin D is obstructed to take place completely.

The reduction of hyperchromicity and high increase of T_m clearly indicate that the interaction of actinomycin D with DNA determine a high stabilization of double helix of DNA. These results are in agreement with the intercalation mode of binding of actinomycin D molecule between the base pairs of DNA. Also, specific hydrogen bonding and other atom-atom intermolecular interactions contribute to the stabilization of the actinomycin D-DNA complexes.⁹

Further, the influence of SDS concentration on (ActD-DNA) complexes was investigated. The use of sur-

factant micelles to sequestrate the drug molecules dissociated from DNA is a well-established method to study the kinetics of dissociation of drug – DNA complexes.^{15,23} Also, the interaction of drug molecules with surfactant micelles is important to understand the nature of drug-biomembrane interactions but can also help in the case of drug overdoses to remove the excess of the drug and the removal of mutagens.^{24,25} Previous studies (absorption, thermal denaturation and circular dichroism) indicate that the native B-form of DNA is not altered by the presence of SDS micelles.²¹ Also, DNA hold its native B-form even in the presence of the highest SDS concentration (6.98×10^{-3} M) used in the present study, as is indicated by the melting curve (Fig. 4) and the value of melting temperature (85.87 °C) which is very close to the value of melting temperature of DNA alone.

The critical micellar concentration (CMC) of pure SDS in 0.1 M phosphate buffer (pH 7.4) was previously determined from conductivity measurements and it is 9.28×10^{-4} M.²⁶ This value is smaller than the CMC of SDS in pure water (8.08×10^{-3} M) and it is an agreement with literature data which indicate that the CMC value decreases in phosphate buffer as the concentration of electrolyte increases.²⁷ Submicellar (6.09×10^{-4} M) and micellar (2.24×10^{-3} M, 4.38×10^{-3} M, 6.98×10^{-3} M) SDS concentrations were used to assess the influence of SDS surfactant on ActD – DNA complexes.

The presence of submicellar SDS concentration does not change significantly the melting temperature and the hyperchromicity of actinomycin D – DNA complexes (Fig. 4). Instead, the presence of increasing micellar SDS concentrations leads to the continuous decrease of melting temperature of actinomycin D-DNA complexes up to almost the melting temperature value of DNA alone. This decrease of T_m after SDS micelles addition signifies that actinomycin D – DNA complex is disrupted and actinomycin D molecules are relocated from DNA into SDS micelles. In other words, the deintercalation of actinomycin D molecules from DNA takes place in the presence of the micelles and not in the presence of monomeric surfactant molecules.

Also, in the presence of increasing micellar SDS concentrations, the hyperchromicity enhances but it does not reach the value obtained for DNA in the absence of drug. Similar with actinomycin D, the intercalative binding of mitoxantrone to DNA induces the increase of melting temperature with about 10 °C.²¹ The addition of SDS micelles conducts to the exclusion of intercalated actinomycin D and mitoxantrone from DNA helix, the melting temperature decreases and reaches the value corresponding to DNA alone. In the case of mitoxantrone – DNA complex, the initial value of DNA hyperchromicity is restored in the presence of SDS micelles,²¹ as against actinomycin D – DNA complex when the hyperchromicity enhances in the presence of micelles but is not recovered completely. The most likely explanation for the lack of recovery of the

hyperchromicity could be the fact that some actinomycin D molecules are still associated with DNA. Also, this different behavior between the two drugs could be due to the more complex structure of actinomycin D and hence probably a more complicated mode of interaction with DNA.

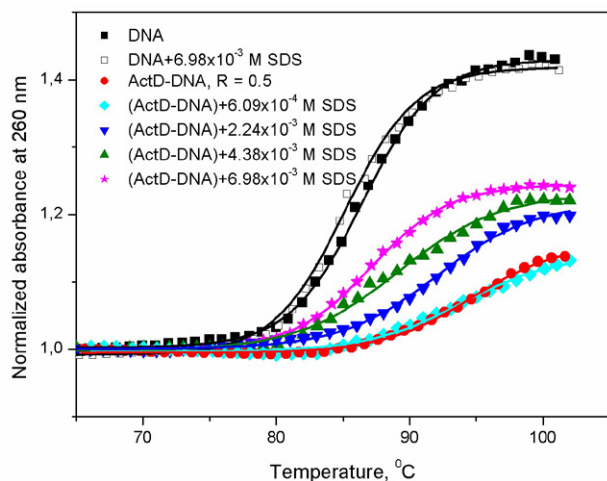


Figure 4. Thermal melting profile of DNA alone, in the presence of 6.98×10^{-3} M SDS, actinomycin D, and actinomycin D and different SDS concentrations.

Table 2. The DNA melting temperature (T_m), the melting shift (ΔT_m) and the hyperchromicity (%H) of actinomycin D-DNA complexes ($R = 0.5$) in the presence of different SDS concentrations.

System	T_m (°C)	ΔT_m (°C)	%H
(ActD-DNA)	95.56	9.05	12.96
(ActD-DNA) + 6.09×10^{-4} M SDS	94.92	8.41	12.37
(ActD-DNA) + 2.24×10^{-3} M SDS	92.07	5.56	20.43
(ActD-DNA) + 4.38×10^{-3} M SDS	89.12	2.61	21.72
(ActD-DNA) + 6.98×10^{-3} M SDS	87.12	0.61	23.68

The deintercalation of actinomycin D molecules from DNA helix is also observed in the absorption spectra when SDS micelles are added to intercalated (ActD-DNA) complex.

The absorption spectrum of actinomycin D is characterized by a broad absorption band around 440 nm. The formation of actinomycin D – DNA complex results in a hypochromic effect and a shift of the maximum towards longer wavelength. In our previous study, these changes in absorption spectra accompanying the titration of actinomycin D with DNA were used to calculate binding constant and the size of binding site.²⁸ The addition of micellar concentrations of SDS leads to an increase in the absorbance and the splitting of the absorption maximum in

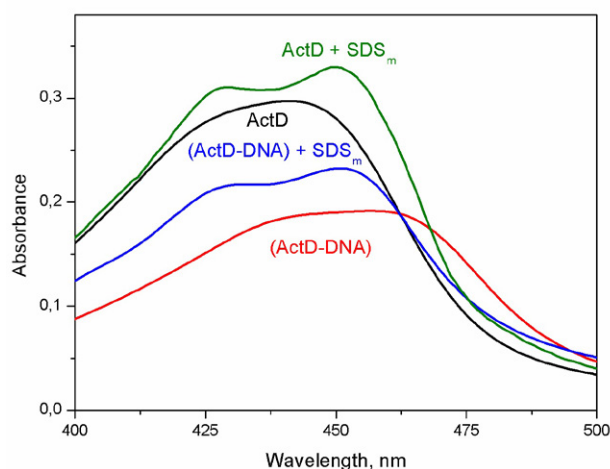


Figure 5. Absorption spectra of actinomycin D, (ActD-DNA) complex, and actinomycin D and (ActD-DNA) complex in the presence of micellar SDS concentration (SDS_m).

two peaks. The spectral modulation in Fig. 5 suggests that upon addition of SDS micelles, actinomycin D molecules experiences a different environment than that in DNA, the absorption spectrum being similar with the spectrum of actinomycin D in SDS micelles.²⁹ These results are in agreement with melting experiments and lead to the conclusion that the presence of SDS micelles induces the deintercalation of actinomycin D molecules from DNA double helix and their further relocation in surfactant micelles.

4. Conclusions

The consequences of actinomycin D – DNA complex formation on the stability of the double helix of DNA as well as the influence of anionic surfactant SDS on drug-DNA complexes were evaluated by recording the DNA melting profiles. The melting temperature values indicate an increasing stabilization of DNA as the concentration of added actinomycin D increases. Also, the large values of melting shift (~ 10 °C) point out for the intercalation mode of binding of actinomycin D to DNA. Addition of SDS micelles to actinomycin D – DNA complexes leads to the deintercalation of drug molecules from DNA helix and their further relocation into surfactant micelles. Besides providing an insight into the stability of actinomycin D – DNA complexes, the present work also demonstrates the excretion of the drug molecules from the biomacromolecular assembly using surfactant micelles.

5. References

1. H. Hosoi, *Pediatr. Int.* **2016**, *58*, 81–87.
DOI:10.1111/ped.12867

2. T. Bunte, U. Novak, R. Friedrich, K. Moelling, *Biochim. Biophys. Acta* **1980**, *610*, 241–247.
DOI:10.1016/0005-2787(80)90006-4
3. H. M. Sobell, *Proc. Natl. Acad. Sci. U.S.A.* **1985**, *82*, 5328–5331. DOI:10.1073/pnas.82.16.5328
4. H. M. Sobell, S. C. Jain, T. D. Sakore, C. E. Nordman, *Nat. New Biol.* **1971**, *231*, 200–205. DOI:10.1038/newbio231200a0
5. H. M. Sobell, S. C. Jain, *J. Mol. Biol.* **1972**, *68*, 21–34.
DOI:10.1016/0022-2836(72)90259-8
6. S. Kamitori, F. Takusagawa, *J. Am. Chem. Soc.* **1994**, *116*, 10, 4154–4165. DOI:10.1021/ja00089a002
6. T. R. Krugh, E. S. Mooberry, Y.-C. C. Chiao, *Biochemistry* **1977**, *16*, 740–747. DOI:10.1021/bi00623a028
7. F. M. Chen, *Biochemistry* **1998**, *37*, 3955–3964.
DOI:10.1021/bi972110x
8. F. Sha, F. M. Chen, *Biophys. J.* **2000**, *79*, 2095–2104.
DOI:10.1016/S0006-3495(00)76457-5
9. C. Bendic, M. Enache, E. Volanschi, *J. Mol. Graph. Model.* **2005**, *24*, 10–16. DOI:10.1016/j.jmglm.2005.03.004
10. J. G. Snyder, N. G. Hartman, B. L. D’Estancoit, O. Kennard, D. P. Remeta, K. J. Breslauer, *Proc. Natl. Acad. Sci. U.S.A.* **1989**, *86*, 3968–3972. DOI:10.1073/pnas.86.11.3968
11. S. A. Bailey, D. E. Graves, R. Rill, *Biochemistry* **1994**, *33*, 11493–11500. DOI:10.1021/bi00204a011
12. R. L. Rill, K. H. Hecker, *Biochemistry* **1996**, *35*, 3525–3533.
DOI:10.1021/bi9530797
13. R. M. Wadkins, E. A. Jares-Erijman, R. Klement, A. Rüdiger, T. M. Jovin, *J. Mol. Biol.* **1996**, *262*, 53–68.
DOI:10.1006/jmbi.1996.0498
14. R. Bittman, L. Blau, *Biochemistry* **1975**, *14*, 2138–2145.
DOI:10.1021/bi00681a015
15. W. Muller, D. M. Crothers, *J. Mol. Biol.* **1968**, *35*, 251–290.
DOI:10.1016/S0022-2836(68)80024-5
16. K. R. Fox, M. J. Waring, *Eur. J. Biochem.* **1984**, *145*, 579–586.
DOI:10.1111/j.1432-1033.1984.tb08596.x
17. P. Kundu, S. Das, N. Chattopadhyay, *Int. J. Pharm.* **2019**, *565*, 378–390. DOI:10.1016/j.ijpharm.2019.04.058
18. H. K. S. Souza, *Thermochim. Acta* **2010**, *501*, 1–7.
DOI:10.1016/j.tca.2009.12.012
19. S. U. Rehman, T. Sarwar, H. M. Ishqi, M. A. Husain, Z. Hasan, M. Tabish, *Arch. Biochem. Biophys.* **2015**, *566*, 7–14.
DOI:10.1016/j.abb.2014.12.013
20. R. Anwer, N. Ahmad, K. I. Al Qumaizi, O. A. Al Khamees, W. M. Al Shaqha, T. Fatma, *J. Mol. Recognit.* **2016**, 1–6.
DOI:10.1002/jmr.2599
21. M. Enache, S. Ionescu, E. Volanschi, *J. Mol. Liq.* **2015**, *208*, 333–341. DOI:10.1016/j.molliq.2015.05.006
22. G. P. Sartiano, W. E. Lynch, W. D. Bullington, *J. Antibiot.* **1979**, *32*, 1038–1045. DOI:10.7164/antibiotics.32.1038
23. F. Westerlund, L. M. Wilhelmsson, B. Norden, P. Lincoln, *J. Am. Chem. Soc.* **2003**, *125*, 3773–3779.
DOI:10.1021/ja029243c
24. A. K. Mora, P. K. Singh, S. Nath, *J. Phys. Chem. B* **2016**, *120*, 4143–4151. DOI:10.1021/acs.jpcc.5b12689
25. M. Varshney, T. E. Morey, D. O. Shah, J. A. Flint, B. M. Moudgil, C. N. Seubert, D. M. Dennis, *J. Am. Chem. Soc.* **2004**, *126*, 5108–5112. DOI:10.1021/ja0394479
26. A. M. Toader, P. Oancea, M. Enache, *Acta Chim. Slov.* **2020**, *67*, 629–637. DOI:10.17344/acsi.2019.5641
27. E. Fuguet, C. Rafols, M. Roses, E. Bosch, *Anal. Chim. Acta* **2005**, *548*, 95–100. DOI:10.1016/j.aca.2005.05.069
28. M. Enache, M. Hillebrand, E. Volanschi, *Romanian J. Biophys.* **2001**, *11*, 93–105.
29. M. Enache, D. Bulcu, I. Serbanescu, E. Volanschi, *Rev. Roumaine Chim.* **2007**, *52*, 725–731.

Povzetek

Termično denaturacijo DNA smo ovrednotili kot merilo učinka protitumorske učinkovine aktinomocina D na stabilnost dvojne vijačnice in tudi učinka micel SDS na komplekse aktinomocin D – DNA. Rezultati so pokazali, da je bila temperatura tališča DNK odvisna od koncentracije zdravila, ki se povečuje s koncentracijo aktinomocina D. Visoka toplotna stabilizacija (približno 10 °C) vijačnice DNA po vezavi z aktinomocinom D jasno kaže interkalativni način vezave. Prisotnost micel SDS vodi do sproščanja interkaliranih molekul aktinomocina D iz dvojne vijačnice DNA in njihove nadaljnje preместitve v micel površinsko aktivne snovi. Ti rezultati so pokazali, da je sproščanje zdravila mogoče nadzorovati pravočasno in s spreminjanjem koncentracije in narave površinsko aktivne snovi.

Scientific paper

Removal of Diazo Dye Direct Red 28 and Tetra Azo Dye Direct Black 22 Using Synthesized Magnetic Kaolin Supported Zinc Ferrite

Serap Findik*

Chemical Engineering Department, Engineering Faculty, Hitit University, Kuzey Yerleşkesi, Cevre Yolu Bulvarı, 19030, Çorum, Turkey

* Corresponding author: E-mail: serapfindik@hitit.edu.tr

Received: 11-21-2021

Abstract

The presence of dye molecules in water resources has harmful effects on environment. Therefore, it is important to remove dyes from wastewater using eco-friendly materials. In this study, adsorptive removal of diazo dye Direct Red 28 (DR-28) and tetra azo dye Direct Black 22 (DB-22) was investigated by using a new composite, kaolin supported zinc ferrite (KZF) as adsorbent. Characteristics of the composite, KZF were determined using various techniques such as FTIR, SEM, XRD, VSM, and EDS/Mapping. The adsorption of DR-28 and DB-22 on KZF was studied as a function of contact time, initial dye concentration, adsorbent amount, temperature, initial pH of the solution as well as the heat treatment of the composite. The removal of DR-28 was found to be 92.4% for the KZF concentration of 1g/200mL, initial dye concentration of 20 mg/L, contact time of 120 min at original pH and 21 °C. On the other hand the removal of DB-22 was found to be 91.7% under the same conditions at 40 °C. The results showed that Langmuir isotherm is suitable for the adsorption of DR-28 and DB-22 on KZF under given conditions. It was found that adsorption of DR-28 on KZF was exothermic while that of DB-22 was endothermic. The enthalpy changes (ΔH^0) for the adsorption of DR-28 and DB-22 dyes on KZF were found to be -24.59 kJ/mol and 61.95 kJ/mol respectively. ΔS^0 for the adsorption of DR-28 dye was found to be negative while ΔS^0 for the adsorption of DB-22 was positive. The kinetic data fitted well to the pseudo second order model for the adsorption of DR-28 and DB-22 on KZF composite. These results showed that the prepared adsorbent KZF could be used as an adsorbent for the efficient removal of anionic dyes.

Keywords: Adsorption, direct black 22, direct red 28, magnetic kaolin, zinc ferrite

1. Introduction

Dyes are chemical compounds used to color products in many fields such as textile, leather, paper, rubber, printing and plastic.¹ Dyes in wastewater are dangerous and negatively affect the water quality. The discharge of wastewater containing dyes into water resources causes a decrease in gas solubility, light and oxygen permeability, and therefore a decrease in photosynthesis. It also affects aquatic life and human life due to its carcinogenic and mutagenic effects.¹⁻⁴ Dyes entering the human body through the food chain cause diseases such as dizziness, jaundice, diarrhea, and nausea. They also damage to organs such as kidney, brain and liver.^{1,3}

Dyes can be divided into two categories: natural and synthetic dyes. With the increase in dye consumption, natural dyes have been replaced by synthetic ones. Synthetic dyes consist of three parts: chromophoric groups, auxo-

chromes and conjugated aromatic structures. Chromophoric groups are unsaturated and they consist of atoms or groups of atoms that allow the light to be absorbed.⁵ Dyes can also be classified according to the chromophoric groups: Azo, Anthraquinone, Indigoid, Nitroso, Nitro, and Triarylmethane.^{1,6} Azo dyes are characterized by the number of azo bond groups such as monoazo, diazo, triazo, polyazo and azoic. Polyazo dyes are complex structures and contain three or more azo groups in the same molecule.⁷

Direct red 28 (DR-28, known as Congo red) and Direct black 22 (DB-22) are widely used in textile, paper and plastic industries.^{8,9} DR-28 contains two azo groups and DB-22 contains tetra azo groups. Both DR-28 and DB-22 are anionic dyes.⁷ DR-28 and DB-22 in wastewater damage the environment due to their carcinogenic and toxic properties. Therefore, DR-28 and DB-22 containing

wastewater should be treated before being released into environment.

Different treatment methods such as coagulation-flocculation¹⁰, Fenton¹¹, ozonation¹², UV¹³, photocatalytic process¹⁴, and adsorption¹⁵ are applied to remove dyes from aqueous solutions. Among these methods, adsorption has gained importance in recent years since it becomes more economical with cheap, simple, and efficient adsorbents. Natural adsorbents such as clinoptilolites, montmorillonites, esmectites, kaolinites, and bentonites have been successfully used for adsorption.¹⁶

Kaolin has a great potential in the removal of dyes from wastewater thanks to its chemical and mechanical stability, high cation exchange capacity, adsorption ability, unique structural properties as well as its low cost, high efficiency, and abundance.^{17,18} On the other hand, the surface properties such as surface area and surface exchange sites of kaolin should be improved to increase the adsorption capacity. For this purpose, physical and chemical processes such as milling, heat treatment, acid treatment, and alkaline treatment can be applied. While alkaline treated kaolin has a small surface area, kaolin with a large surface area can be obtained by acid treatment. However, acid treatment is difficult due to the inert nature of kaolin. Metakaolinite is obtained by the calcination of kaolinite.^{17,19}

Magnetic adsorbents are new generation adsorbents with high adsorption capacity and speed. Compared to other adsorbents, magnetic adsorbents have some advantages such as less production cost, easy separation from solution, low diffusion resistance, and large surface area.⁴ Among the magnetic nanoparticles, spinel ferrites with the chemical composition of MFe_2O_4 ($M=Cu, Mn, Zn, Mg, Co, Ni$ and other metals) have been extensively studied so far due to their special properties, where oxygen ions (O^{2-}) make a cubic structure, Fe^{3+} cations occupy half of the octahedral holes and M^{2+} ion is a divalent cation and place in the eight holes of the tetrahedral.² Zinc, cobalt, and nickel ferrites are widely used as a magnetic support thanks to their high saturation magnetization intensity and excellent mechanical strength.²⁰

The addition of inorganic particles such as spinel ferrite to the matrix of kaolinites can improve the adsorption capacity and facilitate its separation from the aqueous solution by an external magnet. This process improves both the physical and chemical properties of kaolinite and provides high adsorption capacity by preventing agglomeration of inorganic nanoparticles.²¹

The aim of this study was to investigate the performance of magnetic kaolin supported zinc ferrite as an adsorbent for the removal of diazo dye DR-28 and tetra azo dye DB-22 from aqueous solutions. The prepared adsorbent was characterized using FTIR, SEM-EDS, XRD and VSM techniques. In order to determine the optimum adsorption parameters, the effect of process variables such as heat treatment of the composite KZF, adsorbent amount,

initial dye concentration, contact time, initial pH of the solution, and temperature have been investigated. After optimization of the effective factors, the kinetics and isotherm of the adsorption were investigated. A thermodynamic study was realized to understand the behavior of the adsorption process.

2. Materials and Methods

2.1. Materials and Equipments

The kaolin clay with a particle size of 28 μ was procured from a company in Balıkesir, Turkey. It was a commercial product and used without purification. DR-28 was supplied from Isolab, DB-22 (commercial name Direct Black 22 VSF 1600) from a company named “HNY” in Turkey, and $FeSO_4 \cdot 7H_2O$ and $ZnSO_4 \cdot 7H_2O$ from Merck.

A magnetic stirrer (HSD-180), pH meter (C561, Consort), centrifuge (Nuve, NF 200) and oven (Proterm, PLF 120/5) were used in the study. UV- spectrophotometer (Hach, DR-2400) was used to measure the absorbance of the dye samples.

2.2. Preparation of the Adsorbent

The composite kaolin/Zn/Fe was prepared by chemical coprecipitation method. First, iron II sulphate heptahydrate ($FeSO_4 \cdot 7H_2O$) and zinc sulphate heptahydrate ($ZnSO_4 \cdot 7H_2O$) with a molar ratio of 2:1 were dissolved in 200 ml distilled water. Then, kaolin clay was added to the solution and heated to 65–70 °C while stirring with a magnetic stirrer. The mixture was stirred for 30 min. 3M NaOH solution was added dropwise to the solution, and pH of the solution was adjusted to 12. After addition of NaOH solution, stirring was continued for one hour at 100 °C. The prepared composite was left for one day at room conditions and then placed in water bath for 4 h at 95 °C. After that, it was dried at 95 °C for 90 h. Finally, the dried composite was heat treated at 200 °C for 3 h. The composite with and without heat treatment were coded as KZF-200 and KZF, respectively, and the raw kaolin as K.

2.3. Characterization of Adsorbent

The adsorbents used in the study were characterized by XRD, FTIR, SEM, EDS, and VSM. Powder X-ray diffraction (XRD) patterns of the adsorbent were recorded using Rigaku Smart Lab with Cu-K α radiation at 40 kV and 30 mA to determine the crystalline structure of the samples. The samples were scanned from 5°–90° at a rate of 2°/min, and with a step size of 0.01. Fourier transform infrared (FTIR) (PerkinElmer, Spectrum Two) spectroscopy analysis was performed in the range of 400–4000 cm^{-1} to identify the functional groups of the adsorbents before and after adsorption. SEM and EDS analysis were performed using Jeol, JSM 7001F. Magnetic saturation was

measured using a vibrating sample magnetometer (VSM Lake Shore 7407).

2. 4. Adsorption Experiments

A stock solution of dye was prepared using distilled water. Standard dye solutions with known concentration were prepared using stock solution, then absorbance values of the standard dye solutions were recorded using UV-spectrophotometer (Hach, DR-2400). The absorbance of DR-28 and DB-22 solutions was recorded at 497 nm and 481 nm, respectively. The calibration graph was drawn using the absorbance values of the standard solutions.

For the adsorption experiments, the desired amount of adsorbent was put in 200 ml of dye solutions and the sample was magnetically stirred continuously at 600 rpm. The stirring rate was constant in all experiments. The dye solutions were kept at room temperature (21 °C) in all experiments except those in which the effect of temperature was investigated. pH was adjusted with HCl and NaOH solutions to 6.5–9. The original pH of the dye solution was ≈7.4. In the experiments, the amount of adsorbent and the initial dye concentration were changed in the range of 0.6–1.2 g/200mL and 20–50 mg/L, respectively. All the experiments were repeated twice. Process variables such as the heat treatment of the composite KZF, contact time, pH, the initial concentration of dye solution, amount of adsorbent, and temperature were investigated in the study. The samples were withdrawn from the reaction mixture and centrifuged at 5000 rpm for 10 minutes to remove the adsorbent. The absorbance of the samples was measured to find the concentration of dye.

Efficiency of the dye removal, (R) was calculated using Eq. (1).

$$R, \% = [(C_0 - C_t) / C_0] * 100 \quad (1)$$

Equation 2 gives the adsorption capacity of the adsorbent:

$$q_e = ((C_0 - C_e) * V) / W \quad (2)$$

where q_e is the adsorption capacity of the adsorbent at equilibrium (mg/g), C_0 is the initial concentration of dye, C_t is the concentration of dye at any time (mg/L), C_e is the concentration of dye at equilibrium (mg/L), V is the volume of the dye solution (L), and W is the weight of the adsorbent (g).

3. Results and Discussion

3. 1. Adsorbent Characterization

The SEM and EDS/Map analyses were used to examine the structure and distribution of elements at the surface of the adsorbent. SEM, EDS spectra and EDS map-

ping images of the composite KZF are given in Fig. 1. As shown in Fig. 1-a, KZF has an irregular and porous surface structure. The EDS/Map analyses were used to determine the Zn and Fe particles in the kaolin layers, and the results confirm that there are Fe and Zn ions in the structure of KZF. KZF includes iron (7.1%), zinc (4.8%), silisium (6.2%), oxygen (45%), sodium (16.7%), aluminum (4.1%), carbon (9.6%) and sulphur (5.3%). According to the results of EDS analysis, kaolin was successfully loaded with Fe and Zn, and the elements were observed to distribute uniformly.

As shown in Fig. 2, the bands found at ~3690 and 3620 cm^{-1} are the typical bands for the ordered structure of kaolin. The bands at ~3690 cm^{-1} and 3620 cm^{-1} are related to the OH and H-O-H stretchings, respectively.¹⁹ The peaks at 1117, 1030, and 1001 cm^{-1} may be due to Si-O stretching.^{2,19} The peak at 910 cm^{-1} can be attributed to Al-OH-Al stretching vibration.²² The peaks at 796, 752 and 691 cm^{-1} may be due to the tensile vibrations of Si-O-Si, Si-O-Al and Si-O-Mg and the bending vibrations of SiO in the structure of kaolin.²

The peaks detected at 910, 940, 1001, 1030, and 1117 cm^{-1} in the spectrum of kaolin disappeared in the FTIR spectra of KZF and KZF-200. The bands of KZF and KZF-200 (752, 796, 3620 and 3690 cm^{-1}) were similar to those of the raw kaolin but transmittance of these bands was higher than that of the kaolin. The weak and disappeared peaks showed the change in the structure of kaolin. This can be interpreted as the Al^{3+} crystals in the kaolin structure were replaced by Fe^{3+} .¹⁹ There were new bands at 1440, 1100 and 980 cm^{-1} in KZF and KZF-200. The peaks at 1440, 1100 and 980 cm^{-1} may be due to O-H bending, C-O stretching and C=C bending, respectively.

When the FTIR spectra of KZF were compared with the FTIR spectra taken after the adsorption of DR-28 or DB-22 on KZF, it was seen that both had the same bands except the peaks at 1440 and 1100 cm^{-1} . After the adsorption of DR-28 and DB-22 by KZF, the peaks at 1440 and 1100 cm^{-1} disappeared. The transmittance of KZF after the adsorption of dye was lower than that of KZF. This indicates that the functional groups of KZF were involved in the dye adsorption.²³ After the dyes were adsorbed by KZF, some of the peaks disappeared and the range of some of the absorption peaks changed. This may be due to the interaction between the functional groups in the KZF and the dye molecules.²

Fig. 3 shows XRD patterns of K, KZF, and KZF-200. As seen in Fig. 3, kaolin has three intense diffraction peaks at 2θ at 12.34°, 24.87° and 26.61°. These peaks are associated with the presence of kaolinite. Similar diffraction peaks were reported by Meroufel et al.⁸ and Niu et al.²⁴ The diffraction peak at 20.86° is associated with quartz.⁸ In addition to the typical peaks of kaolin, new peaks at 19°, 28.9°, 32.1°, 33.8°, 35°, 48.7°, 54.6°, 59.5° and 62° were observed in XRD spectra of KZF and KZF-200. According to the PDF card, peaks appear at 19°, 28.9°, 35°, 59.5° and 62°

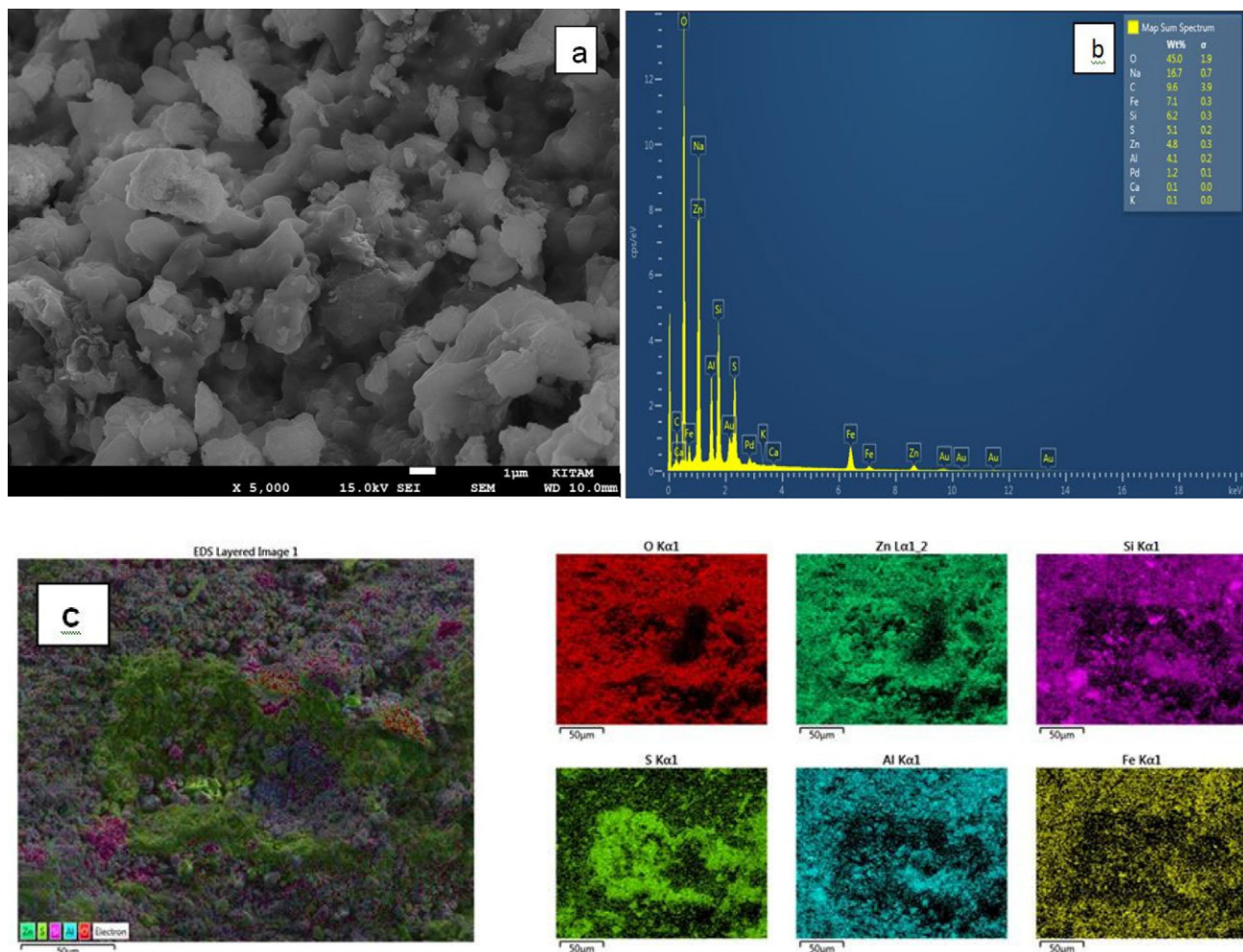


Fig. 1. The SEM (a), EDS spectra (b), EDS Mapping analyses (c) for KZF composite. The functional groups of the kaolin, KZF, KZF-200 and DR-28 or DB-22 adsorbed KZF were determined using FTIR analysis. The related FTIR spectra are shown in Fig. 2.

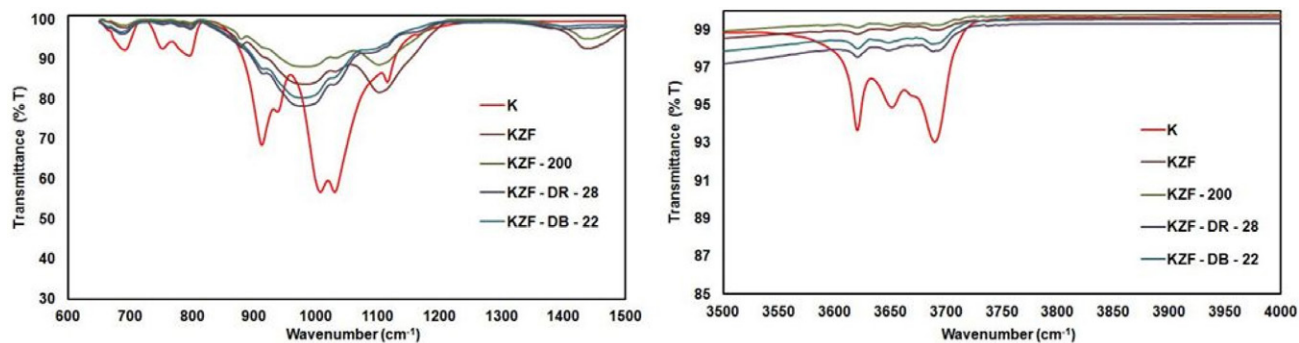


Fig. 2. FTIR spectra of K, KZF, KZF-200, and dye adsorbed KZF

match well with PDF card 00-010-0467 (Franklinite, $\text{Zn-Fe}_2\text{O}_4$).

The peaks at 28.9° and 33.8° indicate that these composites contain typical zinc oxide, magnetite, and zinc ferrite structures. The diffraction peak at 28.9° indicates the successful introduction of Zn to Fe spinel after synthesis. The peak at 35° shows the development of the spinel phase indicating a zinc ferrite formation in the composite.²⁵

The magnetic behavior of KZF at 298K was investigated by VSM analysis. The result is shown in Fig. 4. As can be seen in the Fig. 4, the amount of magnetic saturation for the KZF was determined as 3.3 emu/g. The low value of magnetic saturation for KZF is due to the fact that the magnetite was covered by the kaolin.²⁶ However, KZF can be separated from the solution using a permanent magnet. The magnetization curve of KZF exhibited zero

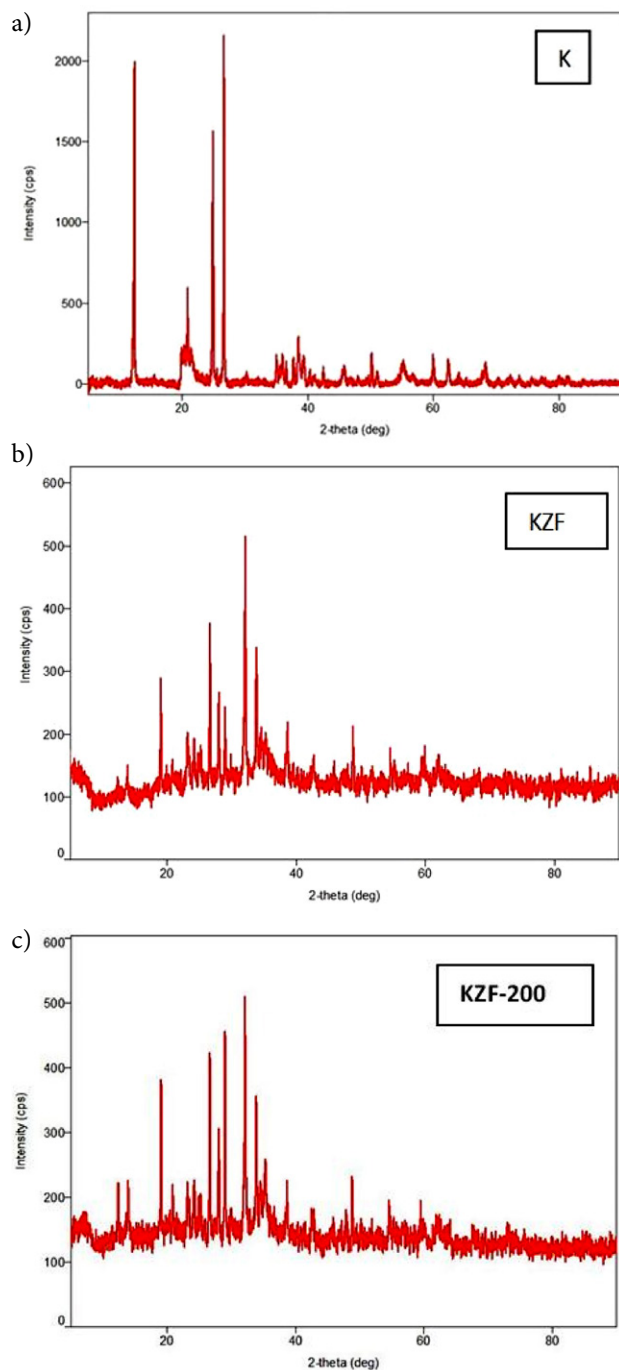


Fig. 3. XRD spectra of K, KZF and KZF-200

coercivities and remanences indicating a superparamagnetic behavior of the sample at room temperature.²⁷

3. 2. Effect of Heat Treatment

KZF and KZF-200 composites were considered to investigate the effect of the heat treatment on dye removal performance of the composites. The experiments were

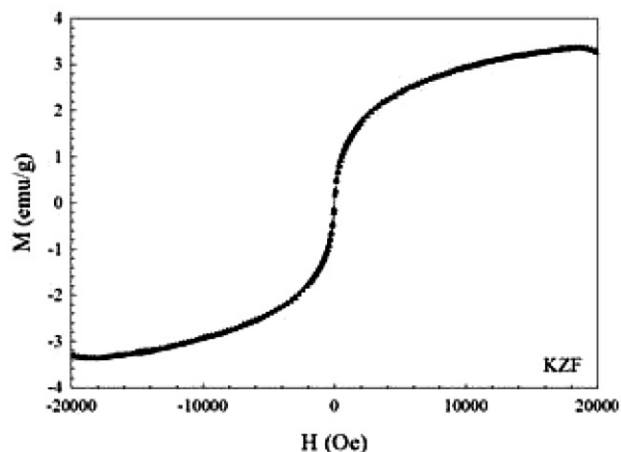


Fig. 4. VSM analysis of KZF at room temperature

performed at an initial dye concentration of 30 mg/L, with an adsorbent amount of 0.6g/200mL, at 21 °C and original solution pH of ≈ 7.4 . As seen in Fig. 5, lower removal rates were obtained for both DR-28 and DB-22 in the experiments with kaolin compared to those with KZF and KZF-200.

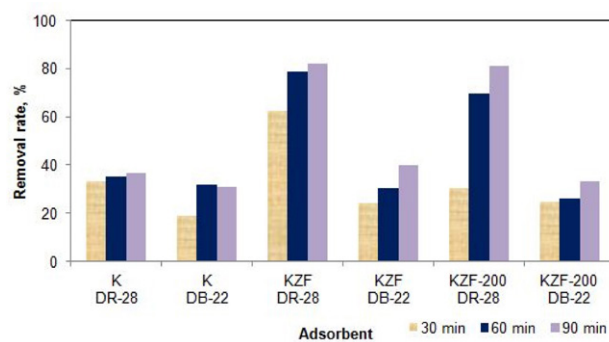


Fig. 5. Effect of the heat treatment on the removal of (a) DR-28 and (b) DB-22 (initial concentration: 30 mg/L, temperature: 21 °C, adsorbent amount: 0.6g/200mL, initial pH: original)

DR-28 removals at the end of 90 minutes were found to be 82.3% and 81.1% in the experiments with KZF and KZF-200, respectively. The removal rates in the contact time of 90 min were almost the same. However, in the contact times of 30 and 60 minutes, KZF provided a higher DR-28 removal than KZF-200. In the experiments, DB-22 removal was found to be higher for the composite KZF. In the contact time of 90 min, the removals of DB-22 were found to be 40% and 33.3% in the experiment with KZF and KZF-200, respectively. Therefore, KZF was chosen as the adsorbent, and the effect of the other parameters was examined using KZF.

The heat treatment temperature affects the structure of the composite. In one study, Olusegun and Mohallem²¹ studied adsorption of Congo red using synthesized kaolinite supported CoFe_2O_4 nanoparticles calcined at different

temperatures. Adsorption capacity of the composite without calcinations was higher than the calcined composite at 700 °C. Calcination temperature up to 700 °C resulted in structural damage to kaolinite.

As shown in Fig. 2, KZF and KZF-200 had the same peaks, but the transmittance of KZF was lower than that of KZF-200. The kaolinite had a disordered structure at lower temperatures due to dehydroxylation.²⁸

The removal rate of DR-28 was found to be higher than that of DB-22. DR-28 has two azo bonds, on the other hand, DB-22 has tetra azo bonds. The higher the number of azo bonds, the higher the stability of dye, which makes the dye removal difficult.

In addition, the molecular weight of the tetra azo dye DB-22 was higher than that of the diazo dye DR-28. The molecular weights of DB-22 and DR-28 were 1084 g/mol and 696.67 g/mol, respectively. The distribution of dyes in water increases with the increase of the molecular weight of the azo dyes, which causes a decrease in the rate of azo dye degradation.⁷

3. 3. Effect of Adsorbent Amount

In the present study, the effect of adsorbent amount on dye removal was also investigated. Experiments were done with a various amounts of adsorbent at the initial concentration of 30 mg/L, at 21 °C and original pH. Fig. 6 shows the effect of adsorbent amounts on the removal of DR-28 and DB-22. The removal of DR-28 increased with

increasing KZF amount from 0.6g/200mL to 0.8g/200mL then remained constant. DR-28 removals at the end of 90 min were found to be 89.7%, 90.2% and 90.1% for the KZF amounts of 0.8, 1, and 1.2g/200mL respectively. At the end of 30 min, the removals of DR-28 were found to be 76.4% and 88.9% in the KZF amounts of 0.8g/200mL and 1g/200mL respectively. Therefore, 1g/200mL of KZF was chosen as the optimum adsorbent amount.

The removal of DB-22 increased with the increasing the amount of adsorbent within the range of 0.6g/200mL–1.2g/200mL. The removals of DB-22 at the end of 90 min, were 40%, 55.3%, 73.2%, and 75.4% in the KZF amounts of 0.6, 0.8, 1, and 1.2g/200mL respectively. There was no significance difference between the DB-22 removals of 1g/200mL and 1.2g/200mL KZF.

DB-22 removal was lower than the removal of DR-28 under the studied conditions. As mentioned in the previous section, removal of tetra azo dyes is more difficult than that of diazo dyes.

The removal of DR-28 and DB-22 increased with the increasing adsorbent amount due to the increase in surface area and number of active sites. After the optimum adsorbent amount, the effective active surface area decreased due to the accumulation of adsorbent particles, and as a result, the removal rate remained almost constant. Nicola et al.²⁷ investigated the adsorption of Congo red using magnetic mesoporous silica. The removal of Congo red increased with increasing the adsorbent amount from 0.5 to 1g/L and after 1g/L adsorbent amount removal rate remained nearly constant. Similarly, Boushehrian et al.², reported that the removal of methylene blue and methyl violet remained almost constant after the adsorbent dosage of 1.5g/L. Cao et al.²⁹ investigated the adsorption of reactive brilliant red using magnetic Fe₃O₄/chitosan nanoparticles and reported that the optimum adsorbent amount was 0.6 g/L, and after the optimum adsorbent amount, the removal rate was almost the same. In another study, Karthikeyan et al.³⁰ studied the adsorption of phosphate and nitrate ions from water using magnetic kaolin (MK) chitosan beads and reported that, the removal of phosphate and nitrate increased with the increasing amounts of MK-chitosan beads due to the increase in reactive vacant sites of the adsorbent surface. Moreover, they also reported that, there was no significant change in the removal rate at the adsorbent amounts greater than 100 mg. Koohi et al.³¹ also reported similar results. They found that the removal efficiency of Congo red increased with the increasing amounts of Fe₃O₄/NiO due to the increase in the active surface area, and after the adsorbent amount of 15 g/L, no significant change was observed in the removal rate. The decrease in the surface area due to the aggregation of particles causes a decrease in the adsorption capacity. Esvandi et al.³ examined the adsorption of sunset yellow and Nile blue using magnetic nanoparticle, and reported that the removal efficiency increased when the adsorbent amount was increased from 0.4 g/L to 1 g/L (optimum adsorbent

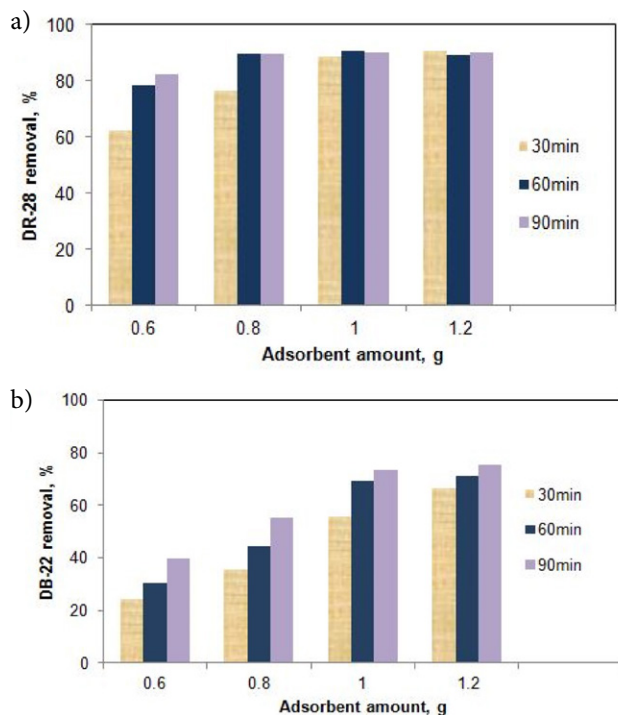


Fig. 6. Effect of KZF amount on the removal of (a) DR-28 and (b) DB-22 (initial concentration: 30 mg/L, temperature: 21 °C, initial pH: original)

amount), and after the adsorbent amount of 1 g/L, the removal rate remained constant. In another study, Mahmoodi et al.³² investigated the adsorption of direct black 22 using polyaminoimide homopolymer. They reported that removal of direct black 22 increases with increasing adsorbent amount due to increased adsorbent surface and availability of more sites.

3. 4. Effect of Initial pH

The pH of solution is an important parameter affecting the adsorption of dye onto the adsorbent. DR-28 is a diazo dye which changes colour at low pHs due to protonation of its amino groups. The red color of DR-28 changes to bluish color below the pH 5.^{8,21,33} For this reason the effect of pH was not investigated under strong acidic conditions.

The effect of pH on the removal of DR-28 and DB-22 was studied at the initial pHs of 6.5, ≈7.4, 8.5, and 9. ≈7.4 is the original pH of the dye solution. The results are presented in Fig. 7. The pH of the dye solution was adjusted at the beginning of the experiment and not controlled during the adsorption process.

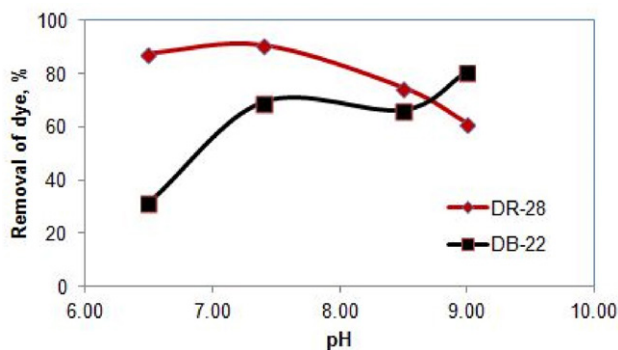


Fig. 7. Effect of initial pH of the dye solution on the removal of DR-28 and DB-22 (initial concentration: 30 mg/L, temperature: 21 °C, adsorbent: KZF, adsorbent amount: 1g/200mL, contact time: 60 min)

The removal rate of DR-28 increased from 87.5% to 90.5% when the pH of the solution was increased from 6.5 to 7.4. After the original pH, the removal rate decreased with the increase in solution pH, which could be attributed to the de-protonation of the adsorbent surface. Similarly, Koohi et al.³¹ reported that the removal of Congo red decreased as the pH was increased after the optimum pH. They also reported that, the adsorption capacity gradually decreased, due to the repulsion between the Congo red ions and the adsorbent molecules. Das et al.³³ investigated the effect of pH on the decolorization of Congo red and reported that, highly acidic and highly basic conditions were not suitable for the decolorization of Congo red solution. They obtained the maximum decolorization of Congo red at pH 7.

The removal of DB-22 increased when the pH was increased from 6.5 to 7.4 (original pH). At the pHs of 7.4

and 8.5, there was no significant change in the removal rate. The removal of DB-22 was found to be 80.4% in pH 9. Sun et al.³⁴ reported similar result for the adsorption of anionic dye reactive red 123 and explained the effect of pH on the adsorption by electrostatic interaction between the adsorbent and the dye molecules. Based on these results, it can be asserted that the adsorption mechanism is not dependent solely on electrostatic interaction. The molecular structure of dyes may also affect the adsorption process.

3. 5. Effect of Temperature

In the study, the effect of temperature on dye removal was also investigated to reveal whether the adsorption process is exothermic or endothermic. The experiments were done at different temperatures at the initial concentration of 30 mg/L, with the adsorbent amount of 1g/200mL and the contact time of 60 min at original pH. Fig. 8 presents the effect of temperature on the removal of DR-28 and DB-22.

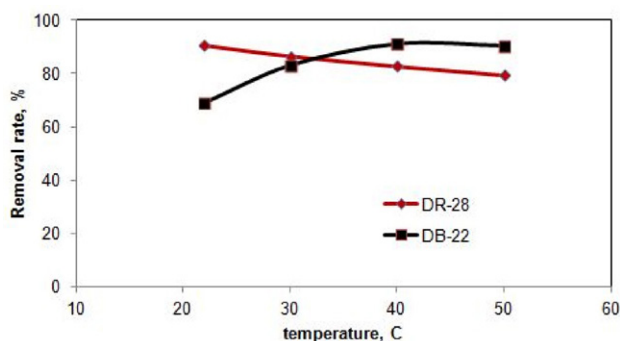


Fig. 8. Effect of temperature on the removal of DR-28 and DB-22 (pH: original, initial concentration: 30 mg/L, adsorbent: KZF, adsorbent amount: 1g/200mL, contact time: 60 min)

The removal of DR-28 decreased with the increasing temperature. This result shows that, the adsorption of DR-28 on KZF was exothermic. As the temperature increases, the tendency of the dye adsorbed on the adsorbent surface to separate from the surface increases.² According to Esvandi et al.³, the adsorption efficiency decreases with increasing the temperature due to the desorption of dye molecules from the adsorbent surface. Maqbool et al.³⁵ investigated the removal of Congo red using free biomass, Na-Alg/CH and PPY/CH conjugates. It was found that the removal of Congo red decreased with increasing temperature due to the weakened Van der Waals force and the H-bonding between the adsorbent and the sorbate.

On the other hand, the removal of DB-22 increased with increasing the temperatures up to 40 °C. The removals of DB-22 at the initial concentration of 30 mg/L and the contact time of 60 min were found to be 69.2%, 83.2% and 91.3% at the solution temperatures of 21, 30, and 40 °C, respectively. After 40 °C, the removal rate remained almost

constant. So, the adsorption of DB-22 on KZF is an endothermic process. Magdy et al.¹⁹ reported similar results for the adsorption of Direct Red 23. The mobility of dye molecules changes with temperature. As the temperature of the solution increases, the mobility of the dye molecules increases and as a result, the number of dye molecules interacting with the free active sites on the composite surface increases.

Based on the experimental results, it can be asserted that the optimum temperatures for the removal of DR-28 and DB-22 were 21 °C and 40 °C, respectively. For this reason, the experiments examining the effect of initial dye concentration were carried out at these optimum temperatures.

3. 6. Effect of Initial Dye Concentration and Contact Time

In the study, the effects of initial dye concentration and contact time on dye removal were also investigated. The experiments were done within an initial concentration range of 20–50 mg/L with an adsorbent amount 1g/200mL, at original pH. The experiments examining the effect of contact time and initial dye concentration were carried out at the optimum temperature values specified in the previous section (i.e., 21 °C for DR-28 and 40 °C for DB-22). Fig. 9 presents the effect of initial dye concentration and contact time on the removal of DR-28 and DB-22.

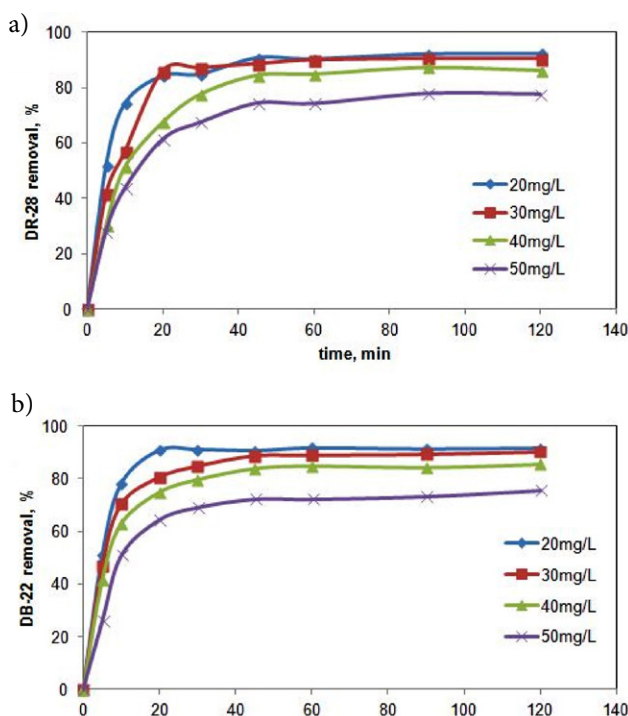


Fig. 9. Effect of initial dye concentration and contact time on the removal of (a) DR-28 and (b) DB-22 (pH: original, temperature: 21 °C (for DR-28), 40 °C (for DB-22), adsorbent: KZF, adsorbent amount: 1g/200mL)

The experimental results showed that the removal rates of DR-28 and DB-22 were faster for the first 20 min, and then slowed down. The removal rate was almost constant after the contact time of 30 min. At the beginning of the adsorption process, active surface area is high. As the time progresses, empty areas begin to fill and the appropriate surface area decreases due to saturation with dye molecules. Accordingly, the rate of the adsorption process decreases and reaches an equilibrium.^{2,30}

As seen in Fig. 9, the removal of DR-28 and DB-22 decreased with the increasing initial dye concentrations. The removals of DR-28 for the contact time of 120 min were found to be 92.4%, 89%, 86% and 77% at the initial dye concentrations of 20, 30, 40, and 50 mg/L, respectively. Similar result was obtained for DB-22. The removals of DB-22 were found to be 91.7%, 90.2%, 85.5%, and 75.6% at the initial DB-22 concentration of 20, 30, 40, and 50 mg/L respectively. Mass transfer occurs due to the concentration difference between the aqueous phase and the adsorbent surface. Initial concentration of the dye solution is the driving force for mass transfer. The removal rate decreases with the increasing initial dye concentration due to the decrease in the number of active sites of the adsorbent.¹⁶ Magdy et al.¹⁹ reported similar results. As the dye concentration increases, the adsorbent reaches saturation quickly for a fixed amount of adsorbent, and the active surfaces are covered with dye molecules. According to Sanad et al.³⁶, at high dye concentrations, the unit mass of the adsorbent is exposed to more dye molecules. As a result, the active sites are gradually filled until they reach saturation causing a decrease in removal efficiency. Boushreen et al.² examined the effect of initial concentration on the removal of methylene blue and methyl violet and reported that the ratio of the active surface area of the adsorbent to the dyes in the solution was high at low dye concentrations, and for this reason, all the dye molecules interacted with the adsorbent, and thus a higher removal efficiency was achieved.

3. 7. Adsorption Isotherms

The adsorption equilibrium data collected at the dye concentrations of 20–50 mg/L were fitted by common isotherms Langmuir and Freundlich models. The Langmuir isotherm model assumes that the adsorbate is coated in a monolayer on the homogeneous adsorbent surface, and the adsorption takes place only at the active sites on the adsorbent. The Freundlich equation is an empirical equation used to describe heterogeneous systems.²⁹

Langmuir and Freundlich models are given in Eqs. (3) and (4), respectively.^{2,22,37}

$$\frac{c_e}{q_e} = \frac{c_e}{q_{max}} + \frac{1}{q_{max}K_L} \quad (3)$$

$$\ln q_e = \ln k_f + \frac{1}{n} \ln c_e \quad (4)$$

$$R_L = \frac{1}{1 + K_L C_0} \quad (5)$$

where q_{\max} is the adsorption capacity (mg/g), K_L is the adsorption energy (L/g), and K_f and n are the Freundlich constants.

The value of R_L specifies whether the adsorption process is irreversible ($R_L=0$), desirable ($0 < R_L < 1$), linear ($R_L=1$) or undesirable ($R_L > 1$). The value of n determines whether the adsorption process is linear ($n=1$), physical ($n > 1$) or chemical ($n < 1$).

The adsorption isotherm models were calculated at the initial dye concentrations of 20–50 mg/L. The other factors, such as initial pH, adsorbent amount, and temperature were kept constant. For DR-28 and DB-22, the initial pH was original pH, and the amount of the adsorbent KZF was 1g/200mL. While the parameters such as adsorbent amount and pH were the same for both dyes, the temperature was 21 °C for DR-28 and 40 °C for DB-22.

The values and constants of the Langmuir and Freundlich isotherm models for DR-28 and DB-22 are given in Table 1. The results of the Langmuir adsorption isotherm models for DR-28 and DB-22 are shown in Fig. 10 and Fig. 11, respectively.

The values of R^2 for the Langmuir model were found to be 0.9969 and 0.9926 for DR-28 and DB-22, respectively. The values of R^2 for the Freundlich model were found to be 0.9308 and 0.8381 for DR-28 and DB-22, respectively. DR-28 and DB-22 adsorptions were found to be in a good agreement with the Langmuir isotherm. The calculated R_L values of DR-28 and DB-22 were between 0 and 1. Based on these results, it can be asserted that the adsorption process was desirable.

Table 1. Langmuir and Freundlich isotherm parameters for the adsorption of DR-28 and DB-22 (pH: original, adsorbent: KZF, adsorbent amount: 1 g/200mL, temperature: 21 °C for DR-28, 40 °C for DB-22)

Isotherm	Constants	DR-28	DB-22
Langmuir	q_{\max} (mg/g)	7.640	8.404
	K_L (L/mg)	0.722	0.605
	R^2	0.9969	0.9926
	R_L	0.027–0.064	0.032–0.076
Freundlich	n	3.59	3.03
	K_f (mg/g)	3.71	3.53
	R^2	0.9308	0.8381

3. 8. Adsorption Thermodynamics

Thermodynamic parameters (ΔG^0 , ΔH^0 , ΔS^0) were calculated using the Eqs. (6), (7), and (8). The values of ΔH^0 and ΔS^0 were calculated from the slope and intercept of a linear plot $\ln K_C$ versus $1/T$.^{4,37,38}

$$\Delta G^0 = \Delta H^0 - T\Delta S^0 \quad (6)$$

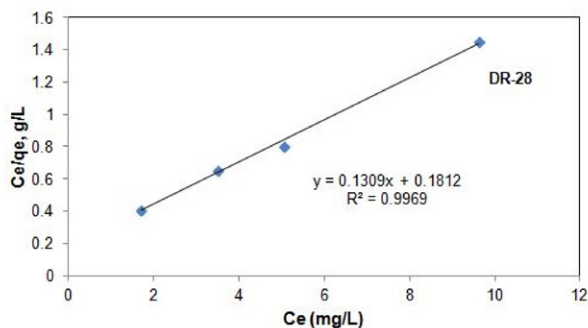


Fig. 10. Langmuir isotherm for DR-28 onto KZF (pH: original, temperature: 21 °C, adsorbent: KZF, adsorbent amount: 1 g/200mL)

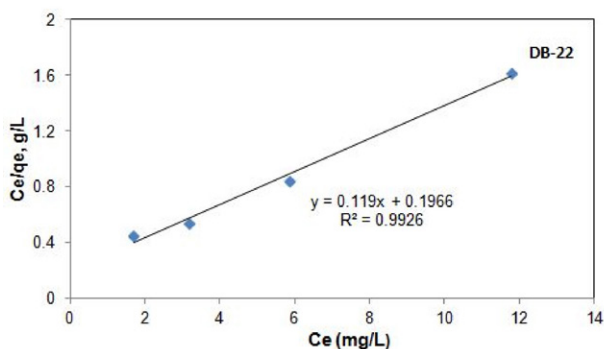


Fig. 11. Langmuir isotherm for DB-22 onto KZF (pH: original, temperature: 40 °C, adsorbent: KZF, adsorbent amount: 1 g/200mL)

$$\ln K_C = -\frac{\Delta G^0}{RT} = \frac{\Delta S^0}{R} - \frac{\Delta H^0}{RT} \quad (7)$$

$$K_C = \frac{q_e}{C_e} \quad (8)$$

where ΔG^0 is the standard change free Gibbs energy (J/mol), ΔH^0 is the standard change enthalpy (J/mol), ΔS^0 is the standard change entropy (J/molK), and R is the universal gas constant (8.314 J/molK), K_C is the ratio of the equilibrium concentration of adsorbate (q_e) loaded to the equilibrium concentration in solution (C_e).

The adsorptions of DR-28 and DB-22 on KZF were thermodynamically studied at an initial concentration of 30 mg/L, with an adsorbent amount of 1g/200mL, and a contact time of 60 min, at the original pH. The results of the thermodynamic study are given in Fig. 12. Table 2 shows the obtained thermodynamic parameters for DR-28 and DB-22.

The enthalpy change (ΔH^0) for DR-28 dyes was found to be -24.59 kJ/mol, which shows that, the adsorption of DR-28 using the composite KZF was exothermic. ΔG^0 values were -1.364 , -0.653 , 0.137 and 0.927 kJ/mol at the adsorption temperatures of 21, 30, 40, and 50 °C, respectively. The negative ΔG^0 values at 21 and 30 °C indicate that the adsorption process occurred spontaneously.²⁹ The positive ΔG^0 values at 40, and 50 °C suggest that the adsorption of DR-28 onto KZF was not a spontaneous pro-

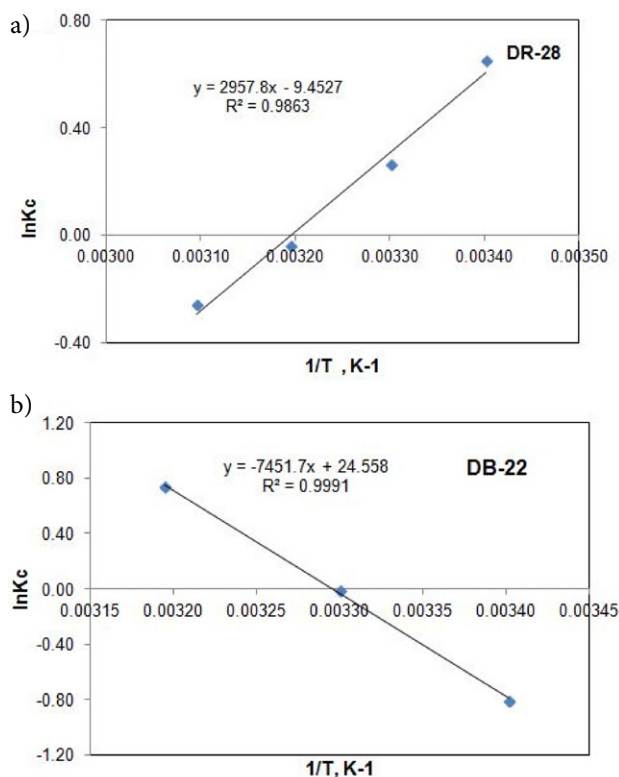


Fig. 12. The thermodynamics of the adsorption of (a) DR-28 and (b) DB-22 on the adsorbent KZF (pH: original, initial concentration: 30 mg/L, contact time: 60 min, KZF amount: 1 g/mL)

cess. The decrease in ΔG^0 value with the decrease in temperature indicates that lower temperatures are suitable for the adsorption of DR-28 molecules onto KZF.²² The value of ΔS^0 for DR-28 dye was also found to be negative. According to Boushehrian et al.², the negative ΔS^0 values indicate a decrease in the random collision of dye molecules and the adsorbent surface during the adsorption process. Maqbool et al.³⁹ reported similar results for the adsorption of BB-41. The negative value of ΔS^0 reveals that the disorder at the solid-solution interface is reduced.

On the other hand, ΔH^0 value for DB-22 was found to be 61.95 kJ/mol, which shows that the adsorption pro-

cess was endothermic. ΔG^0 values were 1.974, 0.138, and -1.902 kJ/mol at the adsorption temperatures of 21, 30, and 40 °C, respectively. The positive ΔG^0 value at 21 and 30 °C indicated that the adsorption process was not spontaneous. The negative ΔG^0 value at 40 °C suggests that the adsorption of DB-22 onto KZF was a spontaneous process.⁴ The decrease in ΔG^0 value with the increase in temperature shows that higher temperatures are suitable for the adsorption of dye molecules onto adsorbent.²² As mentioned in the section 3.5 there was no increase in the removal rate of dye beyond 40 °C. So, there is no need to work at temperatures higher than 40 °C. ΔS^0 was found to be 204 J/mol. The positive ΔS^0 shows the increase in disorder and randomness at the composite KZF and DB-22 dye solution interface during the adsorption process.^{19,40}

3. 9. Adsorption Kinetics

To understand the dynamics of the adsorption process of DR-28 and DB-22 onto KZF, the adsorption kinetic experiments were performed at the adsorbent amount 1g/200mL, with the initial dye concentration of 30 mg/L at original pH. Adsorption temperature was 21 °C for DR-28 and 40 °C for DB-22. Common adsorption kinetic models, pseudo first order equation, and pseudo second order equation were employed to fit the experimental data.

The linear form of the pseudo first order kinetic model is presented as Eq. 9:

$$\ln(q_e - q_t) = \ln q_e - k_1 t \quad (9)$$

In this relation, q_e is the adsorption capacity in the equilibrium state (mg/g), q_t is the adsorption capacity at any time (mg/g), and k_1 is the rate constant (min^{-1}). k_1 can be obtained by drawing the experimental data of $\ln(q_e - q_t)$ versus t .^{2,37}

The pseudo second order kinetic model is given in the Eq. 10:

$$\frac{t}{q_t} = \frac{1}{k_2 q_e^2} + \frac{t}{q_e} \quad (10)$$

where k_2 (g/mg.min) is the rate constant of the pseudo second order kinetics. Drawing the linear graph of t/q_t versus t can provide the pseudo second order kinetic rate parameter.^{2,37,40}

Regression coefficient (R^2) is important to determine the agreement of calculated q_e values with experimental data. A relatively higher R^2 value indicates that the model is suitable for the adsorption process. The values and constants of the pseudo first order and pseudo second order models for DR-28 and DB-22 are given in Table 3 and Table 4, respectively. The results of the pseudo second order model obtained for the adsorption of DR-28 and DB-22 are shown in Fig. 13 and Fig. 14, respectively.

As can be seen in Table 3 and Table 4, the correlation coefficient (R^2) of the pseudo second order model was

Table 2. Thermodynamic parameters for the adsorptions of DR-28 and DB-22 onto KZF

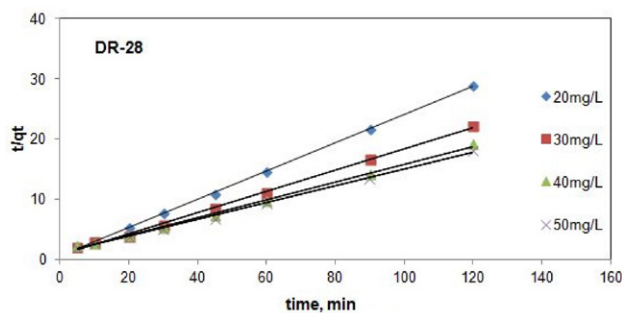
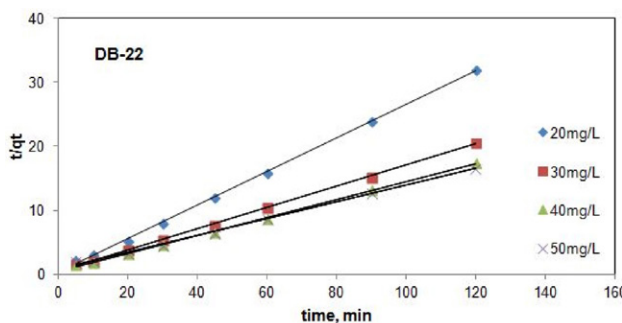
Dye	Temperature (°C)	ΔH^0 (kJ/mol)	ΔS^0 (J/molK)	ΔG^0 (kJ/mol)
DR-28	21	-24.59	-79	-1.364
	30			-0.653
	40			0.137
	50			0.927
DB-22	21	61.95	204	1.974
	30			0.138
	40			-1.902

Table 3. Pseudo first order and pseudo second order kinetic model constants for DR-28 adsorption using the adsorbent KZF

Kinetic model	Parameters	Initial dye concentration of DR-28, mg/L			
		20	30	40	50
Pseudo First Order	R^2	0.9531	0.9205	0.9699	0.8018
	k_1	0.0624	0.0783	0.0727	0.0597
	q_{cal}	1.788	3.009	5.385	4.739
	q_{exp}	4.166	5.434	6.266	6.633
Pseudo Second order	R^2	0.9997	0.9980	0.9974	0.9979
	k_2	0.0755	0.0410	0.0195	0.0177
	q_{cal}	4.292	5.692	6.798	7.179
	q_{exp}	4.17	5.43	6.270	6.63

Table 4. Pseudo first order and pseudo second order kinetic model constants for DB-22 adsorption using the adsorbent KZF

Kinetic model	Parameters	Initial dye concentration of DB-22, mg/L			
		20	30	40	50
Pseudo First Order	R^2	0.532	0.8783	0.7863	0.7998
	k_1	0.0467	0.07	0.0464	0.0338
	q_{cal}	0.372	2.749	2.252	2.718
	q_{exp}	3.754	5.831	6.898	7.265
Pseudo Second order	R^2	0.9992	0.9995	0.9993	0.9976
	k_2	0.145	0.049	0.036	0.021
	q_{cal}	3.83	6.05	7.16	7.65
	q_{exp}	3.75	5.83	6.90	7.27

**Fig. 13** Pseudo second order model for the adsorption of DR-28 onto KZF**Fig. 14** Pseudo second order model for the adsorption of DB-22 onto KZF

higher than that of the pseudo first order. This result shows that the pseudo second order model is the best model for describing the kinetics of KZF toward DR-28 and DB-22.

4. Conclusion

In this study, the adsorption of diazo dye Direct Red 28 (DR-28) and tetra azo dye Direct Black 22 (DB-22) using synthesized magnetic kaolin supported zinc ferrite (KZF) were investigated. KZF was prepared by co-precipitation method. KZF was heat treated at 200 °C for 3h and coded as KZF-200. KZF provided a higher removal of DR-28 and DB-22 than KZF-200. The characteristics of the KZF and KZF-200 were determined using FTIR, SEM, EDS/Elemental Mapping, XRD, and VSM analyses. The highest removal rates of DR-28 and DB-22 with the composite KZF were obtained at the original pH, at the initial dye concentration of 20mg/L, with the adsorbent amount of 1g/200mL, and the contact time of 120 min, and at 21 °C for DR-28 and 40 °C for DB-22. Under these conditions, the removal rates of DR-28 and DB-22 from aqueous solutions were found to be 92.4% and 91.7% respectively. The experimental results were better fitted with the Langmuir isotherm model and adsorption process occurred on the

homogeneous surfaces. The kinetic behavior of the adsorption of DR-28 and DB-22 showed that the pseudo second-order kinetic model was better fitted with the results. The adsorption of DR-28 using KZF resulted in negative ΔH^0 and ΔS^0 values which indicate exothermic in nature and decrease in random collosion. ΔH^0 and ΔS^0 values for the adsorption of DB-22 using KZF were positive. Adsorption of DB-22 was endothermic. The positive ΔS^0 value indicated the increasing of randomness at the solid/liquid interface during the adsorption.

5. References

1. Y. Zhou, J. Lu, Y. Liu, *Env. Pol.* **2019**, *252*, 352–3659. DOI:10.1016/j.envpol.2019.05.072
2. M. M. Boushehrian, H. Hossein Esmaeili, R. Foroutan, *J. Env. Chem. Eng.* **2020**, *8*, 103869. DOI:10.1016/j.jece.2020.103869
3. Z. Esvandia, R. Foroutan, J.S. Peighambaroust, A. Akbari, B. Ramavandi, *Surf. and Int.* **2020**, *21*, 100754. DOI:10.1016/j.surfin.2020.100754
4. M. Fayazi, D. Afzalic, A. Mostafavi, V. K Gupta, *J. Mol. Liq.* **2015**, *212*, 675–685. DOI:10.1016/j.molliq.2015.09.045
5. S. Benkhaya, S. M'rabet, A. El Harfi, A., *In. Chem. Com.* **2020**, *115*, 107891. DOI:10.1016/j.inoche.2020.107891
6. M. Berradi, R. Hsisou, M. Khudhair, M. Assouag, O. Cherkaoui, A. El Bachiri, A. El Harfi, *Hel.* **2019**, *5*, e02711. DOI:10.1016/j.heliyon.2019.e02711
7. S. Benkhaya, S. M'rabet, A. El Harfi, *Hel.* **2020**, *6*, e03271. DOI:10.1016/j.heliyon.2020.e03271
8. B. Meroufel, O. Benali, M. Benyahia, Y. Benmoussa, M. A. Zenasni, *J. Mat. Env. Sc.* **2013**, *4(3)*, 482–491.
9. N. T. Hien, L. H. Nguyen, H. T. Van, T. D. Nguyen, T. H. V. Nguyen, T. H. H. Chu, T. V. Nguyen, V. T. Trinh, X. H. Vu, K. H. H. Aziz, *Sep. Pur. Tech.* **2020**, *233*, 115961. DOI:10.1016/j.seppur.2019.115961
10. H. Patel, R. T. Vashi, *J. Sa. Chem. Soc.* **2012**, *16*, 131–136. DOI:10.1016/j.jscs.2010.12.003
11. R. Saleh, A. Taufik, *Sep. Pur. Tech.* **2019**, *210*, 563–573. DOI:10.1016/j.seppur.2018.08.030
12. M. Khadhraoui, H. Trabelsi M. Ksibi, S. Bouguerra, B. Elleuch, *J. Haz. Mat.* **2009**, *161*, 974–981. DOI:10.1016/j.jhazmat.2008.04.060
13. F. H. AlHamedi, M. A. Rauf, S. S. Ashraf, *Des.* **2009**, *239*, 159–166. DOI:10.1016/j.desal.2008.03.016
14. N. Guy, S. Çakar, M. Özacar, *J. Coll. Int. Sc.* **2016**, *466*, 128–137. DOI:10.1016/j.jcis.2015.12.009
15. M. Hu, X. Yan, X. Hu, J. Zhang, R. Feng, M. Zhou, *J. Coll. Int. Sc.* **2018**, *510*, 111–117. DOI:10.1016/j.jcis.2017.09.063
16. A. Kanwal, H. N. Bhatti, M. Iqbal, S. Noreen, *Wat. Env. Res.* **2017**, *89(4)*, 301–311. DOI:10.2175/106143017x14839994522984
17. Z. Gao, X. Li, H. Wu, H. Zhao, W. Deligeer, S. Asuha, *Mic. Mes. Mater.* **2015**, *202*, 1–7. DOI:10.1016/j.micromeso.2014.09.029
18. Z. Chen, Y. Cheng, Z. Chen, M. Megharaj, R. Naidu, *J. Nanopart. Res.* **2012**, *14:899*, 1–8. DOI:10.1007/s11051-012-0899-0
19. A. Magdy, Y. O. Fouad, M. H. Abdel-Aziza, A. H. Konsowa, *J. Ind. Eng. Chem.* **2017**, *56*, 299–311. DOI:10.1016/j.jiec.2017.07.023
20. F. Sun, Q. Zeng, W. Tian, Y. Zhu, W. Jiang, *J. Env. Chem. Eng.* **2019**, *7*, 103011. DOI:10.1016/j.jece.2019.103011
21. S. J. Olusegun, N. D. S. Mohallem, *Env. Poll.* **2020**, *260*, 114019. DOI:10.1016/j.envpol.2020.114019
22. Q. Huang, M. Liu, J. Chen, K. Wang, D. Xu, F. Deng, H. Huang, X. Zhang, Y. Wei, *J. Mat. Sci.* **2016**, *51*, 8116–8130. DOI:10.1007/s10853-016-0082-6
23. A. H. Jawad, A. S. Abdulhameed, *Surf. Int.* **2020**, *18*, 100422. DOI:10.1016/j.surfin.2019.100422
24. S. Niu, X. Xie, Z. Wang, L. Zheng, F. Gao, Y. Miao, *Env. Tech.* **2021**, *42(10)*, 1472–1481. DOI:10.1080/09593330.2019.1670269
25. D. Ar Rahim, W. Fang, G. Zhu, H. Wibowo, D. Hantoko, Q. Hu, H. Susanto, Z. Gao, M. Yan, *Chem. Eng. Proc.-Pr. Int.* **2021**, *68*, 108565. DOI:10.1016/j.cep.2021.108565
26. D. L. Rossatto, M. S. Netto, S. L. Jahn, E. S. Mallmann, G. L. Dotto, E. L. Foletto, *J. Env. Chem. Eng.* **2020**, *8*, 103804. DOI:10.1016/j.jece.2020.103804
27. R. Nicola, S-G. Muntean, M-A. Nistor, A-M. Putz, L. Almas, L. Sacarescu, *Chemos.* **2020**, *261*, 127737. DOI:10.1016/j.chemosphere.2020.127737
28. A. Souri, F. Golestani-Fard, R. Naghizadeh, S. Veisheh, *App. Cl. Sci.* **2015**, *103*, 34–39. DOI:10.1016/j.clay.2014.11.001
29. C. Cao, L. Xiao, C. Chen, X. Shi, Q. Cao, L. Gao, *Pow. Tech.* **2014**, *260*, 90–97. DOI:10.1016/j.powtec.2014.03.025
30. P. Karthikeyan, S. Meenakshi, *Int. J. Bio. Mac.* **2021**, *168*, 750–759. DOI:10.1016/j.ijbiomac.2020.11.132
31. P. Koohi, A. Rahbar-kelishami, H. Shayesteh, *Env. Tech. Inn.* **2021**, *23*, 101559. DOI:10.1016/j.eti.2021.101559
32. N. M. Mahmoodi, F. Najafi, S. Khorrarnfar, F. Amini, M. Arami, *J Haz Mat.* **2011**, *198*, 87–94. DOI:10.1016/j.jhazmat.2011.10.018
33. R. Das, M. Bhaumik, S. Giri, A. Maity, *Ult. Son.* **2017**, *37*, 600–613. DOI:10.1016/j.ultsonch.2017.02.022
34. D. Sun, X. Zhang, Y. Wu, X. Liu, *J. Haz. Mat.* **2010**, *181*, 335–342. DOI:10.1016/j.jhazmat.2010.05.015
35. M. Maqbool, S. Sadaf, H. N. Bhatti, S. Rehmat, A. Kausar, S. A. Alissa, M. Iqbal, *Surf and Int.* **2021**, *25*, 101183. DOI:10.1016/j.surfin.2021.101183
36. M. M. S. Sanad, M.M. Farahat, M. A. Abdel Khalek, *Adv. Pow. Tech.* **2021**, *32*, 1573–1583. DOI:10.1016/j.apt.2021.03.013
37. R. Salahshour, M. Shanbedi, H. Esmaeili, *Acta Chim. Slov.* **2021**, *68*, 363–373. DOI:10.17344/acs.2020.6311
38. T. A. Aragaw, F. T. Angerasa, *Hel.* **2020**, *6*, e04975. DOI:10.1016/j.heliyon.2020.e04975
39. M. Maqbool, H. N. Bhatti, S. Sadaf, M.M. AL-Anazy, M. Iqbal, *J Mat. Res. Tech.* **2020**, *9(6)*, 14729e14741. DOI: 10.1016/j.jmrt.2020.10.017
40. A. Jabeen, H. N. Bhatti, *Env. Tech and Inn.* **2021**, *23*, 101685. DOI: 10.1016/j.eti.2021.101685

Povzetek

Prisotnost molekul barvil v vodah ima škodljiv vpliv na okolje. Zato je pomembno, da jih odstranimo s pomočjo okolju prijaznih materialov. V tej študiji smo preučevali možnost odstranjevanja diazo barvila Direct Red 28 (DR-28) in tetraazo barvila Direct Black 22 (DB-22) z adsorpcijo na kompozitni nosilec na osnovi kaolina in cinkovega ferita (KZF). Lastnosti KZF kompozita smo določili s pomočjo FTIR, SEM, XRD, VSM in EDS. Adsorpcijo barvil DR-28 in DB-22 na KZF smo preučevali v odvisnosti od kontaktnega časa, začetne koncentracije barvila, količine adsorbenta, temperature, začetne pH vrednosti raztopine ter toplotne obdelave kompozita. Dosegli smo 92.4 % adsorpcijo DR-28 pri KZF koncentraciji 1g/200 mL, začetni koncentraciji barvila 20 mg/L, kontaktnem času 120 min, pri osnovni pH vrednosti in temperaturi 21 °C. Adsorpcija barvila DB-22, pri enakih pogojih le temperaturi 40 °C, pa je bila 91.7 %. Rezultati so pokazali, da je lahko adsorpcijo obeh barvil (DR-28 in DB-22) na KZF opišemo z Langmuirjevo adsorpcijsko izotermo. Adsorpcija barvila DR-28 je eksotermna, medtem ko je adsorpcija barvila DB-22 endotermna. Sprememba entalpije (ΔH^0) pri adsorpciji na KZF je bila 24.59 kJ/mol za DR-28 in 61.95 kJ/mol za DB-22. ΔS^0 adsorpcije je bila pri DR-28 negativna, pri DB-22 pa pozitivna. Hitrost adsorpcije obeh barvil lahko dobro opišemo s kinetiko pseudo-drugega reda. Rezultati kažejo, da lahko pripravljeni KZF kompozit uporabimo za učinkovito odstranjevanje anionskih barvil.



Except when otherwise noted, articles in this journal are published under the terms and conditions of the Creative Commons Attribution 4.0 International License

Scientific paper

Efficient One-Pot Synthesis of 1,4-Dihydropyridines Catalyzed by Magnetic MnFe_2O_4 Nanoparticles

Somayeh Moradi, Mohsen Moradian and Hossein Naeimi*

Department of Organic Chemistry, Faculty of Chemistry, University of Kashan, Kashan, Iran

* Corresponding author: E-mail: naeimi@kashanu.ac.ir

Received: 10-27-2021

Abstract

The efficient one-pot synthesis of some 1,4-dihydropyridines is described by a condensation reaction of some aldehyde derivatives, ethyl acetoacetate and ammonium acetate in the presence of superparamagnetic manganese ferrite nanoparticles at 80 °C. The advantages of this protocol include selectivity, high purity of the products, excellent yields, short reaction times, ease of processing, and environmentally friendly conditions for the synthesis of 1,4-dihydropyridines. In addition, the catalyst can be recovered and reused in multiple runs without significantly reducing the product yield.

Keywords: 1,4-Dihydropyridine; MnFe_2O_4 ; Nanoparticles; Catalyst; Superparamagnetism

1. Introduction

Multicomponent reactions (MCRs) are a very attractive approach as well as an efficient and powerful tool for the synthesis of novel compounds and the discovery of new drugs.^{1–6} In MCRs, three or more flexible and simple compounds are reacted to synthesize complex organic molecules from commercially available starting materials.

The Hantzsch reaction is one of the most popular MCRs and generates 1,4-dihydropyridine (1,4-DHP) derivatives. This reaction, which has received considerable attention in modern synthetic organic chemistry, was first described by A. Hantzsch in 1882.⁷ The Hantzsch reaction is a practical and useful synthetic tool for the preparation of 1,4-dihydropyridines by condensation of ethyl acetoacetate, an aldehyde, and a source of ammonia in the presence of an

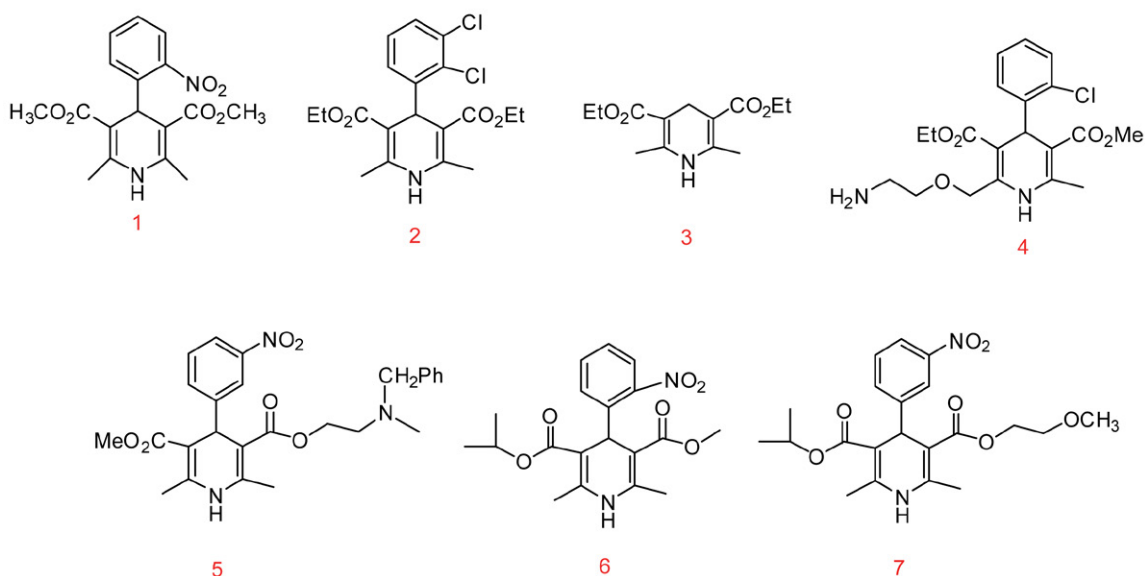


Figure 1. Some biologically active 1,4-dihydropyridines.

alcoholic solvent.⁸ In modern synthetic organic chemistry, 1,4-dihydropyridines are an important group of drugs^{9–11} and calcium channel modulators for the treatment of hypertension,¹² tumors,^{13,14} HIV,¹⁵ cancer,¹⁶ diabetes,¹⁷ apoptosis, and¹⁸ seizures.¹⁹ For example, nifedipine (1), felodipine (2), diludin (3), amlodipine (4), nicardipine (5), nisodipine (6), and nimodipine (7) are synthesized and used worldwide (Figure 1).

Recently, methods have been described using different types of catalysts such as $\text{CeCl}_3 \cdot 7\text{H}_2\text{O}$,²⁰ ionic liquids,^{21,22} TBAB,²³ visible light,^{24,25} chitosan silica sulfate,²⁶ molybdc acid-functionalized nano- $\text{Fe}_3\text{O}_4 @ \text{TiO}_2$,²⁷ $\text{HClO}_4 \cdot \text{SiO}_2$,²⁸ microwave-assisted,²⁹ PW/SiO_2 ,³⁰ solar thermal,³¹ I_2 ,³² sulfonic acid,³³ $\text{Fe}_3\text{O}_4 @ \text{SiO}_2 @ \text{OSO}_3\text{H}$,³⁴ heteropolyacids,³⁵ silica gel/ NaHSO_4 ,³⁶ organocatalysis,³⁷ $\text{AlCl}_3 \cdot 6\text{H}_2\text{O}$,³⁸ and metal triflates.³⁹ Although many of these methods are effective, the search for a more satisfactory catalyst is essential for the preparation of 1,4-DHP. Metal oxide nanocrystals, especially superparamagnetic ones, have recently been used as effective catalysts because of their easy availability and environmentally friendly properties.⁴⁰ Because of the advantages of magnetic nanoparticles, such as low-cost large-scale synthesis, easy separation and reuse using an external magnet, and applicability in industrial processes, their use as catalysts in various organic reactions has been developed.^{41–47} In this research, we describe a useful and simple method for the preparation of 1,4-dihydropyridines from the condensation of ethyl acetoacetate, various aldehydes, and ammonium acetate as a source of ammonia using magnetic MnFe_2O_4 nanoparticles as a catalyst and ethanol as a solvent.

2. Experimental Section

2.1. Apparatus

Chemical reagents and solvents were purchased commercially from Aldrich and Fluka Chemical Companies and used without further purification. A Bruker DRX-400 spectrometer was used to record ^1H NMR and ^{13}C NMR spectra in deuterated chloroform solvent. Infrared spectra (IR) were recorded as KBr pellets using a Nicolet Impact 400 FT-IR spectrophotometer. Elemental analyzes (C, H, and N) were performed using a Perkin Elmer 2400-CHN elemental analyzer. XRD patterns of samples with an X-ray wavelength of 1.54 \AA and Cu anode material were recorded using a Philips X'PertPro X-ray diffractometer at a scanning speed of $2^\circ/\text{min}$ over a range of 10° to 80° (2θ). The powder morphology of the catalyst was determined using a Hitachi S4160 as a field emission scanning electron microscope (FE-SEM). The magnetic properties of the nanoparticles were determined by vibrational magnetometric measurements (VSM, PPMS-9T) at 300 K in Iran (College of Kashan, Iran). The melting points were determined using a Yanagimoto micro-melting point apparatus. The course of the reaction was checked by thin

layer chromatography (TLC) on silica gel polygram SILG/UV 254 plates.

2.2. General Procedure for the Synthesis of MnFe_2O_4 NPs

MnFe_2O_4 nanoparticles were synthesized by simple coprecipitation of $\text{FeCl}_3/\text{MnCl}_2$ in alkaline NaOH medium. First, 100 ml solution of the two salts $\text{FeCl}_3 \cdot 6\text{H}_2\text{O}$ and $\text{MnCl}_2 \cdot 4\text{H}_2\text{O}$ were prepared such that the molar ratio of $\text{Mn}^{2+}:\text{Fe}^{3+}$ molar ratio was 2:1. For this purpose, 0.02 mol of Fe(III) salt and 0.01 mol of Mn(II) salt were dissolved in distilled water and the volume of the solution was made up to 100 mL. Then, the desired solution was added dropwise into a solution of NaOH (100 mL , 3 mol L^{-1}) at 95°C with constant stirring for 2 h. The solution was then added to the solution of NaOH (100 mL , 3 mol L^{-1}). At the end of the desired time, the solid was collected with an external magnetic field, washed with ethanol ($3 \times 20 \text{ mL}$) and deionized water ($5 \times 30 \text{ mL}$), and then dried at 60°C for 12 h. The solid was then removed from the solution. The MnFe_2O_4 nanoparticles were characterized by physical and spectroscopic data.

2.3. A General Method for the Synthesis of 1,4-dihydropyridines

A mixture of ethyl acetoacetate (2.4 mmol), selected aldehyde (1 mmol), NH_4OAc (1.2 mmol), and MnFe_2O_4 (5 mol%) in ethanol (5 mL) as solvent was stirred at 80°C for an appropriate time. The progress of the reaction was followed by thin layer chromatography (TLC). After completion of the reaction, the mixture was diluted with ethyl acetate and the solid catalyst was separated and collected using a magnetic field. The desired product was extracted with ethyl acetate and water and purified by recrystallization from ethanol/water (5:1) to afford pure 1,4-dihydropyridines. The solid magnetic MnFe_2O_4 catalyst was carefully washed with acetone ($3 \times 10 \text{ ml}$) and distilled water ($3 \times 10 \text{ ml}$), and dried at room temperature in a desiccator. The structure of the new compounds was identified from the physical and spectroscopic data.

2.4. Spectral Data for 1,4-dihydropyridine Derivatives

Diethyl 2,6-dimethyl-4-(3-nitrophenyl)-1,4-dihydropyridine-3,5-dicarboxylate (4a); Yellow solid; m.p. = $162\text{--}167^\circ\text{C}$; IR (KBr, cm^{-1}) ν : 3344 (NH), 3093 ($=\text{CH}_2$), 2987 ($-\text{CH}_2$, sp^3), 1706 (C=O), 1645 (C=C), 1213 (C-O); ^1H NMR (400 MHz, CDCl_3 , ppm) δ : 1.23 (t, $J=7.2 \text{ Hz}$, 6H, 2CH_3), 2.36 (s, 6H, 2CH_3), 4.08 (q, 4H, 2CH_2), 5.08 (s, 1H), 5.86 (s, 1H, NH), 7.37 (t, $J=8 \text{ Hz}$, 1H, ArH), 7.64 (d, $J=7.6 \text{ Hz}$, 1H, ArH), 7.99 (d, $J=7.2 \text{ Hz}$, 1H, ArH), 8.12 (s, 1H, ArH).

Diethyl 2,6-dimethyl-4-phenyl-1,4-dihydropyridine-3,5-dicarboxylate (4b); Yellow solid; m.p. = $150\text{--}155^\circ\text{C}$; IR

(KBr, cm^{-1}) v: 3342 (NH), 3061 ($=\text{CH}_2$), 2980 ($-\text{CH}$, sp^3), 1690 ($\text{C}=\text{O}$), 1651 ($\text{C}=\text{C}$), 1211 ($\text{C}-\text{O}$); ^1H NMR (400 MHz, CDCl_3 , ppm) δ : 1.22 (t, $J=7.2$ Hz, 6H, 2CH_3), 2.33 (s, 6H, 2CH_3), 4.10 (q, 4H, 2CH_2), 4.98 (s, 1H), 5.66 (s, 1H, NH), 7.10–7.27 (m, 5H, ArH).

Diethyl 2,6-dimethyl-4-(4-nitrophenyl)-1,4-dihydropyridine-3,5-dicarboxylate (4c); Light yellow solid; m.p. = 125–128 °C; IR (KBr, cm^{-1}) v: 3320 (NH), 3101 ($=\text{CH}_2$), 2980 ($-\text{CH}$, sp^3), 1701 ($\text{C}=\text{O}$), 1646 ($\text{C}=\text{C}$), 1214 ($\text{C}-\text{O}$); ^1H NMR (400 MHz, CDCl_3 , ppm) δ : 1.21 (t, $J=7.2$ Hz, 6H, 2CH_3), 2.36 (s, 6H, 2CH_3), 4.06 (q, 4H, 2CH_2), 5.09 (s, 1H), 5.74 (s, 1H, NH), 7.44 (d, $J=8.8$ Hz, 2H, ArH), 8.07 (d, $J=8.8$ Hz, 2H, ArH).

Diethyl 4-(4-chlorophenyl)-2,6-dimethyl-1,4-dihydropyridine-3,5-dicarboxylate (4d); Yellow solid; m.p. = 140–145 °C; IR (KBr, cm^{-1}) v: 3356 (NH), 3091 ($=\text{CH}_2$), 2988 ($-\text{CH}$, sp^3), 1696 ($\text{C}=\text{O}$), 1651 ($\text{C}=\text{C}$ alkene), 1213 ($\text{C}-\text{O}$); ^1H NMR (400 MHz, CDCl_3 , ppm) δ : 1.22 (t, $J=6.8$ Hz, 6H, 2CH_3), 2.32 (s, 6H, 2CH_3), 4.08 (q, 4H, 2CH_2), 4.95 (s, 1H), 5.70 (s, 1H, NH), 7.16 (d, $J=8.8$ Hz, 2H, ArH), 7.21 (d, $J=8.4$ Hz, 2H, ArH).

Diethyl 4-(2-chlorophenyl)-2,6-dimethyl-1,4-dihydropyridine-3,5-dicarboxylate (4e); White solid. m.p. = 118–120 °C; IR (KBr, cm^{-1}) v: 3325 (NH), 3060 ($=\text{CH}_2$), 2978 ($-\text{CH}$, sp^3), 1699 ($\text{C}=\text{O}$), 1671 ($\text{C}=\text{C}$), 1613, 1491 ($\text{C}=\text{C}$, Ar), 1206 ($\text{C}-\text{O}$); ^1H NMR (CDCl_3 , 400 MHz, δ / ppm): 1.20 (t, $J=7.2$ Hz, 6H, 2CH_3), 2.31 (s, 6H, 2CH_3), 4.07 (q, 4H, 2CH_2), 5.39 (s, 1H), 5.65 (s, 1H, NH), 7.04 (t, $J=7.6$ Hz, 1H, ArH), 7.12 (t, $J=7.6$ Hz, 1H, ArH), 7.22 (d, $J=8$ Hz, 1H, ArH), 7.37 (d, $J=1.6$ Hz, 1H, ArH).

Diethyl 4-(2,4-dichlorophenyl)-2,6-dimethyl-1,4-dihydropyridine-3,5-dicarboxylate (4h); Yellow solid; m.p. = 140–142 °C; IR (KBr, cm^{-1}) v: 3378 (NH), 3087 ($=\text{CH}_2$), 2980 ($-\text{CH}$, sp^3), 1699 ($\text{C}=\text{O}$), 1679 ($\text{C}=\text{C}$), 1617, 1494 ($\text{C}=\text{C}$, Ar), 1201 ($\text{C}-\text{O}$); ^1H NMR (400 MHz, CDCl_3 , ppm) δ : 1.20 (t, $J=7.2$ Hz, 6H, 2CH_3), 2.31 (s, 6H, 2CH_3), 4.07 (q, 4H, 2CH_2), 5.35 (s, 1H), 5.61 (s, 1H, NH), 7.10 (d, $J=7.6$ Hz, 1H, ArH), 7.25 (s, 1H, ArH), 7.31 (d, $J=8.0$ Hz, 1H, ArH).

Diethyl 4-(3-methoxyphenyl)-2,6-dimethyl-1,4-dihydropyridine-3,5-dicarboxylate (4i); Yellow solid; m.p. = 119–123 °C; IR (KBr, cm^{-1}) v: 3342 (NH), 3095 ($=\text{CH}_2$), 2983 ($-\text{CH}$, sp^3), 1699 ($\text{C}=\text{O}$), 1649 ($\text{C}=\text{C}$), 1605, 1487 ($\text{C}=\text{C}$, Ar), 1215 ($\text{C}-\text{O}$); ^1H NMR (400 MHz, CDCl_3 , ppm) δ : 1.23 (t, $J=7.2$ Hz, 6H, 2CH_3), 2.32 (s, 6H, 2CH_3), 3.76 (s, 3H, CH_3), 4.11 (q, 4H, 2CH_2), 4.98 (s, 1H), 5.72 (s, 1H, NH), 6.67 (d, $J=8.8$ Hz, 1H, ArH), 6.84 (s, 1H, ArH), 6.89 (d, $J=6.8$ Hz, 1H, ArH), 7.13 (t, $J=8.0$ Hz, 1H, ArH).

Diethyl 4-(4-methoxyphenyl)-2,6-dimethyl-1,4-dihydropyridine-3,5-dicarboxylate (4j); White solid; m.p. = 150–155 °C; IR (KBr, cm^{-1}) v: 3343 (NH), 2983 ($-\text{CH}$, sp^3), 1689 ($\text{C}=\text{O}$), 1650 ($\text{C}=\text{C}$), 1210 ($\text{C}-\text{O}$); ^1H NMR (400 MHz, CDCl_3 , ppm) δ : 1.23 (t, $J=7.2$ Hz, 6H, 2CH_3), 2.32 (s, 6H, 2CH_3), 3.75 (s, 3H, CH_3), 4.09 (q, 4H, 2CH_2), 4.93 (s, 1H), 5.60 (s, 1H, NH), 6.75 (d, $J=8.8$ Hz, 2H, ArH), 7.20 (d, $J=8.4$ Hz, 2H, ArH).

Diethyl 4-(4-fluorophenyl)-2,6-dimethyl-1,4-dihydropyridine-3,5-dicarboxylate (4i); Yellow solid; m.p. = 145–147 °C; IR (KBr, cm^{-1}) v: 3343 (NH), 3068 ($=\text{CH}_2$), 2983 ($-\text{CH}$, sp^3), 1688 ($\text{C}=\text{O}$), 1652 ($\text{C}=\text{C}$), 1210 ($\text{C}-\text{O}$); ^1H NMR (400 MHz, CDCl_3 , ppm): 1.21 (t, $J=7.2$ Hz, 6H, 2CH_3), 2.33 (s, 6H, 2CH_3), 4.04 (q, 4H, 2CH_2), 4.95 (s, 1H), 5.67 (s, 1H, NH), 6.88 (t, $J=8.4$ Hz, 2H, ArH), 7.23 (t, $J=5.6$ Hz, 2H, ArH).

Diethyl 4-(2-bromophenyl)-2,6-dimethyl-1,4-dihydropyridine-3,5-dicarboxylate (4f); Yellow solid; m.p. = 128–131 °C; IR (KBr, cm^{-1}) v: 3325 (NH), 3058 ($=\text{CH}_2$), 2978 ($-\text{CH}$, sp^3), 1698 ($\text{C}=\text{O}$), 1673 ($\text{C}=\text{C}$), 1613, 1490 ($\text{C}=\text{C}$, Ar), 1208 ($\text{C}-\text{O}$); ^1H NMR (400 MHz, CDCl_3 , ppm) δ : 1.20 (t, $J=7.2$ Hz, 6H, 2CH_3), 2.30 (s, 6H, 2CH_3), 4.08 (q, 4H, 2CH_2), 5.36 (s, 1H), 5.62 (s, 1H, NH), 6.96 (t, $J=8.8$ Hz, 1H, ArH), 7.17 (t, $J=7.2$ Hz, 1H, ArH), 7.38 (d, $J=1.6$ Hz, 1H, ArH), 7.42 (d, $J=8.0$ Hz, 1H, ArH).

Diethyl 4-(4-(dimethylamino) phenyl)-2,6-dimethyl-1,4-dihydropyridine-3,5-dicarboxylate (3k); Yellow solid; m.p. = 195–200 °C; IR (KBr, cm^{-1}) v: 3321 (NH), 3094 ($=\text{CH}_2$), 2978 ($-\text{CH}$, sp^3), 1695 ($\text{C}=\text{O}$), 1674 ($\text{C}=\text{C}$), 1492, 1613 ($\text{C}=\text{C}$, Ar), 1203 ($\text{C}-\text{O}$); ^1H NMR (400 MHz, CDCl_3 , ppm) δ : 1.24 (t, $J=7.2$ Hz, 6H, 2CH_3), 2.32 (s, 6H, 2CH_3), 2.89 (s, 6H, CH_3), 4.08 (q, 4H, 2CH_2), 4.88 (s, 1H), 5.65 (s, 1H, NH), 6.61 (d, $J=8.4$ Hz, 2H, ArH), 7.17 (d, $J=7.2$ Hz, 2H, ArH).

Diethyl 2,6-dimethyl-4-(p-tolyl)-1,4-dihydropyridine-3,5-dicarboxylate (4o); White solid; m.p. = 139–140 °C; IR (KBr, cm^{-1}) v: 3358 (NH), 2986 ($-\text{CH}$, sp^3), 1695 ($\text{C}=\text{O}$), 1652 ($\text{C}=\text{C}$), 1203 ($\text{C}-\text{O}$); ^1H NMR (400 MHz, CDCl_3 , ppm) δ : 1.23 (t, $J=7.2$ Hz, 6H, 2CH_3), 2.27 (s, 3H, CH_3), 2.32 (s, 6H, 2CH_3), 4.08 (q, 4H, 2CH_2), 4.95 (s, 1H), 5.62 (s, 1H, NH), 7.01 (d, $J=7.6$ Hz, 2H, ArH), 7.17 (d, $J=8.0$ Hz, 2H, ArH).

Diethyl 4-(2-fluorophenyl)-2,6-dimethyl-1,4-dihydropyridine-3,5-dicarboxylate (4g); Yellow solid; m.p. = 155–157 °C; IR (KBr, cm^{-1}) v: 3332 (NH), 3104 ($=\text{CH}_2$), 2982 ($-\text{CH}$, sp^3), 1694 ($\text{C}=\text{O}$), 1651 ($\text{C}=\text{C}$), 1215 ($\text{C}-\text{O}$); ^1H NMR (400 MHz, CDCl_3 , ppm) δ : 1.19 (t, $J=7.2$ Hz, 6H, 2CH_3), 2.31 (s, 6H, 2CH_3), 4.03 (q, 4H, 2CH_2), 5.24 (s, 1H), 5.70 (s, 1H, NH), 6.92 (t, $J=9.6$ Hz, 1H, ArH), 6.99 (t, $J=7.6$ Hz, 1H, ArH), 7.08 (t, $J=7.2$ Hz, 1H, ArH), 7.30 (t, $J=7.2$ Hz, 1H, ArH).

Diethyl 2',6'-dimethyl-1',4'-dihydro-[2,4'-bipyridine]-3',5'-dicarboxylate (4n); Brown solid; m.p. = 188–191 °C; IR (KBr, cm^{-1}) v: 3172 (NH), 2982 ($-\text{CH}$, sp^3), 1695 ($\text{C}=\text{O}$), 1670 ($\text{C}=\text{C}$), 1478, 1639 ($\text{C}=\text{C}$, Ar), 1212 ($\text{C}-\text{O}$); ^1H NMR (400 MHz, CDCl_3 , ppm) δ : 1.20 (t, $J=7.2$ Hz, 6H, 2CH_3), 2.26 (s, 6H, 2CH_3), 4.05 (q, 4H, 2CH_2), 5.20 (s, 1H), 7.17 (d, $J=5.2$ Hz, 1H, ArH), 7.43 (d, $J=6.8$ Hz, 1H, ArH), 7.62 (t, $J=7.2$ Hz, 1H, ArH), 8.51 (d, $J=4.4$ Hz, 1H, ArH), 8.71 (s, 1H, NH).

Diethyl 4-(3-hydroxyphenyl)-2,6-dimethyl-1,4-dihydropyridine-3,5-dicarboxylate (4m); White solid; m.p. = 168–170 °C; IR (KBr, cm^{-1}) v: 3351 (NH), 2978 ($-\text{CH}$, sp^3), 1651 ($\text{C}=\text{O}$), 1593 ($\text{C}=\text{C}$), 1217 ($\text{C}-\text{O}$); ^1H NMR (400

MHz, CDCl_3 , ppm) δ : 1.23 (t, $J=7.2$ Hz, 6H, 2CH_3), 2.32 (s, 6H, 2CH_3), 4.10 (q, 4H, 2CH_2), 4.97 (s, 1H), 5.71 (s, 1H, NH), 6.62 (d, $J=7.2$ Hz, 1H, ArH), 6.78 (s, 1H, ArH), 6.87 (d, $J=7.2$ Hz, 1H, ArH), 7.07 (t, $J=7.6$ Hz, 1H, ArH).

Diethyl 4-(9,10-dioxo-9,10-dihydroanthracen-2-yl)-2,6-dimethyl-1,4-dihydropyridine-3,5-dicarboxylate (3p); Brown solid; m.p. = 195–200 °C; IR (KBr, cm^{-1}) ν : 3293 (NH), 2983 (-CH, sp^3), 1670 (C=O), 1637 (C=C), 1214 (C-O); ^1H NMR (400 MHz, CDCl_3 , ppm) δ : 1.20 (t, $J=7.2$ Hz, 6H, 2CH_3), 2.32 (s, 6H, 2CH_3), 4.05 (q, 4H, 2CH_2), 5.33 (s, 1H), 6.17 (s, 1H, NH), 7.74 (m, 4H, ArH), 8.01 (d, $J=8.0$ Hz, 1H, ArH), 8.21 (m, 2H, ArH); ^{13}C NMR (100 MHz, CDCl_3 , ppm) δ : 15.23, 20.18, 41.58, 62.81, 102.05, 126.94, 130.68, 131.36, 132.62, 133.87, 134.18, 134.94, 135.25, 144.76, 152.63, 167.54, 181.94. Anal. Calcd. for $\text{C}_{27}\text{H}_{25}\text{NO}_6$: C, 70.58; H, 5.48; N, 3.05. Found: C, 70.91; H, 5.51; N, 3.07.

3. Results and Discussion

3.1. Characterization of MnFe_2O_4 Nanocrystals.

Exploring new efficient strategies for the synthesis of organic compounds is a crucial approach for the expansion of science and technology. In this research, a magnetic nanoparticle catalyst was used in the Hantzsch reaction to prepare 1,4-dihydropyridine derivatives (DHP) in high yield. Superparamagnetic MnFe_2O_4 nanocrystals prepared from MnCl_2 and FeCl_3 via a co-precipitation routine were confirmed and characterized by a vibrating magnetometer (VSM), a scanning electron microscope (SEM), Fourier transform infrared spectroscopy (FT-IR), and X-ray diffraction (XRD). Figure 2 shows the FT-IR spectra of magnetic MnFe_2O_4 nanoparticles. The FT-IR spectrum shows an absorption band at about 550 cm^{-1} related to the Fe-O stretching vibration. It also shows a band at 1621 cm^{-1} , which is due to the O-H deformation vibration, and a band at 3403 cm^{-1} , which is from the O-H stretching vibration and is related to the surface hydroxyl groups and physisorbed water.

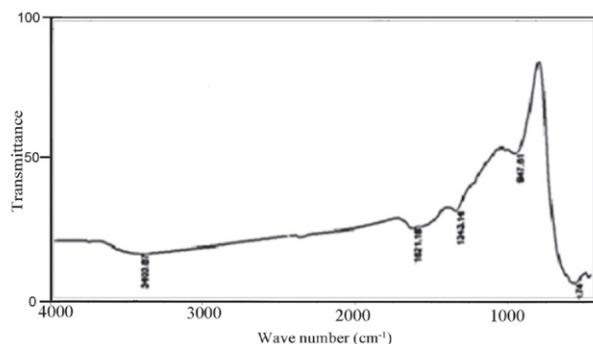


Figure 2. FT-IR spectra of MnFe_2O_4 nanoparticles.

Intensity and position of all peaks agreed well with the standard MnFe_2O_4 X-ray diffraction pattern (JCPDS chart No. 73-1964), and the particle size of about 33 nm was estimated from the line broadening at half maximum intensity (FWHM) at $2\theta = 35.31$ using Debye–Scherrer equation; $D = 0.9\lambda/\beta \cos\theta$ (Figure 3).

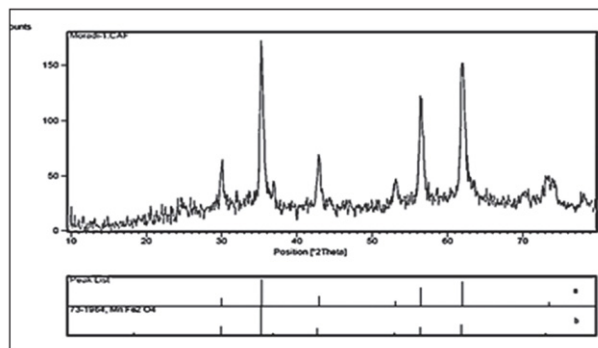


Figure 3. The X-ray diffraction patterns of the prepared MnFe_2O_4 NPs.

The micro- and nanoscale size and morphology of MnFe_2O_4 were studied by scanning electron microscopy (SEM). As Figure 4 shows, MnFe_2O_4 -NP were spherical particles with an average size in the range of 33–35 nm.

VSM measures the magnetic properties of MnFe_2O_4 nanoclusters; hysteresis loops of MnFe_2O_4 nanoparticles were checked using a vibrating sample magnetometer (VSM). Figure 5 shows that the magnetization loop of MNPs exhibits superparamagnetic property with magnetization saturation of 57 emu g^{-1} . The superparamagnetism of MNPs is very advantageous because the particles are magnetized in an existing external magnetic field but show no magnetization in the absence of a magnet. Therefore, they are highly dispersed in the reaction medium and allow rapid penetration of reactants to the surface of the nanoparticles as an efficient catalyst.

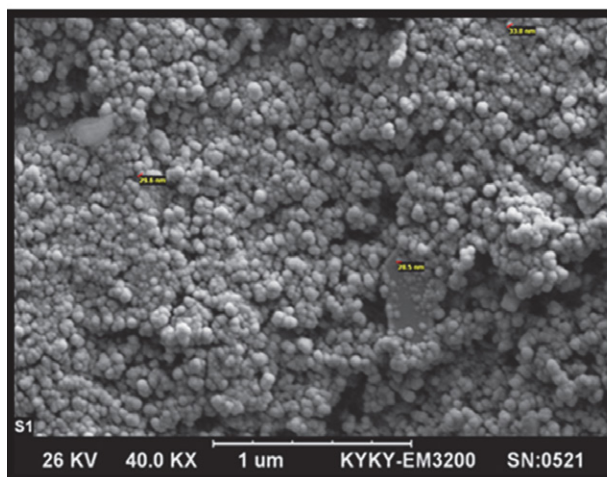


Figure 4. SEM image of MnFe_2O_4 nanoparticles.

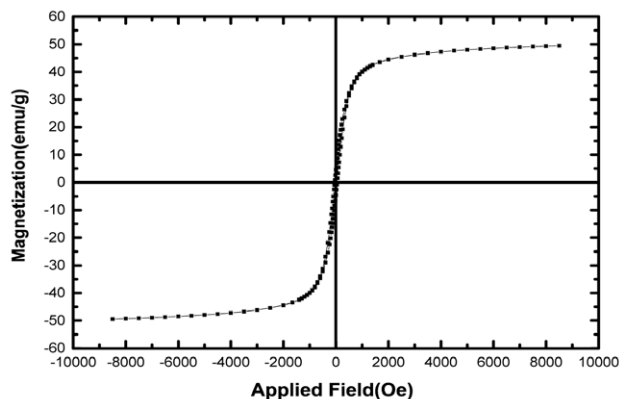


Figure 5. Magnetization curves of the prepared MnFe_2O_4 nanoparticles.

3. 2. Optimization and Generalization of Reaction Conditions

To investigate the catalytic activity of MnFe_2O_4 MNP catalysts, their catalytic performance in the reaction of ethyl acetoacetate (1), 3-nitrobenzaldehyde (2), and ammonium acetate (3) was studied (see Scheme 1).



Scheme 1. Model reaction for the synthesis of diethyl-1,4-dihydro-2,6-dimethyl-4-(3-nitrophenyl)pyridine-3,5-dicarboxylate.

To optimize the reaction, the influence of different polar solvents tested for the preparation of 1,4-dihydro-2,6-dimethyl-4-(3-nitrophenyl)-pyridine-3,5-dicarboxylate was first investigated. Among the solvents used, such as acetonitrile (CH_3CN), ethanol, THF, and H_2O , EtOH is the most suitable for this reaction according to the data in Table 1, entries 5–7, because it is polar and protic (Table 1, entry 3).

Different amounts of catalyst (2, 4, 5, and 8 mol%) were used to optimize the amount of catalyst. It was found that 5 mol% catalyst loading gave the highest yield in the shortest possible time (Table 1, entry 3). Therefore, the optimum catalyst loading was set at 5 mol% MnFe_2O_4 NPs.

To determine the optimum reaction temperature, the sample reaction was carried out at 60 to 90 °C (Table 1, entries 8–11). From the results, it was concluded that the highest yield in the shortest possible time for the synthesis of the product was ob-

Table 1. Optimization of the reaction conditions.^a

Entry	Catalyst (mol %)	Solvent	T (°C)	Time (min)	Yield (%) ^b
1	2	EtOH	78	120	75
2	4	EtOH	78	80	85
3	5	EtOH	78	45	95
4	8	EtOH	78	45	95
5	5	H_2O	80	45	80
6	5	THF	60	130	55
7	5	CH_3CN	80	150	45
8	5	EtOH	60	80	80
9	5	EtOH	70	60	85
10	5	EtOH	78	45	95
11	5	EtOH	90	50	95

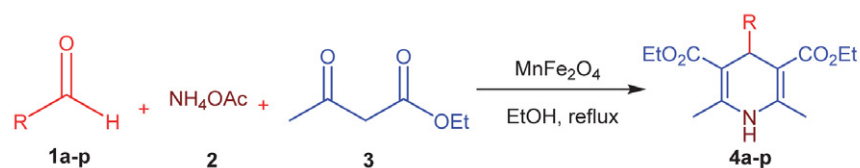
^a Reaction conditions: aldehyde (1 mmol), ethyl acetoacetate (2.4 mmol), ammonium acetate (1.2 mmol). ^b Isolated yields.

tained at a reflux temperature of 78 °C (Table 1, entry 10).

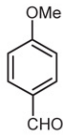
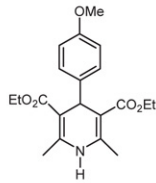
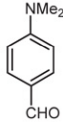
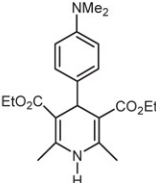
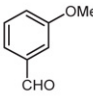
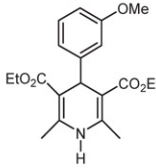
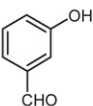
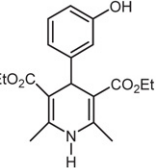
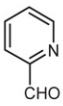
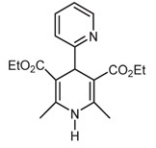
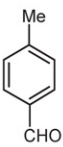
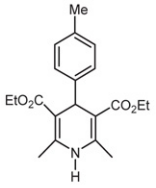
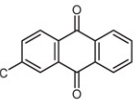
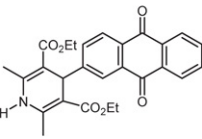
In this study, the reaction for the synthesis of various 1,4-dihydropyridines using MnFe_2O_4 nanoparticles as a heterogeneous catalyst was carried out to develop the scope and generality of this method considering the optimal reaction conditions. In this step,

some aromatic functionalized derivatives of aldehydes with both electron donating and electron withdrawing properties were used for the reaction. The corresponding results are summarized in Table 2. It is noteworthy that the benzaldehyde derivatives with electron-withdrawing functional groups, such as 3-nitrobenzaldehyde and 4-chlorobenzaldehyde, etc., gave excellent yields of the corresponding products (Table 2, entries 1, 3–9), compared with an electron-donating group, which has a lower yield in the reaction (Table 2, entries 10–13).

The structure of MnFe_2O_4 is a mixed spinel that has a close packing of face-centered cubic lattices. The octahedral (Oh) and tetrahedral (Td) sites are occupied by Mn^{2+} and Fe^{3+} cations. The Oh sites are occupied by $\text{Mn}_x^{2+}\text{Fe}_{2-x}^{3+}$, and the metal ions are coordinated with six oxygen atoms, and the Td sites are occupied by $\text{Mn}_{1-x}^{2+}\text{Fe}_x^{3+}$ ($0 < x < 1$), and the metal ions are coordinated with four oxygen atoms. Since the Td sites have low

Table 2. Synthesis of different 1,4-dihydropyridines from several aldehydes.

Entry	Aldehyde	Product	Time (min)	Yield (%) ^b	Ref.
1			45	95	[50]
2			40	90	[51]
3			45	95	[51]
4			40	92	[50]
5			50	89	[50]
6			40	91	[52]
7			40	90	[52]
8			45	92	[53]
9			40	91	[52]

Entry	Aldehyde	Product	Time (min)	Yield (%) ^b	Ref.	
10			4j	70	88	[51]
11			4k	60	85	[50]
12			4l	70	87	[35]
13			4m	50	90	[50]
14			4n	45	90	[54]
15			4o	80	82	[54]
16			4p	50	82	–

– ^a Reaction conditions: aldehyde (1 mmol), ethyl acetoacetate (2.4 mmol), ammonium acetate (1.2 mmol), and Mn-Fe₂O₄ (5 mol%) in ethanol (5 ml) as solvent at 78 °C. ^b Isolated yield.

steric hindrance compared to the Oh sites, the Mn atoms can act as more effective Lewis acid sites. The interaction between the Mn atoms of the nanocatalyst and the active sites of the substrate is more favorable.^{48,49}

In agreement with the reaction mechanism proposed by some research groups,^{55–57} the role of the nanocatalyst can be explained as follows. The activation of the electrophilic components of the carbonyl groups of aldehyde and acetoacetate adducts by Lewis acid moieties on the magnetic nanoparticles could be the driving force of the reaction. The first step involves the condensation of benzaldehyde and the enol form of ethyl acetoacetate to form the

Knoevenagel adduct. At the same time, another intermediate is formed by the reaction of ammonia from ammonium acetate with the second equivalent of ethyl acetoacetate. Subsequently, the two intermediates formed in the above steps are reacted with each other, and the subsequent cyclocondensation and dehydration give the 1,4-dihydropyridine as the target product.

To emphasize the value of this study, the results obtained were compared with recently published work in Table 3. For this comparison, reaction conditions, reaction time and yield were considered in the synthesis of product **4b**. It is worth noting that the efficiency of MnFe₂O₄ NPs

as catalyst in this method is higher and easier to handle than some of the reported methods (Table 3, entry 11 versus entries 1–10).

of the catalyst with a permanent magnet, and reusability of the catalyst five times without significant deterioration of its activity.

Table 3. Comparison of the synthesis of 1,4-DHP (**4b**) using MnFe_2O_4 NPs with methods described in the literature.

Entry	Catalyst (amount)	Reaction conditions	Time (min)	Yield (%)	Ref.
1	$\text{CeCl}_3 \cdot 7\text{H}_2\text{O}$ (10 mol %)	H_3CCN , r.t.,	180	80	[20]
2	[HMIM] BF_4 (Excess)	90 °C	10	95	[21]
3	[(CH_2) $_4\text{SO}_3\text{HMIM}$][HSO_4] (25 mol %)	$\text{C}_2\text{H}_5\text{OH}$, reflux	67	90	[22]
4	MgBr_2 (10 mol %)	solvent-free, 100 °C	45	82	[23]
5	HClO_4 - SiO_2 (50 mg)	solvent-free, 80 °C	25	90	[28]
6	I_2 (30 mol %)	$\text{C}_2\text{H}_5\text{OH}$, r.t.,	150	93	[32]
7	SiO_2 - SO_3H (0.2 g)	<i>n</i> -Hexane, 60 °C	330	90	[33]
8	$\text{H}_{14}[\text{NaP}_5\text{W}_{30}\text{O}_{110}]$ (0.01 g)	water, reflux	480	76	[35]
9	NaHSO_4 - SiO_2 (5 mol %)	H_3CCN , r.t.,	360	85	[36]
10	$\text{AlCl}_3 \cdot 6\text{H}_2\text{O}$ (10 mol %)	solvent-free, 60 °C	60	80	[38]
11	MnFe_2O_4 NPs (5 mol %)	$\text{C}_2\text{H}_5\text{OH}$, 78 °C	45	95	This work

The reusability of the magnetic MnFe_2O_4 nanocatalyst, as shown in Figure 6, was investigated using the desired reaction under optimized conditions. The catalyst was isolated by an external magnet after each reaction and then carefully washed 3–4 times with ethanol and acetone. The catalyst was dried at a temperature of 60 °C and used five times without significant loss of catalytic activity. The weight percentage recovery of the catalyst after the reaction shows a negligible weight loss of about 0.3% and > 99.7% of the catalyst was recovered.

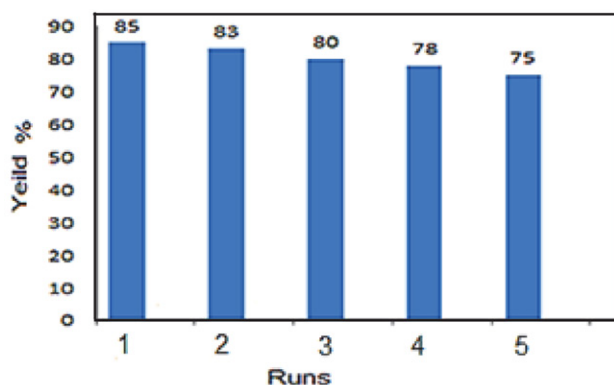


Figure 6. Reusability of the MnFe_2O_4 nanoparticles as catalyst.

4. Conclusion

In this protocol, we synthesized superparamagnetic MnFe_2O_4 nanoparticles and used them as an efficient catalyst in the synthesis of 1,4-dihydropyridines by one-pot condensation of aldehydes, ethyl acetoacetate, and ammonium acetate. The advantages of this method include high purity, good yield, simple work-up procedures, mild reaction conditions, short reaction times, magnetic separation

Acknowledgments

We thank the Research Council of the University of Kashan for supporting this work through grant No. 159148/71.

Declarations: Funding: This research was funded by University of Kashan by grant No. 159148/71.

Conflict of interest: The authors declare that they have no conflict of interest.

5. References

- H. Christopher, G. Vijay. *Curr. Med. Chem.* **2003**, *10*, 51–80. DOI:10.2174/0929867033368600
- M. C. Bagley, M. C. Lubinu. in *Top. Heterocycl. Chem.* (eds Erik Van der Eycken, C. Oliver Kappe), Springer Berlin Heidelberg, 2006, pp. 31–58.
- H. Naeimi, S. Mohammadi. *J. Heterocycl. Chem.* **2020**, *57*, 50–59. DOI:10.1002/jhet.3742
- Z. Ghanbari, H. Naeimi. *J. Heterocycl. Chem.* **2021**, *58*, 1058–1069. DOI:10.1002/jhet.4236
- M. Moradian, M. Nazarabi. *Acta Chim. Slov.* **2021**, *68*, 594–604. DOI:10.17344/acsi.2020.6412
- H. Naeimi, A. Raeisi, M. Moradian. *Arab. J. Chem.* **2017**, *10*, S2723–S2728. DOI:10.1016/j.arabjc.2013.10.017
- A. Hantzsch. *Justus Liebigs Ann. Chem.* **1882**, *215*, 1–82. DOI:10.1002/jlac.18822150102
- J.-J. Xia, G.-W. Wang. *Synthesis* **2005**, 2379–2383. DOI:10.1055/s-2005-870022
- V. K. Sharma, S. K. Singh. *RSC Adv.* **2017**, *7*, 2682–2732. DOI:10.1039/C6RA24823C
- M. Ziaie, K. Akbaridilmaghani, A. Tukmechi. *Acta Chim. Slov.* **2017**, *64*, 895–902. DOI:10.17344/acsi.2017.3506
- M. Moghaddam-Manesh, D. Ghazanfari, E. Sheikhsosseini, M. Akhgar. *Acta Chim. Slov.* **2020**, *67*, 7.

- DOI:10.17344/acsi.2019.5437
12. F. Bossert, H. Meyer, E. Wehinger. *Angew. Chem. Int. Ed. Eng.* **1981**, *20*, 762–769. DOI:10.1002/anie.198107621
13. H. Andreas. *Mini-Rev. Med. Chem.* **2002**, *2*, 235–245. DOI:10.2174/1389557023406241
14. S. Cihat, S. Rahime. *Mini-Rev. Med. Chem.* **2006**, *6*, 747–755. DOI:10.2174/138955706777698606
15. A. Hilgeroth, M. Wiese, A. Billich. *J. Med. Chem.* **1999**, *42*, 4729–4732. DOI:10.1021/jm991115k
16. M. Kawase, A. Shah, H. Gaveriya, N. Motohashi, H. Sakagami, A. Varga, J. Molnár. *Bioorg. Med. Chem.* **2002**, *10*, 1051–1055. DOI:10.1016/S0968-0896(01)00363-7
17. D. Vo, W. C. Matowe, M. Ramesh, N. Iqbal, M. W. Wolowyk, S. E. Howlett, E. E. Knaus. *J. Med. Chem.* **1995**, *38*, 2851–2859. DOI:10.1021/jm00015a007
18. T. Naqvi, A. Amin, S. Ali, M. Y. Lone, N. Bashir, S. U. Khan, T. T. Htare, M. A. Rizvi. *Acta Chim. Slov.* **2021**, *68*, 16. DOI:10.17344/acsi.2021.6684
19. J. M. Tusell, S. Barro, N. J. Serratos. *Brain Res.* **1993**, *622*, 99–104. DOI:10.1016/0006-8993(93)90807-Y
20. G. Sabitha, K. Arundhati, K. Sudhakar, B. S. Sastry, J. S. Yadav. *Synth. Commun.* **2009**, *39*, 2843–2851. DOI:10.1080/00397910802656091
21. S.-J. Ji, Z.-Q. Jiang, J. Lu, T.-P. Loh. *Synlett* **2004**, *2004*, 0831–0835. DOI:10.1055/s-2004-820035
22. M. M. Heravi, M. Saeedi, N. Karimi, M. Zakeri, Y. S. Beheshtiha, A. Davoodnia. *Synth. Commun.* **2010**, *40*, 523–529. DOI:10.1080/00397910902994194
23. H. Salehi, Q. X. Guo. *Synth. Commun.* **2004**, *34*, 171–179. DOI:10.1081/SCC-120027250
24. S. Ghosh, F. Saikh, J. Das, A. K. Pramanik. *Tetrahedron Lett.* **2013**, *54*, 58–62. DOI:10.1016/j.tetlet.2012.10.079
25. G. Ali, N. A. Dangroo, S. Raheem, T. Naqvi, T. Ara, M. A. Rizvi. *Acta Chim. Slov.* **2020**, *67*, 195–202. DOI:10.17344/acsi.2019.5348
26. S. Behrouz, M. N. Abi, M. A. Piltan. *Acta Chim. Slov.* **2021**, *68*, 374–386. DOI:10.17344/acsi.2020.6343
27. J. E. Gholtash, M. Farahi, B. Karami, M. Abdollahi. *Acta Chim. Slov.* **2020**, *67*, 866–875. DOI:10.17344/acsi.2020.5825
28. M. Maheswara, V. Siddaiah, Y. K. Rao, Y.-M. Tzeng, C. Sridhar. *J. Mol. Catal. A: Chem.* **2006**, *260*, 179–180. DOI:10.1016/j.molcata.2006.07.024
29. M. Anniyappan, D. Muralidharan, P. T. Perumal. *Tetrahedron* **2002**, *58*, 5069–5073. DOI:10.1016/S0040-4020(02)00461-1
30. E. Rafiee, S. Eavani, S. Rashidzadeh, M. Joshaghani. *Inorg. Chim. Acta* **2009**, *362*, 3555–3562. DOI:10.1016/j.ica.2009.03.049
31. R. A. Mekheimer, A. A. Hameed, K. U. Sadek. *Green Chem.* **2008**, *10*, 592–593. DOI:10.1039/b715126h
32. S. Ko, M. N. V. Sastry, C. Lin, C.-F. Yao. *Tetrahedron Lett.* **2005**, *46*, 5771–5774. DOI:10.1016/j.tetlet.2005.05.148
33. R. Gupta, R. Gupta, S. Paul, A. Loupy. *Synthesis* **2007**, *2007*, 2835–2838. DOI:10.1055/s-2007-983839
34. M. A. Ghasemzadeh, S. M. Hasan Nasrollahi, M. R. Zolfaghari. *Acta Chim. Slov.* **2018**, *65*, 199–208. DOI:10.17344/acsi.2017.3820
35. A. Gharib, M. Jahangir, M. Roshani, J. W. Scheeren. *Synth. Commun.* **2012**, *42*, 3311–3320. DOI:10.1080/00397911.2011.581405
36. M. Adharvana Chari, K. Syamasundar. *Catal. Commun.* **2005**, *6*, 624–626. DOI:10.1016/j.catcom.2005.03.010
37. S. M. Baghbanian, S. Khaksar, S. M. Vahdat, M. Farhang, M. Tajbakhsh. *Chin. Chem. Lett.* **2010**, *21*, 563–567. DOI:10.1016/j.cclet.2009.12.011
38. S. Das Sharma, P. Hazarika, D. Konwar. *Catal. Commun.* **2008**, *9*, 709–714. DOI:10.1016/j.catcom.2007.08.008
39. L.-M. Wang, J. Sheng, L. Zhang, J.-W. Han, Z.-Y. Fan, H. Tian, C.-T. Qian. *Tetrahedron* **2005**, *61*, 1539–1543. DOI:10.1016/j.tet.2004.11.079
40. F.-P. Ma, P.-H. Li, B.-L. Li, L.-P. Mo, N. Liu, H.-J. Kang, Y.-N. Liu, Z.-H. Zhang. *Appl. Catal. A: General* **2013**, *457*, 34–41. DOI:10.1016/j.apcata.2013.03.005
41. A. Han, J. Liao, M. Ye, Y. Li, X. Peng. *Chin. J. Chem. Eng.* **2011**, *19*, 1047–1051. DOI:10.1016/S1004-9541(11)60090-6
42. J. Mondal, T. Sen, A. Bhaumik. *Dalton Trans.* **2012**, *41*, 6173–6181. DOI:10.1039/c2dt30106g
43. M. Hamidinasab, A. Mobinikhaledi. *ChemistrySelect* **2019**, *4*, 17–23. DOI:10.1002/slct.201802413
44. R. Karimi-Chayjani, N. Daneshvar, H. Tajik, F. Shirini. *ChemistrySelect* **2019**, *4*, 1205–1213. DOI:10.1002/slct.201802916
45. T. T. Nguyen, N. P. Thi Le, T. T. Nguyen, P. H. Tran. *RSC Adv.* **2019**, *9*, 38148–38153. DOI:10.1039/C9RA08074K
46. H. Alinezhad, K. Pakzad, M. Nasrollahzadeh. *Appl. Organomet. Chem.* **2020**, *34*:e5473. DOI:10.1002/aoc.5473
47. M. A. Ashraf, Z. Liu, W. X. Peng, C. Gao. *Catal. Lett.* **2020**, *150*, 683–701. DOI:10.1007/s10562-019-02986-2
48. P. Lahiri, S. K. Sengupta. *Can. J. Chem.* **1991**, *69*, 33–36. DOI:10.1139/v91-006
49. J.-H. Lee, Y.-M. Huh, Y.-W. Jun, J.-W. Seo, J.-T. Jang, H.-T. Song, S. Kim, E.-J. Cho, H.-G. Yoon, J.-S. Suh, J. Cheon. *Nat. Med.* **2007**, *13*, 95–99. DOI:10.1038/nm1467
50. Z. Zarnegar, J. Safari. *Int. J. Biol. Macromol.* **2015**, *75*, 21–31. DOI:10.1016/j.ijbiomac.2015.01.013
51. B. Datta, M. A. Pasha. *Chin. J. Catal.* **2011**, *32*, 1180–1184. DOI:10.1016/S1872-2067(10)60252-5
52. E. Priede, A. Zicmanis. *Helv. Chim. Acta* **2015**, *98*, 1095–1103. DOI:10.1002/hlca.201500009
53. Y. Watanabe, K. Shiota, T. Hoshiko, S. Ozaki. *Synthesis* **1983**, *1983*, 761–761. DOI:10.1055/s-1983-30505
54. J. Safari, F. Azizi, M. Sadeghi. *New J. Chem.* **2015**, *39*, 1905–1909. DOI:10.1039/C4NJ01730G
55. M. José Climent, A. Corma, S. Iborra. *RSC Adv.* **2012**, *2*, 16–58. DOI:10.1039/C1RA00807B
56. M. Leonardi, M. Villacampa, J. C. Menéndez. *Chem. Sci.* **2018**, *9*, 2042–2064. DOI:10.1039/C7SC05370C
57. J.-P. Wan, Y. Liu. *RSC Adv.* **2012**, *2*, 9763–9777. DOI:10.1039/c2ra21406g

Povzetek

V prispevku je opisana učinkovita sinteza nekaterih 1,4-dihidropiridinov s pomočjo kondenzacijske reakcije aldehydov, etilacetoacetata in amonijevega acetata, v prisotnosti superparamagnetnih nanodelcev manganovega ferita pri 80 °C. Prednosti tega postopka so selektivnost, visoka čistost produktov, odlični izkoristki, kratki reakcijski časi, enostavna izolacija in okolju prijazni pogoji sinteze. Poleg tega je mogoče katalizator izolirati in večkrat ponovno uporabiti, ne da bi s tem bistveno zmanjšali izkoristek reakcije.



Except when otherwise noted, articles in this journal are published under the terms and conditions of the Creative Commons Attribution 4.0 International License

Scientific paper

Opportunities for Learning: Analysis of Czech Lower-Secondary Chemistry Textbook Tasks

Karel Vojř^{1,2} and Martin Rusek^{1,*}

¹ Charles University, Faculty of Education, Department of Chemistry and Chemistry Education, Magdalény Rettigové 4, 116 39 Praha

² Charles University, Faculty of Education, Department of Biology and Environmental Studies, Magdalény Rettigové 4, 116 39 Praha

* Corresponding author: E-mail: martin.rusek@pedf.cuni.cz

Received: 10-29-2021

Abstract

Tasks in Czech lower-secondary chemistry textbooks were analysed to describe their position in textbook chapters, required response type, overall task nature, as well as cognitive requirements. The results showed older textbooks contain task banks at the end of chapters suggest a transmissive teaching paradigm, whereas newer textbooks containing tasks within the chapters. As far as the nature of the tasks is concerned, a strong stereotypical genre was found in the chemistry textbooks. Most of the textbook tasks require open-ended answers and target: factual and conceptual knowledge remembering or procedure application. The authors therefore suggest several changes to the tasks, including their position in chapters, cognitive difficulty as well as the required response type in order to meet chemistry education goals.

Keywords: tasks; textbook analysis; chemistry education; lower-secondary school; ISCED 2

1. Introduction

Changes in society, together with an increasing amount of information, place demands on education's transformation. The demands for effective participation in society led to key competences for lifelong learning formulation.¹ As part of the educational process, the emphasis on students was also strengthened. A key element in thinking about education and thus in changing the curriculum is the effort to move from a traditional approach exercising algorithm-based, lower-order cognitive skills to an approach stressing higher-order cognitive skills associated with asking questions, critical or system thinking, decision making and problem solving.² Changes in access to education are gradually being incorporated into the curriculum at a national level. A responsible approach to the changes requires an evidence-based approach. Unfortunately, many curriculum reforms take place without adequate research evidence or mapping educational reality.³

Although the objectives and education content are set out in state curricular documents, textbooks play an important role in the implementation of teaching. These bring a concrete transformation of educational content

and, compared to the higher levels of the curriculum, represent the concretization of the intended curriculum⁴ into concrete activities. They thus represent not only the selection of particular subject-matter, but also its transformation using specific methods and the form of its mediation.

The role of textbooks is twofold: they can be used directly by students as well as by teachers for lesson preparation – which seems to be one of their domineering role.⁵ Textbooks' effect is given by their structural components' utilization. The main structural components in textbooks to mediate the educational content is naturally the text.⁶ The interpretive text itself is not yet a learning tool, as it does not evoke a specific learning activity. The emphasis on the direction of students' own learning activities also comes to the fore with regard to the science (chemistry) education objectives, namely science literacy,⁷ which includes not only the mastery of certain knowledge, but also the development of various science-oriented skills. In order for textbooks to perform their function, they cannot be perceived only as educational content intended for simple memorization. Functional textbooks are an aid that helps to condition the diverse learning situations leading to the students' development in a broad sense.

Students' attention as well as their activity is directed by learning tasks. They represent the students' *opportunity to learn*⁸ and are the key to student activation. Since there is a relationship between questions and answers,⁹ the form of questions and their context determine students' activity, i.e. what about and in what way they think. The authenticity and context of the tasks also influence the students' skill in solving problems¹⁰ and tasks should be relevant not only to the teaching process but also to address authentic issues¹¹.

Students' activation can be accomplished by using textbook. Xin¹² found that task distribution in textbooks affects students' ability to solve certain types of tasks. Yet, as argued by Yang et al.,⁸ that task representation in textbooks does not directly show the textbooks' quality.

Through textbook tasks, students are also presented with the nature of science (NoS), as they are directed towards the way of thinking in a given scientific discipline.¹³ In addition to tools to develop general competences, textbooks can also be a means of scientific enculturation. This puts pressure on the form of textbook tasks so that the NoS presented to students is consistent with real science. As pointed out by Wood,¹⁴ unlike the classical school concept of natural science teaching, in real chemical (science) problems there is usually more than one correct solution, and in many cases only the most appropriate and achievable solution is sought. In this respect, "school tasks" frequently designed to evaluate students deflect from the real tasks as a certain response is needed in order to grade the answer.

It is natural to expect these tasks to be placed inside the chapters as they represent the learning content itself, whereas the role of tasks placed at the end is to evaluate the learning progress. Mediating real science practices in school teaching is one of science education's key challenges.¹⁵

As shown by Andersson-Bakken et al.,¹³ a number of studies focusing on textbook tasks showed a specific culture is evolving in individual school subjects. Bakken and Andersson-Bakken¹⁶ even identified textbook tasks to be a specific genre not only in science textbooks. Textbook tasks are thus influenced by the characteristic standards of their formulation, purpose and educational objectives. The field-specific culture regarding used tasks is further strengthened by textbook use by teachers.

A significant proportion of teachers was found to use textbooks for teaching preparation.^{5, 17} Teachers consider textbooks to be the main source of educational content.^{18–19} At the same time, they also adopt the teaching concept from textbooks and using textbook models²⁰, teaching methods and organizational forms suggested in textbooks.²¹ Since textbooks thus represent curricular material for many teachers (cf.²²) and the conception gives teachers a certain example how to deliver its content.²¹ Textbooks thus represent a potentially implemented curriculum²³ with a direct impact on students. Elaborating on

textbook components then plays a vital role in understanding the teaching-learning process.³⁵

The abovementioned trend was observed²⁴ with significant similarities between the questions used by chemistry teachers in their lessons and the questions in the textbooks they use. Efforts to innovate the curriculum can thus be significantly limited by the lack of textbook innovation. Although textbooks follow different curriculum concepts with different emphases and educational objectives, this is not always clearly reflected in their content. Even in textbooks following a reformed curriculum declaring a focus on developing students' competences, only a limited proportion of tasks targeting higher-order thinking was found.²⁵ Orientation to tasks, i.e. student activity, remains implicit.²⁶

As seen from the above, by analysing textbook tasks, it is possible to identify both the learning opportunities presented to students and the NoS understanding that textbooks convey. However, these aspects have so far received rather partial attention in science textbook research internationally.²⁷

2. Research Aim and Research Questions

As suggested above, from a certain point of view, task elaboration offers a model of curriculum implementation as seen via the student activity perspective. Textbooks therefore become a tool influencing curriculum conception (when textbooks are being used in education) and tasks in them reflect the potential for active learning.

Textbook tasks reflect the potential of students' active learning given the textbook is being used. As research shows, textbooks are an important support for teachers in their work, showing them not only what to teach, but also what methods to use,^{20,22,28} therefore the use of textbook does not mean it is only used in the class with students, but also for teachers' lesson preparation. Understanding current tasks is thus an important element for understanding the current state of the concept of teaching. If certain deflections from an ideal appear, this information is a starting point for innovations.

For these reasons, the aim of the research was to find out *what tasks are contained in lower-secondary school chemistry textbooks* and *What differences there are between the particular lower-secondary school chemistry textbooks in terms of tasks*. These aims were further specified by the following research questions:

- In which parts of lower-secondary chemistry textbooks are tasks placed?
- What type of response is required in the lower-secondary chemistry textbook tasks?
- What are the required cognitive processes and the required types of knowledge in the *in* lower-secondary chemistry textbook tasks?

The placement of tasks in textbooks shows their authors' intended conception of chemistry subject-matter presentation – student activation. There are basically two scenarios: Tasks either induce students' active learning and bring the initial motivation and student activation leading, to their acquisition of new subject-matter, or tasks are designed to fixate subject-matter transmitted by a teacher, therefore conclude non-active methods.

Different types of response required in assigned tasks correspond with a different type of thinking and development of problem-solving strategies. While close-ended tasks require analysis and differentiation of individual submitted claims, open-ended tasks aim to create an individual response. Each type of task therefore aims at a different science education or literacy goal and are supposed to be balanced.

Similarly, the focus on different cognitive processes and types of knowledge shows the emphasis of textbooks on students' specific thought operations and skills. At the same time, they contribute to the formation of a specific picture of scientific knowledge.

3. Methods

To answer the research questions, a quantitative approach based on textbook task closed-coding was chosen.

3. 1. Research Sample

The most commonly used chemistry textbooks (textbooks used at less than 5% of schools were excluded) for lower-secondary schools in Czechia⁵ were analysed. With regard to one textbook's publication of a new edition, this textbook was included in the sample too. It is a direct follow-up to the previous series, and it is therefore reasonable to assume that it will continue to be used, replacing the earlier edition. The analysed textbooks are referenced using abbreviations – see Table 1. All the analysed textbooks are intended for the 8th grade. These are textbooks designed for teaching in the first year students encounter chemistry in the Czech Republic. By analysing these textbooks, the basis of chemistry education is thus evaluated. All analysed textbooks focus on six thematic areas from *Framework education programme for basic education* (state

curricular document): *Observation, experimentation and safety, Mixtures, The molecular composition of substances and chemical elements, Chemical reactions, Inorganic compounds and Chemistry and society*. In Textbooks FR and nFR attention is also paid to the thematic area *Organic compounds*. Only the topic of fuel is included in the textbook nFR in addition. The textbook FR includes the thematic area *Organic compounds* topics hydrocarbons and hydrocarbon derivatives and less attention is paid to the topic of chemical reaction. Entire textbooks were analysed to obtain a comprehensive insight covering both the content of individual chapters as well as the complementary tasks.

3. 2. Procedure and Research Tools

In the first step, all textbook tasks in terms of the means of inducing, guiding and supporting students' learning activities²⁹ were identified and quantified. The identified tasks were further evaluated with regard to their position in the chapter/unit, required response type, cognitive skills and types of knowledge.

The coding was inspired by Gillette and Sanger³⁰ in the categories that corresponded to the component distribution in textbooks as identified by the analysis of textbook didactic equipment.³¹ The following categories were identified:

- *Inside the chapter* – Tasks are integrated between image and text components and are thus part of the explanatory part of the textbook.
- *End of page* – Tasks are used separately from other textbook components on the page. They are placed in the context of the chapter/unit, but after the exposition part.
- *Page margins* – Tasks are placed visually separately within the chapter/unit among other additional information.
- *Tasks banks* – Tasks are classified in separate parts of the textbook separately from the other components included in the chapters.

Closed-ended tasks and *open-ended tasks* were identified as the type of response requested. In this sense, tasks were distinguished only according to the form of the requested response. The response type was further specified on the basis of task typologies according to Kalhous and Obst³² and Jeřábek and Bílek³³. The categories were the following:

Table 1: Analysed textbooks

Textbook title text	Authors	Year of publication	Publishing house	Referenced in the
Základy chemie 1	Beneš, Pumpr, & Banýr	1993	Fortuna	ZCH
Základy praktické chemie 1	Beneš, Pumpr, & Banýr	1999	Fortuna	PCH
Chemie 8	Škoda, & Doulík	2006	Fraus	FR
Chemie 8	Mach, Plucková, & Šibor	2016	Nová škola	NŠ
Chemie 8 (new generation)	Škoda, & Doulík	2018	Fraus	nFR

- *Closed-ended tasks* – multiple choice – multiple-answer, multiple choice – single-answer, dichotomous, coupling/pairing, ordinance,
- *Open-ended tasks* – short answer, gap filling, table filling, long answer.

Based on the previous qualitative analysis of textbook tasks,³⁴ tasks with no required verbal response (non-response tasks) were further coded. Typically, these are tasks consisting of an instruction, e.g. observation, but it is not specified that students should express their observations verbally.

To assess the tasks' cognitive and knowledge domains, Revised Bloom's taxonomy³⁵ was used. Despite its criticism (e.g.³⁶), this taxonomy is used for curricular objectives^{37–39} as well as textbook task evaluation.^{40–41} For this reason, it was also used for the purpose of this study. The highest task potential was considered, and the required student activity was decisive for task categorization. For cognitive processes, the categories: *remember, understand, apply, analyse, evaluate and create* were used. In the knowledge domain, *factual, conceptual, procedural and metacognitive knowledge* were considered.³⁵

3. 3. Data Analysis

The data was processed in MS Excel. To verify that the coding was correct, a randomly selected sample of 10% of the tasks was coded by a second researcher and a match was assessed using the Cohen's kappa coefficient. The kappa values in the individual categories ranging from 0.886 to 1 were found, which can be interpreted as almost perfect or perfect agreement (cf.⁴²) in the 95% confidence interval. With regard to research issues, the

data was further quantitatively processed and descriptively evaluated.

4. Results

4. 1. Frequency of Tasks in Textbooks

In the chemistry textbooks for the 8th grade of lower-secondary school, relatively high numbers of 695 to 1000 tasks were identified (see Table 2).

The different total of tasks in each textbook is mainly related to the different textbook scopes and the topics included. The highest range for chapter pages in textbooks was found in nFR (120), FR (116) and ZCH (114), which corresponds to the overall higher number of tasks (see Table 2). In contrast, the lowest number of tasks was found in the PCH textbook, which has the lowest range of chapter pages (62). Although the average subchapter range corresponding to one comprehensive teaching unit ranges from 1.6 to 2.8 pages, the average number of tasks included in one subchapter is similar among all analysed textbooks (see Table 3).

Differences were identified among the tasks in the individual textbooks. While in most textbooks, about a quarter of the tasks (ZCH and FR – 28%, PCH and nFR – 23 %) fall into the laboratory activities category, i.e. experiment or tasks related to the demonstration of substances and their properties, in the NŠ textbook there are only 14%. Significant differences were also identified in the classification of tasks related to educational content of other fields than chemistry. These were found mainly in FR (16%) and nFR textbooks (19%), while other textbooks contain only a few of these tasks (see Table 2).

4. 2. Task Locations

Significant differences were identified in the location of the tasks in the textbooks. While earlier published textbooks tend to place the tasks at the end of the page (ZCH) or in the task bank (PCH), in the newly published textbooks, FR, NŠ and nFR, the tasks being included directly in the chapters prevails. It shows a shift towards greater individual component interconnectedness in the chapters of newer textbooks. In FR and nFR textbooks, page margins are also used as the only ones for assigning additional tasks (see Table 4).

Table 2: Number of tasks in lower-secondary chemistry textbooks

Textbook	Tasks in total	Laboratory activities	Tasks from other fields (interdisciplinary)
ZCH	561	157	4
PCH	320	74	3
FR	651	181	103
NŠ	517	73	16
nFR	695	163	131

Table 3: Subchapter in textbooks and the tasks they contain

Textbook	Number of chapters	Number of sub-chapters	Mean chapter length (number of pages)	Mean number of tasks in sub-chapters
ZCH	9	41	2.8	13.7
PCH	9	40	1.6	8.0
FR	17	55	2.1	11.5
NŠ	6	43	1.9	11.2
nFR	18	55	2.2	12.3

Table 4: Task location in the textbooks

Textbook	Inside the chapter (%)	Page margins (%)	End of page (%)	Tasks bank (%)
ZCH	19	0	69	12
PCH	22	0	0	78
FR	62	36	0	2
NŠ	68	0	14	18
nFR	61	36	0	3

In the tasks located in each section, differences in the tasks' nature were found in terms of their link with laboratory activities. The tasks included inside the chapters are practically exclusively related to experimental activities in the ZCH and PCH textbooks (ZCH – 95%, PCH – 100%). Other textbooks include theoretical tasks (tasks related to laboratory activities: FR – 41%, NŠ – 17%, nFR – 33%) as a reaction to more safety restrictions as well as plausible usefulness.⁴³

In all the analysed textbooks, the presence of task banks was found. However, their classification in relation to the content of the chapters varies. While in the ZCH and PCH textbooks, task banks are connected with the chapter (in PCH textbooks, it is the main method of consolidating the course), in the FR, NŠ and nFR textbooks, there is also a separate section at the end of the book devoted only to tasks that serve either to repetition of the whole year subject-matter or do not have a direct connection to the subject-matter from the chapters. In the NŠ textbook, 41% of the tasks are placed in the task banks. In the FR and nFR textbooks, all tasks included in task banks are classified in this way and are typically tasks related to laboratory activities (FR – 86%, nFR – 100%). However, compared to other textbooks, the number is low in these categories (cf. Table 4). Tasks linked to laboratory activities are represented in task banks and other textbooks (except for inside the chapter placement, this is the second typical classification of laboratory activities). 58% of tasks placed in task banks in the ZCH textbook are linked to laboratory activities. However, in the PCH textbook, this is only 1%. In the NŠ textbook, 14% of tasks are associated with laboratory activity in the task bank, which is related to the overall lower proportion of these tasks in this textbook (see Table 2).

4. 3. Requested Response Type

In view of the response type required, the analysed textbooks are very similar. In all the textbooks, open-ended tasks significantly dominate. They account for 70 to 92% of all assigned tasks (see Table 5) in textbooks. With the exception of FR and nFR, the most frequently required answers are represented only by individual words or phrases, mainly in the form of free short answers, or by completing a table or filling the gaps. Gap-fill and table-fill is typical, especially for the ZCH textbook (both 5% of tasks). In NS textbooks, 3% of tasks are table-fills, in the case of other textbooks, adding answers appears only for single tasks. In the FR and nFR textbooks, this type of task is non-existent, but open-ended tasks with a long answer dominate, representing more than half of all in the textbooks of the assigned tasks.

None of the close-ended task types (*multiple-answer, single-answer, dichotomous, coupling/pairing, ordinance*) were represented in any textbook in more than 5% of cases. The most close-ended tasks were found in the ZCH and PCH textbooks (see Table 5). Both textbooks include tasks of all types. However, *coupling/pairing* tasks in the ZCH textbook (3%) and multiple choice – single-answer tasks in the PCH textbook (4%) were represented more than once. All types of close-ended tasks were also identified in the NŠ textbook, but only in limited numbers, dichotomous tasks (2%) are the most abundantly represented. Dichotomous tasks are also the most abundant type of close-ended tasks in the FR and nFR textbooks (3%). These contain the lowest variability of close-ended tasks, non-dichotomous tasks did not occur or were represented by only one task.

Table 5: Tasks in textbooks according to the type of response requested

Textbook	Long answer (%)	Short answer (%)	Tables and gaps filling (%)	Closed-ended tasks (%)	Non-answer tasks (%)
ZCH	31	30	9	9	20
PCH	29	38	2	10	20
FR	52	40	0.5	4	4
NŠ	32	46	5	5	12
nFR	51	42	0.6	3	3

A significant proportion of tasks with no required answer were identified in the ZCH, PCH and NŠ textbooks (see Table 4). In all textbooks, most of these tasks are related to laboratory activity (ZCH – 87%, PCH – 98%, FR – 61%, NŠ – 87%, nFR – 79%). The form of laboratory activities is thus reflected in the non-answer tasks. While in the ZCH, PCH and NŠ textbooks, most tasks associated with laboratory activities do not require a response (62%, 86% and 71% of tasks related to laboratory activities) and are only instructions, in the FR and nFR textbooks, tasks associated with laboratory activities are typically open-ended (83 and 82% respectively). Close-ended tasks follow laboratory activities only in the FR and nFR textbooks, in which they represent 9% of tasks related to laboratory activities and are limited in ZCH textbooks (3%).

4. 4. Cognitive and Knowledge Domains in Textbook Tasks

The tasks' cognitive domain analysis also showed significant similarities between textbooks. In all the textbooks, a significant prevalence of tasks focused on lower cognitive operations was identified. The tasks focused on *analyse*, *evaluate* and *create* were not identified in more than 2% of the tasks (see Figure 1), i.e. textbooks practically do not aim at these operations.

Tasks targeting understanding account for the highest share in all textbooks (50–63%). The lowest proportion of these tasks was identified in NŠ textbooks, thanks to a higher representation of tasks aimed at remembering (31%).

About a third of the tasks focused on *remember* were also found in FR and nFR textbooks (37 and 32% respectively). These textbooks however contained the highest variety of tasks compared to the other textbooks. A higher proportion of remember-oriented tasks is influenced by a significantly higher proportion of tasks focused on other educational areas (see Table 2), most of which (79 and 61% of these tasks) aim at *remember*. The remaining tasks in other educational areas in these textbooks are almost exclusively aimed at *understand*. The low representation of application-oriented tasks is also specific to FR and nFR textbooks. Although in other textbooks these tasks represent 18–26%, in FR and nFR textbooks it is only 5 and 4% respectively. This difference partially reflects the different classification of the topic of chemical calculations, which in the case of the FR and nFR textbook series are included in the textbook for the 9th grade which was not analysed. While in the ZCH and PCH textbooks the numerical tasks represent 8% and in the NŠ textbook they represent 7%, in the FR and nFR textbooks they constitute less than 1% of the tasks. However, the main difference is due to a different

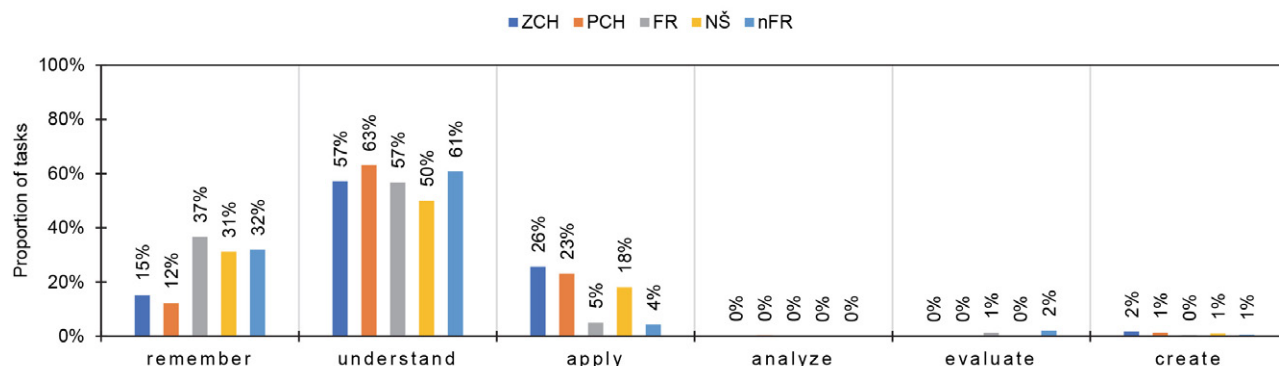


Figure 1 Proportion of tasks in textbooks according to required cognitive operations

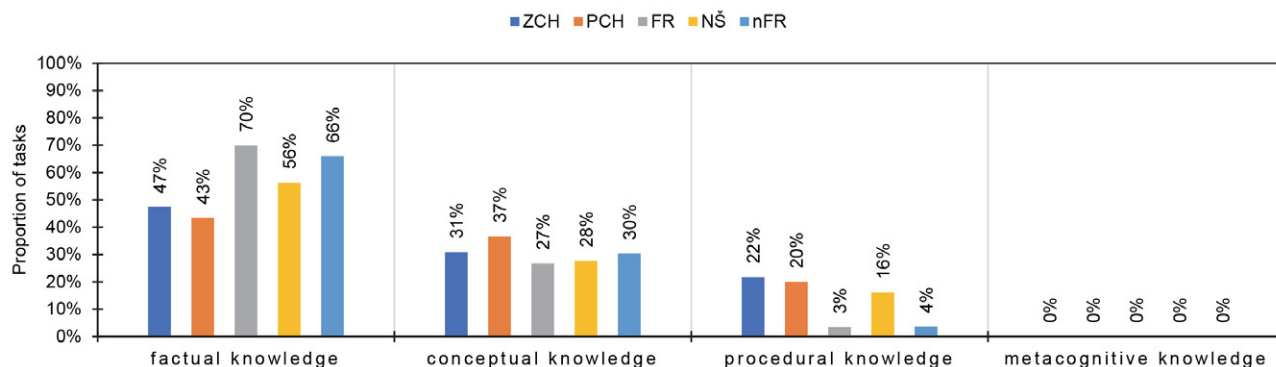


Figure 2 Proportion of textbook tasks according to required knowledge types

approach in the chapters focused on selected substances. Most application tasks are focused on chemical nomenclature and balancing chemical equations. These skills are significantly less stressed in FR and nFR textbooks, and on the contrary, the connection in the wider context and with everyday life is emphasized significantly more.

The abovementioned differences of FR and nFR textbooks are also shown in the tasks according to the required types of knowledge. A lower proportion of chemical nomenclature and equations balancing tasks, respectively calculations, is reflected in a lower proportion of tasks requiring *procedural knowledge*. These represent only 3 and 4% of the tasks in FR and nFR textbooks, compared to 16–22% in other textbooks (see Figure 2).

As far as the knowledge types are concerned, significant similarities were identified between the textbooks' knowledge. Factual knowledge prevails in all textbooks (47–70% of tasks), and the focus on conceptual knowledge was found in about a third of the tasks. No metacognitive knowledge tasks were identified in any of the textbooks.

The higher proportions of tasks requiring *factual knowledge* in FR and nFR textbooks partly reflect the inclusion of tasks focused on other educational areas / school subjects, which target *factual knowledge* (94% and 90% of these tasks, respectively). Even if these tasks were removed from the sample, the proportion of *factual knowledge tasks* is still the highest of all analysed textbooks (65 and 60%, respectively).

5. Discussion

The analysed lower-secondary chemistry textbooks contain a relatively high number of tasks, which is also typical for textbooks in other countries.¹⁶ On average, there are 8 to 14 tasks per subchapter/unit. Due to the usual number of two teaching lessons per week,⁴⁴ the subchapters basically represent the content of one lesson. As the teaching content does not consist only of tasks, the textbooks offer (1) more tasks for teachers to choose from and/or (2) tasks of a nature that allow for short, quick answers. Based on Bakken's⁴⁵ findings, it is reasonable to expect teachers to have the tendency to cover all textbook content. Previous research⁵ showed teachers' use questions and tasks from textbooks often. Therefore, the impact of the tasks is immense. As long as the tasks are an integral part of the textbook (mainly the case of the newer textbooks), those which fit this approach need to be short. This corresponds to the results of the qualitative analysis³⁴ – the tasks in Czech chemistry textbooks typically consist only of a question possibly supplemented by a short accompanying text (maximum a few short sentences). Due to this concept, chemistry textbooks lack tasks focused on working with content representations and a more complex context.

The results of this study fully agree with Bakken and Andersson-Bakken.¹⁶ From various angles, textbook tasks are a very specific genre whose concept, however, is worth reconsidering. Although most of the assigned tasks have

Table 6. Most frequent tasks in textbooks

Textbook	Remember factual knowledge (%)	Understand factual knowledge (%)	Understand conceptual knowledge (%)	Apply procedural knowledge (%)
ZCH	15	31	26	21
PCH	12	31	32	19
FR	35	35	22	3
NŠ	27	29	21	15
nFR	31	34	26	3

A more detailed analysis taking into account both cognitive and knowledge domains identified only four types of tasks that occur in at least 5% of textbook tasks (see Table 6). In the ZCH and PCH textbooks, the most commonly represented task types are the ones on *understand factual knowledge* and *understand conceptual knowledge*. The FR, NŠ and nFR textbooks also include tasks focused on *remember factual knowledge* more abundantly. Tasks from the other fields included mainly in FR and nFR (see Table 2) textbooks are reflected in this category of tasks. When analysing only tasks focused on chemical content, the tasks targeting *factual knowledge remembering* in these textbooks represent 27 and 24% respectively.

an open form of response which seems to require a more complex student answer, if all of them were used, there would not be enough time in class for thorough thought or answer. The culture of using learning tasks is therefore very probably not exploiting the potential of open-ended tasks fully: teachers transform the questions into the format which fits the time constraints⁴⁶ or leave students a very short time to think about the answer after asking a question.⁴⁷ Either way of using the tasks does not leave enough space for the students' learning activity itself and does not provide learning opportunities for all students, thus not fully exploiting the tasks' potential.

Although the analysed textbooks are similar as far as the structural components are concerned,³¹ connecting

these components within the chapters differs significantly. Task analysis then offers better understanding to the textbook authors' conception of chemistry teaching reflected in their textbook. In this study, this was revealed in the textbooks' focus on students' activity, accent on science literacy and, a domain dominated by science education, experimental activities.

The positioning of tasks suggests the required course of the learning activity. In the formerly published ZCH and PCH textbooks (first published before the contemporary curriculum was released), tasks are placed at the end of the chapter. This in itself is an indicator of a proposed learning conception which builds upon an initial transmissive transfer of knowledge to end with questions and task designed to evaluate students' knowledge, i.e. the shape of textbooks from the 90's.⁴⁸ In newer textbooks, tasks are typically placed inside chapters which suggest their authors' attempt to activate students earlier, during new knowledge presentation.

The concept of scientific literacy spread mostly thanks to the PISA project. Naturally, textbooks published before 2000 did not have it incorporated in them. Nevertheless, as curriculum analysis showed, despite not explicitly being named, the content of scientific literacy is reflected in the national curriculum for chemistry.⁴⁹ The declaration that all the chemistry textbooks with a valid approval clause,⁵ are in accordance with the curriculum, is not fully valid. It is the interconnectedness of topics and especially their links to other fields of human knowledge which is (or is not) reflected in textbook tasks. Only the textbooks by one publishing house (FR) contain such links. Other textbooks seem to concentrate on chemistry only, containing interdisciplinary relations only in individual cases.

Another aspect of scientific literacy specific to science disciplines is the accent of experimental activities. Notwithstanding the safety issues, especially in chemistry experiments, see e.g.⁵⁰, educational experiments are cornerstones of science teaching. In this respect, chemistry textbooks with the exception of NŠ textbook maintain the status quo, containing about 25% of the tasks aimed at laboratory activities. However, laboratory activities in Czech chemistry textbooks are typically only demonstrations performed by the teacher and not experiments in the true sense of the word, i.e. laboratory activities performed by students.³⁴ This explains Rusek et al.'s findings⁴³ about demonstrations predominating all chemistry experimental activities in chemistry lessons in Czechia. Moreover, in this particular respect, there seems to be a contradiction between textbook content and teachers' actions. Textbook use reported worldwide shows several aspects teachers from different countries share. They were reported to follow textbooks for the content, i.e. subject-matter (e.g.^{18,19}), used analogies,²⁰ questions²⁴ and also methods²¹ – sometimes even feeling under pressure, considering them compulsory.⁵¹ Yet, as far as laboratory activities are concerned,

despite textbooks being found to contain a high share of experimental tasks, such activities are only seldom.⁴³ Due ZCH, PCH and NŠ's focus on identical topics, the lower proportion (although the absolute number is still high) of the laboratory tasks in the textbook NŠ seems to reflect a school practice more. The fact this textbook is most preferred by majority of Czech teachers⁵ indicates a shift in thinking about didactic transformation in chemistry education. There is also a thought deviation from school experiments visible, which, after all, corresponds to the overall trend of chemistry teaching.⁴⁴ This is, naturally a serious finding as it may lead to students' underdevelopment in one of crucial parts of chemistry/scientific literacy (cf.⁵²⁻⁵³).

As shown in the requested task answer analysis as well as the targeted cognitive and knowledge domain, the genre is not represented only by the tasks' structure. This inertia seems to block any distinct change. A similar phenomenon was also captured by Abd-El-Khalick et al.⁵⁴ in American science textbooks. The impact of former curriculum is therefore being strengthened not only by teachers' relationships to the familiar and well-trying, but also by even new textbooks taking over former structures, including teaching conceptions (see⁵⁵), including tasks. Although the intended curriculum declares a shift in teaching conception, the school reality, i.e. the implemented or experienced curriculum⁵⁶ reflects this shift only in a limited way.

The required task response type analysis showed a strong task culture. All the analysed textbooks significantly predominate open response type tasks, which represent 70–96% of all tasks. In all analysed textbooks, both tasks with a required short and long answer are abundantly represented. In contrast, close-ended tasks are represented only from 3–10%. Although the use of open-ended tasks can be viewed positively due to the students' need to formulate their own response, thus also develop students' communication competence (see e.g.⁵⁷) this significant imbalance in all textbooks points to the one-sidedness of assignment wording. Textbooks thus do not provide students with tools to adopt strategies for comparing, evaluating and selecting the options offered. In contrast, the currently close-ended tasks are widely used for both admission procedures and national and international surveys aimed at students' scientific literacy.^{7,58}

Differences between textbooks in the area of required response type were shown, in particular for tasks related to laboratory activity. While in the ZCH, PCH and NŠ textbooks, tasks associated with laboratory activities are typically formulated without specific verbal response requirements, FR and nFR textbooks typically use open-ended tasks. Students' attention in these textbooks is more clearly directed in the case of these tasks, so it is possible to guide them.²⁹

The high homogeneity of the tasks was also identified in their cognitive demands. All analysed textbooks are dominated by tasks aimed at understanding, followed by

tasks focused on remembering and application. On the contrary, tasks targeting higher-order cognitive operations are almost neglected in textbooks (only 1–3% of tasks were identified). This fact, however, is in contrast with the required students' problem solving skills,⁵⁹ as these students' skills remain underdeveloped,⁶⁰ probably partly because of the lack of emphasis on problem solving in the textbooks.

This is another aspect of textbooks only partial alignment with the national curriculum. Compared to the curricular objectives' cognitive demands (see³⁸), it was expected that most tasks would target understanding followed by remembering and application. Nevertheless, the share of objectives on evaluation is also significant. Although outcomes in the state curriculum target mostly concepts (53%), followed by facts (28%), procedures (21%), but also metacognitive knowledge (20% cit.³⁸). The textbook task analysis, however, revealed that factual knowledge prevails (47–70% of tasks), conceptual knowledge is covered by about one third of the tasks. With the exception of the FR and nFR textbooks, procedural knowledge is represented in about 20% and no metacognitive knowledge tasks were identified in any of the textbooks.

Given the fact the procedural knowledge was represented by considerably one-sided tasks (training nomenclature, balancing formulas and performing calculations), even this category which, judging by the numbers, fits the curriculum needs to be considered only partially fitting.

When combined, most objectives – translated in tasks – are supposed to target understanding concepts, remembering facts, applying procedure and evaluating concepts. The oldest textbooks meet the curriculum in their focus on understand *conceptual knowledge*. The FR, NŠ and nFR textbooks include tasks focused on remember factual *knowledge*, especially when only the chemistry-oriented tasks in FR and nFR are considered. None of the textbooks addressed concept evaluation.

This phenomenon, however, is not caused by the nature of the field requiring only a certain type of questions or tasks. Káčovský et al.'s³⁸ analysis showed Polish or Slovenian curriculum contains a wider range of objectives than the Czech chemistry curriculum. In cases when even curriculum objectives do not contain larger objective variability than the students' cognitive activities, it is not reasonable to expect them in textbooks. This suggests a certain chemistry education culture in Czechia. To confirm, analysis of Polish or Slovenian textbooks tasks needs to be performed. Also, in their analysis of Turkish chemistry textbooks, Zorluoglu, et al.⁴¹ identified not only tasks targeting students' remembering, understanding and application as expected. A significant proportion of tasks targeting evaluation were identified. This is especially surprising in connection to the Turkish curricular objectives' analysis³⁷ which showed the intended chemistry curriculum not to significantly target this cognitive domain. This example then shows a textbooks' positive role in developing the state curriculum in the required manner. Rethinking edu-

cational content and its didactical transformation with regard to active learning and the objectives of science education is thus shown to be crucial in the creation of new textbooks.

The fact that the Czech chemistry textbooks which claim their alignment to the curriculum do not even contain the range from the curriculum, is alarming. Considering the textbooks' effect and the number of tasks, more elaboration, not less, was expected from the textbooks. This finding then stresses an important issue in chemistry (science) education. Despite various efforts to change science education at the level of the intended curriculum, the continued emphasis on knowledge transfer and thus the low proportion of tasks accentuating higher-order cognitive operations is also shown in other countries (cf.²⁶). However, as shown by Gillette and Sanger,³⁰ many studies found that the ability to solve tasks requiring simple knowledge equipment, or their direct application, does not translate into the ability to solve tasks requiring higher cognitive operations. Understanding the concepts of educational content does not in itself lead to the development of skills to analyse, evaluate or create. Surely, many students who underwent such an education (with such textbooks) developed their cognitive skills, though the effect or even contribution of school is disputable. Also, these students' skills could have been developed to a greater extent if addressed at school.

As proved by Robinson,⁶¹ learning to solve tasks algorithmically often leads to mere manipulation with variables according to the learned procedure. Simple task repetition requiring simple application of a known procedure does not lead to understanding scientific concepts the tasks' solution is based on, and learning becomes just a mechanical imitation. In view of the effective learning and deep development of field knowledge and skills, the full absence of metacognitive knowledge tasks identified in all the analysed textbooks also seems problematic. Students are supposed to be encouraged to learn how to learn through textbook tasks, estimate their performance and eventually adapt their learning approach. As shown by Pappa and Tsapalis,⁶² this aspect is also a challenge for curriculum in Greece.

Systematic work with tasks in curricular materials is also proving desirable from the NoS point of view. The analysis performed in this study identified only four dominant types of tasks in which there is only limited scope for students' autonomy in their solution. Therefore, the nature of chemistry (NoS) emphasizes existing knowledge as fixed, while lacking the procedural aspect of the NoS and room for new (out-of-the-box thinking). Simon and Budke⁶³ in their textbook research reached similar conclusions. They identified stress on goals associated with content as opposed to tasks related to methodological aspects and competence development. As pointed out by Osborne,¹⁵ freely paraphrasing scientific literacy definition, natural science knowledge does not only consist of factual

knowledge, but also highlights the way science works, how individual phenomena are related to other aspects, and how knowledge is acquired. These aspects of the NoS in relation to the analyzed textbooks are all the more important as chemical education begins in the 8th grade in the Czech Republic. Since the abovementioned aspects of natural sciences cannot be developed solely through lower cognitive operations, there is a risk of consolidating the image of chemistry as mere isolated, mostly symbolic,⁵⁹ facts students are supposed to acquire (cf.⁶⁴). This tradition needs to be revisited and incorporated into pre-service teacher training as a part of the teachers' professional vision (see⁶⁵) since it is this exact domain in which the content meets the pedagogy.⁶⁶

There are some limitations to the approach presented in this study. First, only the intended curriculum was analysed. In connection with international research, the results provide a vivid picture about the teaching practice, however, without analysing the implemented curriculum, i.e. the textbook tasks in action, conclusions need to be formulated carefully. For this reason, students' activity, performance and results are the next logical step in this area of research.

Second, this study contains results of 8th grade textbooks tasks analysis, despite chemistry is mostly being taught in both 8th and 9th grade (the last two years of compulsory, lower-secondary school in Czechia). Nevertheless, the textbooks are published by the same teams of authors. As a pilot sample of tasks from 9th grade textbooks showed no differences in the tasks' conception, the second books were not submitted to a thorough analysis.

Third, with respect to the analysis' focus, other tasks' qualities should such as their relation to the key competences as the major curricular goal, their accent on science literacy or the Nature of Science be investigated. These are topics which would inform all actors in the field of chemistry education about necessary steps in order textbooks – as the most influential medium in contemporary school – to aim at contemporary (not former) goals of chemistry/science education.

6. Conclusions

This study is directed at chemistry lower-secondary textbook tasks' analysis. It showed several trends which confirm other findings worldwide as well as several specifics which revealed trends in Czech chemistry education conception.

Particular chemistry textbooks differ in task placement. Whereas formerly published textbooks contain tasks at the end, newer textbooks contain them within the chapters. These show authors' effort to connect the tasks with other structural textbook elements and the field's content.

The textbooks contain a relatively large number of

tasks offering a vast database to be used in education. The analysis of tasks from Czech chemistry textbooks confirmed there is a certain task genre from a required answer type to a required performance. Textbooks were found to follow the curriculum as far as the subject-matter is concerned, however they vary from the curriculum as far as the required cognitive processes are concerned.

The textbooks' integral culture consists in the tasks' nature: open-ended tasks predominate, followed by tasks of laboratory nature without required answers. Higher task variability is required. With respect to students' more complex development, richer response types as well as more varying information explanation are suggested. A greater variability is also suggested from the cognitive operations' point of view. Tasks on remembering or understanding facts and conceptual knowledge predominate in the textbooks. Three out of four most often used chemistry textbooks in Czechia also contain procedure application. Tasks on analysis, evaluation or creation, or tasks operating with metacognitive knowledge are lacking. With respect to scientific literacy development, it is important to focus on these domains too.

So far, Czech chemistry textbooks were found to be a suitable educational tool for students to master factual and conceptual knowledge. Their use for skills or developing creative thinking and chemistry (science) problem solving is considerably limited. This study then shows possible ways for future textbook development.

Acknowledgements

This work was supported by Charles University Co-operatio.

7. References

1. Council recommendation of 22 May 2018 on key competences for lifelong learning **2018**, 61, 1–13. [https://eur-lex.europa.eu/legal-content/EN/TXT/PDF/?uri=CELEX:32018H0604\(01\)&rid=7](https://eur-lex.europa.eu/legal-content/EN/TXT/PDF/?uri=CELEX:32018H0604(01)&rid=7)
2. U. Zoller, D. Pushkin, *Matching Higher-Order Cognitive Skills (HOGS) promotion goals with problem-based laboratory practice in a freshman organic chemistry course* **2007**, 8, 153–171. <https://www.scopus.com/inward/record.uri?eid=s2.0-34247493348&partnerID=40&md5=169d3ca34a52b4d704b23b52b7547ce0>
3. K. Schildkamp, W. Kuiper, *Teach. Teach. Educ.* **2010**, 26, 482–496. DOI:10.1016/j.tate.2009.06.007
4. J. Maňák, D. Klapko, *Učebnice pod lupou [Textbooks under the magnifying glass]*. Paido: Brno, **2006**.
5. K. Vojíš, M. Rusek, *J. Balt. Sci. Educ.* **2021**, 20, 316–331. DOI:10.33225/jbse/21.20.316
6. M. Rusek, K. Vojíš, *Analysis of text difficulty in lower-secondary chemistry textbooks* **2019**, 20, 85–94. DOI:10.1039/C8RP00141C

7. OECD, *PISA 2018 Assessment and Analytical Framework*. OECD Publishing: Paris, **2019**; <https://www.oecd-ilibrary.org/content/publication/b25efab8-en>
8. D. C. Yang, Y. K. Tseng, T. L. Wang, *Eurasia J. Math. Sci. T.* **2017**, *13*, 2841–2857. DOI:10.12973/eurasia.2017.00721a
9. T. E. Raphael, *Read. Teach.* **1986**, *39*, 516–522. <https://www.jstor.org/stable/20199149>
10. J. L. Davenport, A. N. Rafferty, D. J. Yaron, *J. Chem. Educ.* **2018**, *95*, 1250–1259. DOI:10.1021/acs.jchemed.8b00048
11. I. Parchmann, C. Grasel, A. Baer, P. Nentwig, R. Demuth, B. Ralle, K. P. G. Chi, “*Chemie im Kontext*”: A symbiotic implementation of a context-based teaching and learning approach **2006**, *28*, 1041–1062. DOI:10.1080/09500690600702512
12. Y. P. Xin, *J. Educ. Res.* **2007**, *100*, 347–359. DOI:10.3200/JOER.100.6.347-360
13. E. Andersson-Bakken, K. M. Jegstad, J. Bakken, *Textbook tasks in the Norwegian school subject natural sciences: what views of science do they mediate?* **2020**, *42*, 1320–1338. DOI:10.1080/09500693.2020.1756516
14. C. Wood, *Chem. Educ. Res. Pract.* **2006**, *7*, 96–113. DOI:10.1039/B6RP90003H
15. J. Osborne, Science for citizenship. In *Good practice in science teaching. What research has to say*, Osborne, J.; Dillon, J., Eds. Open University Press: New York, **2010**; pp 44–67.
16. J. Bakken, E. Andersson-Bakken, *J. Curriculum Stud.* **2021**, *1*–20. DOI:10.1080/00220272.2021.1929499
17. Z. Sikorová, *Učitel a učebnice: užívání učebnic na 2. stupni základních škol*. [A teacher and textbooks: The use of textbooks at lower-secondary education]; Ostravská univerzita v Ostravě, Pedagogická fakulta: Ostrava, **2010**;
18. P.-I. Chou, *Int. J. Sci. Mat. Educ.* **2020**, *1*–19. DOI:10.1007/s10763-020-10083-9
19. M. Johansson. Teaching mathematics with textbooks: a classroom and curricular perspective. Doctoral thesis, Luleå tekniska universitet, **2006**.
20. A. G. Harrison, *Res. Sci. Ed.* **2001**, *31*, 401–435. DOI:10.1023/A:1013120312331
21. A. Bergqvist, S.-N. Chang Rundgren, *Res. Sci. Tech. Educ.* **2017**, *35*, 215–237. DOI:10.1080/02635143.2017.1295934
22. M. Lepik, B. Grevholm, A. Viholainen, *Nord. Stud. Math. Ed.* **2015**, *20*, 129–156. <http://arkiv.ncm.gu.se/node/7993>
23. J. Törnroos, *Stud. Edu. Eval.* **2005**, *31*, 315–327. DOI:10.1016/j.stueduc.2005.11.005
24. C. Nakiboğlu, H. E. Yildirim, *Int. J. Sci. Math. Educ.* **2011**, *9*, 1047–1071. DOI:10.1007/s10763-010-9231-6
25. M. Overman, J. D. Vermunt, P. C. Meijer, A. M. W. Bulte, M. Brekelmans, *Int. J. Sci. Educ.* **2013**, *35*, 2954–2978. DOI:10.1080/09500693.2012.680253
26. K. N. Andersen, *J. Res. Sci. Teach.* **2020**, *57*, 481–509. DOI:10.1002/tea.21599
27. K. Vojří, M. Rusek, *Int. J. Sci. Educ.* **2019**, *41*, 1496–1516. DOI:10.1080/09500693.2019.1613584
28. H. V. Steenbrugge, M. Valcke, A. Desoete, *J. Curriculum Stud.* **2013**, *45*, 322–353. DOI:10.1080/00220272.2012.713995
29. J. Slavík, K. Dyttrtová, M. Fulková, *Pedagogika* **2010**, *60*, 27–46. https://pages.pedf.cuni.cz/pedagogika/files/2013/12/P_2010_3_4_04_Konceptov%C3%A1_27_46.pdf
30. G. Gillette, M. J. Sanger, *Chem. Educ. Res. Pract.* **2014**, *15*, 787–799. DOI:10.1039/C4RP00115J
31. M. Rusek, K. Vojří, Š. Šubová, *Chem. Did. Ecol. Metrol.* **2020**, *25*, 69–77. DOI:10.2478/cdem-2020-0004
32. Z. Kalhous, O. Obst, *Školní didaktika. Portál: Praha*, **2002**;
33. O. Jeřábek, M. Bílek, *Teorie a praxe tvorby didaktických testů*. Univerzita Palackého v Olomouci: Olomouc, **2010**;
34. K. Vojří In: Rusek, M.; Tóthová, M.; Vojří, K. (Eds.) *What tasks are included in chemistry textbooks for lower-secondary schools: A qualitative view: Project-based Education and other activating Strategies in Science Education XVIII.*, **2021**; pp 247–256.
35. L. W. Anderson, D. R. Krathwohl, *A Taxonomy for Learning, Teaching and Assessing: a revision of Bloom's taxonomy of educational objectives*. Longman: New York, **2001**;
36. M. J. Booker, *Ac. Questions* **2007**, *20*, 347–355. DOI:10.1007/s12129-007-9031-9
37. R. Elmas, M. Rusek, A. Lindell, P. Nieminen, K. Kasapoglu, M. Bílek, *Chem. Educ. Res. Pract.* **2020**, *21*, 839–851. DOI:10.1039/D0RP00058B
38. P. Kácovský, T. Jedličková, R. Kuba, M. Snětinová, P. Surynková, M. Vrhel, E. S. Urválková, *J. Curriculum Stud.* **2021**, *1*–22. DOI:10.1080/00220272.2021.1978557
39. Y.-J. Lee, M. Kim, H.-G. Yoon, *Int. J. Sci. Educ.* **2015**, *37*, 2193–2213. DOI:10.1080/09500693.2015.1072290
40. G. Näsström, *Int. J. Res. Math. Educ.* **2009**, *32*, 39–51. DOI:10.1080/17437270902749262
41. S. L. Zorluoglu, A. Kizilaslan, M. Yapucuoglu-Donmez, *Cypriot J Educ. Sci.* **2020**, *15*, 9–20. DOI:10.18844/cjes.v15i1.3516
42. J. R. Landis, G. G. Koch, *Biometrics* **1977**, *33*, 159–174. DOI:10.2307/2529310
43. M. Rusek, K. Chroustová, M. Bílek, P. A. Skřehot, Z. Hon, *Chem. Did. Ecol. Metrol.* **2020**, *15*, 93–100. DOI: 10.2478/cdem-2020-0006 DOI:10.2478/cdem-2020-0006
44. H. Čtrnáctová, J. Zajíček, *Chem. Listy* **2010**, *104*, 811–818. http://www.chemicke-listy.cz/docs/full/2010_08_811-818.pdf
45. A. S. Bakken, *Educ. Res.* **2019**, *61*, 105–122. DOI:10.1080/00131881.2018.1561202
46. J.-W. Son, O.-K. Kim, *Math. Educ. Res. J.* **2015**, *27*, 491–518. DOI:10.1007/s13394-015-0148-9
47. R. Švaříček, *Stud. paed.* **2011**, *16*, 9–46. <https://journals.muni.cz/studia-paedagogica/article/view/18726/14787>
48. H. Čtrnáctová, *Pedagogika* **1997**, *47*, 138–149. DOI:10.1016/S0045-8732(97)83171-3
49. S. Janoušková, V. Žák, M. Rusek, *Stud. paed.* **2019**, *24*, 93–109. DOI:10.5817/SP2019-3-4
50. S. B. Boesdorfer, R. A. Livermore, *Chem. Educ. Res. Pract.* **2018**, *19*, 135–148. DOI:10.1039/C7RP00159B
51. P. Perkkilä, *Opettajien matemaattikkaukomukset ja matemaattikan oppikirjan merkitys alkuopetuksessa [Teachers' mathematical beliefs and the role of the mathematics textbook in primary education]*. Jyväskylän yliopisto: Jyväskylä, **2002**; <http://>

- urn.fi/URN:ISBN:978-951-39-5338-6
52. A. Logar, V. F. Savec, *Acta Chim. Slov.* **2011**, *58*, 866–875. <http://acta-arhiv.chem-soc.si/58/58-4-866.pdf>
53. A. Logar, C. Peklaj, V. F. Savec, *Acta Chim. Slov.* **2017**, *64*, 661–671. DOI:10.17344/acsi.2017.3544
54. F. Abd-El-Khalick, M. Waters, A. P. Le, *J. Res. Sci. Teach.* **2008**, *45*, 835–855. DOI:10.1002/tea.20226
55. K. Vojříř, M. Rusek, *Chem. Listy* **2020**, *114*, 366–369. <http://www.chemicke-listy.cz/ojs3/index.php/chemicke-listy/article/view/3606/3552>
56. J. van den Akker, Curricular development research as specimen of educational design research. In *Educational Design Research*, Plomp, T.; Nieveen, N., Eds. Netherlands Institute for Curriculum Development: Enschede, **2013**; pp 52–71.
57. C. Kulgemeyer, H. Schecker, *Res. Sci. Ed.* **2013**, *43*, 2235–2256. DOI:10.1007/s11165-013-9354-1
58. ČŠI, *Výběrové zjiřtování výsledků řáků na úrovni 5. a 9. ročníků základních řkol ve řkolním roce 2016/2017 – závěrečná zpráva*. [Selective survey on students' results at the level of 5th and 9th lower-secondary school grade in the school year 2016/2017 – Final report]; Česká řkolní inspekce: Praha, **2017**;
59. N. Graulich, *Chem. Educ. Res. Pract.* **2015**, *16*, 9–21. DOI:10.1039/C4RP00165F
60. M. Tóthová, M. Rusek, *Acta Chim. Slov.* **2021**, *68*, 1016–1026. <https://doi.org/10.17344/acsi.2021.7082>
61. W. R. Robinson, *J. Chem. Educ.* **2003**, *80*, 978–982. DOI:10.1021/ed080p978
62. E. T. Pappa, G. Tsaparlis, *Evaluation of questions in general chemistry textbooks according to the form of the questions and the Question-Answer Relationship (QAR): the case of intra- and intermolecular chemical bonding* **2011**, *12*, 262–270. DOI:10.1039/C1RP90031E
63. M. Simon, A. Budke, *Sustainability – Basel* **2020**, *12*, 1–19. DOI:10.3390/su12208344
64. J. K. Gilbert, A. M. Bulte, A. Pilot, *Int. J. Sci. Educ.* **2011**, *33*, 817–837. DOI:10.1080/09500693.2010.493185
65. L. Honskusová, K. Vojříř, M. Rusek, *J. Balt. Sci. Educ.* **2022**, *21*, in press. DOI:10.33225/jbse/22.21.00
66. L. S. Shulman, *Educ. Researcher* **1986**, *15*, 4–14. DOI:10.3102/0013189X015002004

Povzetek

Analizirali smo naloge v čeških učbenikih kemije za nižje srednje šole, da bi opisali njihovo umestitev v poglavjih učbenika, vrsto zahtevanega odgovora, splošno naravo naloge in kognitivne zahteve. Rezultati so pokazali, da starejši učbeniki vsebujejo banke nalog na koncu poglavij, kar kaže na transmisivno paradigmo poučevanja, medtem ko novejši učbeniki vsebujejo naloge znotraj poglavij. Kar zadeva naravo nalog, je bila v učbenikih za kemijo ugotovljena stereotipna zvrst. Večina učbeniških nalog zahteva odprte odgovore in je usmerjena v pomnjenje dejanskega in konceptualnega znanja ali uporabo postopkov. Avtorji zato predlagajo več sprememb nalog, vključno z njihovim položajem v poglavjih, kognitivno zahtevnostjo ter zahtevano vrsto odgovora, da bi izpolnili cilje kemijskega izobraževanja.



Scientific paper

To What Extent do Freshmen University Chemistry Students Master Chemistry Calculations?

Martin Rusek,^{1,*} Karel Vojíš,^{1,2} Iveta Bártová,³ Marta Klečková,³
Vladimír Sirotek⁴ and Jitka Štrofová⁴

¹ Department of Chemistry and Chemistry Education, Faculty of Education, Charles University, M. Rettigové 4, 116 39 Praha 1, Czech Republic

² Department of Biology and Environmental Studies, Faculty of Education, Charles University, M. Rettigové 4, 116 39 Praha 1, Czech Republic

³ Department of Inorganic Chemistry, Faculty of Science, Palacký University Olomouc, 17. listopadu 1192/12, 779 00 Olomouc, Czech Republic

⁴ Department of Chemistry, Faculty of Education, University of West Bohemia, Veslavínova 42, 306 14 Plzeň 3, Czech Republic

* Corresponding author: E-mail: martin.rusek@pedf.cuni.cz

Received: 11-04-2021

Abstract

The research mapped chemistry-oriented university freshman students' ability to solve chemical calculations. Their success was monitored based on several factors such as their faculty, field of studies, the type of calculation and the assignment type (word problem vs. formula). The results indicate a significant need to change the approach to teaching chemical calculations - the students were rather unsuccessful in the tasks. The obstacles they face include the ability to identify a problem, understand the concepts of calculation and appropriately adjust the correct use of the mathematical apparatus. These findings represent an impulse for teaching in upper-secondary school as well as to introductory university courses.

Keywords: Chemistry calculations; students' success; teaching chemistry; freshman students

1. Introduction

Chemistry calculations are a widely discussed area of chemistry in many countries.¹⁻⁴ On the one hand, they represent a very substantial base for chemistry students, which they apply practically throughout their entire university studies, mainly in the laboratory.⁵ On the other hand, research⁶⁻⁷ has shown the topic is considered critical in schools for several reasons: it is a link between mathematical skills and chemical content, pupils consider it difficult and unimportant.⁷ In professional discourse, questions arise as to whether this topic is appropriate in the chemistry curriculum at primary school and in the general educational fields of secondary schools.⁸

As research shows various parallels worldwide, this research conducted in Czechia has the potential to inform other researchers as well as teachers internationally.

2. Theoretical Background

2. 1. Research on Chemistry Calculations

Chemistry calculation tasks represent a special form of tasks. They build on field concepts, however, these are

not the only variable. Mathematical skills, reading skills as well as general problem-solving skills are necessary for successful solutions.

The already mentioned difficulty in students ability to do chemistry calculations has been reported in several studies.^{2-4,9,10} Firstly, some identified the aforementioned mathematical skills to be the cause of pupils or students' failure in chemistry calculations. Leopold and Edgar¹⁰ argued that students' unsatisfactory mathematical skills (mathematics fluency) could be the reason for the limited skills necessary to further understanding of chemical concept development. In connection with this, another study⁹ found unsatisfactory skills among students entering chemistry-oriented university studies. In reaction to this phenomenon, some authors suggested new algorithmic approaches which would make the topic more accessible to students.¹¹

In other studies,^{3,4} however, students' mathematical skills were not found to be such a strong factor, although they appear to play a role. A possible explanation for students' lower ability to solve chemistry calculations may also be caused by the lack of the students' ability to operate with concepts as well as their ability to identify the pro-

blem in the given role. Research showed that pupils have significant gaps in this area.¹² With the obstacle constituted by the difficulty of chemistry concepts and the need to select only the most important,¹³ supportive formulas to work with the commonly used rules were also suggested.¹⁴

Secondly, students' results can be affected by the tasks' context which is carried by text. Added context on one hand brings relevance,¹⁵ but on the other hand it increases the task's difficulty, as students need a certain level of reading literacy.^{16,17} In contrast to rigid tasks containing only values and variables together with a problem to solve, tasks containing context are word problems requiring text processing and understanding and realization of the problem. Only then can particular relationships be understood and a correct mathematical model applied in order to solve the problem.^{18,19}

Thirdly, calculation tasks represent a special form of problems, therefore require problem-solving skills. A significant body of research stresses problem-solving skills as a vital agent in chemistry education.^{20–22} However, several studies suggest these skills are underdeveloped in many students.

As far as particular chemistry calculations topics are concerned, there was only a limited amount of information on the topics' difficulty. Childs & Sheehan found the most difficult topic for upper-secondary and university students were volumetric analysis calculations, redox reactions and concentration of solutions.¹ Rusek et al. identified pH calculations, calculations with the equation of state, calculations from chemical equations to be the most difficult.³ There was an intersection with the aforementioned research in the topic of redox reactions, dilution solutions calculations and calculations of molar concentration.

2. 2. Chemistry Calculations in the Czech Curriculum

According to the currently valid chemistry curriculum, chemical calculations are already encountered by lower-secondary school students and later by the overwhelming majority of upper-secondary school students. The current version of the lower-secondary chemistry curriculum²³ contains the expected outcomes as follows: „calculates the composition of *solutions*, *practically prepares* a solution for a *given composition*“. The grammar school curriculum²⁴ mentions „a student performs *chemical calculations and applies them in solving practical problems*“. This general outcome is complemented by, in secondary schools, binding subject-matter: *quantities and calculations in chemistry*. Therefore, there is no concretization, so the scope of teaching is left to individual schools or teachers. In the Framework Educational Programmes for Secondary Vocational Education (FEP SOV) with a non-academic focus,^{25,26} the topic of chemical calculations is represented by two expected outcomes: „expresses the composition of solutions in different *ways*, prepares a solu-

tion of the desired composition“ and „performs simple chemical calculations in solving practical *chemical problems*“ and further specifies the subject-matter „calculations in *chemistry*“. However, the importance of the turnover of ‚simple calculations‘ is further unspecified. As can be seen above, although the topic of chemical calculations is mandatory in teaching, the content is not further specified and is thus influenced mainly by tradition or with regard to the use of numerous published textbooks²⁷ based on former curriculum (cf. ²⁸).

3. Aims and Methodology

3. 1. Aims

As mentioned above, the extent of chemistry calculation subject-matter may vary from school to school. It is therefore very difficult to map the entire student population's chemical calculation solving skills. However, this skill plays a crucial role for students who have chosen chemistry as their field of study, especially in the early stages of their studies. These students are, on one hand, expected to have mastered the topic of calculations at a higher than basic level, thanks to their study ambitions and interest in the field. At the same time, it is these students who, in case of chemistry calculation solving skills deficits, can be significantly limited in their university studies.

With respect to understanding the results of secondary education in this area as well as mapping the baseline to which higher education courses must respond, the aim of this study was to find out *what chemistry calculation knowledge and skills freshman university students focused on chemistry have at the beginning of their studies*.

The general expectation was that the students are able to solve the chemistry calculation tasks at the chosen level. The study's aim was specified by the following hypotheses:

⁰H₁: There is no statistically significant difference in chemistry calculation test results between students in study programmes focused on chemistry and on chemistry education.

With regard to the double task type (word problem and symbols), the second hypothesis was tested:

⁰H₂: There is no statistically significant difference between the students' results in word problems and tasks assigned using symbols.

This hypothesis was supported by Tóthová and Rusek.¹²

3. 2. The Research Sample

The research sample consisted of 220 students in the first year of bachelor's degrees. 42 % were students of chemistry-focused fields (environmental chemistry, biochemistry, restoration, etc.), 58 % of the sample were students of chemistry teaching-focused fields (combined with bio-

logy, mathematics, health education, etc.). In the academic year 2020/2021, these students studied at four different universities in Czechia.

3.3. The Research Tool

A test consisting of five pairs of tasks was used in the study. The tasks focused on: mass fraction, mixing solutions, molar concentration of solutions, calculations from chemical equations and pH calculations. Each pair of tasks was represented by a word problem and an example specified in symbolic notation using formulas and variables. The aim was to include only basic calculations with few partial steps,¹⁹ which would then not allow us to map the causes of possible solver failures. For illustration, two types of example are shown:

The word problem example

Saline used for medical purposes is a solution of sodium chloride in water in 0.15 mol/dm^3 concentration. Count how much sodium chloride is needed to prepare 30 litres of saline. Molar mass of NaCl is 58.5 g/mol .

The symbol type example

Count $m(\text{CuCl}_2)$ in a solution when you know that: $V(\text{solution}) = 24 \text{ dm}^3$, $c(\text{CuCl}_2) = 0.1 \text{ mol/dm}^3$, $M(\text{CuCl}_2) = 134.45 \text{ g/mol}$.

The test underwent a multi-cycle validation process in an expert panel consisting of six university teachers focused on chemistry calculation teaching and/or on chemistry education. The resulting test was piloted on a convenient sample of bachelor students. After slight changes in formulations, the final version of the test arose. It was given to freshman university students at the beginning of their studies (late September – mid October) in order not to affect the results of ongoing courses.

3.4. Used Methods

Statistical analysis was performed in IBM SPSS Statistics 26. Based on the normality test, which did not enable rejection of the hypothesis about normal distribution of the data (the Saphiro-Wilk test results $p > 0.05$), non-parametric tests were used. To examine differences among students from different universities/faculties, Kruskal-Wallis' test designed for K independent samples' comparison was used. To evaluate both students' results according to their study field as well as the results divided according to the task type, Wilcoxon's single-rank test designed for two dependent samples comparison was used. To calculate the effect-size, r was used as an alternative to the parametric Cohen's d test.

4. Results and Discussion

4.1. Overall Results

The results of the statistical analysis among the students from different universities/faculties ($p > 0.05$) suggested there are no statistically significant difference – the students from faculties of science did not reach better results than students from the faculties of education. Likewise, the differences between the students focused on chemistry and chemistry education ($p > 0.05$) did not suggest any statistically significant difference. The original expectation about chemistry students outperforming chemistry education students was not proven. The sample was then considered homogenous.

The students' success in solving individual calculation types is shown in Figure 1. The students achieved the highest success rate in the mass fraction calculations, with some distance from solutions' concentration and composition. However, even these results do not correspond to expectations for students who have chosen chemistry as

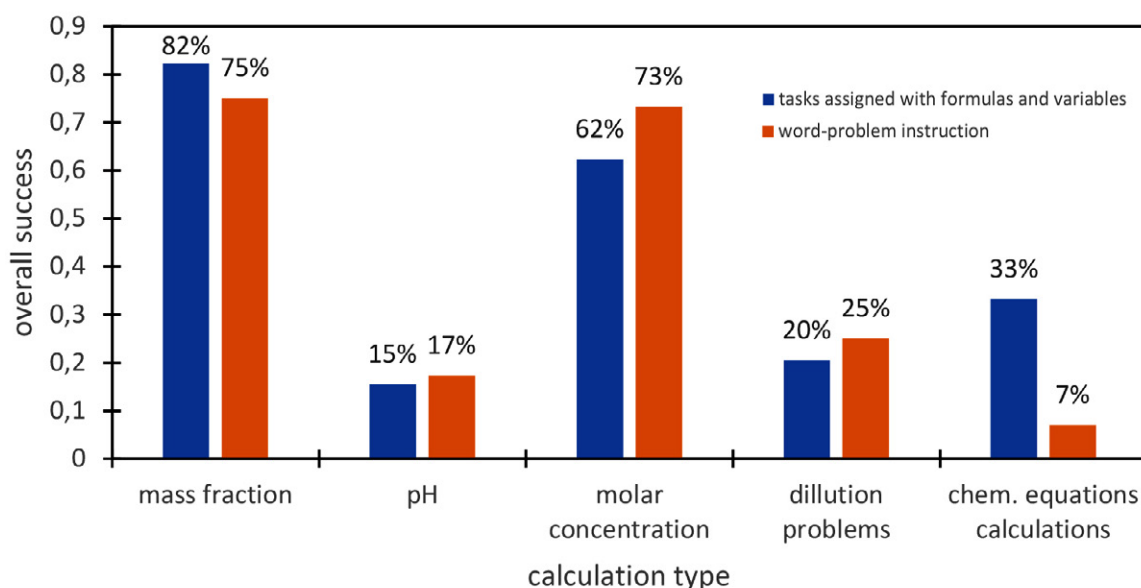


Figure 1. Students' success in solving individual types of chemical calculations depending on the type of assignment

their field of study. Although the composition of solutions calculation is already an obligatory output in lower-secondary education,²³ a fourth of the students failed to solve the task about the components of the mixture's mass proportions. The results for pH calculations, solution mixing and chemical equations, which were solved by only a third of students, are all the more dramatic. These results complete the previously identified problematic calculation types.^{1,3}

4. 2. Differences Between Students' Results by Assignment Type

As proven by Drummond and Selvaratnam,⁹ students often struggle to process mathematical information given in word problems and convert them into appropriate relationships and formulas. This involves both the use of the corresponding mathematical relationships expressed in the word input and the conversion of the verbally described quantities into the marks used in the formulas. Therefore, a higher success rate was assumed when using chemical formulas and variable symbols to specify examples, due to a clearer definition of the example type leading directly to the placement of specific symbols in known definition relationships. Based on previous research, reading demands were considered a hurdle too.^{6,17}

The Kruskal-Wallis test value ($p < 0.05$) enabled us to reject the zero hypothesis of comparable student outcomes according to the assignment type. Specifically, there were differences in calculations focused on the mass fraction ($p = 0.022$; $r = 0.01$), molar concentration and composition of solutions ($p = 0.03$, $r = 0.143$), and calculations from chemical equations ($p < 0.001$, $r = 0.337$). While for examples of calculating the mass fraction and chemical equation calculations, students were statistically significantly more successful in the tasks assigned in formulas and variables, but in the solution concentration calculations, this was the opposite. However, the effect-size value in cases of mass fraction and concentration calculations indicates a *low* effect-size. For calculations from chemical equations, the effect-size was medium. For this reason, the initial assumption was only partially confirmed, and further research is needed on the effect of longer text on student results. Especially in calculations from chemical equations, the result could also be influenced by students' reading literacy. The task focused on this type of calculation contained the longest text describing the reaction, its course and amount of individual reactants due to the information needed to describe the situation. In contrast, in the assignment using chemical equations and variable symbols, it was not necessary to analyze the input to understand the context and identify the variables, and the information was already ready to apply the algorithmic calculation.

A sufficient level of reading literacy appears to be a prerequisite to develop scientific literacy²⁹ and in con-

sequence also for problem solving, including chemical calculations. To initiate any change in this area, it seems desirable to shift the choice of teaching from tasks focusing on isolated field knowledge³⁰ towards the use of tasks including analyzing and choosing appropriate solutions. Since chemistry textbooks do not seem to offer such opportunity,³¹ before the new chemistry textbook paradigm takes over, it is important to develop other supporting materials.

Another explanation could be in the context of the word problems. Students are known to be more active in task solving when they relate to the context.³² The word problem in which the students reached better results – molar concentration – built on a medical context. This could be closer to the students than the chemistry context of the other two types of calculations.

4. 3. Causes of Students' Failure

In the tasks aimed at calculating the mass fraction, the most common cause of students' failure was the non-mention of the relevant mathematical relationship for the weight of the individual components and the whole system. The students who failed usually did not include the dissolved substance's mass to the solvent's mass. Also, some of them failed to provide a mathematical formula or other proportional calculation. Furthermore, numerical errors or unit mis-indications appeared, indicating a fairly common misunderstanding of the concept of mass fraction as a relative quantity. Similarly, for the second type of expressing the solution's composition included in the test (examples of molar concentration calculation), typically unsuccessful students did not even state the basic relationship (formula) required for the calculation. 77 % of the students reported a general formula or otherwise expressed mathematical relationship to calculate molar concentration, and most of them were also able to use it. A similar proportion of students (78 %) introduced a relationship to calculate the weight of a substance from a substance amount. Lower shares of successful solutions were mainly due to the addition of specific values according to the assignment or numerical errors.

While in simple calculations focused on solution composition the success rate was relatively higher, in the examples aimed at mixing solutions, only 34 % of students reported a relevant mathematical relationship (mixing equation or other calculation involving weight-to-mass fraction relationships in mass fraction) and only 30 % of respondents used it in their calculation. Many students were able to express the composition of solutions only in simple examples based on the application of a direct algorithmic solution. Nevertheless, their conceptual understanding of individual quantities and their relationships may not be sufficient to use them in examples requiring more comprehensive judgment. This problem seems to have a wider validity in relation to chemical problem solving (cf.^{21,33}). At the same time, the problems identified in int-

reducing adequate relationships for calculations further confirm that the low success rate in solving chemical calculations cannot be attributed only to students' insufficient mathematical skills^{3–4} and there is a need to focus more on the conceptual understanding of calculated quantities.

Students' difficulties were also identified in the field of using the relationships of quantities students encounter already in the early years of science education. Only 57 % of students provided the relationship for calculating weight when volume and density is given in these examples. This in itself does not represent any significant problem, nevertheless only 50 % used the calculation correctly in their test, which was represented as their understanding of this relationship.

In the examples aimed at calculating pH, ignorance of basic relationships was significant. Only 49 % of students reported the correct relationship to calculate pH and 27 % of pH–pOH relationship which was later mirrored in their test results. However, even if the right relationship was stated, there was a lack of conceptual understanding. Only 20 % of students took into account that sulfuric acid is dibasic. The rest of these only mechanically added a concentration value to the pH calculation formula. The result suggests that these students do not understand the principle of calculation and do not distinguish between the concentration of hydronium and the concentration of acid.

As far as the calculations from chemical equations are concerned, many students failed at the very beginning, i.e. balancing the formula. The chemical formula in the word-problem task was correctly solved by 50 % students, 64 % wrote reactants and products without balancing the formula. The symbolic-assignment task's formula was correctly balanced by 77 % students.

Since in both cases the equations contained only two reactants and one product, which can be considered one of the easiest versions, the result is surprising. Both the nomenclature of inorganic compounds and the balancing of chemical equations are given extensive attention in chemistry teaching,⁷ these topics also take up a significant number of textbook pages even for lower-secondary schools, although at the state curriculum level the emphasis on this topic is being gradually limited.²⁸ The findings show that, although it is a traditional chemistry subject-matter, teaching does not seem to lead to the desired educational outcomes, whereby the series of problematic topics is extended.³⁴ The seriousness of the findings is enhanced by the fact that the respondents were students interested in the field of chemistry. It therefore seems desirable to revise general education leading either to a large-scale innovation in teaching of this topic or to some form of its replacement with other key topics (big ideas), leaving the focus of nomenclature and chemical equation balancing for special seminars.

Although 48 % of respondents correctly established the relationship to calculate the amount of substance in the context of calculations from chemical equations, only 12 %

of respondents correctly used it. The most common problems were the faulty determination of the reactant in surplus, and by far errors in the stoichiometry. These problems suggest only a superficial understanding of the chemical equations' meaning. The simple algorithmic application of relevant quantities' relationships does not subsequently lead to the correct result. A similar problem was found by Mensah and Morabe³⁵. For the relevance of learning numerical algorithms, it is necessary to closely link the tasks with the described situation's conceptual understanding. The teaching process based on the expectation that students will understand the concept of the reaction's course and its outcome based on learning the algorithmic numerical procedures was proven ineffective.³⁵

Due to the fact the student sample was convenient, their relatively high number still did not allow the generalization of results to the entire population of students in the fields of chemistry or chemistry teaching. However, due to the variability of the sample (students came from a high number of secondary schools), the results show possible shortcomings in their preparation and significant limitations that need to be addressed at the beginning of chemistry's higher education.

5. Implications

The results showed critical problems in students' ability to solve chemistry calculations consists in their lack of conceptual understanding to the included variables (cf.¹³). This finding seems to be a product of the contemporary conception of chemistry (calculations') education. Its improvement, however, heavily depends on students' actual potential as too abstract concepts cannot be processed by students not even at lower-secondary,³⁶ but also in upper secondary school.³⁷ With respect to the results, implications for lower-secondary school chemistry calculations' education will be omitted with just a brief remark that only mass-fraction calculations and basic calculations of the amount of substance seem to be sufficient.

More concrete implications in the light of this research's results need to be divided in two parts respecting the actions: 1. secondary school curriculum and 2. reaction from universities.

In order to promote interest in the study of natural sciences as well as the use of skills acquired in general education in an extracurricular environment, rethinking the concept of a curriculum for chemical education needs to be considered. Since there are only sporadic situations when people need to solve a specific chemistry calculation task (in many cases mere rule of three suffices), the topic can hardly be considered important for the field's inner structure. Therefore, it can be removed from the core subject-matter topics placed among broadening topics taught in selective seminars for students with further chemistry

studies ambitions. This act is also in accordance with other research which identified this topic is seen by students as too difficult, useless and with too much attention given to it.⁷ Considering its negative effect on students' attitudes and the fact that despite the perceived high number of lessons devoted to the topic, students mostly fail the tasks, its removal from core-curriculum (at the current extent) should be considered.

The finding that students' results coming into higher education from secondary schools are insufficient in the field of chemical calculations should be reflected in the relevant courses at higher education institutions. This condition represents a potential risk to their successful study. The courses simply cannot start as an extension of upper-secondary subject matter but need to consider starting from a considerably lower level. Also, the students' problems should be taken into account and tackled in the university courses to prevent the students from unnecessary struggle at the very beginning of their university studies. The key aspects are: understanding the key concepts, understanding the role of the formulas and relations in particular calculation types, followed by mastery of these procedures' application first on known, and later on unknown problems.³⁸ Also, with the less-problematic topics identified in this study, such introductory courses could save time not focusing on these topics and directly address the bigger, conceptual, problem before indulging in calculations as such.

6. Conclusion

Although the research sample does not fully allow generalization of the findings, parallels with previous research suggest that students' results in chemical calculations have significant reserves. This is an impulse for a wide range of areas and actors in education. The result is a message towards the content as well as concept of teaching this topic in upper-secondary, and even lower-secondary schools.

According to these partial findings, teaching chemistry at secondary school does not lead to the students mastering basic calculations. The study's results suggest that the output of secondary education is to adopt some algorithmic procedures consisting of placement in remembered definition relationships, but with conceptual understanding of calculated quantities and their relationships at a very low level. The findings are even more dramatic when the research sample is considered. Low conceptual understanding was found in individuals interested in chemistry. It is therefore reasonable to assume that the results would be even more unsatisfactory for secondary school students with interests in a different field than chemistry. For this reason, suggestions to remove this topic from the chemistry curriculum for everyone and its placement among a broadening topic for students with interest in chemistry

was made. However, even for the group of students with chemistry aspirations, the identified problems need to be taken into account during this topic's instruction. This naturally applies also for university courses. Being better prepared for these students' chemistry calculation problems could significantly improve their dropout rate and make their freshman semesters, but also following years, more pleasant and efficient.

7. References

1. P. E. Childs, M. Sheehan, *What's difficult about chemistry? An Irish perspective* **2009**, *10*, 204–218. DOI:10.1039/b914499b
2. F. Ö. Karataş, *Pre-service chemistry teachers' competencies in the laboratory: A cross-grade study in solution preparation* **2016**, *17*, 100–110. <https://www.scopus.com/inward/record.uri?eid=2-s2.0-85016439104&doi=10.1039%2fc5r-p00147a&partnerID=40&md5=e832b80c38b9cbaf1053cd-97b82c4ede> DOI:10.1039/c5rp00147a
3. M. Rusek, K. Vojří, K. Chroustová, An Investigation into Freshman Chemistry Teacher Students' Difficulty in Performing Chemistry Calculations. In *Scientific Thinking in Chemical Education*, Nodzynska, M., Ed. Pedagogical University of Kraków: Kraków, **2021**; pp 61–68.
4. F. J. Scott, *Chem. Educ. Res. Pract.* **2012**, *13*, 330–336. DOI:10.1039/C2RP00001F
5. M. C. Srougi, H. B. Miller, *Chem. Educ. Res. Pract.* **2018**, *19*, 319–330. DOI:10.1039/C7RP00152E
6. J. Rychtera, M. Bílek, I. Bártová, K. Chroustová, R. Sloup, M. Šmídl, V. Machková, J. Štrofová, K. Kolář, O. Kesnerová Řádková, *Arnica* **2018**, *8*, 35–44. https://www.arnica.zcu.cz/imagines/casopis/2018/Arnika_2018_1-5_Rychtera-Bilek--web.pdf
7. M. Rusek. Výzkum postojů žáků středních škol k výuce chemie na základní škole. [Vocational school students' attitudes towards chemistry education at lower-secondary schools research]. Doctoral thesis, Univerzita Karlova, Praha, **2013**.
8. M. Rusek, A. Jančařík, J. Novotná In: Rychtarikova, D.; Szarkova, D.; Balko, L. (Eds.) *Chemical calculations: A necessary evil or an important part of chemistry education?: APLIMAT 2016 – 15th Conference on Applied Mathematics 2016, Proceedings*, Bratislava, **2016**; pp 978–986.
9. H. P. Drummond, M. Selvaratnam, *S. African J. Chem.* **2009**, *62*, 179–184. <http://www.scielo.org.za/pdf/sajc/v62/31.pdf>
10. D. G. Leopold, B. Edgar, *J. Chem. Educ.* **2008**, *85*, 724–731. DOI:10.1021/ed085p724
11. G. Cepria, L. Salvatella, *General Procedure for the Easy Calculation of pH in an Introductory Course of General or Analytical Chemistry* **2014**, *91*, 524–530. DOI:10.1021/ed400089j
12. M. Tóthová, M. Rusek, V. Chytrý, *J. Chem. Educ.* **2021**, *98*, 1831–1840. DOI:10.1021/acs.jchemed.1c00167
13. F. A. Omar, B. L. Dreher, N. S. Winter, *Why Teach Molality in General Chemistry?* **2016**, *93*, 801–802. DOI:10.1021/acs.jchemed.5b00497
14. P. Minkiewicz, M. Darewicz, A. Iwaniak, *Introducing a Simple*

- Equation To Express Oxidation States as an Alternative to Using Rules Associated with Words Alone* **2018**, 95, 340–342. DOI:10.1021/acs.jchemed.7b00322
15. M. Stuckey, A. Hofstein, R. Mamlok-Naaman, I. Eilks, *Stud. Sci. Educ.* **2013**, 49, 1–34. DOI:10.1080/03057267.2013.802463
 16. J. Wellington, J. Osborne, *Language and literacy in science education*. McGraw-Hill Education: Buckingham, **2001**;
 17. N. Cruz Neri, K. Guill, J. Retelsdorf, *Eur. J. Psychol. Educ.* **2021**, 36, 45–61. DOI:10.1007/s10212-019-00453-5
 18. J. Novotná, *Analýza řešení slovních úloh*. [Analysis of word problems' solution]; Univerzita Karlova, Pedagogická fakulta: **2000**
 19. A. Johnstone, H. El-Banna, *Educ. Chem.* **1986**, 23, 80–84. DOI:10.1515/tsd-1986-230211
 20. N. Graulich, *Chem. Educ. Res. Pract.* **2015**, 16, 9–21. DOI:10.1039/C4RP00165F
 21. M. Tóthová, M. Rusek, *Acta Chim. Slov.* **2021**, 68, 1016–1026. DOI:10.17344/acsi.2021.7082
 22. M. Slapnicar, V. Tompa, S. A. Glazar, I. Devetak, J. Pavlin, *Acta Chim. Slov.* **2020**, 67, 904–915. DOI:10.17344/acsi.2020.5908
 23. *Rámcový vzdělávací program pro základní vzdělávání*. MŠMT: Praha, **2021**; http://www.nuv.cz/file/4982_1_1/
 24. *Rámcový vzdělávací program pro gymnázia*. [Framework educational programme for grammar schools]; Výzkumný ústav pedagogický v Praze: Praha, **2007**; http://www.vuppraha.cz/wp-content/uploads/2009/12/RVPG-2007-07_final.pdf
 25. *Rámcový vzdělávací program pro obor vzdělání 23-52-H/01 Nástrojař*. NÚOV: Praha, **2007**; <http://zpd.nuov.cz/RVP/H/RVP%202352H01%20Nastrojar.pdf>
 26. *Rámcový vzdělávací program pro obor vzdělání 78-42-M/02 Ekonomické lyceum*. [Framework educational programme for educational field 78-42-M/02 Economic lyceum]; NÚOV: Praha, **2007**; <http://zpd.nuov.cz/RVP/ML/RVP%207842M02%20Economicke%20lyceum.pdf>
 27. K. Vojíř, M. Rusek, *J. Balt. Sci. Educ.* **2021**, 20, 316–331. DOI:10.33225/jbse/21.20.316
 28. K. Vojíř, M. Rusek, *Chem. Listy* **2020**, 114, 366–369. <http://www.chemicke-listy.cz/ojs3/index.php/chemicke-listy/article/view/3606/3552>
 29. OECD, *PISA 2018 Assessment and Analytical Framework*. OECD Publishing: Paris, **2019**; <https://www.oecd-ilibrary.org/content/publication/b25efab8-en>
 30. K. Vojíř In: Rusek, M.; Tóthová, M.; Vojíř, K. (Eds.) *What tasks are included in chemistry textbooks for lower-secondary schools: A qualitative view: Project-based Education and other activating Strategies in Science Education XVIII.*, **2021**; pp 247–256.
 31. K. Vojíř, M. Rusek, *Opportunities for learning: Analysis of Czech lower-secondary chemistry textbook tasks* **2022**, 69, in press.
 32. R. Havlíčková, *Sci in Educ.* **2020**, 11, 2–21. DOI:10.14712/18047106.1715
 33. M.-H. Chiu, *Algorithmic problem-solving and conceptual understanding of chemistry by students at a local high school in Taiwan* **2001**, 11, 20–38.
 34. M. Rusek, M. Tóthová In: Rusek, M.; Tóthová, M.; Vojíř, K. (Eds.) *Did students reach the periodic table related curricular objectives after leaving from lower-secondary education?: Project-Based Education and Other Activating Strategies in Science Education XVIII.*, Prague, CZECH REPUBLIC, **2021**; pp 178–185.
 35. A. Mensah, O. N. Morabe, *African J. Res. Mat. Sci. Tech. Educ.* **2018**, 22, 174–185. DOI:10.1080/18117295.2018.1475908
 36. J. Piaget, *The Construction of reality in the child*. Routledge & Kegan Paul: London, **1954**; DOI:10.1037/11168-000
 37. J. D. Herron, *Piaget for chemists – explaining what good students cannot understand* **1975**, 52, 146–150. <Go to ISI>://WOS:A1975W028900005 DOI:10.1021/ed052p146
 38. A. H. Johnstone, *Uni. Chem. Educ.* **2001**, 5, 12–18. DOI:10.7748/mhp.4.5.18.s16

Povzetek

Raziskava je prikazala zmožnost reševanja nalog s področja kemijskega računstva pri študentih prvega letnika s kemijско usmeritvijo. Uspešnost reševanja nalog smo spremljali glede na več dejavnikov, kot so fakulteta, smer študija, vrsta računске naloge in vrsta naloge (besedilna naloga ali formula). Rezultati kažejo na precejšnjo potrebo po spremembi pristopa k poučevanju kemijskega računanja, saj so bili študenti pri nalogah dokaj neuspešni. Ovire vključujejo sposobnost prepoznavanja problema, razumevanja konceptov kemijskega računanja in nenazadnje ustrezna uporaba matematičnega znanja. Ta opažanja predstavljajo vzpodbudo za poučevanje kemije na srednjih šolah in uvodnih univerzitetnih predmetih.



Except when otherwise noted, articles in this journal are published under the terms and conditions of the Creative Commons Attribution 4.0 International License

Scientific paper

The Use of Yeast *Saccharomyces Cerevisiae* as a Biorecognition element in the Development of a Model Impedimetric Biosensor for Caffeine Detection

Zala Štukovnik,¹ Regina Fuchs Godec¹ and Urban Bren^{1,2,*}¹ University in Maribor, Faculty for Chemistry and Chemical Engineering, Smetanova 17, 2000 Maribor, Slovenia² University of Primorska, Faculty of Mathematics, Natural sciences and Information Technologies, Glagoljaška 8, 6000 Koper, Slovenia

* Corresponding author: E-mail: urban.bren@um.si

Received: 11-26-2021

Abstract

In the present study, an electrochemical-impedimetric biosensor using *Saccharomyces cerevisiae* as an effective biorecognition element was designed to detect caffeine. The presented biosensor consists of a previously developed stainless steel electrochemical cell constructed as a three-electrode system in the RCW side-by-side configuration. The electrochemical stability of the sensing electrode was evaluated by measuring the open circuit potential (OCP), and electrochemical impedance spectroscopy (EIS) was applied to determine the impedimetric response of the biosensor with *Saccharomyces cerevisiae* cells attached to the working electrode (WE) in the absence (0.9% NaCl) and presence (10 mg/mL in 0.9% NaCl) of caffeine. Moreover, the limit of detection (LOD) was determined. In this way, a new approach in biosensor development has been established, which involves assembling a low-cost and disposable electrochemical system to detect alkaloids such as caffeine. The developed biosensor represents a good candidate for detecting caffeine in beverages, foods, and drugs with the merits of time-saving, robustness, low cost, and low detection limit.

Keywords: Impedimetric biosensor, *Saccharomyces cerevisiae*, electrochemical impedance spectroscopy, caffeine

1. Introduction

The demand for biosensors has increased significantly in the recent years due to the need for specific sensors that can provide fast and reliable measurements in various research areas. The development of biosensors is of interest for different applications ranging from biochemical profiling of normal and pathologic cells, over clinical diagnostics and drug discovery to more straightforward analyses such as fermentation, process monitoring, environmental testing, and food and beverages quality control.^{1–3} Detection of alkaloids such as caffeine has attracted abundant attention due to their extensive occurrence in beverages and drugs.⁴ However, conventional detection methods for caffeine (high-performance liquid chromatography-mass spectrometry (HPLC-MS), thin-layer chromatography (TLC), and immunoassay) have several drawbacks, including expensive equipment as well as complex and laborious sample preparation.⁵

Biosensors, as analytical devices, convert a biological response into an electrical signal and provide us with the

information on the concentration of the target analyte.^{6,7} Biosensors may present the best candidates for detecting caffeine with the merits of high sensitivity and specificity, convenience, time-saving, low cost, and low detection limit.⁸ Biosensors can be based on animal tissues, bacteria, or eukaryotic microorganisms such as yeasts.⁹ Although yeasts are highly resistant to adverse environmental conditions, they can sense and respond to a variety of stimuli and, unlike several alternative biological components, do not require sophisticated sterile techniques or complex media.^{10,11} Yeast *Saccharomyces cerevisiae* represents a single-cell eukaryotic organism used primarily in the food industry to produce bakery products and alcoholic beverages.^{9,12} It is chemoorganotrophic and anaerobic organism classified in the kingdom of Fungi, phylum *Ascomycota*, class *Saccharomycetes*, order *Saccharomycetales*, and family *Saccharomycetaceae*.¹³ *Saccharomyces cerevisiae* can exist in two different forms, the haploid or the diploid form.^{13,14} A yeast cell possesses the typical characteristics of a eukaryotic cell and characteristic organelles such as vacuoles

and lipid droplets.¹² It is usually spherical to slightly spherical and occasionally ellipsoidal to cylindrical.¹⁵

Caffeine (1,3,7-trimethylxanthine), with the chemical molecular formula of $C_8H_{10}N_4O_2$, has been used for thousands of years and represents one of the most widely consumed food ingredient throughout the world.^{1,16} It is found in common beverages such as coffee, tea, and soft drinks, as well as in products containing cocoa or chocolate, and in a variety of medications and dietary supplements.^{17,18} Due to the high consumption of caffeinated foods, beverages, and medicines worldwide, caffeine is also considered to be the most representative pharmaceutically active pollutant with regard to its abundance in the environment.¹⁹ Based on the data reviewed, it is concluded that in the healthy adult population, daily caffeine intake at a dose exceeding 400 mg is associated with adverse effects such as general toxicity, cardiovascular effects, effects on bone status and calcium balance, changes in adult behavior, increased cancer incidence and effects on male fertility.²⁰ The caffeine content in coffee products ranges from 0.27 to 1.85 mg/mL, in tea from 0.11 to 0.23 mg/mL, in energy drinks from 0.30 to 0.37 mg/mL, and in soft drinks such as regular cola from 0.10 to 0.13 mg/mL.^{21–23} Given these values, the biosensor may be sufficiently sensitive and robust enough to cover the range of caffeine concentrations present in beverages.

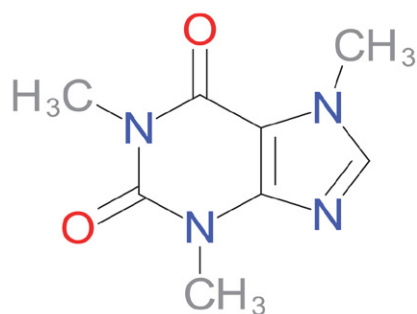


Figure 1: Chemical structure of the caffeine molecule

For the detection of different caffeine concentrations, the electrochemical impedance spectroscopy (EIS) method was applied. EIS is widely used in the production and optimization of biosensors as this method allows for the characterization of the biological component attached to the sensor and of the analyte present in the sample.^{24,25} Because biosensors produce a rapid response, they can be applied to monitor molecular events in real-time.²⁶ The EIS method was used to measure the frequency response of the electric current, which provides data on the adhesion layer of *Saccharomyces cerevisiae* on the electrode surfaces.

The aim of this study was to develop a model electrochemical impedimetric biosensor for the detection of caffeine using *Saccharomyces cerevisiae* as an effective bi-

orecognition element with many advantageous properties such as cell robustness, ease of maintenance, and cell production rate.

2. Experimental

The developed biosensor consists of a stainless steel electrochemical cell (Figure 2) constructed as a three-electrode system in the RCW-side by side configuration, including the working electrode (WE) with yeast cells on the surface, the reference electrode (RE), and the counter electrode (CE). Such electrochemical cell was previously developed and tested.¹⁰ In assembling the electrochemical cell, stainless steel type SS316 (manufacturer TBJ Industries, Germany) was used. The electrodes were manufactured with a dimension of electrode 20 mm × 5 mm, where the active component was applied to the 5 mm × 5 mm. The electrodes were insulated on the fixation side, and the system was sealed with glass.

Saccharomyces cerevisiae was applied to the working electrode using a technique involving a mold made with a 3D printer, which ensured that the layer thickness (0.10 mm) was similar for all measurements. 3.8 g *Saccharomyces cerevisiae* was mixed with 1 mL 0.9% NaCl to ensure that the mixture was viscous. The mixture was applied on the stainless-steel electrode inserted in the mold. The process of coating the working electrode (WE) was taken at 25 °C and took approximately 30 seconds.

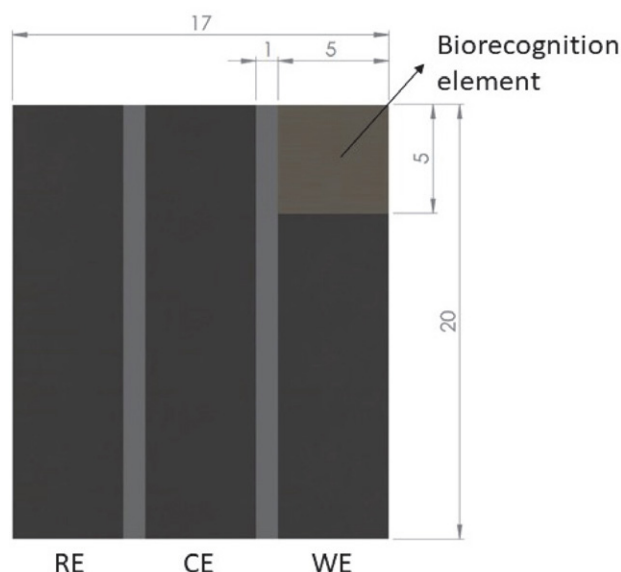


Figure 2: Electrochemical cell in the RCW-side-by-side configuration and the *Saccharomyces cerevisiae* cells attached to the working electrode (WE).

Two solutions were prepared for the measurements, the 0.9% NaCl solution (Sigma Aldrich, CAS: 7647-14-5, M: 58.44 g/mol) and 10 mg/mL caffeine (Sigma Aldrich,

CAS: 58-08-2, M: 194.19 g/mol) in 0.9% NaCl solution. The electrochemical cell with *Saccharomyces cerevisiae* on the working electrode was connected to the Multi Palm-sens4 potentiostat. Initially, 1 mL of the 0.9% NaCl solution was injected into the system, and the open circuit potential (OCP) and EIS measurements were performed. Then, the excess saline (0.9% NaCl) was drained. Afterward, 1 mL of the 10 mg/mL caffeine solution was injected into the system, and OCP and EIS measurements were repeated.

The electrochemical characterization of the working electrode was evaluated by measuring the OCP to assess the stability of the electrode. The duration of the measurement was 600 seconds since living yeast cells were utilized.

The EIS method was applied to evaluate the biosensor with yeast on the stainless-steel surface. Impedance spectra were obtained at a steady open circuit potential (OCP) in the frequency range from 100 kHz to 10 mHz with 10 points per decade and a 20 mV amplitude of the excitation signal. The potential amplitude was chosen at 20 mV since the lower amplitudes have not provided the stable signal due to the yeast layer on the stainless-steel electrode.

The EIS measurement's expected duration was 2 minutes and 15 seconds, although this time was often extended up to 3 minutes. EIS was used to obtain data on the processes on the surface of the electrode and the applied layers, and the Bode and Nyquist plots were interpreted as the results.

Moreover, the limit of detection (LOD) was determined based on the impedance drop with the increasing concentration of caffeine in 0.9% NaCl. For the measurement, eight different caffeine concentrations in saline (0.0 mg/mL, 0.05 mg/mL, 0.01 mg/mL, 0.1 mg/mL, 0.25 mg/mL, 0.5 mg/mL, 1.0 mg/mL, and 5.0 mg/mL) were prepared and 1 mL of each sample was injected into the system separately. The blank solution consisted of 0.9% NaCl solution (saline). Three measurements were taken for each concentration, where the mean value (MV), standard deviation (SD), precision, and accuracy of the measurements were calculated. The measurements were taken using identical parameters as in the measurements mentioned before, and the data were obtained at the frequency 125 mHz.

3. Results and Discussion

3.1. Open Circuit Potential (OCP) Measurements

The electrochemical characterization of the sensing electrode was evaluated by measuring the OCP to assess the stability of the electrode. The OCP provides valuable insight into the thermodynamic stability of the electrode material involved in the electrochemical response.²⁷

The results are represented in Figure 1S in the Supplementary information. The data provided from the meas-

urements indicate that the system was thermodynamically stable. When measuring with *Saccharomyces cerevisiae* on the stainless steel surface of the working electrode (WE) with the addition of 0.9% NaCl and the addition of 10 mg/ml caffeine in 0.9% NaCl, a slight difference is observed at OCP in each measurement. The slight change in OCP is due to the living cells on the surface, which react to environmental conditions.

3.2. Electrochemical Impedance Spectroscopy (EIS)

EIS represents a non-destructive method that can be used to quantify specific parameters and simultaneously monitor multiple electrochemical processes.²⁸ The measurements are explained with the real (electrical resistance) and imaginary (capacitance) components of the impedance response of an electrochemical system.¹⁰

In the Nyquist diagram (Figure 3), the decrease in the resistance (real component, x-axis) and the decrease in the capacitance (imaginary component, y-axis) when 10 mg/mL caffeine in 0.9% NaCl was added to the system compared to the blank solution (0.9% NaCl) is seen. The results indicate that the electrode surface was released due to the detachment of yeast cells from the electrode surface.

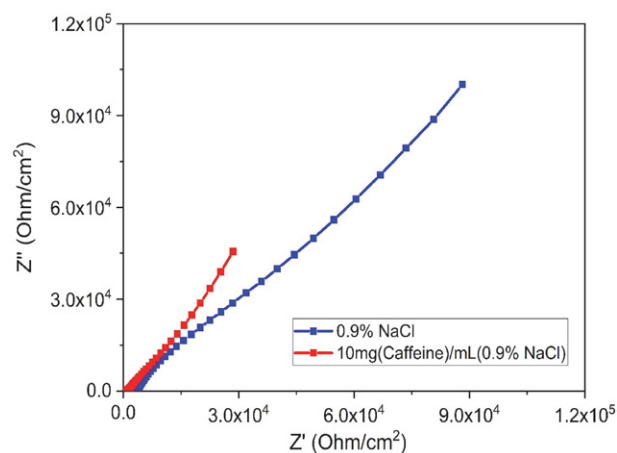


Figure 3: Nyquist diagram of the EIS measurement of the biosensor containing *Saccharomyces cerevisiae* on the WE, with the addition of 0.9% NaCl (blue) and 10 mg Caffeine in 1 mL 0.9% NaCl (red).

Bode plots consist of two spectra simultaneously, the impedance spectrum and the phase spectrum, in which the dependence of impedance (Z) and the dependence of phase angle on the frequency is shown. In the impedance spectrum, the activity at the working electrode is determined from the slopes of the line, and in the phase spectrum, the activity is determined from a phase angle.

Based on the impedance spectrum of the Bode diagram (Figure 4), the solution resistance (R_s) was determined with a slope of approximately 0 (high-frequency range), the capacitance of the electrical double layer (C_{dl}) was deter-

mined with a slope of approximately -0.8 , which occurs at the phase boundary between the electrode and the electrolyte (middle-frequency range), the charge transfer resistance was determined with a slope of approximately 0 (R_{ct}) which occurs due to the electrochemical reaction or due to the charge transfer between the electrolyte and the metal (middle-frequency range), as well as the diffusion with a slope approximately -0.5 (low-frequency range) was determined.

In the phase spectrum of the Bode diagram (Figure 5), the resistance is described as the negative phase at approximately 0° , the non-ideal capacitance with the negative phase at approximately 55° , the diffusion at the negative phase at approximately 45° .

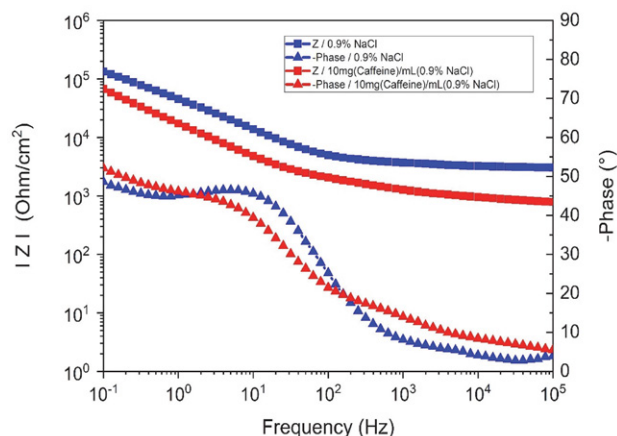


Figure 4: Bode diagram of the EIS measurement of the biosensor containing *Saccharomyces cerevisiae* on the WE, with the addition of 0.9% NaCl (blue) and 10 mg Caffeine in 1 mL 0.9% NaCl (red). The Bode diagram includes an impedance diagram described with squares and a phase diagram described with triangles, where $|Z|$ represents an impedance and $-Phase$ presents a negative phase shift.

The equivalent electrical circuits (EEC) of the stainless steel electrochemical cell without and with the yeast on the working electrode (WE) are shown in Figure 5.

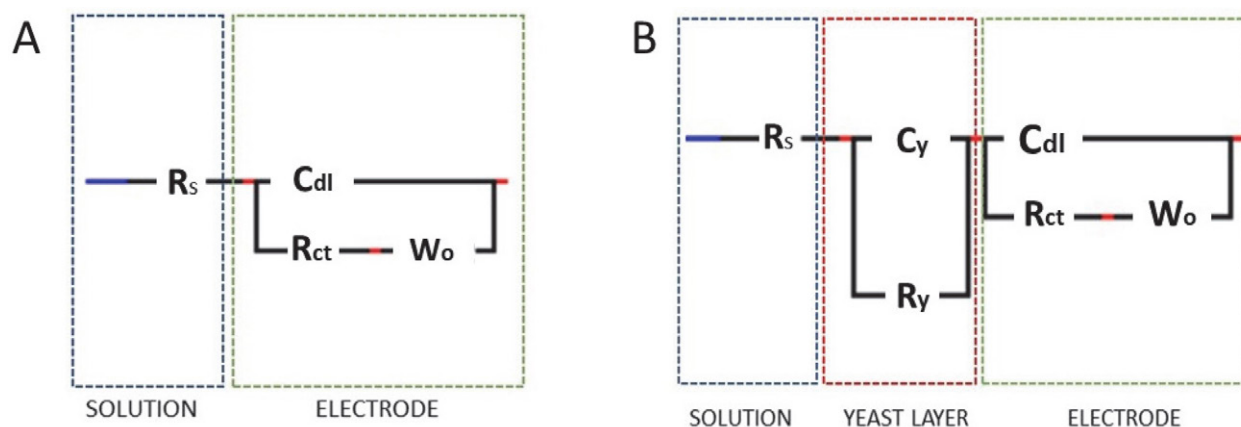


Figure 5: The equivalent electrical circuit (EEC) of the electrochemical cell without the yeast attached to the working electrode (Figure 5A) and with the electrochemical cell with yeast attached to the working electrode (Figure 5B). Figure 5A consists of the solution resistance (R_s), the capacitance of the electrical double layer (C_{dl}), the charge transfer resistance (R_{ct}), and the Warburg impedance (W_o). Figure 5B consists of the solution resistance (R_s), the yeast layer capacitance (C_y), the yeast layer resistance (R_y), the capacitance of the electrical double layer (C_{dl}), the charge transfer resistance (R_{ct}), and the Warburg open diffusion (W_o).

The EEC of the electrochemical cell without yeast cells attached to the stainless steel electrode is depicted in Figure 5A. The equivalent circuit consists of the solution resistance (R_s), the capacitance of the electrical double layer (C_{dl}), the charge transfer resistance (R_{ct}), and the Warburg impedance (W_o).

The EEC of the electrochemical cell with the yeast cells attached to the working electrode is shown in the Figure 5B and consists of the solution resistance (R_s), the yeast layer capacitance (C_y), the yeast layer resistance (R_y), the capacitance of the electrical double layer (C_{dl}), the charge transfer resistance (R_{ct}), and the Warburg open diffusion (W_o).

The comparison of the values of the parameters where the 0.9% NaCl and the 10 mg/mL caffeine in 0.9% NaCl were separately added to the system is provided in Table 1.

When caffeine was added to the system, the *Saccharomyces cerevisiae* cells detached from the stainless steel surface, and consequently, the electrode surface was released. Consequently, the resistance of the system dropped, and the capacitance and the impedance of diffusion increased. The χ^2 of the measurement where 0.9% NaCl was added to the system was 2.94×10^{-3} , and for the measurement where the 10 mg/mL caffeine in 0.9% NaCl was added 1.48×10^{-3} .

Table 1: Comparison of the EEC parameters when the 0.9% NaCl and the 10 mg/mL caffeine in 0.9% NaCl were added to the system.

Parameters	0.9% NaCl	10 mg/mL Caffeine
R_s (kOhm/cm ²)	3.07	0.69
R_y (kOhm/cm ²)	55.65	1.08
R_{ct} (kOhm/cm ²)	103.35	78.97
C_y (μ F/cm ²)	21.17	2237.20
C_{dl} (μ F/cm ²)	77.26	208.72
W_{or} (kOhm/cm ²)	8.42	12.68
W_{oc} (Ohm/cm ²)	0.09	1.21

3. 3. Limit of Detection (LOD) and Limit of Quantification (LOQ)

In Table 2, the decrease in impedance ($|Z|$) with the increasing concentration of caffeine in saline (c) is reported. Compared to the blank solution, the decrease in impedance is observed with the addition of 0.1 mg/mL of caffeine in 0.9% NaCl. The data were obtained at a frequency of 125 mHz. Three measurements were taken for each concentration, where the mean value (MV), standard deviation (SD), precision, and accuracy of the measurements were calculated.

Table 2: The decrease in impedance with increasing concentration of caffeine in 0.9% NaCl

C (mg/mL)	logC (mg/mL)	MV $\log Z $ (kOhm/cm ²)	SD (kOhm/cm ²)	Precision (%)	Accuracy (%)
0.00	/	237.472	0.539	99.503	99.681
0.01	-2.00	231.935	2.895	97.051	98.318
0.05	-1.30	221.839	2.998	96.827	98.166
0.10	-1.00	106.922	1.929	96.161	97.515
0.25	-0.61	98.402	0.555	98.627	99.310
0.50	-0.30	94.551	0.272	99.312	99.616
1.00	0.00	88.514	0.583	97.949	98.859
5.00	0.70	75.801	0.332	98.175	99.010

The impedance decrease with increasing concentrations is also represented as a box plot (Figure 6). The data were obtained at a frequency of 125 mHz. The box plot shows the mean values as a dot, the upper whiskers represent the maximum, the lower whiskers represent the minimum, and the box represents the interquartile range. The distinct decrease in the impedance is observed at 0.1 mg/mL concentration.

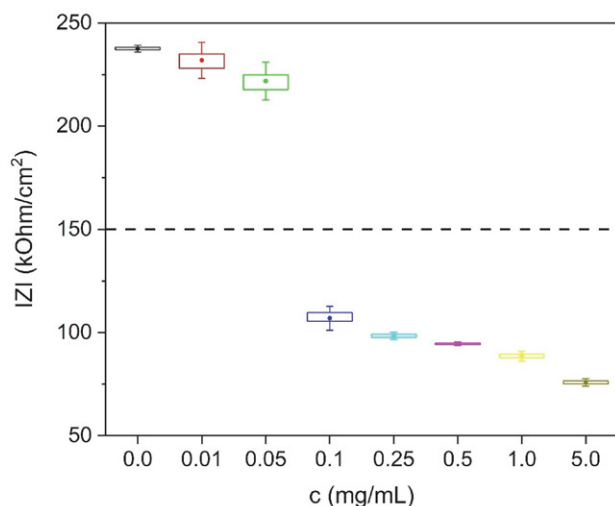


Figure 6: Box plot representing the impedance ($\log|Z|$) decrease with the increasing concentrations (c) of caffeine

The system's linearity was obtained in the concentration range from 0.1 mg/mL to 5 mg/mL with R^2 of 0.997 (Figure 7). The concentrations were calculated to logarithmic values (Table 2) to obtain linear regression since the impedance values read from the Bode plot were logarithmic. Based on the 3-Sigma criteria, the LOD was determined at 0.728 mg/mL, and based on the 10-sigma criteria, the LOQ was determined at a concentration of 0.382 mg/mL. It was observed that the impedance decreased with the increasing concentration of the caffeine in the solution. Thus, it can be concluded that the biosensor can sense the presence of caffeine in the solution.

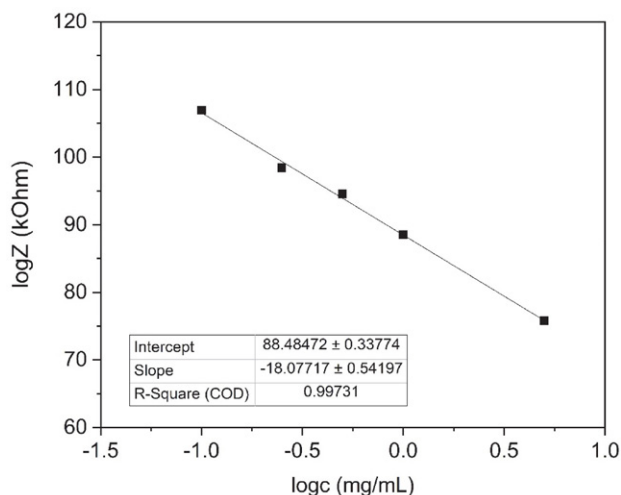


Figure 7: Calibration curve between the impedance ($\log|Z|$) and the caffeine concentrations ($\log c$)

In conclusion, the Nyquist plot and the Bode plot of the investigated biosensor show that adding 10 mg/mL of caffeine in saline decreased the resistance and increased the capacitance, indicating that the electrode surface is released. Due to the *Saccharomyces cerevisiae* detachment from the stainless steel surface, the parameters of the EEC changed: the system's resistance decreased, and the capacitance increased. Consequently, it can be indeed concluded that caffeine can cause the desorption and death of *Saccharomyces cerevisiae* cells.

Some other research was done in the field of electrochemical biosensors and caffeine detection. An amperometric biosensor for the determination of caffeine in solutions was developed, where whole cells of *Pseudomonas alcaligenes* were utilized. The biosensor system was able to detect caffeine in solution over a concentration range of 0.1 to 1 mg/mL.¹ In comparison, the linearity range with our biosensor was in the range of 0.1 to 5 mg/mL. A biosensor based on the inhibition of alkaline phosphatase (ALP) enzyme was developed for caffeine determination, where caffeine concentration can be determined accurately between 0.1 and 10 μ M and the LOD of the biosensor was 0.08 μ M.

This biosensor, compared to ours, had a lower LOD and linearity range as the enzymes were used as a biorecognition element. Also, an electrochemical impedance aptasensor based on a porous organic framework supported silver nanoparticles for ultrasensitively detecting theophylline, with the LOD of 0.191 pg/mL (1.06 pmol/L) in a wide concentration range of 5.0×10^{-4} to 5.0 ng/mL (2.78×10^{-3} to 27.8 nmol/L) was developed.²⁹

4. Conclusions

A new approach in biosensor development has been established, which involves assembling a low-cost and disposable electrochemical system for the detection of alkaloids such as caffeine. The caffeine detection with the presented method avoids an excessive use of solvents, requires only a small amount of analyte, and does not require lengthy preparation.

It was observed that the impedance decreased with the increasing concentration of the caffeine in the solution. It can be concluded that the developed biosensor is robust enough to detect the various caffeine concentrations. Based on the linear calibration curve of the impedance decrease with the increasing caffeine concentration, the LOD was determined at 0.728 mg/mL, and the LOQ was determined at 0.382 mg/mL. Therefore, it can be concluded that yeasts, although very resistant to adverse environmental conditions, can sense and respond to caffeine as stimuli.

Biosensors have the potential to represent the best candidate for caffeine detection with the merits of time-saving, robustness, low cost, and low detection limit. In the future, an upgraded impedimetric biosensor with the biorecognition element *Saccharomyces cerevisiae* could be used to detect the caffeine content in various beverages, foods, and medicines. Furthermore, impedimetric biosensors based on the described approach and using a simplified potentiostat/galvanostat, which is transferable and compared to other conventional methods cost less, could also be applied on a large scale for food monitoring, environmental monitoring, or even medical diagnostics.

Acknowledgments

Financial support from the Slovenian Research Agency through project (J1-2471) and programme (P2-0046) grants is gratefully acknowledged.

5. References

- V. R. S. Babu, S. Patra, N. G. Karanth, M. A. Kumar and M. S. Thakur, *Analytica Chimica Acta* **2007**, 582, 329–334. DOI:10.1016/j.aca.2006.09.017
- H. Kaur, A. Bhosale and S. Shrivastav, *Int J Health Sci Res* **2018**, 8, 315–333.
- P. Mehrotra, *J Oral Biol Craniofac Res* **2016**, 6, 153–159. DOI:10.1016/j.jobocr.2015.12.002
- J. dePaula and A. Farah, *Beverages* **2019**, 5, 37. DOI:10.3390/beverages5020037
- W. Ye, T. Liu, W. Zhang, M. Zhu, Z. Liu, Y. Kong and S. Liu, *Toxins (Basel)* **2019**, 12, 1. DOI:10.3390/toxins12010001
- I. E. Tothill and A. P. F. Turner, in: B. Caballero (Ed.): *Encyclopedia of Food Sciences and Nutrition (Second Edition)*, Academic Press, Oxford, **2003**, pp. 489–499. DOI:10.1016/B0-12-227055-X/01374-2
- B. Caballero, L. C. Trugo and P. M. Finglas, *Book Encyclopedia of food sciences and nutrition*, Academic, **2003**.
- A. Elif Burcu, A. Muhammet and S. Mustafa Kemal, *Current Analytical Chemistry* **2019**, 15, 467–484. DOI:10.2174/1573411014666180912131811
- H. Martin-Yken, *Biosensors* **2020**, 10, 51. DOI:10.3390/bios10050051
- Z. Štukovnik, U. Bren and M. Rozman, *Acta Chimica Slovenica* **2021**. DOI:10.17344/acsi.2020.6545
- W. Xu, T.-H. Kim, D. Zhai, J. C. Er, L. Zhang, A. A. Kale, B. K. Agrawalla, Y.-K. Cho and Y.-T. Chang, *Scientific Reports* **2013**, 3, 2255. DOI:10.1038/srep02255
- G. G. Stewart, in: C. A. Batt and M. L. Tortorello (Eds.): *Encyclopedia of Food Microbiology (Second Edition)*, Academic Press, Oxford, **2014**, pp. 309–315. DOI:10.1016/B978-0-12-384730-0.00292-5
- S.-O. Suh, M. Blackwell, C. P. Kurtzman and M.-A. Lachance, *Mycologia* **2006**, 98, 1006–1017. DOI:10.1080/15572536.2006.11832629
- B. C. Viljoen and G. M. Heard, in: R. K. Robinson (Ed.): *Encyclopedia of Food Microbiology*, Elsevier, Oxford, **1999**, pp. 1918–1925. DOI:10.1006/rwfm.1999.1355
- J. I. Pitt and A. D. Hocking: *Fungi and Food Spoilage*, Springer US, Boston, MA, **1997**, pp. 439–468. DOI:10.1007/978-1-4615-6391-4_10
- S. Li, J. Wen, B. He, J. Wang, X. Hu and J. Liu, *Environmental Pollution* **2020**, 263, 114371. DOI:10.1016/j.envpol.2020.114371
- M. A. Heckman, J. Weil and E. G. De Mejia, *Journal of Food Science* **2010**, 75, R77–R87. DOI:10.1111/j.1750-3841.2010.01561.x
- J. L. Temple, C. Bernard, S. E. Lipshultz, J. D. Czachor, J. A. Westphal and M. A. Mestre, *Front Psychiatry* **2017**, 8, 80–80. DOI:10.3389/fpsy.2017.00080
- C. V. T. Rigueto, M. T. Nazari, C. F. De Souza, J. S. Cadore, V. B. Brião and J. S. Piccin, *Journal of Water Process Engineering* **2020**, 35, 101231. DOI:10.1016/j.jwpe.2020.101231
- P. Nawrot, S. Jordan, J. Eastwood, J. Rotstein, A. Hugenoltz and M. Feeley, *Food Additives & Contaminants* **2003**, 20, 1–30. DOI:10.1080/0265203021000007840
- J. C. Verster, C. Aufricht and C. Alford, *Int J Gen Med* **2012**, 5, 187–198. DOI:10.1080/10408390701522445
- L. Bagwath Persad, *Frontiers in Neuroscience* **2011**, 5. DOI:10.3389/fnins.2011.00116
- S. E. George, K. Ramalakshmi and L. J. Mohan Rao, *Critical Reviews in Food Science and Nutrition* **2008**, 48, 464–486.

DOI:10.1080/10408390701522445

24. X. Fan, Z. Li, S. Wang, L. Liu, P. Liu, F. Chen and X. Zheng, *Journal of the Brazilian Chemical Society* **2019**, *30*, 1762–1768.
25. E. Randviir and C. Banks, *Analytical methods* **2013**, *5*, 1098–1115. DOI:10.1039/c3ay26476a
26. K. Kivirand, M. Min and T. Rincken: Environmental Biosensors, IntechOpen, **2019**.
27. A. S. Tanak, B. Jagannath, Y. Tamrakar, S. Muthukumar and S. Prasad, *Analytica Chimica Acta: X* **2019**, *3*, 100029. DOI:10.1016/j.acax.2019.100029

28. N. Meddings, M. Heinrich, F. Overney, J.-S. Lee, V. Ruiz, E. Napolitano, S. Seitz, G. Hinds, R. Raccichini, M. Gaberšček and J. Park, *Journal of Power Sources* **2020**, *480*, 228742. DOI:10.1016/j.jpowsour.2020.228742
29. Z.-Y. Han, H.-K. Li, Q.-Q. Zhu, R. Yuan and H. He, *Chinese Chemical Letters* **2021**, *32*, 2865–2868. DOI:10.1016/j.ccllet.2021.02.013

Povzetek

Za detekcijo kofeina smo razvili elektrokemijski-impedančni biosenzor, ki kot biološko komponento uporablja kvasovke vrste *Saccharomyces cerevisiae*. Predstavljen biosenzor je sestavljen iz predhodno razvite elektrokemijske celice, narejene iz nerjavnega jekla v RCW konfiguraciji. Elektrokemijska stabilnost delovne elektrode je bila ocenjena s potencialom odprtega tokokroga (OCP). Elektrokemijska impedančna spektroskopija (EIS) je bila uporabljena za spremljanje impedimetričnega odziva biosenzorja s celicami *Saccharomyces cerevisiae* na površini delovne elektrode (WE) pri odsotnosti (0.9% NaCl) in prisotnosti (10 mg/mL v 0.9% NaCl) kofeina. Določena je bila tudi meja zaznavnosti (LOD). Razvit je bil nov pristop v razvoju biosenzorjev, ki vključuje sestavo ekonomično dostopnega biosenzorja, namenjenega enkratni uporabi za detekcijo alkaloidov kot je kofein. Razvit biosenzor je dober kandidat za detekcijo kofeina v pijači, hrani ter zdravilih, saj omogoča hitro detekcijo, z nizko mejo zaznavnosti ter z nizko mejo določljivosti, hkrati pa je tudi ekonomičen.



Except when otherwise noted, articles in this journal are published under the terms and conditions of the Creative Commons Attribution 4.0 International License

Scientific paper

Synthesis, Biological Evaluation, and Molecular Docking Studies of Hydrazones as Novel Xanthine Oxidase Inhibitors

Ling-Wei Xue,^{1,*} Shi-Tong Li,² Yong-Jun Han¹ and Xiao-Qiang Luo¹¹ School of Chemical and Environmental Engineering, Pingdingshan University, Pingdingshan Henan 467000, P. R. China² Department of Materials, School of Natural Sciences, The University of Manchester, Manchester M13 9PL, United Kingdom

* Corresponding author: E-mail: pdsuchemistry@163.com

Received: 11-02-2021

Abstract

A series of hydrazones, 2-cyano-*N*'-(4-diethylamino-2-hydroxybenzylidene)acetohydrazide (**1**), *N*'-(5-bromo-2-hydroxy-3-methoxybenzylidene)-3-chlorobenzohydrazide monohydrate (**2·H₂O**), *N*'-(2-hydroxy-3-methylbenzylidene)-4-nitrobenzohydrazide (**3**), and *N*'-(2-hydroxy-3-trifluoromethoxybenzylidene)-4-nitrobenzohydrazide (**4**), were prepared and structurally characterized by elemental analysis, IR and ¹H NMR spectra, and single crystal X-ray determination. Xanthine oxidase inhibitory activities of the compounds were studied. Among the compounds, 2-cyano-*N*'-(4-diethylamino-2-hydroxybenzylidene)acetohydrazide shows the most effective activity. Docking simulation was performed to insert the compounds into the crystal structure of xanthine oxidase at the active site to investigate the probable binding modes.

Keywords: Hydrazone; xanthine oxidase; inhibition; crystal structure; molecular docking study.

1. Introduction

Enzyme inhibitors can interact with enzymes and block their activity towards natural substrates. The importance of enzyme inhibitors as drugs is enormous since these molecules have been used for treating a number of pathophysiological conditions.¹ Xanthine oxidase (XO; EC 1.17.3.2), a molybdenum hydroxylase, catalyses the hydroxylation of hypoxanthine and xanthine to yield uric acid and superoxide anions. These superoxide anions have been linked to post ischaemic tissue injury and edema as well as to vascular permeability.² XO can oxidize synthetic purine drugs, such as antileukaemic 6-mercaptopurine, with the loss of their pharmacological properties. XO has also been linked to conditions such as hepatic and kidney damage, atherosclerosis, chronic heart failure, hypertension and sickle-cell disease due to the production of reactive oxygen species (ROS) alongside uric acid.³ Then, control of the action of XO may help the therapy of some diseases. Nowadays, the treatment of gout makes use of allopurinol, a potent inhibitor of XO known for a long time.⁴ The mode of action of allopurinol involves the direct coordination of its active metabolite, oxypurinol (al-

loxanthine), to the molybdenum centre in the active site of the enzyme.⁵ However, given its side effects, toxicity, and its inability to prevent the formation of free radicals by the enzyme,⁶ the research on new XO inhibitors is needed. A number of compounds with various types like carboxylic acids and pyrimidines,⁷ pyrimidinones and 3-cyano indoles,⁸ amides,⁹ pyrazoles,¹⁰ thiobarbiturates,¹¹ hydrozingerones,¹² have been reported with XO inhibitory activities. Schiff bases have been of great interest in biological chemistry for a long time.¹³ Leigh and co-workers have reported some Schiff bases as novel XO inhibitors.¹⁴ However, the study on hydrazones is limited, and no rational structure-activity relationships have been achieved so far. As an extension of the work on the exploration of effective XO inhibitors related to Schiff bases, in this paper, a series of hydrazone type Schiff bases, 2-cyano-*N*'-(4-diethylamino-2-hydroxybenzylidene)acetohydrazide (**1**), *N*'-(5-bromo-2-hydroxy-3-methoxybenzylidene)-3-chlorobenzohydrazide monohydrate (**2·H₂O**), *N*'-(2-hydroxy-3-methylbenzylidene)-4-nitrobenzohydrazide (**3**), and *N*'-(2-hydroxy-3-trifluoromethoxybenzylidene)-4-nitrobenzohydrazide (**4**), were synthesized and structurally characterized. The XO inhibitory activities of the com-

pounds were investigated from both experimental and molecular docking study.

2. Experimental

2.1. Materials and Methods

Starting materials, reagents and solvents with AR grade were purchased from commercial suppliers and used without further purification. Elemental analyses were performed on a Perkin-Elmer 240C elemental analyzer. IR spectra were recorded on a Jasco FT/IR-4000 spectrometer as KBr pellets in the 4000–400 cm^{-1} region. ^1H NMR data were recorded on a Bruker 300 MHz instrument. X-ray diffraction was carried out on a Bruker SMART 1000 CCD area diffractometer.

2.2. General Method for the Synthesis of the Compounds

The compounds were prepared according to the literature method.¹⁵ Equimolar quantities (1.0 mmol each) of hydrazide and aldehyde were dissolved in methanol (30 mL) and stirred at room temperature for 30 min to give clear solution. X-ray quality single crystals were formed by slow evaporation of the solution in air for a few days.

2-Cyano-*N'*-(4-diethylamino-2-hydroxybenzylidene)acetohydrazide (1)

Yield: 0.22 g (82%). Mp 133–135 °C, IR (KBr, cm^{-1}) ν 3195, 3143, 2066, 1649, 1466, 1395, 1323, 1264, 1127, 1074, 963, 859, 820, 748, 520. ^1H NMR (300 MHz, DMSO- d_6) δ 10.97 (s, 1H, OH), 9.70 (s, 1H, NH), 9.62 (s, 1H, CH=N), 7.41 (d, 1H, $J = 9.0$ Hz, ArH), 6.25 (d, 1H, $J = 9.0$ Hz, ArH), 6.24 (s, 1H, ArH), 3.42 (m, 4H, CH_2), 3.33 (s, 2H, CH_2), 1.15 (t, 6H, $J = 6.0$ Hz, CH_3). Anal. Calcd for $\text{C}_{14}\text{H}_{18}\text{N}_4\text{O}_2$: C, 61.3; H, 6.6; N, 20.4; Found: C, 61.1; H, 6.7; N, 20.5%.

N'-(5-Bromo-2-hydroxy-3-methoxybenzylidene)-3-chlorobenzohydrazide monohydrate (2·H₂O)

Yield: 0.37 g (93%). Mp 221–223 °C, IR (KBr, cm^{-1}) ν 3430, 3195, 1668, 1629, 1518, 1401, 1342, 1244, 1127, 1081, 781, 709, 520. ^1H NMR (300 MHz, DMSO- d_6) δ 12.20 (s, 1H, OH), 11.72 (s, 1H, NH), 8.64 (s, 1H, CH=N), 8.02 (s, 1H, ArH), 7.87 (d, 1H, $J = 9.0$ Hz, ArH), 7.68 (d, 1H, $J = 9.0$ Hz, ArH), 7.56 (t, 1H, $J = 9.0$ Hz, ArH), 7.41 (s, 1H, ArH), 7.19 (s, 1H, ArH), 3.83 (s, 3H, CH_3). Anal. Calcd for $\text{C}_{15}\text{H}_{14}\text{BrClN}_2\text{O}_4$: C, 44.9; H, 3.5; N, 7.0; Found: C, 44.7; H, 3.6; N, 6.8%.

N'-(2-Hydroxy-3-methylbenzylidene)-4-nitrobenzohydrazide (3)

Yield: 0.26 g (86%). Mp 252–253 °C, IR (KBr, cm^{-1}) ν 3435, 3228, 1651, 1605, 1554, 1519, 1341, 1287, 1075, 853, 713, 627. ^1H NMR (300 MHz, DMSO- d_6) δ 12.67 (s, 1H, OH), 11.83 (s, 1H, NH), 8.60 (s, 1H, CH=N), 8.40 (d,

2H, $J = 8.6$ Hz, ArH), 8.19 (d, 2H, $J = 8.6$ Hz, ArH), 7.32 (d, 1H, $J = 7.6$ Hz, ArH), 7.25 (d, 1H, $J = 7.2$ Hz, ArH), 6.88 (t, 1H, $J = 7.5$ Hz, ArH), 2.23 (s, 3H, CH_3). Anal. Calcd for $\text{C}_{15}\text{H}_{13}\text{N}_3\text{O}_4$: C, 60.2; H, 4.4; N, 14.0. Found: C, 60.4; H, 4.3; N, 14.0%.

N'-(2-Hydroxy-3-trifluoromethoxybenzylidene)-4-nitrobenzohydrazide (4)

Yield: 0.33 g (89%). Mp 245–247 °C, IR (KBr, cm^{-1}) ν 3434, 3112, 1648, 1536, 1401, 1255, 1160, 1115, 1040, 862, 785, 710, 670. ^1H NMR (300 MHz, DMSO- d_6) δ 12.15 (s, 1H, OH), 12.01 (s, 1H, NH), 8.71 (s, 1H, CH=N), 8.39 (d, 2H, $J = 8.6$ Hz, ArH), 8.18 (d, 2H, $J = 8.5$ Hz, ArH), 7.67 (s, 1H, ArH), 7.33 (d, 1H, $J = 9.0$ Hz, ArH), 7.03 (d, 1H, $J = 8.9$ Hz, ArH). Anal. Calcd for $\text{C}_{15}\text{H}_{10}\text{F}_3\text{N}_3\text{O}_5$: C, 48.8; H, 2.7; N, 11.4. Found: C, 48.7; H, 2.9; N, 11.5%.

2.3. Measurement of the XO Inhibitory Activity

The XO activities with xanthine as the substrate were measured spectrophotometrically, based on the procedure reported by L. D. Kong *et al.*, with modification.¹⁶ The activity of xanthine oxidase is measured by uric acid formation monitored at 295 nm. The assay was performed in a final volume of 1 mL 50 mM K_2HPO_4 at pH 7.8 in a quartz cuvette. The reaction mixture contains 200 μL of 84.8 mg/mL xanthine in 50 mM K_2HPO_4 , 50 μL of the various concentrations tested compounds. The reaction is started by addition of 66 μL 37.7 mU/mL xanthine oxidase. The reaction is monitored for 6 min at 295 nm and the product is expressed as mmol uric acid per minute. The reactions kinetic were linear during these 6 min of monitoring.

2.4. Docking Simulations

Molecular docking study of the compounds into the 3D X-ray structure of XO (entry 1FIQ in the Protein Data Bank) was carried out by using the AutoDock version 4.2. First, AutoGrid component of the program precalculates a 3D grid of interaction energies based on the macromolecular target using the AMBER force field. The cubic grid box of $60 \times 70 \times 60 \text{ \AA}^3$ points in x , y , and z direction with a spacing of 0.375 \AA and grid maps were created representing the catalytic active target site region where the native ligand was embedded. Then automated docking studies were carried out to evaluate the binding free energy of the inhibitor within the macromolecules. The GALS search algorithm (genetic algorithm with local search) was chosen to search for the best conformers. The parameters were set using the software ADT (AutoDockTools package, version 1.5.4) on PC which is associated with AutoDock 4.2. Default settings were used with an initial population of 100 randomly placed individuals, a maximum number of 2.5×10^6 energy evaluations, and a maximum number of 2.7

$\times 10^4$ generations. A mutation rate of 0.02 and a crossover rate of 0.8 were chosen. Given the overall consideration of the most favorable free energy of binding and the majority cluster, the results were selected as the most probable complex structures.

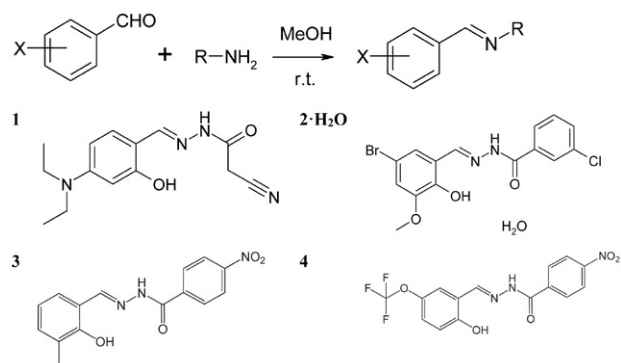
2. 5. Data Collection, Structural Determination and Refinement

Diffraction intensities for the compounds were collected at 298(2) K using a Bruker D8 VENTURE PHOTON diffractometer with Mo K α radiation ($\lambda = 0.71073$ Å). The collected data were reduced using the SAINT program,¹⁷ and multi-scan absorption corrections were performed using the SADABS program.¹⁸ The structures were solved by direct methods and refined against F^2 by full-matrix least-squares methods using the SHELXTL.¹⁹ All of the non-hydrogen atoms were refined anisotropically. The amino and water H atoms were located in difference Fourier maps and refined isotropically, with N–H, O–H and H...H distances restrained to 0.90(1), 0.85(1) and 1.37(2) Å, respectively. All other H atoms were placed in idealized positions and constrained to ride on their parent atoms. The crystallographic data for the compounds are summarized in Table 1. Hydrogen bonding information is given in Table 2.

3. Results and Discussion

3.1. Chemistry

The compounds were readily synthesized by reaction of 1:1 molar ratio of aldehydes with primary amines in methanol at room temperature (Scheme 1), with high yields (over 90%) and purity. Single crystals suitable for X-ray diffraction were obtained by slow evaporation of the solutions containing the compounds in air. The compounds have been characterized by elemental analyses and IR spectra. Structures of the compounds were further confirmed by single crystal X-ray crystallography.



Scheme 1. The synthesized hydrazones 1–4

Table 1. Crystallographic and experimental data for compounds 1–4.

Compound	1	2·H ₂ O	3	4
Formula	C ₁₄ H ₁₈ N ₄ O ₂	C ₁₅ H ₁₄ BrClN ₂ O ₄	C ₁₅ H ₁₃ N ₃ O ₄	C ₁₅ H ₁₀ F ₃ N ₃ O ₅
<i>Mr</i>	274.3	401.6	299.3	369.3
<i>T</i> (K)	298(2)	298(2)	298(2)	298(2)
Crystal system	Monoclinic	Monoclinic	Monoclinic	Monoclinic
Space group	<i>P</i> 2 ₁ / <i>c</i>	<i>P</i> 2 ₁ / <i>n</i>	<i>P</i> 2 ₁ / <i>c</i>	<i>P</i> 2 ₁ / <i>c</i>
<i>a</i> (Å)	12.582(3)	5.999(2)	11.158(1)	11.672(2)
<i>b</i> (Å)	14.562(3)	14.323(2)	13.448(1)	15.011(3)
<i>c</i> (Å)	8.389(2)	19.372(2)	9.278(1)	8.785(2)
α (°)				
β (°)	107.116(2)	96.624(2)	91.366(2)	94.744(3)
γ (°)				
<i>V</i> (Å ³)	1469.0(6)	1653.3(5)	1391.8(2)	1533.9(5)
<i>Z</i>	4	4	4	4
<i>D_c</i> (g cm ⁻³)	1.240	1.614	1.428	1.599
<i>m</i> (Mo-K α) (mm ⁻¹)	0.086	2.668	0.106	0.145
<i>F</i> (000)	584	808	624	752
Reflections collected	11691	8041	13528	14416
Unique reflections	3213	3590	2582	2697
Observed reflections ($I \geq 2s(I)$)	1345	1939	2146	1471
Parameters	187	219	204	241
Restraints	1	4	1	2
Goodness-of-fit on F^2	0.999	0.999	1.055	1.028
$R_1, wR_2 [I \geq 2s(I)]^a$	0.0548, 0.1269	0.0412, 0.0801	0.0424, 0.1142	0.0568, 0.1124
R_1, wR_2 (all data) ^a	0.1442, 0.1709	0.1059, 0.1006	0.0515, 0.1216	0.1358, 0.1427
Large diff. peak and hole (eÅ ⁻³)	0.202, -0.139	0.315, -0.362	0.186 and -0.146	0.331 and -0.284

^a $R_1 = F_o - F_c/F_o$, $wR_2 = [\sum w(F_o^2 - F_c^2)]/\sum w(F_o^2)^{1/2}$

Table 2. Hydrogen bond distances (Å) and bond angles (°) for the compounds.

<i>D</i> – <i>H</i> ... <i>A</i> (<i>D</i> – <i>H</i> ... <i>A</i>)	<i>d</i> (<i>D</i> – <i>H</i>)	<i>d</i> (<i>H</i> ... <i>A</i>)	<i>d</i> (<i>D</i> ... <i>A</i>)	Angle
1				
N3–H3...O2 ^{#1}	0.91(1)	1.98(2)	2.889(3)	172(2)
O1–H1...N2	0.82	1.90	2.631(3)	147(2)
2·H₂O				
O4–H4B...O3 ^{#2}	0.84(1)	1.96(2)	2.754(3)	158(4)
O4–H4A...O2 ^{#3}	0.84(1)	2.44(3)	3.070(4)	133(3)
O4–H4A...O1 ^{#3}	0.84(1)	2.28(2)	3.042(4)	150(4)
N2–H2...O4 ^{#4}	0.90(1)	1.96(2)	2.830(3)	162(4)
O1–H1...N1	0.82	1.86	2.580(3)	145(3)
3				
N2–H2...O2 ^{#5}	0.90(1)	2.08(1)	2.920(2)	159(2)
O1–H1...N1	0.82	1.94	2.654(2)	146
4				
O1–H1...N1	0.85(1)	1.91(2)	2.661(4)	150(4)
N2–H2...O2 ^{#6}	0.90(1)	2.02(1)	2.900(3)	166(4)

Symmetry codes: #1) $2 - x, -y, 3 - z$; #2) $1 + x, -1 + y, z$; #3) $x, -1 + y, z$; #4) $1/2 - x, 1/2 + y, 1/2 - z$; #5) $x, 1/2 - y, -1/2 + z$; #6) $x, 3/2 - y, -1/2 + z$.

3. 2. Structure Description of the Compounds

Figure 1 gives perspective view of compounds 1–4 with atomic labeling systems. X-ray crystallography reveals that the compounds are similar benzohydrazone derivatives. The asymmetric unit of compound **2·H₂O** contains a benzohydrazone molecule and a water molecule of crystallization, which is isostructural with the bromo-containing hydrazone compound 3-bromo-*N'*-(5-bromo-2-hydroxy-3-methoxybenzylidene)benzohydrazone mo-

nohydrate,²⁰ and similar to *N'*-[(*E*)-5-bromo-2-hydroxy-3-methoxybenzylidene]benzohydrazone monohydrate.²¹ All the benzohydrazone molecules of the compounds adopt *E* configuration with respect to the methyldiene units. The distances of the methyldiene bonds, ranging from 1.26 to 1.29 Å, confirm them as typical double bonds. The shorter distances of the C–N bonds and the longer distances of the C=O bonds for the –C(O)–NH– units than usual, suggest the presence of conjugation effects in the molecules. The remaining bond lengths in the

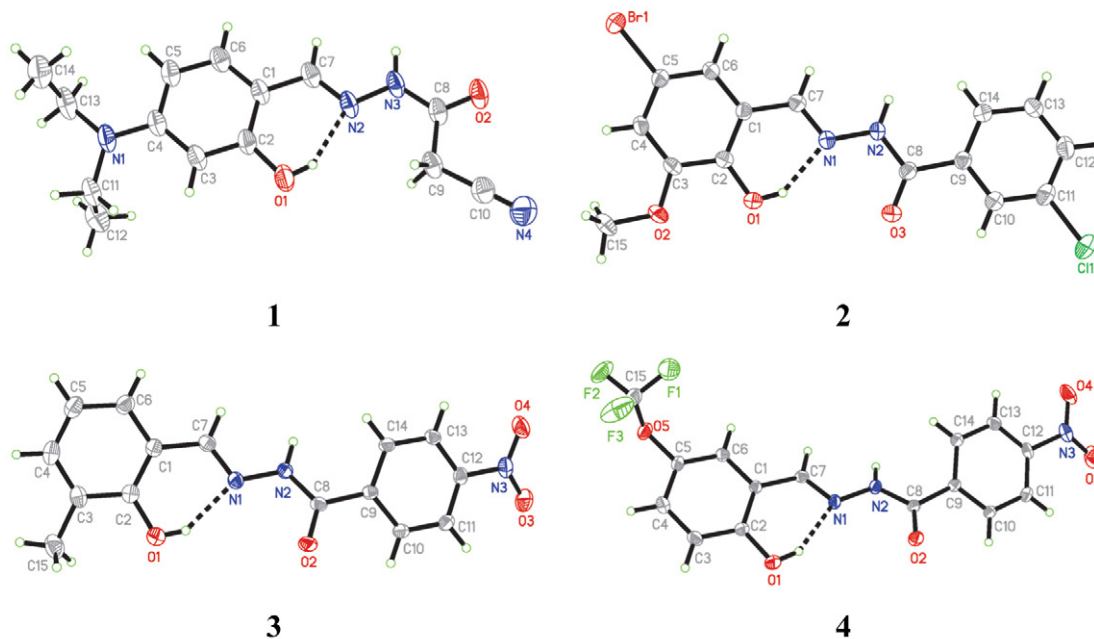


Figure 1. A perspective view of the molecular structures of the compounds 1–4 with the atom labeling scheme. Thermal ellipsoids are drawn at the 30% probability level. Hydrogen bonds are shown as dashed lines.

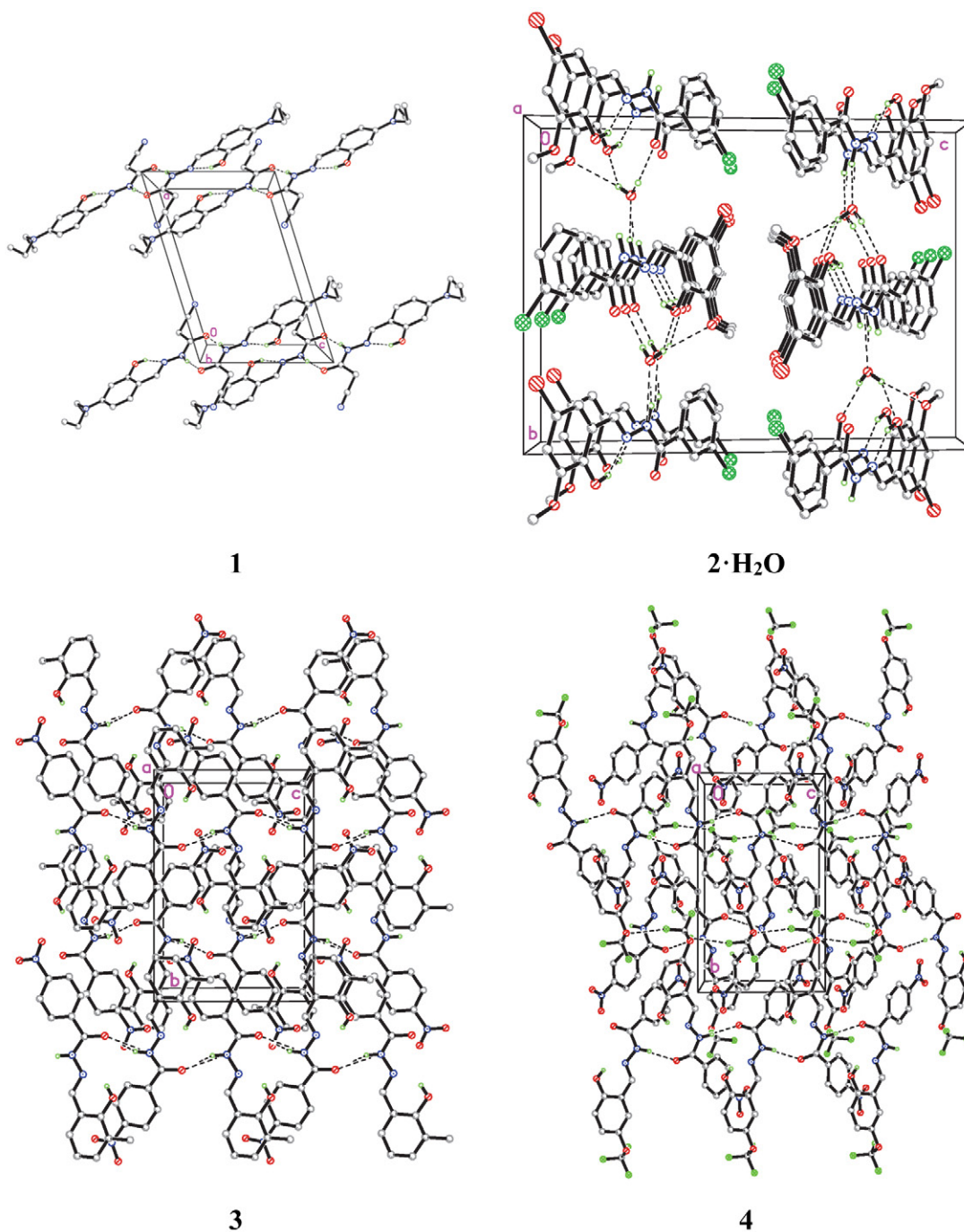


Figure 2. Molecular packing diagrams of the compounds 1–4. Hydrogen bonds are shown as dashed lines.

compounds are comparable to each other, and are within normal values.²² The dihedral angles between the two aromatic rings are $9.8(3)^\circ$ for $2 \cdot \text{H}_2\text{O}$, $12.9(5)^\circ$ for 3, and $14.9(3)^\circ$ for 4. The crystal structures of the compounds are stabilized by intermolecular hydrogen bonds (Table 2, Figure 2). As expected, the crystal packing structure of compound $2 \cdot \text{H}_2\text{O}$ is also very similar to the similar compounds mentioned above.^{13,14}

In ^1H NMR, the absence of NH_2 signals and the appearance of a peak for NH proton in the region δ

12.01–9.70 ppm and imine CH proton in the region δ 9.62–8.60 ppm confirmed the synthesis of the hydrazones. The aromatic proton signals were found in their respective regions with different multiplicities, confirming their relevant substitution pattern.

3.3. Pharmacology

The measurement of XO inhibitory activity was carried out for three parallel times. The percents of inhibition

at the concentration of 100 μM and IC_{50} values for the compounds against XO are summarized in Table 3.

Table 3. Inhibition of XO by the tested materials.

Tested materials	Percent of inhibition ^b	IC_{50} (μM)
1	74.0 \pm 3.3	15.8 \pm 1.5
2	44.5 \pm 2.8	—
3	25.5 \pm 2.0	—
4	31.2 \pm 1.7	—
Allopurinol	80.7 \pm 4.3	8.7 \pm 2.3

^bThe concentration of the tested material is 100 μM .

Allopurinol was used as a reference with the percent of inhibition of 80.7 \pm 4.3 and with IC_{50} value of 8.7 \pm 2.3 μM . Compound **1** shows the most effective activity with the percent of inhibition of 74.0 \pm 3.3 and with IC_{50} value of 15.8 \pm 1.5 μM . Although the number of tested compounds is limited, some structural features, important to the xanthine oxidase inhibitory effect, can be inferred. The merely difference of compounds **3** and **4** is the substituent groups of the benzene rings, *viz.* CH_3 for **3** and OCF_3 for **4**. As a result, the XO inhibitory activity of **3** is less than **4**. Detailed investigation of the structure-activity relationship reveals that the presence of Cl and Br substituent groups may contribute to the inhibition, which is revealed by compound **2**. These findings are coherent with the results reported in the literature that the presence of electron-withdrawing groups in the benzene rings can enhance the activities,²³ and also comparable to that compounds with the presence of bulky ethyl group have stronger activity than those bearing methyl group.²⁴ As a comparison, compound **1** has stronger activity than the Schiff base copper complexes,^{14b} and the OH and Br substituted hydrazone compounds,²⁶ but lower activity than *N*-(3-cyano-1*H*-indol-5/6-yl)-6-oxo-1,6-dihydropyrimidine-4-carboxamides and 5-(6-oxo-1,6-dihydropyrimidin-2-yl)-1*H*-indole-3-carbonitriles,⁸

N-(3-cyano-1-cyclopentyl-1*H*-indol-5-yl)-1*H*-benzo[*d*]imidazole-5-carboxamide,⁹ and the Cl and CN substituted hydrazone compounds.^{14b}

3. 4. Molecular Docking Study

In order to give an explanation and understanding of potent inhibitory activity observed from the experiment, molecular docking study was performed to investigate the binding effects between the compound **1** and the active sites of XO (entry 1FIQ in the Protein Data Bank). Allopurinol was used to verify the model of docking, and gave satisfactory results. Figure 3 is the binding model for the compound **1** in the enzyme active site of XO. The docking score is -7.12 . As a comparison, the docking score for Allopurinol is -6.27 .

From the docking results, it can be seen that the molecule of compound **1** is well filled in the active pocket of XO. The molecule of **1** binds with the enzyme through four hydrogen bonds with Ser876, Ala1011 and Thr1010. In addition, there exist hydrophobic interactions among the compounds with the active sites of the enzyme. The results of the molecular docking study could explain the effective inhibitory activity of compound **1** on XO.

4. Conclusion

The present study reports the synthesis, crystal structures and XO inhibitory activities of a series of hydrazones. The compounds were characterized by elemental analysis, IR and ¹H NMR spectra, as well as single crystal X-ray diffraction. Among the compounds, 2-cyano-*N*'-(4-diethylamino-2-hydroxybenzylidene) acetohydrazide has effective XO inhibition with IC_{50} value of 15.8 \pm 1.5 μM , which may be used as a potential XO inhibitor, and deserves further study. The molecule of the compound can be well filled and combined with hydrogen bonds in the active pocket of XO.

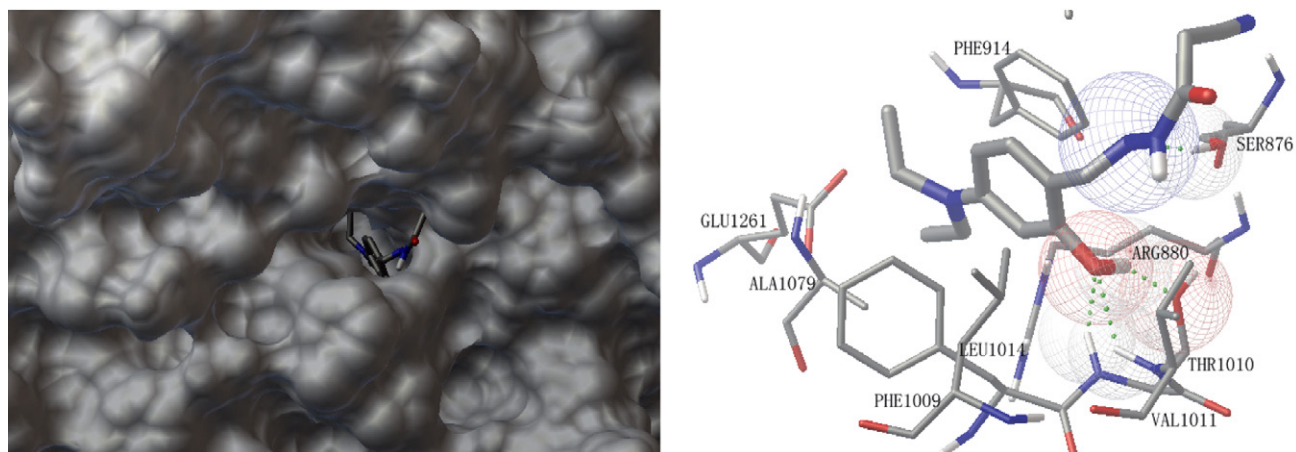


Figure 3. 3D (left) and 2D (right) binding mode of **1** with the active site of XO. Hydrogen bonds are shown as dashed lines.

Supplementary Material

CCDC – 892363 for **1**, 892364 for **2·H₂O**, 1041580 for **3**, and 1041581 for **4** contain the supplementary crystallographic data for this article. These data can be obtained free of charge at <http://www.ccdc.cam.ac.uk/const/retrieving.html> or from the Cambridge Crystallographic Data Centre (CCDC), 12 Union Road, Cambridge CB2 1EZ, UK; fax: +44(0)1223-336033 or e-mail: deposit@ccdc.cam.ac.uk.

5. References

- (a) R. Roncato, J. Angelini, A. Pani, E. Cecchin, A. Sartore-Bianchi, S. Siena, E. de Mattia, F. Scaglione, G. Toffoli, *Inter. J. Mol. Sci.* **2020**, *21*, 6350; DOI:10.3390/ijms21176350
(b) S. Kaur, Y. Bansal, R. Kumar, G. Bansal, *Bioorg. Med. Chem.* **2020**, *28*, 115327; DOI:10.1016/j.bmc.2020.115327
(c) D. W. Banner, P. Hadvary, *J. Biol. Chem.* **1991**, *266*, 20085–20093; DOI:10.1016/S0021-9258(18)54894-8
(d) E. Sandstrom, *Drugs* **1989**, *38*, 417–450. DOI:10.2165/00003495-198938030-00005
- (a) T. Mori, H. Muramatsu, T. Matsui, A. McKee, T. Asano, *Neuropath. Appl. Neurobiol.* **2000**, *26*, 31–40; DOI:10.1046/j.1365-2990.2000.00215.x
(b) A. Pinto, M. Kornfeld, H. Aubin, P. Akhyari, A. Lichtenberg, *Free Rad. Biol. Med.* **2014**, *76*, S52–S52; DOI:10.1016/j.freeradbiomed.2014.10.420
(c) L. Tiano, R. Belardinelli, P. Carnevali, F. Principi, G. Seddaiu, G. P. Littarru, *Eur. Heart J.* **2007**, *28*, 2249–2255; DOI:10.1093/eurheartj/ehm267
(d) P. H. Chan, J. W. Schimidley, R. A. Fishman, S. M. Longar, *Neurology* **1984**, *34*, 315–320. DOI:10.1212/WNL.34.3.315
- (a) E. O. Dangana, T. E. Omolekulo, E. D. Areola, K. S. Olaniyi, A. O. Soladoye, L. A. Olatunji, *Chem. Biol. Interact.* **2020**, *316*, 108929; DOI:10.1016/j.cbi.2019.108929
(b) Y. Q. Wu, H. He, T. Hou, *J. Food Sci.* **2021**, *86*, 1081–1088; DOI:10.1111/1750-3841.15603
(c) X. Yu, L. Zhang, P. Zhang, J. Zhi, R. N. Xing, L. Q. He, *Pharm. Biol.* **2020**, *58*, 944–949; DOI:10.1080/13880209.2020.1817951
(d) J. Nomura, N. Busso, A. Ives, C. Matsui, S. Tsujimoto, T. Shirakura, M. Tamura, T. Kobayashi, A. So, Y. Yamanaka, *Sci. Rep.* **2014**, *4*, 4554; DOI:10.1038/srep04554
(e) M. M. Kolomiets, A. Bilchenko, *Eur. J. Heart Fail.* **2019**, *21*, 356–356;
(f) B. Butts, D. A. Calhoun, T. S. Denney, S. G. Lloyd, H. Gupta, K. K. Gaddam, I. Aban, S. Oparil, P. W. Sanders, R. Patel, J. F. Collawn, L. J. Dellitalia, *Free Rad. Biol. Med.* **2019**, *134*, 343–349; DOI:10.1016/j.freeradbiomed.2019.01.029
(g) P. Pacher, A. Nivorozhkin, C. Szabo, *Pharmacol. Rev.* **2006**, *58*, 87–114; DOI:10.1124/pr.58.1.6
(h) A. A. Fatokun, T. W. Stone, R. A. Smith, *Neurosci. Lett.* **2007**, *416*, 34–38. DOI:10.1016/j.neulet.2007.01.078
- (a) P. C. Robinson, N. Dalbeth, P. Donovan, *Arthr. Care Res.* **2021**, *73*, 1537–1543; DOI:10.1002/acr.24357
(b) C. A. Hay, J. A. Prior, J. Belcher, C. D. Mallen, E. Roddy, *Arthr. Care Res.* **2021**, *73*, 1049–1054; DOI:10.1002/acr.24205
(c) S. Z. Zhang, T. Xu, Q. Y. Shi, S. Y. Li, L. Wang, Z. M. An, N. Su, *Front. Med.* **2021**, *8*, 698437; DOI:10.3389/fmed.2021.698437
(d) L. G. Gao, B. Wang, Y. Pan, Y. Lu, R. Cheng, *Clin. Cardiol.* **2021**, *44*, 907–916;
(e) A. Jeyaruban, W. Hoy, A. Cameron, H. Healy, Z. Wang, J. Zhang, A. Mallett, *J. Nephrol.* **2021**, *34*, 753–762; DOI:10.1007/s40620-020-00937-4
(f) T. Novinsion, B. Bhooshan, T. Okabe, G. R. Revankar, R. K. Robins, K. Senga, H. R. Wilson, *J. Med. Chem.* **1976**, *19*, 512–516. DOI:10.1021/jm00226a013
- K. Okamoto, B. T. Eger, T. Nishino, E. F. Pai, T. Nishino, *Nucleos. Nucleot. Nucl. Acids* **2008**, *27*, 888–893. DOI:10.1080/15257770802146577
- (a) A. Smelcerovic, K. Tomovic, Z. Smelcerovic, Z. Petronijevic, G. Kocic, T. Tomasic, Z. Jakopin, M. Anderluh, *Eur. J. Med. Chem.* **2007**, *135*, 491–516;
(b) G. Beyer, M. F. Melzig, *Biol. Pharm. Bull.* **2005**, *28*, 1183–1186; DOI:10.1248/bpb.28.1183
(c) A. Haberland, H. Luther, I. Schinker, *Agents Actions* **1991**, *32*, 96–97. DOI:10.1007/BF01983326
- (a) J. X. Zhao, Q. Mao, F. W. Lin, B. Zhang, M. Sun, T. J. Zhang, S. J. Wang, *Eur. J. Med. Chem.* **2022**, *229*, 114086;
(b) N. Zhai, C. C. Wang, F. S. Wu, L. W. Xiong, X. G. Luo, X. L. Ju, G. Y. Liu, *Inter. J. Mol. Sci.* **2021**, *22*, 8122. DOI:10.3390/ijms22158122
- (a) T.-J. Zhang, S. Tu, X. Zhang, Q.-Y. Wang, S.-S. Hu, Y. Zhang, Z.-H. Zhang, Z.-R. Wang, F.-H. Meng, *Bioorg. Chem.* **2021**, *117*, 105417; DOI:10.1016/j.bioorg.2021.105417
(b) B. Zhang, Y. L. Duan, Y. W. Yang, Q. Mao, F. W. Lin, J. Gao, X. W. Dai, P. Zhang, Q. H. Li, J. X. Li, R. H. Dai, S. J. Wang, *Eur. J. Med. Chem.* **2022**, *227*, 113928.
- S. Tu, T.-J. Zhang, Y. Zhang, X. Zhang, Z.-H. Zhang, F.-H. Meng, *Bioorg. Chem.* **2021**, *115*, 105181.
- A. Alsayari, M. Z. Hassan, Y. I. Asiri, A. Bin Muhsinah, M. Kamal, M. S. Akhtar, *Indian J. Heterocycl. Chem.* **2021**, *31*, 635–640.
- J. L. Serrano, D. Lopes, M. J. A. Reis, R. E. F. Boto, S. Silvestre, P. Almeida, *Biomedicines* **2021**, *9*, 1443. DOI:10.3390/biomedicines9101443
- H. Hayun, R. Hanifati, A. D. Pratiwik, *Indian J. Pharm. Sci.* **2021**, *83*, 1074–1080.
- (a) M. Kaur, S. Kumar, M. Yusuf, J. Lee, R. J. C. Brown, K. H. Kim, A. K. Malik, *Coord. Chem. Rev.* **2021**, *449*, 214214; DOI:10.1016/j.ccr.2021.214214
(b) G.-X. He, L.-W. Xue, Q.-L. Peng, P.-P. Wang, H.-J. Zhang, *Acta Chim. Slov.* **2019**, *66*, 570–575; DOI:10.17344/acsi.2018.4868
(c) C.-L. Zhang, X.-Y. Qiu, S.-J. Liu, *Acta Chim. Slov.* **2019**, *66*, 484–489; DOI:10.17344/acsi.2019.5019
(d) J. Qin, Q. Yin, S.-S. Zhao, J.-Z. Wang, S.-S. Qian, *Acta Chim. Slov.* **2016**, *53*, 55–61; DOI:10.17344/acsi.2015.1918

- (e) F. Qureshi, M. Y. Khuhawar, T. M. Jahangir, A. H. Chanar, *Acta Chim. Slov.* **2016**, *63*, 113–120; DOI:10.17344/acsi.2015.1994
- (f) X.-Q. Luo, Q.-R. Liu, Y.-J. Han, L.-W. Xue, *Acta Chim. Slov.* **2020**, *67*, 159–166; DOI:10.17344/acsi.2019.5303
- (g) K. M. El-Mahdy, A. M. E.-Kazak, M. Abdel-Megid, M. Seada, O. Farouk, *Acta Chim. Slov.* **2016**, *67*, 18–25. DOI:10.17344/acsi.2015.1555
14. (a) N. Choudhary, D. L. Hughes, U. Kleinkes, L. F. Larkworthy, G. J. Leigh, M. Maiwald, C. J. Marmion, J. R. Sanders, G. W. Smith, C. Sudbrake, *Polyhedron* **1997**, *16*, 1517–1528; DOI:10.1016/S0277-5387(96)00436-6
(b) M. Leigh, C. E. Castillo, D. J. Raines, A. K. Duhme-Klair, *ChemMedChem* **2011**, *6*, 612–616. DOI:10.1002/cmcd.201000429
15. (a) Y. Lu, D.-H. Shi, Z.-L. You, X.-S. Zhou, K. Li, *J. Coord. Chem.* **2012**, *65*, 339–352; DOI:10.1080/00958972.2011.653785
(b) D. Qu, F. Niu, X. Zhao, K.-X. Yan, Y.-T. Ye, J. Wang, M. Zhang, Z. You, *Bioorg. Med. Chem.* **2015**, *23*, 1944–1949. DOI:10.1016/j.bmc.2015.03.036
16. L.D. Kong, Y. Zhang, X. Pan, R. X. Tan, C. H. K. Cheng, *Cell Mol. Life Sci.* **2000**, *57*, 500–505. DOI:10.1007/PL00000710
17. Bruker, SMART and SAINT. Bruker AXS Inc., Madison, Wisconsin, USA (2002).
18. G. M. Sheldrick, SADABS. Program for Empirical Absorption Correction of Area Detector, University of Göttingen, Germany (1996).
19. G. M. Sheldrick, *Acta Crystallogr.* **2008**, *A64*, 112–122. DOI:10.1107/S0108767307043930
20. H.-Y. Zhu, *Asian J. Chem.* **2012**, *24*, 558–560.
21. J. Emmanuel, M. Sithambaresan, M. R. Prathapachandra Kurup, *Acta Crystallogr.* **2013**, *E69*, o1775–o1776. DOI:10.1107/S1600536813030572
22. (a) F. H. Allen, O. Kennard, D. G. Watson, L. Brammer, A. G. Orpen, R. Taylor, *J. Chem. Soc. Perkin Trans.* **1987**, *2*, S1–19;
(b) M. Zhang, D.-M. Xian, H.-H. Li, J.-C. Zhang, Z.-L. You, *Aust. J. Chem.* **2012**, *65*, 343–350; DOI:10.1071/CH11424
(c) F.-M. Wang, L.-J. Li, G.-W. Zang, T.-T. Deng, Z.-L. You, *Acta Chim. Slov.* **2021**, *68*, 541–547; DOI:10.17344/acsi.2020.6051
(d) G.-X. He, L.-W. Xue, *Acta Chim. Slov.* **2021**, *68*, 567–574; DOI:10.17344/acsi.2020.6333
(e) H.-Y. Zhu, *Acta Chim. Slov.* **2021**, *68*, 65–71.
23. S. Gupta, L. M. Rodrigues, A. P. Esteves, A. M. F. Oliveira-Campos, M. S. J. Nascimento, N. Nazareth, H. Cidade, M. P. Neves, E. Fernandes, M. Pinto, N. M. F. S. A. Cerqueira, N. Bras, *Eur. J. Med. Chem.* **2008**, *43*, 771–780. DOI:10.1016/j.ejmech.2007.06.002
24. S. Wang, J. Yan, J. Wang, J. Chen, T. Zhang, Y. Zhao, M. Xue, *Eur. J. Med. Chem.* **2010**, *45*, 2663–2670. DOI:10.1016/j.ejmech.2010.02.013
25. Y.-Q. Cui, Z.-L. You, X.-F. Li, X.-L. Wang, Y.-P. Ma, C. Wang, C.-L. Zhang, *Transition Met. Chem.* **2010**, *35*, 159–163. DOI:10.1007/s11243-009-9309-6

Povzetek

Sintetizirali smo serijo hidrazonov: 2-ciano-*N'*-(4-dietilamino-2-hidroksibenziliden)acetohidrazid (**1**), *N'*-(5-bromo-2-hidroksi-3-metoksibenziliden)-3-klorobenzohidrazid monohidrat (**2**·H₂O), *N'*-(2-hidroksi-3-metilbenziliden)-4-nitrobenzohidrazid (**3**) in *N'*-(2-hidroksi-3-trifluorometoksibenziliden)-4-nitrobenzohidrazid (**4**). Pripravljene spojine smo strukturno karakterizirali z elementno analizo, IR in ¹H NMR spektroskopijo ter rentgensko difrakcijo na monokristalu. Preučili smo tudi inhibitorno aktivnost proti ksantin oksidazi. Izmed vseh spojin se je 2-ciano-*N'*-(4-dietilamino-2-hidroksibenziliden)acetohidrazid izkazal kot najbolj učinkovit. Da bi ugotovili verjetne načine vezave preučevanih hidrazonov v aktivno mesto ksantin oksidaze, smo izvedli tudi molekulske sidranje spojin v kristalno strukturo tega encima.



Except when otherwise noted, articles in this journal are published under the terms and conditions of the Creative Commons Attribution 4.0 International License

Scientific paper

Computational Molecular Modeling Studies of Some *Mycobacterium Tuberculosis* Alanine Racemase Inhibitors

Unni Jayaram* and Mohammed Afzal Azam

Department of Pharmaceutical Chemistry, JSS College of Pharmacy, Udthagamandalam - 643001, Tamil Nadu, India
(A Constituent College of JSS Academy of Higher Education and Research, Mysuru).

* Corresponding author: E-mail: jayaramkvt@gmail.com

Received: 11-10-2021

Running title: *Mycobacterium tuberculosis* alanine racemase.

Abstract

Alanine racemase is a pyridoxal-5'-phosphate dependent bacterial enzyme that provides the essential peptidoglycan precursor D-alanine, utilized for cell wall synthesis. This enzyme is ubiquitous throughout bacteria, including *Mycobacterium tuberculosis*, making it an attractive target for antibacterial drug discovery. We investigated the binding mode of twenty five reported *Mycobacterium tuberculosis* alanine racemase inhibitors. The results obtained from molecular docking studies emphasized the importance of inhibitor interaction with Lys42, Tyr46, Arg140, His172 and Tyr175 residues at the catalytic binding pocket of alanine racemase enzyme. The predicted binding free energies showed that van der Waals and nonpolar solvation interactions are the driving force for binding of inhibitors. Molecular dynamics simulation studies of four such inhibitor-alanine racemase systems were further explored to study the inhibition mechanism. The quantum chemical parameters calculated at the B3LYP/6-31G**++ level of theory indicated that the inhibitors must have low values of the lowest unoccupied molecular orbital energy and high values of electrostatic potential for stronger interactions. We expect that this study can provide significant theoretical guidance for design of potent *Mycobacterium tuberculosis* alanine racemase inhibitors in future.

Keywords: Molecular docking; binding free energy; alanine racemase; molecular dynamics simulations.

1. Introduction

One-third of world's population is infected with *Mycobacterium tuberculosis* (*M. tuberculosis*) and remains a serious global health concern. Hence, discovery and development of effective chemotherapeutic agents against *M. tuberculosis* is of top health priority.¹ Alanine racemase (AlaR) is a pyridoxal-5'-phosphate (PLP) dependent enzyme required for bacterial cell wall synthesis. This enzyme catalyses the conversion of L-alanine to D-alanine which is required for the synthesis of the peptidoglycan in both Gram-positive and Gram-negative bacteria.² Generally, AlaR is absent in higher eukaryotes but is ubiquitous throughout bacteria. Its inhibition is lethal to prokaryotes, hence making it an attractive target for the antibacterial drug discovery.³ This enzyme exists as a homodimer in which two monomers interact in a head-to-tail fashion, making two active sites, where PLP and alanine bind. AlaR from numerous bacteria has been structurally characterized including *M. tuberculosis* ala-

nine racemase (*MtAlaR*).⁴ The substrate entryway and active site of enzymes are shown to be highly conserved.^{5,6} The 3D crystal structure of *MtAlaR* monomer consists of 384 residues and two different domains.⁴ The *N*-terminal domain is made up of an eight-stranded α/β -barrel from residues 1–246 and the *C*-terminal domain contains predominantly β -strands formed by residues 247–384. The approximate 130° angle between the *N*- and *C*-terminal domains is unique for *MtAlaR*. The substrate binding cavity having cofactor PLP390 forms an internal aldimine linkage with the highly conserved catalytic Lys42 residue which is surrounded by the side chains of Tyr175, Tyr46 and Tyr364. The binding cavity of this enzyme is compact (5.5 Å × 5.0 Å × 2.5 Å), making it difficult for the larger molecules to reach the active site. The putative substrate binding site of *MtAlaR* exhibits structural similarity with AlaR binding sites of *Pseudomonas aeruginosa*,⁴ *Geobacillus stearothermophilus*⁷ and *Staphylococcus aureus*.^{8,9} *MtAlaR* uses Lys42 and Tyr271 for the racemization reaction.^{10–12} Site-directed mutagenesis and kinetic studies

revealed that Tyr271 serves as the base acting on the L-enantiomer¹³ and Lys42 on the antipode. It also showed that mutation of Arg219 to a glutamate residue reduced the pH independent K_{cat} value by more than 3 orders of magnitude¹¹ which is supported qualitatively by the quantum chemical calculations.¹² Several reports described the role of key binding residues Lys42, Tyr46, His172, Arg228, Tyr271 and Met319 in the enzyme catalytic steps.^{5,7,13,14} The amino acid residues outside the binding site but near to the entryway of the active site are highly conserved⁴ and can be exploited for the design of larger and potentially more specific inhibitors.

There are several well-known inhibitors of AlaR. Among them D-cycloserine and *O*-carbamyl-D-serine are two natural compounds known to inhibit AlaR.^{15,16} But only D-cycloserine is approved commercially for the treatment of tuberculosis. However, its clinical use is limited due to severe toxic effects arising due to the lack of target specificity.¹⁷ D-cycloserine inhibits alanine racemase by interacting with the enzyme-bound co-factor PLP. There are several PLP dependent enzymes in nature, hence D-cycloserine is not target-specific. Several structural modifications of D,L-cycloserine have been made to improve the activity and target specificity but not to date resulted in development of AlaR specific inhibitors^{18a,b} with high potency. Several other scaffolds have also been investigated as AlaR inhibitors. These include β,β,β -trifluoroalanine, alanine phosphonate,¹⁹ 1-amino-cyclopropane phosphonate,²⁰ β -chloro- and β -fluoroalanine,²¹ phosphonopeptides,^{22,23} and thiazolidinones.²⁴ Most of the substrate analogs, like D-cycloserine engage co-factor PLP.

The interest in identifying small molecule inhibitors of AlaR to overcome the liabilities of the existing compounds has intensified the structure-based drug design approach.^{25,26} In addition, there is a considerable research effort to discover AlaR inhibitors that are not substrate analogs and that act through different mechanisms of enzyme inhibition.^{24,27} In this study, we present the results of molecular docking, binding free-energy calculation, molecular dynamics (MD) simulation and quantum chemical calculation on literature reported *MtAlaR* inhibitors to get further insight into the binding mechanism of these inhibitors. The role of hydrogen bonding with key residues of *MtAlaR* catalytic pocket with these inhibitors is examined in detail. Binding free energies of protein with inhibitors were calculated by molecular mechanics-generalized born/surface area (MM-GBSA) and analysed. MD simulations were performed to investigate the stability and dynamical changes of predicted binding conformations. Using B3LYP/6-31G**++ level of theory, quantum chemical parameters were calculated to understand the mechanism of interaction between inhibitors and biological system. The information from this study provides further insight into the key structural features required to design or optimize alanine racemase inhibitors.

2. Materials and Methods

Computational Methods

2.1. Molecular Docking

Twenty-five *MtAlaR* inhibitors (**1-25**) with wide range biological activity and structural diversity (Supplementary Table S1) were collected from literatures^{24,27} (Table 1) and used in the present study. The 3D structures of ligands were generated using the builder panel in Maestro 10.5 and subsequently optimized with the LigPrep module (Schrödinger 2017-2, LLC, New York, NY). Partial atomic charges were ascribed and possible ionization states were generated at a pH of 7.0. The energy minimization for each ligand was performed using OPLS3 force field.²⁸ The structure of *MtAlaR* (PDB-ID: 1XFC, 1.9 Å resolution) was retrieved from the protein data bank and prepared using protein preparation wizard²⁹ (Epik v4.0, Schrödinger 2017-2). Crystallographic water molecules (less than 3 hydrogen bonds) were deleted and hydrogen bonds (corresponding to pH 7.0) were added. Missing side chain atoms were added and breaks present in the structure were built using Prime (v4.8, Schrödinger 2017-2).³⁰ Then the energy of protein was minimized under OPLS3 force field²⁸ with the convergence of heavy atoms to a RMSD of 0.3 Å. The Ramachandran plot³¹ (Supplementary figure S1) showed 97.90% of the residues in the most favoured regions and none of the non-glycine residues in disallowed regions. The active site was defined with a 10 Å radius around the Lys42 residue present in the crystal structure and a grid box was generated at the centroid of this active site for docking. All compounds were docked into the catalytic pocket of prepared protein using Glide (v7.5, Schrödinger 2017-2)³² in extra precision (XP) mode without applying any constraints (Figure 1a-d and Supplementary figure S2). Best docked structures were selected based on Glide score function, Glide energy and Glide model energy (Supplementary Table S2). The best pose of **10**, **19**, **21** and **25/1XFC** complexes were selected to run the molecular dynamics. Further, electrostatic potential surfaces for **21** and **25** (Supplementary figure S3a and S3b) and hydrophobic and hydrophilic map for **19**, **21** and **25** (Supplementary figure S3c) were generated in the binding pocket of 1XFC enzyme.

2.2. Binding Free Energy Calculation

Molecular mechanics-generalized born surface area (MM-GBSA) method is used to calculate the binding free energies of macromolecules, and serve as a powerful tool for the design of inhibitors.³³ The XP-molecular docking receptor-ligand complex structures ranking were minimized with Prime (v4.8, Schrödinger 2017-2).³⁰ Binding free energies of complexes were computed using MM-GBSA continuum solvent model (Table 1) with OPLS3 force field²⁸ and VSGB 2.0 solvation model.³⁴

2. 3. Quantum Chemical Parameters

The molecular electrostatic potential (MEP)³⁵ calculations provide detailed stereoelectronic information and are useful to study the biological activity of a compound.³⁶ We calculated mean MEP of best binding conformations of inhibitors **1-25** by Jaguar (v9.1, Schrödinger 2017-2) using basis set 6-31G**++ and hybrid density functional theory with Hamiltonian-Nonrelativistic correlation functional (B3LYP) in gas phase. ESP maps of compounds **19**, **21** and **25**, which is an estimate of overall molecular size and location of regions of negative and positive electrostatic potential are shown in supplementary figure 4a-c. The deepest red color represents the most electronegative potential, whereas deepest blue indicates the most positive potential site in inhibitors.³⁷ A semi-empirical Neglect of Diatomic Differential Overlap (NDDO) module with RM1³⁸ method and RHF wave function (Schrödinger 2017-2) was used to calculate highest occupied molecular orbital (HOMO), lowest unoccupied molecular orbital (LUMO), electrophilic, nucleophilic and radical super delocalizability energies (Supplementary Table S3). The frontier molecule orbital density distributions of HOMO and LUMO for compounds **19**, **21** and **25** are shown in supplementary figure S5.

2. 4. Molecular Dynamics Simulations

In order to investigate the stability of the XP-docked inhibitor **10**, **19**, **21** and **25**/1XFC complexes, 10 ns molecular dynamics simulations³⁹ were performed using the Desmond (v5.0) computational package. The systems were explicitly solvated in orthorhombic boxes (volume **10**/1XFC = 460130 Å³; volume **19**/1XFC = 1016870 Å³; volume **21**/1XFC = 459351 Å³; **25**/1XFC = 985370 Å³) with a shell of TIP4P^{40a,b} water molecules within Desmond molecular dynamics system and allowing for a 10 Å buffer region between protein atoms and box sides. Overlapping water molecules were deleted and the systems were neutralized by counter ions. The total numbers of atoms in solvated protein structures of **10**, **19**, **21** and **25**/1XFC complexes for the MD simulations are 43992, 44104, 44348 and 42692, respectively. Each system was placed at a distance of 10 Å from the edge of the box and LBFGS minimization was performed with 3 vectors and minimum 10 steepest descent steps until a gradient threshold of 25 kcal/mol/Å was reached. Smooth particle mesh Ewald⁴¹ method was used for long range electrostatic interactions at a tolerance of 1e-09 and a cut-off radius of 9 Å was selected for short range electrostatic interactions. After minimization, systems were gradually heated in the NPT ensemble to 300° K with a time step of 2 fs. For bonded, near non-bonded, and far nonbonded interactions, a multiple time step RESPA integration algorithm was used throughout the dynamics with time steps of 2, 2 and 6 fs, respectively. Systems were then subjected to 10 ns MD simulations in the NPT ensemble (T = 300° K, thermostat relaxation time

= 200 ps; P = 1 atm; barostat relaxation time = 200 ps) using a Nose-Hoover thermostat⁴² and Martyna-Tobias-Klein barostat.⁴³ For each system, trajectories and 3D structures were visually analysed using the Maestro graphical interface.

3. Results and Discussion

3. 1. Molecular Docking

We compared different XP-docked poses (Figure 1 and also Supplementary figure S2) for the better understanding of interactions between *MtAlaR* and its inhibitors **1-25**. It is evident that most of these inhibitors adopt similar hydrogen bond pattern at the ligand-receptor interface. Earlier studies have indicated that the difference in activities of different *AlaR* inhibitors are primarily due to their binding orientations and spatial arrangement towards Lys42, Tyr46, Arg140, His172, Tyr175 and Tyr364 core residues and formation of hydrogen bonding network and hydrophobic interaction^{4,6,7,9} within the catalytic pocket. In the present investigation, inhibitors binding to the *MtAlaR* were observed to be driven by the π - π stacking, π -cation and hydrogen bonding interactions with the conserved residues near to the PLP390. It is important to note that none of the selected inhibitors showed any interaction with the co-factor PLP390. To explain the binding mode, compounds **10**, **19**, **21** and **25** were selected for more detailed analysis. Figure 1d shows the docked pose of the most active compound **25** (IC₅₀ 0.03 μ M) within the active site of 1XFC protein. Precisely, fifth position >C=O of thiadiazolidine-3,5-dione ring accepted a hydrogen bond from the backbone OH of Tyr175 (OH...O=C<, 2.1 Å). Another hydrogen bonding interaction was observed between third position >C=O of thiadiazolidine-3,5-dione ring and the side chain NH of Met173 (NH...O=C<, 2.0 Å). These hydrogen bonds are important for positioning and orienting the thiadiazolidine-3,5-dione ring of this inhibitor closer for π - π interactions with imidazole ring of His172 and phenyl ring of Try175. In another high active compound **19** (Figure 1b, IC₅₀ 0.05 μ M), a total of three hydrogen bonds were observed with 1XFC. The nitro oxygen atom of 2-chlorophenyl-4-nitrophenyl moiety accepted hydrogen bond from the side chain NH of Asn141 (NH...O(NO), 1.8 Å). Carbonyl oxygen atoms of thiadiazolidine-3,5-dione ring exhibited hydrogen bonding interactions one each with the side chain imidazole ring NH of His172 (rNH...O=C<, 2.1 Å) and the side chain OH of Tyr46 (OH...O=C<, 2.1 Å). Our Glide XP-docking also exposed two π - π stacking interactions of this inhibitor. Phenyl ring of 2-chlorophenyl-4-nitrophenyl moiety and phenyl ring of 2,3-dihydro-1*H*-indene moiety exhibited π - π interactions, respectively with imidazole ring of His172 and phenyl ring of Tyr175. These attractive and non-covalent interactions are responsible for further stabilization of inhibitor **19** at the active site. In the lowest active inhibitor **21** (Figure 1c, IC₅₀ 28.76 μ M), only one π -cation interaction was ob-

served between thiazolidine-3,5-dione ring and nitrogen atom of Lys42 side chain NH_2 . For this inhibitor, hydrogen bonding and π - π stacking interactions were not observed and probably this may be the reason for the lower activity of this compound. In case of another less active compound **10** (Figure 1a, IC_{50} 13.1 μM) a single hydrogen bond was observed. Precisely, (carbamothioylsulfanyl)acetic acid moiety NH formed a hydrogen bond with the side chain imidazole ring nitrogen of His172 ($r = \text{N} \cdots \text{NH}-\text{C}(=\text{S})-\text{S}$) (2.0 Å). This compound also showed a π - π stacking interaction of its pyridine ring with indole phenyl ring of Trp88. However, like high active inhibitors **19** and **25**, no π - π stacking interactions with Tyr46, His172 and Tyr175 residues were observed for this inhibitor. It is evident from the docking results that apart from the hydrogen bonding network, π - π stacking interactions with Tyr46, His172 and Tyr175 residues are important for the stabilization within the catalytic pocket and inhibitory activity of *MtAlaR* inhibitors.

As shown in supplementary figure S3b, **25** fully occupied the binding pocket and oriented in a way to block the approach of substrate near to the Lys 42 and co-factor PLP390. Moreover, the positively charged (blue colour) Lys42 residue is in the region of negative (red colour) surface electrostatic potential of **25**, which favour the stabili-

zation of this inhibitor within the catalytic pocket. While the inhibitor **21**, did not occupy the whole binding pocket (Supplementary figure S3a) and oriented in a way that indene ring is exposed to the solvent pocket, disfavoured the binding of this inhibitor. Further, it can be seen from the supplementary figure S3c that inhibitors **19** and **25** phenyl rings are in close contact with the hydrophobic pocket, while the thiazolidine-3,5-dione rings are buried in the hydrophilic pocket. In case of inhibitor **21**, part of the 2,3-dihydro-1*H*-indene ring is buried in hydrophilic pocket while, the ethyl carboxylate group is located within the hydrophobic pocket (Supplementary figure S3c), disfavoured the binding.

3. 2. Binding Free Energy Calculation

To get a quantitative comparison of the binding strengths between diverse structure inhibitors **1-25** and 1XFC, the binding free energies (ΔG_{binds}) were computed by using the MM-GBSA approach (Li *et al.*, 2011). In the present study a moderate correlation ($R^2 = 0.573$) was observed between the computed ΔG_{binds} and IC_{50} values of selected inhibitors **1-25**. It is evident from the energy components of the calculated binding free energies (Table 1)

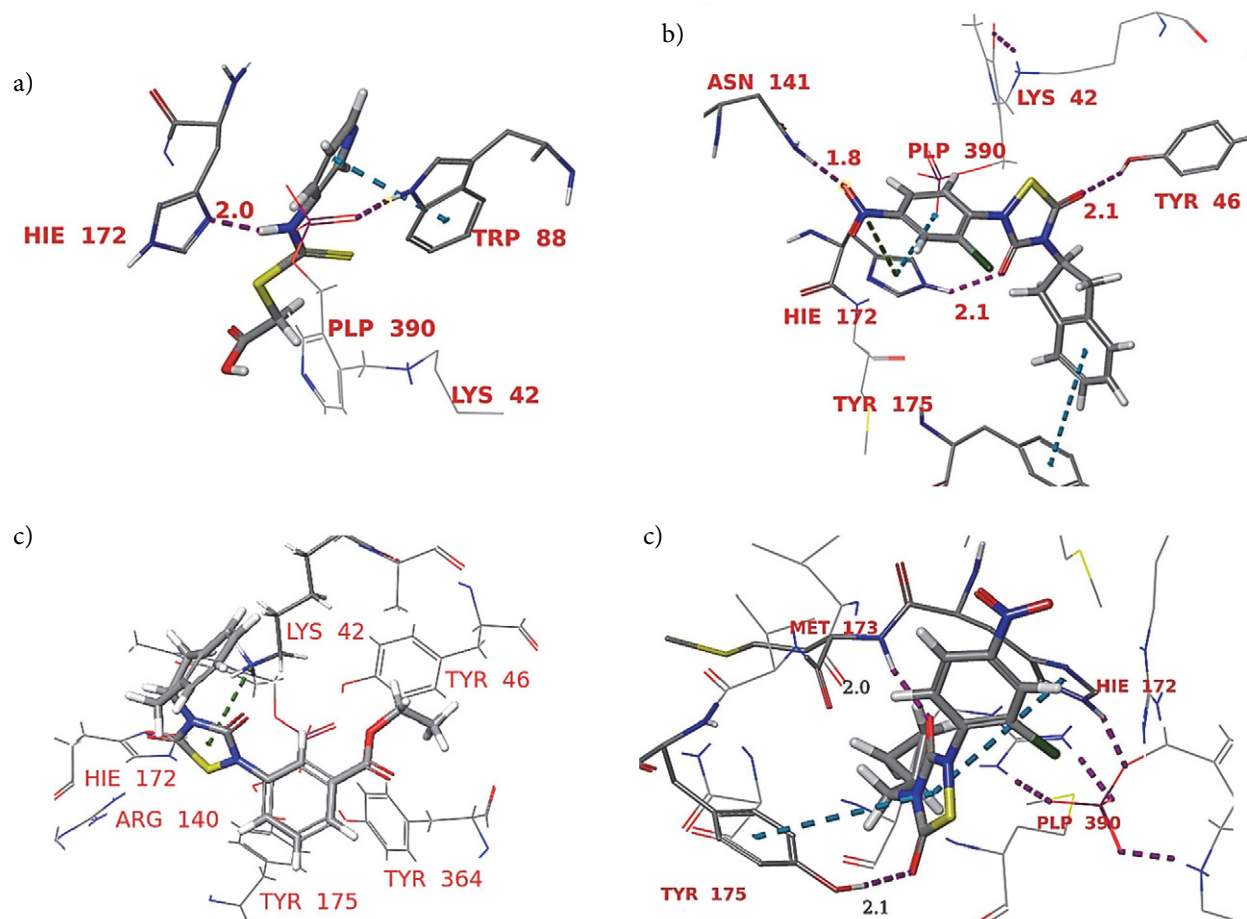


Figure 1: Binding modes of compounds (a) **10** (b) **19** (c) **21** and (d) **25** in the catalytic pocket of *M. tuberculosis* AlaR enzyme (PDB ID: 1XFC).

Table 1: Contribution to the free energy of binding (mm-gbsa) for ligands 1–25 with 1XFC (kcal/mol).

Compd. No.	IC ₅₀ (μM)	^a ΔG _{Coul}	^b ΔG _{Cov}	^c ΔG _{H-bond}	^d ΔG _{vdW}	^e ΔG _{Lipo}	^f ΔG _{Solv}	^g ΔG _{bind}
1.	5.2	-33.713	2.605	0.317	-23.690	-21.036	13.815	-60.087
2.	8.2	-29.817	-1.214	-0.428	-21.324	-22.045	28.677	-45.4426
3.	1.0	-43.348	-1.849	-5.124	-31.954	-21.937	39.614	-53.3249
4.	5.7	-48.829	-2.445	-0.657	-10.810	-14.137	29.585	-48.7813
5.	0.12	-14.652	8.125	-0.322	-27.265	-29.148	17.119	-45.1766
6.	4.48	-25.131	15.666	-1.376	-27.085	-34.652	23.502	-47.7372
7.	3.3	-3.618	-1.077	0.797	-24.274	-25.189	12.226	-41.4227
8.	6.5	21.218	-21.045	0.975	-26.127	-31.154	1.225	-56.0666
9.	9.0	77.783	-1.501	1.083	-31.825	-26.723	-23.612	-32.1513
10.	13.1	-9.601	6.504	-1.333	-20.895	-9.6544	19.690	-21.5392
11.	0.82	-9.454	-3.512	0.927	-25.370	-38.742	8.915	-61.989
12.	0.29	-54.104	24.440	-2.991	-25.605	-33.075	22.886	-57.7316
13.	2.6	-13.699	5.534	-1.351	-10.300	-18.288	-1.185	-41.3644
14.	8.2	-8.832	6.480	-1.556	-32.968	-32.636	24.397	-51.4349
15.	1.46	-40.730	6.015	-2.836	-26.248	-35.996	39.831	-59.7989
16.	0.13	3.913	-1.156	0.893	-27.383	-28.121	13.004	-42.6172
17.	4.9	20.307	1.304	-0.315	-17.582	-22.819	-30.085	-50.5578
18.	6.8	24.923	6.666	-2.189	-27.740	-18.081	-8.493	-29.8858
19.	0.05	-18.082	-4.375	-0.779	-22.054	-33.262	16.623	-63.3841
20.	6.0	8.003	-9.162	0.950	-20.613	-27.058	-1.843	-48.2484
21.	28.76	-8.562	-6.816	-1.094	-17.350	-26.901	15.372	-33.1315
22.	2.8	-1.611	-7.988	-3.683	-16.635	-10.579	6.723	-36.685
23.	0.17	0.258	-3.931	-0.221	-19.133	-26.945	-4.626	-57.9106
24.	1.6	6.098	5.407	-0.682	-29.088	-30.205	-26.703	-58.8693
25.	0.03	-23.355	3.334	-0.215	-24.938	-29.498	25.507	-63.1989

^a Coulomb energy; ^b covalent energy (internal energy); ^c hydrogen bonding; ^d van der Waals energy; ^e hydrophobic energy (nonpolar contribution estimated by solvent accessible surface area); ^f free energy of binding; ^g electrostatic solvation energy.

that the major favourable contributors to ligand binding are van der Waals (ΔG_{vdW}) and nonpolar solvation (ΔG_{lipo}) terms. Whereas in all active inhibitors covalent and electrostatic solvation (ΔG_{solv}) energy terms strongly disfavour the inhibitor binding except inhibitors **9**, **17**, **18** and **24** which showed moderate (ΔG_{solv}) energy terms. The highly active inhibitors **19** and **25** (IC₅₀ 0.05 and 0.03 μM respectively) showed a slightly higher van der Waals (-22.05 and -24.938 kcal/mol, respectively) and nonpolar solvation (-33.26 and -29.49 kcal/mol, respectively) contributions. Also, both inhibitors exhibited higher favourable Coulomb energy terms (-18.082 and -23.355 kcal/mol, respectively) compared to the other less active inhibitors **10** and **21** (-9.601 and -8.562 kcal/mol, respectively). It is clearly evident from result that ΔG_{vdW} and ΔG_{lipo} terms are the driving force for ligand binding and this is in well agreement with our XP-Glide docking result (Supplementary Table S2).

3. 3. Quantum Chemical Parameters

The mean electrostatic potential (ESP) of potent inhibitors **19** and **25** are +3.55 and +4.45 kcal/mol, respectively, clearly indicating that positive electrostatic potential of molecules will favour the binding of inhibitors into the

binding pocket of *MtAlaR*. The negative electrostatic potential of inhibitor **8**, **10** and **21** (-0.03, -71.79 and -0.12 kcal/mol, respectively) may be one of the reason for low inhibitory activity (IC₅₀ 8.2, 13.1 and 28.76 μM, respectively) against 1XFC. In addition, the similarity in electrostatic potential profile of compound **19** and **25** was akin to the similarity in the inhibitory activity (IC₅₀ 0.05 and 0.03 μM, respectively) against *MtAlaR* enzyme. The quantum chemical calculation results show that the optimizations of ESP may lead to the potent *MtAlaR* inhibitor. It is evident from supplementary Table S3 that in high active compounds **19** and **25**, the high negative E_{LUMO} (-1.555 and -1.630 eV, respectively) and positive nucleophilic superdelocalizability (703.455 and 178.047, respectively) favours the inhibitors binding. Whereas in the less active compounds **10** and **21** positive E_{LUMO} (1.810 and 0.681 eV, respectively) and negative nucleophilic superdelocalizability (-8.571 and -79.09, respectively) disfavour inhibitor binding into the catalytic pocket of 1XFC.

It appears from the LUMO shape that the molecular orbital involved in bonding with the catalytic pocket residues is located on the 2-(2-chloro-4-nitrophenyl)-1,2,4-thiadiazolidine-3,5-dione ring of compounds **19** and **25**, but it is spread over the 3-aminopyridine ring in case of compound **10**. The relative smaller size of LUMO lobes in com-

pound **10** explains the low inhibitory activity of this compound. A plot of the LUMO vs. HOMO energies (Supplementary figure S6) showed statistically significant correlation coefficient of $R^2 = 0.71$ with a slope and intercept of 0.67 and 5.14 eV, respectively. The slope showed consistent increase in the excitation binding energy with increasing electron affinity. These data indicates that the potent molecules should have a higher negative E_{LUMO} , positive nucleophilic superdelocalizability and positive ESP values for the inhibitory activity. This is in well agreement with the MM-GBSA result where Coulomb energy term favours binding of compounds **19** and **25** in the catalytic pocket of 1XFC.

3. 4. Molecular Dynamics Studies

A 10 ns molecular dynamics (MD) was performed to explore the atomic details of molecular interactions. Root

mean square deviations (RMSD) from the starting structures were analysed to explore the dynamic stability of systems. The convergence of RMSD values (Figure 2a-d) at approximately 2 ns of the simulation time indicates that the systems were well equilibrated and have attained stability. The time-dependent average RMSDs of **10**, **19**, **21** and **25**/1XFC complexes backbone (0.37, 0.26, 0.74, 0.605 Å) and C- α (0.38, 0.345, 0.72, and 0.61 Å) atoms indicated less conformational changes in protein during MD simulation. It is also evident from the RMSD plots (Figure 2a-d) that the tendency of catalytic pocket residues RMSD copes well with the ligand movement. During MD simulations ligands **10**, **19**, **21** and **25** showed conformational variations up to 2 ns and then were stable for rest of the simulation period.

The protein backbone, C- α and heavy atoms of ligand binding residues for complexes **10**, **19**, **21** and **25**/1XFC showed root-mean-square fluctuations (RMSF)

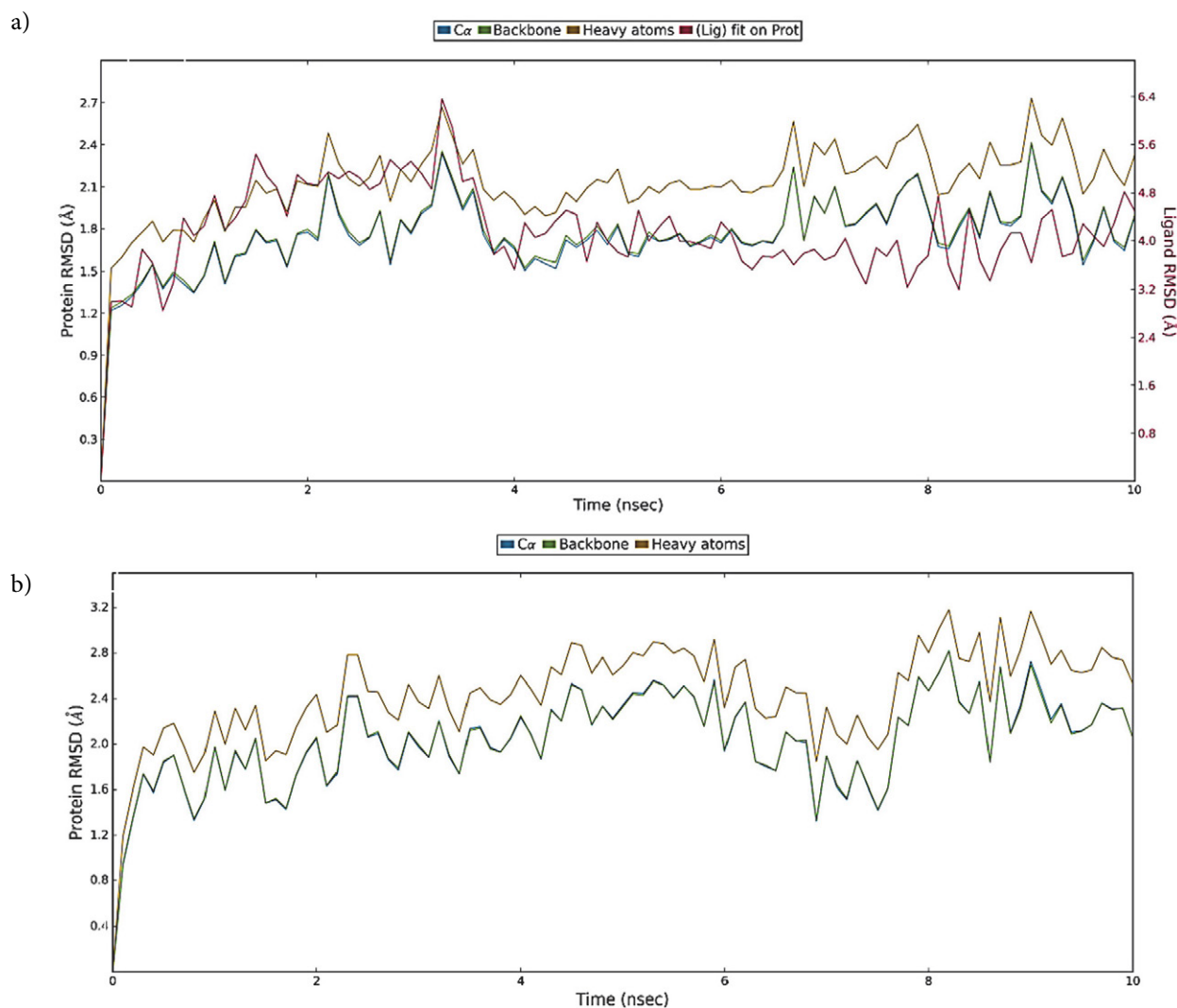


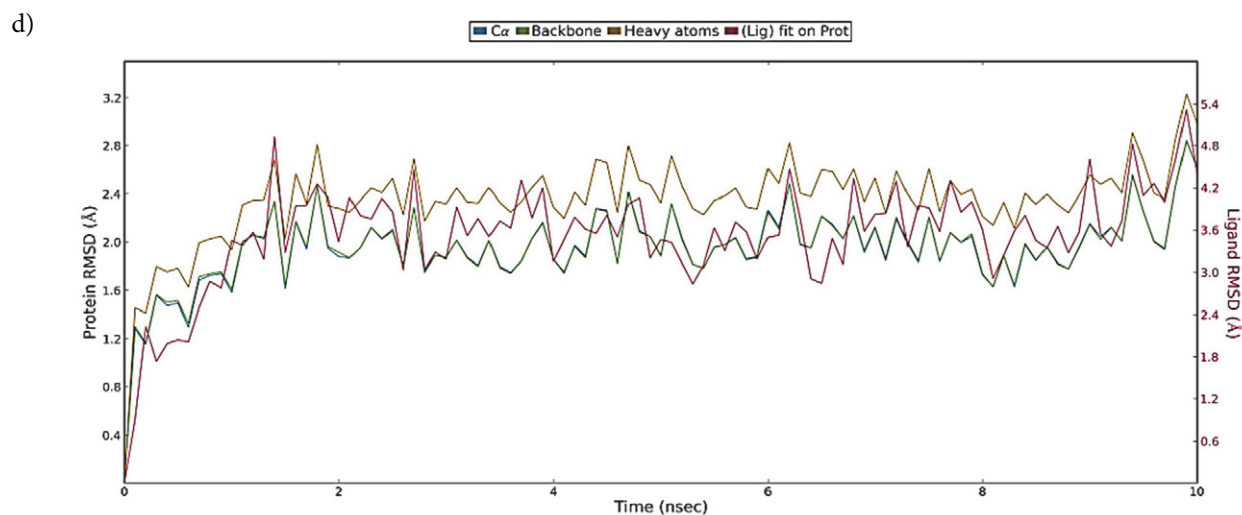
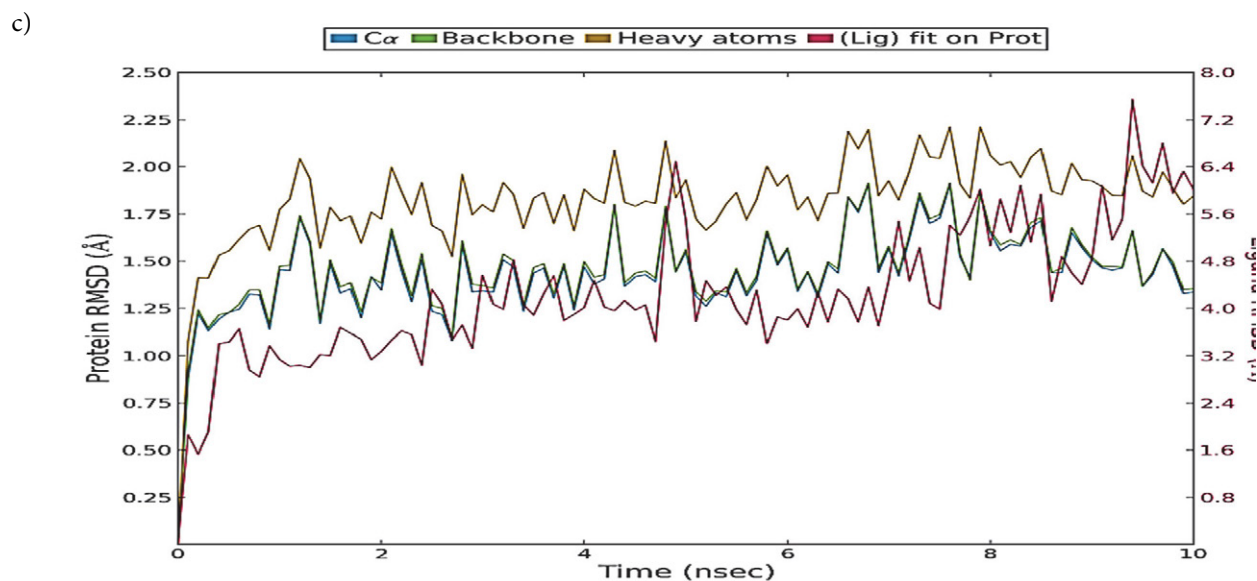
Figure 2: Represents the RMSDs (Å) of the simulated positions of (a) **10** (b) **19**

values in the range 0.62–2.87, 0.5–2.10 and 0.48–3.13 Å, respectively (Figure 3a–d) which is indicative of the moderate fluctuations in these residues. The high fluctuations in RMSFs of **10**, **19**, **21** and **25**/IXFC complexes backbone (2.55–2.91, 2.87–2.96, 2.98–3.32 and 1.76–1.86 Å, respectively) and C- α (2.51–2.89, 2.61–2.88, 2.86–3.11 and 1.72–1.83 Å, respectively) atoms were observed inflexible loop between amino acid stretch Ser270 to Thr274, connecting two short β -sheets (amino acid stretches Trp275-Ile276 and Val269-Gly268). These residues are away from the catalytic pocket.

During MD simulation the low mean fluctuations of radius of gyration (rGyr) in the backbone (blue circle, 0.677 and 0.30 Å, respectively) and C α (red thin diamond, 0.35 and 0.31 Å, respectively) atoms for **19** and **25**/IXFC complexes (Supplementary figure S7b and S7d) further indicated low degree of flexibilities in protein complexes. However, in **10** and **21**/IXFC complexes, a little higher

mean fluctuations of rGyr in the backbone (0.677 and 1.0 Å, respectively) and C α atoms (1.37 and 0.81 Å, respectively) (Supplementary figure S7a and S7c) showed higher degree of flexibilities in protein complexes. These results indicate that the whole **19** and **25**/IXFC systems were in more relaxed conformations compared to the **10** and **21**/IXFC complexes. In comparison to the protein crystal structure average B-factor (28 Å²), a little higher average B-factor of 30.26 Å² was observed for the catalytic pocket residues during MD simulations of four complexes. During MD simulations of all four complexes, five residues Gly137, Leu138, Asn139, Arg140 and Asn141 located on the flexible loop between amino acids stretch Asp135-Gln147 showed higher B-factor in the range 48.40–74.30 Å² but lower RMSF values for the protein backbone and C α atoms (0.68–1.46 Å and 0.67–1.31 Å, respectively).

MD simulations of **10**, **19**, **21** and **25**/IXFC complexes showed similar binding interactions as predicted in



(c) **21** and (d) **25** /IXFC complexes backbone.

the extra-precision molecular docking. During MD simulation of **19**/1XFC complex, all three hydrogen bonds (Asn141 NH...O(NO), His172 rNH...O=C< and Tyr46 OH...O=C<) predicted in the XP molecular docking was preserved, respectively in 7, 34 and 62% of MD trajectory (Figure 4b also Supplementary figure S8b and S9b). For this inhibitor a strong hydrogen bond interaction was observed between fifth position >C=O of thiadiazolidine-3,5-dione ring and the backbone OH of Tyr46 (>C=O...HO) (~62% of the trajectory) in a bidentate manner. Another moderate frequency hydrogen bonding interaction was observed between third position >C=O of thiadiazolidine-3,5-dione ring and the side chain NH of His172 ring (>C=O...HNr) (~34% of the trajectory). Conformational flexibility of His172 side chain ($\psi = 110^\circ$, Supplementary figure S10b) was observed to be less during first 8.5 ns of simulation and it is considerably less for this inhibitor compared to conformational flexibility of His172 observed for the lowest active inhibitor **10**. These hydrogen bonding networks stabilized the positions of thiadiazolidine-3,5-dione and 4-nitro-2-chlorophenyl rings for π - π stackings respectively, with Tyr364 phenyl (~21% of the trajectory) and His172 imidazole (~26% of the trajectory) rings. Additional stabilization was achieved by the

low frequency π - π stacking of 2,3-dihydro-1H-indene phenyl ring with Tyr175 (~11% of the trajectory) and hydrogen bonding network between the backbone of Tyr175 and third position >C=O of thiadiazolidine-3,5-dione ring (~13% of the trajectory). These low frequency interactions are due to the conformational flexibility of Tyr175 backbone brought about by the flexible body movement of the Ser171-Asp181 stretch in loop. Our MD simulation result also exposed salt bridge interaction of nitro oxygen atom with Arg140 (~21% of the trajectory). Another salt bridge interaction was observed between oxygen atom of fifth position >C=O of thiadiazolidine-3,5-dione ring and Lys42 (~13% of the trajectory). These interactions are in good agreement with the calculated ΔG_{binds} value of this inhibitor (Table 1). These hydrogen bonds, hydrophobic and salt bridge interactions are responsible for the stabilization of this inhibitor within the catalytic pocket.

During MD simulation of the highest active inhibitor **25**/1XFC complex, among the two hydrogen bonds (Tyr175 OH...O=C<, Met173 NH...O=C<) predicted in XP-docking, only one (Met173 NH...O=C<) was preserved in 37% of MD trajectory (Figure 4d also Supplementary figure S8d and S9d). A moderate frequency hydrogen bond was observed between the second position >C=O of

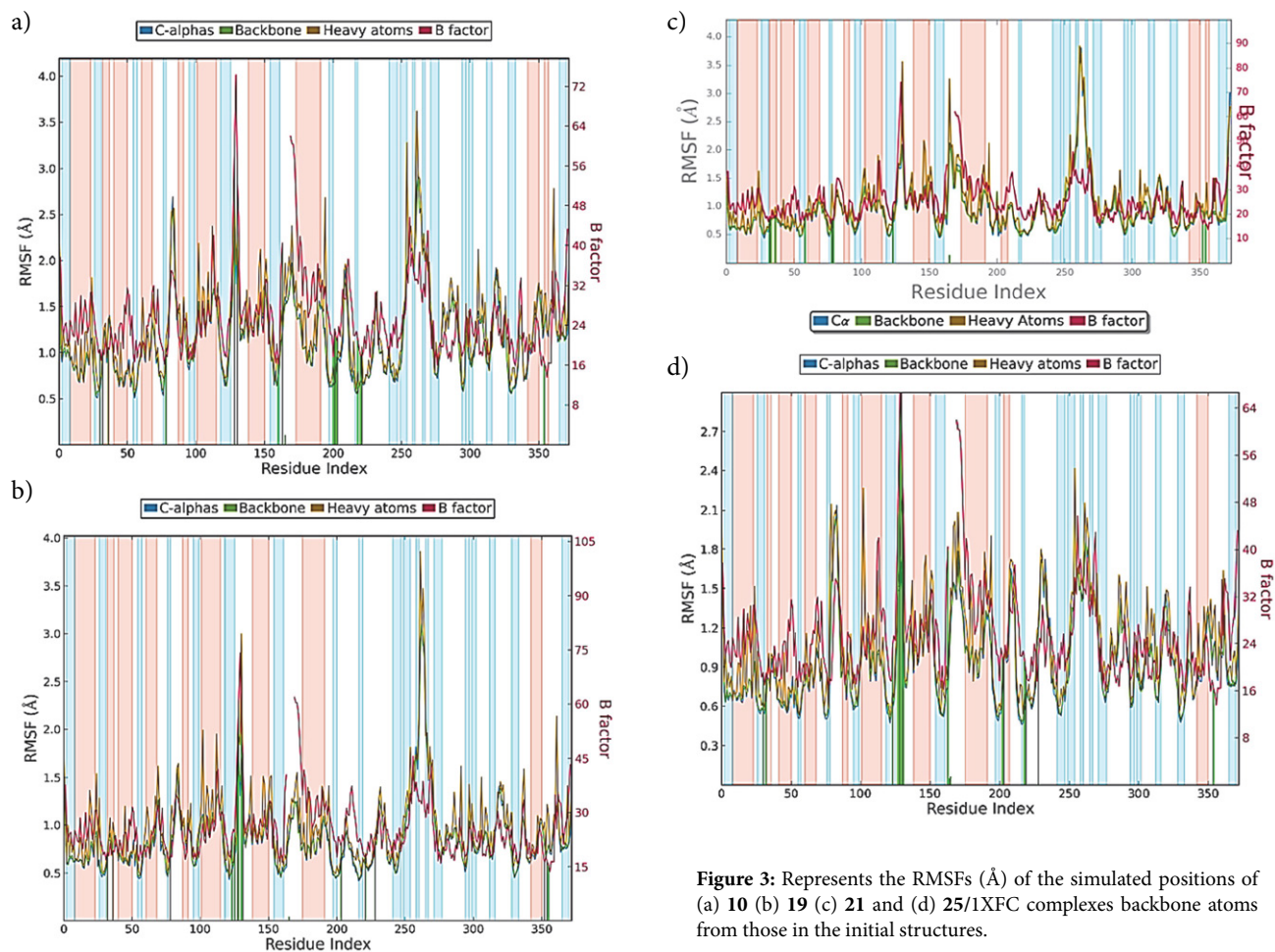


Figure 3: Represents the RMSFs (Å) of the simulated positions of (a) **10** (b) **19** (c) **21** and (d) **25**/1XFC complexes backbone atoms from those in the initial structures.

thiadiazolidine-3,5-dione ring and backbone NH ($r > C=O \cdots HN$) of Met173 (~37% of the trajectory). Precisely, fifth position $>C=O$ of thiadiazolidine-3,5-dione ring formed low frequency hydrogen bond networks with the side chain of Asn212 ($>C=O \cdots HN(H)-$ and $>C=O \cdots H-O-H \cdots HN(H)$) in a bidentate manner (~18% of the trajectory). Imidazole ring of His172 residue exhibited weak $\pi-\pi$ stacking interactions, one each with thiadiazolidine-3,5-dione and phenyl rings of inhibitor **25**. This weak interaction is due to the higher conformational flexibility of His172 side chain ($\psi = 340^\circ$, Supplementary figure S10d during first 5 ns of MD simulation and then ($\psi = 80^\circ$) during further last 5 ns. These hydrophobic interactions further stabilized the inhibitor **25** in the catalytic pocket of 1XFC and positioned the inhibitor near to the Lys42 and PLP390. Additionally, nitro group of 2-chloro-4-nitrophenyl moiety showed two moderate frequency water mediated hydrogen bonding networks with the side chain of Lys133 (~21% of the trajectory), back bone of Arg140 (~29% of the trajectory) and a low frequency water mediated hydrogen bonding interaction with the backbone of Leu138 (~18% of the trajectory) during MD simulation. These hydrogen bonding networks probably forms the basis for the high activity of this inhibitor compared to the low active compounds **10** and **21**.

For the low active **10**/1XFC complex, one hydrogen bond (His172r $=N \cdots NH-C(=S)S-$), predicted in glide XP-docking simulation was preserved in 25% of MD simulation trajectory. This inhibitor exhibited a total of six

moderate to low frequency hydrogen bonds (Figure 4a, also Supplementary figure S8a and S9a). Precisely, nitrogen of pyridine ring accepted a moderate frequency hydrogen bond from the side chain of Arg228 (~45% of the trajectory) and also exhibited salt bridge interaction (~39% of the trajectory) with the same residue. These interactions stabilize the position of the pyridine ring with regard to the Trp88 phenyl and His172 imidazole rings to form low frequency $\pi-\pi$ stacking interactions. His172 imidazole ring nitrogen atom also accepted a low frequency hydrogen bond (~25% of the trajectory) from the NH of (carbamothioylsulfanyl)acetic acid moiety ($r = N \cdots HN$) of this compound. This low frequency hydrogen bond is due to the higher conformational flexibility of His172 side chain ($\psi = 350^\circ$, Supplementary figure S10a) during last 4 ns of simulation. This conformational flexibility is brought about by the flexible body movement of the Ser171-Asp181 stretch in loop. Another moderate frequency hydrogen bond was observed between $>C=O$ of carboxylate and the side chain OH ($>C=O \cdots HO$) of Tyr46 (~31% of the trajectory). In addition, compound **10** showed four more low frequency hydrogen bond networks with Arg140, Ser213 and Arg228 residues.

During MD simulation of **21**/1XFC complex, the π -cation interaction between thiadiazolidine-3,5-dione ring and the side chain NH_2 of Lys42 predicted in the XP molecular docking was preserved during MD simulation (~11% of MD trajectory) (Figure 4c, also Supplementary figure S8c and S9c). An additional π -cation interaction

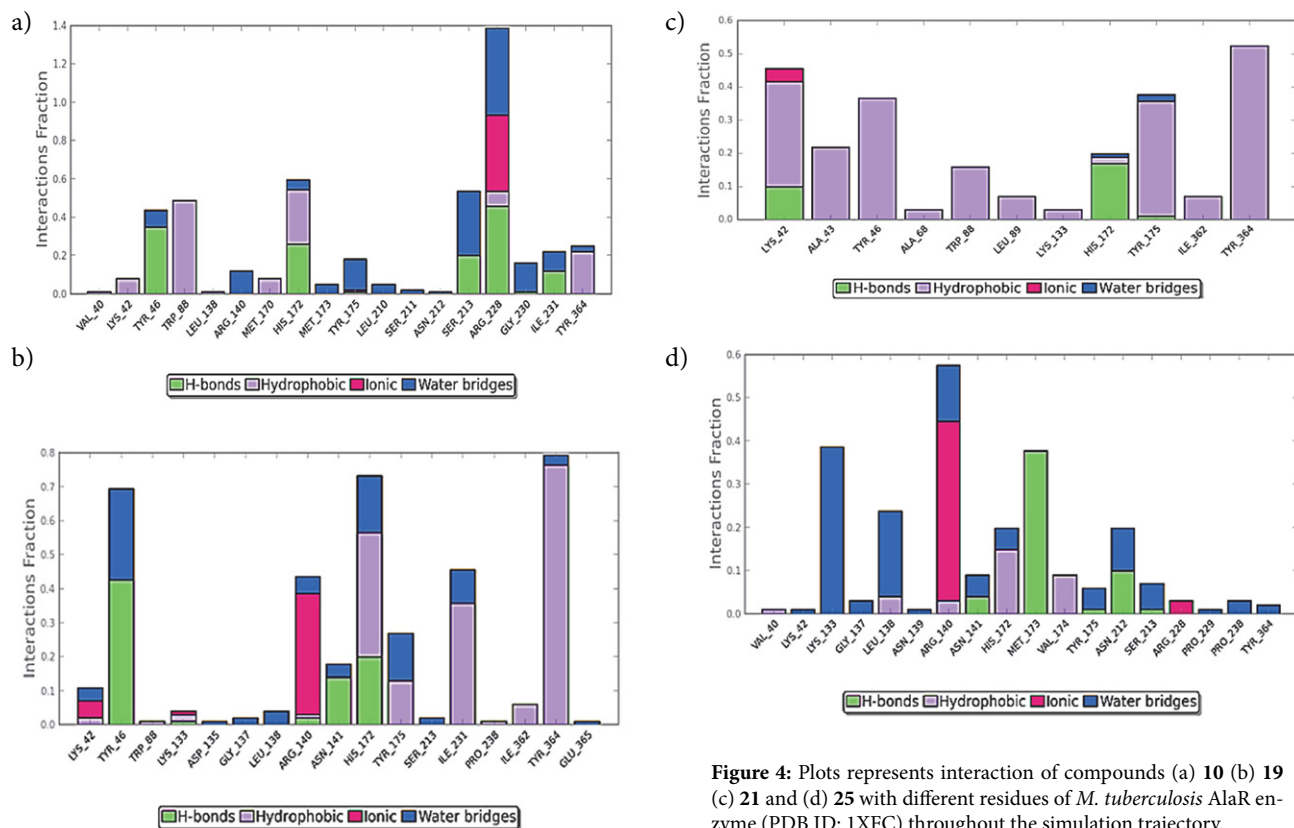


Figure 4: Plots represents interaction of compounds (a) **10** (b) **21** (c) **21** and (d) **25** with different residues of *M. tuberculosis* AlaR enzyme (PDB ID: 1XFC) throughout the simulation trajectory.

(~11% of MD trajectory) was observed between Lys42 and the phenyl ring of ethyl benzoate moiety. The side chain NH_2 of this residue also exhibited a weak hydrogen bonding interaction (~9% of MD trajectory) with position five $>\text{C}=\text{O}$ of thiazolidine-3,5-dione ring. This carbonyl oxygen atom showed another weak hydrogen bonding interaction (~16% of MD trajectory) with the side chain imidazole ring NH of His172. This low frequency hydrogen bonding interaction is due to the higher conformational flexibility of His172 side chain ($\psi = 325^\circ$, Supplementary figure S10c), observed during entire 10 ns MD simulation. This conformational flexibility of His172 is more compared to the conformational flexibility of His172 observed for inhibitors **19** and **25**. In addition, three weak π - π stacking interactions (~5–17% of MD trajectory) were also observed for this inhibitor with Tyr46, Trp88 and Tyr175 residues. Probably these weak hydrophobic and hydrogen bonding interactions are responsible for the low activity of this compound.

The gyration radius (r_{Gyr}) measures the extendedness of a ligand. It was found to be stable after 2 ns of MD simulations of **21** and **25**/1XFC complexes and the average values were 0.215, 0.24, 0.67 and 0.11 Å, respectively (Supplementary figure S12a-d). The average RMSD of these inhibitors were 0.48, 0.465, 0.67 and 0.475 Å, respectively. As evident by the lower RMSD values, inhibitors **19** and **25** showed less conformational changes and more stability during simulation. Inhibitors **19** and **25** also exhibited lower changes in the polar surface area (PSA) (157.75–169.16 and 156.71–139.4 Å², respectively) compared to the less active compounds **10** and **21** (MolSA: 203.5–210 and 344.6–355.58 Å², respectively; PSA: 121.20–141.44 and 86.72–108.73 Å², respectively) during MD simulation, fur-

ther indicating less conformational flexibility of inhibitors **19** and **25** before stabilization within the catalytic pocket.

Further, similar orientation was observed between the superposition of the conformations of **10** after MD simulation and best XP-docking pose (RMSD: 1.23 Å) (Supplementary figure S11a); conformations of **19** after MD simulation and best XP-docking pose (RMSD: 1.53 Å) (Supplementary figure S11b); conformations of **21** after MD simulation and best XP-docking pose (RMSD: 1.35 Å) (Supplementary figure S11c) and conformations of **25** after MD simulation and best dock pose (RMSD: 0.77 Å) (Supplementary figure S11d). Conformational changes of 2-chloro-4-nitrophenyl moiety arising due to the rotation about PhC-N< thiazolidine-3,5-dione ring bond probably resulted in slightly higher RMSDs after superposition of the conformations of **19** best XP-docking pose with the pose of MD simulation.

The designing of novel *MtAlaR* inhibitors targeting the blockade of bacterial AlaR enzyme is considered to be a futuristic approach as reflected by the availability of limited number of known inhibitors. The only marketed drug D-cycloserine however, faces the issues associated with the lack of target specificity and selectivity. The partial agonism offered at the glycine site of NMDA receptor and non-selective inhibition towards other PLP dependent enzymes are proven causes for the concerned drawbacks. For further evaluation, the results of the current study were compared with the AlaR inhibitory activity of the literature molecules as reported by Anthony K.G. et al.^{24,27} The compound **19** ($\text{IC}_{50} = 0.05 \mu\text{M}$) and **25** ($\text{IC}_{50} = 0.03 \mu\text{M}$) showed potent activity against the *MtAlaR*. The compounds (**19**; $\text{IC}_{50} = 0.36 \mu\text{M}$) and **25**; ($\text{IC}_{50} = 0.49 \mu\text{M}$) were also able to exhibit prominent inhibitory activity against

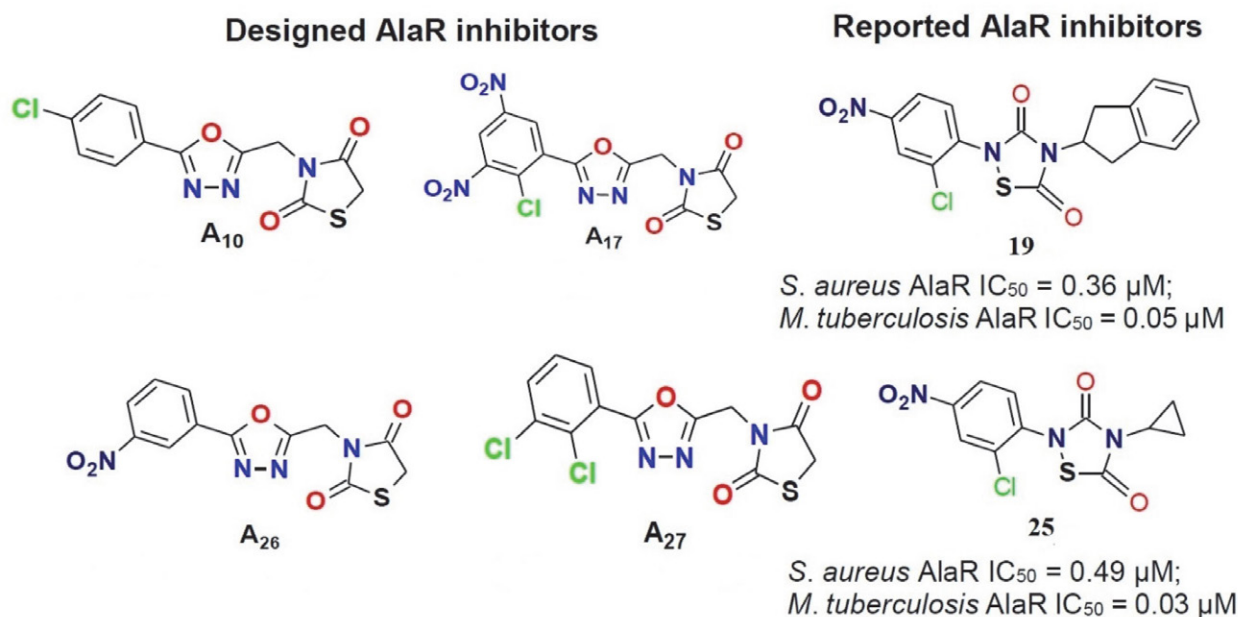


Figure 5: Structural comparison of designed AlaR inhibitors (**A₁₀**, **A₁₇**, **A₂₆** and **A₂₇**) with that of reported AlaR inhibitors (**19** and **25**).

Staphylococcus aureus AlaR. When the structural aspects of the inhibitors **19** and **25** were compared, it was found that, three ring system scaffold, aryl ring with electron withdrawing groups like -Cl and -NO₂, and thiazolidin-2,4-dione/thiadiazolidine-3,5-dione ring scaffold are essential requirements for imparting the activity (Figure 5). The reported molecule although showed high inhibitory action towards *Mt*AlaR, but their further development as drug candidate still needs to be investigated in terms of target specified action and non-interaction with other PLP dependent enzymes. Based on the above observation, some novel AlaR inhibitors (**A**₁₀, **A**₁₇, **A**₂₆ and **A**₂₇) were designed which may be considered as promising lead molecules for AlaR inhibitory action. These designed molecules may assure target selectivity and enzyme inhibitory action which has to be evaluated by computational protocols and *in vitro* enzymatic assays.

4. Conclusion

To date, most known inhibitors of alanine racemase bind solely to the substrate binding region proximal to the PLP. In the present study, a combined computational approach was applied to gain insight into the structural basis for *Mt*AlaR inhibitors. We obtained several possible binding poses for structurally diverse set of 25 *Mt*AlaR inhibitors using Glide XP-docking. Docking interaction profile showed that residues Lys42, Tyr46, Arg140, His172 and Tyr175 are mainly responsible for the stabilization of inhibitors within the catalytic pocket. MM-GBSA rescoring result revealed that ΔG_{vdW} and ΔG_{lipo} terms are the driving force for ligand binding. Further, the negative values of van der Waals (ΔG_{vdW} -22.05 and -24.93 kcal/mol, respectively) and non-polar solvation (ΔG_{lipo} -33.26 and -29.49 kcal/mol, respectively) binding energy terms for the high active inhibitors **19** and **25**, also indicated that hydrophobic interactions are primarily responsible for the stable complex formation. A computational study on inhibitors **1-25** with the B3LYP/6-31G**++ quantum chemical method was performed in an attempt to correlate stereoelectronic features with AlaR inhibitory activity. The molecular electrostatic potential of the inhibitors in specific regions of the molecules appears to play a pivotal role in the activity. Further, results showed that positive electrostatic potential, high negative E_{LUMO} and positive nucleophilic superdelocalizability favours inhibitors binding in the catalytic pocket. 10 ns MD simulations used here revealed the importance of hydrogen bonding and hydrophobic interactions of compounds with *M. tuberculosis* AlaR. Moreover, similar orientations were observed between the superposition of the conformations of **21** and **25** after MD simulation and respective best XP-docking poses. Based on the above finding we hereby propose the chemical structures of 4 lead molecules which may exhibit potent *Mt*AlaR action and can be considered as a promising scaffold for further drug design and synthesis.

Acknowledgements

We would like to thank University Grants Commission (UGC), Government of India, for the financial support (No. F1-17.1/2014-15/RGNF-2014-15-SC-KER-61880).

5. References

1. D. T. Hoagland, J. Liu, R. B. Lee, R. E. Lee, *Adv Drug Del Rev* **2016**, 102, 55–72. DOI:10.1016/j.addr.2016.04.026
2. N. V. Grishin, M. A. Phillips, E. J. Goldsmith, *Protein Sci* **1995**, 4, 1291. DOI:10.1002/pro.5560040705
3. A. Watanabe, T. Yoshimura, B. Mikami, H. Hayashi, H. Kagamiyama, N. Esaki, *J Biol Chem* **2002**, 277, 19166–19172. DOI:10.1074/jbc.M201615200
4. P. LeMagueres, H. Im, J. Ebalunode, U. Strych, M. J. Benedik, J. M. Briggs, H. Kohn, K. L. Krause, *Biochem.* **2005**, 44, 1471–1481. DOI:10.1021/bi0486583
5. E. Davis, E. S. Hutchinson, H. O. Reading, Y. Nakatani, K. L. Krause, *Acta Cryst.* **2014**, F70, 1199–1205. DOI:10.1107/S2053230X14017725
6. P. Le Magueres, H. Im, A. Dvorak, U. Strych, M. Benedik, K. L. Krause, *Biochem.* **2003**, 42, 14752–14761. DOI:10.1021/bi030165v
7. J. P. Shaw, G. A. Petsko, D. Ringe, *Biochem.* **1997**, 36, 1329–1342. DOI:10.1021/bi961856c
8. E. R. Scaletti, S. R. Luckner, K. L. Krause, *Acta Crystallogr. D. Biol. Crystallogr.* **2012**, 68, 82–92. DOI:10.1107/S0907444911050682
9. G. F. Stamper, A. A. Morollo, D. Ringe, *Biochem.* **1998**, 37, 10438–10445. DOI:10.1021/bi980692s
10. A. Watanabe, T. Yoshimura, B. Mikami, N. Esaki, *J. Biochem.* **1999**, 126, 781–786. DOI:10.1093/oxfordjournals.jbchem.a022517
11. S. Sun, M. D. Toney, *Biochem.* **1999**, 38, 4058–4065. DOI:10.1021/bi982924t
12. D. T. Major, G. Jiali, *J. Am. Chem. Soc.* **2006**, 128, 16345–16357. DOI:10.1021/ja066334r
13. U. Strych, M. Davlieva, J. P. Longtin, E. L. Murphy, H. Im, Benedik, K. L. Krause, *BMC Microbiol.* **2007**, 7, 40–45. DOI:10.1186/1471-2180-7-40
14. T. Yoshimura, M. Goto, *FEBS J.* **2008**, 275, 3527–3537. DOI:10.1111/j.1742-4658.2008.06516.x
15. F. C. Neuhaus, in: D. Gottlieb, P. Shaw (Ed.): *Antibiotics*, Springer-Verlag Berlin Heidelberg, 1967, 1, pp. 40–83.
16. F. C. Neuhaus, W. P. Hammes, *Pharmacol. Ther.* **1981**, 14, 265–319. DOI:10.1016/0163-7258(81)90030-9
17. W. W. Yew, C. F. Wong, P. C. Wong, J. Lee, C. H. Chau, *Clin. Infect. Dis.* **1993**, 17, 288–289. DOI:10.1093/clinids/17.2.288
18. (a) M. G. Kim, U. Strych, K. Krause, M. Benedik, H. Kohn, *J. Antibiot.* **2003**, 56, 160–168. DOI:10.7164/antibiotics.56.160
(b) M. G. Kim, U. Strych, K. Krause, M. Benedik, H. Kohn, *Med. Chem. Res.* **2003**, 12, 130–138.
19. V. Copie, W. S. Faraci, C. T. Walsh, R. G. Griffin, *Biochem.* **1988**, 27, 4966–4970. DOI:10.1021/bi00414a002

20. M. D. Erion, C. T. Walsh, *Biochem.* **1987**, 26, 3417–3425. DOI:10.1021/bi00386a025
21. B. Badet, D. Roise, C. T. Walsh, *Biochem.* **1984**, 23, 5188–5194. DOI:10.1021/bi00317a016
22. F. R. Atherton, M. J. Hall, C. H. Hassall, R. W. Lambert, W. J. Lloyd, P. S. Ringrose, *Antimicrob. Agents Chemother.* **1980**, 18, 897–905. DOI:10.1128/AAC.18.6.897
23. F. R. Atherton, M. J. Hall, C. H. Hassall, R. W. Lambert, W. J. Lloyd, P. S. Ringrose, D. Westmacott, *Antimicrob. Agents Chemother.* **1982**, 22, 571–578. DOI:10.1128/AAC.22.4.571
24. Y. Lee, S. Mootien, C. Shoen, M. Destefano, P. Cirillo, O. A. Asojo, K. R. Yeung, M. Ledizet, M. H. Cynamon, P. A. Aristoff, R. A. Koski, P. A. Kaplan, K. Anthony, *Biochem. Pharmacol.* **2013**, 86, 222–230. DOI:10.1016/j.bcp.2013.05.004
25. G. I. Mustata, T. A. Soares, J. M. Briggs, *Biopolymers.* **2003**, 70, 186–200. DOI:10.1002/bip.10425
26. G. I. Mustata, J. M. Briggs, *J. Comput. Aided Mol. Des.* **2002**, 16, 935–953. DOI:10.1023/A:1023875514454
27. K. G. Anthony, U. Strych, K. R. Yeung, C. S. Shoen, O. Perez, K. L. Krause, M. H. Cynamon, P. A. Aristoff, A. Raymond, R. A. Koski, *PLoS One.* **2011**, 6, e20374. DOI:10.1371/journal.pone.0020374
28. E. Harder, W. Damm, J. Maple, C. Wu, M. Reboul, J. Y. Xiang, L. Wang, M. K. L. Dahlgren, J. L. Knight, J. W. Kaus, D. S. Cerutti, G. Krilov, W. L. Jorgensen, R. Abel, R. A. Friesner, *J. Chem. Theo. Comput.* **2016**, 12, 281–296. DOI:10.1021/acs.jctc.5b00864
29. G. M. Sastry, M. Adzhigirey, T. Day, R. Annabhimoju, W. Sherman, *J. Comput. Aided Mol. Des.* **2013**, 27, 221–234. DOI:10.1007/s10822-013-9644-8
30. M. P. Jacobson, D. L. Pincus, C. S. Rapp, T. J. F. Day, B. Honig, D. E. Shaw, R. A. Friesner, *Proteins.* **2004**, 55, 351–367. DOI:10.1002/prot.10613
31. G. N. Ramachandran, C. Ramakrishnan, V. Sasisekharan, *J. Mol. Biol.* **1963**, 7, 95–99. DOI:10.1016/S0022-2836(63)80023-6
32. R. A. Friesner, R. B. Murphy, M. P. Repasky, L. L. Frye, J. R. Greenwood, T. A. Halgren, P. C. Sanschagrin, D. T. Mainz, *J. Med. Chem.* **2006**, 49, 6177–6196. DOI:10.1021/jm051256o
33. J. M. Wang, T. J. Hou, X. J. Xu, *Curr. Comput. Aided Drug Des.* **2006**, 2, 287–306. DOI:10.2174/157340906778226454
34. J. Li, R. Abel, K. Zhu, Y. Cao, S. Zhao, R. A. Friesner, *Proteins.* **2011**, 79, 2794–2812. DOI:10.1002/prot.23106
35. A. Pullman, B. Pullman, *Q. Rev. Biophys.* **1981**, 14, 289–380. DOI:10.1017/S0033583500002341
36. V. Prasad, E. T. Birzin, C. T. McVaugh, R. D. van Rijn, S. P. Rohrer, G. Chicchi, D. J. Underwood, E. R. Thornton, A. B. Smith, R. Hirschmann, *J. Med. Chem.* **2003**, 46, 1858–1869. DOI:10.1021/jm0205088
37. S. R. Gadre, P. K. Bhadane, *Reson.* **1999**, 4, 14–23. DOI:10.1007/BF02839010
38. G. B. Rocha, R. O. Freire, A. M. Simas, J. J. Stewart, *J. Comput. Chem.* **2006**, 27, 1101–1111. DOI:10.1002/jcc.20425
39. Z. Guo, U. Mohanty, J. Noehre, T. K. Sawyer, W. Sherman, G. Krilov, *Chem. Biol. Drug Des.* **2010**, 75, 348–359. DOI:10.1111/j.1747-0285.2010.00951.x
40. (a) W. L. Jorgensen, J. D. Madura, *Mol. Phys.* **1985**, 56, 1381–1392. DOI:10.1080/00268978500103111
(b) C. P. Lawrence, J. L. Skinner, *Chem. Phys. Lett.* **2003**, 372, 842–847. DOI:10.1016/S0009-2614(03)00526-8
41. U. Essmann, L. Perera, M. L. Berkowitz, T. Darden, H. Lee, L. G. Pedersen, *J. Chem. Phys.* **1995**, 103, 8577–8593. DOI:10.1063/1.470117
42. G. J. Martyna, M. L. Klein, M. Tuckerman, *J. Chem. Phys.* **1992**, 97, 2635–2643. DOI:10.1063/1.463940
43. G. J. Martyna, D. J. Tobias, M. L. Klein, *J. Chem. Phys.* **1994**, 101, 4177–4189. DOI:10.1063/1.467468

Povzetek

Alanin racemaza je piridoksal-5'-fosfat odvisen bakterijski encim, ki zagotavlja esencialni peptidoglikanski prekurzor D-alanin, ki ga bakterija uporablja za sintezo celične stene. Ta encim je prisoten v vseh bakterijah, vključno z *Mycobacterium tuberculosis*, zaradi česar je pomembna tarča za odkrivanje novih antibakterijskih zdravil. Raziskali smo način vezave petindvajsetih znanih zaviralcev alanin racemaze bakterije *Mycobacterium tuberculosis*. Rezultati pridobljeni s študijami molekulskega prileganja so pokazali interakcije zaviralcev z aminokislinskimi ostanki Lys42, Tyr46, Arg140, His172 in Tyr175 na katalitskem veznem mestu encima alanin racemaze. Izračunane proste vezavne energije so pokazale, da predstavljajo van der Waalove in nepolarne solvatacijske interakcije gonilno sila vezave inhibitorjev. Inhibicijski mehanizem štirih preučevanih sistemov inhibitor-alanin racemaza smo nadalje preučili s pomočjo simulacije molekulske dinamike. Kvantno kemijski parametri izračunani z B3LYP/6-31G**++ pristopom so pokazali, da morajo imeti zaviralci nizke energijske vrednosti najnižje nezasedene molekulske orbitale in visoke vrednosti elektrostaticnega potenciala za močnejše interakcije. Rezultati te teoretične študije lahko služijo kot smernica pri bodočem načrtovanju močnih zaviralcev alanin racemaze *Mycobacterium tuberculosis*.



Except when otherwise noted, articles in this journal are published under the terms and conditions of the Creative Commons Attribution 4.0 International License

Scientific paper

Synthesis, Characterization, Biological Activities and Ab-initio Study of Transition Metal Complexes of [Methyl 2-((4-chlorophenyl)(hydroxy)methyle) Acrylate]

Shazia Ishfaq,¹ Shazia Nisar,^{1,*} Saqib Ali,² Sadaf Iqbal,¹ Saima Imad,³ Samina Iqbal,³ Saeeda Bano,³ Syeda Kanwal Zahid,¹ Nasreen Fatima¹ and Muhammad Shahzaman⁴

¹ Department of Chemistry, Faculty of Sciences, University of Karachi, 75270, Pakistan

² Department of Chemistry, Faculty of Sciences, University of Kotli, 11100, Pakistan

³ PCSIR Laboratories Complexes, Karachi, 75270, Pakistan

⁴ School of Atmospheric Sciences, Nanjing University of Information Science and Technology, Nanjing 210044, China

* Corresponding author: E-mail: shazian@uok.edu.pk

Phone No.00923343519338

Received: 11-29-2021

Abstract

Taking cognizance of the medicinal significance and diverse functions of synthetic Morita-Baylis-Hillman adducts (MBHA), the title ligand was synthesized and purified through column chromatography. Cr⁺³, Mn⁺², Co⁺³, Ni⁺², Cu⁺² complexes of the ligand were synthesized under basic conditions, subjected to characterization through spectral analyses and verified with the IR spectrum that was generated computationally by the DFT B3LYP method, with 6-311++ G (d,p) basis set and Hartree Fock (HF) B3LYP method in conjunction with 3-21G(d,p) basis set. Powder XRD helped to testify crystals of the complexes. Moreover, the antibacterial, and antioxidant characteristics of MBHA and its complexes were also established. All of them were found to be active antioxidants. The antibacterial activities, examined against *S. aureus*, *E. coli*, *B. pumilis* and *S. typhi* have revealed that its Cobalt complex has an excellent potential to act against all of them. Hence, these compounds maybe having potentialities for the discovery of new, cheaper and efficient drugs against various infectious diseases. The study also uncovers the first example of utilization of MBHA towards metal complex formation.

Keywords: MBH Adduct; transition Metal Complexes; XRD; antibacterial Activities; antioxidant Activities

1. Introduction

The significance of reactions that proceed through Carbon-Carbon bond forming, which in turn involves the coupling of the α -position of activated alkenes with carbon electrophiles under the influence of a catalyst, cannot be overlooked in atom economy.^{1,2} The reaction ends up in the formation of Michael type dimers. There are many other synthetic routes by which effectual and perfect C-C bond emerging reactions take place.³ Further to that medicinally relevant pharmaceutical compounds and natural products are very useful multifunctional building blocks for C-C bond formation which is vital for the synthetic organic chemistry.^{4,5} Besides this, Morita-Baylis-Hillman (MBH) compounds, especially the ones which are carbon-

ate, aldehyde, ester, or acetate-based derivatives act as an important intermediate in the synthesis of different structures. These compounds have become important MBH originators and represent a valuable class of substrates for synthetic purposes. These derivatives are widely employed as intermediates in the preparation of significant classes of compounds, as building blocks for natural products. Moreover, Michael/aldol cyclic reactions, that involve multiple C-C bond formations, also lead to important carbon frames that can be employed in drug synthesis.⁶ The MBH reaction is mainly a three-component reaction between the α -position of activated alkenes e.g ethyl or methyl acrylate, acrylonitrile and methyl vinyl ketones and electrophilic sp² carbon of aldehyde or imines in the presence of an appropriate catalyst, usually a tertiary

amine or phosphine.⁵ The resulting Morita-Baylis-Hillman adducts (MBHA) have diverse functionalities and versatile reactivity. Consequently, they have been widely used as powerful precursors for the building of various carbocyclic, heterocyclic and biologically important compounds.⁷ These compounds that are economical and biologically friendly, perform a number of functions and most importantly can be synthesized following green- one-step synthetic protocols. The anti-fungal, antimalarial, anti-tubercular activities of some MBHAs have been reported.⁸ The antileishmanial/antibacterial activities of some MBHA indicate that they can prove to be a novel and promising class of anti-parasitic compounds.^{9,10}

In this scenario a discovery that paved the way for some newer treatments has been that of an uncharted world of metal-based chemotherapeutic agents which have dissimilar kinetic and mechanisms of action from those of traditional organic medications. Curative potentialities of metal complexes in tumor/cancer therapy as well as other biological functions develop certain intricacies because central metals exhibit some special features. These metal-based complexes have variable coordination modes, that generate curing drug activity and provide excellency in terms of reactivity in the realm of the organic substrate.^{11,12} Through metal complexation of ligands, comprising of oxygen, nitrogen, hydroxyl, or ester functional groups, with metals like copper, zinc, cobalt, and iron, numerous finely-tuned therapeutic activities such as antihypertensive, antimalarial, and antimicrobial get enhanced. In addition, transition metal ion complexes are known to have a key electron transfer role in many biological processes.¹³ Metals have long been used for medicinal purposes in a more or less empirical fashion, in a wide variety of chelating modes, geometrical forms, and redox states. Presently identified thermodynamic and kinetic properties of the metal cation and ligand itself, however, provide the medicinal chemist a wide spectrum of reactive sites that can be highly mobilized.¹⁴ Thus, the biological diversity of the transition metal complexes along with their pharmacological specificity is to be established. Promising physiological responses would be drugs need to be demonstrated by in vitro study with targeted biomolecules and tissues as well as in-vivo. Therefore, studies pertaining to ligands with multiple, medicinally dynamic binding sites may serve as models for ensuring biochemical processes.^{11,15,16} In this context, the wide variety of potent biotic activities of MBHA encouraged us to synthesize new series of products belonging to this class of compounds, possessing different functionalities and exhibiting potential antioxidant activity. Keeping in view the significance of reported research on synthetic MBH adducts as medicinally important candidates and having the diversity of functions, we conferred them as ligands for the novel drug synthesis composed of their transition metal complexes. The present study is directed towards synthesis, characterization, and computational studies of halo/chloro-benzaldehyde

based MBH adducts and some of their novel metal complexes.

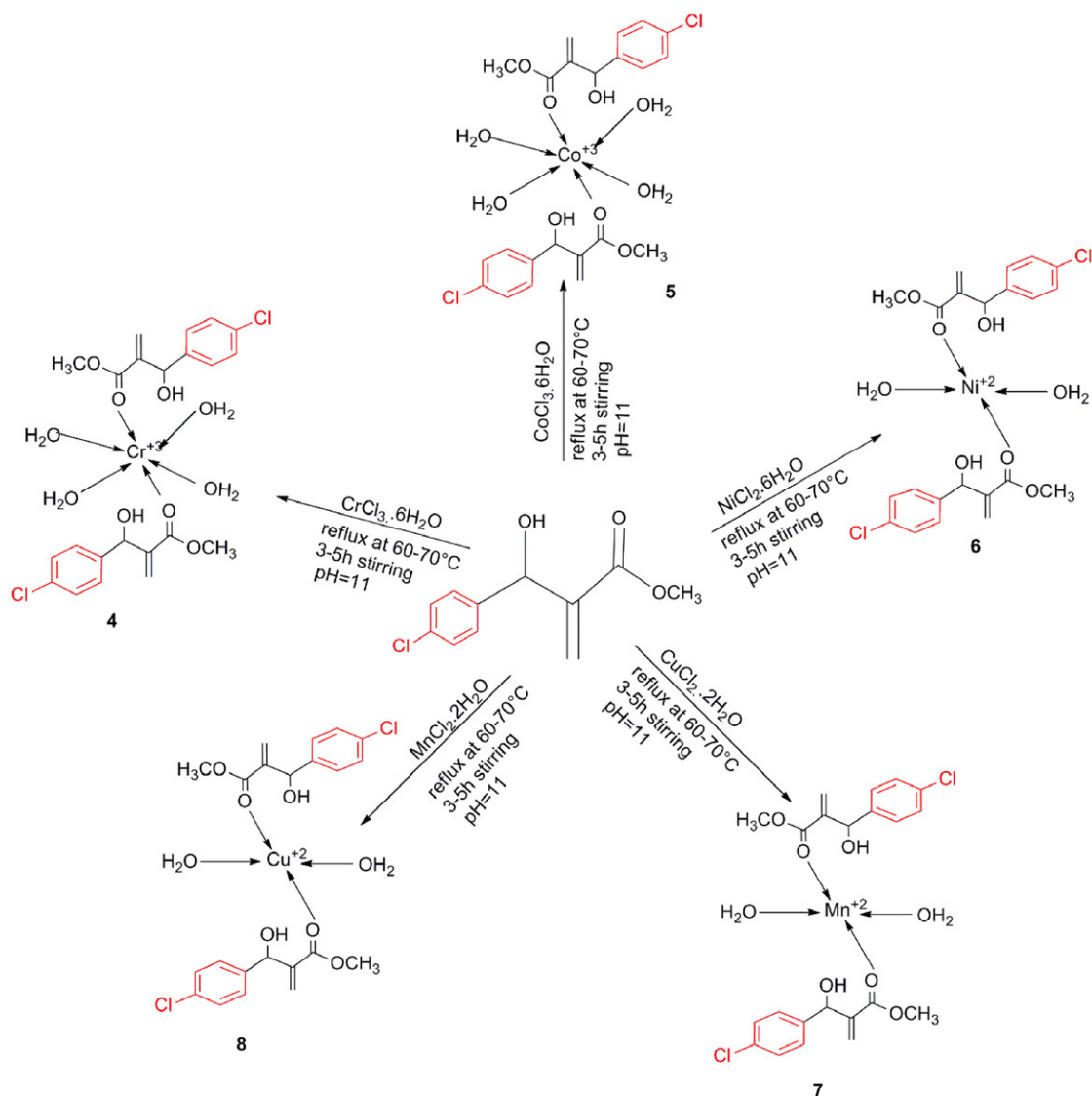
2. Materials and Methods

2.1. General

In the present study various solvents such as n-hexane, methanol and ethyl acetate of synthetic grade were used. In addition to that chemicals 4-Chlorobenzaldehyde (Sigma Aldrich), DABCO (Sigma Aldrich), Methyl Acrylate (Dae-Jung Kosdaq Reagents and Chemicals), NaCl (Sigma Aldrich), MgSO₄ anhydrous (Sigma Aldrich), NaOMe (Dae-Jung Kosdaq Reagents and Chemicals), CuCl₂ · 2H₂O (Sigma Aldrich), MnCl₂ · 2H₂O (Sigma Aldrich), NiCl₂ · 6H₂O (Sigma Aldrich), CoCl₃ · 6H₂O (Sigma Aldrich) and CrCl₃ · 6H₂O (Sigma Aldrich) were used. Further to that equipments like UV lamp (monitoring TLC card), Digital hot plate with constant temperature and stirring system, Gallen Kamp melting point instrument, LAMBDA 1050+ UV/Vis/NIR spectrophotometer, FTIR Spectrophotometer of Shimadzu Company prestige-21. The ¹H NMR spectrum of the ligand was recorded on AVANCE NEO NMR spectrometer (500 MHz for ¹H) in CDCl₃ solvent. Chemical shifts are reported as δ ppm against TMS as internal reference and coupling constants (*J*) are reported in Hz units. Mass spectrophotometer instrument of JEOL 600H1, for transition metal complexes used Electrospray ionization mass spectrometry (ESI MS) at QTrap hybrid triple-quadrupole (QTrap 2000, Applied Biosystems/MDS Sciex) and XRD Pananalytical company X-pro serial No. DYH313 for powder diffraction were the major instruments used for data analysis.

2.2. Synthesis of MBHA (Methyl 2-((4-chlorophenyl) (hydroxy)methyl) acrylate) L1

MBHA was prepared by addition of 5 equivalents of methyl acrylate to 4-chloro benzaldehyde (1 equivalent). The reaction mixture was further treated with 0.65 equivalents of Lewis base DABCO, using 5% THF solvent in round bottom flask with constant stirring at room temperature. The progress of the reaction was monitored at regular intervals of one hour through TLC under UV lamp and the completion time was recorded as 24 hours. The excess of methyl acrylate was evaporated which furnished gummy crude material upon complete evaporation. This was diluted further with 15 mL each of ethyl acetate and brine solutions. The organic layer developed in this mixture was separated through separating funnel, collected and this process was repeated thrice. Furthermore, the organic phase was concentrated by removing EtOAc through evaporation and concentrated crude was subjected to column chromatographic purification. Mobile phase system of ethyl acetate and n-hexane in ratio of 5:95 to 35:65 (v/v) was used for this



Scheme 2. Molecular modifications by reacting the MBHA as Ligand with transition metal salts to synthesize corresponding metal complexes

2. 6. X-Ray Diffraction

The XRD study (powder pattern) of the complexes were made with the help of X-ray diffractometer (Goniometer Radius mm = 240.00 and Dist. Focus-Diverg. Slit mm = 91.00) with Cu- anode material, $K\alpha [A^\circ] = 1.54060$ and the generator settings 30 mA, 40 kV.

2. 7. Antibacterial Assay

The antibacterial activity of L1 and its complexes was evaluated by agar diffusion method,^{26,27} against two Gram-negative bacteria (*Staphylococcus aureus*, *Escherichia coli*) and two Gram- positive bacteria (*Bacillus pumilis*, *Salmonella typhi*). All extracts were sterilized by sterile membrane syringe filter (pore size 0.45 μm , Millipore). For assay, 1mL of culture suspension of each strain (25% transmittance, 530 nm) was added in 100 mL antibiotic agar

No.11 (45 °C) and mixed well. 25mL of inoculated agar was poured in each petri dish (20 × 100 mm) and kept for solidification. After solidification 4 holes were made using sterile borer of 8mm diameter with 6mm internal diameter. Holes were marked and each extract (100 μL) was poured in the respective well, and incubated for 24 hours at 37 °C. The experiment was performed in triplicate under strict aseptic conditions. After incubation, zone of inhibition (mm) produced by each extract was measured and antibacterial activity expressed in terms of percent inhibition. Gentamycin (0.3%) was used as a standard antibiotic in comparison to L1 and complexes.

2. 8. DPPH Radical Scavenging Activity

The free radical scavenging action was determined by using the DPPH (2,2-diphenyl-1-picrylhydrazyl) radi-

cal scavenging method with some modification.^{28,29} The 0.3 mM solution of DPPH was prepared in methanol. 10 μL of each sample of different concentration (25 μg –100 μg) was mixed with 1.0 mL of DPPH solution. The reaction mixture was incubated at 37 $^{\circ}\text{C}$ for about 30 min. The absorbance at 515 nm was measured by spectrophotometer and percent radical scavenging activity was determined in comparison with the methanol treated control. Ascorbic acid was used as standard for further samples analysis.³⁰ By using this standard the antioxidant activity of the MBHA (L1) and its metal complexes were determined and recorded in the Table 4.

3. Results and Discussions

The present work was initiated with (i) the synthesis of ligand MBHA ($\text{C}_{11}\text{H}_{11}\text{ClO}_3$) through MBH reaction scheme where the choice of catalyst in appropriate amount and solvent often have a significant effect on the efficiency, rate and stability of the reactions.^{31,32} Using DABCO as catalyst and THF as solvent, the MBH adducts form exclusively or as major products in moderate to good yields in stable form upon continues stirring.^{33,34} The stability of the adduct was further confirmed via spectral analysis, which demonstrated no dimerization (Scheme 1), its transition metal complexes with five biologically significant transition metal ions

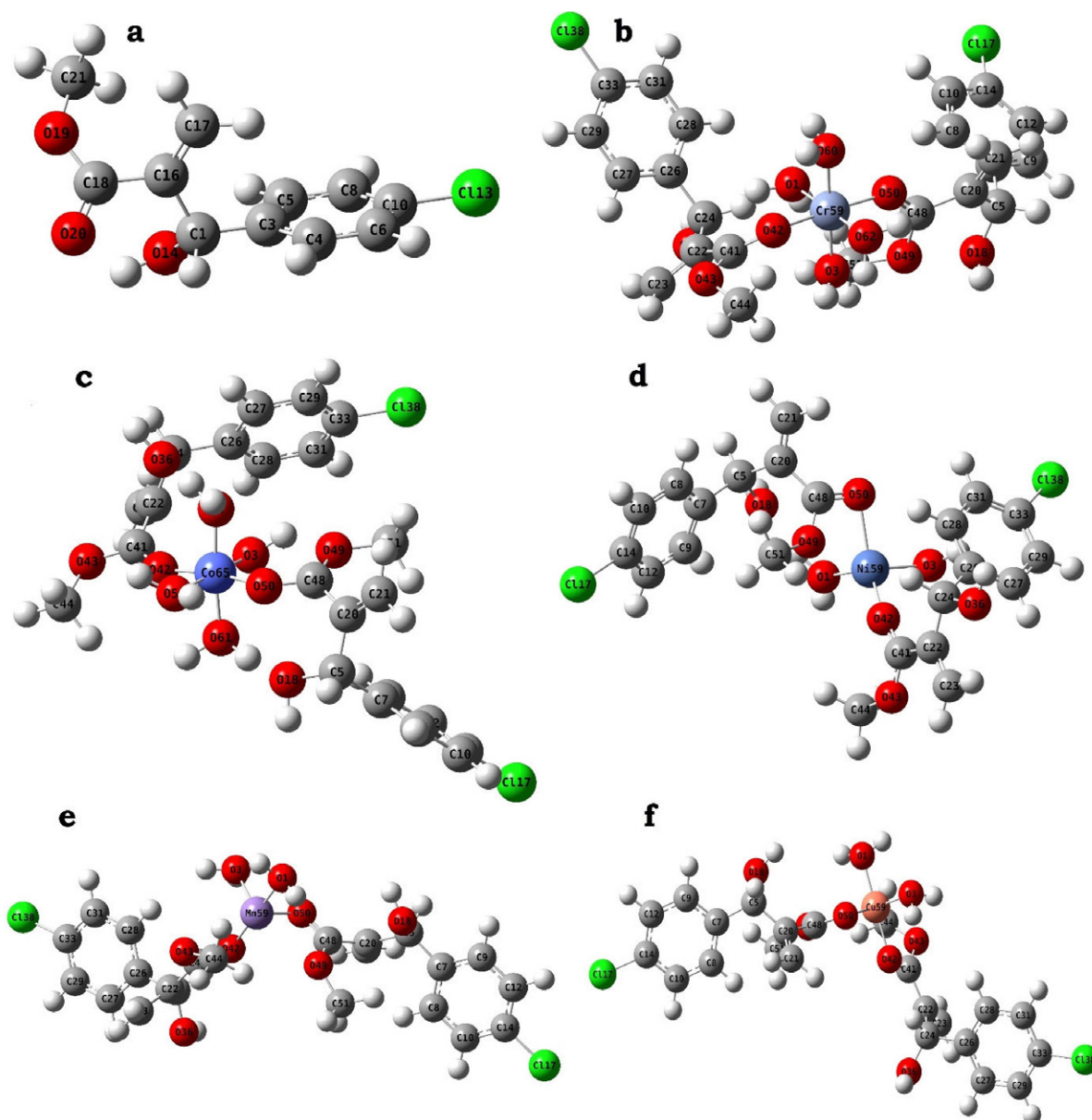


Fig. 1. Theoretically optimized geometry of the (a) MBHA (L1), and its corresponding complexes, (b) $\text{Cr}^{+3}\text{L1}$, (c) $\text{Co}^{+3}\text{L1}$, (d) $\text{Ni}^{+2}\text{L1}$, (e) $\text{Mn}^{+2}\text{L1}$ and (f) $\text{Cu}^{+2}\text{L1}$. The results have confirmed that each metal is coordinated by two ligand molecules, Cr^{+3} , Co^{+3} are octahedral and Ni^{+2} , Mn^{+2} , Cu^{+2} are tetrahedral as per optimized geometrical structures.

(Scheme 2), (ii) characterization of these compounds and finally (iii) their subsequent biological and antioxidant investigations. The UV-Visible spectroscopic results have revealed the formation of metal complexes, which was observed between 250 nm–265 nm of wavelength, in contrast to MBHA (L1) that shows a $\lambda_{\text{max}} = 267$ nm. Additionally, the m/z ratio and relative abundance (%) of MBHA have also been observed using Electrospray ionization-mass spectrometry (ESI-MS).³⁵ While, the ^1H NMR of MBHA was recorded at 500MHz using CDCl_3 as solvent. MBHA (compound 3) showed four signals at δ 3.29, 3.71, 5.83 and 6.34 ppm as singlet corresponding to proton of $-\text{OH}$ and three proton of $-\text{OCH}_3$, one proton of $-\text{CH}$ and one $-\text{CH}$ aromatic proton, respectively, in ^1H NMR spectrum. Furthermore, one signal of multiplet was appeared at δ 5.55 because of two protons of $-\text{CH}_2$ and neighboring proton effect. The other aromatic protons have been shown in the region δ 7.47–7.49 and 7.60–7.62 as doublet ppm in consensus with the structure.^{36–38} In Mass spectrum,⁸ a prominent peak of 227 m/z at 56.5% noted for M^+ , while 207 m/z (25%), 191 m/z (100%), 160 m/z (90%), 132 m/z (66%), 104 m/z (70%) and 77 m/z (64%) for fragmentation peaks pertaining to synthesized MBHA were recorded. The ^1H NMR and ESI-MS spectral data are consistent with the assigned structure

(compound 3). Additionally, the results of computational and spectral studies confirm that each transition metal (Cr^{+3} , Co^{+3} , Ni^{+2} , Mn^{+2} , Cu^{+2}) complex with MBHA (L1) has 1:2 stoichiometric ratios (Fig. 1).

3. 1. Theoretical and Experimental FTIR Analysis of Ligand (MBHA)/Compound 3

The FTIR spectra of MBHA (L1) and their complexes $[\text{M}(\text{L1})_2(\text{H}_2\text{O})_4]^{+3}$, $[\text{M}(\text{L1})_2(\text{H}_2\text{O})_2]^{+2}$ were recorded between 4000–500 cm^{-1} using KBr disk and the data is presented in Table-2. The FTIR data corresponding to compound 3, has shown the characteristics $-\text{OH}$ broad peak in 3446 cm^{-1} , prominent stretch of $=\text{C}-\text{H}$ at 2953 cm^{-1} and Sp^3 C-H stretch at 2897 cm^{-1} . The band observed at 1714 cm^{-1} is due to ester carbonyl vibration. Furthermore, the frequency ($\bar{\nu}$) of $\text{C}=\text{C}$ aromatic, $-\text{CH}_3$, C-O and C-Cl were designated as 1631 cm^{-1} , 1440 cm^{-1} , 1278 cm^{-1} and 540 cm^{-1} respectively (Fig. 2a).³⁹ Moreover, in computational IR analysis, it was observed that OH peak is somewhat different from the observed spectrum. This fact is because of the breadth of OH band appeared by the water vapors. It might be obtained due to greater number of OH ions appeared in the same intensity.⁴⁰ The peak intensities

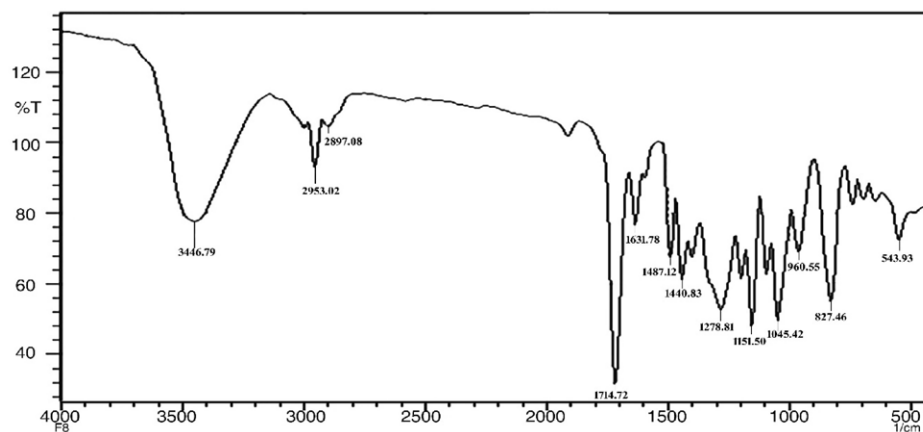


Fig. 2a. Experimental FTIR spectrum of Methyl 2-((4-chlorophenyl)(hydroxy)methyl) acrylate [MBHA (L1)]

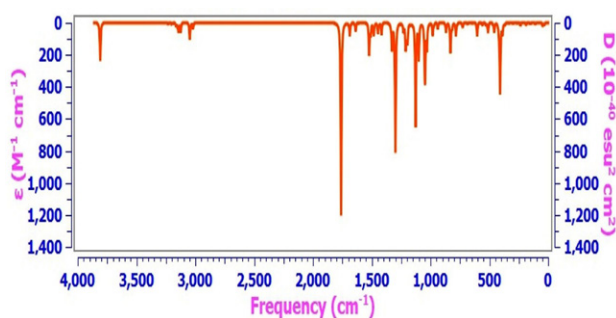


Fig. 2b. Theoretical FTIR spectrum of Methyl 2-((4-chlorophenyl)(hydroxy)methyl) acrylate [MBHA (L1)]

of left aforementioned fragments (Fig. 2b) in calculated spectrum more about the similar values. The slight change may be observed because of the theoretical results presented to isolated functional groups in gaseous state, while the experimental calculations belong to the molecules in solid state.⁴¹

3. 2. Characterization of MBHA Based Metal Complexes

The transition metals (Cr^{+3} , Co^{+3} , Ni^{+2} , Mn^{+2} , Cu^{+2}) complexes of MBHA (L1) were synthesized. Initially, Cr^{+3}

based complex **4** of ligand was prepared by employing a reported method.⁴² The existence of a single complex species in the reaction mixture and hence, the purity of the complex was confirmed through TLC, until a single spot was achieved on TLC plate (expected product **4**) (Scheme 2). In addition to this, the major spot upon purification was subjected to UV- visible analysis, which presented considerable difference from MBHA band (expected product **4**). By repeating the procedure with slight modification such as increasing the pH, precipitates were observed in 2.5 hours. Furthermore, the TLC analysis indicated 20–30 percent conversion with less spots and change in color. Based on current observation (TLC in 1.5h), any increase in the concentration of base up to 4M, maximum conversion of the reactants into product was observed (Scheme 2).

All the transition metal complexes (**4–8**) were subjected to characterization through their physical characteristics. Their molecular and structural formulae were established with the help of m/z ratio obtained through powder XRD and FTIR analyses. The data presented for m/z ratio of the ligand and compound **4–8** shows a good agreement between the calculated and observed values and thus support the suggested structures of the complexes.

3. 3. Theoretical and Experimental FTIR Analysis of the Compounds 4-8

Table 1 provides the details of the experimental and computed IR vibrational frequencies of MBHA (compound **3**) and metal complexes (compounds **4–8**). Considering FTIR spectrum of compound **4**, a broad band at 3500–3380 cm^{-1} (–OH) can be observed, which might be either due to moisture or coordinated water in the complex. Moreover, we observed peak shifts toward lower frequency value for C=O group from a sharp peak of ligand at 1725 cm^{-1} to a small peak at 1625 cm^{-1} . It suggests the coordination of carbonyl group through oxygen to the Cr^{+3} metal which ultimately reduces strength of the car-

bonyl group in complex. These results are also supported by literature.¹⁴ Similarly, the peaks of ligand and its C-O (of ester) appeared 1278 cm^{-1} which showed a shift from 1105 cm^{-1} (Table 1). Which may change because of environmental effect regarding C=O coordination towards the metal ion.^{43,44} Some additional peaks have also been observed to appear at 603 and 520 cm^{-1} . These peaks were assigned to Cr-O and C-Cl, respectively.⁴⁵ These findings have confirmed the participation of carbonylic functional group of the ligand in complex formation. No significant change in the IR frequency of C=C double bond was seen upon complex formation and hence, it is inferred that this group doesn't participate in complexation (Fig. 1b). Based on these observations, the molecular and structural formulae of the compound **4** were deduced as $[\text{Cr}(\text{L1})_2(\text{H}_2\text{O})_4]^{+3}$.

In FTIR spectral results for the compound **5** we observed that –OH group has shown a broad signal ranging from 3400–3300 cm^{-1} . This signal was relatively at similar position as in the ligand. While comparing the C=C frequencies of both the ligand and complex **5**, the peak was found to be slightly shifted from 1631 cm^{-1} to 1620 cm^{-1} which suggests that this functional group was not involved in coordination. The aromatic ring has shown frequencies (1604 and 1521 cm^{-1}) almost at similar position as that of the ligand aromatic pi bonds which also suggests non coordination behavior of the aromatic ring in respective complex formation. A clearer signal appeared at 1651 cm^{-1} was probably due to the carbonyl group and has significantly shifted from 1714 cm^{-1} to 1651 cm^{-1} upon complexation. This kind of shift has also been reported in literature,¹⁴ thus confirming the coordination of the ligand's carbonyl site to the Co^{+3} metal. Another significant variation in the IR spectrum of complex was a slight shift to the higher frequencies in IR signal of C-O (of ester) i.e. ligand C-O frequency shifted from 1278 to 1386 (C-O of the complex) (Table 1). Additionally, a unique signal attributable to Co-O appeared at 607 cm^{-1} and another noticeable

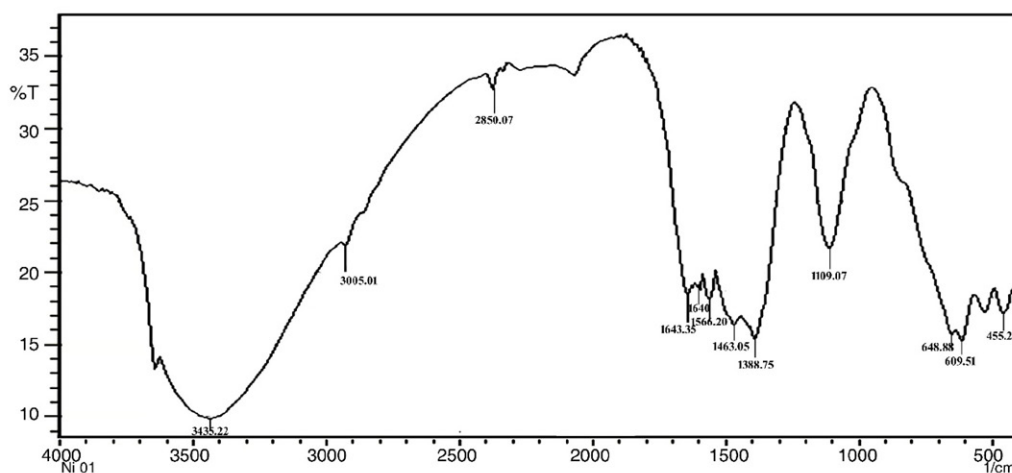


Fig. 3a. Observed FT-IR spectrum of Nickel Transition Metal with MBHA (L1)

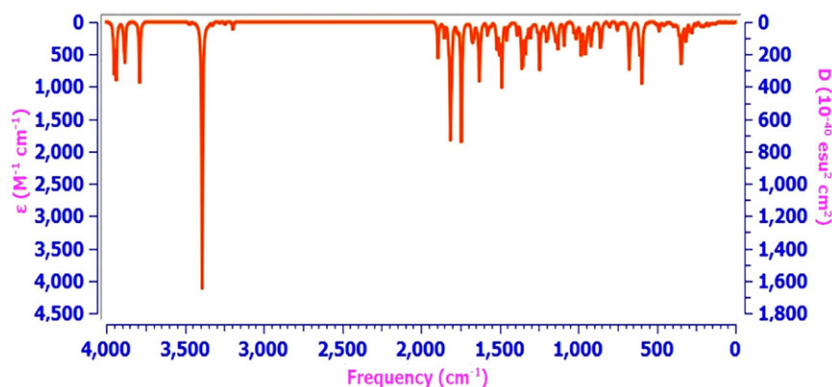


Fig. 3b. Theoretical FT-IR spectrum of Nickel Transition Metal with MBHA (L1)

variation in C-Cl frequency from 540 cm^{-1} to 518 cm^{-1} was also observed. Based on the overall information discussed above, the molecular formula $[\text{Co}(\text{L1})_2(\text{H}_2\text{O})_4]^{+3}$ and structural formula (Fig. 1c) was established for the compound 5.

FTIR analysis for the Ni^{+2} complex (compound 6) showed peaks for all the prominent functional groups along with some informative shifts which revealed the complex formation. Such as, an extremely weak band, almost negligible at 1640 cm^{-1} correspond to carbonyl group which was comparatively at lower frequency than its precursor (Ligand) carbonyl absorption (1714 cm^{-1}). It suggests carbonyl coordination upon complex formation. Moreover, the peaks at 609 cm^{-1} and 455 cm^{-1} were assigned to Ni-O and C-Cl groups, respectively. Additionally the -OH and =CH groups exhibited peaks at 3450–3350 cm^{-1} (broad) and 3005 cm^{-1} , respectively. Furthermore, we have also observed peaks for C=C bond at 1643 cm^{-1} with no significant shift and simultaneously demonstrating that C=C do not participate in complexation (Fig. 1d). In spite of that we have also observed sharp peak instead at 3880–3886 cm^{-1} of same (-OH) functional group. The difference is observed due to the presence of moisture in the compound, which has pro-

vided interference during recording of spectrum.⁴¹ Likewise, the remaining functional groups show a little change in the calculated values as is evident from their sharp pointed peaks at exact frequencies. In the observed spectrum these small peaks overlap with each other to give loops instead of sharp pointed peaks obtained in the theoretical spectrum (Fig. 3a & Fig. 3b).⁴⁰ Nevertheless, we have obtained good agreement in the observed and calculated values of frequencies and deduced the formula $[\text{Ni}(\text{L1})_2(\text{H}_2\text{O})_2]^{+2}$.⁴⁶

FTIR spectral results for the compound 7 (Fig. 1e) reveal that -OH group gives a broad band ranging from 3505–3310 cm^{-1} with relatively no change in its position as compared to the ligand. Similarly, the C=C $\bar{\nu}$ (1631 cm^{-1}) remains about the same upon complex formation i.e. at 1629 cm^{-1} suggesting that this functional group was not involved in coordination. A clear disappearance of signal of the carbonyl group and its appearance at an entirely new position (Table 1) was probably due to its coordination with the metal ion. This kind of shift has also been reported in the literature,¹⁴ hence confirms the coordination of the ligand's carbonyl site to the Mn^{+2} metal ion. Moreover, the appearance of new peak at 603 cm^{-1} was attributed to Mn-O while C-Cl 540 cm^{-1} shifted towards 523 cm^{-1} . The

Table 1. Characteristic FTIR bands of the MBHA (L1) and its metal complexes (cm^{-1}) $\bar{\nu}$

Functional groups	(L1)	Calc. (L1)	CrL1	CoL1	NiL1	Calc. NiL1	MnL1	CuL1
$\bar{\nu}$ (-OH)	3446	3808	3500–3380	3300–3400	3350–3450	3880–3886	3310–3505	3350–3480
$\bar{\nu}$ (=C-H)	2953	3150	2915	2950	3005	3194	3005	3115
$\bar{\nu}$ (Sp^3 C-H stretch),	2897	3020	2810–2980	2860–2935	2850	3244	2980	2980
$\bar{\nu}$ (ester C=O),	1714	1760	1625	1651	1640	1669	–	–
$\bar{\nu}$ C=C (aromatic),	1631	1637	1550	1620	1643	1627	1629	1673
$\bar{\nu}$ C=C	–	1446	1438	1483	1566	1576	1500	1604
$\bar{\nu}$ (-CH ₃)	1440	1482	–	–	1463	1485	1566	1521
$\bar{\nu}$ (C-O)	1278	1299	1105	1386	1388	1358	1386	1388
$\bar{\nu}$ (C-OCH ₃)	–	1212	1382	1109	1109	1128	1111	1112
$\bar{\nu}$ (M-O)	–	–	603	607	609	606	603	605
$\bar{\nu}$ (C-Cl)	540	459	520	518	455	485	523	486

Only the observed changes in specified functional groups are represented

molecular $[\text{Mn}(\text{L1})_2(\text{H}_2\text{O})_2]^{+2}$ and structural formula were established for the compound 7.

FTIR results for the compound 8 (Fig. 1f) have revealed the presence of $-\text{OH}$ functional group by a peak almost at similar position ($3480\text{--}3350\text{ cm}^{-1}$) as that of the ligand precursor. Almost similar results were obtained for the presence of sp^2 and sp^3 C-H bonds of the complex i.e. their peaks were observed at $3115, 2980\text{ cm}^{-1}$ respectively. The ester carbonyl absorption (1705 cm^{-1}) has completely disappeared as compared to that of the ligand carbonyl (1714 cm^{-1}) which suggests its participation in complex formation. No marked difference was observed in the frequency due to the C=C double bond (1673 cm^{-1}) and aromatic C=C bond (1604 cm^{-1}) suggesting no contribution in complex formation. These assumptions were further supported by appearance of IR peaks at 605 cm^{-1} , and 486 cm^{-1} due to presence of Cu-O and C-Cl bond. Based on all these physical, analytical and spectral results the prepared complex was assigned the structure presented above in scheme 2 as compound 8 formulated as $[\text{Cu}(\text{L1})_2(\text{H}_2\text{O})_2]^{+2}$.

3. 4. X-Ray Diffraction

The structure resolved from powder XRD analysis is a successful process that leads to evaluation of an exact crystal structure depending on the cautious handling of each step. Microcrystalline materials mainly organic based metal complexes can easily be resolved by XRD powder diffraction.^{13,28} The accuracy of a material whose structure is to be determined depends on the quality of

the powder diffraction data. Besides, nature of the asymmetric unit such as the number, type of atoms, atomic arrangement and molecular geometry involves to prove the quality of the complex. However, for successful structure determination, monophasic powder sample of good crystallinity should be available for the material of interest.⁴⁷ The recorded result was summarized in Table 2. & Table 3.

X-ray diffraction was performed for further confirmation of the structure of transition metal complexes. The patterns of diffractograms obtained for complexes are given in Fig. 4. Each metal complex pattern has one sharp peak of metal oxide (Fig. 4). This clearly gives an idea of the coordination of one oxygen atom from the ligand to the metal ions. Hence, the idea of coordination of ligand with the metal ions through the same site has been confirmed. Moreover, these patterns indicate crystalline nature of all the complexes. It can be observed that the rest of the pattern of metal complexes is almost dissimilar from each other owing to the formation of a distinct distorted crystalline structure. Most probably, this difference is due to the coordination of water molecules into the coordination sphere.^{15,16} Besides, they have different unit cell number and radius intensity ratio, because of this they belong to non-identical but unique crystal class. The resultant XRD output such as density, volume, radius intensity ratio, lattice parameters ($a, b, c, \alpha, \beta, \gamma$) and probable crystal class have been given in the Table 2. The chromium complex (compound 4) was isolated, and crystallized in the orthorhombic system (space group Pmmn (59) with $Z = 2$). In the cobalt complex, the molecule contains one Cr^{+3} atom, two

Table 2. Crystallographic data and observed refinement parameters for complexes 4-8

S. No.	Sample complexes	S. Group (G. No.)	Volume (10^6pm^3)	Density (g/cm^3)	Unit Cell Dimensions (Å)	Crystal Class	No. of unit cells (Z)	Reference Intensity Ratio (RIR)
1	CrL1	Pmmn (59)	94.58	3.63	$a \neq b \neq c$ $a = 3.8630$ $b = 3.1820$ $c = 7.6940$	Orthorhombic	2	4.60
2	CoL1	Fd-3m (223)	93.82	6.09	$a = b = c$ $a = 8.0840$ $b = 8.0840$ $c = 8.0840$	Cubic	2	6.39
3	NiL1	R-3m (166)	99.78	4.53	$a = b \neq c$ $a = 2.8353$ $b = 2.8353$ $c = 14.3319$	Hexagonal	3	6.38
4	MnL1	141/amd (141)	518.94	$a = b = c$ $a = 8.0360$ $b = 8.0360$ $c = 8.0360$	Cubic	4	4.21
5	CuL1	Cc (9)	81.12	6.51	$a \neq b \neq c$ $a = .6890$ $b = 3.4200$ $c = 5.1300$	Monoclinic	4	3.72

Table 3. Crystal lattice Data and Summary of Data Collection and Refinement for complexes 4-8

S.NO.	Complex Compound	Miller Indices			d [Å]	2θ	Intensity (%)
		h	k	l			
1	[Cr(L1) ₂ (H ₂ O) ₄] ⁺³	0	0	1	7.6940	11.492	100.0
		1	0	1	3.4523	25.785	48.3
		1	1	0	2.4519	36.620	37.2
		1	1	1	2.3397	38.443	14.1
2	[Co(L1) ₂ (H ₂ O) ₄] ⁺³	2	2	0	2.8600	31.249	40.0
		3	1	1	2.4380	36.837	100.0
		5	1	1	1.5559	59.350	35.0
		4	4	0	11.4293	65.222	45.0
3	[Ni(L1) ₂ (H ₂ O) ₂] ⁺²	1	1	0	4.7773	18.558	100.0
		1	0	1	2.4201	37.119	26.9
		1	0	4	2.0254	44.706	36.9
		1	0	7	1.5724	58.663	9.4
4	[Mn(L1) ₂ (H ₂ O) ₂] ⁺²	2	1	1	3.4037	26.160	100.0
		1	0	3	2.9359	30.421	20.8
		2	2	0	2.8850	30.972	22.1
		2	2	4	1.8266	49.883	30.9
5	[Cu(L1) ₂ (H ₂ O) ₂] ⁺²	0	2	2	2.5300	35.452	100.0
		2	0	2	2.3600	38.100	79.7
		0	0	4	2.3350	38.525	36.2
		2	2	0	2.0241	44.735	42.2

Each set of indices was chosen on the basis of highest intensity (%) of sharp peak

coordinated MBHA (L1) molecules at the two sites in a mononuclear complex.

It is noteworthy that the complexes cobalt and manganese (compound 5 and 7) were found to have cubic crystalline nature, having space group Fd-3m (223) and 141/

amd (141), whereas they have 2 and 4, Z values, respectively. The indexing related to their structure elucidation as well as peak intensities and diffraction angle (2θ) is given in the Table 3. It is illustrated that the prepared complex of nickel (compound 6) has the space group R-3m (166), Z =

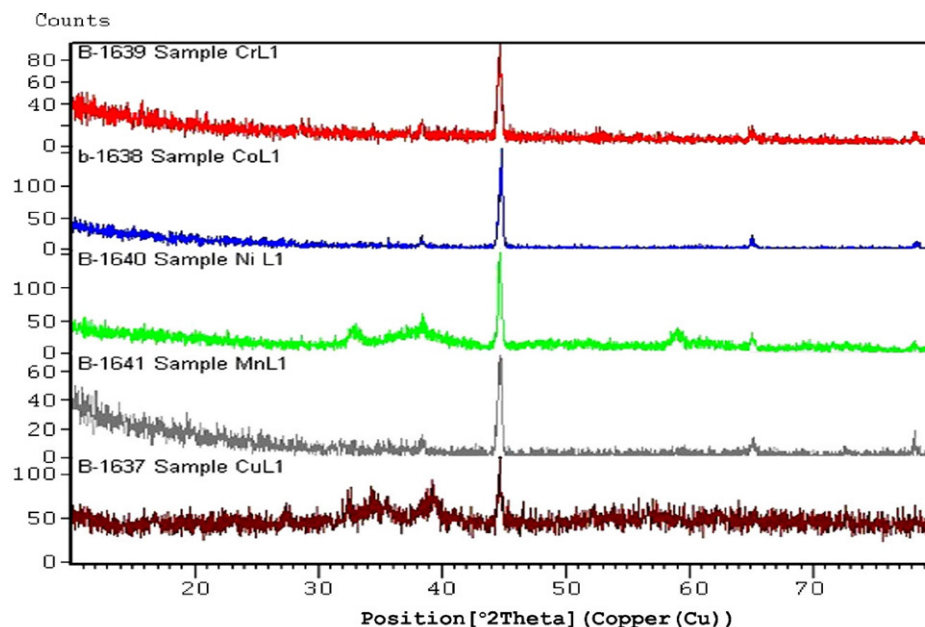


Fig. 4. X-ray diffraction patterns of complexes [M(L1)₂(H₂O)₄]⁺³ with M=Cr⁺³, Co⁺³ and [M(L1)₂(H₂O)₂]⁺² with M= Ni⁺², Mn⁺² and Cu⁺²

3 and belongs to hexagonal crystal class. While, copper metal (compound 8) coordinated with MBHA has monoclinic crystalline nature. It has the space group Cc (9) and $Z = 4$. Based on aforementioned analysis and to provide more strength in verdicts (energy balance and mass balance) the computational modeling was further performed.

3. 5. Antioxidant Activities of MBHA and Metal Complexes

These compounds (3-8) were tested to determine their efficiency for scavenging the DPPH radicals using

ascorbic acid as standard, which has a known free radical scavenging activity. The potential of MBHA and metal complexes as antioxidants has been plotted in (Fig. 5 and Fig. 6). The alcoholic MBHA and ester containing compounds are highly active against antioxidant exhibition.^{28,48} The antioxidant potential of the MBHA and its transition metal complexes along with the standard (ascorbic acid) is documented in Table 4.

The results have indicated that ascorbic acid has exhibited the highest antioxidant activity at high concentration. When the highest antioxidant exhibition percent among synthesized metal moieties was compared with

Table 4. Antioxidant activity of MBHA (compound 3) and its formed metal complexes (compound 4-8)

S. No.	Concentration (mM)	Ascorbic Acid (%)	Ligand/Complexes	Antioxidant Activity (%)
1	1.00	20	L1	56.7
2	2.00	39.4	CrL1	9.7
3	3.00	58.1	CoL1	17.1
4	4.00	76	NiL1	10.8
5	5.00	92.7	MnL1	19.7
6	6.00	96.8	CuL1	18.7

DPPH scavenging effect (%) = $(Ac - As)/Ac \times 10$, Ac = Absorbance of Control

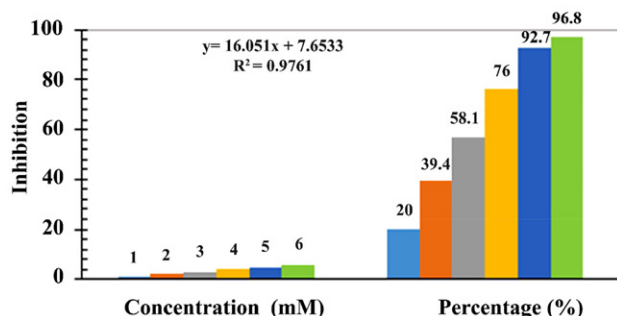


Fig. 5. Graphical representation of Antioxidant Activities of the Standard (Ascorbic Acid)

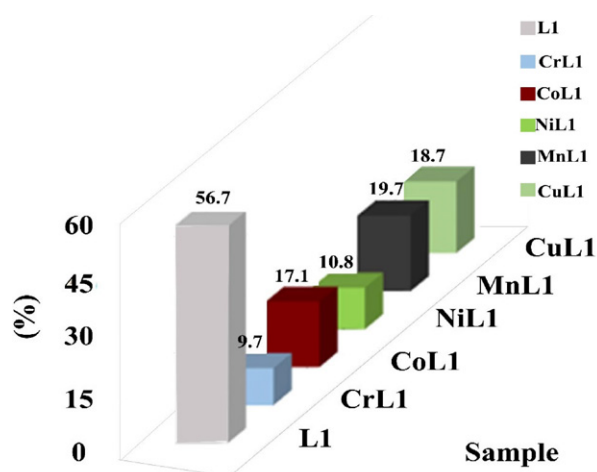


Fig. 6. Graphical representation of Antioxidant Activities of MBHA (L1) and compounds 4-8

MBHA, it was observed that MnL1 (compound 7) has the highest (19.7%) antioxidant activity. Additionally, the copper complex with MBHA has shown almost the same inhibition. However, L1 (MBHA) has comparatively maximum antioxidant activity. It is interesting to note that all these novel compounds (MBHA, $[M(L1)_2(H_2O)_4]^{+3}$ and $[M(L1)_2(H_2O)_2]^{+2}$) possess positive inhibition (Fig. 6).

3. 6. Antibacterial Assay

The antibacterial activity of these compounds was screened by using agar disc diffusion method against four

Table 5. Antibacterial activities of the MBHA and the complexes (compound 4-8)

S. No	Ligand/Complexes	<i>S.aureus</i> (%)	<i>E.coli</i> (%)	<i>B.pumilis</i> (%)	<i>S.typhi</i> (%)
1	L1	71.4	62.5	80.3	45.8
2	CrL1	A	A	40.7	A
3	CoL1	95.21	99.1	81.4	50.0
4	NiL1	44.6	45.8	40	50.0
5	MnL1	47.6	A	46.2	A
6	CuL1	52.3	A	44.4	48.0

Antimicrobial activity, expressed as inhibition zone diameter in millimeters (mm), of synthesized compounds against pathological strains based on agar well diffusion assays at 1 mg mL^{-1} . The experiment was carried out in triplicate and the average zone of inhibition was calculated.

A = Non active inhibition zone

bacterial strains (*Staphylococcus aureus*, *Escherichia coli*, *Bacillus pumilis*, *Salmonella typhi*) while Gentamycin is used as standard (Table 5).

The efficiency of compounds was categorized into three classes such as sensitive, transitional and resistant. The reported analysis is consistent with our findings that if a compound is found to be sensitive, it could be a valuable medication against bacterial disease. Though, non-active compounds are found to be as least resistant.^{26,49,50} In contrast to the ligand an enhanced antibacterial potential was observed in metal complexes. Consequently, opening new ways in the fight against antibiotic resistance. This is because of coordination (ligand to metal) which could be best explained on the basis of chelation theory.^{16,51} The comparison of antibacterial activity, shown in Fig. 7 confirms that metal complex of cobalt (compound 5) was highly active than its corresponding MBHA ligand against all bacterial strains. It is evident from the results that all metal complexes and MBHA are significantly active against *B.pumilis*, however, chromium (compound 4) complex is completely resistive against the remaining bacterial strains (*S.aureus*, *E.coli*, *S.typhi*). It is interesting to note that compound 7 (manganese complex) is found non-reactive against two bacterial strains (*E.coli* and *S.typhi*), while compound 8 (copper complex) is resistant against *E.coli* only. Thus, all remaining complexes indicate extremely positive activity against the bacterial strains.

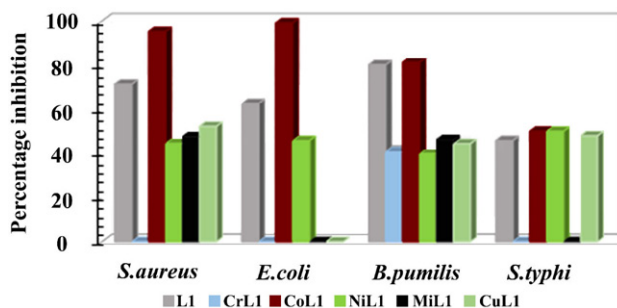


Fig. 7. A comparative histograms inhibition zone Antibacterial Assay of MBHA and compound 4-8, *S.typhi*, *E.coli* are two Gram-negative bacteria and *B.subtilis*, *S.aureus* are two Gram-positive bacteria

4. Conclusions

An aromatic MBHA Methyl 2-((4-chlorophenyl)(hydroxy)methyl) acrylate (compound 3) was prepared successfully by a well-known MBH reaction scheme and used further in synthesis of metal complexes by transition metal salts (Cr^{+3} , Co^{+3} , Ni^{+2} , Mn^{+2} , Cu^{+2}). Through modified aforementioned scheme synthesis of five novel compounds is being reported (4-8). The ligand MBHA (L1) and its corresponding complexes were characterized by carrying out their physical, analytical, spectral and computational analysis. The IR spectrum of the synthesized

ligand is optimized by using DFT B3LYP method and 6-311++ G (d,p) basis set. Whereas, five metal complexes were generated computationally by the Hartree Fock (HF) B3LYP method in conjunction with the 3-21G(d,p) basis set and we found good agreement with their observed FT-IR spectrum. These investigations have collectively suggested the molecular and structural formula. It has been found that MBHA (L1) coordinated with all the central metal ion in stoichiometric of 2:1 ligand to metal ratio. The well-defined crystalline homogeneous nature of all metal complexes was observed and confirmed through XRD powder diffraction analysis. Moreover, different crystal structures were found for each metal complex. Such as, compound 4 is orthorhombic, compound 6 is hexagonal, and compound 8 is monoclinic while compounds 5 and 7 both lie in cubic crystal class. For antibacterial assay, four pathogenic strains (*S. aureus*, *E. coli*, *B. pumilis*, *P. mirabilis*, and *S.typhi*) were examined and compared with standard antibiotic, Gentamycin. It was inferred that Cobalt complexes displayed uppermost antibacterial potential compared to MBHA (L1). Whereas, Nickel based complex showed good inhibition against all four bacterial strains. Chromium based complexes were found active against *B.pumilis* only. Both Manganese and Copper based complexes were seen inactive against *E. coli*. Manganese complex inhibition potential against *S.typhi* indicated non-active, conversely, again showed good inhibition zone against the remaining bacterial strains. Furthermore, the DPPH radical scavenging assay (antioxidant) of compounds 3-8 demonstrated the positive inhibition with context to the standard (ascorbic acid). This study can be expanded further by synthesizing some other novel MBHA ligands and their metal complexes, in order to identify the most suitable medication against infectious diseases.

Acknowledgement

The authors are thankful to University of Karachi for providing such an appreciative infrastructure and environment. We are highly gratified to PCSIR laboratories Complex-Karachi, Pakistan and NED University of Engineering and Technology for their support in bioactivity studies and XRD analysis opportunity.

Conflict of interest

All authors declare that they have no conflict of interest.

5. References

1. F. Collet, R. H. Dodd, P. Dauban, *Chem. Commun.* **2009**, Vol. 20 (34), pp. 5061–5074.
DOI:10.1039/b905820f
2. E. C. Tavares, M. M. M. Rubinger, E. V. Filho, M. R. L. Ol-

- iveira, D. Piló-Veloso, J. Ellena, S. Guilardi, R. A. C. Souza, L. Zambolim, *J. Mol. Struct.* **2016**, Vol. 1106, pp. 130–140.
DOI:10.1016/j.molstruc.2015.10.097
3. R. O. M. A. de Souza, V. L. P. Pereira, M. F. Muzitano, C. A. B. Falcão, B. Rossi-Bergmann, E. B. A. Filho, M. L. A. A. Vasconcellos, *Eur. J. Med. Chem.* **2007**, Vol. 42 (1), pp. 99–102.
DOI:10.1016/j.ejmech.2006.07.013
4. J. Du, Y. Ma, F. Meng, R. Zhang, R. Wang, H. Shi, Q. Wang, Y. Fan, H. Huang, J. Cui, et al., **2019**, pp. 9–12.
DOI:10.1021/acs.orglett.8b03709
5. T. Narendar Reddy, V. Jayathirtha Rao, *Tetrahedron Lett.* **2018**, Vol. 59 (30), pp. 2859–2875.
DOI:10.1016/j.tetlet.2018.06.023
6. M. Tsednee, Y. C. Huang, Y. R. Chen, K. C. Yeh, *Sci. Rep.* **2016**, Vol. 6 (May), pp. 1–13. DOI:10.1038/srep26785
7. V. Carrasco-Sanchez, M. J. Simirgiotis, L. S. Santos, *Molecules.* **2009**, Vol. 14 (10), pp. 3989–4021.
DOI:10.3390/molecules14103989
8. G. W. Amarante, M. Benassi, R. N. Pascoal, M. N. Eberlin, F. Coelho, *Tetrahedron.* **2010**, Vol. 66 (24), pp. 4370–4376.
DOI:10.1016/j.tet.2010.04.018
9. C. G. L. Junior, P. A. C. De Assis, F. P. L. Silva, S. C. O. Sousa, N. G. De Andrade, T. P. Barbosa, P. L. N. Neris, L. V. G. Segundo, Í. C. Anjos, G. A. U. Carvalho, et al., *Bioorg. Chem.* **2010**, Vol. 38 (6), pp. 279–284. DOI:10.1016/j.bioorg.2010.08.002
10. R. V. Pirovani, B. R. V. Ferreira, F. Coelho, *Synlett.* **2009**, (14), pp. 2333–2337. DOI:10.1055/s-0029-1217725
11. S. Rehman, M. Ikram, F. Subhan, M. Sinnokrot, W. Khan, *Open Chem.* **2019**, Vol. 17 (1), pp. 936–942.
DOI:10.1515/chem-2019-0108
12. D. C. Crans, J. J. Smee, E. Gaidamauskas, L. Yang, *Chem. Rev.* **2004**, Vol. 104 (2), pp. 849–902. DOI:10.1021/cr020607t
13. P. C. Bruijninx, P. J. Sadler, *Curr. Opin. Chem. Biol.* **2008**, Vol. 12 (2), pp. 197–206. DOI:10.1016/j.cbpa.2007.11.013
14. J. Martí-Rujas, *Dalt. Trans.* **2020**, Vol. 49 (40), pp. 13897–13916. DOI:10.1039/D0DT02802A
15. S. Y. Liu, I. D. Hills, G. C. Fu, *Organometallics.* **2002**, Vol. 21 (21), pp. 4323–4325. DOI:10.1021/om020533b
16. V. B. M. Brito, G. F. Santos, T. D. S. Silva, J. L. C. Souza, G. C. G. Militão, F. T. Martins, F. P. L. Silva, B. G. Oliveira, E. C. C. Araújo, M. L. A. A. Vasconcellos, et al., *Mol. Divers.* **2020**, Vol. 24 (1), pp. 265–281. DOI:10.1007/s11030-019-09950-7
17. J. da Câmara Rocha, K. A. da Franca Rodrigues, P. L. do Nascimento Néris, L. V. da Silva, F. S. Almeida, V. S. Lima, R. F. Peixoto, J. da Câmara Rocha, F. de L. A. A. de Azevedo, R. C. Veras, et al., *Parasitol. Res.* **2019**, Vol. 118 (10), pp. 3067–3076.
DOI:10.1007/s00436-019-06403-w
18. F. Coelho, W. P. Almeida, D. Veronese, C. R. Mateus, E. C. Silva Lopes, R. C. Rossi, G. P. C. Silveira, C. H. Pavam, *Tetrahedron.* **2002**, Vol. 58 (37), pp. 7437–7447.
DOI:10.1016/S0040-4020(02)00822-0
19. M. Saikia, J. C. Sarma, *Can. J. Chem.* **2010**, Vol. 88 (12), pp. 1271–1276. DOI:10.1139/V10-133
20. H. Y. Qian, *Acta Chim. Slov.* **2019**, Vol. 66 (4), pp. 995–1001.
DOI:10.17344/acsi.2019.5247
21. R. Gaussian, G. Trucks, H. Schlegel, G. Scuseria, M. Robb, J. Cheeseman, G. Scalmani, V. Barone, B. Mennucci, G. Petersson, et al., *Gaussian, Inc., Wallingford CT.* **2004**.
22. H. Ahmed, A. Hashim, H. M. Abduljalil, *Egypt. J. Chem.* **2019**, Vol. 62 (4), pp. 1167–1176.
DOI:10.21608/ejchem.2019.6241.1522
23. A. D. Becke, *J. Chem. Phys.* **1992**, Vol. 96 (3), pp. 2155–2160.
DOI:10.1063/1.462066
24. T. Lecklider, *EE Eval. Eng.* **2011**, Vol. 50 (11), pp. 36–39.
25. L. S. Kassel, *J. Chem. Phys.* **1936**, Vol. 4 (4), pp. 276–282.
DOI:10.1063/1.1749835
26. S. Kirbag, F. Zengin, S. Fac, F. Processing, *Antimicrob. Act. Some Euphorbia Species.* **2013**, Vol. 10 (12), pp. 305–309.
DOI:10.4314/ajtcam.v10i5.13
27. V. Alfredo Rodriguez, V. Alfredo, **2018**.
28. H. Elleuch, W. Mihoubi, M. Mihoubi, E. Ketata, A. Gargouri, F. Rezgui, *Bioorg. Chem.* **2018**, Vol. 78, pp. 24–28.
DOI:10.1016/j.bioorg.2018.03.004
29. A. L. Dawidowicz, D. Wianowska, M. Olszowy, *Food Chem.* **2012**, Vol. 131 (3), pp. 1037–1043.
DOI:10.1016/j.foodchem.2011.09.067
30. I. Gülçin, *Arch. Toxicol.* **2012**, Vol. 86 (3), pp. 345–391.
DOI:10.1007/s00204-011-0774-2
31. J. Mack, M. Shumba, *Green Chem.* **2007**, Vol. 9 (4), pp. 328–33. DOI:10.1039/B612983H
32. L. Wang, J. N. Tan, M. Ahmar, Y. Queneau, *Comptes Rendus Chim.* **2019**, Vol. 22 (9–10), pp. 615–620.
DOI:10.1016/j.crci.2019.09.002
33. D. K. Jangid, **2020**, pp. 1–17.
DOI:10.2174/2213346107666191227101538
34. K. Rad-moghadam, L. Youseftabar-miri, **2011**, Vol. 2011 (xi), pp. 43–50. DOI:10.3998/ark.5550190.0012.b04
35. M. Tsednee, Y.-C. Huang, Y.-R. Chen, K.-C. Yeh, *Sci. Rep.* **2016**, Vol. 6 (1), pp. 26785. DOI:10.1038/srep26785
36. E. B. A. Filho, I. A. Moraes, K. C. Weber, G. B. Rocha, M. L. A. A. Vasconcellos, *J. Mol. Struct.* **2012**, Vol. 1022, pp. 72–80.
DOI:10.1016/j.molstruc.2012.04.051
37. P. Marinova, M. Marinov, M. Kazakova, Y. Feodorova, A. Slavchev, D. Blazheva, D. Georgiev, P. Penchev, V. Sarafian, N. Stoyanov, *Acta Chim. Slov.* **2016**, Vol. 63 (1), pp. 26–32.
DOI:10.17344/acsi.2015.1591
38. A. Srinivas, *Acta Chim. Slov.* **2016**, Vol. 63 (1), pp. 173–179.
DOI:10.17344/acsi.2015.2124
39. B. Kavitha, M. Sravanthi, P. Saritha Reddy, *J. Mol. Struct.* **2019**, Vol. 1185, pp. 153–167.
DOI:10.1016/j.molstruc.2019.02.093
40. B. Kosar, C. Albayrak, *Spectrochim. Acta - Part A Mol. Biomol. Spectrosc.* **2011**, Vol. 78 (1), pp. 160–167.
DOI:10.1016/j.saa.2010.09.016
41. N. Sundaraganesan, S. Kalaichelvan, C. Meganathan, B. D. Joshua, J. Cornard, *Spectrochim. Acta - Part A Mol. Biomol. Spectrosc.* **2008**, Vol. 71 (3), pp. 898–906.
DOI:10.1016/j.saa.2008.02.016
42. Z. Yekke-Ghasemi, M. Ramezani, J. T. Mague, R. Takjoo, *New J. Chem.* **2020**, Vol. 44 (21), pp. 8878–8889.
DOI:10.1039/D0NJ01187H
43. D. A. Köse, H. Nəcəfoğlu, *J. Therm. Anal. Calorim.* **2008**, Vol.

- 93 (2), pp. 509–514. DOI:10.1007/s10973-007-8712-5
44. I. Kostova, I. Manolov, I. Nicolova, S. Konstantinov, M. Karaivanova, *Eur. J. Med. Chem.* **2001**, Vol. 36 (4), pp. 339–347. DOI:10.1016/S0223-5234(01)01221-1
45. T. Aiyelabola, E. Akinkunmi, I. Ojo, E. Obuotor, C. Adebajo, D. Isabirye, *Bioinorg. Chem. Appl.* **2017**, Vol. 2017. DOI:10.1155/2017/2956145
46. M. A. Asraf, M. M. Rahman, D. C. Kabiraz, R. H. Ansary, M. F. Hossen, M. F. Haque, C. M. Zakaria, *Asian J. Appl. Chem. Res.* **2019**, Vol. 3 (3), pp. 1–15. DOI:10.9734/ajacr/2019/v3i330093
47. A. Jacques, T. Auvray, R. Bevernaegie, F. Loiseau, M. Cibian, G. S. Hanan, A. Kirsch-De Mesmaeker, B. Elias, *Inorganica Chim. Acta.* **2018**, Vol. 471 (Iii), pp. 8–16. DOI:10.1016/j.ica.2017.10.018
48. P. Jeslin Kanaga Inba, B. Annaraj, S. Thalamuthu, M. A. Neelakantan, *Bioinorg. Chem. Appl.* **2013**, Vol. 2013. DOI:10.1155/2013/439848
49. B. Possato, L. F. Dalmolin, L. M. Pereira, J. Q. Alves, R. T. C. Silva, R. V. Gelamo, A. P. Yatsuda, R. F. V. Lopez, S. de Albuquerque, N. B. Leite, et al., *Eur. J. Pharm. Sci.* **2021**, Vol. 162 (April). DOI:10.1016/j.ejps.2021.105834
50. K. G. Harmon, J. R. Clugston, K. Dec, B. Hainline, S. Herring, S. F. Kane, A. P. Kontos, J. J. Leddy, M. McCrea, S. K. Poddar, et al., *Br. J. Sports Med.* **2019**, Vol. 53 (4), pp. 213–225. DOI:10.1136/bjsports-2018-100338
51. M. I. Khan, A. Khan, I. Hussain, M. A. Khan, S. Gul, M. Iqbal, Inayat-Ur-Rahman, F. Khuda, *Inorg. Chem. Commun.* **2013**, Vol. 35 (June), pp. 104–109. DOI:10.1016/j.inoche.2013.06.014

Povzetek

Naslovni ligand smo sintetizirali in očistili s kolonsko kromatografijo, pri čemer smo upoštevali pomen in različna področja uporabe sintetičnih Morita-Baylis-Hillmanovih aduktov (MBHA). Pod bazičnimi pogoji smo pripravili Cr^{+3} , Mn^{+2} , Co^{+3} , Ni^{+2} in Cu^{+2} komplekse s sintetiziranim ligandom, ga karakterizirali s spektroskopskimi metodami in preverili IR spekter z izračunanim z DFT B3LYP metodo, z 6-311++ G (d,p) naborom osnov in Hartree Fock (HF) B3LYP metodo z 3-21G(d,p) naborom osnov. Dobljene kristale smo dodatno karakterizirali z rentgensko praškovno difrakcijo. Preučevali smo tudi antibakterijske in antioksidativne lastnosti MBHA in njegovih kompleksov. Vse navedene spojine so aktivni antioksidanti. Antibakterijske študije, opravljene na *S. aureus*, *E. coli*, *B. pumilis* in *S. typhi* so pokazale odlično delovanje kobaltovega kompleksa. Tovrstne spojine imajo potencial za razvoj novih, cenejših in učinkovitih zdravil za bakterijska obolenja. Raziskava predstavlja prvi primer uporabe MBHA za tvorbo kovinskih kompleksov.



Except when otherwise noted, articles in this journal are published under the terms and conditions of the Creative Commons Attribution 4.0 International License

Scientific paper

Novel Benzimidazole-Based Compounds as Antimicrobials: Synthesis, Molecular Docking, Molecular Dynamics and *in silico* ADME Profile Studies

Elif Yeşilçayır,¹ İsmail Çelik,² Hasan Tahsin Şen,^{1,3} Suna Sibel Gürpınar,⁴ Müjde Eryılmaz,⁴ Gülgün Ayhan-Kılıçgil^{1*}

¹ Ankara University, Faculty of Pharmacy, Department of Pharmaceutical Chemistry, Ankara, Turkey

² Erciyes University, Faculty of Pharmacy, Department of Pharmaceutical Chemistry, Kayseri, Turkey

³ Lokman Hekim University, Faculty of Pharmacy, Department of Pharmaceutical Chemistry, Ankara, Turkey

⁴ Ankara University, Faculty of Pharmacy, Department of Pharmaceutical Microbiology, Ankara, Turkey

* Corresponding author: E-mail: kilcigil@pharmacy.ankara.edu.tr

Received: 12-03-2021

Abstract

Some novel benzimidazole derivatives were synthesized and their antimicrobial activities were evaluated. Compounds **3a** and **3b** exhibited excellent antibacterial activity with MIC values <4 µg/mL against *Staphylococcus aureus* ATCC 29213 (MSSA) and *Staphylococcus aureus* ATCC 43300 (MRSA). Molecular docking analyzes of compounds with MIC values of 16 µg/mL and below against gram-positive bacteria and fungi were performed using FabH (β-ketoacyl-acyl carrier protein synthase III) as bacterial protein and CYP51 (sterol 14α-demethylase) as the fungal target protein. According to the molecular docking analysis, it was calculated that sufficient protein-ligand interaction energy was liberated between the compounds **2f**, **3a**, **3b**, **3e** and **3h** and the antibacterial target protein FabH and strong interactions were formed between **2f** and **3h** and the antifungal target protein. According to RMSD, RMSF and MMPBSA measurements obtained from molecular dynamics, it is understood that compounds **3a** and **3b** maintain protein-ligand stability *in silico* physiological conditions.

Keywords: Benzimidazole, antimicrobial activity, molecular docking, molecular dynamics

1. Introduction

Microbes are disease agents that cause death. Today, the transmission of diseases to large masses has become an increasing threat to human health. Antibiotic resistance remains at dangerously high levels around the world. This situation leads to new resistance mechanisms and spreads the resistance globally, making it difficult to treat infectious diseases. Furthermore, antimicrobial resistance is recognized globally as one of the greatest health threats; thus, the discovery of alternative antibacterial agents to address antimicrobial resistance is a priority target. Effective treatment of infections and complete elimination of antimicrobial resistance can be achieved with the use of new antimicrobial compounds.

It is well known that benzimidazoles have antibacterial,¹ antimicrobial,^{2–5} and antifungal⁶ activities. Furthermore, several benzimidazoles show promising pharmacological

activities such as antioxidant,^{7–9} anticancer,¹⁰ anti-inflammatory,¹¹ antiprotozoal,¹² antiviral,¹³ antidiabetic,¹⁴ antihypertensive,¹⁵ antimycobacterial,¹⁶ and antithrombin,¹⁷ as well as tubulin¹⁸ and dipeptidyl peptidase III¹⁹ inhibitors.

In view of extending our previous studies on the synthesis and bioactivity of benzimidazole derivatives,^{20–21} we synthesized a series of 4-(1*H*-benzimidazol-2-yl)-6-arylpiperidin-2-amines. Moreover, we also evaluated their antibacterial and antifungal activities and carried out molecular docking and molecular dynamics simulation studies.

2. Experimental

2.1. Chemistry

All reagents and solvents were used as purchased, without further purification. The reactions were moni-

tored by thin-layer chromatography (TLC) analysis using silica gel plates (Kieselgel 60F254, E. Merck). Column chromatography was performed on Silica Gel 60 M (0.040–0.063 mm, E. Merck). Melting points were determined on a Büchi B540 capillary melting point apparatus and are uncorrected. The ^1H and ^{13}C NMR spectra were recorded on a Varian 400 MHz and Bruker 500 MHz FT spectrometer in $\text{DMSO}-d_6$, shift values are given in parts per million relative to tetramethylsilane as internal reference and coupling constants (J) are reported in Hertz. Mass spectra were taken on a Waters Micromass ZQ connected with Waters Alliance HPLC, using ESI+ method, with the C-18 column. Elemental analyses were performed by Leco CHNS-932 analyzer.

2. 1. 1. Synthesis of 2-(α -Hydroxyethyl) benzimidazole

o-Phenylenediamine (0.025 mol) and lactic acid (3.2 mL) were refluxed for 3 h. The reaction mixture was cooled and made alkaline with 10% aq. NaOH. The crude product obtained was dissolved in boiling water and decolorized with activated charcoal. The mixture was filtered and washed with cold water.^{22–24}

2. 1. 2. Synthesis of 2-Acetylbenzimidazole

To the solution of $\text{K}_2\text{Cr}_2\text{O}_7$ (0.15 mol) in H_2SO_4 (25%, 10 mL) was added dropwise a solution of 2-(α -hydroxyethyl)benzimidazole (0.01 mol) in 5% H_2SO_4 (5 mL) while stirring at room temperature over a period of 20 min. The reaction mixture was stirred at room temperature for 2 h. The reaction mixture was neutralized with aqueous NH_3 solution (1:1) and the precipitated solid was filtered, washed with water, dried and recrystallized from ethyl acetate.^{23,24}

2. 1. 3. Synthesis of 1-(1*H*-Benzimidazol-2-yl)-3-aryl-prop-2-en-1-ones 2a–h

2-Acetylbenzimidazole (0.01 mol) and aromatic aldehydes (0.01 mol) were mixed with ethanol (20 mL) and added 60% aq. KOH (5 mL) at 0 °C and the mixture were stirred at room temperature for 4 h. After completion of the reaction (controlling TLC, chloroform:hexane 1/3), the reaction mixture was poured into ice-cold water and neutralized with dilute HCl solution. The solid formed was filtered, washed, dried and recrystallized from ethanol.^{23,24}

(*E*)-1-(1*H*-Benzimidazol-2-yl)-3-(3-bromo-4-fluorophenyl)prop-2-en-1-one (2a)

Yield 73%; mp 214 °C. ^1H NMR (400 MHz, $\text{DM-SO}-d_6$) δ 7.3–7.5 (m, 3H, Ar-H), 7.56 (d, 1H, $J_o = 8$ Hz, Ar-H), 7.83–7.95 (m, 3H, Ar-H and $\text{CH}=\text{CH}$), 8.09 (d, 1H, $J_{trans} = 16$ Hz, $\text{CH}=\text{CH}$), 8.25–8.26 (m, 1H, Ar-H), 13.51 (s, 1H, NH); ^{13}C NMR (100 MHz, $\text{DMSO}-d_6$) δ 108.9 (d, $J =$

21.4 Hz), 112.94, 117.4 (d, $J = 22.9$ Hz), 121.7, 112.7, 123.2, 125.8, 130.3 (d, $J = 8.45$ Hz), 132.8 (d, $J = 3.11$ Hz), 134.0, 134.8, 141.6, 143.0, 148.8, 159 (d, $J = 250.05$ Hz), 180.8; MS (ESI+) m/z 345.40 (M+H), 347.39 (M+H+2). Anal. Calcd for $\text{C}_{10}\text{H}_{10}\text{BrFN}_2\text{O}$: C, 55.68; H, 2.92; N, 8.12. Found: C, 55.83; H, 3.19; N, 7.88.

(*E*)-1-(1*H*-Benzimidazol-2-yl)-3-(naphthalen-2-yl)prop-2-en-1-one (2b)

Yield 34%; mp 225 °C. ^1H NMR (500 MHz, $\text{DM-SO}-d_6$) δ 7.35–7.37 (m, 1H, Ar-H), 7.41–7.44 (m, 1H, Ar-H), 7.90 (d, 1H, $J_o = 8.15$ Hz, Ar-H), 7.98–8.06 (m, 4H, Ar-H), 8.15 (d, 1H, $J_{trans} = 16$ Hz, $\text{CH}=\text{CH}$), 8.26 (d, 1H, $J_{trans} = 16$ Hz, $\text{CH}=\text{CH}$), 8.43 (s, 1H, Ar-H), 13.52 (s, 1H, NH); ^{13}C NMR (125 MHz, $\text{DMSO}-d_6$) δ 113.39, 121.63, 122.32, 123.71, 124.76, 126.28, 127.39, 128.23, 129.24, 129.28, 131.42, 132.39, 133.45, 134.62, 135.29, 143.54, 144.80, 181.39; MS (ESI+) m/z 299.60 (M+H). Anal. Calcd for $\text{C}_{20}\text{H}_{14}\text{N}_2\text{O}$: C, 80.52; H, 4.73; N, 9.39. Found: C, 80.23; H, 4.41; N, 9.80.

(*E*)-1-(1*H*-Benzimidazol-2-yl)-3-(naphthalen-1-yl)prop-2-en-1-one (2c)

Yield 44%; mp 216 °C. ^1H NMR (500 MHz, $\text{DM-SO}-d_6$) δ 7.35–7.41 (m, 2H, Ar-H), 7.35–7.43 (m, 2H, Ar-H), 7.61–7.70 (m, 4H, Ar-H), 7.90 (d, 1H, $J = 7.6$ Hz, Ar-H), 8.04 (d, 1H, $J = 8.30$ Hz, Ar-H), 8.10 (d, 1H, $J = 8.10$ Hz, Ar-H), 8.18–8.23 (2H, Ar-H and $\text{CH}=\text{CH}$), 8.36 (d, 1H, $J = 8.45$ Hz, Ar-H), 8.82 (d, 1H, $J_{trans} = 15.85$ Hz, $\text{CH}=\text{CH}$), 13.57 (brs, 1H, NH); ^{13}C NMR (125 MHz, $\text{DM-SO}-d_6$) δ 113.41, 121.68, 123.50, 123.70, 124.57, 126.28, 126.35, 126.93, 127.91, 129.36, 131.51, 131.70, 131.83, 133.91, 135.31, 140.85, 143.57, 149.44, 181.29; MS (ESI+) m/z 299.55 (M+H). Anal. Calcd for $\text{C}_{20}\text{H}_{14}\text{N}_2\text{O}$: C, 80.52; H, 4.73; N, 9.39. Found: C, 80.33; H, 4.92; N, 9.15.

(*E*)-1-(1*H*-Benzimidazol-2-yl)-3-(4-bromophenyl)prop-2-en-1-one (2d)

Yield 80%; mp 229 °C. ^1H NMR (400 MHz, $\text{DM-SO}-d_6$) δ 4.82 and 5.46 (td, 1H, $J = 7.6$ Hz, Ar-H), 7.21–7.47 (m, 5H, Ar-H), 7.67–7.85 (m, 3H, Ar-H), 7.94 and 8.14 (d, 1H, $J_{trans} = 16$ Hz, $\text{CH}=\text{CH}$), 13.18 and 13.53 (s, 1H, NH); ^{13}C NMR (100 MHz, $\text{DMSO}-d_6$) δ 119.81, 122.27, 124.52, 129.86, 130.84, 130.86, 132.13, 133.57, 138.21, 142.87, 147.76, 148.90, 180.88, 192.09; MS (ESI+) m/z 327.51 (M+H), 329.49 (M+H+2). Anal. Calcd for $\text{C}_{16}\text{H}_{11}\text{BrN}_2\text{O}$: C, 58.74; H, 3.39; N, 8.56. Found: C, 59.07; H, 3.72; N, 8.24.

(*E*)-1-(1*H*-Benzimidazol-2-yl)-3-phenylprop-2-en-1-one (2e)

Yield 71%; mp 224 °C (lit.²³ 162–164 °C). ^1H NMR (400 MHz, $\text{DMSO}-d_6$) δ 7.36–7.38 (m, 2H, Ar-H), 7.47–7.49 (m, 3H, Ar-H), 7.70–7.89 (m, 4H, Ar-H), 7.98 (d, 1H, $J_{trans} = 16$ Hz, $\text{CH}=\text{CH}$), 8.13 (d, 1H, $J_{trans} = 16$ Hz, $\text{CH}=\text{CH}$), 13.51 (brs, 1H, NH); ^{13}C NMR (100 MHz, $\text{DM-SO}-d_6$) δ 113.41, 121.68, 123.50, 123.70, 124.57, 126.28, 126.35, 126.93, 127.91, 129.36, 131.51, 131.70, 131.83, 133.91, 135.31, 140.85, 143.57, 149.44, 181.29; MS (ESI+) m/z 299.55 (M+H). Anal. Calcd for $\text{C}_{20}\text{H}_{14}\text{N}_2\text{O}$: C, 80.52; H, 4.73; N, 9.39. Found: C, 80.33; H, 4.92; N, 9.15.

SO- d_6) δ 121.53, 128.94, 129.14, 131.11, 134.30, 144.25, 148.99, 180.96; MS (ESI+) m/z 249.47 (M+H). Anal. Calcd for C₁₆H₁₂N₂O: C, 77.40; H, 4.87; N, 11.28. Found: C, 77.65; H, 5.21; N, 10.91.

(E)-1-(1H-Benzimidazol-2-yl)-3-(2-fluorophenyl)prop-2-en-1-one (2f)

Yield 13%; mp 212 °C. ¹H NMR (400 MHz, DM-SO- d_6) δ 7.29–7.38 (m, 4H, Ar-H), 7.52–7.55 (m, 2H, Ar-H), 7.86 (d, 1H, J = 6.8 Hz, Ar-H), 7.97–8.01 (m, 2H, Ar-H and CH=CH), 8.18 (d, 1H, J_{trans} = 16.4 Hz, CH=CH), 13.52 (brs, 1H, NH); ¹³C NMR (100 MHz, DMSO- d_6) δ 113.36, 116.75 (d, J = 21.3 Hz), 121.70, 123.47 (d, J = 11.5 Hz), 123.71, 124.49 (d, J = 6.1 Hz), 125.73, 126.36, 130.66, 133.52 (d, J = 8.4 Hz), 135.29, 136.60, 143.49, 149.23, 160.66 (d, J = 250.7 Hz), 181.33 (d, J = 3.8 Hz); MS (ESI+) m/z 267.49 (M+H). Anal. Calcd for C₁₆H₁₁FN₂O: C, 72.17; H, 4.16; N, 10.52. Found: C, 71.79; H, 4.49; N, 10.86.

(E)-1-(1H-Benzimidazol-2-yl)-3-[4-(benzyloxy)phenyl]prop-2-en-1-one (2g)

Yield 45%; mp 240 °C. ¹H NMR (400 MHz, DM-SO- d_6) δ 5.2 (s, 2H, CH₂), 7.13 (d, 2H, J = 8.8 Hz, Ar-H), 7.34–7.49 (m, 7H, Ar-H), 7.6 (brs, 1H), 7.84–8.03 (m, 5H, Ar-H and CH=CH); ¹³C NMR (100 MHz, DMSO- d_6) δ 69.88, 115.73, 115.92, 119.54, 127.59, 128.24, 128.32, 128.51, 128.94, 128.95, 131.42, 132.34, 137.07, 144.69, 149.62, 161.32, 181.27; MS (ESI+) m/z 355.54 (M+H). Anal. Calcd for C₂₃H₁₈N₂O₂: C, 77.95; H, 5.12; N, 7.90. Found: C, 77.52; H, 4.79; N, 8.28.

(E)-1-(1H-Benzimidazol-2-yl)-3-(thiophen-2-yl)prop-2-en-1-one (2h)

Yield 67%; mp 224 °C. ¹H NMR (400 MHz, DM-SO- d_6) δ 7.22–7.24 (m, 1H, Ar-H), 7.31–7.42 (m, 2H, Ar-H), 7.73 (d, 1H, J = 3.6 Hz, Ar-H), 7.80 (d, 1H, J_{trans} = 15.6 Hz, CH=CH), 7.85–7.88 (m, 2H, Ar-H), 8.15 (d, 1H, J_{trans} = 16 Hz, CH=CH); ¹³C NMR (100 MHz, DMSO- d_6) δ 180.35, 148.94, 143.51, 139.69, 137.01, 135.26, 134.27, 131.17, 129.09, 126.23, 123.68, 121.62, 119.86, 113.31; MS (ESI+) m/z 255.30 (M+H). Anal. Calcd for C₁₄H₁₀N₂OS: C, 66.12; H, 3.96; N, 11.02; S, 12.61. Found: C, 65.83; H, 3.50; N, 11.45; S, 12.97.

2. 1. 4. Synthesis of 4-(1H-Benzimidazol-2-yl)-6-arylpyrimidin-2-amines 3a–h

0.81 mmol arylidene benzimidazole **2a–h** was added at 0 °C to the mixture of 1.08 mmol (103.4 mg) guanidine hydrochloride and 2.16 mmol (51.94 mg) sodium hydride in 2.7 mL DMF, stirred for 1 h at room temperature and for another 3 h at 100 °C. The reaction mixture was poured onto the crushed ice and pH adjusted to 7 with dilute HCl. The precipitate was filtered and purified by column chromatography using chloroform/methanol, 10/0.5 as the eluent.²⁵

4-(1H-Benzimidazol-2-yl)-6-(3-bromo-4-fluorophenyl)pyrimidin-2-amine (3a)

Yield 26%; mp 130 °C. ¹H NMR (500 MHz, DM-SO- d_6) δ 6.91 (brs, 2H, NH₂), 7.24–7.32 (m, 2H, Ar-H), 7.55 (td, 1H, J = 8.65 Hz, 8.60 Hz, Ar-H), 7.61 (d, 1H, J_o = 7.85 Hz, Ar-H), 7.75 (d, 1H, J_o = 7.9 Hz, Ar-H), 7.98 (s, 1H, pyrimidine H-5), 8.25–8.28 (m, 1H, Ar-H), 8.54 (dd, 1H, J_o = 6.8 Hz, J_m = 2.6 Hz, Ar-H), 13.04 (s, 1H, NH); ¹³C NMR (125 MHz, DMSO- d_6) δ 102.93, 109.10–109.27 (d, J = 21.26 Hz), 112.96, 117.56–117.73 (d, J = 22.46 Hz), 120.03, 122.77–124.29 (d, J = 190.65 Hz), 128.92–128.98 (d, J = 7.96 Hz), 132.39, 135.24–135.31–135.34 (2 \times d, J = 9.34 Hz, 3.44 Hz), 144.13, 149.85, 158.00, 158.25, 161.24, 163.00, 164.20; MS (ESI+) m/z 384.48 (M+H), 386.50 (M+H+2). Anal. Calcd for C₁₇H₁₁BrFN₅: C, 43.90; H, 2.60; N, 15.06. Found: C, 44.39; H, 2.98; N, 14.85.

4-(1H-Benzimidazol-2-yl)-6-(naphthalen-2-yl)pyrimidin-2-amine (3b)

Yield 29%; mp 231 °C. ¹H NMR (500 MHz, DM-SO- d_6) δ 6.87 (brs, 2H, NH₂), 7.25–7.33 (m, 2H, Ar-H), 7.60–7.64 (m, 3H, Ar-H), 7.77 (d, 1H, J_o = 7.9 Hz, Ar-H), 8.00–8.02 (m, 1H, Ar-H), 8.09 (d, 1H, J_o = 8.75 Hz, Ar-H), 8.15–8.17 (m, 2H, Ar-H), 8.34 (dd, J_o = 8.65 Hz, J_m = 1.75 Hz, Ar-H), 8.83 (s, 1H, pyrimidine H-5), 13.05 (s, 1H, NH); ¹³C NMR (125 MHz, DMSO- d_6) δ 103.28, 112.97, 120.01, 122.73, 124.20, 124.41, 127.15, 127.45, 127.91, 128.06, 128.81, 129.47, 133.33, 134.59, 134.64, 135.28, 144.18, 150.08, 157.68, 164.35, 165.41; MS (ESI+) m/z 338.58 (M+H). Anal. Calcd for C₂₁H₁₅N₅: C, 74.76; H, 4.48; N, 20.76. Found: C, 74.29; H, 4.75; N, 20.38.

4-(1H-Benzimidazol-2-yl)-6-(naphthalen-1-yl)pyrimidin-2-amine (3c)

Yield 26%; mp 152 °C. ¹H NMR (500 MHz, DM-SO- d_6) δ 6.91 (brs, 2H, NH₂), 7.24 (td, 1H, J = 8.15 Hz, 1.15 Hz, Ar-H), 7.30 (td, 1H, J = 8.15 Hz, 1.15 Hz, Ar-H), 7.57–7.67 (m, 5H, Ar-H), 7.71 (d, 1H, J = 8.10 Hz, Ar-H), 7.78 (dd, 1H, J = 7.05 Hz, 1.15 Hz, Ar-H), 8.04–8.09 (m, 2H, Ar-H), 8.29–8.31 (m, 1H, Ar-H); ¹³C NMR (125 MHz, DMSO- d_6) δ 107.82, 112.95, 120.07, 122.73, 124.23, 125.74, 125.90, 126.64, 127.24, 127.68, 128.92, 130.19, 130.47, 133.89, 135.27, 136.80, 144.15, 149.91, 157.11, 164.14, 168.33; MS (ESI+) m/z 338.56. Anal. Calcd for C₂₁H₁₅N₅: C, 74.76; H, 4.48; N, 20.76. Found: C, 75.11; H, 4.82; N, 20.99.

4-(1H-Benzimidazol-2-yl)-6-(4-bromophenyl)pyrimidin-2-amine (3d)

Yield 24%; mp 102 °C. ¹H NMR (500 MHz, DM-SO- d_6) δ 6.87 (brs, 2H, NH₂), 7.26–7.30 (m, 2H, Ar-H), 7.60–7.61 (m, 2H, Ar-H), 7.75 (d, 2H, J_o = 8.5 Hz, Ar-H), 7.97 (s, 1H, pyrimidine H-5), 8.15 (d, 2H, J_o = 8.5 Hz, Ar-H), 13.3 (s, 1H, NH); ¹³C NMR (125 MHz, DMSO- d_6) δ 102.88, 112.97, 120.05, 122.78, 124.25, 124.91, 129.37, 131.56, 132.29, 135.25, 136.45, 144.17, 149.93, 157.87,

164.29, 164.39, 172.49; MS (ESI+) m/z 366.51 (M+H), 368.51 (M+H+2). Anal. Calcd for $C_{17}H_{12}BrN_5$: C, 55.75; H, 3.30; N, 19.12. Found: C, 56.18; H, 3.74; N, 19.50.

4-(1H-Benzimidazol-2-yl)-6-phenylpyrimidin-2-amine (3e)

Yield 17%; mp 172 °C (lit.²⁴ 192–194 °C). ¹H NMR (500 MHz, DMSO- d_6) δ 6.95 (brs, 2H, NH₂), 7.20 (brs, 1H), 7.35–7.36 (m, 2H, Ar-H), 7.56–7.59 (m, 2H, Ar-H), 7.72–7.74 (m, 3H, Ar-H), 8.16 (s, 1H, Ar-H), 8.21–8.23 (m, 2H, Ar-H); ¹³C NMR (100 MHz, DMSO- d_6) δ 104.47, 116.18, 124.32, 127.08, 127.37, 129.34, 129.51, 131.50, 136.93, 149.23, 152.20, 156.00, 158.76, 164.12, 165.85; MS (ESI+) m/z 288.5 (M+H). Anal. Calcd for $C_{17}H_{13}N_5$: C, 71.06; H, 4.56; N, 24.37. Found: C, 69.59; H, 4.82; N, 24.80.

4-(1H-Benzimidazol-2-yl)-6-(2-fluorophenyl)pyrimidin-2-amine (3f)

Yield 15%; mp 121 °C. ¹H NMR (500 MHz, DMSO- d_6) δ 6.88 (brs, 2H, NH₂), 7.23–7.31 (m, 2H, Ar-H), 7.38–7.42 (m, 2H, Ar-H), 7.57–7.76 (m, 2H, Ar-H), 7.75 (d, 1H, $J_o = 7.95$ Hz, Ar-H), 7.87 (d, 1H, $J = 2.45$ Hz, Ar-H), 8.09 (tdd, 1H, $J = 7.9$ Hz, 7.8 Hz, 1.8 Hz, 1.75 Hz, Ar-H), 13.04 (s, 1H, NH); ¹³C NMR (125 MHz, DMSO- d_6) δ 106.85–106.93 (d, $J = 10.27$ Hz), 112.95, 116.93–117.12 (d, $J = 22.58$ Hz), 120.12, 122.74, 124.26, 125.29–125.31 (d, $J = 2.98$ Hz), 125.51–125.60 (d, $J = 10.66$ Hz), 130.87, 132.85–132.92 (d, $J = 8.77$ Hz), 135.27, 144.14, 149.80, 157.48, 160.09, 161.95–162.08 (d, $J = 16$ Hz), 164.24; MS (ESI+) m/z 306.5 (M+H). Anal. Calcd for $C_{17}H_{12}FN_5$: C, 66.88; H, 3.96; N, 22.94. Found: C, 66.39; H, 3.74; N, 23.26.

4-(1H-Benzimidazol-2-yl)-6-[4-(benzyloxy)phenyl]pyrimidin-2-amine (3g)

Yield 10%; mp 240 °C. ¹H NMR (500 MHz, DMSO- d_6) δ 5.24 (2, 2H, CH₂), 6.72 (brs, 2H, NH₂), 7.15–7.50 (m, 9H, Ar-H), 7.60 (d, 1H, $J = 7.80$ Hz, Ar-H), 7.75 (d, 1H, $J = 7.85$ Hz, Ar-H), 7.91 (s, 1H, pyrimidine H-5), 8.17 (d, 2H, $J = 8.80$ Hz, Ar-H); ¹³C NMR (125 MHz, DMSO- d_6) δ 69.87, 102.26, 112.90, 114.77, 115.47, 119.98, 122.67, 124.11, 128.26, 128.42, 128.96, 129.76, 131.37, 135.21, 137.24, 144.14, 150.17, 157.33, 161.09, 164.20, 165.04; MS (ESI+) m/z 394.7 (M+H). Anal. Calcd for $C_{24}H_{19}N_5O$: C, 73.27; H, 4.87; N, 17.80. Found: C, 73.61; H, 4.45; N, 18.09.

4-(1H-Benzimidazol-2-yl)-6-(thiophen-2-yl)pyrimidin-2-amine (3h)

Yield 13%; mp 118 °C. ¹H NMR (400 MHz, DMSO- d_6) δ 6.77 (brs, 2H, NH₂), 7.21–7.26 (m, 3H, Ar-H), 7.60 (brs, 1H, Ar-H), 7.71 (brs, 1H, Ar-H), 7.78 (dd, 1H, $J = 4$ Hz, 1.2 Hz, thiophene-H), 7.87 (s, 1H, pyrimidine H-5), 8.05 (dd, 1H, $J = 4$ Hz, 1.2 Hz, thiophene-H), 13.00 (brs, 1H, NH); ¹³C NMR (100 MHz, DMSO- d_6) δ 101.45, 112.94, 120.02, 122.74, 124.23, 128.69, 129.18, 130.86, 135.19, 143.01, 144.10, 149.89, 157.29, 160.67, 163.93; MS

(ESI+) m/z 294.47 (M+H), 296.27 (M+H+2). Anal. Calcd for $C_{15}H_{11}N_5S$: C, 61.42; H, 3.78; N, 23.87; S, 10.93. Found: C, 61.20; H, 3.39; N, 24.15; S, 10.58.

2. 2. Antimicrobial Activity Tests

In the antibacterial activity tests, *Staphylococcus aureus* ATCC 29213 (methicillin-susceptible, MSSA), *Staphylococcus aureus* ATCC 43300 (methicillin-resistant, MRSA), *Escherichia coli* ATCC 25922, and *Pseudomonas aeruginosa* ATCC 27853 were used as test bacteria. For the determination of minimum inhibitory concentration (MIC) values, the broth microdilution method was used.²⁶ Serial two-fold dilutions ranging from 512 μ g/mL to 4 μ g/mL were prepared in Mueller-Hinton Broth (Difco, Difco Laboratories, Detroit, MI, USA). The inoculums were prepared from subcultures for 24 h. The final test concentration of the bacteria was adjusted to 5×10^5 cfu/mL. The microplates were incubated at 35 °C for 18–24 h. The last well that completely inhibited visual microbial growth was noted as the MIC value (μ g/mL).

The antifungal activity of the compounds was also evaluated by the determination of the MIC values (μ g/mL). *Candida albicans* ATCC 10231 was used as the test organism. Serial two-fold dilutions ranging from 512 μ g/mL to 4 μ g/mL were prepared in RPMI 1640 broth (ICN-Flow, Aurora, OH, USA, with glutamine, without bicarbonate, and with pH indicator). The final test concentration of the fungus was 0.5 to 2.5×10^3 cfu/mL. The microplates were incubated at 35 °C for 48 h. The last well that completely inhibited visual microbial growth was noted as the MIC value (μ g/mL).²⁷

Test compounds were dissolved in dimethyl sulfoxide (DMSO; Sigma, USA) and 10% DMSO was used as the negative control. Ciprofloxacin (Sigma, USA) and gentamicin (Sigma, USA), fluconazole (Sigma, USA) were used as reference drugs.²⁸ Each experiment was performed in triplicate.

2. 3. Molecular Docking

Molecular docking studies were performed using the Maestro module of Schrödinger software 2021.2 version. Protein preparation was done with the 'Protein Preparation Wizard' module. FabH and CYP51 target proteins were prepared to add H atoms, creating disulfide bonds and removing waters and other heteroatoms. H bonds assignment for protein optimization according to sample water orientations with PROPKA pH:7.0 was performed. The protein minimization stage was performed with converging heavy atoms to RMSD:0.3 Å and OPLS4²⁸ force field. Ligand 3D minimized structures were prepared using OPLS4 force field in pH 7±2 with the 'LigPrep' module. The active site was determined according to the native ligands of target proteins, and the 20·20·20 Å³ area was created by the 'Receptor Grid Generation' module. Molecular

docking was carried out using the 'Glide XP'²⁹ module, and Molecular Mechanics Generalized Born Surface Area (MM-GBSA) dG bind (binding free energy, kcal/mol) was measured using Prime module of Schrödinger software. 2D protein-ligand interactions and 3D binding mode analysis were performed with Chimera v.1.15, and Discovery Studio Visualizer v2021.

2. 4. Molecular Dynamics

Molecular dynamics simulation was performed with Gromacs 2019.2 version (GRONingen MACHine for Chemical Simulations) to investigate the FabH-**3a** and the FabH-**3b** complex's protein-ligand stability. The **3a** and **3b** compounds structure's topology was created by the Glyco-BioChem PRODRG2 server, the topology file of the FabH enzyme was created with the GROMOS 43a1 force field^{31,32} and SCP water model. The energy of the formed protein, ligand, ion, and solvent system was minimized in 5000 steps with the steepest descent integrator algorithm. The system was balanced with 0.3 ns NVT and 0.3 ns NPT stages at 1 atm pressure and 300 K temperature according to the V-rescale³² thermostat and Parrinello-Rahman³⁴ barostat. The 100 ns molecular dynamics simulation was performed with leap-frog MD integrator. Trajectory analysis was performed with gmx scripts, the root mean square deviation (RMSD) and the root mean square fluctuation (RMSF) measurements were performed. MD trajectory analysis results were monitored with VMD-Visual Molecular Dynamics v.1.9.3, BIOVIA Discovery Studio Visualizer v.2021, and graphs were generated with GraphPad

Prism v.8.0.1. The binding free energy calculation by molecular mechanics Poisson-Boltzmann surface area (MM-PBSA) was performed between 80 and 100 ns using RashmiKumari's g_mmpbsa package.^{35–37} The average binding free energy was calculated by using the 'MmPbSa-Stat' Python script provided in g_mmpbsa.

2. 5. ADME Predictions

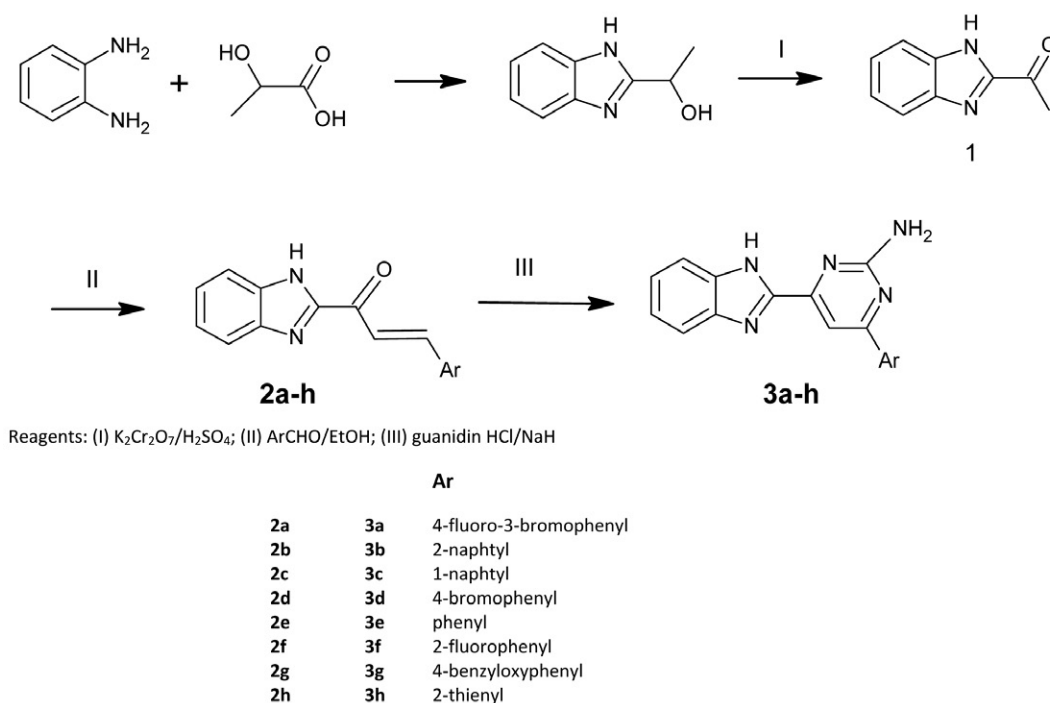
The theoretical ADME parameters of the selected compounds were calculated with the Schrödinger software 'QikProp' module. Molecular weight, QPlogPo/w, QPlogHERG, QPPCaco, QPlogBB, QPPMDCK, percentage human oral absorption, rule of five, and rule of three were calculated.

3. Results

3. 1. Chemistry

Novel 1-(1*H*-benzimidazol-2-yl)-3-aryl-prop-2-en-1-ones and 4-(1*H*-benzimidazol-2-yl)-6-arylpyrimidin-2-amine derivatives were synthesized as described in Scheme 1. 2-Acetylbenzimidazole (**1**) was prepared by condensation of *o*-phenylenediamine and lactic acid^{22–24} and followed by oxidation with potassium dichromate in the presence of sulfuric acid.^{23–24}

The arylidene derivatives **2a–h** were synthesized *via* Claisen-Schmidt condensation of 2-acetyl benzimidazole (**1**) with aromatic aldehydes in ethanol at room temperature, the reaction was catalyzed by potassium hydroxide solution.²⁵ Although two types of geometric isomers could



Scheme 1. Synthesis of compounds 2 and 3

be expected for compounds **2a–h**, only (*E*) isomers were obtained. This is demonstrated by the ^1H NMR spectra, supported by the appearance of characteristic *trans*-coupling constants belonging to the arylidene protons in the range of 15.85–16.4 Hz.

The reaction of compounds **2a–h** with guanidine hydrochloride in the presence of NaH^{25} was conducted to give the respective 4-(1*H*-benzimidazol-2-yl)-6-(aryl)pyrimidin-2-amines **3a–h**.

3. 2. Antimicrobial Activity

All the synthesized compounds **2** and **3** were evaluated for their antimicrobial activities *in vitro* against *Staphylococcus aureus* (ATCC 29213-methicillin-susceptible, MSSA, and ATCC 43300-methicillin-resistant, MRSA) as gram-positive, two gram-negative (*Escherichia coli* ATCC 25922, and *Pseudomonas aeruginosa* ATCC 27853) bacteria, and *Candida albicans* ATCC 10231 as fungus using the standard two-folds serial dilution method in 96-well micro-test plates recommended by the National Committee for Clinical and Laboratory Standards Institute.^{26,27} Minimal inhibitory concentration (MIC, $\mu\text{g}/\text{mL}$) was defined as the lowest concentration of new compounds that completely inhibited the growth of bacteria and fungus. Ciprofloxacin, gentamicin, and fluconazole were used as the reference drugs.²⁸

The antimicrobial results *in vitro* (Table 1) revealed that most of the prepared compounds could effectively inhibit the growth of some tested strains and that gram-positive bacteria are more sensitive to the tested compounds

than the gram-negative bacteria and fungus. Moreover, in most of the compounds, amino pyrimidines were observed to be more active than the arylidene counterparts.

Regarding the activity of individual compounds, it is noteworthy that bearing 4-fluoro-3-bromophenyl (**3a**) and 2-naphthyl (**3b**) as aryl group at the position 4 of pyrimidine ring are the most active analogs; they exhibited $<4 \mu\text{g}/\text{mL}$ MIC values against both *S. aureus*. **2f** (Ar = 2-fluorophenyl), **3e** (Ar = phenyl), and **3h** (Ar = thienyl) also displayed moderate to good activities against the gram-positive bacterial strains. In addition, compounds **2f** and **3h** showed moderate antifungal efficacy toward *C. albicans* with $16 \mu\text{g}/\text{mL}$ MIC values. The rest of the investigating benzimidazoles exerted either weaker activity or were totally inactive toward the tested microbial strains.

3. 3. Computational Studies

3. 3. 1. Molecular Docking Analysis

Molecular docking studies are computational methods frequently used in drug design to predict how small molecule compounds interact with target macromolecules at the atomic level.^{38–40} In this study, molecular docking analyses of compounds with MIC values of $16 \mu\text{g}/\text{mL}$ and below against gram-positive bacteria and fungi were performed. FabH (β -ketoacyl-acyl carrier protein synthase III) was preferred as the bacterial target protein and CYP51 (sterol 14 α -demethylase) was preferred as the fungal target protein. To validate the molecular docking process, the natural ligand re-docking process in the crystal structures of the target enzymes was performed. Ligand and protein

Table 1. MIC values ($\mu\text{g}/\text{mL}$) of the synthesized compounds

Compound	Gram-positive bacteria		Gram-negative bacteria		Fungus
	<i>S. aureus</i> ATCC 29213 (MSSA)	<i>S. aureus</i> ATCC 43300 (MRSA)	<i>E. coli</i> ATCC 25922	<i>P. aeruginosa</i> ATCC 27853	<i>C. albicans</i> ATCC 10231
2a	64	64	256	128	–
2b	128	128	–	–	128
2c	64	64	–	128	128
2d	64	64	–	–	–
2e	128	128	256	128	64
2f	16	16	256	256	16
2g	64	64	–	–	–
2h	128	128	256	256	128
3a	<4	<4	256	256	–
3b	<4	<4	256	256	64
3c	32	64	256	256	128
3d	64	128	–	128	128
3e	16	16	256	128	64
3f	32	64	256	256	64
3g	64	128	–	–	128
3h	16	16	256	256	16
Ciprofloxacin	<0.25	0.5	<0.25	<0.25	NT
Gentamicin	0.5	<0.25	0.5	<0.25	NT
Fluconazole	NT	NT	NT	NT	1.56

NT: Not tested “–”: represents no activity

Table 2. Glide XP molecular docking, prime binding free energy and protein-ligand interactions results performed against bacterial (FabH) and fungal (CYP51) target enzymes

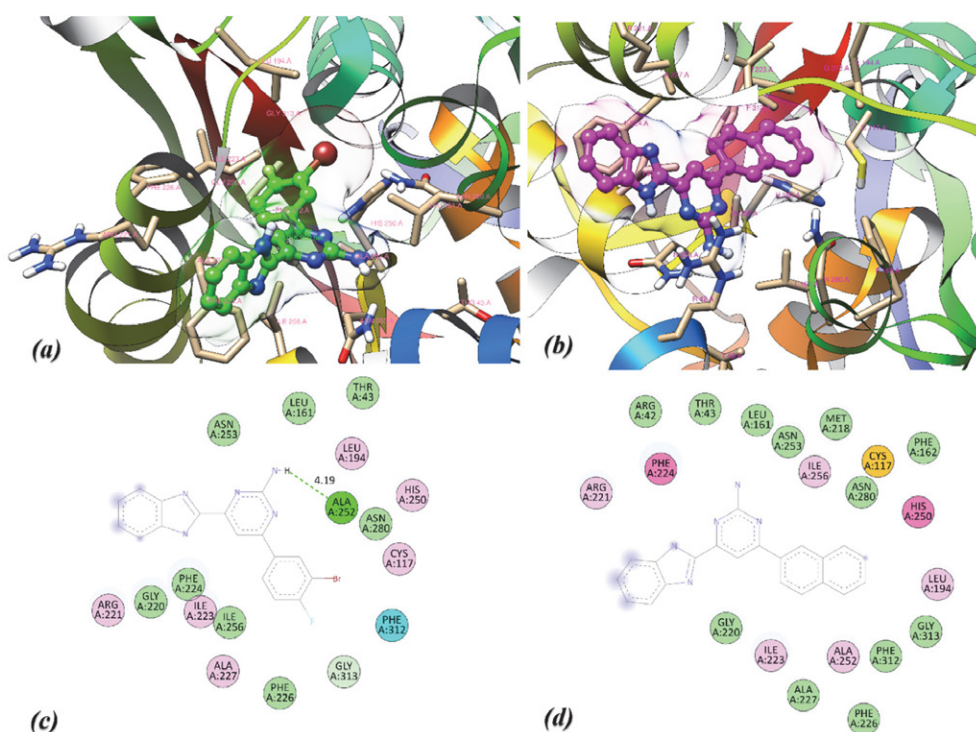
Target enzymes	Comp.	XP GScore	MMGBSA dG Bind	Protein-ligand interactions
FabH (PDB ID: 3IL5)	2f	-8.75	-60.11	Asn253 (2.50 Å), Asn280 (2.80 Å, 1.96 Å), Asn280, Phe312, Ile223, Ala227, Ala252, Ile223, Ala252
	3a	-8.50	-65.52	Ala252 (2.06 Å), Gly313, Phe312, Cys117, Leu194, His250, Arg221, Ala252, Ile223, Ala227, Ala252
	3b	-7.90	-60.64	Cys117, His250, Phe224, Arg221, Ile223, Ala252, Ile256, Leu194, Ile223, Ala252
	3e	-8.33	-56.69	Gly220 (2.51 Å), Ala252 (1.97 Å), Met218, Phe312, Ala252, Ile223, Ala227, Ala252
	3h	-7.51	-61.75	Gly220 (2.42 Å), Ala252 (2.24 Å), Ala252, Met218, Phe312, Ile223, Ile223, Ala227, Ala252
CYP51 (PDB ID: 5TZ1)	2f	-7.97	-47.97	Phe380, Phe233, Leu376, Leu376, Ile131, Hem601
	3h	-7.07	-47.94	Met508 (3.69 Å), Tyr118, Tyr118, His377, Pro230, Pro230, Met508, Leu121, Leu376, Met508, Leu376, Met508

FabH: β -ketoacyl-acyl carrier protein synthase III (PDB ID: 3IL5), CYP51: sterol 14 α -demethylase, XP Gscore (kcal/mol): Extra Precision Glide Score, MMGBSA dG Bind (kcal/mol): Molecular Mechanics Generalized Born Surface Area total binding energy.

structures were minimized using the OPLS4 force field. As given in Table 2, Glide XP binding energies were below -7 kcal/mol and MMGBSA binding free energy values were below -47 kcal/mol. Again, in Table 2, the protein-ligand interaction details of the selected compounds are explained.

The binding poses and schematic protein-ligand interactions of the two most active compounds, **3a** and **3b**, at

the FabH active site are shown in Figure 1. Compound **3a** showed H bond between -NH group of 2-aminopyrimidine structure and Ala252, hydrophobic interactions with Gly313, Phe312, Cys117, Leu194, His250, Arg221, Ala252, Ile223, and Ala227. Compound **3b**, on the other hand, formed hydrophobic interactions with Cys117, His250, Phe224, Arg221, Ile223, Ala252, Ile256, Leu194, and Ile223, although there was no H bond formation.

**Figure 1.** Visualization of the results from the Glide XP molecular docking study performed against bacterial target enzyme FabH. (a) Binding pose of compound **3a** and (b) compound **3b**, and 2D schematic protein-ligand interactions of (c) compound **3a** and (d) compound **3b**

3.3.2. Molecular Dynamics Simulations

Molecular dynamics simulations are widely used to study the stability of protein-ligand complexes obtained from molecular docking.^{37,40,41} By modeling the protein-ligand complex *in silico* physiological conditions, the variation and stability of the protein-ligand interaction can be predicted. Accordingly, the protein-ligand interaction of FabH-**3a** and FabH-**3b** complexes obtained from the Glide XP molecular docking study was investigated for the two most active compounds. 100 ns molecular dynamics simulation was performed, RMSD and RMSF trajectory analyzes were performed. RMSD is one of the most basic parameters used to analyze aberrations in protein structure. As seen in Figure 2, after the first 20 ns, just above 0.4 nm, the deviations continue to be stable at a minor level after the system stabilizes. The mean RMSD value of the FabH-**3a** and FabH-**3b** complex was measured as 0.44 nm and 0.41, respectively. RMSF is another analysis parameter that provides information on protein fluctuations and conformational changes. As seen in Figure 2, some different fluctuations occurred with the binding of **3a** and **3b** with FabH. The lower RMSF value than **3b** was measured around the Ser41 residues, where **3a** gave H-bond interaction. This H bond reduced protein mobility and made it more stable. **3b**, on the other hand, formed strong hydrophobic interactions with Phe312, significantly reducing FabH mobility.

To examine the protein-ligand interaction and binding pose during the molecular dynamics simulation of compound **3a**, its changes in the middle and at the end of the 100 ns simulation were analyzed. As shown in Figure 3, compound **3a** remained stable at the active site. The H bond and basic hydrophobic interactions between –NH of the benzimidazole core and Ser41 were preserved.

Measuring the binding free energy between protein and ligand in molecular dynamics simulations is another important approach. MMPBSA is obtained by summing the averages of Van der Waals, electrostatic, polar solvation, and solvent accessible surface area (SASA) energies. In this study, the average binding free energy of **3a** and **3b** compounds with FabH was calculated between 80 ns and

Table 3. MM-PBSA binding free energies of FabH with compounds **3a** and **3b** between 80 ns and 100 ns.

Parameters (Energy)	Enzyme-ligand complexes	
	FabH · 3a (kJ/mol)	FabH · 3b (kJ/mol)
Van der Waals	-207.305 ± 12.271	-272.200 ± 10.109
Electrostatic	3.695 ± 3.356	1.563 ± 2.200
Polar solvation	41.219 ± 13.297	45.524 ± 6.006
SASA	-18.603 ± 10.999	-20.690 ± 0.835
Binding free	-180.993 ± 15.364	-245.803 ± 10.893

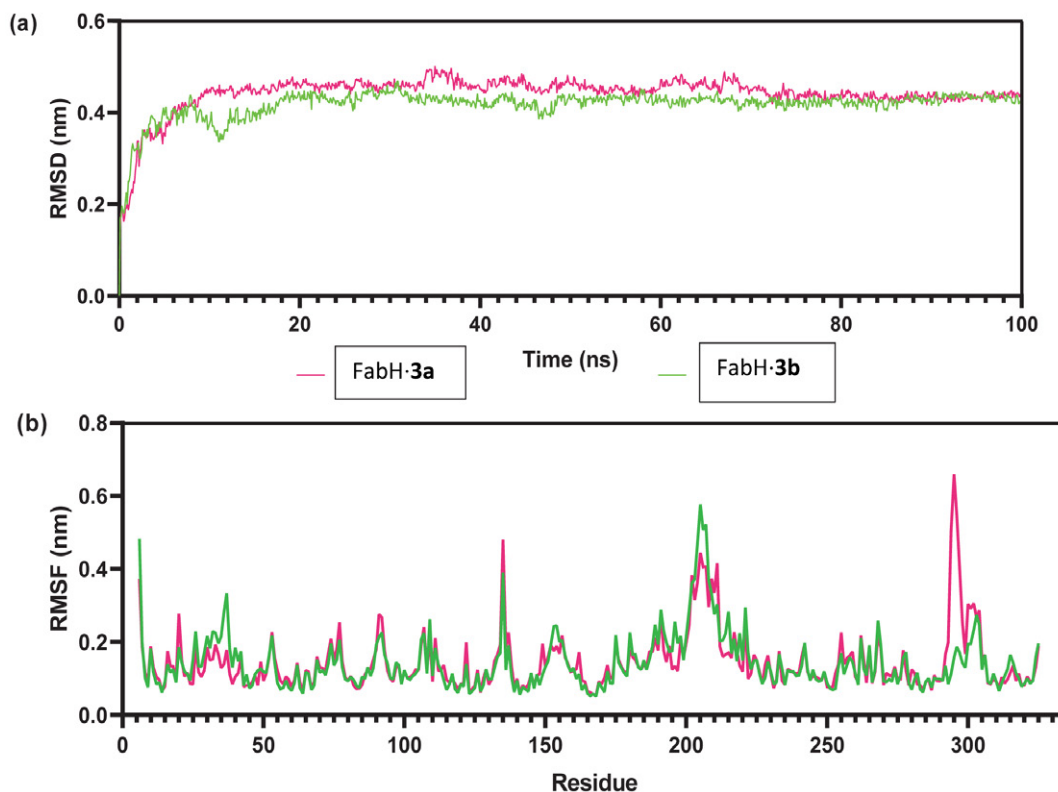


Figure 2. Molecular dynamics simulation trajectory analysis of **3a** and **3b** with FabH enzyme throughout 100 ns (a) RMSD of ligand-bound FabH-**3a** (magenta) and FabH-**3b** (green), (b) RMS fluctuation values during the period of simulation

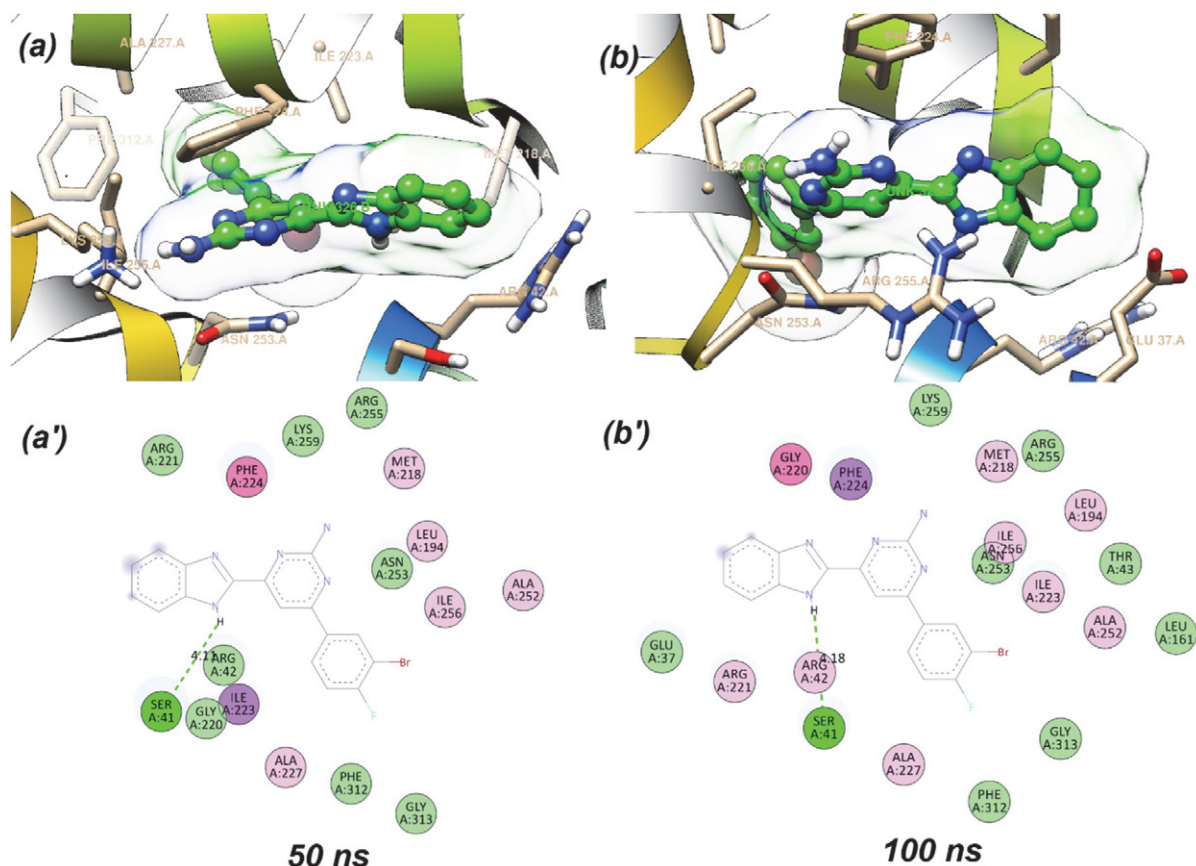


Figure 3. Binding pose and protein-ligand schematic interactions of compound **3a** in the FabH active site (a, a') in the middle (50 ns), (b, b') and at the end (100 ns) of the molecular dynamics simulations.

100 ns. The average of -180.993 kJ/mol and -245.883 kJ/mol binding free energy was found between **3a** and **3b** compounds and FabH, respectively. Interactions energy details are given in Table 3.

3. 3. 3. ADME Estimations

Drug discovery is a long, expensive and risky process that includes drug candidate identification, candidate validation, pharmacokinetics, and preclinical toxicity assessment studies. *In silico*, drug discovery technology plays an important role in the pharmaceutical industry. One of these technologies is *in silico* ADME prediction. ADME parameters, together with the drug discovery process, contribute to the selection of the therapeutic dose and identification of molecules with the optimal safety profile. Early prediction of ADME parameters has been shown to significantly reduce the pharmacokinetics failure rate at clinical stages during the discovery phase and avoid wasting time and resources in the discovery of drug molecules.⁴³ ROF value Lipinski's rule of five, also known as Pfizer's five rules or only the five rules (ROF), is a rule of thumb for assessing drug similarity or determining whether a chemical compound with a particular pharmacological or bio-

logical activity has favorable chemical and physical properties. According to this rule, the ligand molecule should have no more than 5 hydrogen bond donors, no more than 500 molecular weight, no more than 5 log *P*, and no more than 10 N and O atoms.⁴⁴ ROT value should be greater than the estimated aqueous solubility (log*S*) -5.7 , predicted apparent Caco-2 cell permeability (PCaco) greater than 22 nm/s, and primary metabolites (PM) less than 7 according to Jorgensen's rule of three. The QPlogPo/w value is the estimated octanol/water coefficient and should be in the range of -2.0 to 6.5 . QPlogHERG is the estimated IC₅₀ for blocking HERG K⁺ channels below -5 is of concern. QPPCaco Estimated apparent Caco-2 cell permeability in nm/second Caco-2 cells are a model for the intestinal blood barrier. QikProp estimates are for inactive transport. Values below 25 are weak, above 500 are great. QPlogBB is the estimated brain/blood partition coefficient and should has a value between -3.0 and 1.2 . QPPMDCK Estimated apparent MDCK cell permeability in nm/s. MDCK cells are considered a good mimic of the blood-brain barrier. QikProp estimates are for inactive transport. Percent Human Oral Absorption (PHOA) is estimated human oral absorption on a scale of 0% to 100%. Values above 80% are great, below 20% are weak. For this pur-

Table 4. ADME parameters data of selected compounds

Compounds	MW	QPlogPo/w	QPlogHERG	QPPCaco	QPlogBB	QPPMDCK	PHOA	ROF	ROT
2f	266.2	3.287	-6.0	1483.2	-0.411	1226.717	100.0	0	0
3a	384.2	3.507	-6.2	652.5	-0.531	1330.029	100.0	0	0
3b	337.3	3.677	-7.0	639.4	-0.845	305.129	100.0	0	0
3e	287.3	2.752	-6.4	643.1	-0.780	307.012	93.3	0	0
3h	293.3	2.672	-6.0	637.6	-0.599	529.965	92.7	0	0

pose, some important physicochemical properties, and descriptors of **2f**, **3a**, **3b**, **3e**, and **3h** were calculated theoretically using Schrödinger Maestro's QikProp module and are presented in Table 4. According to Lipinski's five rules and Jorgensen's three rules in these calculations, drug candidates should not have more than one violation in their ADME profile. All compounds in the table appear to comply with these rules.

These results increase the possibility that the compounds are potential drug molecules, given the promising antimicrobial activity results.

4. Conclusion

Results from molecular docking and molecular dynamics simulation studies show that active compounds **3a** and **3b** form strong interactions at the FabH active site. According to the molecular docking analysis, it was calculated that sufficient protein-ligand interaction energy was formed between the compounds **2f**, **3a**, **3b**, **3e**, and **3h** and the antibacterial target protein FabH, and strong interactions were formed between the compounds **2f** and **3h** and the antifungal target protein. It is understood that compounds **3a** and **3b** with MIC values below 4 µg/mL maintain protein-ligand stability *in silico* physiological conditions, according to RMSD, RMSE, and MMPBSA measurements obtained from molecular dynamics.

Conflicts of Interests

The authors declare that there are no conflicts of interests.

Acknowledgement

The authors thank to Ankara University-Scientific Research Unit supplying the Schrödinger software program purchased under grant project number BAP-21B0237004.

All molecular dynamics simulations reported were performed utilizing TÜBİTAK (The Scientific and Technological Research Council of Turkey), ULAKBİM (The Turkish Academic Network and Information Center), and the High Performance and Grid Computing Center (TRUBA resources).

5. References

- R. Srivastava, S. K. Gupta, F. Naaz, A. Singh, V. K. Singh, R. Verma, N. Singh, R. K. Singh, *Comput. Biol. Chem.* **2018**, *76*, 1–16. DOI:10.1016/j.compbiolchem.2018.05.021
- M. Abdel-Motaal, K. Almohawes, M. A. Tantawy, *Bioorg. Chem.* **2020**, *101*, 103972. DOI:10.1016/j.bioorg.2020.103972
- S. Malasala, N. Ahmad, R. Akunuri, M. Shukla, G. Kaul, A. Dasgupta, Y. V. Madhavi, S. Chopra, S. Nanduri, *Eur. J. Med. Chem.* **2021**, *212*, 112996. DOI:10.1016/j.ejmech.2020.112996
- E. M. E. Dokla, N. S. Abutaleb, S. N. Milik, D. Li, K. El-Baz, M. W. Shalaby, R. Al-Karaki, M. Nasr, C. D. Klein, K. A. M. Abouzid, M. N. Seleem, *Eur. J. Med. Chem.* **2020**, *186*, 111850. DOI:10.1016/j.ejmech.2019.111850
- H. Chaurasia, V. K. Singh, R. Mishra, A. K. Yadav, N. K. Ram, P. Singh, R. K. Singh, *Bioorg. Chem.* **2021**, *115*, 105227. DOI:10.1016/j.bioorg.2021.105227
- C. Sun, S. Zhang, P. Qian, Y. Li, H. Deng, W. Ren, L. Jiang, *Bioorg. Med. Chem. Lett.* **2021**, *47*, 128210. DOI:10.1016/j.bmcl.2021.128210
- I. Kerimov, G. Ayhan-Kilcigil, E. D. Ozdamar, B. Can-Eke, T. Coban, S. Ozbey, C. Kazak, *Arch. Pharm.* **2012**, *345*(7), 549–556. DOI:10.1002/ardp.201100440
- A. S. Alp, G. Kilcigil, E. D. Özdamar, T. Çoban, B. Eke, *Turk. J. Chem.* **2015**, *39*(1), 42–53. DOI:10.3906/kim-1403-44
- G. Ayhan-Kilcigil, C. Kus, T. Coban, E. D. Ozdamar, B. Can-Eke, *Arch. Pharm.* **2014**, *347*(4), 276–282. DOI:10.1002/ardp.201300324
- R. Sireesha, R. Sreenivasulu, C. Chandrasekhar, S. S. Jadav, Y. Pavani, M. V. B. Rao, M. Subbarao, *J. Mol. Struct.* **2021**, *1226*, Part B, 129351. DOI:10.1016/j.molstruc.2020.129351
- M. T. E. Maghraby, O. M. F. Abou-Ghadir, S. G. Abdel-Moty, A. Y. Ali, O. I. A. Salem, *Bioorg. Med. Chem.* **2020**, *28*(7), 115403. DOI:10.1016/j.bmc.2020.115403
- F. Doganc, I. Celik, G. Eren, M. Kaiser, R. Brun, H. Goker, *Eur. J. Med. Chem.* **2021**, *221*, 113545. DOI:10.1016/j.ejmech.2021.113545
- M. Bessières, E. Plebanek, P. Chatterjee, P. Shrivastava-Ranjan, M. Flint, C. F. Spiropoulou, D. Warszycki, A. J. Bojarski, V. Roy, L. A. Agrofoglio, *Eur. J. Med. Chem.* **2021**, *214*, 113211. DOI:10.1016/j.ejmech.2021.113211
- S. Hussain, M. Taha, F. Rahim, S. Hayat, K. Zaman, N. Iqbal, M. Selvaraj, M. Sajid, M. A. Bangesh, F. Khan, K. M. Khan, N. Uddin, S. A. A. Shah, M. Ali, *J. Mol. Struct.* **2021**, *1232*, 130029. DOI:10.1016/j.molstruc.2021.130029
- Z. Wu, M. B. Xia, D. Bertsetseg, Y. H. Wang, X. L. Bao, W. B.

- Zhu, T. Xu, P. R. Chen, H. S. Tang, Y. J. Yan, Z.-L. Chen, *Bioorg. Chem.* **2020**, *101*, 104042. DOI:10.1016/j.bioorg.2020.104042
16. M. M. Sirim, V. S. Krishna, D. Sriram, O. Unsal Tan, *Eur. J. Med. Chem.* **2020**, *188*, 112010. DOI:10.1016/j.ejmech.2019.112010
17. T. Zhang, Q. Liu, Y. Ren, *Tetrahedron* **2020**, *76*(13), 131027. DOI:10.1016/j.tet.2020.131027
18. S. Sana, V. G. Reddy, T. S. Reddy, R. Tokala, R. Kumar, S. K. Bhargava, N. Shankaraiah, *Bioorg. Chem.* **2021**, *110*, 104765. DOI:10.1016/j.bioorg.2021.104765
19. V. Rastija, D. Agić, S. Tomić, S. Nikolić, M. Hranjec, G. Karminski-Zamola, M. Abramić, *Acta Chim. Slov.* **2015**, *62*, 867–878. DOI:10.17344/acsi.2015.1605
20. I. Celik, G. Ayhan-Kilcigil, B. Guven, Z. Kara, S. Gurkan-Alp, A. Karayel, A. Onay-Besikci, *Eur. J. Med. Chem.* **2019**, *173*, 240–249. DOI:10.1016/j.ejmech.2019.04.012
21. C. Kus, G. Ayhan-Kilcigil, S. Ozbey, F. B. Kaynak, M. Kaya, T. Coban, B. Can-Eke, B, *Bioorg. Med. Chem.* **2008**, *16*(8), 4294–4303. DOI:10.1016/j.bmc.2008.02.077
22. M. Chandran, *J. Pharm. Res.* **2012**, *5*(1), 324–326.
23. R. R. Kunduru, M. R. Vanga, S. Boche, *Int. J. Pharm. Sci. Invent.* **2014**, *3*(6), 27–31.
24. R. R. Kunduru, M. R. Vanga, S. Boche, *Int. J. Pharm. Sci. Drug. Res.* **2014**, *6*(4), 278–282.
25. H. B. Liu, W. W. Gao, V. K. R. Tanganchu, C. H. Zhou, R. X. Geng, *Eur. J. Med. Chem.* **2018**, *143*, 66–84. DOI:10.1016/j.ejmech.2017.11.027
26. Clinical and Laboratory Standards Institute (CLSI). **2009**, Methods for dilution antimicrobial susceptibility tests for bacteria that grow aerobically. Approved standard. In: CLSI Publication M07-A8, 8th ed. Wayne, PA, USA.
27. Clinical and Laboratory Standards Institute (CLSI). **2008**, Reference method for broth dilution antifungal susceptibility testing of yeasts; approved standard. M27-A3, vol 29, 3rd ed., Wayne: PA, USA.
28. European Committee on Antimicrobial Susceptibility Testing. Breakpoint tables for interpretation of MICs and zone diameters. Version 3.1., valid from 2013-02-11.
29. E. Harder, W. Damm, J. Maple, C. Wu, M. Reboul, J. Y. Xiang, R. A. Friesner, *J. Chem. Theory Comput.* **2016**, *12*(1), 281–296. DOI:10.1021/acs.jctc.5b00864
30. E. P. Glide, *J. Med. Chem.* **2006**, *4*, 6177–6196.
31. M. J. Abraham, T. Murtola, R. Schulz, S. Páll, J. C. Smith, B. Hess, E. Lindahl, “GROMACS: High performance molecular simulations through multi-level parallelism from laptops to supercomputers,” *SoftwareX*, **2015**, *1–2*, 19–25. DOI:10.1016/j.softx.2015.06.001
32. C. Oostenbrink, A. Villa, A. E. Mark, W. F. Van Gunsteren, *J. Comput. Chem.* **2004**, *25*(13), 1656–1676. DOI:10.1002/jcc.20090
33. G. Bussi, D. Donadio, M. Parrinello, *J. Chem. Phys.* **2007**, *126*(1), 014101. DOI:10.1063/1.2408420
34. M. Parrinello, A. Rahman, *J. Appl. Phys.* **1981**, *52*(1), 7182–7190. DOI:10.1063/1.328693
35. R. Kumari, R. Kumar, Open Source Drug Discovery Consortium, A. Lynn, *J. Chem. Inf. Model.* **2014**, *54*(7), 1951–1962. DOI:10.1021/ci500020m
36. N. A. Baker, D. Sept, S. Joseph, M. J. Holst, J. A. McCammon, *Proc. Natl. Acad. Sci.* **2001**, *98*(18), 10037–10041. DOI:10.1073/pnas.181342398
37. N. Homeyer, H. Gohlke, *Mol. Inform.* **2012**, *31*(2), 114–122. DOI:10.1002/minf.201100135
38. H. Ahmad, F. Ahmad, S. Parveen, S. Ahmad, S. S. Azam, A. Hassan, *Bioorg. Chem.* **2020**, *105*, 104426. DOI:10.1016/j.bioorg.2020.104426
39. Y. Huang, H. Hu, R. Yan, L. Lin, M. Song, X. Yao, *Arch. Pharm.* **2021**, *354*(2), 2000165. DOI:10.1002/ardp.202000165
40. I. Celik, A. Onay-Besikci, G. Ayhan-Kilcigil, *J. Biomol. Struct. Dyn.* **2020**, *39*(15), 5792–5798. DOI:10.1080/07391102.2020.1792993
41. K. N. Venugopala, M. Kandeel, M. Pillay, P. K. Deb, H. H. Abdallah, M. F. Mahomoodally, D. Chopra, *Antibiotics* **2020**, *9*(9), 559. DOI:10.3390/antibiotics9090559
42. I. Celik, M. Erol, Z. Duzgun, *Mol. Divers.* **2021**, 1–14. DOI:10.1007/s11030-021-10215-5
43. L. L. Ferreira, A. D. Andricopulo, *Drug Discov. Today* **2019**, *24*(5), 1157–1165. DOI:10.1016/j.drudis.2019.03.015
44. İ. Şahin, M. Çeşme, F. B. Özgeriş, F. Güngör, F. Tümer, *J. Mol. Struct.* **2022**, *1247*, 131344. DOI:10.1016/j.molstruc.2021.131344

Povzetek

Sintetizirali smo serijo novih derivatov benzimidazola ter določili njihove antimikrobne aktivnosti. Spojini **3a** in **3b** sta proti *Staphylococcus aureus* ATCC 29213 (MSSA) in *Staphylococcus aureus* ATCC 43300 (MRSA) pokazali odlično antibakterijsko aktivnost z MIC vrednostjo <4 µg/mL. Molekulsko sidranje spojin, ki so se proti gram-pozitivnim bakterijam in glivam izkazale z MIC vrednostmi 16 µg/mL in manj, smo izvedli z uporabo bakterijskega proteina FabH (β-ketoacil-acil protein sintaza III) oz. CYP51 (sterol 14α-demetilaza), ki je protein glive. Glede na rezultate molekulskega sidranja, smo ugotovili, da se pri interakciji proteina z ligandom sprosti dovolj energije v primerih, ko spojine **2f**, **3a**, **3b**, **3e** in **3h** interagirajo z antibakterijskim tarčnim proteinom FabH; močne so tudi interakcije v primeru, ko spojini **2f** in **3h** interagirata s tarčnim proteinom v primeru glive. Skladno z RMSD, RMSF in MMPBSA rezultati, dobljenimi z molekulskega dinamiko, izgleda, da spojini **3a** and **3b** ohranjata stabilno interakcijo proteina in liganda pod *in silico* fiziološkimi pogoji.



Except when otherwise noted, articles in this journal are published under the terms and conditions of the Creative Commons Attribution 4.0 International License

Scientific paper

Effects of Extraction Period on Bioactive Compounds Extracted from *Olea Europaea* (var. Domat) Leaves by Ultrasound-Assisted Extraction

Dua Danjoli-Hashani^{1,2,*} and Şebnem Selen-Işbilir²¹ Heimerer College, Health Sciences of Diagnostic Profile: Laboratory Technician, 10000, Pristina, Kosovo² Trakya University, Faculty of Science, Department of Chemistry, 22030, Edirne, Turkey

* Corresponding author: E-mail: dua_danjolli@hotmail.com

Phone: +383 49 850662

Received: 12-22-2021

Abstract

In this study, polyphenols from olive leaves (Domat var.) were compared by shaking water bath and ultrasound-assisted extraction to compare the polyphenol contents and antioxidant activity in olive leaves. The effects of the extraction time on the antioxidant activity of olive leaves will be analyzed depending not only on the extraction method but also on the extraction time, due to the extraction yield, antioxidant activity, as well as the type of polyphenols recovered.

Objective: To obtain high antioxidant results and to determine the phenolic compounds contained in olive leaf (Domat var.) by LC-MS/MS after ultrasonic water bath and shaking water bath extraction comparison in a shorter time instead of 2 h.

Conclusions: The phenolic compounds contained in olive leaf by ultrasound-assisted extraction were higher than water bath extraction. We said that there is no significant difference between the extraction time and TPC and TFC. There was also no relationship between extraction time and DPPH and ABTS EC50 values ($p < 0.05$), which means that 15 min of sonication can be performed instead of 120 min.

Keywords: Ultrasound-assisted extraction; Domat olive tree leaves; antioxidant activity; phenolic compounds; LC-MS/MS

1. Introduction

Antioxidants are endogenous or exogenous substances that protect metabolism against the harmful effects of free radicals. They are also used in the food industry, cosmetics, and pharmaceutical industries to prevent lipid peroxidation. In these sectors, it is preferred to use natural antioxidants found in herbal sources instead of the synthetic antioxidants. The antioxidant properties of plants are due to their contents phytochemicals, especially polyphenolic compounds, carotenoids, and ascorbic acid. Polyphenolic compounds including mainly phenolic acids, flavanones, flavones, anthocyanins, isoflavones, tannins which are the secondary metabolites of plants. It is known that olive tree (*Olea europaea* L.) leaf, which is rich in phenolic compounds,¹⁻³ has antioxidant properties⁴ as well as antimicrobial,⁵⁻⁶ antihypertensive⁷⁻⁸ and cholesterol-lowering⁹ properties. The positive effects and antioxidant properties of olive tree leaf on health are related to its phenolic components such as oleuropein, verbascoside, rutin, hydroxytyrosol, luteolin-7-glucoside, and tyrosol.

Besides there are studies on the pharmacological effects of oleuropein, which is the major phenolic component of olive tree leaf.¹⁰⁻¹¹

Olive tree is an economically important tree, especially in Mediterranean countries. Although the minor part of leaves is traditionally drunk as tea, the others are by-product of table olive and olive oil industries, or natural waste as fallen leaf. Therefore, the phenolic-rich extract could be obtained from olive leaves, and this extract can be evaluated in food additive as antioxidant, functional food production or drug candidate search studies because of their rich bioactive components and inexpensiveness. There is an increasing effort of some industries to obtain bioactive compounds from natural products through extraction and purification for food additive manufacturing.¹²⁻¹⁴ The first and most important step in obtaining the phytochemicals of natural products such as plant leaves is an efficient extraction process. Especially oleuropein is extracted from olive leaves, fruits, and olive seeds.¹⁵ To extraction of phenolic compounds from plants the organic solvents are used most and, the extraction procedures are

divided into two groups as traditional and modern methods. Traditional methods such as maceration, percolation, infusion and soxhlet extraction are inexpensive, but have very solvent-used, longer extraction time. Recently, modern techniques such as supercritical fluid extraction, microwave-assisted extraction (MAE), ultrasound-assisted extraction (UAE) are replacing these traditional methods.^{16–17} These alternative techniques are green extraction processes, and both reduce the use of solvents and speed up the extraction procedure.

Polyphenolic compounds are secondary metabolites of plants with various biological effects¹⁸. Due to the variety and structural differences of phenolic compounds, it is difficult to develop an optimum extraction procedure. In recent years, techniques such as UAE, MAE, supercritical and accelerated extraction have been used to obtain biologically active extracts from plants^{19–20}. These techniques have specific benefits such as environmental friendliness, cost, and time savings. In addition, the fact that some of them offer high temperature or high-pressure operation which significantly shortens the extraction time.^{21–22} In recent years, studies on ultrasonic applications have been increasing due to its use in food processing and preservation.²³ The efficiency of ultrasound-assisted extraction is that it allows the intracellular material to pass into the solvent by disrupting the plant cell wall.

Various parameters such as extraction method, time, temperature, solvent type and solvent-sample ratio affect the yield of the bioactive compounds obtained. Since olive tree leaf is known to be effective as antioxidants,⁴ it was used as a model in this study. In the study, the olive tree (*Olea europaea* L.) leaves belong to Domat variety were extracted both by shaking in a water bath, which is a traditional extraction method, and ultrasound-assisted extraction method at the same conditions as a modern extraction method. Domat variety originates from Akhisar district of Manisa province (Turkey) and, has large fruits. It is the best green olive variety grown in Turkey. Firstly the two extraction methods were compared in terms of antioxidant activity and polyphenolic compounds content. In the other part of study the UAE conditions were constant, namely, extraction solvent, temperature and solid-solvent ratio, and the ultrasound treatment was performed in intervals 15 min, 30 min, 60 min and 120 min. Although there are few studies about the UAE of polyphenols from other varieties of olive leaves (Serrana variety from Spain and Tavsan Yuregi variety from Turkey),^{24–25} this is the first report on time effect in UAE for antioxidant compound recovery from Domat variety of olive leaves.

2. Experimental

2.1. Materials

All the reagents and solvents used in the experiments were of analytical grade. Olive tree leaf which is Domat

variety (2019 November) was obtained from Olive Research Institute in Izmir-Turkey. Olive tree leaves were dried at room conditions in airy environment without direct sunlight and then ground in a Waring blender.

2.2. Extraction Procedure

In the extraction with shaking water bath (WBE), samples are shaken with a 75% (v/v) ethanol solvent at 30 °C and 125 rpm with a sample:solvent ratio of 1:10 (w/v) during 2 h. Ultrasound-assisted extraction (UAE) was carried out in an ultrasonic bath (Daihan WiseClean, Korea, 230 V, 296 Watt and 50 Hz) at 30 °C for 2 h with 75% (v/v) ethanol solvent at a sample:solvent ratio of 1:10 (w/v). In the second part of the study, samples were sonicated for 15, 30, 60 and 120 min under the same conditions. After the extraction procedures, the samples were filtered through filter paper and their solvents were evaporated at 35 °C in the evaporator. The obtained crude extracts were used in all experiments.

2.3. Determination of Total Phenolic Content

The determination of total phenolic content was performed according to the method of Singleton and Rossi²⁶ using Folin-Ciocalteu reagent (FCR). Gallic acid solutions in the concentration range of 50–500 µg / mL were used as the standard phenolic substance. The total phenolic content of the samples was calculated using the equation ($y = 0.0011x - 0.0372$, $R^2 = 0.996$) obtained from the concentration-absorbance graph.

2.4. Determination of Total Flavonoid Content

It was determined according to Zhishen, Mengcheng and Jianming.²⁷ Rutin solution was used as standard flavonoid in the concentration range of 25–200 µg / mL. Total flavonoid contents of the samples were calculated from the equation of the standard graph ($y = 0.0012 + 0.0206$, $R^2 = 0.9996$).

2.5. DPPH Radical Scavenging Assay

The free radical scavenging capacity of the samples was determined using the DPPH radical scavenging method. According to the method of Blois,²⁸ 0.1 mM DPPH solution was added to the sample or standard solutions (BHA, butylatedhydroxy anisole) which were prepared at different concentrations (100–1000 µg / mL). The samples were kept in the dark for 30 min at room conditions, and absorbances at 517 nm were measured. The control was prepared using ethanol or water instead of the sample. Free radical scavenging efficiencies of the standards and samples were calculated as % inhibition using Equation 2.1. A_{control} is the absorbance of the con-

trol tube and A_{sample} is the absorbance of the sample or standard compound.

$$\% I = [(A_{\text{Control}} - A_{\text{Sample}}) / A_{\text{Control}}] \times 100 \quad (1)$$

2. 6. ABTS Cationic Radical Scavenging

Assay

In the ABTS radical scavenging method, ABTS solution and sodium persulphate solution were mixed at a ratio of 1: 0.5 and kept for 16 h and then ABTS radical ($\text{ABTS}^{\bullet+}$) was formed. The absorbance of the prepared solution was used after diluting with ethanol to give an absorbance of 0.70 at 734 nm. The samples (100–1000 $\mu\text{g}/\text{mL}$) to which ABTS radical solution was added were kept in the dark for 30 min and their absorbance were measured at 734 nm.²⁹ Radical scavenging capacities were calculated using the formula in Equation 2.1.

Free radical scavenging results of olive leaf extracts were given as EC50 value. EC50 (effective concentration) value is defined as the amount of extract required to remove half of the radical in the environment and is calculated by plotting inhibition (%) against extract concentrations graph. The EC50 value is the most used parameter to evaluate antioxidant activity.

2. 7. Identification of Phenolic Content with LC-MS/MS

LC-MS/MS analysis was used for identification of phenolic compounds quantitatively. Phenolic content of olive leaf extracts was compared to standard thirty-three organic compounds. The chromatographic separation was performed on a C8 (150 mm \times 3 mm, 3.5 μm) reversed phase analytical column (Agilent Zorbax SB-C8). The mobile phase A consisted of 5 mM ammonium acetate and ultrapure water. The mobile phase B consisted of 5 mM acetonitrile: methanol (1:1, v/v) and 0.1 % acetic acid. The injection volume of sample was 5 μL . It was runned at 0.7 mL/min flow. For the mass spectrometry analysis, it was carried out using the Agilent Technologies 6460 Triple Quad LC/MS system. The ionizations were detected by ESI. The other parameters were ion spray (IS) voltage 3500 V; 10 L/min for nebulizing gas flow; nitrogen as nebulizer gas and source temperature 375 $^{\circ}\text{C}$. The multiple reaction monitoring (MRM) mode was used to quantify the analyzes.

2. 8. Statistical Analysis

In the experiments, each sample was analyzes two times in parallel, and each experiment was carried out in duplicate (n=2). Data were expressed as means \pm standard deviation. Pearson correlation test was used to determine the correlation between the antioxidant properties and extraction time. The value of $p < 0.05$ was considered to be statistically significant. The statistical analysis was done using SPSS 21 programme.

3. Results and Discussion

Due to the biological activities of polyphenolic compounds, they are extract from plant materials using various extraction methods. The ultrasound-assisted extraction is also used as a cheap and simple extraction technique that provides high extraction yield and quality, especially in the extraction of phenolic compounds from various natural and waste herbal sources.^{30–31} The extraction yield, total phenolic and flavonoid contents of extracts obtained from ultrasound-assisted and shaking water bath extraction techniques are presented in Table 1. The extraction yields (gram extract/100 g dried leaves) were 18.7% for WBE and 16.5% for UAE. Although UAE has a slightly lower extraction yield than WBE, total phenolic amount of UAE was twice that of WBE (Table 1). The extract obtained by the ultrasound-assisted extraction showed higher antioxidant activity due to its high phenolic and flavonoid contents. In addition, the low EC50 value indicates high antioxidant capacity. The EC50 values of extracts obtained from UAE are lower than these of other extraction method in both of free radical scavenging assays (Table 1). According to Table 1, the difference was found between the two methods in the free radical activities, the phenolic and flavonoid contents of the extracts.

Phenolic contents of olive leaf extract were compared to standard thirty-three organic compounds and thirteen of them were identified in both extracts at quantifiable levels. The flavonol quercetin, isorhamnetin, luteolin, five phenolic acids (chlorogenic, protocatechuic, 2,5-dihydroxybenzoic, caffeic and gallic acid) and as well as glycosides oleuropein, verbascoside and rutin were determined higher amount at olive leaf extract obtained by UAE (Table 2) and (Figure 1). As seen in Table 1, in the determination of total phenolic and flavonoid contents by spectrophotometric method, the contents of ultrasonic extract were already determined higher than the water bath

Table 1. Effect of UAE and WBE methods on antioxidant properties of olive leaf extract.

Extraction Conditions	Extraction Method	Extract yield (%)	TPC (GAE $\mu\text{g}/\text{mg}$)	TFC (Rutin $\mu\text{g}/\text{mg}$)	DPPH EC50 assay mg/mL	ABTS assay EC50 mg/mL
75% EtOH, 2h, 30 $^{\circ}\text{C}$	UAE	16.5	111.9 \pm 0.018	534.44 \pm 0.045	138.1	245.9
	WBE	18.7	56.9 \pm 0.0013	528.11 \pm 0.072	284.1	650.0

Table 2. Content of individual phenolics of olive leaf extracts by LC-MS/MS

Phenolic compound	UAE (ppb)	WBE (ppb)
Oleuropein	34090.33	30715.84
Chlorogenic Acid	2621.13	2395.64
Protocatechuic Acid	1088.58	710.85
Verbascoside	515.37	178.54
Rutin	417.76	325.78
Quercetin	224.19	20.80
Isorhamnetin	197.97	39.02
2,5-dihydroxybenzoic acid	121.96	88.76
Luteolin	111.37	76.36
Caffeic acid	88.35	76.12
Gallic acid	20.88	5.58
Salicylic acid	9.95	15.94
Apigenin	6.52	10.47

extract. This indicates that the high antioxidant capacity in the olive leaf extract obtained UAE is due to its high phenolic composition in comparison with WBE.

Researchers who interested in natural products have been studying on extraction process to compare the efficiency of the UAE method with others by using various plant sources. Similar to our study, it was observed that the extracts obtained from ultrasonic application were more efficient in other studies performed to compare traditional and ultrasound-assisted extraction techniques for the extraction of bioactive components. It has been reported that

UAE technique from the leaves of lemon scented tea tree (*Leptospermum petersonii*) is more efficient in terms of total phenolics and antioxidant capacity compared to traditional shaking water bath extraction.¹⁷ Ali and Kumar (2015) used two extraction methods (UAE and Soxhlet extraction) for the extraction of bioactive compound from the pomegranate peel. They reported that UAE extract showed higher antioxidant activity and had a higher amount of chlorogenic acid.³⁰ In another study, *Bauhinia purpurea* leaf was extracted by Soxhlet, ultrasonication and maceration extraction methods, and it was reported that UAE was better method for the extraction of antioxidant and antibacterial substances compared to others.³² Similarly, Wang et al. (2011) compared ultrasound extraction, high-pressure liquid extraction, and Soxhlet extraction for antioxidants from *C. sulcate* fruit and peel and suggested that UAE is the ideal method for the extraction of antioxidants.³¹

In our study, similarly other studies in the literature, the extract from UAE showed better results compared to its extract by obtained WBE for Domat variety of olive leaf. Since extraction conditions have an effect on the extraction of phenolic and biocomponents, it was aimed to investigate the effect of extraction duration on extraction yield by keeping other conditions same in the continuation of the study. If the extraction time is shortened without changing antioxidant capacity of the extract significantly, time and energy will be saved that is important for manufacturing cost industrially. Therefore, in the present study, olive leaf

Table 3. Effect of ultrasonication period on antioxidant properties of olive leaf extract

Extract	Yield (%)	TPC ($\mu\text{g GAE/mg}$)	TFC ($\mu\text{g Rutin/mg}$)	EC50 mg/mL	
				DPPH assay	ABTS assay
UAE-15	14.2 ^a	99.7 \pm 0.12 ^a	421.3 \pm 0.10 ^a	130.3 ^a	411.3 ^a
UAE-30	15.4 ^a	97.5 \pm 0.03 ^a	410.1 \pm 0.04 ^a	137.6 ^a	376.9 ^a
UAE-60	19.1 ^a	102.7 \pm 0.04 ^a	418.7 \pm 0.02 ^a	127.6 ^a	409.2 ^a
UAE-120	19.4 ^a	104.5 \pm 0.018 ^a	530.2 \pm 0.045 ^a	122.8 ^a	406.7 ^a

SD = standard deviation (n=2)

Different letters of upper index within the column indicate significant differences at p<0.05 level.

Table 4. Linear correlations between the analyzed parameters

	Time	TPC (GAE)	TFC (Rutin)	DPPH assay (EC50 value)	ABTS assay (EC50 value)
Time	1	0.865	0.911	-0.789	-0.904
TPC (GAE)		1	0.089	0.211	0.096
TFC (Rutin)			1	-0.972*	0.334
DPPH assay (EC50 value)				1	0.656
ABTS assay (EC50 value)					1

*Correlation is significant at the 0.05 level (2-tailed).

was extracted by ultrasound-assisted extraction at a different interval of time (15 min, 30 min, 60 min, 120 min) at 30 °C using ethanol (75%) as the solvent. According to results (Table 3), it was seen that the maximum extraction yield was obtained by 120 min of sonication in comparison with 15 min, 30 min and 60 min intervals of sonication. The sonication interval was increased the extraction yield (%), however, there are not significantly differences between the sonication time and both total phenolic and flavonoid contents ($p < 0.05$).

According to Table 4, it can be inferred that extraction time values are not significantly correlated with TPC, TFC, DPPH, ABTS, but DPPH values are significantly correlated with TPC, and ABTS values are significantly correlated with TFC. We said that there is no significant difference between the extraction time and TPC and TFC which responsible antioxidant activity. There was also no relationship between extraction time and DPPH and ABTS EC₅₀ values ($p < 0.05$), which means that 15 min of sonication can be done instead of 120 min. In recent studies, the extraction time has been reported at different timings. The most efficient extraction time of the total polyphenol contained in soybeans extract with solid-liquid extraction has been reported as 120 min.³³ It has been shown that the pepper pulp extract obtained by ultrasonic bath and shaking water bath methods was obtained with the 20 min extraction process in terms of the highest total phenolic substance and antioxidant activity which is similar with our results.³⁴ Altemimi et al. was reported the optimum extraction process time of spinach leaves with ultrasound-assisted extraction method was reported as 30 min.³⁵

In other studies, about comparing microwave-assisted extraction and ultrasound-assisted extraction methods, the extraction times for optimum antioxidant activity were reported as 30.5 for *Prunella vulgaris* L. extract.³⁶ Similarly, the extraction time was reported as 5–30 min by keeping temperature and power constant as the optimum extraction conditions of Nettle and Chokeberries extracts by comparing microwave-assisted extraction and ultrasound-assisted extraction methods.^{37–38} According to the reports of other researchers, Wang et al. also indicated that the ultrasound-assisted extraction method is a convenient and economical method for the extraction of total phenolic compounds for *Inula helenium* sample.³⁹

The olive tree leaf is a source of valuable active compounds such as oleuropein, verbascoside and rutin, which has benefit in health promoting potential, and also have an importance in agricultural as industrial waste. Therefore, the extraction process for biophenols obtained from olive leaf is important and the researchers focused on optimum extraction conditions. Nowadays, ultrasound-assisted extraction methods have been studied mostly because of its advantages.

There are few studies about olive leaf extraction by ultrasound-assisted extraction method related to Serrana variety from Spain²⁵ and Tavsan Yuregi variety from Tur-

key.²⁴ In this study, we studied another variety of olive leaf which is Domat variety from Manisa/Turkey. Ahmad-Qasem et. al. has addressed the ultrasound-assisted extraction of Serrana var. olive leaf bioactive compounds and evaluated the influence of some process parameters such as the electric amplitude, the emitter surface and temperature. Also, they reported that olive leaf extracts were similar content of bioactive compounds, such as oleuropein, verbascoside and luteolin-7-O-glucoside in comparing the conventional technique with ultrasound-assisted extraction method. In their results, the extraction time of conventional technique reduced from 24 h reduced to 15 min with ultrasound-assisted extraction method.²⁵ In another study by Sahin and Samli for ultrasound-assisted extraction of olive leaves (Tavsan Yuregi variety) with response surface methodology, were reported the optimum extraction conditions such as 0.5 g sample to 10 mL solvent ratio, 50% ethanol and 60 min of extraction time²⁴. As stated above, different extraction process times have been reported so far regarding to antioxidant activity, total phenolic and flavonoid contents of different plants, so the results of our study may suggest the best extraction time for olive leaf (Domat var.) as 15 min with ultrasound-assisted extraction. Comparing to the conventional extraction process, ultrasound-assisted extraction can use for reducing the long extraction time, and to decrease the risk of biocompound degradation.

4. Conclusions

This study aimed to analyse whether high antioxidant results of olive leaf extracts in a shorter time instead of two hours by ultrasound-assisted extraction, and to determine the phenolic compounds contained in olive leaf (Domat var.) by LC-MS/MS. So, choosing the right extraction method is important for obtaining extracts with various pharmacological activities expected from plants and also it is important to minimize or avoid degradation of biocompounds and to select the best working conditions. For the extraction of antioxidant compounds from Domat variety olive leaves, the UAE technique gave better results than the extraction with shaking water bath technique. When the effect of time on ultrasound-assisted extraction is examined, it can be said that the extraction time of 15 minutes instead of 2 hours is sufficient, according to the results obtained from the antioxidant activity trials of the extracts and their extract yields. The results show that the UAE method provides time and energy saving, and can be used in biocomponent recovery, which is faster and more effective than traditional methods. This technique can also find application in the development of industrial extraction processes. In order to contribute to the industrial field, extraction-time optimization or other extraction parameters can be also investigated by using different herbal materials with biological activity.

Acknowledgements

The authors wish to thank TUTAGEM for the phenolic profile analysis by LC-MS/MS, and Olive Research Institute-Izmir for providing the olive leaves sample. This work was supported financially by the Scientific Research Fund of Trakya University, Project number TUBAP-2019/159.

5. References

- S. De Marino, C. Festa, F. Zollo, A. Nini, L. Antenucci, G. Raimo, M. Iorizzi, *Anticancer Agents Med. Chem.* **2014**, *14*, 1376–1385. DOI:10.2174/1871520614666140804153936
- A. Guinda, J. M. Castellano, J. M. Santos-Lozano, T. Delgado-Hervás, P. Gutiérrez-Adánez, M. Rada, *Food Sci. Technol.* **2015**, *64*, 431–438. DOI:10.1016/j.lwt.2015.05.001
- S. Lockyer, P. Yaqoob, J. Spencer, I. Rowland, *Nutrition Aging* **2012**, *1*, 125–140. DOI:10.3233/NUA-2012-0011
- H. H. Orak, S.S. Isbilir, H. Yagar, *Food Sci. Biotechnol.* **2012**, *21*, 1065–1074. DOI:10.1007/s10068-012-0138-6
- S. Himour, A. Yahia, H. Belattar, *Eur. Sci. J.* **2017**, *13*, 1857–7881. DOI:10.19044/esj.2017.v13n6p342
- M. Bayram, S. Topuz, C. Kaya, *Turk. J. Agric. - Food Sci. Technol.* **2020**, *8*, 337–347. DOI:10.24925/turjaf.v8i2.337-347.3039
- K. Mmopele, K. S. Combrinck, J. Hamman, C. Willers, W. Chen, A. Viljoen, *Planta Med.* **2018**, *84*, 886–894. DOI:10.1055/a-0583-0543
- E. Susalit, N. Agus, I. Effendi, R. R. Tjandrawinata, D. Nofiarny, T. Perrinjaquet-Moccetti, M. Verbruggen, *Phytomedicine*, **2011**, *18*, 251–258. DOI:10.1016/j.phymed.2010.08.016
- H. Jemai, M. Bouaziz, I. Fki, A. El Feki, S. Sayadi, *Chem. Biol. Interact.* **2008**, *176*, 88–98. DOI:10.1016/j.cbi.2008.08.014
- S. H. Omar, *Sci Pharm.* **2010**, *78*, 133–154. DOI:10.3797/scipharm.0912-18
- L. Di Donna, F. Mazzotti, A. Naccarato, R. Salerno, A. Tagarelli, D. Taverna, G. Sindona, *Food Chem.* **2010**, *121*, 492–496. DOI:10.1016/j.foodchem.2009.12.070
- I.C.F.R. Ferreira, L. Barros, M. S. Soares, M. L. Bastos J. A. Pereira, *Food Chem.* **2007**, *103*, 188–195. DOI:10.1016/j.foodchem.2006.08.006
- Y. H. Chen and C. Y. Yang, *Processes* **2020**, *8*, 1218. DOI:10.3390/pr8101218
- L. Wen, Z. Zhang, D. Rai, D. Sun, B. Tiwari, *J. Food Process Eng.* **2019**, *42*, 1–11. DOI:10.1111/jfpe.13191
- F. Nicoli, C. Negro, M. Vergine, A. Aprile, E. Nutricati, E. Sabella, L. De Bellis, *Molecules* **2019**, *24*, 1998. DOI:10.3390/molecules24101998
- Q. He, B. Du, B. Xu, *Appl. Sci.* **2018**, *8*, 1905. DOI:10.3390/app8101905
- M. Saifullah, R. McCullum, A. McCluskey, Q. Vuong, *Heliyon*, **2020**, *6*, e03666. DOI:10.1016/j.heliyon.2020.e03666
- L. J. Cseke, A. Kirakosyan, P. B. Kaufman, S. Warber, J. A. Duke, H. L. Briemann, (Eds.): *Natural Products from Plants*, CRC Press, United States of America, **2006**, pp. 442–468.
- M. Tranfić Bakić, S. Pedisić, Z. Zorić, V. Dragović-Uzelac, A. Ninčević Grassino, *Acta Chim. Slov.* **2019**, *66*, 367–377. DOI:10.17344/acsi.2018.4866
- T. Ismandari, S. Kumalaningsih, S. Wijana, S. A. Mustaniroh, *Scientific World J.* **2020**, *2020*, 1–8. DOI:10.1155/2020/9105847
- J. A. Perez-Serradilla, F. Priego-Capote, M. D. Luque de Castro, *Anal. Chem.* **2007**, *79*, 6767–6774. DOI:10.1021/ac0708801
- L. Wang, C. L. Weller, *Trends Food Sci. Technol.* **2006**, *17*, 300–312. DOI:10.1016/j.tifs.2005.12.004
- Ş. Tavman, S. Kumcuoğlu, Z. Akkaya, *Gıda* **2009**, *34*, 175–182.
- S. Şahin, R. Samli, *Ultrason. Sonochem.* **2013**, *20*, 595–602. DOI:10.1016/j.ultsonch.2012.07.029
- M. H. Ahmad-Qasem, J. Cánovas, E. Barrajón-Catalán, V. Micol, J. A. Cárcel, J. V. García Pérez, *Innov. Food Sci. Emerg. Technol.* **2013**, *17*, 120–129. DOI:10.1016/j.ifset.2012.11.008
- V. L. Singleton, J.A. Rossi, *Am. J. Enol. Vitic.* **1965**, *16*, 144–158.
- J. Zhishen, T. Mengchneq, W. Jianming, *Food Chem.* **1999**, *64*, 555–559. DOI:10.1016/S0308-8146(98)00102-2
- M. S. Blois, *Nature* **1958**, *181*, 1199–1200. DOI:10.1038/1811199a0
- R. Re, N. Pellegrini, A. Proteggente, A. Pannala, M. Yang, C. Rice-Evans, *Free Radic. Biol. Med.* **1999**, *26*, 1231–1237. DOI:10.1016/S0891-5849(98)00315-3
- U. Ali, P. Kumar, *Int. J. Food Nutr. Sci.* **2015**, *3*, 265–270.
- A. Y. Wang, M. Y. Zhou, W. C. Lin, *Food Chem.* **2011**, *124*, 958–963. DOI:10.1016/j.foodchem.2010.07.035
- H. V. Annegowda, M. N. Mordij, S. Ramanathan, M.R. Hamdan, S. M. Mansor, *Food Anal. Methods* **2012**, *5*, 226–233. DOI:10.1007/s12161-011-9228-y
- S. Jokić, D. Velić, M. Bilić, A. Bucić-Kojić, M. Planinić, S. Tomas, *Czech J. Food Sci.* **2010**, *28*, 206–212. DOI:10.17221/200/2009-CJFS
- M. Civan, S. Kumcuoğlu, Ş. Tavman, *Akad. Gıda* **2019**, *17*, 351–361. DOI:10.24323/akademik-gida.647717
- A. Altemimi, R. Choudhary, D. G. Watson, D. A. Lightfoot, *Ultrason. Sonochem.* **2015**, *24*, 247–255. DOI:10.1016/j.ultsonch.2014.10.023
- G. Zhang, L. He, M. Hu *Innov. Food Sci. Emerg. Technol.* **2011**, *12*, 18–25. DOI:10.1016/j.ifset.2010.12.003
- A. E. İnce, S. Şahin, G. Sumnu, *J. Food Sci. Technol.* **2014**, *51*, 2776–2782. DOI:10.1007/s13197-012-0828-3
- V. M. Simić, K. M. Rajković, S. S. Stojičević, D. T. Veličković, N. Č. Nikolić, M. L. Lazić, I. T. Karabegović, *Sep. Purif. Technol.* **2016**, *160*, 89–97. DOI:10.1016/j.seppur.2016.01.019
- J. Wang, Y. M. Zhao, Y. T. Tian, C. L. Yan, C. Y. Guo, *Scientific World J.* **2013**, *2013*, 1–5. DOI:10.1155/2013/157527

Povzetek

V tej raziskavi smo primerjali učinkovitost ekstrakcije polifenolov iz oljčnih listov (Domat) s pomočjo stresane vodne kopeli in ultrazvoka ter rezultate primerjali z vsebnostjo polifenolov in antioksidativno aktivnostjo oljčnih listov. Učinkovitost ekstrakcije na antioksidativno aktivnost oljčnih listov smo preverjali preko izkoristka ekstrakcije, antioksidativne aktivnosti in vrste pridobljenih polifenolov, pri čemer smo poleg same metode spreminjali tudi trajanje ekstrakcije.

Cilj: doseči visoke antioksidativne vrednosti in določiti vrste fenolnih spojin v oljčnih listih (Domat) z LC-MS/MS pri uporabi ekstrakcije z ultrazvokom ali stresano vodno kopelijo v prej kot 2 urah

Zaključki: Ugotovili smo, da z ekstrakcijo z ultrazvokom dosežemo višjo koncentracijo fenolnih komponent kot pri ekstrakciji s stresano vodno kopeljo. Obenem pa smo ugotovili, da pri tem tipu ekstrakcije čas ekstrakcije ne vpliva na celotno vsebnost fenolov in flavonoidov, kot tudi ne na antioksidativne vrednosti določene z DPPH in ABTS EC 50 ($p < 0.05$), kar pomeni, zadostuje že 15 minut namesto 120 min ultrazvočne ekstrakcije.



Except when otherwise noted, articles in this journal are published under the terms and conditions of the Creative Commons Attribution 4.0 International License

Scientific paper

Design of “Turn-Off” Fluorescent Nanoprobe for Highly Sensitive Detection of Uric Acid using Green Synthesized Nitrogen-Doped Graphene Quantum Dots

Sopan Nangare,¹ Shweta Baviskar,² Ashwini Patil³ and Pravin Patil^{2,*}

¹ Department of Pharmaceutics, H. R. Patel Institute of Pharmaceutical Education and Research, Shirpur-425405, Dist: Dhule, Maharashtra state, INDIA-425405

² Department of Pharmaceutical Chemistry, H. R. Patel Institute of Pharmaceutical Education and Research, Shirpur-425405, Dist: Dhule, Maharashtra state, INDIA-425405

³ Department of Microbiology, R. C. Patel Arts, Science, and Commerce College, Shirpur, Dist: Dhule, Maharashtra state, INDIA-425405

* Corresponding author: E-mail: rxpatilpravin@yahoo.co.in

Received: 02-24-2022

Abstract

Green synthesized graphene quantum dots (GQD) have been doped with nitrogen in an attempt to boost their optical characteristics and application sectors. In the present investigation, the blue luminescent nitrogen-doped GQDs (N-GQDs) were synthesized by single-step hydrothermal synthesis using tamarind shell powder as a precursor. The particle size and zeta potential of N-GQDs were found to be 11.40 nm and be -35.53 mV, respectively. A quantum yield as high as 23.78 % was accomplished at an excitation wavelength of 330 nm at neutral pH. It gets quenched sensitively in the existence of uric acid (UA) combining static quenching, electron transfer, and an inner filter effect mechanism. A linear range was obtained for UA from 10 μ M to 100 μ M, with a limit of detection (LOD) of 401.72 ± 0.04 pM. Additionally, the N-GQDs were selective toward UA in presence of metal ions and biomolecules that indicated its impending use to monitor UA in clinical samples. In conclusion, this work demonstrates that the N-GQDs as a sensing probe for UA recognition with notable advantages including socioeconomic, simple, and less time-consuming methods as compared to other methods. In the future, it can be potentially explored as a biosensor for UA detection in clinical samples.

Keywords: Graphene Quantum Dots; N-GQDs; Uric acid; Biosensor; Tamarind Shell Powder

1. Introduction

Principally, UA (2,6,8-trihydroxypurine) is the primary product of purine synthesis.¹ As per literature, in the general population, UA is referred to between 0.13 mM to 0.46 mM and 2.49 mM to 4.46 mM in serum and urine, respectively.² As we know, the abnormal levels of such metabolites in body fluids can cause several diseases.³ Plentiful literature revealed that the increased UA levels in body samples are indicative of hypertension, gout, cardiovascular disease, kidney disease, high cholesterol, and many more.⁴ In comparison, low concentrations of UA are also connected with multiple sclerosis and oxidative stress.^{5,6} In diagnosis and healthcare, it is crucial to quantify me-

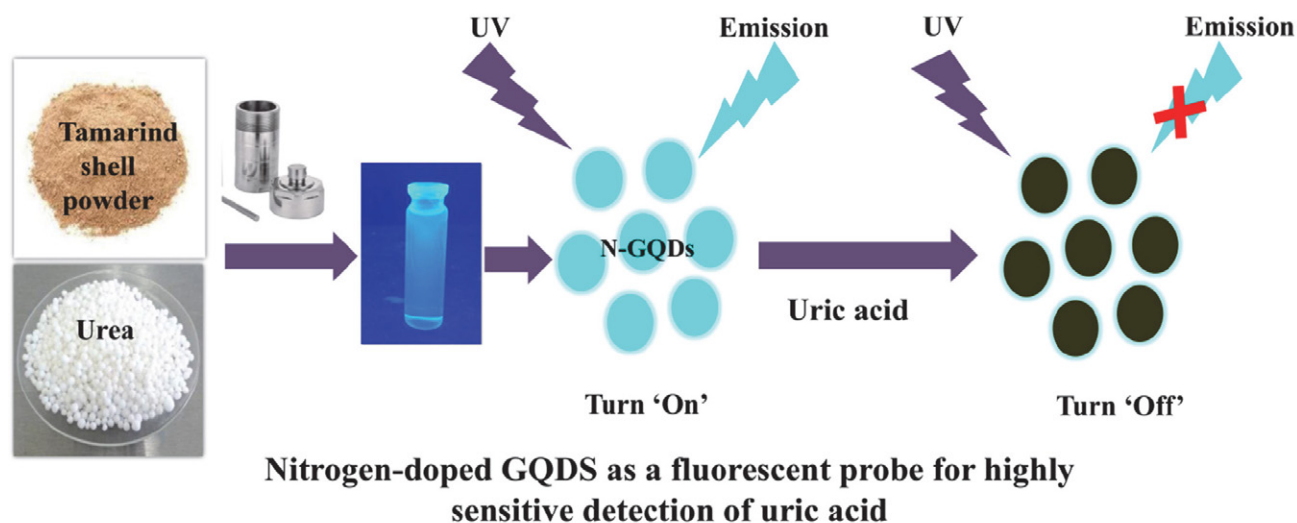
tabolites in blood or other biological samples. Therefore, a rapid, responsive, precise, and cheap method of assessment must be developed to track such metabolites in body fluids including serum and urine.⁵

Literature survey reported that electrochemical sensing,⁷ a colorimetric method,⁸ a chromatographic method,⁹ etc. are currently engaged detection techniques for UA in different body fluid samples. However, some in-conveniences such as complicated synthesis or challenging extraction, advanced equipment, expensive and tedious limiting their practical uses, are present in these approaches.⁵ There are no exceptions for benefit of fluorescence. It is highly sensitive, and it shows a fast reaction, and operative simplicity in contrast to the oth-

er existing approaches.^{5, 10} From the last decades, ample reports have been reported for the detection of UA using fluorescent nanomaterials. Ding *et al.*, designed the graphene oxide-based carbon quantum dots (CQDs) as an electrochemical sensor for detection UA.¹¹ In another study, CQDs- hybrid composites-based electrochemical sensor has been constructed by Abbas and colleagues for recognition of UA.¹² Currently, application of GQDs as a sensing material is gaining much consideration from research fraternities. Thanks to its tunable photoluminescence properties GQDs have created substantial interest as a potential new class of carbon-based, luminescent nanomaterials.¹⁰ The growing advancement in fluorescent sensors and bioimaging has been growing for the GQD because of their high bio-compatibility and photostability.^{13,14} Applications of GQDs in UA sensing a redox modulated fluorescent strategy for a finding of UA and glucose using fluorescent GQDs based probe has been reported.⁵ Kunpatee and co-authors reported the detection of UA using GQDs mediated ionic liquid modified screen-printed carbon electrode that offers the 0.03 μM of lowest detection limit.¹⁵ However, the QY of GQDs mentioned is far lower than traditional quantum dots (QDs), which restricts QD's wide-ranging use for different purposes. Hence, the improvement of QYs has become one of the obstacles to the use of GQDs. Several scholars have successfully shown that GQDs can be reliably transformed into an amino-functionalized GQD or π -conjugated system employing doping of heteroatoms.¹⁴ As per literature, doping is an efficient method to alter the electronic density of bulk semiconductor materials. Besides, it helps to tune the optical and electrical properties. Recently, nitrogen doping in graphene structure enabled the in-plane substitution of nitrogen atoms to graphene as an *n*-type semiconductor.¹⁶ Therefore, in this work we developed the doped GQDs as fluorescent nanomaterials.

Nitrogen doping is a feasible approach for altering the electrical, chemical, and structural functions of GQDs to boost their efficiency in sensing applications.¹⁷ Li and co-authors found, owing to the intense electron-withdrawing outcome of the doped 'N' atom, that the as-prepared N-GQDs have special optoelectronic properties.¹⁸ Besides, a potential mechanism for tuning GQDs fluorescent properties via the charge transfer effect of the functional group was suggested by the Chattopadhyay group.¹⁹ Due to the high QY and superb bleaching resistance of fluorescent materials, many research groups have been used N-GQDs as fluorescent sensors for sensing biological small macromolecules, organic small molecules, and metal or non-metal ions.²⁰ It is intended, by adjusting the surface characteristics and the associated fluorescent property, the design of realistic sensors for the assessment of UA in the urine can be promising. In the meantime, N-GQDs normally have greater amounts of QY than GQDs and are good for the fluorescence study in spiked real-time body fluid (urine). A preference of methods has been developed for the N-GQDs preparation including hydrothermal method,²¹ direct electrolysis,²² pyrolysis,²³ etc. using different chemicals as a precursor. Additionally, owing to the costly facilities, complex and time-consuming processes, the aforementioned protocols are unconvincing.

In this study, we illustrate a single step, relatively inexpensive and environmentally safe in preparing N-doped GQDs through hydrothermal treatment of Tamarind seed as a green source. We present a new kind of fluorescent sensor for UA detection based on the fluorescence Turn On-Off strategy. The synthesized N-GQDs show a high quantity of QY and emit light blue luminescence. Interestingly, owing to the stronger electrostatic interaction and electron transfer between blue luminescent N-GQDs and UA, the photoluminescence intensity of the N-GQDs could be quenched efficiently (Scheme 1). Finally, based



Scheme 1: One spot synthesis of N-GQDs using tamarind shell powder and sensing of UA

on a finding of the proposed N-GQDs fluorescent sensor, it could be an exceptional alternative as high sensitivity and selectivity for UA recognition.

2. Materials and Methods

2.1. Materials

Uric acid (2, 6, 8-trihydroxypurine, $\geq 99\%$) and urea ($\geq 99\%$) were purchased from Sigma-Aldrich. The sodium hydroxide, sodium chloride, calcium chloride, glycine, glucose, sucrose, lysine, alanine, quinine sulfate were collected from Lobachemie, Chemicals. Pvt. Ltd. Mumbai, India. All chemicals plus reagents utilized for synthesis and characterization of N-GQDs were of analytical grade (AR) and applied as received without purification. Double distilled water (DDW) was prepared in the laboratory. Tamarind seed was collected from the local market of Shirpur, Maharashtra (India).

2.2. Methods

2.2.1. Processing of Tamarind Shell

In the beginning, 0.5 kg of tamarind shell (*Tamarindus indica*) waste was collected from the local market, Shirpur city (Dhule, Maharashtra). Further, the tamarind shell waste was dried using a laboratory hot air oven. The temperature was programmed at 60 °C and then decreased to 40 °C at the rate of -0.14 °C/minutes for 12 h. After drying, the dried shells were checked for stuck dirty materials on the shells. Finally, shells were crushed into tiny pieces via a mortar pestle. Further, the obtained powder was subjected to grinding to obtain fine tamarind shell powder.

2.2.2. Synthesis of N-GQDs

The N-GQDs synthesis from Tamarind shell powder and urea was achieved through the one-pot hydrothermal method. Briefly, 500 mg of fine tamarind shell powder was dispersed in 20 mL of double-distilled water (DDW) followed by 20 minutes of sonication. After that, 100 mg urea was added to the above dispersion. Finally, the prepared dispersion was transferred into a Teflon-lined autoclave in a stainless-steel hydrothermal reactor in a hot air oven at 200 °C for 8 h. After the end of the hydrothermal process, the resultant solution was kept to bath sonication for 20 minutes at 25 °C, which gives uniform dispersion of N-GQDs. For purification purposes, the obtained N-GQDs were shifted to the dialysis (for 24 h) using a dialysis bag (12,000 kDa, 0.22 μm), which help to remove the insoluble carbon materials. Afterward, the final dialyzed solution was transferred to centrifugation (Refrigerated Centrifuge, Elteck Overseas Pvt. India) at 9000 rpm for 20 minutes (4 °C to 10 °C) to remove the impurities.

2.2.3. Freeze-Drying of N-GQDs

In this study, liquid N-GQDs solution was processed for lyophilization by using a laboratory freeze dryer (Freezone12, Labconco, MO, USA). Briefly, the N-GQDs solution was pre-freeze at -30 °C for 36 h at the laboratory deep freezer (Southern Scientific Lab Instrument, India). After that, the primary drying of N-GQDs was performed at -53 °C and 0.016 mBar for 24 h. Afterward, the secondary drying of N-GQDs was performed at 10 °C for 8 h and was followed by drying at 25 °C for 4 h with a steady increase in temperature at 1 °C/min. Finally, the temperature of the cold trap was maintained at -53 °C until the end of the drying process.

2.2.4. Characterizations of N-GQDs

The synthesized N-GQDs were characterized by the UV-visible spectra was recorded between 800 to 400 nm on UV-vis spectrophotometer (UV 1800 Shimadzu, Japan) using a quartz cuvette. FT-IR spectra of N-GQD were recorded using an FT-IR spectrophotometer (Agilent CARY 630 FT-IR) at 4 cm^{-1} resolution in the absorption area of 4000 to 1000 cm^{-1} . Energy Dispersive X-ray Spectroscopy (EDAX) was used to provide qualitative and quantitative surface analysis. The particle size of synthesized N-GQDs was measured via Nanoplus 3 Particulate System (Micromeritics, USA). The green synthesized N-GQDs shape, size, and crystalline nature were obtained using HR-TEM (HR-TEM, Jeol/JEM 2100) with a LaB6 light source at 200 kV. The fluorescence study of N-GQDs was performed using a UV chamber (details) at different wavelengths such as 254 nm and 365 nm along with visible light.

2.2.5. pH Influence Study

The pH of the N-GQDs solution actively affects the fluorescence properties of the N-GQDs since the pH affects the surface stability and molecularity of the surface functional groups. The prepared N-GQDs were subjected to different pH ranges from 1 to 12 to study the pH dependant changes in the fluorescence intensity.²⁴ Herein, different predefined pH such as 1, 3, 7, 9, and 12 of N-GQDs solution was adjusted using 1.5 M solution of sodium hydroxide and 0.5 M hydrochloric acid at room temperature. Then, the pH value of the N-GQDs solution was recorded using a digital pH meter, and solutions were kept aside for 60 min. After that, the fluorescence intensity was recorded at excitation 330 nm and corresponding changes in the intensities were recorded.

2.2.6. Quantum Yield (QY)

In this study, the 'QY' of the N-GQDs was calculated by using a comparative method. Quinine sulfate was dissolved in 0.1 M sulphuric acid ($\phi_{\text{st}} = 54\%$) as a standard for QY determination. Then, the dilutions were prepared

using double distilled water (DDW). The absorbance was measured at 350 nm via a UV-Vis spectrophotometer and optical density values were kept below 0.1 to reduce the re-absorption effect. Fluorescence emission spectra of quinine sulfate, as well as N-GQDs, were recorded at 350 nm excitation and a graph was plotted for integrated fluorescence intensity against absorbance. The 'QY' of N-GQDs was calculated using the following equation,

$$\varphi_x = \varphi_{st} \left(\frac{\text{Grad}_x}{\text{Grad}_{st}} \right) \left(\frac{\eta_x}{\eta_{st}} \right)$$

wherein, ' φ ' is representing the QY. The subscripts 'x' and 'st' represent test (N-GQDs) and standard (quinine sulfate) respectively. Grad is the slope of fluorescence intensity vs. absorbance plot. The ' η ' is the refractive index of the solvent.

2. 2. 7. Uric Acid-Sensing Study

Detection of UA was carried out by using a spectrofluorometer (JASCO FP8200 spectrofluorometer) at neutral pH. Initially, 2 mL of synthesized N-GQDs solution were taken in a quartz cuvette and excited at 330 nm with a slit width of 5 nm for both excitations as well as emission wavelength at a scanning range of 335 nm to 520 nm at room temperature. To study the sensitivity of N-GQDs for UA detection, different concentrations of UA from 10 μM to 1000 μM were incorporated into an aqueous solution of N-GQDs (2 mL) and uniformly shaken followed by 5 minutes of incubation time at controlled room temperature (25 $^{\circ}\text{C}$). Afterward, fluorescence intensities were measured in triplicate for more accuracy. Notably, N-GQDs probe fluorescence intensity and the concentration of UA were found to have a linear function as the calibration curve. Different analytical characteristics including the limit of detection and the limit of quantification were calculated using slope and standard deviation. Moreover, the precision of the proposed sensing method was measured as interday and intraday variations.

2. 2. 8. Interference Study

The selectivity of N-GQDs (2 mL) was analyzed against a range of metal ions and biomolecules. For the interference study, an aliquot of the stock solutions of non-target samples namely, Na^+ , K^+ , Ca^+ , Ag^+ , bovine serum albumin, lysine, glycine, alanine, glucose, sucrose, lactose, ascorbic acid, etc. were prepared in DDW (pH 7). A concentration of 100 μM was chosen for all the metal ions and biomolecules for interference study. Briefly, the 1 mL of N-GQDs solution was mixed with 500 μL of these interfering substance solutions, separately. After 10 minutes, the fluorescence intensity of all samples was recorded at 330 nm (excitation wavelength) with 5.0 nm slit width for both excitation and emission wavelength. In addition, the mixture of all metal ions and biomolecules with UA

(sample A) was investigated to confirm the interference of foreign substances in the UA sample. The repeatability of N-GQDs was measured by the proposed method using 30 μM of UA samples ($n = 6$).

3. Results and Discussion

3. 1. Characterization of N-GQDs

In the present study, the applicability of N-GQDs as a fluorescent nanomaterial belonging to the 'C' family was explored for the recognition of UA in aqueous media. Briefly, a one-step, facile and eco-friendly method was preferred to synthesize N-GQDs using tamarind shell powder in a Teflon-lined hydrothermal stainless-steel autoclave reactor. Accordingly, the tamarind shell was proved to be an efficient and reliable waste material for synthesizing of GQDs while urea successfully donated nitrogen for the doping of nitrogen on the GQD structure. Inside the reactor, under high pressure and temperature conditions, tamarind shell powder forms the primary graphitic frame, and the nitrogen atoms were doped onto the graphitic structure. The synthesis procedure was optimized by altering the precursor's concentration as well as by changing the reaction time. The various batches were thus synthesized. As a result, it displayed momentous variation in the fluorescence properties. From these results; the final optimized parameters were identified for the synthesis of N-GQDs. Briefly, the fluorescence spectra were recorded at a fixed and varying wavelength to measure the excitation-dependent behavior. The synthesized N-GQDs were obtained in liquid form and then subjected to the different wavelengths in a UV-cabinet for fluorescence study. The solution of synthesized N-GQDs was looking pale yellow (or brownish) in visible light (Figure 1A). When a solution was transferred to the UV light excitation wavelength 254 nm, green fluorescence was observed (Figure 1B). In the case of UV light excitation wavelength 365 nm, the bright blue fluorescence of N-GQDs was obtained.²⁵ The varied colors observed in N-GQDs fluorescence were most possibly caused by solvent attachment/ different emissive traps of 'N' on green synthesized GQDs surface.²⁶ The oxygen-rich group provides the blue shift in photoluminescence emission from N-GQDs. Moreover, 'N' contains a strong electron affinity that offers the photoluminescence blue shift.¹⁸

For further investigation of optical properties of green synthesized GQDs, the UV-vis absorption spectra and fluorescence spectra were recorded. Figure 1D depicted the typical absorption peak at 229 nm that confirmed establishment of the graphitic structure of N-GQDs. It shows the absorption peak of N-GQDs in water at 200 nm to 800 nm against DDW (as a blank). The UV visible spectra of synthesized N-GQDs showed a maximum absorption peak at ~ 235 nm due to the π - π^* transition of C=C. The shoulder peak at ~ 344 nm is due to n - π^* transitions of

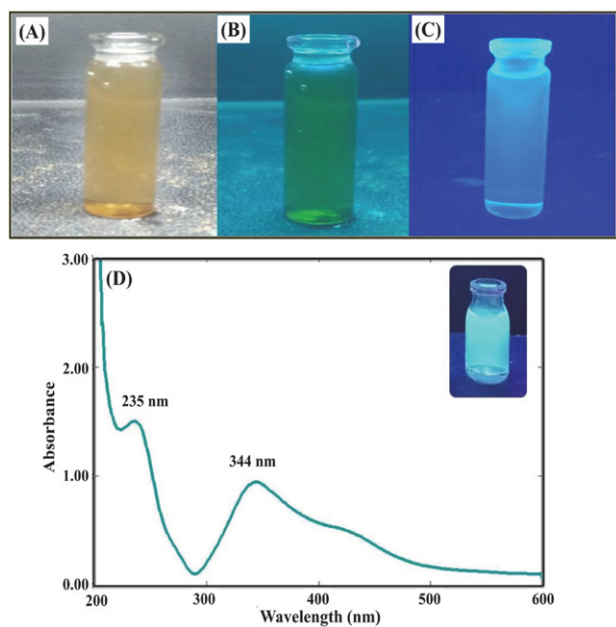


Figure 1: (A) N-GQDs in Visible Light, (B) N-GQDs excited in UV light wavelength 254 nm, (C) N-GQDs excited in UV light wavelength 365 nm, (D) UV-Visible spectra of N-GQDs

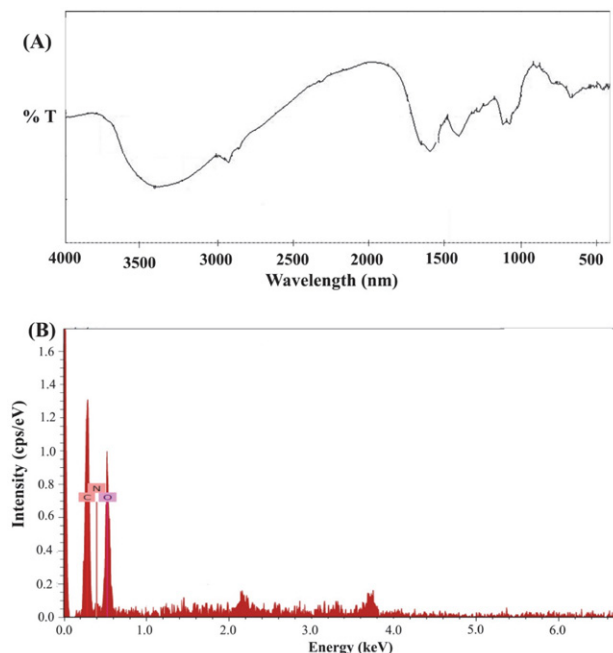


Figure 2: (A) FT-IR Spectra of N-GQDs, (B) EDAX spectra of N-GQDs

C=O.²⁷ Herein, these two absorption peaks confirmed that there is a certain absorption peak in N-GQDs. In conclusion, it confirmed the green synthesis of N-GQDs using the hydrothermal method.^{20, 25}

FT-IR was used to characterize the presence of major functional groups in synthesized N-GQDs (Figure 2A). The FT-IR spectrum of N-GQDs showed the absorption peak of the stretching vibration of the -OH group at 3412.0 cm^{-1} whereas the strong absorption peak 3230 cm^{-1} can vibrate of amine (NH_2) bond. The overlapping of -OH and

NH_2 was obtained due to the aqueous form of N-GQDs. Moreover, the peak at 1408.0 cm^{-1} can be attributed to the bimodal bending vibration of -NH. The C-N stretching vibration was obtained at 1276.92 cm^{-1} . Accordingly, it confirms the chemical interaction between the 'N' source and carboxyl. Moreover, it assures the existence of N on green synthesized GQDs surface.²⁵ The vibration peaks at 1658.84 cm^{-1} , 1120.68 cm^{-1} , and 1026.16 cm^{-1} can be ascribed to C=O stretching, C-O stretching, and C-O bending, respectively. In conclusion, the different functional

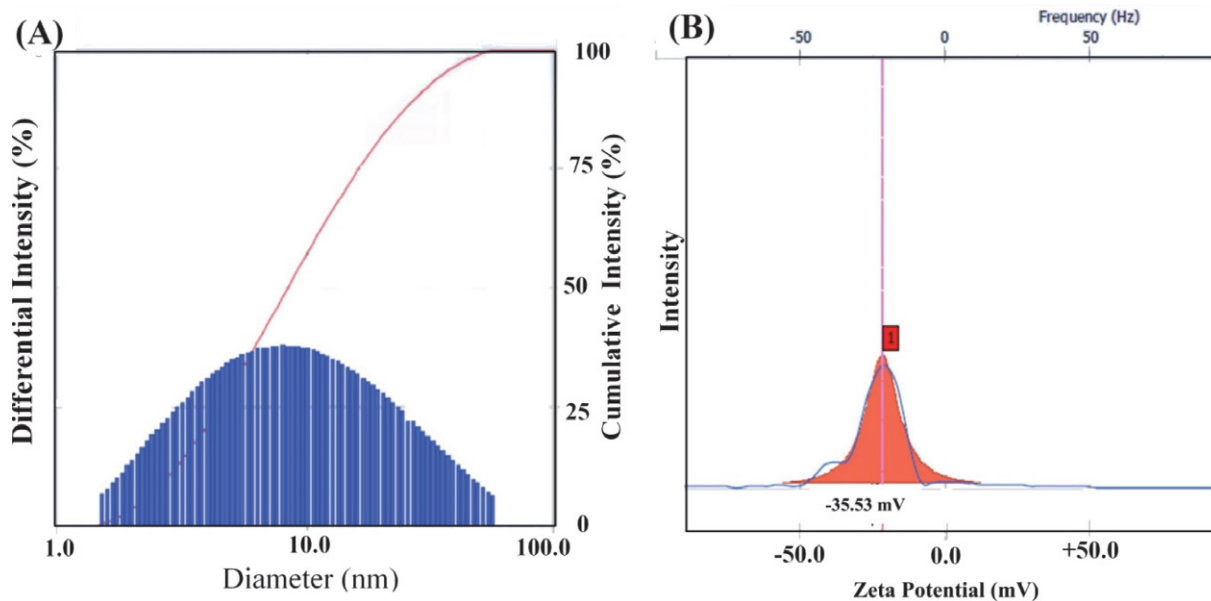


Figure 3: Particle size analysis (A) and zeta potential (B) of green synthesized N-GQDs

groups including –OH, –NH, and –COOH on N-GQDs surface confirmed the hydrophilicity and stability of the N-GQDs in an aqueous system.²³

The elemental analysis of synthesized N-GQDs was conducted for authentication of the occurrence of C, O, and N (Figure 2B) elements. In brief, it provides the details of wt.% of these mentioned elements in synthesized N-GQDs from green precursors. Herein, the presence of C, O, and N was found to be 41.09 wt%, 49.00 wt%, and 9.91 wt% respectively. Therefore, the existence of these elements demonstrates the successful formation of the N-GQDs.²⁸ Moreover, the confirmation of the amide group in N-GQDs can form the hydrogen bonds between water molecules and N-GQDs, which helps to improve the water solubility of prepared N-GQDs.²⁰ It is worthy to mention that particle size is the foremost critical factor since particle size is a potential technique for confirming the transformation of a micro-sized structure to a nano-sized structure. In this study, the particle size of green synthesized N-GQDs was found to be 12.6 ± 11.1 nm that confirming the synthesis of nanosized N-GQDs (Figure 3A). The polydispersity index (PDI) was found to be 0.35 ± 0.09 . It assured that the prepared N-GQDs exhibited uniform distribution in media. The zeta potential of N-GQDs was checked to confirm the surface charge as well as stability. The zeta potential of N-GQDs was found to be -35.53 mV (Figure 3B), which assures that the prepared N-GQDs exhibited good stability.

The morphological features of purified N-GQDs were characterized using HR-TEM. As depicted in Figure 3A, the GQDs are small, rounded, and uniformly dispersed with an average particle of size 7 nm. Moreover, the typical

lattice spacing was found to be 0.23 nm demonstrating a graphitic structure of green synthesized N-GQDs. Figure 3B showed the selected area diffraction (SAED) pattern of N-GQDs that assured the crystalline nature of N-GQDs. In conclusion, it confirmed the successful synthesis of nanosized N-GQDs.²⁰

3. 2. pH-Dependent Fluorescence Study of N-GQDs

Nitrogen doping is a feasible approach for altering the electrical, chemical, and structural functions of GQDs to boost their efficiency in sensing applications. The synthesized N-GQDs solution was excited at different excitation wavelengths from 300 to 400 nm length, with an increment of 10 nm, slit width is 5 nm and scanning range is 315–525 nm at 25 °C (Figure 5A). The N-GQDs showed the emission at 400 nm when excited from 300 nm to 330 nm and the emission peak was decreased and shifted towards the longer wavelength when excited from 340 nm to 400 nm. The strongest emission peak was obtained at 400 nm when excited at 330 nm. In this study, the emission spectrum of the N-GQDs was showed excitation-dependent PL behavior. Literature survey reported that the shift in emission peak positions with different excitation wavelengths is depending on several key factors such as quantum confinement effect, size effect, elemental composition, edge states, surface functional groups, conjugated π -domains, and defects in the carbon framework.¹⁰ The effect of pH on synthesized N-GQDs was also studied by fluorescence spectroscopy. The fluorescence intensity of N-GQDs at different pH was shown in Figure 5B. The syn-

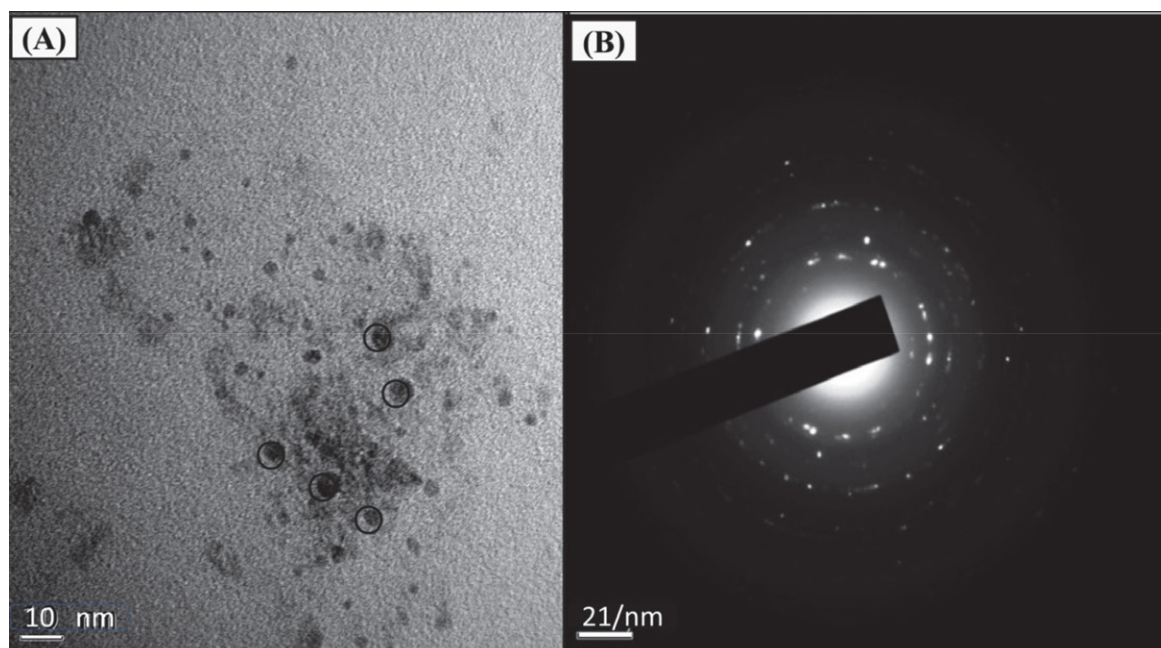


Figure 4: (A) HR-TEM and (B) SAED images of N-GQDs

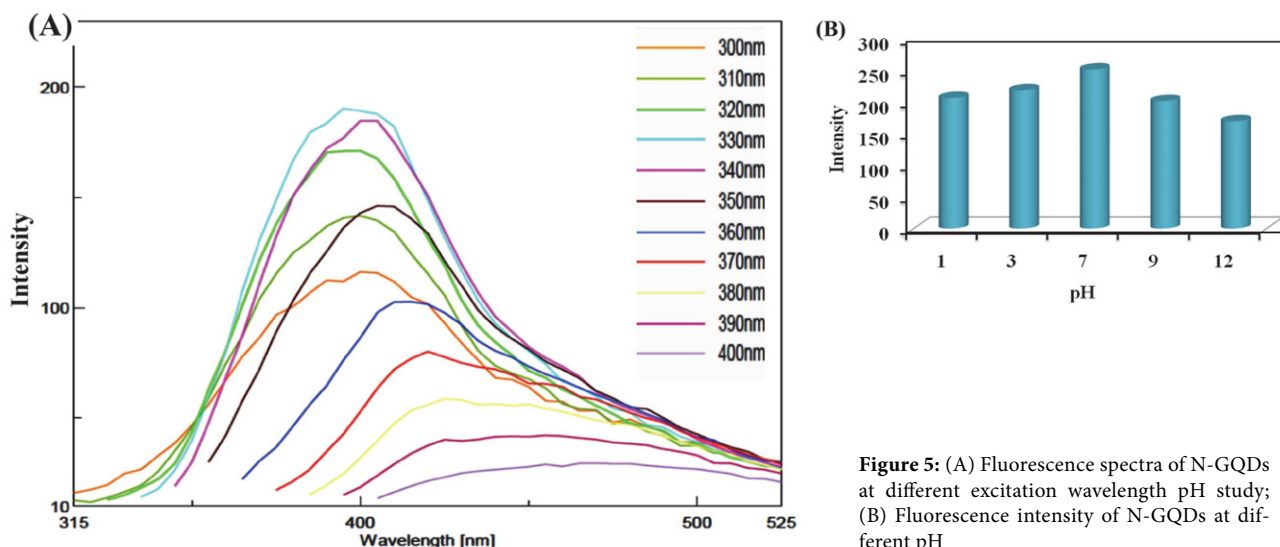


Figure 5: (A) Fluorescence spectra of N-GQDs at different excitation wavelength pH study; (B) Fluorescence intensity of N-GQDs at different pH

thesized N-GQDs were dispersed in a solution of varying pH mainly 1, 3, 7, 9, and 12. The N-GQDs fluorescence intensity was gradually increased with increment in pH of N-GQDs. As a result, the synthesized N-GQDs show the highest fluorescence intensity at neutral pH. On contrary, the fluorescence intensity of N-GQDs was decreased at pH 9 and 12.²⁹ Therefore, neutral pH was selected for further sensing study of UA. Importantly, the protonation state of N-GQDs could influence fluorescence intensity. In brief, owing to protonation or deprotonation of N-GQDs containing amide and carboxylic functional groups, it gives a carbene-like triplet state that causes changes in photoluminescence.^{30–32} The change in pH from 1 to 7 resulted in a high degree of deprotonation of N-GQDs. Subsequently, it generates the deprotonated oxygen atoms and nitrogen atoms on the N-GQDs surface that facilitated the alteration in electron distribution. Hence, the present N-GQDs mediated sensor shows a high fluorescence intensity at the physiological range.³² At neutral pH, the Quantum yield (QY) of synthesized N-GQDs was found to be 23.78%. Figure 4B concludes that the neutral pH (7) has the highest fluorescence intensity as compared to acidic pH (1, 3) and basic pH (9, 12).

3. 3. Detection of UA using N-GQDs

The fluorescence quenching of N-GQDs was studied by adding different concentrations of UA at 25 °C (Figure 6A). The fluorescence of N-GQDs was observed in the UV cabinet shown in Figure 6B (i and ii). In this study, the fluorescence of N-GQDs (i) gets quenched after UA addition (ii). To study the sensitivity of N-GQDs for UA detection, different concentrations of UA were added to the aqueous solution of N-GQDs followed by measurement of fluorescence intensities. When UA with concentrations ranging from 10 μM to 1000 μM was added to the as-prepared N-GQDs, the fluorescence intensity of N-GQDs was grad-

ually decreased at 245 nm. It presents the relationship of the fluorescent quenching value $\Delta F = F_0 - F^*100$ (F_0 and F are the fluorescence intensities of N-GQDs at 400 nm in the absence and presence of UA, respectively) in varying concentrations of UA (Figure 6C and D). As a result, the ΔF has a good linear relationship with the concentration of UA in the range of 10 μM to 50 μM and 60 μM to 100 μM wherein the linear regression equation was found to be $y = 0.337x + 2.614$ [$R^2 = 0.989$, CI: (0.202, 0.472)] and $y = 0.300x + 8.947$ [$R^2 = 0.981$, CI: (0.165, 0.435)], respectively at 95% of confidence level. It shows both static and dynamic fluorescence quenching in presence of UA³³. The lowest detection limit of 401.72 ± 0.04 pM ($n = 3$) was obtained based on a $3.3 \sigma/\text{Slope}$ (σ : Standard deviation). The comparison of different sensors for the detection of UA is depicted in Table 1. The limit of quantification was found to be 1.217 ± 12 nM, which was calculated based on $10^* \sigma/\text{Slope}$. The precision of the sensor was measured based on intraday ($n = 6$) and interday ($n = 6$) analysis of UA concentration. The percent relative standard deviation (% RSD) was found to be 0.901% and 2.547% for intraday and interday, respectively assuring the high precision for sensing of UA. Importantly, at neutral pH, the fluorescence of N-GQDs was gets quenched sensitively in the existence of UA. It may be because of different possible mechanisms such as static quenching, electron transfer, and an inner filter effect mechanism. Notably, the N-GQDs were exhibited as hydrophilic which may be due to the continuation of surface nitrogen, oxygen functionality. This hydrophilic surface can facilitate the better accessibility of interest analytes in the aqueous media to the 'C' surface. Particularly, it may be because of high surface coverage, and more efficient adsorption ability towards interest analyte. This mechanism can alter the surface ion interaction at the edge or on the basal plane of N-GQDs by the modification of surface charge properties. Besides, the occurrence of oxygen functionalities in N-GQDs offers more interaction among the

analyte and carbon surface of N-GQDs.¹⁶ Literature survey divulged that nitrogen doping on nanomaterials surface could change the electrical conductivity and alter the band-gap. Additionally, it can produce electronic defects that can increase the charge transfer ability of nanomaterials. Accordingly, it gives good sensitivity and stability.³⁴ Herein, doping of nitrogen into GQDs shows high electronegativity and it can transfer lone pair of an electron to electron-deficient molecules.³⁵ In the present investigation, N-GQDs can transfer two electrons to UA which shows the quenching of fluorescence of N-GQDs.³⁶ Overall, it is notable that the doping of nitrogen not only enhanced the QY but also improves the chelation ability like oxygen functional groups with the presence of a target marker such as UA that offers the effectual quenching of fluorescence.¹⁴ Taken as a whole, modification of chemical and electronic properties by nitrogen doping into GQDs shows the boosted fluorescence presentation for UA.³³ Herein, more research is necessary to comprehend the quenching mechanics of N-GQDs. For further study, optimizing the doping of nitrogen in the structure of GQDs is essential in N-GQDs-based fluorescent nanosensors for monitoring an analyte.

3. 4. Interference Study

To estimate the selectivity of the proposed method for the determination of UA, the effects of some common metal ions and biomolecules such as NaCl, KCl, CaCl₂, AgNO₃, lysine, glycine, alanine, glucose, sucrose, and lactose were investigated in triplicates, individually (n = 3). Figure 7 shows the selectivity of N-GQDs towards different interfering substances in presence of the different interfering substances. Herein, common ions and biomolecules had little effect (or slight quenching effect) on the fluorescence of N-GQDs, which was considered to be tolerable. It may be due to available active sites in metal ions and biomolecules that get co-interacted with functionality present on the surface of N-GQDs. Importantly, slight N-GQDs fluorescence quenching effect of different interfering substances was observed that assured the low affinity of N-GQDs towards the selected metal ions and biomolecules.⁴⁴ In addition, the fluorescent color alters of N-GQDs upon adding the common ions and biomolecules can be examined by the naked eye below the UV lamp. Moreover, a mixture of numerous metal ions and biomolecules (sample A) had no obvious interference in the de-

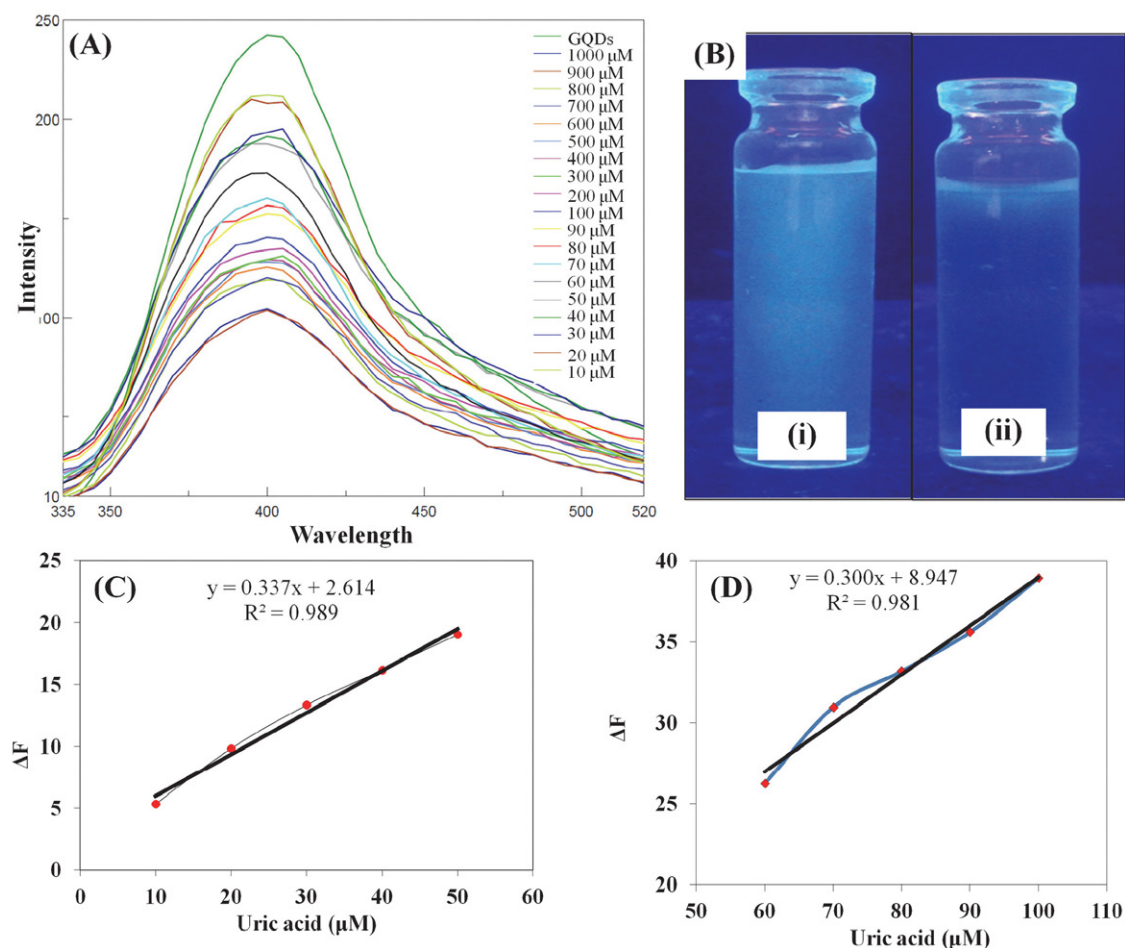


Figure 6: (A) Fluorescence spectra of N-GQDs with different concentrations of UA; (B) Fluorescence of N-GQDs before (i) and after addition of UA (ii); Fluorescence quenching linearity curve [ΔF vs UA concentration ranging from 10 μM to 50 μM (C) and (D) 60 μM to 100 μM , n = 3].

Table 1: Summary of different types of sensors for detection of UA

Sr. No.	Composite	Sensor type	Linearity range	Limit of detection	Ref.
1.	Citrate-capped -PtNPs	Colorimetric	0 mM to 8 mM	4.2 μM	37
2.	Poly(dipicolinic acid)/SiO ₂ @Fe ₃ O ₄	Electrochemical	1.2 μM to 1.8 μM	0.4 μM	38
3.	CNCo/GCE	Electrochemical	2 μM to 110 μM	0.83 μM	39
4.	MoS ₂	Electrochemical	10 μM to 400 μM	1.169 μM	40
5.	ZnNi@f-MWCNT	Electrochemical	0.2 mM to 1.1 mM	0.51 μM	41
6.	r-GO/AuNPs	Electrochemical	10 to 500 $\mu\text{mol dm}^{-3}$	3.6 μM	42
7.	Cu ²⁺ @MIL-91(Al:Eu)	Optical	10 μM to 1200 μM	1.6 μM	43
8.	N-GQDs	Optical	10 μM to 100 μM	401.72 \pm 0.04 pM	Present work

tection of UA. These results demonstrate that the method possesses a good selectivity for the determination of UA. Overall, N-GQDs could be a promising biosensing stage for UA detection in complex samples. The repeatability of the proposed N-GQDs based fluorescent sensor was performed ($n = 6$) for detection of UA. As a result, it provides the %RSD of 0.802 that confirmed the repeatability of a proposed sensor for the detection of UA. Table 3 shows the summary of analytical characteristics of the N-GQDs based fluorescent biosensor for the determination of UA.

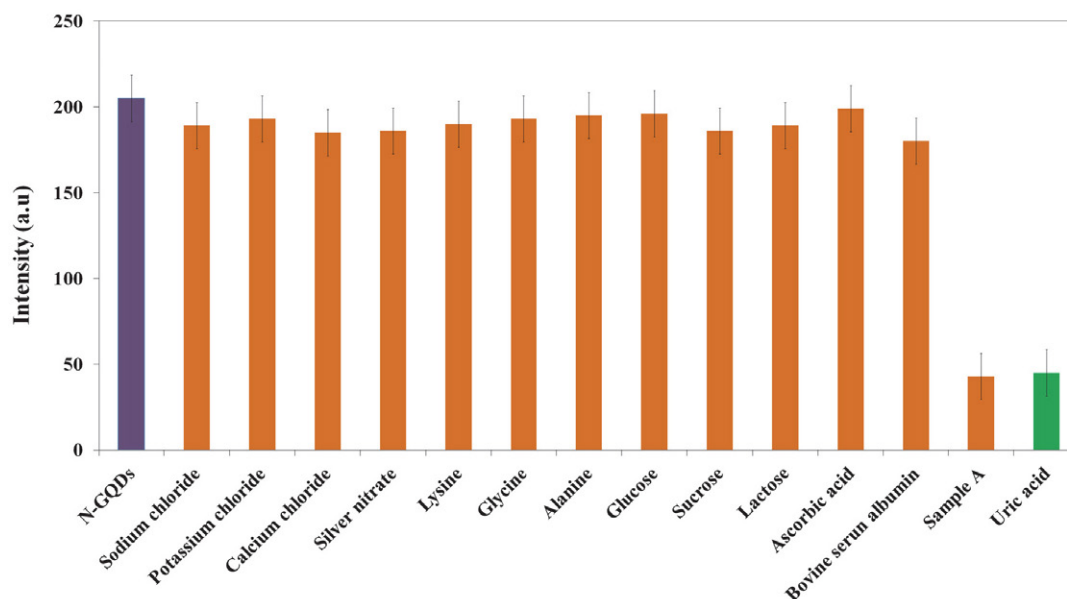
4. Conclusion

In conclusion, a novel, extremely sensitive, and efficient label-free fluorescence sensing substrate has been developed using N-GQDs. Compared to methods reported in previous studies for N-GQDs synthesis, we have reported a single step, facile, and green synthesis method, which is more economical and less time-consuming. As a result, the prepared N-GQDs were demonstrated excel-

Table 3: Analytical characteristics of the N-GQDs based fluorescent biosensor for determination of UA.

Analytical parameters	Uric acid
	10 μM to 50 μM
	$y = 0.337x + 2.614$
	$[R^2 = 0.989, \text{CI}: (0.202, 0.472)]$
	60 μM to 100 μM
	$y = 0.300x + 8.947$
	$[R^2 = 0.981, \text{CI}: (0.165, 0.435)]$
Limit of detection (n = 3)	401.72 \pm 0.041 pM
Limit of quantification (n = 3)	1.217 \pm 12 nM
Precision (% RSD)	
Intraday analysis (n = 6)	0.901 %
Interday analysis (n = 6)	2.547 %
Repeatability (RSD, n = 6)	0.802 %

lent optical properties and graphene structure. The as-synthesized N-GQDs emitted strong blue color fluorescence and showed good stability at neutral pH. Afterward, the prepared N-GQDs were utilized for fluorescence detection

**Figure 7:** Fluorescence intensity ($n = 3$) in presence of different ions and biomolecules

of UA. Owing to synergistic static quenching, electron transfer, and inner filter effect mechanisms, the fluorescent N-GQDs nanoprobe exhibited high sensitive detection of UA upto 401.72 ± 0.04 pM. Under the optimum condition, it shows a wide linear response and high selectivity in presence of numerous interfering agents. For further development, there is a major need to control on doping of nitrogen in the structure of GQDs. In a nutshell, N-GQDs can be synthesized from different kinds of waste materials, which are existed in nature. In the upcoming days, the proposed N-GQDs based fluorescent nanoprobe can be used for the determination of UA and other biomarkers in human plasma and urine samples.

Declaration of interest

The authors declare no conflict of interest.

Acknowledgment

Authors are thankful to H. R. Patel Institute of Pharmaceutical Education and Research, Shirpur and Sophisticated Test and Instrumentation Center (STIC), Cochin (Kerala), India, for providing necessary facilities.

5. References

- J. Du, R. Yue, Z. Yao, F. Jiang, Y. Du, P. Yang and C. Wang, *Colloids Surf A: Physicochem Eng Asp* **2013**, *419*, 94–99
DOI:10.1016/j.colsurfa.2012.11.060
- M. Alam, A. M. Asiri, M. Uddin, M. Islam, M. R. Awual and M. M. Rahman, *New J Chem* **2019**, *43*, 8651–8659.
DOI:10.1039/C9NJ01287G
- N. Chauhan and C. S. Pundir, *Anal Biochem* **2011**, *413*, 97–103. DOI:10.1016/j.ab.2011.02.007
- Y. Saito, A. Tanaka, K. Node and Y. Kobayashi, *J Cardiol* **2020**, *78*, 51–57. DOI:10.1016/j.jcc.2020.12.013
- H. Liu, X. Li, M. Wang, X. Chen and X. Su, *Analytica chimica acta* **2017**, *990*, 150–156. DOI:10.1016/j.aca.2017.07.031
- A. Vernerová, L. K. Krčmová, B. Melichar and F. Švec, *Clin Chem Lab Med (CCLM)* **2020**, *59*, 797–812.
DOI:10.1515/cclm-2020-1533
- K. Shi and K. K. Shiu, *Electroanalysis: An International Journal Devoted to Fundamental and Practical Aspects of Electroanalysis* **2001**, *13*, 1319–1325. DOI:10.1002/1521-4109(200111)13:16<1319::AID-ELAN1319>3.0.CO;2-C
- J. Lu, Y. Xiong, C. Liao and F. Ye, *Anal Methods* **2015**, *7*, 9894–9899. DOI:10.1039/C5AY02240A
- Q. Li, Y. Qiu, W. Han, Y. Zheng, X. Wang, D. Xiao, M. Mao and Q. Li, *RSC Adv* **2018**, *8*, 25808–25814.
DOI:10.1039/C7RA12702B
- R. S. Tade, S. N. Nangare, A. G. Patil, A. Pandey, P. K. Deshmukh, D. R. Patil, T. N. Agrawal, S. Mutalik, A. M. Patil and M. P. More, *Nanotechnology* **2020**, *31*, 292001.
DOI:10.1088/1361-6528/ab803e
- L. Ding, H. He, J. Zhou, D. Wang, Q. Nian, S. Li, S. Qian, W. Li, C. Liu, Z. Liang, *Nanotechnology* **2021**, *32*(13), 135501.
DOI:10.1088/1361-6528/abd12a
- M. W. Abbas, R. A. Soomro, N. H. Kalwar, M. Zahoor, A. Avci, E. Pehlivan, K. R. Hallam, M. Willander, *Microchem J* **2019**, *146*, 517–524. DOI:10.1016/j.microc.2019.01.034
- R. S. Tade and P. O. Patil, *ACS Biomater Sci Eng* **2020**, *6*, 5987–6008. DOI:10.1021/acsbomaterials.0c01045
- J. Ju, R. Zhang, S. He and W. Chen, *Rsc Adv* **2014**, *4*, 52583–52589. DOI:10.1039/C4RA10601F
- K. Kunpatee, S. Traipop, O. Chailapakul, S. Chuanuwatanakul, *Sensors and Actuators B: Chemical* **2020**, *314*, 128059.
DOI:10.1016/j.snb.2020.128059
- S. Gu, C.-T. Hsieh, Y.-Y. Tsai, Y. Ashraf Gandomi, S. Yeom, K. D. Kihm, C.-C. Fu and R.-S. Juang, *ACS Appl Nano Mater* **2019**, *2*, 790–798. DOI:10.1021/acsnm.8b02010
- M. Kaur, M. Kaur and V. K. Sharma, *Adv Colloid Interface Sci* **2018**, *259*, 44–64. DOI:10.1016/j.cis.2018.07.001
- Y. Li, Y. Zhao, H. Cheng, Y. Hu, G. Shi, L. Dai and L. Qu, *J Am Chem Soc* **2012**, *134*, 15–18. DOI:10.1021/ja206030c
- G. S. Kumar, R. Roy, D. Sen, U. K. Ghorai, R. Thapa, N. Mazumder, S. Saha and K. K. Chattopadhyay, *Nanoscale* **2014**, *6*, 3384–3391. DOI:10.1039/c3nr05376h
- F. Lu, Y.-h. Zhou, L.-h. Wu, J. Qian, S. Cao, Y.-f. Deng and Y. Chen, *Int J Opt* **2019**, *2019*. DOI:10.1155/2019/8724320
- Y. Yang, X. Xiao, X. Xing, Z. Wang, T. Zou, Z. Wang, R. Zhao and Y. Wang, *Mater Res Express* **2019**, *6*, 095615.
DOI:10.1088/2053-1591/ab3006
- F. Yang, W. Bao, T. Liu, B. Zhang, S. Huang, W. Yang, Y. Li, N. Li, C. Wang and C. Pan, *Microchim Acta* **2020**, *187*, 1–10.
DOI:10.1007/s00604-020-04294-8
- H. M. Kashani, T. Madrakian and A. Afkhami, *New J Chem* **2017**, *41*, 6875–6882. DOI:10.1039/C7NJ00262A
- S.-H. Song, M. Jang, H. Yoon, Y.-H. Cho, S. Jeon, B.-H. Kim, *RSC Adv* **2016**, *6*(100), 97990–97994.
DOI:10.1039/C6RA21651J
- J. Yu, C. Xu, Z. Tian, Y. Lin and Z. Shi, *New J Chem* **2016**, *40*, 2083–2088. DOI:10.1039/C5NJ03252K
- Z. Yan, X. Qu, Q. Niu, C. Tian, C. Fan and B. Ye, *Anal Methods* **2016**, *8*, 1565–1571. DOI:10.1039/C5AY03208C
- J. Ju, S. Regmi, A. Fu, S. Lim and Q. Liu, *J Biophotonics* **2019**, *12*, e201800367. DOI:10.1002/jbio.201800367
- J. Soleymani, M. Hasanzadeh, M. H. Somi, S. A. Ozkan and A. Jouyban, *Int J Biol Macromol* **2018**, *118*, 1021–1034.
DOI:10.1016/j.ijbiomac.2018.06.183
- M. Aghelifar, S. Kimiagar, *Phy Chem Res.* **2018**, *6*(2), 237–250.
- N. R. Mohanty, Kansas State University, **2011**. Web:https://krex.k-state.edu/dspace/handle/2097/9264
- Q. Li, B. Chen and B. Xing, *Environ Sci Technol* **2017**, *51*, 1364–1376. DOI:10.1021/acs.est.6b04178
- B. Shi, L. Zhang, C. Lan, J. Zhao, Y. Su, and S. Zhao, *Talanta* **2015**, *142*, 131–139. DOI:10.1016/j.talanta.2015.04.059
- J. Ju, and W. Chen, *Biosens Bioelectron* **2014**, *58*, 219–225.
DOI:10.1016/j.bios.2014.02.061
- K. Jindal, M. Tomar and V. Gupta, *Analyst* **2013**, *138*, 4353–4362. DOI:10.1039/c3an36695b

35. L. Zhao, H. Li, Y. Xu, H. Liu, T. Zhou, N. Huang, Y. Li, and L. Ding, *Anal Bioanal Chem* **2018**, 410(18), 4301–4309. DOI:10.1007/s00216-018-1079-6
36. T. S. Thanh, P. T. Qui, N. T. T. Tu, T. T. T. Toan, T. T. B. Hoa, L. V. T. Son, D. M. Nguyen, T. N. Tuyen, and D.Q. Khieu, *J Nanomater* **2021**, 2021. DOI:10.1155/2021/9914062
37. M. Ali, M. A. U. Khalid, I. Shah, S. W. Kim, Y. S. Kim, J. H. Lim, and K. H. Choi, *New J Chem* **2019**, 43(20), 7636–7645. DOI:10.1039/C9NJ01257E
38. Y. V. M. Reddy, B. Sravani, S. Agarwal, V. K. Gupta, and G. Madhavi, *J Electroanal Chem* **2018**, 820, 168–175. DOI:10.1016/j.jelechem.2018.04.059
39. L. Liu, L. Liu, Y. Wang, and B.-C. Ye, *Talanta* **2019**, 199, 478–484. DOI:10.1016/j.talanta.2019.03.008
40. R. Sha, N. Vishnu, and S. Badhulika, *Sens Actuators B Chem* **2019**, 279, 53–60. DOI:10.1016/j.snb.2018.09.106
41. A. Savk, B. Özdil, B. Demirkan, M. S. Nas, M. H. Calimli, M. H. Alma, A. M. Asiri, and F. Şen, *Mater Sci Eng C* **2019**, 99, 248–254. DOI:10.1016/j.msec.2019.01.113
42. F. Mazzara, B. Patella, G. Aiello, A. O’Riordan, C. Torino, A. Vilasi, and R. Inguanta, *Electrochim Acta* **2021**, 388, 138652. DOI:10.1016/j.electacta.2021.138652
43. X. Lian, and B. Yan, *Inorg.Chem.* **2017**, 56(12), 6802–6808. DOI:10.1021/acs.inorgchem.6b03009
44. Y. Wang, S. Zhao, M. Li, W. Li, Y. Zhao, J. Qi, and X. Cui, *J Electroanal Chem* **2017**, 797, 113–120. DOI:10.1016/j.jelechem.2017.05.031

Povzetek

Zelene sintetizirane grafenske kvantne pike (GQD) smo dopirali z dušikom, da bi povečali njihove optične značilnosti in sektorje uporabe. V tej preiskavi so bili modri luminiscentni GQD, dopirani z dušikom (N-GQD), sintetizirani z enostopenjsko hidrotermalno sintezo z uporabo prahu lupine tamarinda kot prekursorja. Ugotovljeno je bilo, da sta velikost delcev in zeta potencial N-GQD 11,40 nm in $-35,53$ mV. Kvantni izkoristek do 23,78 % je bil dosežen pri valovni dolžini vzbujanja 330 nm pri nevtralnem pH. Fluorescenca se občutljivo zniža v prisotnosti sečne kisline (UA) na podlagi treh mehanizmov: statično dušenje fluorescence, prenos elektronov in mehanizem učinka notranjega filtra. Za UA smo dobili linearno območje od $10 \mu\text{M}$ do $100 \mu\text{M}$ z mejo detekcije (LOD) $401,72 \pm 0,04$ pM. Poleg tega so bili N-GQD selektivni proti UA v prisotnosti kovinskih ionov in biomolekul, kar kaže na njihovo potencialno uporabo za spremljanje UA v kliničnih vzorcih. Skratka, to delo dokazuje, da imajo N-GQD kot zaznavna sonda za prepoznavanje UA določene prednosti pred ostalimi metodami, kot je enostavnost, hitrost analize, pa tudi z družbenoekonomskih aspektov. V prihodnosti je mogoče razcito metodologijo potencialno uporabiti za odkrivanje UA v kliničnih vzorcih.



Except when otherwise noted, articles in this journal are published under the terms and conditions of the Creative Commons Attribution 4.0 International License

Scientific paper

Optimisation of Amphiphilic-Polymer Coatings for Improved Chemical Stability of NaYF₄-based Upconverting Nanoparticles

Tina Černič,^{1,2} Monika Koren,^{3,4} Boris Majaron,^{3,4} Maja Ponikvar-Svet⁵ and Darja Lisjak^{1,*}

¹ Jožef Stefan Institute, Department for Materials Synthesis, Ljubljana, Slovenia

² Jožef Stefan International Postgraduate School, Ljubljana, Slovenia

³ Jožef Stefan Institute, Department of Complex Matter, Ljubljana, Slovenia

⁴ Faculty of Physics and Mathematics, University of Ljubljana, Slovenia

⁵ Jožef Stefan Institute, Department of Inorganic Chemistry and Technology, Ljubljana, Slovenia

* Corresponding author: E-mail: darja.lisjak@ijs.si
+386 1 4773879

Received: 12-20-2021

Abstract

NaYF₄ nanoparticles codoped with Yb³⁺ and Tm³⁺ exhibit upconversion fluorescence in near-infrared and visible spectral range. Consequently, such upconverting nanoparticles (UCNPs) can be used as contrast agents in medical diagnostics and bioassays. However, they are not chemically stable in aqueous dispersions, especially in phosphate solutions. Protective amphiphilic-polymer coatings based on poly(maleic anhydride-*alt*-octadec-1-ene) (PMAO) and bis(hexamethylene)tri-amine (BHMT) were optimised to improve the chemical stability of UCNPs under simulated physiological conditions. Morphologies of the bare and coated UCNPs was inspected with transmission electron microscopy. All samples showed intense UC fluorescence at ~800 nm, typical for Tm³⁺. The colloidal stability of aqueous dispersions of bare and coated UCNPs was assessed by dynamic light scattering and measurements of zeta potential. The dissolution of UCNP in phosphate-buffered saline at 37 °C, was assessed potentiometrically by measuring the concentration of the dissolved fluoride. Protection against the dissolution of UCNPs was achieved by PMAO and PMAO crosslinked with BHMT.

Keywords: Nanoparticles; upconversion; dissolution; chemical stability; coatings

1. Introduction

Upconverting nanoparticles (UCNPs) show great potential for various applications in biomedicine as multimodal contrast agents in bioimaging and bioanalysis, nanothermometry, biosensorics and nanotheranostics.^{1–4} These applications are based on the UC fluorescence of visible or near-infrared (NIR) light. The sensitising Yb³⁺ ions are excited with NIR light around 980 nm, and the absorbed energy is transferred to the activator Er³⁺, Yb³⁺ or Ho³⁺ ions emitting light with lower wavelengths.⁵ The NIR emission of Tm³⁺ around 808 nm is of particular interest for biomedicine, due to its deeper penetration in bi-

ological tissues compared to visible or ultraviolet light. To achieve a high quantum yield of UC fluorescence, fluoride crystalline matrices are preferred to incorporate lanthanide dopants. One of such matrices is β-NaYF₄ with hexagonal structure, where Na⁺ and Y³⁺ occupy two different sites among the close-packed F⁻ ions.⁶

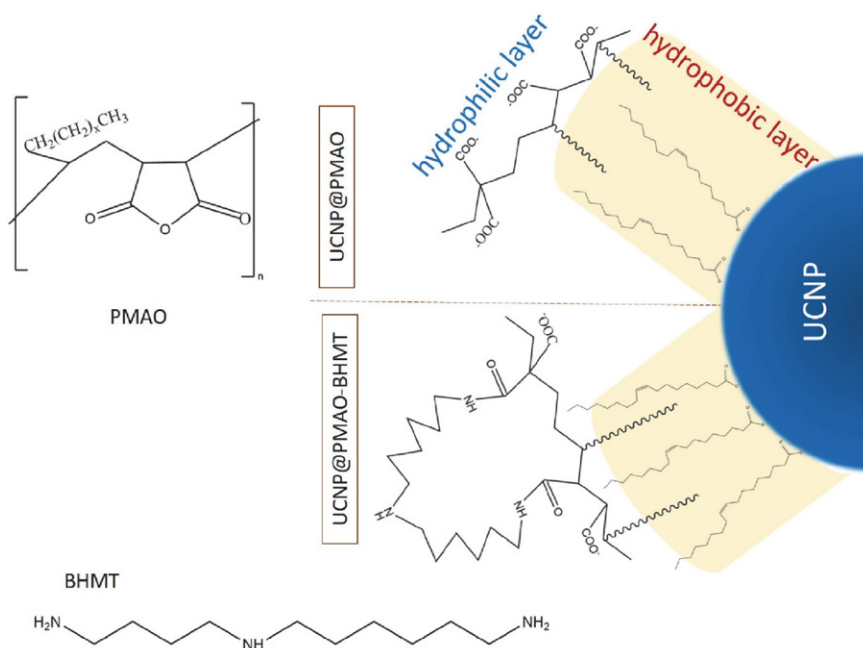
The first condition for practical application of any nanoparticles is their chemical and colloidal stability, which strongly depends on their surface chemistry and surrounding medium. Nanoparticles are prone to fast surface reactions, dissolution and severe agglomeration due to their large surface area. Specifically, UCNPs intended for biomedicine must be stable in aqueous media, includ-

ing physiological buffers. The colloidal stability of nanoparticles is achieved by optimising their surface chemistry to induce: (i) electrostatic repulsion by tuning the surface charge or/and (ii) steric repulsion with large molecules (e.g., polymers). The chemical and colloidal stability of nanoparticles becomes more challenging with the increasing complexity of the aqueous media. The primary origin of the colloidal destabilisation of nanoparticles in physiological buffers is high ionic strength that decreases the repulsive electrostatic energy between the nanoparticles, which is otherwise sufficiently high in pure water. Additionally, the colloidal destabilisation of nanoparticles in complex aqueous media can also be induced by the exchange of the stabilising surface ligands with species having a higher affinity towards the surface metal ions but lower surface charge. Similarly, the dissolution of nanoparticles can be promoted when the exchanging species bond more strongly with the surface ions than the latter are bonded with the crystalline core. For example, the fluoride-based UCNP dissolve in phosphate solutions (e.g., in phosphate-buffered saline; PBS) due to strong interaction between the surface rare-earth ions and dissolved phosphate ions, thus inducing the coprecipitation of highly stable rare-earth phosphates.⁷ Any dissolution of fluoride-based UCNP *in vivo* can cause various adverse effects^{4,8–11} which questions their suitability for applications in biomedicine. The protection of fluoride-based UCNP against the dissolution and interaction with solutes from the surrounding media is necessary also to ensure stable optical properties. It was shown that even a minor dissolution of the NaYF₄-UCNP deteriorates their

UC fluorescence properties,^{12–15} limiting their general applicability.

Possible protective coatings against the dissolution of the NaYF₄-based UCNP in aqueous media were studied in the last few years, starting from silica and phosphonates to more complex polymer coatings.^{15–21} Most of these coatings decelerated the dissolution of the UCNP in water or PBS at room temperature. However, only thick microporous silica coating and amphiphilic poly(maleic anhydride-*alt*-octadec-1-ene) crosslinked with bis(hexamethylene)tri-amine (PMAO-BHMT) coating significantly suppressed the dissolution of NaYF₄-UCNP in PBS at body temperature. Under the same conditions, bare UCNP almost completely disintegrated.^{16,20} Such a high protective efficiency of the thick silica coatings was attributed to the mechanical barrier for the diffusion of aqueous molecules and solute ions to/from the UCNP surface. Alternatively, the protection of UCNP by the PMAO-BHMT was attributed to the coating stability, achieved by crosslinking PMAO with BHMT at the UCNP surfaces.

This study focuses on amphiphilic coatings since they have been recognised as a suitable strategy towards biocompatible inorganic NPs.²² We hypothesise that a hydrophobic surface layer from an amphiphilic polymer can form an effective diffusion barrier and suppresses the dissolution of UCNP. We coated Yb³⁺,Tm³⁺-codoped β -NaYF₄ with different surface fractions of amphiphilic PMAO or PMAO additionally crosslinked with BHMT (PMAO-BHMT, Scheme 1). We compared the colloidal and chemical stability of differently coated UCNP in aqueous media.



Scheme 1. Chemical formulae of poly(maleic anhydride-*alt*-octadec-1-ene) (PMAO) and bis(hexamethylene)tri-amine (BHMT) with a schematic presentation of the PMAO (top) and PMAO-BHMT (bottom) coating on an upconverting nanoparticle (UCNP). The inner layer of the coating (yellow) is hydrophobic, while the outer layer is hydrophilic.

2. Experimental

2.1. Chemicals

Unless otherwise specified, chemicals were used as received. Deionised water was used in all experiments. Ammonium fluoride (98.0%), yttrium(III) chloride hydrate (99.99%), ytterbium(III) chloride hydrate (99.9%), thulium(III) chloride hydrate (99.9%), 1-octadecene (tech. 90%) and oleic acid (tech. 90%) were purchased from Alfa Aesar. The concentration of rare earths in chlorides were determined with an inductively-coupled optical emission spectrometer (ICP-OES, Agilent 720). Poly(maleic anhydride-*alt*-1-octadecene) (PMAO, M_n 30000–50000), bis(hexamethylene)triamine (BHMT, high purity), sodium hydroxide (≥98%) and chloroform (≥99.8%) were purchased from Sigma Aldrich. Acetone (≥99.8%) and absolute ethanol (≥99.9%) were purchased from Carlo Erba Reagents, while methanol (100%) was purchased from VWR Chemicals. Phosphate-buffered saline (PBS, 10x) was purchased from Alfa Aesar and diluted 10-times before usage to mimic blood's pH and ionic strength.

2.2. Materials

β -NaYF₄ upconverting nanoparticles codoped with Yb³⁺ and Tm³⁺ (named shortly as UCNPs in the subsequent text) with nominal composition NaY_{0.78}Yb_{0.20}Tm_{0.02}F₄ were synthesised with a high-temperature coprecipitation, similarly as reported previously.^{23,24} In short, lanthanide

chlorides (2 mmol) in the stoichiometric ratio were mixed with 12 ml of oleic acid and 30 ml of 1-octadecene in a 100 ml three-neck flask and heated to 156 °C for 30 min. After that, the solution was cooled down to 70 °C, and 10 ml methanol solution of NH₄F (8 mmol) and NaOH (5 mmol) was slowly added. The mixture was stirred for 40 min at 50 °C until methanol evaporated. After that, the solution was heated to 300 °C under an argon atmosphere for 1.5 h. When the reaction solution cooled down to room temperature, acetone was added to sediment the UCNPs. UCNPs were washed several times with ethanol and deionised water, centrifuged (3016 rcf for 5 min), and finally dispersed in chloroform. Three UCNPs batches were distinguished by the average particle diameter (Table 1 and Figure S1 in Supporting Information).

The UCNPs were coated with poly(maleic anhydride-*alt*-octadec-1-ene) (PMAO) and subsequently cross-linked with bis(hexamethylene)triamine (BHMT) by optimising the procedure from Ref.²⁵. In short, as-synthesised UCNPs in chloroform were diluted to a concentration of 0.1 mg/ml. The nominal fraction of the PMAO monomer units per UCNPs' surface varied between $n = 7$ –300 MAO/nm². First, a chloroform solution of PMAO polymer (100 mg/ml) was admixed to the diluted UCNPs dispersion in a 50-ml flask and stirred for 2 h. Then chloroform solution of BHMT (50 mg/ml) was added with the ratio of 0.5–30 BHMT molecules/nm² (i.e., MAO:BHMT = 10:1) and mixed for 30 min. After mixing, chloroform was evaporated using a rotary evaporator. The solid residual was re-dis-

Table 1. Selected samples used in specific comparative studies

Coated polymer	Nominal MAO fraction (no./nm ²)	Sample name UCNPs@...	Average equivalent diameter of the core UCNPs (nm)	Comparative study
PMAO-BHMT	300	PB-300	69 ± 3	DLS: Effect of the polymer nominal fraction on the colloidal stability
	105	PB-105	52 ± 2	
	20	PB-20	52 ± 2	
	7	PB-7	52 ± 2	
PMAO	210	P-210	52 ± 2	DLS: Long-term colloidal stability (4 months)
	105	P-105	52 ± 2	
	20	P-20	52 ± 2	
	7	P-7	52 ± 2	
PMAO-BHMT	150	PB-150	67 ± 5	Chemical stability: dissolution in PBS at physiological conditions
	105	PB-105	52 ± 2	
	20	PB-20	52 ± 2	
	7	PB-7	52 ± 2	
PMAO	150	P-150	67 ± 5	
	105	P-105	52 ± 2	
	20	P-20	52 ± 2	
	7	P-7	52 ± 2	

persed in 20 ml of water with 0.5 ml of 1M NaOH and sonicated for 30 min. The dispersion was first filtered with 0.45 μm pore size filters and later centrifuged (15294 rcf for 30 min). The sedimented coated UCNPs were dispersed in deionised water. The samples were labelled as UCNPs@PB-*n*.

An additional set of samples was prepared by coating the UCNPs with PMAO omitting the crosslinking with BHMT. All other parameters were kept the same as above. These samples are labelled as UCNPs@P-*n*.

Firstly, we determined the optimal concentration of as-synthesised UCNPs for the coating procedure, which was 0.1 mg/ml. Secondly, we identified a side reaction when the polymers were used in too large excess. In such a case, the polymers also precipitated homogeneously, not only on the UCNPs surfaces. Therefore, we were lowering the nominal surface density of PMAO from approximately 300 MAO/nm² (as in Ref.²⁵) down to 7 MAO/nm². This optimisation step was done for both types of coatings, UCNPs@PB-*n* and UCNPs@P-*n*. A list of the coated samples used in different comparative studies is given in Table 1.

For comparison, a batch of bare UCNPs was prepared by stripping the surface oleate ligands from the as-synthesised UCNPs. The process was done with a known procedure in conc. HCl.²⁶

2. 3. Characterisation

As-synthesised and polymer-coated UCNPs were analysed with a transmission electron microscope (TEM, Jeol 2100). Size distribution of the as-synthesised UCNPs was determined from their surface area as an equivalent diameter using the DigitalMicrograph software (Gatan Inc.). A minimum of 250 particles per sample were accounted for statistics. The crystalline structure of the as-synthesised UCNPs was verified with an X-ray diffractometer (XRD, PANalytical X'Pert pro) using CuK_{α1} irradiation. The UC fluorescence emission of the UCNPs dispersions was induced with a focused beam from a diode laser emitting 2 W of light at 980 ± 2 nm, and analysed using a compact diffraction spectrometer (Ocean FX Vis-NIR, Ocean Optics) in the 400–900 nm spectral range. Zeta-potential behaviour vs pH was measured in 0.1 mg/ml aqueous dispersions of bare and coated UCNPs with Anton Paar Litesizer™ 500. The pH value was adjusted with 0.1 or 1 M solutions of HCl or NaOH. Hydrodynamic sizes of these aqueous dispersions were measured with dynamic light scattering (DLS, Fritsch, Analysette 12 DynaSizer). The presented results are statistical averages from five measurements with a time interval of 30 s. DLS and zeta potential were also measured in the dispersions of coated UCNPs (0.1 mg/ml) in PBS (both with Litesizer™ 500, Anton Paar).

2. 4. Chemical Stability Studies

Bare and polymer-coated UCNPs were aged under physiological conditions for 3 days. Aqueous dispersions

of all samples were filtered beforehand (see Materials Section) to eliminate any potential aggregates that could affect the results. 0.1 mg/ml of bare or coated UCNPs were dispersed in PBS and aged in a thermostatic water bath at 37 °C for 3 days. For comparison, selected samples were also aged at a concentration of 5 $\mu\text{g}/\text{ml}$. After 3 days, the dispersions were cooled to room temperature. The solid fraction was sedimented in a centrifuge (3016 rcf for 5min). For complete removal of the smallest nanoparticles, the supernatant was subsequently ultrafiltered through a 30-kDa membrane. The dissolved fluoride was determined in the filtrates potentiometrically with Orion 960 Autochemistry System, equipped with a temperature sensor and a ion-selective electrode (ISE, Orion 96-09).²⁷ Three samples were analysed per batch, each one at least in duplicate. For comparison with previous studies, the dissolved fluoride was expressed as the molar fraction of the released fluoride (X_{F}), calculated by considering the nominal chemical composition of the as-synthesised NPs (Eq. S1 in Supporting Information).

3. Results and Discussion

3. 1. UCNPs with Amphiphilic Polymer Coatings

All as-synthesized UCNPs have the typical shape of hexagonal discs, resulting from their hexagonal crystal structure (Figure 1). Most of the UCNPs lie flat on the sample support, while some are oriented perpendicularly (encircled in Figure 1a), showing that their thickness is approximately one half of their diameter. The UCNPs were relatively homogenous in size; however, the average sizes (i.e., diameters) varied between different synthesis batches (Figure S1 in Supporting Information). Therefore, all direct comparisons were performed on series of samples originating from the same synthesis batch of the UCNPs (Table 1).

TEM investigation revealed the presence of an amorphous layer on the surfaces of all coated UCNPs. The PB coatings appeared thicker than the P coatings (Figure 2). Most of the coated UCNPs were well separated on the TEM-sample support, with a small fraction of (apparent) aggregates of 2–3 UCNPs (Figure S2 in Supporting Information). However, such aggregation may have been induced during the drying of the TEM samples and does not necessarily reflect the situation in the dispersion. In addition, amorphous impurities were observed in the sample coated with the nominal fraction of 300 MAO/nm². We assume that the impurities were homogeneously precipitated polymers, since only C and O were identified with EDXS analyses. This was a result of a highly excessive PMAO fraction, in addition to the limited solubility of BHMT in the reaction medium, i.e., chloroform. Therefore, only the samples with ≤ 150 MAO/nm² were used in the subsequent studies.

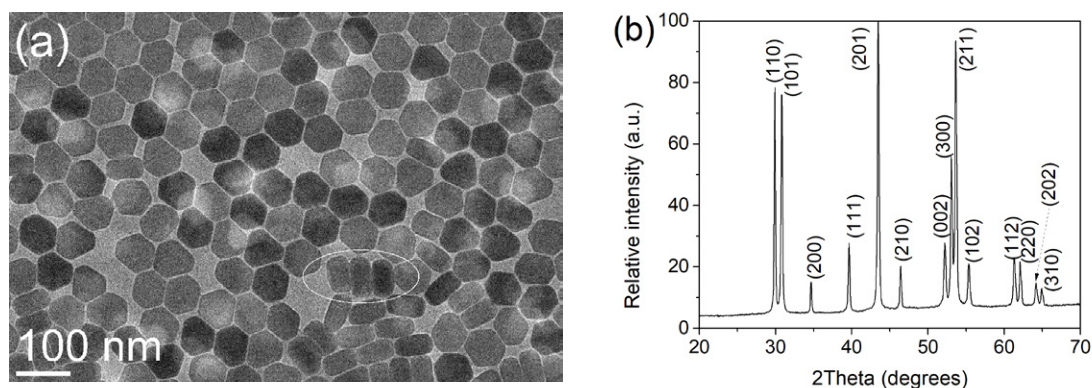


Figure 1. TEM image of the as-synthesised UCNPs (a) and their XRD pattern (b) with indices corresponding to space group $P6_3/m$. Some UCNPs lying perpendicularly to the sample support are encircled in panel (a).

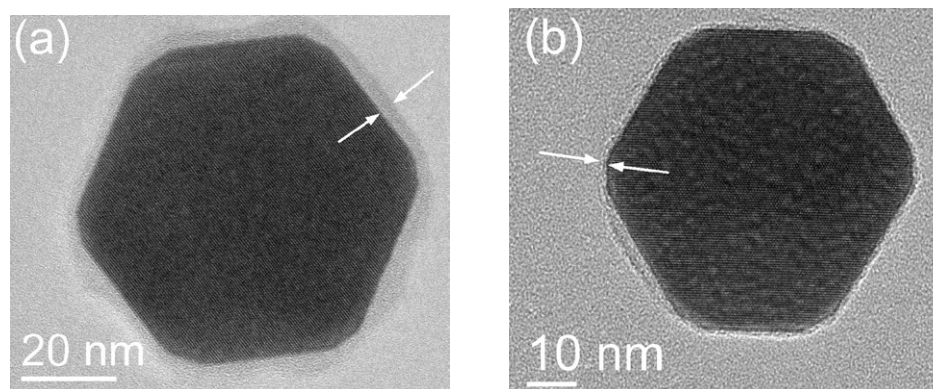


Figure 2. TEM image of a UCNP coated with: @PB-150 (a) and @P-150 (b). Arrows point at the amorphous surface layer.

Successful incorporation of Yb^{3+} and Tm^{3+} into the NaYF_4 crystal lattice was confirmed by the characteristic UC fluorescence spectra upon excitation at 980 nm, within the strong absorption band of the Yb^{3+} ion (Figure 3). The dominant peak centred at 804 nm corresponds to the transition ${}^3\text{H}_4 \rightarrow {}^3\text{H}_6$ of the Tm^{3+} ion, broadened by the Stark splitting of the Tm^{3+} ground-state manifold. The UC fluorescence in the visible region is significantly weaker in comparison. Nevertheless, emission peaks at 452, 477, 648 and 698 nm can be easily identified (see the inset) and assigned to radiative transitions originating from the higher excited levels of the Tm^{3+} ions.

In Figure 3, we can also see a decrease of the UC fluorescence intensities (normalised to the same UCNP mass concentration) upon stripping of the oleate ligands from the as-synthesised UCNPs (dispersed in chloroform) and their transfer to water (bare UCNPs). This is a well-known effect, indicative of the surface quenching by the high-energy vibrations of the water molecules, favouring non-radiative relaxation of the excited levels in Yb^{3+} and Tm^{3+} ions. However, the UC fluorescence spectra of the coated UCNPs in water dispersions demonstrate that both polymer coatings with a high nominal fraction of MAO (*i.e.*, the @PB-150 and @P-150) provide

some protection against the surface quenching. In both these cases, the dominant UC emission line (around 800 nm) is $\sim 30\%$ stronger than the bare UCNPs of the same diameter (67 nm).

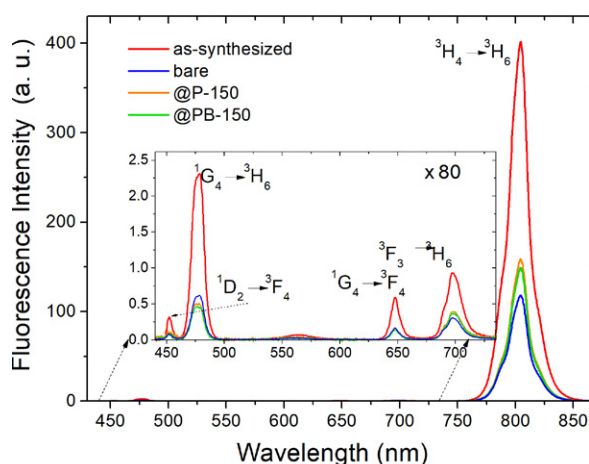


Figure 3. UC fluorescence spectra with the assigned electronic transitions of the as-synthesised oleate-capped UCNPs in chloroform, and bare as well as polymer-coated UCNPs in water. All UCNPs have a core diameter of 67 nm.

The zeta potential of the coated UCNPs is negative at the neutral pH range, and its absolute value decreases with the decreasing pH (Figure 4). This can be explained by deprotonation of surface carboxylic groups, resulting in the negative zeta potential at higher pH values. The carboxylic groups are exposed at the UCNPs surface after the MAO anhydride ring opens in water (Scheme 1). Alternatively, the anhydride ring also opens to react with amine groups of BHMT, and the negative surface-charge density of UCNPs@PB is lower than that of UCNPs@P. The same trend was observed for other nominal fractions. Such zeta-potential behaviour is also an indication that PMAO is crosslinked with BHMT at the UCNPs surfaces, as concluded previously¹⁶ from infrared spectroscopy analysis.

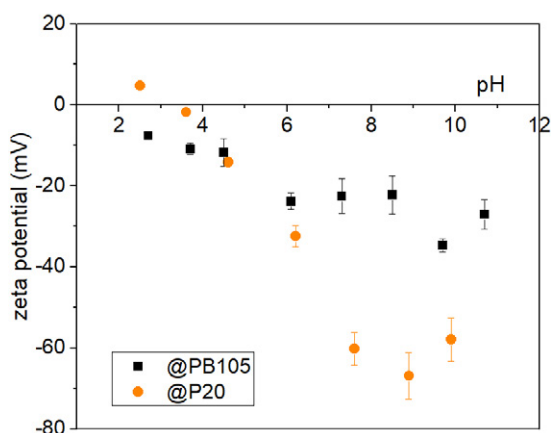


Figure 4. Zeta-potential dependence on pH of the polymer-coated UCNPs.

The colloidal stability of differently coated UCNPs in water was assessed from DLS measurements of the coated UCNPs with an average core diameter of 52 ± 2 nm (Figure 5a and b). The hydrodynamic sizes of the coated UCNPs were, in general, larger than the crystalline core, which can be attributed to the polymer coating and hydration surface layer. The fractions with hydrodynamic sizes ≥ 100 nm indicate some smaller aggregates (Figure S2b in Supporting Information). The absence of larger agglomerates was also in accordance with the transparency of all the dispersions, with the exception of a turbid dispersion of UCNPs@PB-7 containing some fraction of ~ 300 nm large NPs. Another exception was the UCNPs@P-105 dispersion with a small fraction of ~ 250 nm sized NPs (see the arrow in Figure 5b), suggesting minor aggregation in this sample. In contrast, the dispersion of the UCNPs@PB-210 contained a significant fraction of ~ 35 nm sized NPs. These NPs, with the sizes lower than the as-synthesised core UCNPs, were homogeneously precipitated polymer NPs, also identified with TEM and EDXS.

Long-term colloidal stability was examined for the coated UCNPs with 150 MAO/nm² within 4 months (Fig-

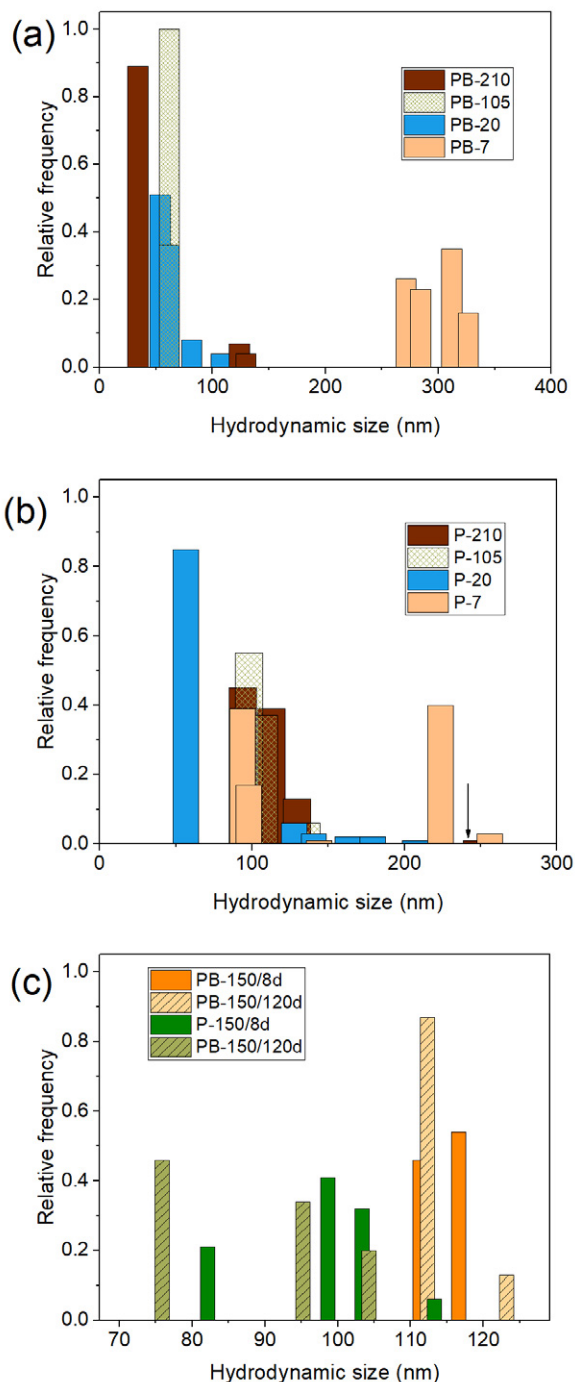


Figure 5. Number-weighted hydrodynamic-size distribution of differently coated UCNPs in water; fresh (a and b) and aged dispersions (c). Core diameters of UCNPs are ~ 50 nm (a and b), and ~ 70 nm (c). The arrow in panel (b) points at the very low fraction of the UCNPs@P-210 at ~ 250 nm. 8d and 120d in panel (c) denote 8 and 120 days, respectively.

ure 5c). The UCNPs@PB-150 were, on average, larger than the UCNPs@P-150, but the hydrodynamic sizes of both samples were in the range of 1–2 UCNP core sizes (~ 70 nm) at all times. This demonstrates their long-term stability in water.

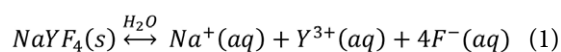
We have also verified the colloidal stability of the coated samples in a physiological buffer, i.e., PBS, used in our chemical-stability studies of the UCNPs. We selected two colloidally stable UCNPs samples in water with the lowest and highest nominal polymer fraction, i.e., UCNP@P-20 and UCNP@PB-150. The hydrodynamic size of fresh dispersions of UCNP@PB-150 in PBS (Figure 6) was comparable to that in water (Figure 5). However, it increased slightly in 3 days, indicating a slow aggregation of the UCNP@PB-150 in PBS, whereas the aggregation of UCNP@P-20 in PBS was more significant. After 3 days, a noticeable fraction of aggregates with hydrodynamic sizes of several microns was detected. The colloidal instability can be ascribed to the relatively low absolute value of the zeta potential, i.e., around -10 mV in the fresh PBS dispersions, compared to much higher negative zeta-potential values in water (Figure 4). In addition, the decreasing zeta-potential value with time ($>50\%$ in 3 days) indicates some changes in the UCNPs surface chemistry. A TEM inspection of dried PBS dispersions (older than 1 month) did not reveal any significant morphological changes of the coated UCNPs (see example in Figure S3 in Supporting Information). This result demonstrates that the phosphate ions from PBS did not destroy the studied coatings at room temperature. Note that characteristic fibrous decomposition product of bare UCNPs in PBS was observed with TEM even at room temperature,¹⁵ which was not the case in this study. The observed limited colloidal stability of the coated UCNPs in PBS is not critical for their use, since other aqueous media can be used for their storage.

3. 2. Chemical Stability of UCNPs

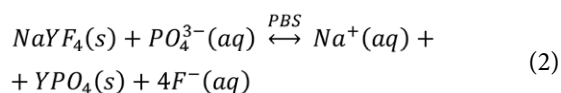
Our dissolution study represents the most rigorous chemical test of the UCNPs chemical stability under simulated physiological conditions. Namely, the fastest dissolution of UCNPs was so far observed in PBS.^{7,12,20} The effect of polymer coatings on the UCNPs dissolution was evaluated by comparing the bare and coated UCNPs aged under

the same conditions (Table 2). No significant difference in the X_F -values was observed if the coating was only PMAO or PMAO-BHMT. Both types of polymer coatings almost completely prevented the dissolution of UCNPs. Although differences were not significant, a trend of increasing protecting efficiency in line with the increasing nominal MAO was found. Moreover, no significant difference in the dissolution was found for differently large UCNP, i.e., between ~ 50 and ~ 70 nm.

Most of the analysed dispersions contained 0.1 mg/ml of bare or coated UCNPs, which is about the maximum NPs concentration typically used in cytotoxicity and biocompatibility studies (i.e., 1 – 100 $\mu\text{g/ml}$).^{28–30} It was reported previously that the dissolution of bare UCNPs is more significant for aqueous dispersion with lower concentrations of UCNPs.¹² This was explained with the chemical equilibrium between the dissolved and crystalline fluoride:



The lower is the concentration of dispersed UCNPs, the larger fraction of UCNPs (i.e., larger X_F) dissolves to reach the equilibrium in Eq. 1. The decomposition mechanism of UCNPs in PBS is not that simple because it is accompanied by the precipitation of Y-phosphates:



Eq. 2 is a simplified equilibrium where we consider only one phosphate form. The concentration of all solutes in PBS (phosphates, NaCl, KCl) is very large and can be considered constant. Therefore, the fraction of dissolved fluoride should also increase with the decreasing UCNPs concentration in PBS as in pure water (Eq. 1). For the verification, we analysed a couple of dispersions containing only 5 $\mu\text{g/ml}$ UCNPs in PBS. Indeed, the X_F -values of the

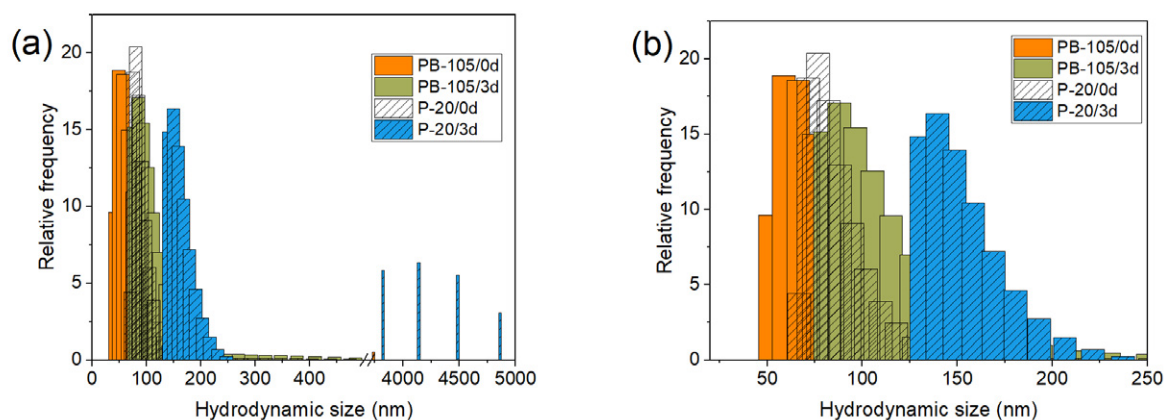


Figure 6. Number-weighted hydrodynamic-size distribution of differently coated UCNPs in PBS; fresh (0d) and 3-days old dispersions (3d). Core diameters of UCNPs ~ 50 nm. Panel (b) shows an enlarged section of panel (a)

Table 2. Released fluoride concentration after ageing the aqueous dispersions bare or polymer-coated UCNPs (0.1 mg/ml) in PBS at pH 7.4 and 37 °C for 3 days: measured concentration (C_F), molar fraction considering the total solid content (X_F ; Eq. S1 in Supporting Information).

Coating	Size of core UCNPs (nm)	C_F ($\mu\text{g/ml}$)	X_F (mol. %)
none	67 ± 5	30 ± 1	83 ± 4
@PB-150	67 ± 5	0.19 ± 0.04	0.52 ± 0.04
@PB-105	52 ± 2	<0.1	<0.27
		0.07 ± 0.05*	3.8 ± 2.9*
@PB-20	52 ± 2	0.2 ± 0.1	0.6 ± 0.4
@PB-7	52 ± 2	0.33 ± 0.05	0.9 ± 0.1
@P-150	67 ± 5	0.4 ± 0.1	1.1 ± 0.3
@P-105	52 ± 2	<0.1	<0.27
@P-20	52 ± 2	0.20 ± 0.01	0.55 ± 0.02
		0.03 ± 0.01*	1.4 ± 0.6*
@P-7	52 ± 2	0.15 ± 0.03	0.41 ± 0.08

* dispersions with 5 $\mu\text{g/ml}$ UCNPs

UCNPs@PB-105 and @P-20 were larger for lower (5 $\mu\text{g/ml}$) than for the higher UCNPs concentrations (0.1 mg/ml) (Table 2). This indicates that the hydrophobic surface layer is an efficient barrier to significantly slow down the dissolution of UCNPs, but it does not prevent it completely.

The X_F values of the UCNPs@P and @PB are comparable to those obtained with UCNPs coated with a thick (~70 nm) silica shell and by far lower than with any other protective coatings tested at similar conditions.^{15,20,21} This means that our ~1 nm-thick polymer coating with the solvation layer of ≤ 25 nm (as estimated from the hydrodynamic size) provides for equivalent protection against the dissolution of UCNPs as the 70-nm silica shell.²⁰

If the dissolution cannot be completely prevented, it is crucially important for *in vivo* applications to, at least, reduce the dissolution rate to such an extent that the concentration of dissolved species remains insignificant until the UCNPs are excreted from the body. We estimate that 3 days would be the required time for their excretion after being used as contrast agents. The measured concentration of released fluoride (C_F , Table 2) is the fluoride concentration that would interact *in vivo* if the dissolution kinetics is assumed similar to the studied system. The studied polymer coatings suppress the dissolution of UCNPs to such an extent that the released fluoride (≤ 0.33 $\mu\text{g/ml}$) would not exceed the acceptable daily intake of fluoride for humans, ADI = 50 $\mu\text{g/kg}$ body mass/day,¹¹ even if 10 ml of the coated-UCNPs dispersion with a concentration of 0.1 mg/ml would be administered. Although, we have not found any data on the toxicity of rare earths in humans, a rough estimation was done. If we consider complete dissolution of studied UCNPs as in water (Eq. 1) with the dissolution rate comparable to that in PBS, the released ~0.5 $\mu\text{g/ml}$ of rare-earth ions (Y^{3+} , Yb^{3+} and Tm^{3+}) from 10 ml of dispersion would not exceed the median lethal dose, LD_{50} = 500 mg/kg body mass determined in mice.³¹ So, we con-

clude that the studied polymer coatings, PMAO and PMAO-BHMT, show a promise for safe application of UCNPs in biomedical diagnostics. Moreover, free carboxyl groups of PMAO can be subsequently functionalised for specific *in vivo* applications.

4. Conclusions

We studied amphiphilic-polymer coatings made of poly(maleic anhydride-*alt*-octadec-1-ene) (PMAO) and bis(hexamethylene)triamine (BHMT) to improve the chemical stability of upconverting nanoparticles (UCNPs) based on NaYF_4 codoped with Yb^{3+} and Tm^{3+} that decompose in aqueous phosphate solutions. The decomposition of UCNPs was followed by measuring the concentration of released fluoride phosphate-buffered saline (PBS) at physiological conditions. PMAO coating formed directly on the as-synthesised oleate-capped UCNPs. Hydrophobic chains of the amphiphilic PMAO and oleate formed a diffusion barrier for the solutes and solvent molecules. Consequently, the decomposition of the PMAO-coated UCNPs in PBS at physiological conditions was almost completely suppressed. Subsequent crosslinking of PMAO coating with BHMT resulted in a similarly low concentration of the released fluoride, which was for all samples ≤ 0.33 $\mu\text{g/ml}$, i.e., well below the acceptable daily intake of fluoride for humans. We conclude that the chemical stability of UCNPs was achieved with the hydrophobic diffusion barrier and that the crosslinking of PMAO with BHMT on the UCNPs surface was not necessary. The PMAO-coated UCNPs can be subsequently bioconjugated to be suitable for diagnostic applications *in vivo*.

Conflicts of Interest: The authors declare no conflict of interest.

Supporting Information includes the calculation of the molar fraction of the released fluoride (Eq. S1), size-distribution graph of the as-synthesized UCNPs (Figure S1), TEM images of the coated UCNPs (Figure S2) and of the coated UCNPs after being aged in PBS (Figure S3).

Acknowledgement

The authors acknowledge the financial support from the Slovenian Research Agency (research core funding P2-0089, P1-0192, P1-0045, and P3-0067). We thank Center of Excellence in Nanoscience and Nanotechnology (CENN) for the use of TEM (Jeol 2100).

5. References

- H. Guo, S. Sun, *Nanoscale* **2012**, *4* (21), 6692–6706. DOI:10.1039/c2nr31967e
- H. H. Gorris, U. Resch-Genger, *Anal. Bioanal. Chem.* **2017**, *409* (25), 5875–5890. DOI:10.1007/s00216-017-0482-8
- F. Vetrone, R. Naccache, A. Zamarrón, A. Juarranz de la Fuente, F. Sanz-Rodríguez, L. Martínez Maestro, E. Martín Rodríguez, D. Jaque, J. García Solé, J. A. Capobianco, *ACS Nano* **2010**, *4* (6), 3254–3258. DOI:10.1021/nn100244a
- B. Del Rosal, D. Jaque, *Methods Appl. Fluoresc.* **2019**, *7* (2), 22001. DOI:10.1088/2050-6120/ab029f
- F. Auzel, *Chem. Rev.* **2004**, *104* (1), 139–174. DOI:10.1021/cr020357g
- F. Wang, Y. Han, C. S. Lim, Y. Lu, J. Wang, J. Xu, H. Chen, C. Zhang, M. Hong, X. Liu, *Nature* **2010**, *463* (7284), 1061–1065. DOI:10.1038/nature08777
- D. Lisjak, O. Plohl, J. Vidmar, B. Majaron, M.; Ponikvar-Svet, *Langmuir* **2016**, *32* (32), 8222–8229. DOI:10.1021/acs.langmuir.6b02675
- A. Gnach, T. Lipinski, A. Bednarkiewicz, J. Rybka, J. A. Capobianco, *Chem. Soc. Rev.* **2015**, *44* (6), 1561–1584. DOI:10.1039/C4CS00177J
- H. Oliveira, A. Bednarkiewicz, A. Falk, E. Fröhlich, D. Lisjak, A. Prina-Mello, S. Resch, C. Schimpel, I. V. Vrčec, E. Wysokińska, H. H. Gorris, *Adv. Healthc. Mater.* **2019**, *8* (1), 1801233. DOI:10.1002/adhm.201801233
- N. I. Agalakova, G. P.; Gusev, *ISRN Cell Biol.* **2012**, *2012*, 403835. DOI:10.5402/2012/403835
- J. Han, L. Kiss, H. Mei, A. M. Remete, M. Ponikvar-Svet, D. M. Sedgwick, R. Roman, S. Fustero, H. Moriwaki, V. A. Soloshonok, *Chem. Rev.* **2021**, *121* (8), 4678–4742. DOI:10.1021/acs.chemrev.0c01263
- S. Lahtinen, A. Lyytikäinen, H. Pääkilä, E. Hömppi, N. Perälä, M. Lastusaari, T. Soukka, *J. Phys. Chem. C* **2017**, *121* (1), 656–665. DOI:10.1021/acs.jpcc.6b09301
- O. Plohl, M. Kraft, J. Kovač, B. Belec, M. Ponikvar-Svet, C. Würth, D. Lisjak, U. Resch-Genger, *Langmuir* **2017**, *33* (2), 553–560. DOI:10.1021/acs.langmuir.6b03907
- A. Sedlmeier, H. H.; Gorris, H. H. *Chem. Soc. Rev.* **2015**, *44*, 1526–1560. DOI:10.1039/C4CS00186A
- E. Andresen, C. Würth, C. Prinz, M. Michaelis, U. Resch-Genger, *Nanoscale* **2020**, *12* (23), 12589–12601. DOI:10.1039/D0NR02931A
- O. Plohl, S. Kralj, B.; Majaron, E.; Fröhlich, M.; Ponikvar-Svet, D.; Makovec, D.; Lisjak, *Dalt. Trans.* **2017**, *46* (21), 6975–6984. DOI:10.1039/C7DT00529F
- N. Estebanez, M. González-Béjar, J. Pérez-Prieto, *ACS Omega* **2019**, *4* (2), 3012–3019. DOI:10.1021/acsomega.8b03015
- E. Palo, M.; Salomäki, M.; Lastusaari, *J. Colloid Interface Sci.* **2019**, *538*, 320–326. DOI:10.1016/j.jcis.2018.11.094
- E. Palo, H.; Zhang, M.; Lastusaari, M.; Salomäki, *ACS Appl. Nano Mater.* **2020**. DOI:10.1021/acsnm.0c01245
- M. I. Saleh, B. Rühle, S. Wang, J. Radnik, Y. You, U. Resch-Genger, *Sci. Rep.* **2020**, *10* (1), 19318. DOI:10.1038/s41598-020-76116-z
- M. Vozlič, T. Černič, S. Gyergyek, B. Majaron, M. Ponikvar-Svet, U. Kostiv, D. Horak, D. Lisjak, *Dalt. Trans.* **2021**, *50*, 6588–6597. DOI:10.1039/D1DT00304F
- G. Palui, F. Aldeek, W. Wang, H. Mattoussi, *Chem. Soc. Rev.* **2015**, *44* (1), 193–227. DOI:10.1039/C4CS00124A
- H.-S. Qian, Y. Zhang, *Langmuir* **2008**, *24* (21), 12123–12125. DOI:10.1021/la802343f
- E. Palo, M. Tuomisto, I. Hyppänen, H. C. Swart, J. Hölsä, T. Soukka, M. Lastusaari, *J. Lumin.* **2017**, *185*, 125–131. DOI:10.1016/j.jlumin.2016.12.051
- G. Jiang, J. Pichaandi, N. J. J. Johnson, R. D. Burke, F. C. J. M. van Veggel, *Langmuir* **2012**, *28* (6), 3239–3247. DOI:10.1021/la204020m
- N. Bogdan, F. Vetrone, G. A. Ozin, J. A. Capobianco, *Nano Lett.* **2011**, *11* (2), 835–840. DOI:10.1021/nl1041929
- D. Štepec, G. Tavčar, M. Ponikvar-Svet, *Environ. Pollut.* **2019**, *248*, 958–964. DOI:10.1016/j.envpol.2019.02.046
- E. Wysokińska, J. Cichos, E. Ziolo, A. Bednarkiewicz, L. Strzadała, M. Karbowski, D. Hreniak, W. Kałas, *Toxicol. Vitr.* **2016**, *32*, 16–25. DOI:10.1016/j.tiv.2015.11.021
- R. Li, Z. Ji, J. Dong, C. H. Chang, X. Wang, B. Sun, M. Wang, Y.-P. Liao, J. I. Zink, A. E. Nel, T. Xia, *ACS Nano* **2015**, No. 3, 3293–3306. DOI:10.1021/acsnano.5b00439
- B. Pem, D. González-Mancebo, M. Moros, M. Oca a, A. I. Becerro, I. Pavičić, A. Selmani, M. Babič, D. Horák, I. Vinković Vrčec, *Methods Appl. Fluoresc.* **2019**, *7* (1). DOI:10.1088/2050-6120/aae9c8
- S. Hirano, K. T. Suzuki, *Environ. Health Perspect.* **1996**, *104* (suppl 1), 85–95. DOI:10.1289/ehp.96104s185

Povzetek

Nanodelci NaYF_4 , sočasno dopirani z Yb^{3+} in Tm^{3+} , izkazujejo fluorescenco z energijsko pretvorbo navzgor v bližnjem infrardečem in vidnem spektru. Tovrstne nanodelce z energijsko pretvorbo navzgor (NDEPN) lahko uporabljamo kot kontrastna sredstva v medicinski diagnostiki in bioloških testih. Pomanjkljivost NDEPN je omejena kemijska stabilnost v vodnih disperzijah, še posebej v fosfatnih raztopinah. Optimizirali smo zaščitne amfifilne polimerne prevleke na osnovi poli(maleinski anhidrid-*alt*-oktadec-1-en) (PMAO) in bis(heksametilen)triamin (BHMT) za izboljšavo kemijske stabilnosti NDEPN pri simuliranih fizioloških pogojih. Morfologijo izhodnih in prevlečenih NDEPN smo analizirali s presevno elektronsko mikroskopijo. V vseh vzorcih smo izmerili intenzivno fluorescenco pri ~ 800 nm, značilno za Tm^{3+} . Koloidno stabilnost vodnih disperzij izhodnih in prevlečenih NDEPN smo ocenili z meritvami dinamičnega sipanja svetlobe in zeta potenciala. Raztapljanje NDEPN pri 37°C v fosfatnem fiziološkem pufru smo spremljali s potenciometričnimi meritvami koncentracije raztopljenega fluorida. Ugotovili smo, da NDEPN lahko pred raztapljanjem zaščitimo s PMAO in s PMAO zamreženim z BHMT.



Except when otherwise noted, articles in this journal are published under the terms and conditions of the Creative Commons Attribution 4.0 International License

Scientific paper

Adsorption Properties of Low-Cost Synthesized Nanozeolite L for Efficient Removal of Toxic Methylene Blue Dye from Aqueous Solution

Neda Salek Gilani,^{1,*} Salma Ehsani Tilami² and Seyed Naser Azizi¹¹ Analytical division, Faculty of Chemistry, University of Mazandaran, Postal code 47416-95447, Babolsar, Iran² Department of basic science, Farhangian University, Postal code 19989-63341, Tehran, Iran

* Corresponding author: E-mail: salekgilani@gmail.com

Received: 01-07-2022

Abstract

In this study, nanozeolite L was applied for the removal of toxic methylene blue dye (MB) to evaluate its feasibility as an effective adsorbent. Synthesized nanozeolite L was characterized by X-ray diffraction (XRD), Fourier transform infrared (FTIR), scanning electronic microscopy (SEM), Brunauer–Emmett–Teller (BET), and energy-dispersive X-ray analysis (EDX) methods to determine its basic physicochemical properties. Batch adsorption studies were performed as a function of pH, adsorbent dose, contact time, initial MB concentration, and temperature. The adsorption behavior of MB was fitted better by the Langmuir isotherm than by the Freundlich isotherm, and the maximum adsorption capacity of nanozeolite L was obtained 80.64 mg g⁻¹. The negative values of Gibbs free energy change (ΔG°) and the positive value of the standard enthalpy change (ΔH°) affirmed that the adsorption process is spontaneous and endothermic. Based on these findings, nanozeolite L, with high surface area, great adsorption capacity, and low synthetic cost, can be an effective and economical adsorbent for MB removal.

Keywords: Nanozeolite L; Hydrothermal synthesis; Methylene blue; Adsorption

1. Introduction

The discharge of dye effluents from various industries such as paper, textiles, leather, plastics, rubber, cosmetics, and food beverages to the environment, especially to the water system, is becoming a major concern because of their toxicity. The considerable release of dyes from these industries is a major problem of pollution, leading to severe damages to aquatic life. Dyes can consume the dissolved oxygen necessary for aquatic life, and also some of them have direct toxicity to microbial populations and even can be toxic and carcinogenic to mammals.^{1–3}

Methylene blue (MB) is a cationic aromatic dye and has several adverse effects on Homo sapiens, such as an increase in hypertension, nausea, diarrhea, headache, dizziness, and eye injuries. So it must be removed from wastewater before discharge into water bodies.^{4–6}

Various physical and chemical methods such as coagulation, sedimentation, ozonation, membrane separation, photocatalysis, and adsorption have been used for the removal of dyes from wastewaters.^{7,8} Among these meth-

ods, the adsorption process is preferred because of its high efficiency and cost-effectiveness.^{9,10} The selection of adsorbent plays a significant role in determining its cost-effectiveness, and the search for efficient and low-cost adsorbents such as natural, agricultural, and industrial byproduct waste is still underway.^{11–13} Clay materials such as bentonite, montmorillonite, kaolinite, and zeolite have received much attention due to their unique structural and surface features, which offer high chemical stability and specific surface area that conduces to high adsorption capacities.^{14–22} Among these clays, zeolite has received the greatest consideration and recognition as an appropriate adsorbent.

Among a large number of zeolites, zeolite L is one of the most interesting and versatile adsorbents. It contains one-dimensional (1D) channels running along the length of its hexagonal crystals. The unique configuration of its large pores with a diameter of 7.1 Å makes this kind of zeolite an excellent candidate for shape-selective catalysis, for the adsorption of various species such as ions, metals, and organic molecules and mass transport and/or occlu-

sion.^{23,24} The reduction of zeolite size from the micrometer to the nanometer scale leads to unique properties such as decreased diffused path lengths and large external surfaces, which are effective for improving the adsorption of organic dye pollutants.^{25,26} Most nanozeolites are synthesized in the presence of costly organic structure-directing agents (OSDAs), but nanozeolite L could be synthesized in the absence of OSDAs, which is desirable due to economic considerations.²⁷

The main objective of the present study is to evaluate the feasibility of using synthesized nanozeolite L as a cost-effective adsorbent for removing MB from aqueous solution. The effects of various adsorption parameters such as solution pH, adsorbent dose, reaction time, initial pollutant concentration, and temperature on adsorption of MB were investigated. Also, the adsorption isotherm, kinetic, and thermodynamic were studied. This fundamental study would be useful for further application in designing a batch reactor for the treatment of dye-containing wastewaters coming out from various industries.

2. Experimental

2.1. Chemicals and Apparatus

Silicic acid, potassium hydroxide ($\geq 85.0\%$), and hydrochloric acid (37%) were purchased from Merck, and aluminum foil and MB were purchased from Fluka. X-ray diffraction (XRD) pattern was recorded with an X-ray diffractometer (SHIMADZUXD-DL) using $\text{CuK}\alpha$ radiation ($\lambda = 1.5418 \text{ \AA}$) at 35.4 kV and 28 mA with a scanning speed of $2\theta = 10^\circ \text{ min}^{-1}$. Fourier transform infrared (FTIR) spectrum was recorded with an FTIR spectrometer (Tensor 27Bruker) at room temperature in the range of 400–1300 cm^{-1} . Scanning electron microscopy (SEM; EM-3200, KYKY) was used to determine the crystallite size and morphology of the sample. Nitrogen adsorption-desorption isotherms were measured at 77 K using a Quantachrome NovaWin2 apparatus. For each set of experiments, the residual MB concentrations in the supernatant were analyzed using a T90+ -UV-vis spectrophotometer. The pH measurements were made with a pH meter, model 827 pH lab, Metrohm, Switzerland.

2.2. Synthesis of Nanozeolite L

In order to synthesize nanozeolite L, silica and alumina solutions were prepared by dissolving 20 mmol silicic acid and 2 mmol aluminum foil in potassium hydroxide solutions, respectively. Then, the silica solution was added dropwise to the alumina solution under vigorous stirring. The resulting aluminosilicate gel was transferred into a Teflon-lined stainless steel autoclave and heated at 170°C for 2 days. The resulting product was then centrifuged, washed with deionized water, and dried at 80 °C.

2.3. MB Sorption Experiments

Batch adsorption experiments were performed to investigate the adsorption behavior of MB onto synthesized nanozeolite L in aqueous solution at 25°C. The effect of pH was studied in the range of 2–10 and the pH values were adjusted using 0.1 M HCl and 0.1 M NaOH solutions. To investigate the effect of pH, 5 mg of nanozeolite L was added to 10 mL of each MB solution (20 mg L^{-1}) and the solutions were shaken for 30 minutes.

To study the effect of adsorbent dosage, 10 mL of 20 mg L^{-1} MB solution at pH = 9 was shaken with 2–15 mg of nanozeolite L for 30 minutes.

To study the kinetics of the adsorption process, MB solution containing 0.5 g L^{-1} of nanozeolite L at pH = 9 was vigorously agitated for different times in the range of 5–40 minutes. For adsorption isotherm studies, constant dosages of nanozeolite L (0.5 g L^{-1}) were agitated with different initial concentrations of MB in the range of 20–100 mg L^{-1} at pH = 9.

Also, the temperature effect on adsorption was studied by mixing 5 mg of nanozeolite L with 10 mL of 40 mg L^{-1} MB solution at different temperatures ranged from 25 to 55 °C.

At the end of the experiments, samples were centrifuged and the residual concentrations of MB were determined using UV-Vis spectrophotometer. The removal percentage was determined from equation (1):

$$\text{Removal (\%)} = \frac{C_i - C_e}{C_i} \times 100 \quad (1)$$

where C_i and C_e (mg L^{-1}) are the concentrations of MB in initial solution and the aqueous phase after adsorption, respectively. Also, the adsorption capacity (q_e , mg g^{-1}) of nanozeolite L was calculated using the following equation:

$$q_e = \frac{(C_i - C_e)V}{m} \times 100 \quad (2)$$

where V (L) is the volume of the aqueous phase and m is the weight of adsorbent.

3. Results and Discussion

3.1. Characterization of Nanozeolite L

Figure 1a shows the XRD pattern of nanozeolite L. The presence of the characteristic peaks of nanozeolite L at $2\theta = 5.5^\circ, 19.4^\circ, 22.7^\circ, 25.6^\circ, 28.0^\circ, 29.1^\circ,$ and 30.7° in the diffraction pattern indicates that the pure phase of nanozeolite L is formed.²⁸ The FTIR spectrum (inset, Fig 1a) shows the characteristic vibrational bands of nanozeolite L in the range of 400–1300 cm^{-1} . The broadband in the range 1008–1145 cm^{-1} shows the asymmetric stretching vibrations of O–T–O (T=Si, Al) tetrahedral. The adsorption

band near 721 cm^{-1} belongs to the symmetric stretching vibrations of O–T–O, and the band near 765 cm^{-1} is related to the symmetric stretching vibrations of AlO_4 tetrahedral. The band around 605 cm^{-1} is attributed to the vibration of double six-membered rings (D6Rs), and the band near 476 cm^{-1} is assigned to the O–T–O bending vibrations.²⁹

The size and surface morphology of synthesized nanozeolite L was revealed from its SEM image. The formation of spherical-like nanoparticles with an average diameter of about 20 nm could be observed in Figure 1b.

The elemental analysis of the synthesized nanozeolite L was investigated through EDX studies, and the results are represented in Figure 1c. As can be seen in the figure, the elemental content of synthesized nanozeolite consists of oxygen (O), aluminum (Al), silicon (Si), and potassium (K), with the weight percentages of 42.37, 27.48, 20.14, and 10.01.

The textural properties of nanozeolite sample were investigated by N_2 sorption analysis. The nitrogen adsorption-desorption isotherms of nanozeolite L prepared sample is shown in Fig 1d. It shows type IV isotherm with an H_1 type hysteresis loop which is found in well-defined cylindrical pores or material agglomerates consisting of extremely uniform particles.³⁰ The results showed that the

specific surface area of the prepared sample is $215\text{ m}^2\text{ g}^{-1}$. Also, the pore volume of synthesized nanozeolite obtained 0.4 cc g^{-1} , and its pore size distribution is centered at about 3.65 nm (inset, Figure 1d).

3. 2. Adsorption Studies

3. 2. 1. Effect of pH

The initial pH plays an important role in the adsorption process. The effect of solution pH on MB removal by the synthesized nanozeolite was investigated in the range of 2–10. As shown in Figure 2, the adsorbed MB increased

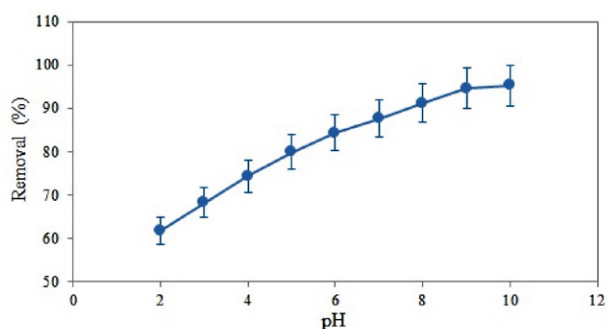


Figure 2. Effect of pH on MB adsorption by nanozeolite L

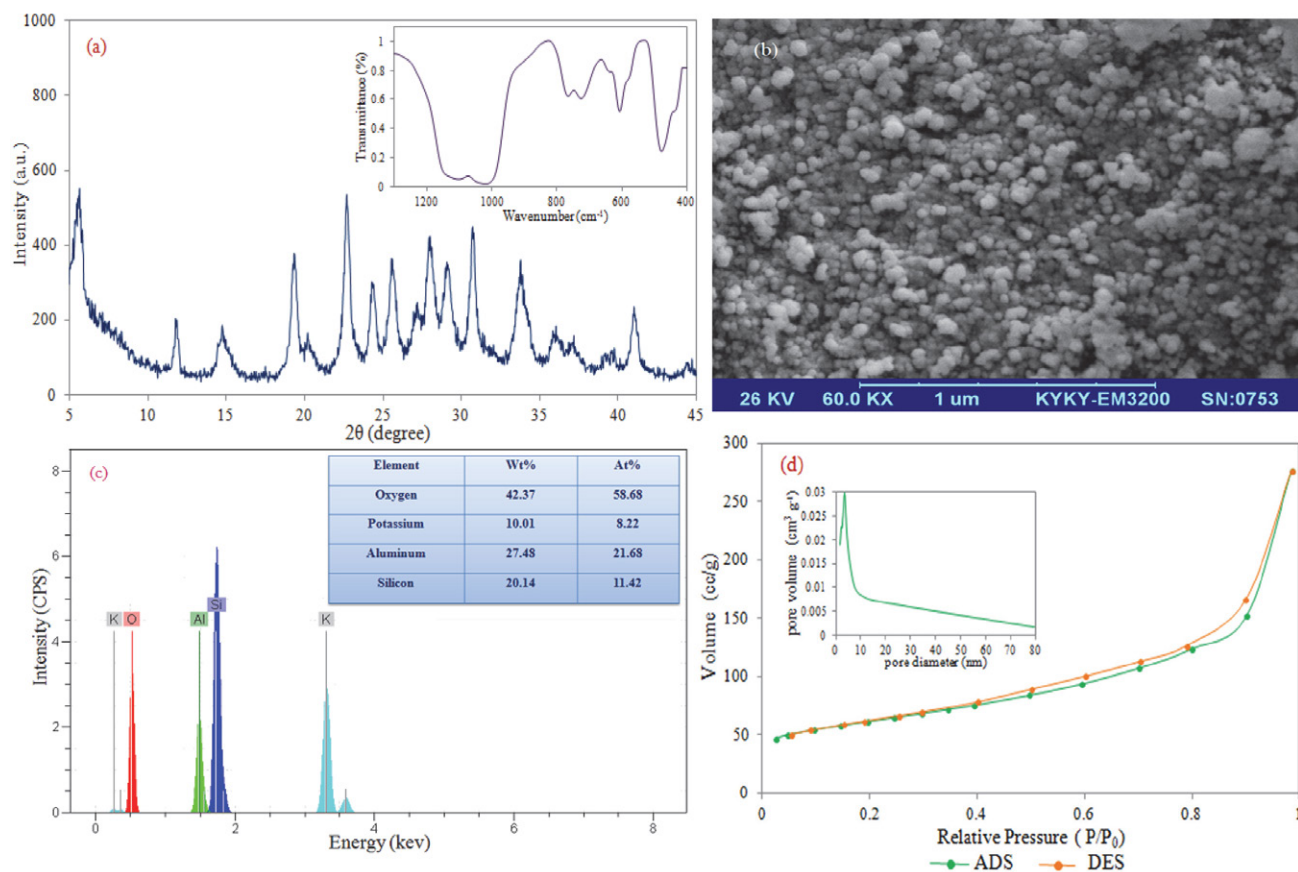


Figure 1. (a) XRD pattern of synthesized nanozeolite L, Inset: FT-IR spectrum of nanozeolite L, (b) SEM image of nanoparticles of zeolite L, (c) EDX spectrum of nanozeolite L, (d) Nitrogen adsorption-desorption isotherms of nanozeolite L, Inset: pore size distribution of nanozeolite L

with increasing solution pH and reached its maximum at pH = 9. It is probably due to the presence of H⁺ ions at lower pH, which will compete with cationic MB for adsorption sites. As pH increases, the zeolite surface is more negatively charged, which results in an increment of adsorption because of the decrease in the electrostatic repulsion force between MB and zeolite surface.^{31,32}

3. 2. 2. Effect of Adsorbent Dosage

Adsorbent dosage is an important factor in the adsorption process because it defines the capacity of an adsorbent for a given initial concentration of the adsorbate. Figure 3 shows the effect of adsorbent dosage on the adsorption of MB. The figure shows that the optimum dosage of nanozeolite L for the removal of MB is 5 mg. The further increase in the amount of MB removal was found to be negligible above a dose of 5 mg. The increase in the extent of MB removal with the adsorbent dose is attributed to the increase in the adsorbent surface area and thus the number of adsorption sites available for adsorption.³³

3. 2. 3. Effect of Contact Time and Kinetic Studies

Figure 4a shows the effect of contact time on the adsorption process of MB on synthesized nanozeolite sodalite. As can be observed in the figure, the dye removal efficiency was increased as the contact time increased until equilibrium.³⁴ The adsorption equilibrium with nanozeolite sodalite was reached at 30 min.

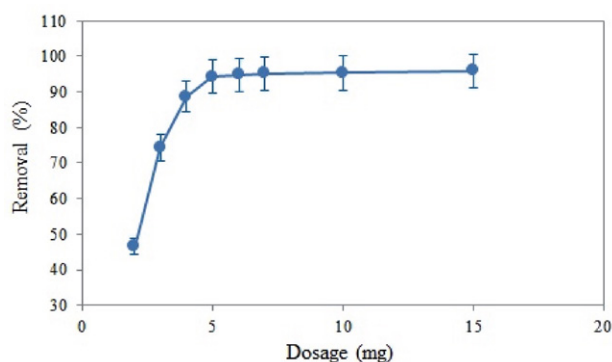


Figure 3. Effect of adsorbent dosage on MB adsorption by nanozeolite L

To evaluate the mechanism of adsorption, pseudo-first-order and pseudo-second-order models were investigated to find the best-fitted model for the experimental data. When the adsorption process is diffusion-controlled, the kinetics follows the pseudo-first-order model, and when the adsorption process occurs through the chemisorption mechanism, the adsorption kinetics follows the pseudo-second-order model. These models are expressed by the following equations:^{35,36}

$$\log(q_e - q_t) = \log q_e - \frac{K_1}{2.303} t \quad (3)$$

$$\frac{t}{q_t} = \frac{1}{K_2 q_e^2} + \frac{1}{q_e} t \quad (4)$$

where q_e and q_t are the adsorption capacity (mg g^{-1}) of the adsorbent at the equilibrium and at time t , respectively. Also, K_1 (min^{-1}) and K_2 ($\text{g mg}^{-1} \text{min}^{-1}$) are the rate constants of the pseudo-first-order and the pseudo-second-order adsorption and can be obtained from the $\log(q_e - q_t)$ versus t plot (Figure 4b) and t/q_t versus t plot (Figure 4c), respectively.

The obtained kinetic parameters of the models and coefficients of determination (R^2) are presented in Table 1. From the R^2 values, it can be deduced that the pseudo-second-order model fits the experimental data slightly better than the pseudo-first-order model.

3. 2. 4. Effect of MB Concentration and Isotherms Studies

The effect of the initial concentration of MB on its removal percentage by nanozeolite L was investigated, and the results are presented in Figure 5a. The results show that as the initial dye concentration increases, the removal percentage decreases due to the consumption of the available active adsorption sites on the adsorbent.³⁷

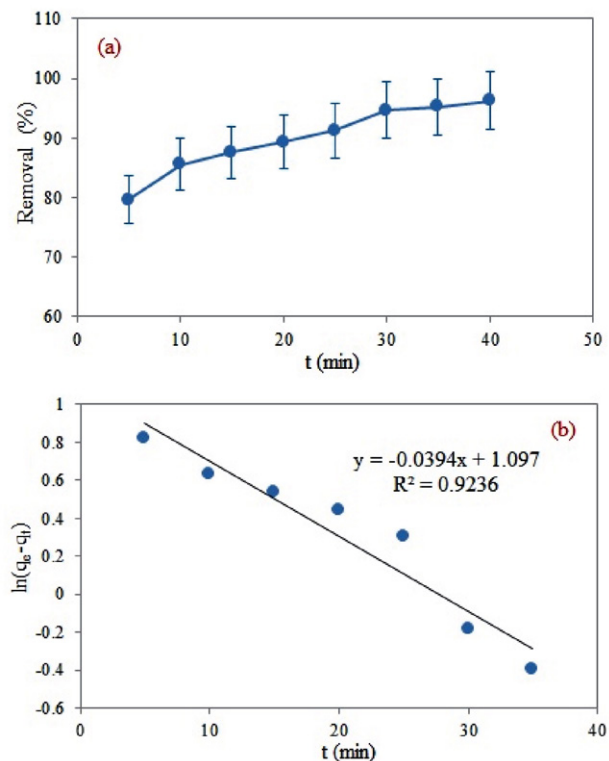


Figure 4. (a) Effect of contact time on MB adsorption by nanozeolite L, (b) Pseudo-first-order kinetics plots for adsorption of MB by nanozeolite L and (c) Pseudo-second-order kinetics plots for adsorption of MB by nanozeolite L

Table 1. Kinetic parameters of pseudo-first-order model and pseudo-second-order model for MB adsorption by nanozeolite L

Models	Parameters	values
pseudo-first-order	K_1 (min^{-1})	0.0907
	$q_{e, \text{cal}}$ (mg g^{-1})	12.50
	R^2	0.9236
pseudo-second-order	K_2 ($\text{g mg}^{-1} \text{min}^{-1}$)	0.0140
	$q_{e, \text{cal}}$ (mg g^{-1})	39.84
	R^2	0.9989
Experimental data	$q_{e, \text{exp}}$ (mg g^{-1})	38.49

The adsorption isotherm studies are important for distinguishing the nature of adsorption. The adsorption isotherm experimental data were analyzed with Langmuir and Freundlich models.

Langmuir isotherm is used for the monolayer adsorption on a homogenous surface and is expressed as follows:³⁸

$$\frac{C_e}{q_e} = \frac{1}{q_{\text{max}} K_L} + \frac{1}{q_{\text{max}}} C_e \quad (5)$$

where C_e is the dye concentration at the equilibrium (mg L^{-1}); q_e is the equilibrium adsorption capacity (mg g^{-1}); q_{max} is the maximum monolayer uptake capacity of the adsorbent and K_L is the Langmuir equilibrium constant (L mg^{-1}). q_{max} and K_L can be obtained from the plot of C_e/q_e versus C_e (Figure 5b).

Freundlich isotherm is used to describe the multilayer adsorption equilibrium on the heterogeneous surface and is mathematically described by the following equation:³⁹

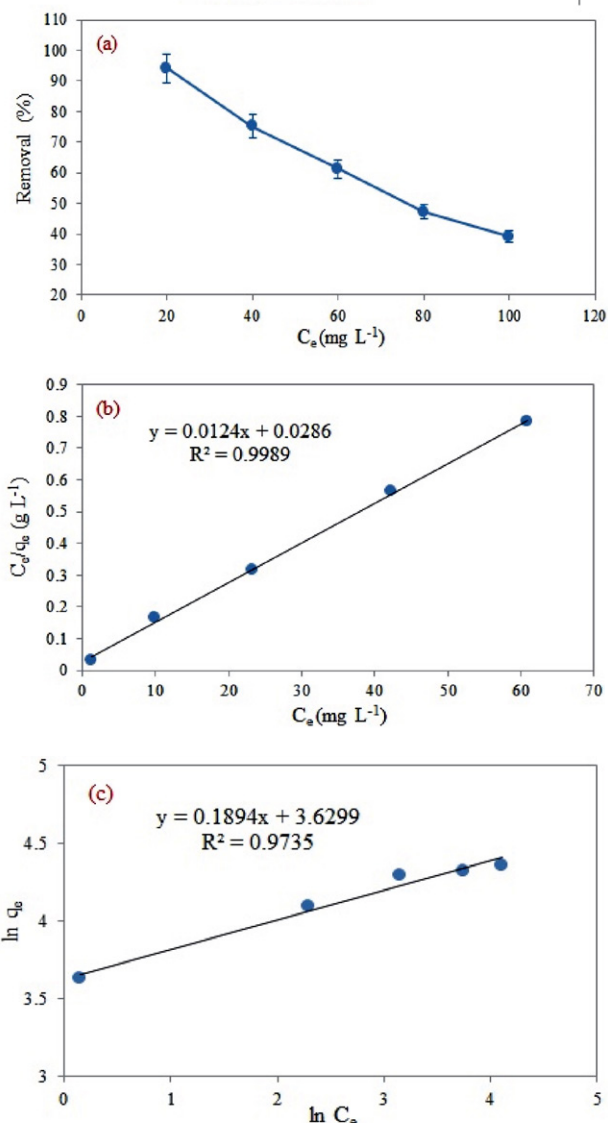
$$\ln q_e = \ln K_F + \left(\frac{1}{n}\right) \ln C_e \quad (6)$$

where K_F is the Freundlich constant related to adsorbent capacity, and n is the heterogeneity factor which indicates the adsorption intensity. The values of K_F and n can be obtained from $\ln q_e$ versus $\ln C_e$ plot (Figure 5c).

The Langmuir and Freundlich isotherm constants, along with the correlation coefficients, are presented in Table 2. As can be seen in the table, the obtained correlation coefficient value is better for Langmuir isotherm, and the equilibrium adsorption capacity ($q_{\text{max, cal}}$) obtained from the Langmuir model is close to the experimentally observed saturation capacity ($q_{\text{max, exp}}$). So, it could be concluded that the equilibrium data for MB adsorption onto nanozeolite L gave a better fit to the Langmuir model.

3. 2. 5. Comparison with Other Adsorbents

Among several adsorbents reported in the literature for the removal of MB from aqueous solutions, some of them are summarized in Table 3. It can be observed that the adsorption capability of nanozeolite L is greater than

**Figure 5.** (a) Effect of initial concentration on MB adsorption by nanozeolite L, (b) Langmuir isotherm for MB adsorption by nanozeolite L and (c) zeolite Freundlich isotherm for MB adsorption by nanozeolite L

most of those reported for other adsorbents. This can be attributed to a higher amount of adsorption sites of nanozeolite L and confirms that it can be used as a promising sorbent for MB removal from its aqueous solution.

Table 2. Isotherm parameters for MB adsorption by nanozeolite L

Isotherm	Parameters	values
Langmuir	$q_{\text{max, cal}}$ (mg g^{-1})	80.64
	K_L (L mg^{-1})	0.43
	R^2	0.9989
Freundlich	K_F ($\text{mg g}^{-1} (\text{L mg}^{-1})^{1/n}$)	37.71
	n_F (mg g^{-1})	5.28
	R^2	0.9735
Experimental data	$q_{\text{max, exp}}$ (mg g^{-1})	78.00

3. 2. 6. Effect of Temperature and Thermodynamic Studies

In this study, the effect of temperature on MB adsorption was investigated in the range of 298–328 K. The results (Figure 6) showed that the percentage removal increased with the increment of temperature. This can be attributed to the increase of dye molecule mobility with temperature.

As the reaction temperature in the solution increases, the number of molecules which have enough energy to undergo an interaction with active sites at the surface increases.^{40,41}

Table 3. Comparison of maximum adsorption capacities of various adsorbents for MB

Adsorbent	q_m (mg g ⁻¹)	Reference
Kaolinite	45.60	42
Magnetic multi-wall carbon nanotube	15.87	43
Walnut shells	51.55	44
Freeze-dried agarose gel	10.40	45
Zeolite A	64.80	46
Cortaderia selloana flower spikes	47.90	47
ZSM-5	8.67	48
Algerian palygorskite powder	57.50	49
(Chit/AILP-Kao) nanocomposite	99.01	50
Fly ash based spheres	79.70	51
Sodium dodecyl benzenesulfonate modified ZSM-5	15.68	48
Rice husk	40.59	52
Zeolite/Ferrite Nickel/Alginate nanocomposite	54.05	53
Nanozeolite L	80.64	This work

The Increase of percentage removal with temperature demonstrates that the adsorption process is endothermic. Thermodynamic parameters (ΔG° , ΔH° ; ΔS°) values were calculated using the following equations:

$$\Delta G^\circ = -RT \ln K_c \quad (7)$$

$$\ln K_c = \frac{\Delta S^\circ}{R} - \frac{\Delta H^\circ}{RT} \quad (8)$$

where R (8.314 J mol⁻¹K⁻¹) is the universal gas constant, T (K) is the absolute temperature, and K_c is the ratio of MB concentration adsorbed on the adsorbent at equilibrium and MB concentration remaining in solution at equilibrium. The values of ΔH° and ΔS° can be obtained from the slope and intercept of $\ln k_d$ versus $1/T$ plot, respectively. The obtained values of thermodynamic parameters are tabulated in Table 4. ΔG° values obtained negative, indicating that the adsorption process is thermodynamically feasible and spontaneous at room temperature.

The positive ΔS° value for MB adsorption onto nanozeolite L is due to increasing randomness at the solid-solution interface during the adsorption process.

The Values of ΔG° are negative, confirming that the adsorption process is thermodynamically feasible and spontaneous in nature. The obtained positive value of ΔH° reveals the endothermic nature of the adsorption process, and the calculated positive value of ΔS° is related to the increase of randomness at the solid-solution interface during the adsorption process.

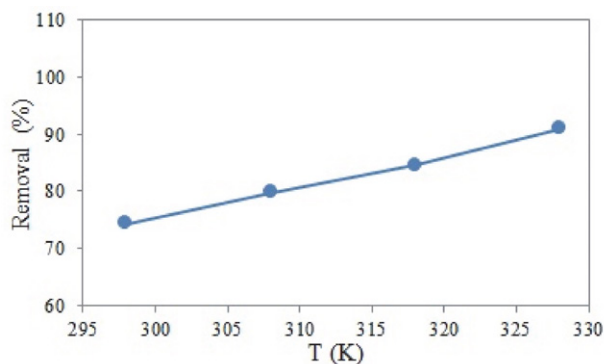


Figure 6. Effect of temperature on MB adsorption by nanozeolite L

Table 4. Thermodynamic parameters for MB adsorption by nanozeolite L

Temperature (K)	K_c	ΔG° (kJ mol ⁻¹)	ΔH° (kJ mol ⁻¹)	ΔS° (J K ⁻¹ mol ⁻¹)
298	2.880	-2.621	-26.256	96.66
308	3.998	-3.549		
318	5.446	-4.481		
328	7.690	-5.563		

4. Conclusion

Uniform nanoparticles of zeolite L were synthesized via a hydrothermal approach. Then the feasibility of using synthesized nanozeolite L as an adsorbent for MB removal was investigated.

The removal efficiency was optimized at a reaction time of 30 min at pH 9 and an adsorbent dose of 0.5 g l⁻¹. The experimental adsorption isotherm data were best fitted with the Langmuir model with a maximum sorption capacity of 80.64 mg g⁻¹. The better R² showed that the kinetics of the system could be conveniently modeled by the pseudo-second-order model, indicating that the rate controlling step is a chemisorption mechanism. The thermodynamic studies represent that the adsorption process is endothermic, feasible, and spontaneous in nature.

Based on these evidences, nanozeolite L with high adsorption capacity and low preparation cost can be used as an efficient and cost-effective adsorbent for the removal of MB from wastewater. For example, using this zeolite to separate MB from wastewater of dye and textile factories

can be applicative; also the ability of this zeolite can be examined to separate other industrial dyes wastewater.

5. References

- V. K. Gupta, A. Mittal, L. Krishnan, J. Mittal, *J. Colloid. Interf. Sci.* **2006**, *293*, 16–26. DOI:10.1016/j.jcis.2005.06.021
- R. Han, Y. Wang, W. Zou, Y. Wang, J. Shi, *J. Hazard. Mater.* **2007**, *145*, 331–335. DOI:10.1016/j.jhazmat.2006.12.027
- E. N. El-Qada, S. J. Allen, G. M. Walker, *Chem. Eng. J.* **2006**, *124*, 103–110. DOI:10.1016/j.cej.2006.08.015
- M. Ghaedi, S. Heidarpour, S. Nasiri Kokhdan, R. Sahraie, A. Daneshfar, B. Brazesh, *Powder Technol.* **2012**, *228*, 18–25. DOI:10.1016/j.powtec.2012.04.030
- K. Mahapatra, D. S. Ramteke, L. J. Paliwal, *J. Anal. Appl. Pyrol.* **2012**, *95*, 79–86. DOI:10.1016/j.jaap.2012.01.009
- J. Z. Yi, L. M. Zhang, *Bioresour. Technol.* **2008**, *99*, 2182–2186. DOI:10.1016/j.biortech.2007.05.028
- N. Salek Gilani, S. Ehsani Tilami, S. N. Azizi, *J. Chin. Chem. Soc.* **2021**, *68*, 2264–2273. DOI:10.1002/jccs.202100258
- A. E. Ofomaja, *Chem. Eng. J.* **2008**, *143*, 85–95. DOI:10.1016/j.cej.2007.12.019
- V. K. Garg, R. Gupta, A. Bala Yadav, R. Kumar, *Bioresour. Technol.* **2003**, *89*, 121–124. DOI:10.1016/S0960-8524(03)00058-0
- A. R. Tehrani-Bagha, H. Nikkar, N. M. Mahmoodi, M. Markazi, F. M. Menger, *Desalination* **2011**, *266*, 274–280. DOI:10.1016/j.desal.2010.08.036
- B. H. Hameed, A. L. Ahmad, and K. N. A., Latiff, *Dyes Pigm.* **2007**, *75*, 143–149. DOI:10.1016/j.dyepig.2006.05.039
- S. M. Sidik, A. A. Jalil, S. Triwahyono, S. H. Adam, M. A. H. Satar, B. H. Hameed, *Chem. Eng. J.* **2012**, *203*, 9–18. DOI:10.1016/j.cej.2012.06.132
- A. A. Jalil, S. Triwahyono, M. R. Yaakob, Z. Z. A. Azmi, N. Sapawe, N. H. N. Kamarudin, H. D. Setiabudi, N. F. Jaafar, S. M. Sidik, S. H. Adam, B. H. Hameed, *Bioresour. Technol.* **2012**, *120*, 218–224. DOI:10.1016/j.biortech.2012.06.066
- E. Bulut, M. Ozacar, I. A. Sengil, *J. Hazard. Mater.* **2008**, *154*, 613–622. DOI:10.1016/j.jhazmat.2007.10.071
- C. C. Wang, L. C. Juang, T. C. Hsu, C. K. Lee, F. C. Huang, *J. Colloid Interface Sci.* **2004**, *273*, 80–86. DOI:10.1016/j.jcis.2003.12.028
- M. H. Karaoglu, M. Dogan, M. Alkan, *Micropor. Mesopor. Mat.* **2009**, *122*, 20–27.
- R. Han, Y. Wang, Q. Sun, L. Wang, J. Song, X. He, C. Dou, *J. Hazard. Mater.* **2010**, *175*, 1056–1061. DOI:10.1016/j.jhazmat.2009.10.118
- S. J. Allen, E. Ivanova, B. Koumanova, *Chem. Eng. J.* **2009**, *152*, 389–395. DOI:10.1016/j.cej.2009.04.063
- B. A. Shah, A. V. Shah, R. V. Tailor, *J. Disper. Sci. Technol.* **2012**, *33*, 41–51. DOI:10.1080/01932691.2010.530079
- B. A. Shah, C. B. Mistry, A. V. Shah, *Chem. Eng. J.* **2013**, *220*, 172–184. DOI:10.1016/j.cej.2013.01.056
- A. S. Ozcan, B. Erdem, A. Ozcan, *Colloid Surface A* **2005**, *266*, 73–81.
- S. N. Azizi, S. Ghasemi S, and N. Salek Gilani, *Chinese J. Catal.* **2014**, *35*, 383–390. DOI:10.1016/S1872-2067(14)60002-4
- A. Mech, A. Monguzzi, F. Meinardi, J. Mezyk, G. Macchi, R. Tubino, *J. Am. Chem. Soc.* **2010**, *132*, 4574–4576. DOI:10.1021/ja907927s
- S. N. Azizi, S. Ghasemi S, N. Salek Gilani, *Monatsh. Chem.* **2016**, *147*, 1467–1474. DOI:10.1007/s00706-016-1664-3
- M. J. Climent, A. Corma, S. Iborra, *Chem. Rev.* **2011**, *111*, 1072–1133. DOI:10.1021/cr1002084
- L. Tosheva L, V. P. Valtchev, *Chem. Mater.* **2005**, *17*, 2494–2513. DOI:10.1021/cm047908z
- N. Salek Gilani, S. N. Azizi, S. Ghasemi, *Bull. Mater. Sci.* **2017**, *40*, 177–185. DOI:10.1007/s12034-016-1351-3
- L. J. Garces, V. D. Makwana, B. Hincapie, A. Sacco, S. L. Suib, *J. Catal.* **2003**, *217*, 107–116.
- Y. S. Ko, W. S. Ahn, *Bull. Korean Chem. Soc.* **1999**, *20*, 1–6.
- M. Thommes, **2010**, *82*, 1059–1073. DOI:10.1002/cite.201000064
- G. Zhang, Y. Bao, *Energy Proc.* **2011**, *16*, 1141–1146. DOI:10.1016/j.egypro.2012.01.182
- P. K. Mondal, R. Ahmad, R. Kumar, *Environ. Eng. Manag. J.* **2014**, *13*, 231–240. DOI:10.30638/eemj.2014.026
- R. Ahmad, *J. Hazard. Mater.* **2009**, *171*, 767–773. DOI:10.1016/j.jhazmat.2009.06.060
- T. C. R. Bertolini, J. C. Izidoro, C. P. Magdalena, D. A. Fungaro, *Orbital: Electron J. Chem.* **2013**, *5*, 179–191.
- Y. S. HO, G. McKay, *Can. J. Chem. Eng.* **1998**, *76*, 822–826. DOI:10.1002/cjce.5450760419
- Y. S. Ho, D. J. Wase, C. F. Forster, *Technol.* **1996**, *17*, 71–77. DOI:10.1080/09593331708616362
- S. A. Drweesh, N. A. Fathy, M. A. Wahba, A. A. Hanna, A. I. Akarish, E. A. Elzahany, K. S. J. *Environ. Chem. Eng.* **2016**, *4*, 1674–1684. DOI:10.1016/j.jcece.2016.02.005
- I. Langmuir, *J. Am. Chem. Soc.* **1918**, *40*, 1361–1403. DOI:10.1021/ja02242a004
- H. M. F. Freundlich, *J. Phys. Chem.* **1906**, *57*, 385–470. DOI:10.1515/zpch-1907-5723
- S. Netpradit, P. Thiravetyan, S. Towprayoon, *J. Colloid Interface Sci.* **2004**, *270*, 255–261. DOI:10.1016/j.jcis.2003.08.073
- F. Birch, *J. Geophys. Res.* **1986**, *91*, 4949–4954. DOI:10.1029/JB091iB05p04949
- S. Asuha, F. Fei, W. Wurendaodi, S. Zhao, H. Wu, and X. Zhuang, *Powder Technol.* **2019**, *361*, 624–632. DOI:10.1016/j.powtec.2019.11.068
- J. L. Gong, B. Wang, G. M. Zeng, C. P. Yang, C. G. Niu, Q. Y. Niu, W. J. Zhou, Y. Liang, *J. Hazard. Mater.* **2009**, *164*, 1517–1522. DOI:10.1016/j.jhazmat.2008.09.072
- R. Tang, C. Dai, C. Li, W. Liu, S. Gao, C. Wang, *J. Chem.* **2017**, *2017*, 1–10. DOI:10.1155/2017/8404965
- W. Y. Seow, C. A. E. Hauser, *J. Environ. Chem. Eng.* **2016**, *4*, 1714–1721. DOI:10.1016/j.jcece.2016.02.013
- N. Sapawe, A. A. Jalil, S. Triwahyono, M. I. A. Shah, R. Jusoh, N. F. M. Salleh, A. H. Karim, *Chem. Eng. J.* **2013**, *229*, 388–398. DOI:10.1016/j.cej.2013.06.005

47. N. Mechi, I. B. Khemis, G. L. Dotto, D. Franco, L. Sellaoui, A. B. Lamine, *J. Mol. Liq.* **2019**, *280*, 268–273. DOI:10.1016/j.molliq.2019.02.024
48. X. Jin, M. Jiang, X. Shan, Z. Pei, Z. Chen, *J. Colloid Interface Sci.* **2008**, *328*, 243–247. DOI:10.1016/j.jcis.2008.08.066
49. L. D. Youcef, L. S. Belaroui, A. L. Galindo, *Appl. Clay Sci.* **2019**, *179*, 105145. DOI:10.1016/j.clay.2019.105145
50. R. Ahmad, K. Ansari, *Process Biochem.* **2021**, *108*, 90–102. DOI:10.1016/j.procbio.2021.05.013
51. R. M. Novais, J. Carvalheiras, D. M. Tobaldi, M. P. Seabra, R. C. Pullar, J. A. Labrincha, *J. Clean. Prod.* **2019**, *207* 350–362. DOI:10.1016/j.jclepro.2018.09.265
52. V. Vadivelan, K. V. Kumar, *J. Colloid Interface Sci.* **2005**, *286*, 90–100. DOI:10.1016/j.jcis.2005.01.007
53. M. Bayat, V. Javanbakht, J. Esmaili, *Int. J. Biol. Macromol.* **2018**, *116*, 607–619. DOI:10.1016/j.ijbiomac.2018.05.012

Povzetek

Nanozeolit L je bil uporabljen kot adsorbent z namenom določitve njegove učinkovitosti za odstranjevanje strupenega barvila metilen modro (MB). Sintetizirani nanozeolit L je bil okarakteriziran z rentgensko difrakcijo (XRD), infrardečo Fourierjevo transformacijo (FTIR), elektronsko mikroskopijo (SEM), Brunauer-Emmett-Teller analizo (BET) in energijsko-disperzivno rentgensko spektroskopijo (EDX) za določitev njegovih osnovnih fizikalno-kemijske lastnosti. Adsorpcija je bila preučevana v odvisnosti od pH, količine adsorbenta, kontaktnega časa, začetne koncentracije MB in temperature. Adsorpcijsko obnašanje MB je bilo bolje opisano z Langmuirovo izotermo kot s Freundlichovo, največja adsorpcijska zmogljivost nanozeolita L pa je bila dosežena pri $80,64 \text{ mg g}^{-1}$. Negativna vrednost Gibbsove proste energije (ΔG°) in pozitivna vrednost standardne spremembe entalpije (ΔH°) sta potrdili, da je proces adsorpcije spontan in endotermen. Na podlagi teh ugotovitev je nanozeolit L z veliko površino, veliko adsorpcijsko zmogljivostjo in nizkimi stroški sinteze lahko učinkovit in ekonomičen adsorbent za odstranjevanje MB.



Except when otherwise noted, articles in this journal are published under the terms and conditions of the Creative Commons Attribution 4.0 International License

Synthesis, Characterization and Thermal Degradation Kinetics of a New Pyrazole Derived Methacrylate Polymer, Poly(1,3-Diphenyl-1H-Pyrazol-5-Yl Methacrylate)

Adnan Kurt^{1,*} and Murat Koca²

¹ Department of Chemistry, Faculty of Science and Arts, Adiyaman University, Adiyaman, Turkey

² Department of Pharm. Chemistry, Pharmacy Faculty, Adiyaman University, Adiyaman, Turkey

* Corresponding author: E-mail: akurt@adiyaman.edu.tr

Received: 03-09-2022

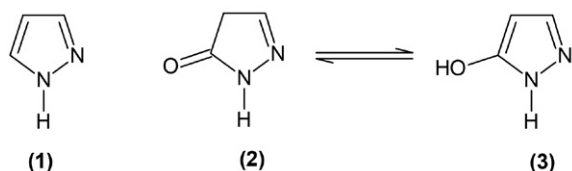
Abstract

Since the behavior and properties of macromolecular pyrazole derived polymers differ from their small molecules, such polymers are in the class of well-defined functional polymers due to the fact that the pyrazole ring contains two π -bonds as well as two hetero atoms in its structure, and this feature makes them important in the fields of scientific and technological applications. In present study, therefore, we synthesized a new pyrazole derived methacrylate monomer, 1,3-diphenyl-1H-pyrazol-5-yl methacrylate, from the reaction of 1,3-diphenyl-5-pyrazolone with methacryloyl chloride in the presence of triethylamine. After that, its homopolymerization was carried out by free radical polymerization method at 60 °C initiated with benzoyl peroxide. Spectral characterizations were achieved by ¹H-NMR and FTIR spectroscopies. The kinetics of thermal degradation of the new polymer, poly(1,3-diphenyl-1H-pyrazol-5-yl methacrylate), poly(DPPMA), were investigated by thermogravimetric analysis (TGA) at different heating rates. The initial decomposition temperature of the polymer changed from 216.3 °C to 243.5 °C depending on the increasing heating rate. The thermal decomposition activation energies in a conversion range of 7–19% were 79.45 kJ/mol and 81.56 kJ/mol by the Flynn–Wall–Ozawa and Kissinger methods, respectively. Thermodegradation mechanism of the poly(DPPMA) were investigated in detail by using different kinetic methods available in the literature such as Coats-Redfern, Tang, Madhusudanan and Van Krevelen. Among all these methods, the best result was obtained for Coats-Redfern method ($E = 90.93$ kJ/mol) at the optimum heating rate of 15 °C/min for D₁ mechanism that is a one-dimensional diffusion type deceleration mechanism.

Keywords: Pyrazole derived polymer; synthesis and characterization; thermal degradation kinetics; activation energy; reaction mechanism

1. Introduction

As is known, briefly, pyrazoles (or 1H-pyrazol) (1) are compounds in the class of heteroaromatic molecules containing two nitrogen atoms in the quintuple ring systems. When this five-membered lactam ring contains a ketonic group and two nitrogen atoms in its structure, it is called pyrazolone (or 1H-pyrazol-5(4H)-one) (2). There is also a tautomerization in the pyrazolone ring and, in that



case, the resulting compound is named as pyrazolol (or 1H-pyrazol-5-ol) (3).^{1,2}

The studies on the pyrazole/pyrazolones have gained importance recently, especially because of the broad pharmacological properties of these compounds. Some of these features are cytotoxic,³ anti-inflammatory,⁴ antimicrobial,⁵ antioxidant,⁶ antiviral,⁷ oral hypoglycemic activity,⁸ analgesic,⁹ etc. In addition, these compounds are widely used in the preparation of herbicides,¹⁰ liquid crystals,¹¹ dyes,¹² thermally stable polymers.^{13,14} Since pyrazolones have different biochemical and physicochemical properties, new scientific research programs have been developed in the synthesis of these compounds.¹ In this context, pyrazolones are traditionally prepared from the reaction of beta-keto esters with hydrazine derivatives in an acidic environment at high temperatures.¹⁵ In addition, the so-

lid-phase synthesis reaction,¹⁶ two-step reaction of benzoyl hydrazones with silyl enolates in catalytic medium,¹⁷ microwave synthesis method,¹⁸ solvent-free medium reaction¹⁴ are also available in literature.

Some of the features as above stated generally include the synthesis and application of these compounds in the form of small molecules. However, pyrazole/pyrazolone chemistry is also important for polymers. The behavior and properties of macromolecular pyrazole-derived polymers differ from these small molecules, and therefore, such polymers are in the class of well-defined functional polymers.¹⁹ The most important factor causing this is that the pyrazole ring contains two π -bonds as well as two hetero atoms in its structure. Thus, the electro-optical properties and thermal properties of polymers containing pyrazole ring comes to the fore.^{13,19–24} These polymers can be used in the semiconductor class thanks to their good optical properties such as refractive index, absorption, optical band gap, which are important for the electro-optical parts such as various diodes and transistors.^{22–24} On the other hand, the presence of such a hetero ring in the polymer main chain, as well as the partial delocalization of the π -bonds, cause side group interactions between polymer chains and on the polymer main chains. This significantly restricts the movement of polymer chains and also delays the thermal degradation of polymers. Therefore, these structural behaviors allow the preparation of thermally stable polymers.^{19–21} There are some studies in the literature investigating the thermal properties of pyrazole-derived polymers. One of these is reported by Connell et al, in that study, thermally stable polypyrazoles have been prepared by using the reactions of bis-hydrazines with acetylenic ketones and esters.²⁰ Moore and Mehta have developed a new way to synthesize polypyrazole by reacting bis-chloro vinylidene cyanides with diamines. They have succeeded in increasing the thermal stability of the synthesized polypyrazoles using the vinylic nucleophilic substitution reaction.²¹

Free radical addition polymerization is a well-known polymerization method that has been studied in detail. This method has been one of the most useful and beneficial areas of chemistry ever discovered. It is widely used in scientific and technological fields. It has been one of the most preferred polymerization methods in almost every period and platform. The free radical polymerization method is highly tolerant of functional groups in monomers and polymerization can occur in a wide variety of environments.²⁵ Free radical polymerization takes place in three different stages: initiation, propagation and termination.²⁶ In addition to chemical initiators such as organic peroxides, azo compounds, redox initiators as initiator system, radical polymerization can also be initiated with different physical factors such as heat, light, high energy, electrochemical method, etc.²⁷ In addition, radical polymerization is a very effective polymerization method in the polymerization of olefins, styrene and its derivatives, acrylamides, acrylates, methacrylates and their derivatives, and many other vinylic mono-

mers, including unsaturated alkene chemistry.²⁸ On the other hand, there are different polymerization techniques in polymer chemistry and they are widely used for the purpose. Suspension and emulsion polymerizations have been used in important industrial processes for years. Apart from these, step growth polymerization techniques, ionic addition, coordination, ring opening, electrochemical polymerization etc. have been used for years.²⁵ In recent years, controlled polymerization techniques such as atom transfer radical polymerization (ATRP), degenerative transfer (DT), reversible addition fragmentation chain transfer processes (RAFT), nitroxide mediated polymerization (NMP), stable free radical polymerization (SFRP) have been developed to control the molecular weight distribution.²⁹ Generally, in these methods, since special reaction conditions and reagents are required, the application area is relatively limited, costly and mostly preferred in the synthesis of specific polymers. However, some factors such as ease of application, cheapness, low number of reagents (monomer and initiator), etc. make free radical polymerization more advantageous and common.³⁰

As mentioned above, most of the reported studies on pyrazole/pyrazolone derivatives are for the synthesis of small molecules using different organic synthesis reactions and some applications. Within our knowledge of the literature, the studies on the synthesis of polymers derived from the pyrazole molecule, especially the methacrylate polymers containing it as a side group, is quite limited. Unfortunately, the study investigating the thermal degradation kinetics of pyrazole-derived methacrylate polymers is not seen in the literature. In order to fill this lack of literature, we aim the synthesis and spectral characterization of a new pyrazole-derived methacrylate polymer, poly(1,3-diphenyl-1H-pyrazol-5-yl methacrylate), poly(DPPMA), in the present study. The thermal behavior of the polymer is determined using the thermogravimetric analysis method (TGA). In addition, the thermal decomposition kinetics of the polymer have been investigated in detail by using different kinetic methods available in the literature. Kinetic parameters such as the activation energy and thermal decomposition mechanism are reported.

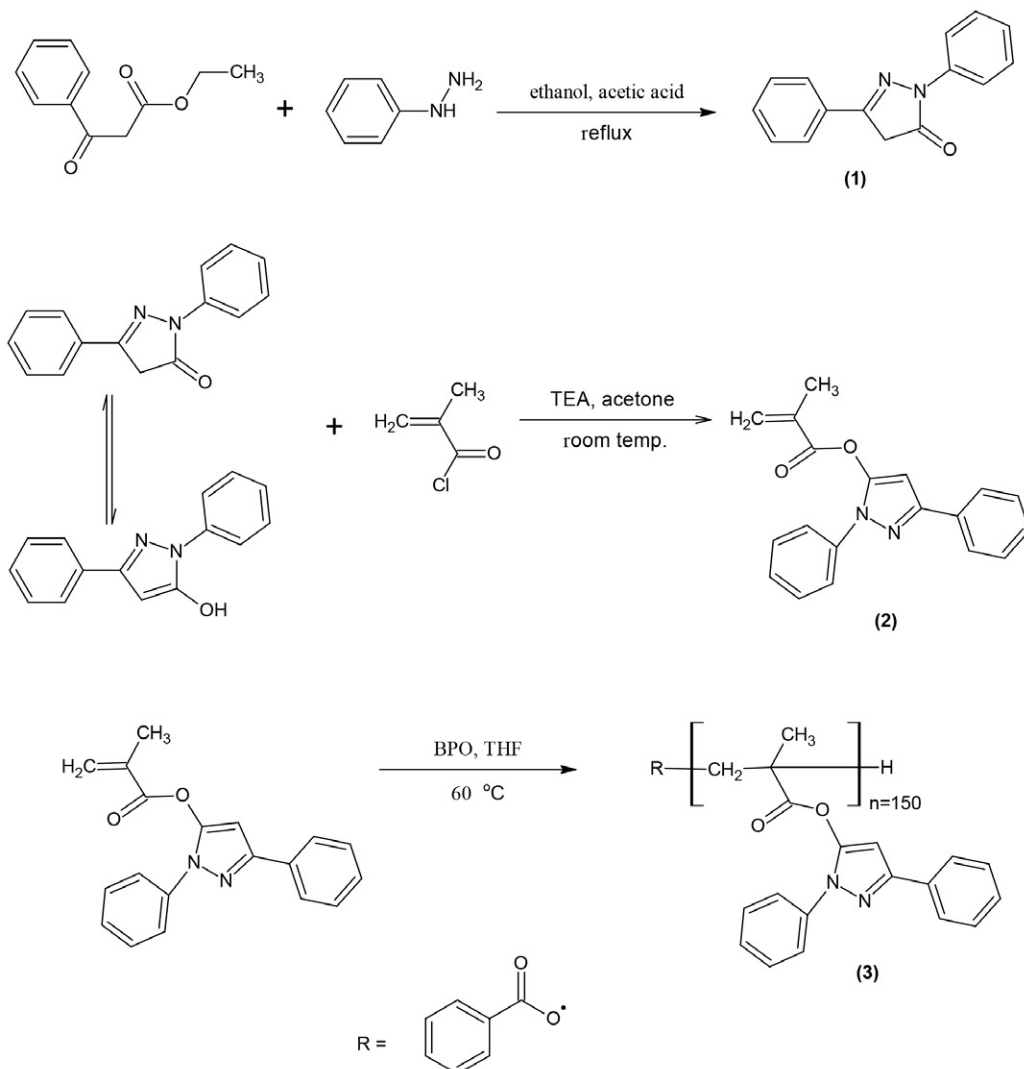
2. Experimental

2.1. Materials

Ethyl benzoylacetate, phenylhydrazine, methacryloyl chloride, triethylamine (TEA), benzoyl peroxide (BPO), acetone, acetic acid, chloroform, ethyl alcohol and tetrahydrofuran (THF) were purchased from Sigma-Aldrich. Benzoyl peroxide before use in the polymerization as initiator was crystallized in ethanol.

2.2. Synthesis of 1,3-diphenyl-5-pyrazolone

Ethyl benzoylacetate (1.921 g, 10 mmol), phenylhydrazine (1.081 g, 10 mmol), ethanol (25 ml) and catalytic



Scheme 1. Homopolymerization of 1,3-diphenyl-1H-pyrazol-5-yl methacrylate monomer

amount of acetic acid were added into a 50 ml single-necked reaction flask and refluxed for 12 h on a magnetic stirrer using a method similar to that previously reported.¹ After the mixture was cooled to room temperature, it was precipitated in water. The product was then recrystallized in ethanol, and dried. The yield (1) was calculated as 94%.

FTIR (cm^{-1}): 3067–3044 (aromatic C-H stretching), 2956–2911 (aliphatic C-H stretching), 1699 (pyrazolone C=O stretching).

$^1\text{H-NMR}$ (600MHz, CDCl_3): δ (ppm) = 7.4–8.1 (multiple, 10H, phenyl ring protons), 3.8 (singlet, 2H, pyrazolone ring protons)

2. 3. Synthesis of 1,3-diphenyl-1H-pyrazol-5-yl Methacrylate

1,3-diphenyl-5-pyrazolone (2.3627 g, 10 mmol), methacryloyl chloride (1.0453 g, 10 mmol), triethylamine (1.0119 g, 10 mmol) and acetone (50 ml) were added into

a 100 ml single-necked reaction flask and stirred for 24 h at room temperature. The crude product was precipitated in water. It was crystallized again in ethanol. The yield (2) was calculated as 74%.

FTIR (cm^{-1}): 3085–3036 (aromatic C-H stretching), 2987–2903 (aliphatic C-H stretching), 1744 (methacrylate ester C=O stretching), 1635 (aliphatic C=C stretching), 1596 (aromatic C=C stretching), 1109 (-COC- stretching).

$^1\text{H-NMR}$ (600MHz, CDCl_3): δ (ppm) = 7.4–8.0 (multiple, 10H, phenyl ring protons), 6.8 (singlet, 1H, pyrazolone ring proton), 6.4 (singlet, 1H vinyl proton) 5.8 (singlet, 1H, vinyl proton), 2.0 (singlet, 3H, methyl protons next to vinyl group)

2. 4. Synthesis of Poly(1,3-diphenyl-1H-pyrazol-5-yl methacrylate)

The homopolymerization of 1,3-diphenyl-1H-pyrazol-5-yl methacrylate monomer was carried out under

conventional free radical polymerization conditions. For this purpose, monomer (1.000 g), benzoyl peroxide (0.0100 g, 1% w/w of monomer) as initiator and THF (3 ml) as solvent were added into a polymerization tube, respectively, and the mixture was dissolved. It was then passed through argon gas for about 15 minutes. The tube was closed and immersed in an oil bath preheated to 60 °C. After a 21 h polymerization time, the polymer mixture was cooled to room temperature, and then precipitated twice in excess ethanol. The resulting polymer (3) was filtered, and dried under vacuum overnight. The appropriate scheme for this synthesis is shown in Scheme 1.

FTIR (cm^{-1}): 3095–3030 (aromatic C-H stretching), 2996–2909 (aliphatic C-H stretching), 1764 (methacrylate ester carbonyl stretching), 1595 (aromatic C=C stretching), 1072 (-COC- stretching)

$^1\text{H-NMR}$ (300MHz, CDCl_3): δ (ppm) = 7.7–6.8 (phenyl ring protons), 6.6 (pyrazol ring proton), 1.8 and 0.8 (methylene and methyl protons in the polymer main chain, respectively).

2. 5. Characterization Techniques

The spectral characterizations were performed with a Perkin Elmer Spectrum 100 FTIR spectrometer with an attenuated total reflectance accessory and also with a high resolution Bruker Avance III HD 600 MHz NMR Spectrometer (its 300 MHz version used for homopolymer). NMR measurements were taken at room temperature using deuterated chloroform solvent and tetramethylsilane standard. Molecular weight and molecular weight distribution of polymer was determined by gel permeation chromatography (GPC) a Malvern Viscotek GPCmax system equipped with a refractive index detector. The eluting solvent was tetrahydrofuran (THF) and calibrated by using polystyrene as standard. A Perkin Elmer Differential Scanning Calorimeter (Pyris 6 DSC) was used to determine the glass transition temperature of poly(DPPMA) in the temperature range of 30–210 °C at a heating rate of 5 °C/min under a nitrogen atmosphere (100 ml/min). TGA analysis was performed on a Seiko SII 7300 TG/DTA thermobalance for obtaining the TG/DTG curves. Polymer samples were added to aluminum pans and then submitted to a controlled temperature program from ambient temperature to 500 °C in nitrogen flow of 25 mL/min. The samples were heated at various heating rates of 5, 10, 15 and 20 °C/min, respectively, in order to determine the kinetic parameters of the thermal decomposition of polymer.

3. Results and Discussion

Figure 1a shows the FTIR spectrum of 1,3-diphenyl-5-pyrazolone compound. The most characteristic absorption bands are observed at the frequencies of 3067–

3044 cm^{-1} (aromatic C-H stretching), 2956–2911 cm^{-1} (aliphatic C-H stretching), 1699 cm^{-1} (pyrazolone C=O stretching). FTIR spectrum of 1,3-diphenyl-1H-pyrazol-5-yl methacrylate monomer is shown in Figure 1b where the aromatic and aliphatic C-H stretchings are absorbed at 3085–3036 cm^{-1} and 2987–2903 cm^{-1} , respectively. The other important bands are recorded at 1744 cm^{-1} for methacrylate ester C=O stretching, 1635 cm^{-1} for aliphatic C=C stretching, 1596 cm^{-1} for aromatic C=C stretching, 1109 cm^{-1} for -COC- stretching. Figure 1c shows the FTIR spectrum of poly(1,3-diphenyl-1H-pyrazol-5-yl methacrylate). In this figure, the most significant change is that the signal observed at 1635 cm^{-1} characteristic for C=C stretching in the vinyl group is lost due to polymerization. The disappearance of this signal is the most obvious evidence that polymerization has taken place, so it can be easily detected by FTIR.³¹ The characteristic absorptions are also attributed to aromatic C-H stretching (3095–3030 cm^{-1}), aliphatic C-H stretching (2996–2909 cm^{-1}), methacrylate ester carbonyl stretching (1764 cm^{-1}), aromatic C=C stretching (1595 cm^{-1}) and -COC- stretching (1072 cm^{-1}).

$^1\text{H-NMR}$ spectra of all compounds are shown in Figure 2. Among them, Figure 2a is recorded for 1,3-diphenyl-5-pyrazolone in which the multiple peaks in the range of 7.4–8.1 ppm are due to the phenyl ring protons. The singlet observed at 3.8 ppm is for the protons in the pyrazolone ring.

Figure 2b is also recorded for 1,3-diphenyl-1H-pyrazol-5-yl methacrylate monomer. As a result of tauterization in pyrazolone ring and then bonding of the methacryl group to it, the protons in the pyrazole ring decreased to one proton, which is resonated in the low chemical shift region at 6.8 ppm as a singlet. The location of the protons in the phenyl ring did not change significantly and signaled at 7.4–8.0 ppm. Two singlet at 5.8 and 6.4 ppm, which are new signals proving that the methacrylate group

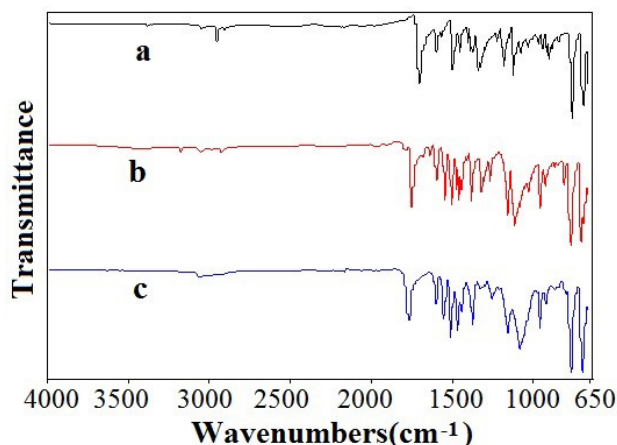


Figure 1. FTIR spectra: a) 1,3-diphenyl-5-pyrazolone, b) 1,3-diphenyl-1H-pyrazol-5-yl methacrylate, c) poly(1,3-diphenyl-1H-pyrazol-5-yl methacrylate)

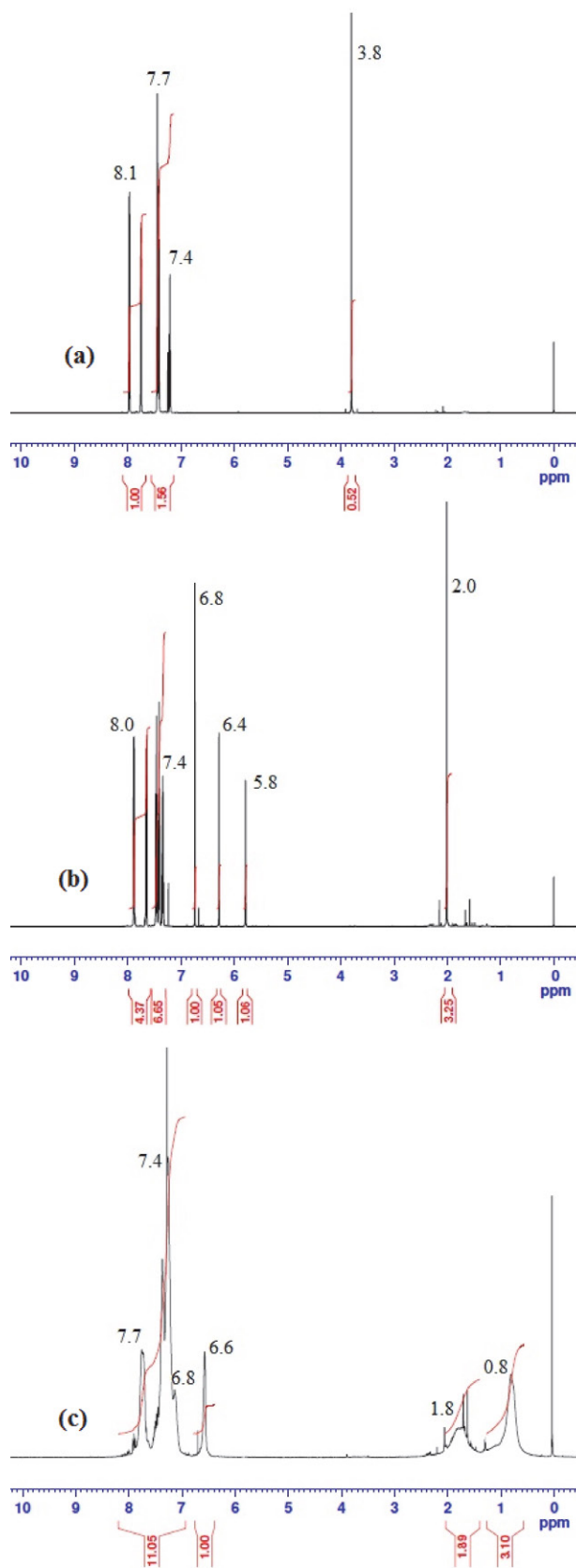


Figure 2. $^1\text{H-NMR}$ spectra: a) 1,3-diphenyl-5-pyrazolone, b) 1,3-diphenyl-1H-pyrazol-5-yl methacrylate, c) poly(1,3-diphenyl-1H-pyrazol-5-yl methacrylate)

is in the structure, are attributed to methylene protons in the vinyl group. In addition, the singlet corresponding to 3 protons at 2.0 ppm is characteristic for the methyl protons adjacent to the vinyl group. $^1\text{H-NMR}$ spectrum of poly(1,3-diphenyl-1H-pyrazol-5-yl methacrylate) homopolymer is shown in Figure 2c. The 5.8 ppm and 6.4 ppm signals, the two most important characteristic signals for the monomer, are disappeared due to polymerization. These signals are shifted to 1.8 ppm as a new signal group and appeared as methylene protons in the polymer main chain. Methacrylate methyl protons are also shifted to 0.8 ppm. The signal at 6.6 ppm is due to the proton in the pyrazol ring, and the 7.7–6.8 ppm signals are also due to the protons in the phenyl ring.

Figure 3 shows the chromatogram output of the gel permeation chromatography (GPC). The number – average molecular weight of the pyrazole derived poly(1,3-diphenyl-1H-pyrazol-5-yl methacrylate) polymer is measured to be 45800 and its molecular weight distribution (polydispersity) is 3.24. Since the free radical polymerization method is used, the measured polydispersity value is relatively moderate and in the acceptable range for this method. As seen in the literature, a precise molecular weight and distribution control cannot be achieved in the free radical polymerization process. This is because all polymer chains cannot be started at the same time, and undesirable events such as chain termination, chain transfers, etc. also occur simultaneously. Thus, very large and small chains may form during polymerization and the chain distribution may often wide (polydispersity ≥ 2).³² In addition, the molecular mass of present DPPMA monomer is 304.342 g/mol, and thus the degree of polymerization (D_p) is calculated as 150.

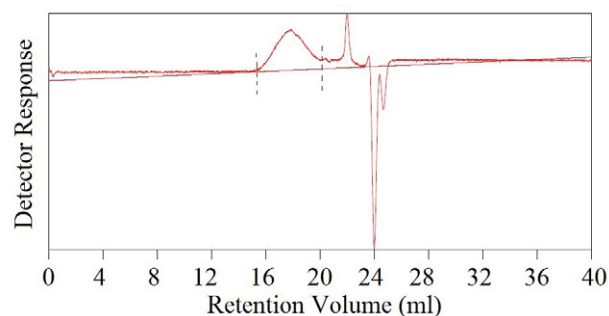


Figure 3. GPC chromatogram of poly(1,3-diphenyl-1H-pyrazol-5-yl methacrylate)

The glass transition temperature of poly(1,3-diphenyl-1H-pyrazol-5-yl methacrylate) was determined by using differential scanning calorimetry technique (DSC) and its thermogram is illustrated in Figure 4. As can be seen from that thermogram, the glass transition temperature of poly(1,3-diphenyl-1H-pyrazol-5-yl methacrylate) was measured to be 158.1 °C. Similar results to this measured value are seen in the literature for pyrazole derived hetero-

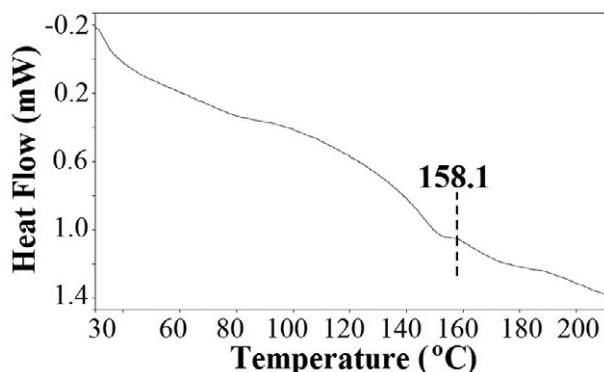


Figure 4. DSC thermogram of poly(1,3-diphenyl-1H-pyrazol-5-yl methacrylate)

cyclic polymers. Wang and Cheng synthesized a series of 3,5-disubstituted pyrazole polymers and found that the glass transition temperatures of these polymers varied in the range of 147 °C–158 °C.³³

Thermal analysis of poly(1,3-diphenyl-1H-pyrazol-5-yl methacrylate) was performed by thermogravimetric analysis (TGA). The thermal decomposition process was followed on a temperature range of ~25–500 °C in nitrogen gas atmosphere in order to detect the possible data of decomposition phases. Therefore, a controlled heating program at different rates of 5, 10, 15 and 20 °C/min was applied to this process. TGA thermograms recorded from these heatings are given in Figure 5 comparatively.

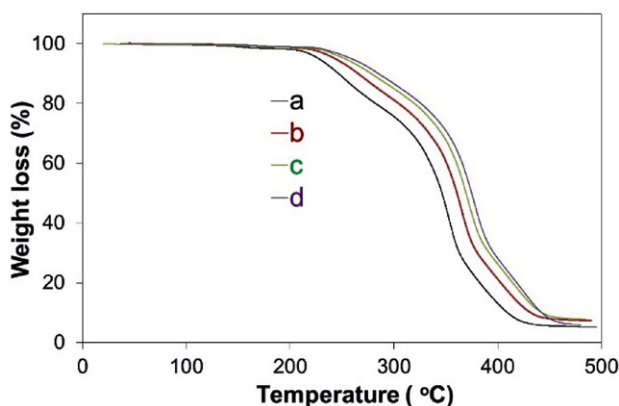


Figure 5. TGA curves of poly(1,3-diphenyl-1H-pyrazol-5-yl methacrylate) at different heating rates of a) 5, b) 10, c) 15 and d) 20 °C/min.

Table 1. Thermal data of poly(1,3-diphenyl-1H-pyrazol-5-yl methacrylate)

Reaction rate (°C/min)	T _{initial} (°C)	T _{final} (°C)	T _{%50} (°C)	%Weight loss at 300 °C	%Weight loss at 350 °C	%Weight loss at 400 °C	%Residue at 500 °C
5	216.3	431.6	346.3	24.4	54.5	86.9	5.1
10	230.9	445.2	360.7	18.9	39.5	78.8	7.2
15	238.8	454.2	369.5	15.0	32.2	73.7	7.7
20	243.5	463.7	374.8	13.4	29.1	71.9	5.9

In general, at these heating conditions, the degradation of the poly(1,3-diphenyl-1H-pyrazol-5-yl methacrylate) took place in three stages. The first one, with up to 20% weight loss at ~215–300 °C usually caused by volatile hydrocarbons, the second decomposition stage is about between 300–380 °C with up to 70% weight loss, and the third one is ~380–450 °C with up to 93% weight loss (according to 10 °C/min used as reference). These results are in good agreement with the thermal behavior of pyrazole polymers. Wang and Cheng reported 3,5-disubstituted polypyrazoles synthesized by click polymerization procedure were decomposed at ~290 °C about 10% of their weight losses.³³ Some thermal data obtained in the thermal decomposition of the polymer, such as the initial decomposition temperature, the final decomposition temperature, the temperature at 50% mass loss, the % decomposition values at different temperatures, the % residual value, etc. are determined. These values are summarized in Table 1. As can be seen from the Table 1, the initial degradation temperatures of the polymer were calculated as 216.3, 230.9, 238.8 and 243.5 °C at heating rates of 5, 10, 15 and 20 °C/min. As expected, there is a positive correlation between heating rate increase and thermal stability. Similar results for thermal degradation of heterocyclic polymers have been reported in our previous publications and also by different researchers.^{34–42} For example, Kurt et al.³⁷ reported the degradation temperatures of an isocoumarin derived polymer changed in a positive direction, which increased 256.6 °C to 286.1 °C by increasing heating rate from 5 to 20 °C/min. Meng and friends investigated the thermal degradation kinetics of a polyimide polymer containing 2,6-benzobisoxazole units and reported the onset decomposition temperatures increased with increase of heating rates.⁴⁰

A typical kinetic process for thermal decomposition of polymeric materials can be given by the following equation:⁴³

$$\frac{d\alpha}{dt} = A \exp\left(-\frac{E}{RT}\right) f(\alpha) \quad (1)$$

where $f(\alpha)$ is the differential function of a kinetic model, A is the pre-exponential factor, E is activation energy, R is the ideal gas constant (8.314 J/mol K), T is the absolute temperature (K), α is the extent of reaction and t is the time.

The integral function of a kinetic model, $g(\alpha)$, can be expressed as:

$$g(\alpha) = \int_0^{\alpha_p} \frac{d\alpha}{f(\alpha)} = \frac{A}{\beta} \int_0^{T_p} e^{-\frac{E}{RT}} dT \quad (2)$$

where β is the heating rate and T_p is the peak temperature (K). Thermal degradation of polymers mostly proceeds via a sigmoidal type mechanism or a deceleration type mechanism.⁴³ Different versions of these mechanisms are stated in Table 2. These $g(\alpha)$ functions allow the determination of thermal degradation mechanism of polymer by thermogravimetry method.⁴⁴ Besides, derivative thermogravimetry (DTG) method is also used to determine the thermal decomposition mechanisms of polymers and to determine the physical or chemical interaction types during decomposition. Therefore, kinetic parameters of thermal degradation can be determined based on TG/DTG data. These kinetic parameters are highly dependent on the calculation methods due to the different solutions of Equation 2. There are many methods in which the apparent activation energies are determined based on the data obtained from TGA curves recorded at different heating rates. Here, we used some kinetic methods namely, Flynn-Wall-Ozawa, Kissinger, Coats-Redfern, Tang, Madhusudanan and Van Krevelen method in order to determine kinetic parameters and decomposition mechanism for the degradation of poly(1,3-diphenyl-1H-pyrazol-5-yl methacrylate).

Of the kinetic methods mentioned, Flynn-Wall-Ozawa^{45,46} and Kissinger⁴⁷ methods do not depend on the reaction mechanism and the degree of reaction. Therefore, it is used to calculate the thermal degradation activation energy of the polymer.^{37,40,43} The Flynn-Wall-Ozawa equation is expressed as:

$$\log \beta = \log \left[\frac{AE}{g(\alpha)R} \right] - 2.315 - \frac{0.457 E}{RT} \quad (3)$$

Table 2. Algebraic expressions for $g(\alpha)$ for the most frequently used mechanisms of solid state processes

Symbol	$g(\alpha)$	Solid state processes
Sigmoidal curves		
A ₂	$[-\ln(1-\alpha)]^{1/2}$	Nucleation and growth (Avrami equation 1)
A ₃	$[-\ln(1-\alpha)]^{1/3}$	Nucleation and growth (Avrami equation 2)
A ₄	$[-\ln(1-\alpha)]^{1/4}$	Nucleation and growth (Avrami equation 3)
Deceleration curves		
R ₁	α	Phase boundary controlled reaction (One-dimensional movement)
R ₂	$[1-(1-\alpha)^{1/2}]$	Phase boundary controlled reaction (contraction area)
R ₃	$[1-(1-\alpha)^{1/3}]$	Phase boundary controlled reaction (contraction volume)
D ₁	α^2	One-dimensional diffusion
D ₂	$(1-\alpha)\ln(1-\alpha)+\alpha$	Two-dimensional diffusion
D ₃	$[1-(1-\alpha)^{1/3}]^2$	Three-dimensional diffusion (Jander equation)
D ₄	$(1-2/3\alpha)(1-\alpha)^{2/3}$	Three-dimensional diffusion (Ginstling-Brounshtein equation)
F ₁	$-\ln(1-\alpha)$	Random nucleation with one nucleus on the individual particle
F ₂	$1/(1-\alpha)$	Random nucleation with two nuclei on the individual particle
F ₃	$1/(1-\alpha)^2$	Random nucleation with three nuclei on the individual particle

According to this equation, in order to calculate the activation energy, $\log \beta$ values versus $(1000/T)$ values are plotted and the E value is calculated from the slope of the obtained line. For this, the decomposition temperatures corresponding to 7%, 9%, 11%, 13%, 15%, 17% and 19% conversions at different heating rates were measured and these values were plotted for each conversion as shown in Figure 6.

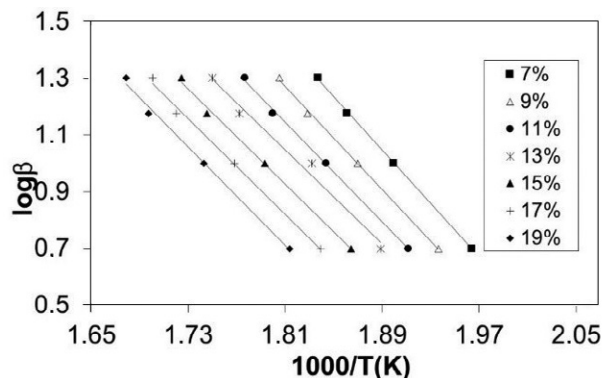


Figure 6. Flynn-Wall-Ozawa lines at different conversion values.

As can be seen from the figure, the lines of all conversions in an almost parallel order. In addition, the linear regression value of each line is also a high level. This increases the reliability of the calculations. The activation energy value corresponding to each conversion mentioned above was calculated separately. The results are given in Table 3. According to the table, activation energy values varied between the lowest value 75.43 kJ/mol and the highest 85.82 kJ/mol in the studied conversion range. The mean thermal decomposition activation energy value of poly(1,3-diphenyl-1H-pyrazol-5-yl methacrylate) according was calculated as 79.45 kJ/mol. The closest activation

Table 3. Activation energies of poly(1,3-diphenyl-1H-pyrazol-5-yl methacrylate) obtained by Flynn-Wall-Ozawa method

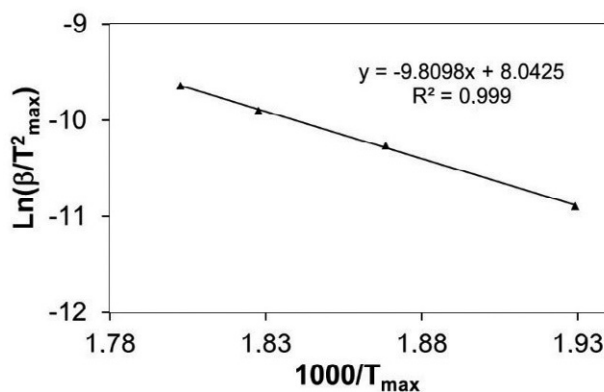
α (%)	E (kJ/mol)	R
7	85.82	0.9996
9	82.71	0.9990
11	80.16	0.9985
13	75.43	0.9840
15	76.23	0.9965
17	76.75	0.9956
19	79.06	0.9951
Mean	79.45	

energy value to that was reached at a conversion of 19%, with a value of 79.06 kJ/mol.

The activation energy of thermal decomposition of poly(1,3-diphenyl-1H-pyrazol-5-yl methacrylate) was also determined by the Kissinger method. This method, like the Flynn-Wall-Ozawa method, does not depend on the reaction mechanism and order. This method is expressed by following equation:

$$\ln\left(\frac{\beta}{T_{\max}^2}\right) = \left\{ \ln\frac{AR}{E} + \ln\left[n(1 - \alpha_{\max})^{n-1}\right] \right\} - \frac{E}{RT_{\max}} \quad (4)$$

where n is the reaction order, T_{\max} is the temperature at the maximum reaction rate, α_{\max} is the maximum conversion at T_{\max} . According to this method, $\ln(\beta/T_{\max}^2)$ versus $1000/T_{\max}$ values are plotted and the activation energy is determined from the slope of this line. Figure 7 shows these plots. The T_{\max} values required to determine the activation energy according to the Kissinger method were measured from the DTG curves. These temperatures were 245.12, 262.04, 273.98 and 281.59 °C for the rates of 5, 10, 15 and 20 °C/min, respectively. Accordingly, the activation energy value was determined as 81.56 kJ/mol with a high linear regression ($R = 0.9990$) using the Kissinger method. When the results are examined, an energy difference of only 2.11 kJ/mol is detected among the energy values of these integral methods. This result also shows that there is

**Figure 7.** $\ln(\beta/T_{\max}^2)$ versus $1000/T_{\max}$ plots obtained from Kissinger method.

a very good agreement between the methods used and the reliability of the results is high.

There are some kinetic methods in which the different sigmoidal and deceleration type $g(\alpha)$ functions given in Table 2 are analyzed with different approaches in determining the thermal degradation mechanism of the polymer. One of these methods is the Coats-Redfern method.⁴⁸ This method is used the below equation:

$$\ln\frac{g(\alpha)}{T^2} = \ln\frac{AR}{\beta E} - \frac{E}{RT} \quad (5)$$

From the fitting $\ln[g(\alpha)/T^2]$ vs. $1000/T$ plots, the activation energy corresponding to different $g(\alpha)$ functions is obtained at constant heating rates. Another method to determine thermodegradation mechanism is Tang method,⁴⁹ and which used:

$$\ln\left[\frac{g(\alpha)}{T^{1.89466100}}\right] = \left[\ln\frac{AE}{\beta R} + 3.63504095 - 1.89466100 \ln E\right] - 1.00145033\frac{E}{RT} \quad (6)$$

The plots of $\ln[g(\alpha)/T^{1.89466100}]$ vs. $1000/T$ give a straight line and from its slope, E can be calculated for each $g(\alpha)$ function. Madhusudanan method⁵⁰ is another one, and which is expressed as:

$$\ln\left[\frac{g(\alpha)}{T^{1.921503}}\right] = \left[\ln\frac{AE}{\beta R} + 3.772050 - 1.921503 \ln E\right] - 1.000955716\frac{E}{RT} \quad (7)$$

E values for each $g(\alpha)$ mechanisms can be calculated from the slope of $\ln[g(\alpha)/T^{1.921503}]$ vs. $1000/T$ plots. As a final method, the Van Krevelen method⁵¹ is proposed by the following equation:

$$\log g(\alpha) = \log B + \left(\frac{E}{RT_r} + 1\right) \log T \quad (8)$$

where T_r corresponds the reference temperature which is taken as the temperature of the maximum reaction rate obtained by derivative thermogravimetry. E is defined from a linear fitting of $\log g(\alpha)$ vs. $\log T$ plots for every $g(\alpha)$ mechanisms.

In general, each activation energy value calculated for the $g(\alpha)$ mechanisms in different states and for the heating rates is compared with the Flynn-Wall-Ozawa and Kissinger methods to determine the thermal degradation mechanism of the polymer. Because, as is known, these two methods are independent of the reaction mechanism and order. The activation energies, obtained from the other methods, closest to Flynn-Wall-Ozawa and Kissinger methods are determined. The corresponding $g(\alpha)$ mechanism is accepted as the thermal decomposition mechanism of the pro-

Table 4. Activation energies of poly(1,3-diphenyl-1H-pyrazol-5-yl methacrylate using Coats-Redfern Method

Mechanism	Heating Rate							
	5 °C/min		10 °C/min		15 °C/min		20 °C/min	
	E (kJ/mol)	R	E (kJ/mol)	R	E (kJ/mol)	R	E (kJ/mol)	R
A ₂	20.57	0.9659	19.02	0.9719	17.43	0.9825	18.22	0.9858
A ₃	10.78	0.9445	9.63	0.9506	8.50	0.9661	8.99	0.9730
A ₄	5.88	0.8977	4.94	0.8968	4.04	0.9157	4.38	0.9351
R ₁	46.17	0.9729	43.56	0.9783	40.79	0.9866	42.39	0.9888
R ₂	48.04	0.9751	45.34	0.9803	42.48	0.9882	44.13	0.9902
R ₃	48.67	0.9758	45.95	0.9809	43.05	0.9887	44.72	0.9907
D ₁	101.16	0.9776	96.26	0.9824	90.93	0.9894	94.24	0.9912
D ₂	103.61	0.9787	98.60	0.9834	93.15	0.9902	96.54	0.9919
D ₃	106.15	0.9799	101.03	0.9845	95.45	0.9910	98.91	0.9926
D ₄	104.46	0.9791	99.41	0.9838	93.92	0.9905	97.33	0.9921
F ₁	49.95	0.9772	47.17	0.9822	44.20	0.9896	45.92	0.9915
F ₂	-1.08	0.9731	-1.75	0.9845	-2.35	0.9744	-2.24	0.9603
F ₃	6.66	0.9961	5.65	0.9908	4.65	0.9648	4.99	0.9590

cess. The heating rate corresponds to the optimum heating rate.^{37,43} The activation energy values calculated for each $g(\alpha)$ function for different heating rates using the above kinetic methods are given in Tables 4–7. Conversion percentages for this process are between 7% and 19%. When these tables were analyzed in detail, it was determined that the degradation of polymer progressed through the D_n mechanism, which is a common degradation mechanism for all methods. Because, the activation energy values calculated for the D_n mechanisms (deceleration-type dimensional diffusions) are the closest to the Flynn-Wall-Ozawa and Kissinger methods. In addition, linear regression values determined for D_n mechanisms are relatively high. In order to see the results more clearly, the activation energy values corresponding to the D_n mechanisms calculated for all methods are also summarized in Table 8.

Table 4 shows the results obtained for the Coats Redfern method. Compared to other methods and their D_n

mechanisms, especially for the D_1 mechanism, the activation energy value at the heating rate of 15 °C is 90.93 kJ/mol. This value is very close to the values obtained from Flynn-Wall-Ozawa ($E = 79.45$ kJ/mol) and Kissinger ($E = 81.56$ kJ/mol) methods, and the results are quite compatible. According to the results calculated by the Coats Redfern method, it can be said that the thermal degradation mechanism of poly(1,3-diphenyl-1H-pyrazol-5-yl methacrylate) proceeds strongly through the D_1 mechanism, deceleration type one-dimensional diffusion mechanism.

Activation energy and linear regression values calculated according to the Tang method are given in Table 5. As can be seen from this table, the closest result to Flynn-Wall-Ozawa and Kissinger methods among all $g(\alpha)$ mechanisms is obtained for D_1 mechanism at 15 °C heating rate, which is $E = 91.29$ kJ/mol. The results obtained from Tang method also support the Coats Redfern method and increase the reliability of their results.

Table 5. Activation energies of poly(1,3-diphenyl-1H-pyrazol-5-yl methacrylate using Tang Method

Mechanism	Heating Rate							
	5 °C/min		10 °C/min		15 °C/min		20 °C/min	
	E (kJ/mol)	R	E (kJ/mol)	R	E (kJ/mol)	R	E (kJ/mol)	R
A ₂	20.57	0.9659	19.02	0.9719	17.43	0.9825	18.22	0.9858
A ₃	10.78	0.9445	9.63	0.9506	8.50	0.9661	8.99	0.9730
A ₄	5.88	0.8977	4.94	0.8968	4.04	0.9157	4.38	0.9351
R ₁	46.17	0.9729	43.56	0.9783	40.79	0.9866	42.39	0.9888
R ₂	48.04	0.9751	45.34	0.9803	42.48	0.9882	44.13	0.9902
R ₃	48.67	0.9758	45.95	0.9809	43.05	0.9887	44.72	0.9907
D ₁	101.16	0.9776	96.26	0.9824	90.93	0.9894	94.24	0.9912
D ₂	103.61	0.9787	98.60	0.9834	93.15	0.9902	96.54	0.9919
D ₃	106.15	0.9799	101.03	0.9845	95.45	0.9910	98.91	0.9926
D ₄	104.46	0.9791	99.41	0.9838	93.92	0.9905	97.33	0.9921
F ₁	49.95	0.9772	47.17	0.9822	44.20	0.9896	45.92	0.9915
F ₂	-1.08	0.9731	-1.75	0.9845	-2.35	0.9744	-2.24	0.9603
F ₃	6.66	0.9961	5.65	0.9908	4.65	0.9648	4.99	0.9590

Table 6. Activation energies of poly(1,3-diphenyl-1H-pyrazol-5-yl methacrylate using Madhusudanan Method

Mechanism	Heating Rate							
	5 °C/min		10 °C/min		15 °C/min		20 °C/min	
	E (kJ/mol)	R	E (kJ/mol)	R	E (kJ/mol)	R	E (kJ/mol)	R
A ₂	20.90	0.9670	19.36	0.9729	17.78	0.9833	18.58	0.9864
A ₃	11.11	0.9479	9.98	0.9541	8.86	0.9690	9.36	0.9752
A ₄	6.22	0.9081	5.29	0.9096	4.40	0.9287	4.75	0.9447
R ₁	46.47	0.9733	43.88	0.9786	41.11	0.9868	42.72	0.9890
R ₂	48.34	0.9755	45.66	0.9806	42.80	0.9884	44.46	0.9904
R ₃	48.97	0.9762	46.26	0.9812	43.37	0.9889	45.05	0.9908
D ₁	101.40	0.9778	96.52	0.9826	91.21	0.9895	94.52	0.9912
D ₂	103.86	0.9789	98.87	0.9836	93.43	0.9903	96.81	0.9919
D ₃	106.39	0.9800	101.29	0.9846	95.72	0.9911	99.18	0.9926
D ₄	104.70	0.9793	99.68	0.9839	94.19	0.9906	97.60	0.9922
F ₁	50.25	0.9775	47.48	0.9825	44.53	0.9898	46.24	0.9917
F ₂	-0.73	0.9423	-1.39	0.9747	-1.99	0.9635	-1.86	0.9427
F ₃	6.99	0.9965	6.00	0.9918	5.01	0.9693	5.36	0.9640

Table 7. Activation energies of poly(1,3-diphenyl-1H-pyrazol-5-yl methacrylate using Van Krevelen Method

Mechanism	Heating Rate							
	5 °C/min		10 °C/min		15 °C/min		20 °C/min	
	E (kJ/mol)	R	E (kJ/mol)	R	E (kJ/mol)	R	E (kJ/mol)	R
A ₂	24.39	0.9808	22.93	0.9849	21.46	0.9910	22.34	0.9924
A ₃	14.82	0.9808	13.80	0.9849	12.79	0.9910	13.36	0.9924
A ₄	10.04	0.9808	9.24	0.9849	8.46	0.9910	8.86	0.9924
R ₁	49.40	0.9779	46.79	0.9824	44.15	0.9889	45.85	0.9906
R ₂	51.22	0.9794	48.53	0.9837	45.79	0.9900	47.55	0.9915
R ₃	51.84	0.9798	49.12	0.9841	46.35	0.9903	48.13	0.9918
D ₁	103.11	0.9779	98.04	0.9824	92.85	0.9889	96.31	0.9906
D ₂	105.51	0.9789	100.33	0.9833	95.02	0.9896	98.55	0.9912
D ₃	107.99	0.9798	102.69	0.9841	97.25	0.9903	100.87	0.9918
D ₄	106.34	0.9792	101.11	0.9836	95.76	0.9899	99.32	0.9914
F ₁	53.09	0.9808	50.31	0.9849	47.48	0.9910	49.29	0.9924
F ₂	3.26	0.9994	2.75	0.9990	2.26	0.9965	2.44	0.9956
F ₃	10.82	0.9994	9.95	0.9990	9.08	0.9965	9.49	0.9956

Table 8. Activation energies for Dn mechanisms of all methods

Method	Mechanism	5 °C/min E (kJ/mol)	10 °C/min E (kJ/mol)	15 °C/min E (kJ/mol)	20 °C/min E (kJ/mol)
Coats-Redfern	D ₁	101,16	96,26	90,93	94,24
	D ₂	103,61	98,60	93,15	96,54
	D ₃	106,15	101,03	95,45	98,91
	D ₄	104,46	99,41	93,92	97,33
Tang	D ₁	101,47	96,60	91,29	94,60
	D ₂	103,93	98,94	93,51	96,89
	D ₃	106,46	101,36	95,80	99,26
	D ₄	104,77	99,75	94,27	97,68
Madhusudanan	D ₁	101,40	96,52	91,21	94,52
	D ₂	103,86	98,87	93,43	96,81
	D ₃	106,39	101,29	95,72	99,18
	D ₄	104,70	99,68	94,19	97,60
Van Krevelen	D ₁	103,11	98,04	92,85	96,31
	D ₂	105,51	100,33	95,02	98,55
	D ₃	107,99	102,69	97,25	100,87
	D ₄	106,34	101,11	95,76	99,32

Table 6 shows the results obtained by the Madhusudan method in which activation energy is found to be $E = 91.21$ kJ/mol and linear regression is $R = 0.9895$ for the D_1 mechanism at a heating rate of 15 °C/min. These values are also in good agreement with the Flynn-Wall-Ozawa and Kissinger methods. In addition to the results obtained from the above kinetic methods, the latest Van Krevelen method is used. The results determined by this method are summarized in Table 7. Similar results to other methods are also available for this method. Accordingly, the activation energy ($E = 92.85$ kJ/mol) value and linear regression ($R = 0.9889$) value are close to Flynn-Wall-Ozawa ($E = 79.45$ kJ/mol) and Kissinger ($E = 81.56$ kJ/mol) methods. These results show that there is a very good agreement between all the kinetic methods used and also the degradation mechanism proceeds through the D_1 mechanism, one-dimensional diffusion-type deceleration mechanism.

4. Conclusions

A new pyrazole derived methacrylate polymer poly(1,3-diphenyl-1H-pyrazol-5-yl methacrylate) poly(DP-PMA) was synthesized and spectrally characterized. Then, it was tested for determining the thermal characteristics by TGA method at various heating rates. The initial decomposition temperature of the polymer changed from 216.3 °C to 243.5 °C depending on the increasing heating rate. The thermal decomposition activation energies in a conversion range of 7–19% were 79.45 and 81.56 kJ/mol by the Flynn-Wall-Ozawa and Kissinger methods, respectively. Thermodegradation mechanism of the poly(DPPMA) were investigated in detail by using different kinetic methods available in the literature. The best result was obtained for Coats-Redfern method ($E = 90.93$ kJ/mol) at the optimum heating rate of 15 °C/min for D_1 mechanism, one-dimensional diffusion type deceleration mechanism.

Acknowledgements

We wish to thank the Adiyaman University Scientific Research Projects Unit for financially supporting this study with project number (ADYÜBAP/ FEFMAP/2021-0002).

5. References

- M. I. Marzouk, G. H. Sayed, M. S. Abd ElHalim, S. Y. Mansour, *Eur. J. Chem.* **2014**, *5*, 24–32
DOI:10.5155/eurjchem.5.1.24-32.870
- L. Kumar, C. Thakur, V. Sharma, *Int. J. Res. Pharm. Sci.* **2012**, *2*, 13–22.
- H. P. Devnath, M. R. Islam, *Bangladesh J. Pharmacol.* **2010**, *5*, 30–33. DOI:10.3329/bjp.v5i1.4693
- J. P. Soni, D. J. Sen, K. M. Modh, *J. Appl. Pharm. Sci.* **2011**, *1*, 115–120.
- S. Sunitha, K. K. Aravindakshan, *Int. J. Pharm. Bio. Sci.* **2011**, *2*, 108–113.
- K. S. Kumar, A. Rajasekharan, *Int. J. Res. Pharm. Chem.* **2012**, *2*, 327–337.
- A. N. Evstropov, V. E. Yavorovskaya, E. S. Vorobev, Z. P. Khudonogova, S. G. Medvedeva, V. D. Filimonov, T. P. Prishchep, A. S. Saratikov, *Pharm. Chem. J.* **1992**, *26*, 426–430. DOI:10.1007/BF00772907
- D. Nirupam, V. Abilasha, K. Shrivastava, P. Shrivastva, K. Su-shant, *Indian J. Chem. B* **2008**, *47*, 1555–1558.
- M. Amir, K. Shikha, *Indian J. Chem. B* **2005**, *44*, 2532–2537.
- Y. Fu, M. X. Wang, D. Zhang, Y. W. Hou, S. Gao, L. X. Zhao, F. Ye, *RSC Adv.* **2017**, *7*, 46858–46865. DOI:10.1039/C7RA09858H
- C. Cativiela, J. L. Serrano, M. M. Zurbano, *J. Org. Chem.* **1995**, *60*, 3074–3083. DOI:10.1021/jo00115a023
- S. Sugiura, S. Ohno, O. Ohtani, K. Izumi, T. Kitamikado, H. Asai, K. Kato, M. Hori, H. Fujimura, *J. Med. Chem.* **1977**, *20*, 80–85. DOI:10.1021/jm00211a016
- M. W. Sabaa, F. H. Oraby, A. S. Abdel-Naby, R. R. Mohamed, *Polym. Degrad. Stab.* **2006**, *91*, 911–923. DOI:10.1016/j.polymdegradstab.2005.05.031
- M. M. Mojtahedi, M. Javadpour, M. S. Abaee, *Ultrason Sonochem.* **2008**, *15*, 828–832. DOI:10.1016/j.ultsonch.2008.02.010
- L. F. Tietze, A. Steinmetz, *Synlett.* **1996**, *7*, 667–668. DOI:10.1055/s-1996-5548
- L. F. Tietze, H. Evers, T. Hippe, A. Steinmetz, E. Topken, *Eur. J. Org. Chem.* **2001**, *9*, 1631–1634. DOI:10.1002/1099-0690(200105)2001:9<1631::AID-EJOC1631>3.0.CO;2-
- S. Kobayashi, T. Furuta, K. Sugita, H. Oyamada, *Synlett.* **1998**, *9*, 1019–1021. DOI:10.1055/s-1998-1843
- M. M. Mojtahedi, M. R. Jalali, M. S. Abaee, M. Bolourtchian, *Heterocycl. Commun.* **2006**, *12*, 225–228. DOI:10.1515/HC.2006.12.3-4.225
- Z. Liang, L. R. Dalton, S. M. Garner, S. Kalluri, A. Chen, W. H. Steier, *Chem. Mater.* **1995**, *7*, 1756–1758. DOI:10.1021/cm00058a002
- J. W. Connell, R. G. M. Bass, S. Sinsky, R. O. Waldbauer, P. M. Hergenrother, *J. Polym. Sci. Polym. Chem. Ed.* **1987**, *25*, 2531–2542. DOI:10.1002/pola.1987.080250918
- J. A. Moore, P. G. Meththa, *Macromolecules* **1995**, *28*, 444–453. DOI:10.1021/ma00106a007
- A. Cetin, B. Gündüz, N. Menges, I. Bildirici, *Polym. Bull.* **2017**, *74*, 2593–2604. DOI:10.1007/s00289-016-1846-5
- Z. Duan, D. Hu, H. Ohuchi, M. Zhao, G. Zhao, Y. Nishioka, *Synth. Metals* **2012**, *162*, 1292–1298. DOI:10.1016/j.synthmet.2012.05.002
- J. Y. Back, Y. Kim, T. K. An, M. S. Kang, S. K. Kwon, C. E. Park, Y. H. Kim, *Dyes Pigm.* **2015**, *112*, 220–226. DOI:10.1016/j.dyepig.2014.07.008
- M. L. Coote, T. P. Davis, in: G. Wypych (Ed.): Handbook of Solvents (Second Edition), ChemTec Publishing, **2014**, pp. 811–833. DOI:10.1016/B978-1-895198-64-5.50021-0
- A. Lamaoui, J. J. García-Guzmán, A. Amine, J. M. Palacios-Santander, L. Cubillana-Aguilera, in: M. P. Sooraj, A. S.

- Nair, B. Mathew, S. Thomas (Ed.): Molecularly Imprinted Polymer Composites, In Woodhead Publishing Series in Composites Science and Engineering, Woodhead Publishing, **2021**, pp.49-91. DOI:10.1016/B978-0-12-819952-7.00002-0
27. H. A. Pearce, Y. S. Kim, L. Diaz-Gomez, A. G. Mikos, in: W. R. Wagner, S. E. Sakiyama-Elbert, G. Zhang, M. J. Yaszemski: Biomaterials Science (Fourth Edition), Academic Press, **2020**, pp. 1317–1334, DOI:10.1016/B978-0-12-816137-1.00082-9
28. B. Love, in: B. Love (Ed.): Biomaterials, Academic Press, **2017**, pp. 205-238. DOI:10.1016/B978-0-12-809478-5.00009-2
29. K. Matyjaszewski, J. Xia, *Chem. Rev.* **2001**, *101*, 2921–2990. DOI:10.1021/cr940534g
30. K. Hong, H. Zhang, J. W. Mays, A. E. Visser, C. S. Brazel, J. D. Holbrey, W. M. Reichert, R. D. Rogers, *Chem. Commun.* **2002**, *13*, 1368-1369. DOI:10.1039/b204319j
31. A. Kurt, *J. Appl. Polym. Sci.* **2009**, *114*, 624-629. DOI:10.1002/app.30576
32. D. Colombani, *Prog. Polym. Sci.* **1997**, *22*, 1649–1720. DOI:10.1016/S0079-6700(97)00022-1
33. S. Wang, B. Cheng, *Sci. Rep.* **2017**, *7*, 12712. DOI:10.1038/s41598-017-12727-3
34. A. Kurt, M. Koca, *Arab. J. Sci. Eng.* **2014**, *39*, 5413–5420. DOI:10.1007/s13369-014-1103-x
35. A. Kurt, P. Yilmaz, *Kuwait J. Sci.* **2016**, *43*, 172–184.
36. A. Kurt, M. Koca, *J. Eng. Res.* **2016**, *4*, 46–65.
37. A. Kurt, H. I. Avci, M. Koca, *Maced. J. Chem. Chem. Eng.* **2018**, *37*, 173–184. DOI:10.20450/mjccce.2018.1503
38. A. Kurt, I. Kılınc, M. Koca, *Iran. J. Sci. Technol. Trans. A Sci.* **2020**, *44*, 1039–1050. DOI:10.1007/s40995-020-00926-z
39. A. Kurt, H. Andan, M. Koca, *Maced. J. Chem. Chem. Eng.* **2020**, *39*, 227–237. DOI:10.20450/mjccce.2020.2025
40. X. L. Meng, Y. D. Huang, H. Yu, Z. S. Lv, *Polym. Degrad. Stab.* **2007**, *92*, 962–967. DOI:10.1016/j.polymdegradstab.2007.03.005
41. J. D. Peterson, S. Vyazovkin, C. A. Wight, *Macromol. Chem. Phys.* **2001**, *202*, 775–784. DOI:10.1002/1521-3935(20010301)202:6<775::AID-MACP775>3.0.CO;2-G
42. S. C. Turmanova, S. D. Genieva, A. S. Dimitrova, L. T. Vlaev, *Express Polym. Lett.* **2008**, *2*, 133–146. DOI:10.3144/expresspolymlett.2008.18
43. L. Núñez, F. Fraga, M. R. Núñez, M. Villanueva, *Polymer*, **2000**, *41*, 4635–41. DOI:10.1016/S0032-3861(99)00687-4
44. S. Ma, J. O. Hill, S. Heng, *J. Therm. Anal.* **1991**, *37*, 1161–77. DOI:10.1007/BF01913852
45. J. H. Flynn, L. A. Wall, *J. Polym. Sci. B*, **1966**, *4*, 323-328. DOI:10.1002/pol.1966.110040504
46. T. Ozawa, *J. Therm. Anal.* **1986**, *31*, 547–551. DOI:10.1007/BF01914230
47. H. E. Kissinger, *Anal. Chem.* **1957**, *29*, 1702–1706. DOI:10.1021/ac60131a045
48. A. W. Coats, J. P. Redfern, *Nature*, **1964**, *201*, 68–69. DOI:10.1038/201068a0
49. W. Tang, Y. Liu, H. Zhang, C. Wang, *Thermochim. Acta*, **2003**, *408*, 39–43. DOI:10.1016/S0040-6031(03)00310-1
50. P. M. Madhusudanan, K. Krishnan, K. N. Ninan, *Thermochim. Acta*, **1993**, *221*, 13–21. DOI:10.1016/0040-6031(93)80519-G
51. D. W. Van Krevelen, C. Van Herden, F. J. Hutjens, Kinetic study by thermogravimetry, *Fuel*, **30**, 253–258 (1951).

Povzetek

Obnašanje in lastnosti polimerov, pridobljenih iz makromolekularnega pirazola, se razlikujejo od njihovih osnovnih molekul. Temu ustrezno takšni polimeri spadajo v razred dobro opredeljenih funkcionalnih polimerov zaradi dejstva, da pirazolni obroč vsebuje dve π -vezi in dva heteroatoma v svoji strukturi, kar jih dela pomembne na področju znanstvenih in tehnoloških aplikacij. V tej študiji je bil tako sintetiziran nov metakrilatni monomer, pridobljen iz pirazola, 1,3-difenil-1H-pirazol-5-il metakrilata, prek reakcije 1,3-difenil-5-pirazolona z metakrilolil kloridom v prisotnosti trietilamina. Za tem je bila izvedena njegova homopolimerizacija z metodo polimerizacije prostih radikalov pri 60 °C, začeta z benzoil peroksidom. Produkt je bil okarakteriziran z $^1\text{H-NMR}$ in FTIR spektroskopijo. Kinetika termične razgradnje novega polimera, poli(1,3-difenil-1H-pirazol-5-il metakrilata), poli(DPPMA), je bila raziskana s termogravimetrično analizo (TGA) pri različnih hitrostih segrevanja. Začetna temperatura razgradnje polimera je v območju od 216,3 °C do 243,5 °C, odvisno od naraščajoče hitrosti segrevanja. Aktivacijski energiji termičnega razpada v območju pretvorbe 7–19 % sta bili 79,45 kJ/mol po Flynn-Wall-Ozawa in 81,56 kJ/mol po Kissingerjevi metodi. Mehanizem termičnega razpada poli(DPPMA) je bil podrobno raziskan z različnimi kinetičnimi metodami, ki so na voljo v literaturi, kot so Coats-Redfern, Tang, Madhusudanan in Van Krevelen. Med vsemi omenjenimi metodami je bil najboljši rezultat dosežen pri Coats-Redfernovi metodi ($E = 90,93$ kJ/mol) pri optimalni hitrosti segrevanja 15 °C/min za mehanizem D_1 , opredeljen kot enodimenzionalni zaviralni mehanizem difuzijskega tipa.

Scientific paper

iFIT: An Automated Web Tool for Determining Enzyme-kinetic Parameters Based on the High-curvature Region of Progress Curves

Boštjan Petrič, Marko Goličnik and Aljoša Bavec*

University of Ljubljana, Institute of Biochemistry and Molecular Genetics, Faculty of Medicine,
Vrazov trg 2, SI-1000 Ljubljana, Slovenia

* Corresponding author: E-mail: aljosa.bavec@mf.uni-lj.si

Received: 02-16-2022

Abstract

The area where a progress curve exhibits maximum curvature contains the most information about kinetic parameters. To determine these parameters more accurately from progress curves, we propose an iterative approach that calculates the area of maximum curvature based on an estimate of kinetic parameters and then recalculates the parameters based on time-concentration data points within this area. Based on this algorithm, we developed a computer script called iFIT as a free web application at <http://www.i-fit.si>. The benefits of working with iFIT are that it decreases the importance of initial substrate concentration and the impact of certain side reactions on the final calculated kinetic parameters.

Keywords: Progress curves; integrated Michaelis-Menten equation; Lambert W

1. Introduction

The classical way to determine enzyme-kinetic parameters, such as the Michaelis constant K_m and limiting rate V_{max} , was via initial-velocity-based approaches, such as the Michaelis-Menten (MM) diagram and its linearized derivations, e.g., the Lineweaver-Burk diagram. In recent decades, analyzing entire progress curves has mostly superseded the former approach as a simple way of determining kinetic parameters with greater accuracy and precision and using fewer measurements.¹ While a common problem of analyzing initial velocities is a shortage of experimental data points, progress curves often have too many data points, which may counterintuitively decrease the quality of the fitted parameters.

It is well understood that information about kinetic parameters is not equally encoded in all parts of a progress curve. Once the curve reaches its plateau, recording additional time-concentration points does not provide any further information about K_m or k_{cat} . Fitting a model function onto a curve with a long plateau might result in a model curve that fits perfectly onto the measured plateau, but at the expense of the area of maximum curvature (see Figure 1). Similarly, for progress curves at high substrate concentration relative to K_m , the initial part of the progress curve will be almost linear (zero-order), and similar consider-

ations apply to it as to the plateau. The most information about kinetic parameters can be extracted from the progress curve's area of maximum curvature.²

To ensure that the model function fits well onto the area of maximum curvature, different weights can be assigned to different areas of the progress curve, or parts of the curve (e.g., the plateau) can be manually removed. However, to avoid accusations of tampering with raw data, any such method for optimizing progress curves must be clearly defined, universally applicable, and based on sound mathematical principles. We here propose such a method, based on the theoretical work of Stroberg and Schnell². They published an equation that calculates the area of maximum curvature of a progress curve from already known kinetic parameters. Based on this, we developed an iterative approach for calculating the area without known kinetic parameters. Furthermore, we developed a computer script to automatically perform the iterative process.

2. Experimental

2.1. Study Design

Our study was designed only for the development of simple and quick methodology for determination of serum paraoxonase 1 (PON1) kinetic characteristics. We

utilized a leftover routine blood sample of a healthy blood-donor. Since the biological material used in this report has been obtained from a leftover specimen, and the sample was not used for any other particular study, informed consent from volunteers and ethical approval was unnecessary because the sample was no longer traceable.

2. 2. Methods

The blood sample was collected in a heparin tube, immediately centrifuged at 2200 g, 4 °C for 10 min, and the plasma was removed and stored at –80 °C until measurement. Enzyme activity measurements were performed as in Goličnik and Bavec.³ Briefly, the measurements were conducted at room temperature, in a buffer consisting of 50 mM Tris and 1 mM CaCl₂, pH = 8. The substrate was dihydrocoumarin, prepared as a 25 mM stock solution in methanol. Each reaction had a total volume of 2 mL and was performed in a 1 cm cuvette.

For each measurement, 20 µL of substrate stock solution (final concentration: 250 µM) and 10 µL of plasma were added to 1970 µL of buffer. Substrate was added last, after which we started the measurement. Absorbance at 270 nm was measured every second until after the progress curve had clearly reached its plateau. Afterwards, the progress curve was analyzed using iFIT, which is explained in detail in the main text of the present article.

2. 3. Data Analysis

Stroberg and Schnell introduce the concept of t_Q , i.e., the length of time during which the progress curve is at its maximum curvature. t_Q depends on K_m , V_{max} , and initial substrate concentration ($[S]_0$), according to Equation 1:

$$t_Q = \frac{27K_m \cdot [S]_0}{4V_{max}(K_m + [S]_0)} \quad (1)$$

When an entire progress curve has been measured, and the extinction coefficient for the product is known, S_0 can be easily calculated. However, calculating K_m and V_{max} from a progress curve is not trivial, even if we are only interested in an estimate. Hence, using t_Q for an improved way to calculate K_m results in a chicken-and-egg problem, which can be solved with an iterated approach. We start by applying the integrated MM equation (Equation 2) to the entire progress curve to acquire estimates for K_m and V_{max} . We then use these estimates to calculate t_Q and subsequently analyze only the t_Q -bound region of the progress curve again with the model function to acquire more precise estimates of K_m and V_{max} . We continue this process until the calculated t_Q interval, i.e., the number of experimental time-concentration data points selected by the algorithm, is the same in two successive iterations.

Several approaches for calculating kinetic parameters directly from progress curves have been proposed.

Briefly, it is possible to (1) model the enzymatic reaction with a system of differential equations (an example of such a program is Dynafit);⁴ (2) treat each derivative of the progress curve with respect to time as an initial velocity and plot these “initial velocities” onto the standard MM diagram;⁵ or (3) use an integrated version of the MM equation. We decided to use the latter: a numerical approximation by Goličnik (Equations 2 and 3).⁶

$$[P]_t = [S]_0 - K_m \cdot (1.45869 \cdot \ln(1.2 \cdot \frac{x}{\ln(2.4 \cdot \frac{x}{\ln(1 + 2.4x)})}) - 0.45869 \cdot \ln(2 \cdot \frac{x}{\ln(1 + 2x)})) \quad (2)$$

where

$$x = \frac{[S]_0}{K_m} \cdot e^{\frac{([S]_0 - V_{max} \cdot t)}{K_m}} \quad (3)$$

Goličnik's approximation is based on an integrated MM equation (based on the Lambert Omega function) that was published by Schnell and Mendoza (Equation 4).⁷

$$[P]_t = [S]_0 - K_m \cdot W_0\left(\frac{[S]_0}{K_m} \cdot \exp\left(\frac{[S]_0 - V_{max} \cdot t}{K_m}\right)\right) \quad (4)$$

3. Results and Discussion

Performing the entire iterative procedure manually would be extremely time-consuming. Therefore, we developed a computer script in Python, provisionally referred to as iFIT. The script takes a progress curve as its input, asks the user for an initial selection of an area of the curve (not necessary) and an extinction coefficient, and automatically calculates estimates for substrate concentration, baseline, and V_{max} . The user then inputs an estimate for K_m , which is required by the integrated MM equation to start the fitting procedure. iFIT begins the iterative process of calculating t_Q from kinetic parameters and then recalculating kinetic parameters from the part of the curve described by t_Q . The area of the curve that is being fitted can expand, contract, or move left or right on the x-axis between successive iterations.

When two successive iterations produce the same selection of time-concentration data points as the result, it is output by the script as the final result, including calculated values for K_m , V_{max} , $[S]_0$, and the baseline. If iFIT does not converge to a t_Q value after 100 iterations (usually this occurs when the script oscillates between two values of t_Q), the procedure is terminated without a final result. Additionally, iFIT always draws all the intermediate graphs as well as the final graph, with both the data points and model curve displayed, so that the user can visually check whether the final fit is indeed sensible. An example of an initial and final graph is displayed in Figure 1. More de-

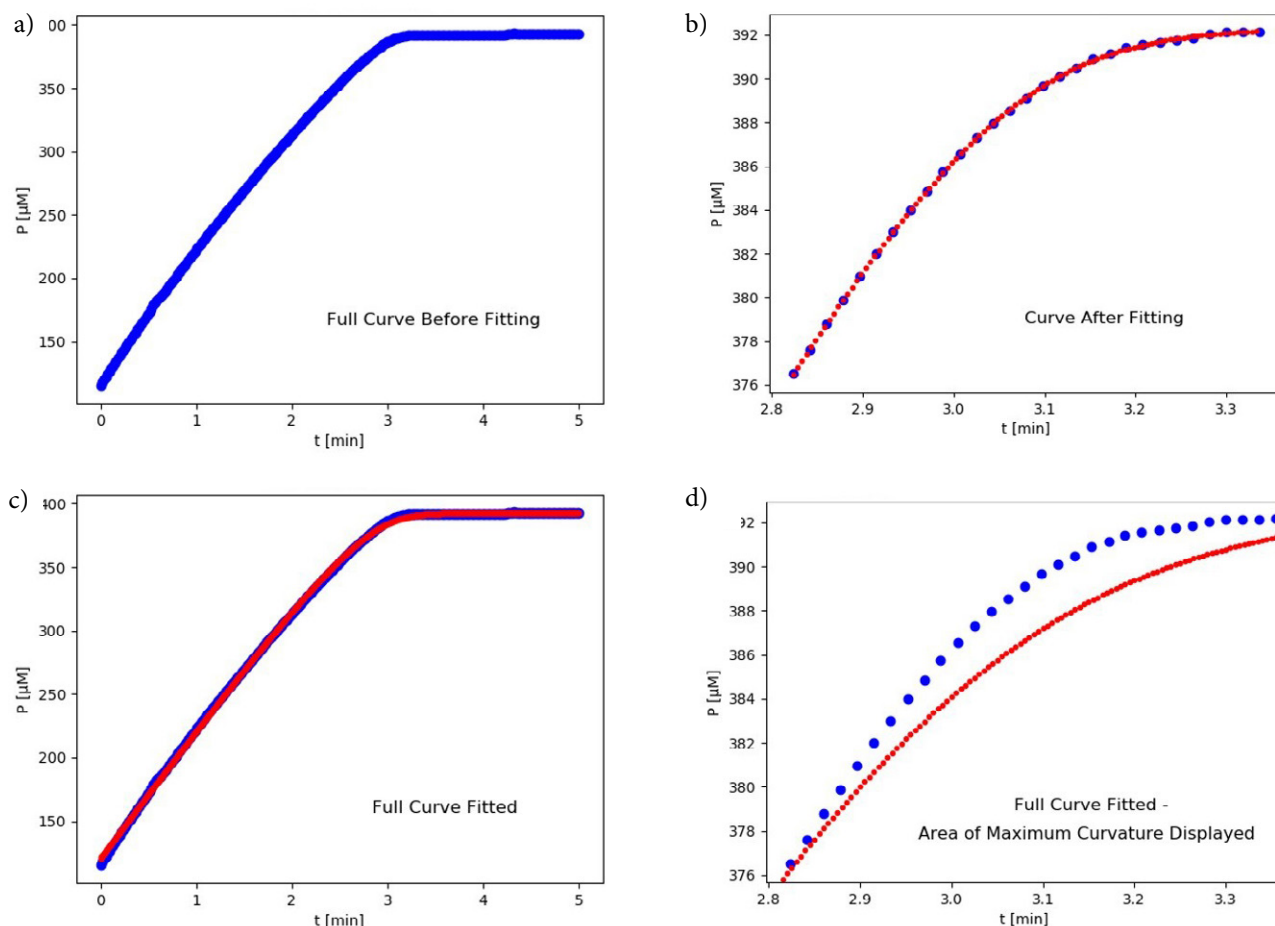


Figure 1: The fit of kinetic progress curve data by iFIT for human PON1. **a)** The entire curve (blue) before fitting with a model function, with the area of maximum curvature shown in the shaded window. **b)** The area of maximum curvature (blue) of the progress curve in **a)** and the best-fit curve calculated with Equation 2 (red) after the final iteration of iFIT. The calculated value of K_m is $6.70 \mu\text{M}$. **c)** The entire progress curve from **a)** (blue) fitted with the model function (red) after the first iteration of iFIT; the area of maximum curvature is shown in the shaded window and is the same as in **a)**. The calculated value of K_m is $17.33 \mu\text{M}$. **d)** The area of maximum curvature zoomed in after the entire curve (blue) was fitted with the model function (red). It is apparent from the comparison between **b)** and **d)** that iFIT can produce model functions which fit much more closely to the area of maximum curvature.

tailed information on how to use the iFIT web application is available in the Supplementary material.

iFIT has two main requirements. 1) The progress curve must be smooth, without a substantial amount of noise. Even if each part of the curve can be fitted well with the integrated MM equation, noise may cause iFIT to oscillate between two or more different values of t_Q (and, consequently, two or more different output values of K_m). 2) The initial substrate concentration must not be substantially below K_m . In such cases, iFIT will conclude that the area of maximum curvature lies before the beginning of the progress curve, i.e., at a “negative” time interval. Since such intervals do not contain time-concentration data points, iFIT will be unable to continue the calculation. The same thing will happen if we try to input an exponential progress curve, e.g., from a first-order reaction.

Conversely, it is not a problem for iFIT if the initial substrate concentration is significantly above K_m , which is advised against in conventional enzyme-kinetic guidelines. As long as there are enough time-concentration data points in the high-curvature region of the progress curve, it does not matter how many other points lie outside of this region. It also does not matter if the progress curve’s plateau is very long, noisy, or deviates from a straight line; iFIT will simply not consider these points in the final result.

A related advantage of iFIT is that it can decrease the influence of certain side reactions on the final calculated value of K_m . During a MM reaction with a low K_m and an $[S]_0$ sufficiently above K_m , the rate of the reaction will slowly decrease as substrate is being consumed. If we perform the same reaction with a lower-affinity enzyme, the reaction rate will decrease more quickly as substrate is being consumed. The example of this is a first-order reaction,

such as spontaneous substrate hydrolysis, where the reaction rate will decrease even more rapidly with respect to substrate concentration. This means that the side reactions of either an impure sample, containing an unwanted enzyme that catalyzes the same substrate (but with a higher K_m), or a substrate that undergoes first-order spontaneous hydrolysis, will have the smallest impact on the total reaction just before the plateau of the progress curve, i.e., in the area of highest curvature. In such cases, fitting a model function on the entire progress curve produces a poorer fit and less accurate output kinetic parameters than fitting the same model function on only the high-curvature region using iFIT (see Figure 1).

Many methodological articles on enzyme kinetics conclude with recommendations regarding proper experimental design. The value of iFIT, however, is that it renders precise experimental design less important. Using progress curves instead of initial velocities minimizes the importance of ensuring precise initial substrate concentration or immediately starting the measurement, as long as the product's extinction coefficient is known. An additional advantage of using iFIT is that we do not need to worry about substrate concentration at all. The script will trim any progress curves with excessive substrate concentration down to size, and iFIT can immediately notify that the substrate concentration is too small by calculating a t_Q interval that falls outside of the measured progress curve. When measuring progress curves, we must only ensure that the total absorbance of the solution does not exceed the functional range of the instrumentation being utilized.

Apart from reducing noise, it is also helpful to record as many time-concentration data points per unit of time as possible when measuring progress curves for iFIT. Especially when K_m is low and V_{max} is high, t_Q will be short as well, i.e., only a small part of the progress curve will end up being fitted by the model function. If this part of the curve contains only a few data points, the resulting fit might be less accurate.

For enzymatic reactions where the integrated MM equation cannot be applied to progress curves, iFIT cannot be applied as well. This includes equilibrium reactions (i.e. reaction that are not irreversible), reactions which involve cosubstrates that are not present sufficiently in excess, reactions with enzymes that degrade substantially over the course of the reaction, and reactions with strong product inhibition. If progress curves cannot be measured at all because substrates and products have the same spectral properties, then iFIT obviously cannot help us either.

Obviously, we cannot know whether a previously unstudied enzyme-substrate pair exhibits any of the above properties and whether it follows Michaelis-Menten kinetics at all. iFIT is primarily valuable not as a tool for studying novel enzymes or analysing one-time measurements, but as an accessory for routine kinetic parameter determination. Researchers often wish to determine K_m for a known enzyme-substrate pair on a number of samples, e.g.

medical samples from different patients. In such cases, a simple and routine tool for progress curve analysis like iFIT is vastly preferable to initial-velocity calculations. However, for poorly understood enzymes, we recommend first comparing several approaches for kinetic parameter determination (including initial velocities) and making sure that we are indeed dealing with simple MM kinetics before settling for iFIT for routine work.

4. Conclusions

Utilizing Stroberg & Schnell's equation to improve the determination of kinetic parameters does not require a scripted approach or the integrated MM equation as part of the iterative algorithm. However, the script that we have developed is quick and easy to use. As it is based on the integrated MM equation, complex differential-equation-based models, such as those behind Dynafit or ENZO, are unnecessary.^{4,8} At the same time, on a set of data with a purified recombinant enzyme, iFIT has been shown to compare favorably with Dynafit, the initial velocities approach, and the integrated MM equation without data point removal.⁹ Using iFIT at <http://www.i-fit.si> (last accessed 16. February 2022), any research group that determines MM kinetic parameters from progress curves can solve the problem of unwanted data points at the beginning or end of progress curves.

Acknowledgements

This study was supported by the Slovenian Research Agency (grant P1-170). The authors thank Marjan Kužnik for his kind help with experimental work.

Potential conflict of interests

There are none.

CRediT authorship contribution statement

Boštjan Petrič: Conceptualization, Formal analysis, Investigation, Writing – original draft, Writing – review & editing, Visualization. **Marko Goličnik:** Conceptualization, Methodology, Software, Formal analysis, Investigation. **Aljoša Bavac:** Conceptualization, Methodology, Software, Formal analysis, Investigation, Writing – review & editing.

5. References

1. B. Choi, G. Rempala, J. K. Kim. *Sci Rep.* **2017**, 7(1), 17018. DOI:10.1038/s41598-017-17072-z
2. W. Stroberg, S. Schnell, *Biophys. Chem.* **2016**, 219, 17–27. DOI:10.1016/j.bpc.2016.09.004

3. M. Goličnik and A. Bavec, *J Enzyme Inhib Med Chem.* **2020**, 35, 261–264. DOI:10.1080/14756366.2019.1695792
4. P. Kuzmič, *Anal. Biochem.* **1996**, 237, 260–273. DOI:10.1006/abio.1996.0238
5. S.L. Yun, C.H. Suelter, *Biochim. Biophys Acta* **1977**, 480(1), 1–13. DOI:10.1016/0005-2744(77)90315-1
6. M. Goličnik, *Biochem. Mol. Biol. Educ.* **2011**, 39(2), 117–125. DOI:10.1002/bmb.20479
7. S. Schnell, C. Mendoza, *J. Theor. Biol.* **1997**, 187, 207–212. DOI:10.1006/jtbi.1997.0425
8. S. Bevc, J. Konc, J. Stojan, M. Hodošček, M. Penca, M. Praprotnik, D. Janežič, *PLoS ONE* **2011**, 6(7), e22265. DOI:10.1371/journal.pone.0022265
9. B. Petrič, M. Goličnik, A. Bavec, *Molecules* **2022**, 27(4), 1306. DOI:10.3390/molecules27041306

Povzetek

Območje, kjer je krivulja časovnega poteka nastajanja produkta encimske reakcije najbolj ukrivljena, vsebuje največ informacij o kinetičnih parametrih. Za natančnejšo določitev teh parametrov iz krivulj časovnega poteka nastajanja produkta predlagamo iterativni pristop, ki izračuna območje največje ukrivljenosti na podlagi ocene kinetičnih parametrov in nato ponovno izračuna parametre na podlagi območja največje ukrivljenosti. Na podlagi tega algoritma smo razvili računalniški program iFIT kot brezplačno spletno aplikacijo na naslovu <http://www.i-fit.si>. Prednosti dela z iFIT so, da se zmanjša pomen začetne koncentracije substrata in vpliv nekaterih stranskih reakcij na končne izračunane kinetične parametre.



Except when otherwise noted, articles in this journal are published under the terms and conditions of the Creative Commons Attribution 4.0 International License

Scientific paper

Ibuprofen Loaded Electrospun Polymeric Nanofibers: A Strategy to Improve Oral Absorption

Dibya Sundar Panda,¹ Nabil K. Alruwaili,¹ Kalpana Swain²
and Satyanarayan Pattnaik^{2,*}

¹ *Pharmaceutics Department, College of Pharmacy, Jouf University, Sakaka, Kingdom of Saudi Arabia*

² *Talla Padmavathi College of Pharmacy, Warangal, India*

* *Corresponding author: E-mail: drsatyapharma@gmail.com
Mobile +91-9849337607*

Received: 01-21-2022

Abstract

The poor aqueous solubility of candidate drugs has presented a great challenge to formulation scientists for their effective oral delivery. Poor solubility is often associated with poor dissolution behavior and, subsequently, poor bioavailability for those drugs when intestinal absorption is dissolution rate limited. In the present study electrospun polymeric nanofibers were developed to address the poor aqueous solubility of ibuprofen, a Biopharmaceutic Classification System (BCS) class-II drug. Hydrophilic spinnable polymers like polyvinyl pyrrolidone were deployed as a carrier system for the fabrication of nanofibers. The electrospinning parameters like flow rate, voltage, and spinneret to collector distance were optimized. The fabricated ibuprofen-loaded nanofibers were characterized using scanning electron microscopy and differential scanning calorimetry. Drug release studies and ex vivo intestinal absorption studies were also carried out. The nanofiber-based platform significantly improved in vitro absorption of ibuprofen compared to pure ibuprofen crystals.

Keywords: Electrospinning; Nanomedicine; Bioavailability; Absorption; Ibuprofen.

1. Introduction

Effective delivery of active ingredients (APIs) to the target site at the desired concentration and rate is of paramount importance in systemic drug therapy. Poorly soluble drug candidates continue to pose challenges to their optimal administration and have therefore drawn the attention of researchers around the world.^{1–5} Poor water solubility of drug molecules often limits gastrointestinal absorption and hence oral bioavailability, leading to therapeutic failure. The aggressive research efforts to provide solutions to drug insolubility problems are evident from the abundance of literature available.

Based primarily on the physicochemical properties of the active ingredients, a diverse strategy for active ingredient delivery has been proposed to increase the solubility and/or the rate of dissolution of such molecules.⁶ These fascinating techniques include chemical modification,⁷ co-crystals,⁸ micro- / nanonization,^{3,5,6} polymorphic improvements,⁹ lipid-based systems,^{6,10} micellar solubilization in-

cluding self-emulsifying drug delivery systems,¹¹ inclusion complexes,^{12–15} amorphous solid dispersion/solution^{16–18} etc. In addition, nanotechnology has provided solutions for improving the solubility and/or bioavailability of active ingredients.^{19–23} Among all of these available techniques, strategies involving the development of amorphous solid drug products have received much attention in the recent past due to the tremendous improvement in the solubility of drug candidates under this approach.^{3,19} Electrospinning is widely used by pharmaceutical researchers to deliver a wide variety of active ingredients to treat various disease states. The very efficient amorphization effect of electrospinning is based on the immediate evaporation of the solvent, which leads to a solid solution of the active ingredient in the polymer matrix.²⁴ Amorphous solid dispersions based on electrospun fibers can retain an incorporated active substance in the amorphous physical form for longer periods due to their homogeneous distribution of active substances within the matrix and the possibility of inhibiting molecular mobility, which leads to impaired devitrifica-

tion. In an attempt to improve the dissolution of ibuprofen, a co-axial solid core spinneret-based electrospinning method was adopted and the dissolution was reportedly improved drastically.²⁵ The objective of the study was mostly to characterize the fast dissolution of the cargo molecule.

In the present study, attempts were made to explore a convenient and efficient electrospinning approach to amorphizing ibuprofen (a poorly soluble drug candidate) to improve its oral absorption.

2. Materials and Methods

2. 1. Materials

Ibuprofen was obtained as a gift sample from Cipla Ltd (Mumbai, India). Polyvinylpyrrolidone K30 (CAS Number-9003-39-8; PVP K30, MW= about 40,000 g/mol), and ethanol (analytical grade) were obtained from Sigma-Aldrich Corp (India). All other chemicals used were of analytical grade and procured locally.

2. 2. Fabrication of Nanofibers

The ibuprofen loaded PVP-based nanofibers and only PVP nanofibers were prepared by electrospinning equipment (Super ES 2; E-Spin Nanotech, India). The nanofibers were electrospun from 8% (w/v) PVP solution with or without 2% (w/v) ibuprofen at an applied DC voltage of 12 kV. The working solution was initially stirred magnetically for 2–3 h to completely dissolve PVP in ethanol. Subsequently, ibuprofen was added to the polymer solution and stirred for another 1 h to completely dissolve the drug. This solution was then electrospun at a flow rate of 2.0 ml/h using a syringe pump. The spinneret-to-collector distance was fixed at 15 cm and a plate collector was used for the collection of the nanofibers. The spinning parameters were optimized after the trial batches.

2. 3. Scanning Electron Microscopy

The fiber morphology and diameter were analyzed using a scanning electron microscope (SEM). Samples were coated with 20 nm of gold under a vacuum using a sputter coater. All micrographs were taken at an acceleration voltage of 5 kV. The secondary electrons were detected using an Everhart-Thornley detector.

2. 4. X-ray Diffraction Studies

The samples of nanofibers and raw ibuprofen were assessed for crystallinity using an X-ray diffractometer (Model: SEIFERT, C-3000, Germany) using Nickel-filtered CuK α radiation ($k = 1.54 \text{ \AA}$). The voltage and current were 35 kV and 30 mA, respectively, and smoothed 95. Measurements were carried out in the angular range from 5° to 40° (2 θ) using step sizes 0.05 and 0.25 s per step.

2. 5. Differential Scanning Calorimetry

The solid-state properties of the raw ibuprofen and fabricated nanofiber samples were studied using differential scanning calorimetry (DSC 822, Mettler Toledo). Each powdered sample (5 mg) was placed in an aluminum pan, sealed, and heated to 200 °C at a heating ramp rate of 10 °C / min under nitrogen gas (50 L/min). Before each measurement, the sample was allowed to equilibrate for 5 min at 30 °C. Transition temperatures and enthalpy readings were automatically calculated using Mettler Toledo software for each peak.

2. 6. Drug Entrapment Efficiency (DEE)

The drug loading efficiency was calculated using the following equation (Eq 1).

$$\text{DEE (\%)} = (W_m/W_a) \times 100\% \quad (1)$$

where W_m is the ibuprofen content measured in the electrospun nanofibers, and W_a is the ibuprofen added to the working fluid during the preparation. All tests were repeated in triplicate and the mean is reported. The ibuprofen content in the generated fibers was determined by dissolving the fibers in ethanol. The solutions were then analyzed spectrophotometrically at 220 nm to assess the amounts of ibuprofen in each sample.

2. 7. In Vitro Dissolution and Solubility Studies

Samples of pure ibuprofen drug (10 mg) and nanofiber sample equivalent to 10 mg ibuprofen were subjected to dissolution studies in 900 ml of distilled water under sink conditions (USP paddle method: Thermonic, Campbell Electronics, Mumbai, India, at 100 rpm and 37 °C).¹⁹ At predetermined intervals, a sample of the solution was removed and filtered through a 0.45 μm filter, and the same amount of medium was replaced at the same temperature. The drug content in the withdrawn aliquots was spectrophotometrically analyzed at 220 nm (UV-160, Shimadzu, Japan). The experimental points were the average of at least three repetitions. To assess the solubility of ibuprofen in studied dissolution media, an excess of ibuprofen was added to distilled water and stirred for 24 hours. Later the suspension was centrifuged and the supernatant was filtered using Whatman filter paper. Further, the drug concentration was measured spectrophotometrically at 220 nm.

2. 8. Ex Vivo Intestinal Permeation Studies

The ex vivo intestinal permeation studies were performed as per a previously reported method by the author.¹⁹ The goat's small intestine was collected from a local slaughterhouse for the study, kept in buffer fluid (Krebs-

Ringer solution), and used immediately without storage for a prolonged period. The tissue sample was properly cleaned to separate the mesentery, rinsed with the buffer, and then cut into different sections. Each section was everted on a Teflon rod and fixed on its location using a thread. The setup consisted of an intestinal holder which was a cylindrical glass vessel connected to a “U” glass tube whose one portion was represented by the intestine. Intestine holders (four in one set) filled with buffer fluid represented the receiver environment (4×12 mL) and the holder was placed in the donor environment. Both the receiver and donor phases were continuously aerated to keep the intestine cells alive during experimentation. At regular intervals of time, after the beginning of the permeation test, 4 mL of the receiver phase were sampled from each intestine holder and replaced with pure buffer, for a time duration of 120 min. The concentration of ibuprofen in each of the four liquid phases sampled was estimated using a UV spectrophotometer (UV-160, Shimadzu, Japan).

2.9. Statistical Analysis

The performance of raw ibuprofen and ibuprofen-loaded nanofibers in the *in vitro* dissolution studies and the *ex vivo* intestinal permeation studies were analyzed following a t-test at an overall significance level of 0.05 using Sigma Stat software (Sigma Stat 3.5, SPSS Inc, Chicago, IL).

3. Results and Discussions

Hydrophilic and water-soluble polymers have been widely exploited by formulation scientists to enhance the solubility of poorly soluble drugs.^{19, 23–26} It is supposed that these polymers act as antinucleating agents and stabilizers inhibiting the devitrification of amorphized drugs.⁶ Moreover, nanotechnology-based drug delivery approaches have gained a lot of momentum providing viable solutions for optimal therapeutic delivery of poorly soluble drug candidates.^{27, 28} In the present work, PVP was used for the preparation of nanofibers due to its inherent properties such as outstanding physiological compatibility, and satisfactory solubility in water along with other organic solvents. The solvent plays a vital role in the successful

preparation of electrospun nanofibers. The solvent should dissolve the drug conveniently while keeping the electrospinnability of polymer solutions intact. Amongst several solvents screened for solubilization of ibuprofen and PVP, ethanol was found to be suitable.

3.1. Scanning Electron Microscopic Investigation

The formation of nanoscopic fibers was confirmed using SEM (Fig. 1). The nanofiber diameter, as revealed by SEM, fell in the approximate range of 450–500 nm. The SEM images revealed no visible surface deposition of drug crystals indicating molecular dispersion of the loaded ibuprofen in the PVP matrices. On the other hand, SEM images of pure ibuprofen revealed distinct needle-shaped crystals.

3.2. X-ray Diffraction Studies

X-ray diffraction studies of the prepared samples were carried out to assess the polymorphic transitions (if any) that might have been taken place in ibuprofen when

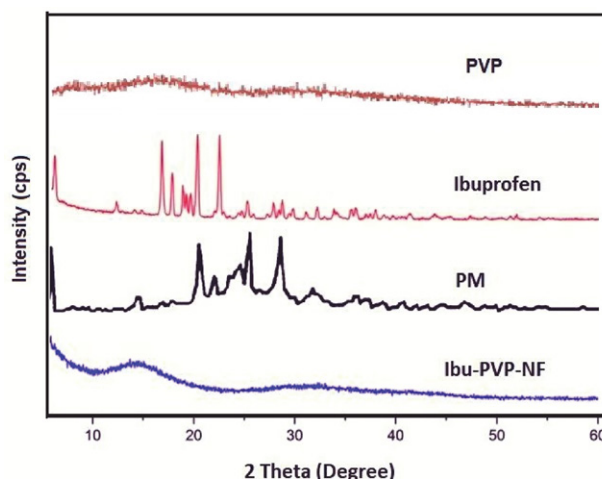


Fig 2. X-ray diffraction patterns of the studied samples indicated negligible or no crystallinity in the ibuprofen-loaded nanofiber sample (Ibu-PVP-NF). The raw ibuprofen (Ibuprofen) and physical mixture (PM) samples retained the crystalline peaks. PVP nanofibers (PVP) exhibited no crystalline peak indicating their amorphous nature.

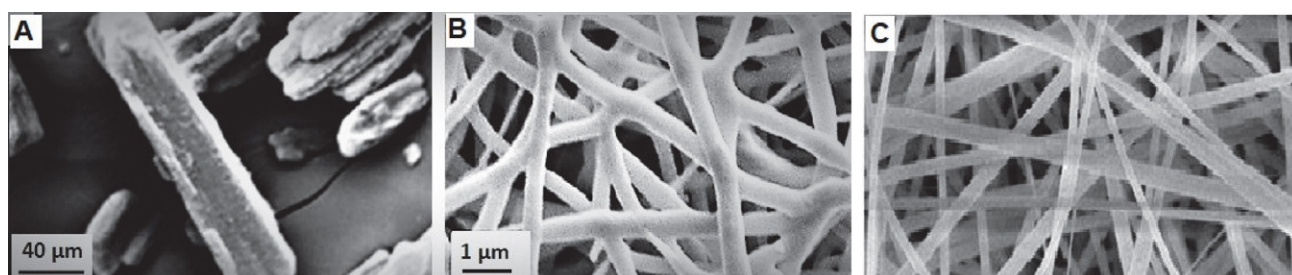


Fig 1. Scanning electron microscopy of (A) raw ibuprofen, (B) ibuprofen loaded PVP nanofibers, and, (C) PVP nanofibers.

formulated as nanofibers. The X-ray diffraction patterns of ibuprofen alone, as a physical mixture with the matrix-forming polymer and ibuprofen, loaded nanofibers are depicted in Fig. 2. The XRD pattern of ibuprofen alone exhibited intense peaks of high-intensity reflections to the interplanar distances 13.5, 7.2, 5.3, 4.7, and 4.0 Å at 6.3°, 12.4°, 15.9°, 18.2°, and 22.5° (2 θ), respectively which reveal its crystalline nature. However, the pattern of ibuprofen-loaded nanofibers showed broad and diffuse maxima peaks which may be attributed to the amorphization of ibuprofen in the nanofiber samples. Furthermore, the physical mixture (PM) samples prepared by physically mixing ibuprofen and PVP, exhibited the retained crystalline properties of ibuprofen. It has been well documented that the amorphous state of drug substances possesses many advantages including enhanced solubility, improved wettability, and increased dissolution rate when compared to its crystalline counterpart.^{29–30}

3. 3. Differential Scanning Calorimetry (DSC)

The DSC thermograms of samples are in agreement with the results of XRD studies (Fig. 3). Ibuprofen alone showed a sharp endothermic peak at 79.8 °C corresponding to its melting point confirming its crystalline nature. The physical mixture sample retained the melting endotherm of ibuprofen in the DSC studies. However, the peak associated with ibuprofen melting was significantly affected (small peak) in the nanofiber samples indicating its significant amorphization. Thus, the results of DSC studies were in agreement with the XRD analysis.

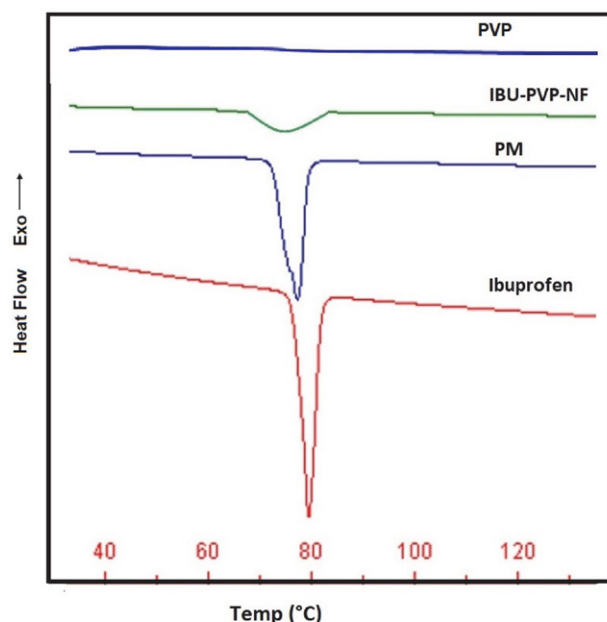


Fig 3. DSC thermograms of the studied samples indicate sharp melting endotherms at the melting point of ibuprofen in raw ibuprofen (Ibuprofen) and physical mixture (PM) samples. Ibuprofen-loaded nanofiber sample (IBU-PVP-NF) lacks a sharp endothermic peak. PVP nanofiber sample (PVP) exhibited no endothermic peak indicating its amorphous nature.

3. 4. Drug Loading Efficiency

Drug loading in drug delivery systems is considered an important parameter when assessing the suitability of the drug carrier systems. The methods of drug loading in polymeric nanofibers are diverse and include blending (the drug is dissolved/dispersed in polymer solution), surface modification (drugs are conjugated to the nanofiber surfaces), co-axial process (co-electrospinning of drug solution as core and polymer solution as a sheath), etc. The present study adopted the blending method for loading ibuprofen. The ibuprofen loading efficiency in the fabricated electrospun nanofibers was found to be as high as $93.42 \pm 4.21\%$ w/w.

3. 5. In Vitro Dissolution Studies

For BCS II drug candidates like ibuprofen, dissolution is the rate-limiting step for oral absorption. In such, a scenario, improving the dissolution of the drug has been an ideal strategy for its effective oral delivery. The raw ibuprofen (Ibu) dissolution in distilled water was found slow and incomplete ($55.72 \pm 4.82\%$). Moreover, the solubility of raw ibuprofen in distilled water was also found very poor (10.23 ± 1.44 mcg/ml). The dissolution profile of the studied samples (Fig. 4) revealed a significant improvement ($p < 0.05$; t-test) in drug release from the nanofiber samples (Ibu-PVP-NF) when compared to native raw ibuprofen (Ibu). The improved dissolution of ibuprofen ($88.96 \pm 3.22\%$) from the nanofiber samples may be due to the amorphous state of the drug.^{31,32} In our previous report, a similar improvement in dissolution was observed while attempting co-processing with hydrophilic polymers like hydroxypropyl methylcellulose.¹⁹

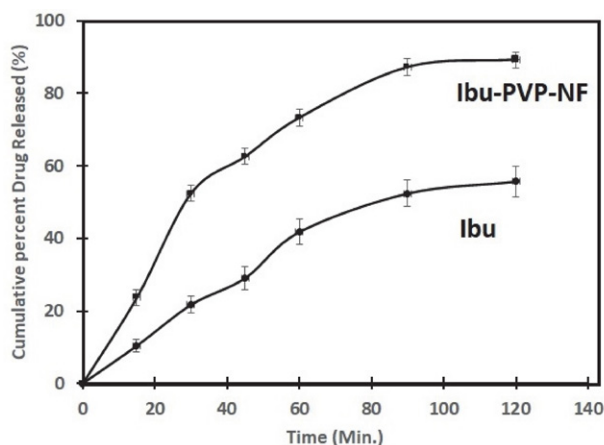


Fig 4. The dissolution profile of the raw ibuprofen (Ibu) and nanofiber (Ibu-PVP-NF) samples.

3. 6. Ex vivo intestinal permeation studies

As a surrogate for in vivo bioavailability studies, we have carried out ex vivo intestinal permeation studies to confirm dissolution data. The study conducted for two

hours revealed a significant ($p < 0.05$) improvement in the rate and extent of permeation of ibuprofen from nanofiber samples (equivalent weight of nanofiber containing 50 mg of ibuprofen) when compared to raw ibuprofen samples (50 mg) (Fig. 5). Raw ibuprofen (Ibu) exhibited a lower percentage of permeation ($34.66 \pm 5.27\%$). However, the nanofiber samples exhibited significantly ($p > 0.05$) higher intestinal permeation ($79.83 \pm 7.29\%$). Since, intestinal permeation of ibuprofen is dissolution rate limited, the present approach to enhance the dissolution of ibuprofen using nanofiber technology successfully improved the ex vivo intestinal permeation of the cargo.

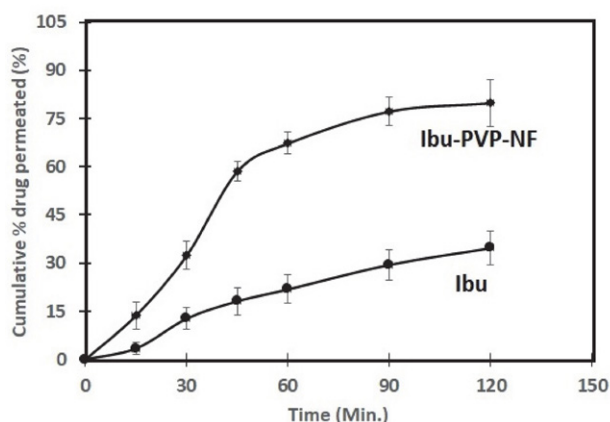


Fig 5. Ex vivo intestinal permeation pattern of raw ibuprofen (Ibu) and nanofiber (Ibu-PVP-NF) samples.

4. Conclusion

Hydrophilic polymer electrospun nanofibers for oral delivery of ibuprofen are reported with enhanced dissolution and ex vivo permeation. The results are very promising with the existence of ibuprofen in an amorphous state in the nanofiber matrix evident from the DSC and XRD investigations. The apparent absence of crystalline traces of ibuprofen in the nanofiber samples may be due to the antinucleating properties of PVP. The study has provided enough supporting data for further preclinical investigations.

Conflict of Interest

The authors declare no conflict of interest. The authors alone are responsible for the content and writing of the article.

Acknowledgment

This work was funded by the Deanship of Scientific Research at Jouf University, Kingdom of Saudi Arabia under grant No. DSR-2021-01-03135.

5. References

1. S. Mallick, S. Pattnaik, K. Swain, P. De, *Drug Dev Ind Pharm* **2007**, *33*, 535–541. DOI:10.1080/03639040601050130
2. S. S. Hota, S. Pattnaik, S. Mallick, *Acta Chimica Slovenica* **2020**, *67*, 179–188. DOI:10.17344/acsi.2019.5311
3. Y. C. Yadav, S. Pattnaik, K. Swain, *Drug Dev Ind Pharm* **2019**, *45*, 1889–1895. DOI:10.1080/03639045.2019.1672717
4. S. Pattnaik, K. Pathak, *Curr Pharm Des* **2017**, *23*, 467–480. DOI:10.2174/1381612822666161026162005
5. K. Pathak, S. Pattnaik, K. Swain, In: S. M. Jafari and D. J. McClements (Eds.): *Nanoemulsions: Formulation, Applications and Characterization*, Academic Press (Elsevier), Amsterdam, **2018**, pp.415–433. DOI:10.1016/B978-0-12-811838-2.00013-8
6. S. Mallick, S. Pattnaik, K. Swain, P. De, *Drug Dev Ind Pharm* **2007**, *33*, 865–873. DOI:10.1080/03639040701429333
7. J. Morimoto, K. Miyamoto, Y. Ichikawa, et al., *Sci Rep* **2021**, *11*, 12697. DOI:10.1038/s41598-021-92028-y
8. S. Abd Rahim, N. A. Rosli, and S. S. Mohd Khalid, *Advanced Materials Research* **2015**, *1113*, 417–421. DOI:10.4028/www.scientific.net/AMR.1113.417
9. L. Nicoud, F. Licordari, and A. S. Myerson, *Crystal Growth & Design* **2018**, *18*, 7228–7237. DOI:10.1021/acs.cgd.8b01200
10. C. Porter, N. Trevaskis, & W. Charman, *Nat Rev Drug Discov* **2007**, *6*, 231–248. DOI:10.1038/nrd2197
11. A. Malkawi, A. Jalil, I. Nazir, B. Matuszczak, R. Kennedy, and A. Bernkop-Schnürch, *Molecular Pharmaceutics* **2020**, *17*, 3709–3719. DOI:10.1021/acs.molpharmaceut.0c00389
12. A. K. Mahapatra, P. N. Murthy, R. K. Patra, S. Pattnaik, *Drug Delivery Letters* **2013**, *3*, 210–219. DOI:10.2174/22103031113039990005
13. S. B. Carneiro, F. I. Costa Duarte, L. Heimfarth, J. S. Siqueira Quintans, L. J. Quintans-Júnior, V. F. D. Veiga Júnior, A. A. Neves de Lima, *Int J Mol Sci* **2019**, *20*, 642. DOI:10.3390/ijms20030642
14. S. Pattnaik, K. Pathak, *Current Pharmaceutical Design* **2017**, *23*, 467–480. DOI:10.2174/1381612822666161026162005
15. N. Roy, B. Ghosh, D. Roy, B. Bhaumik, and M. N. Roy, *ACS Omega* **2020**, *5*, 30243–30251. DOI:10.1021/acsomega.0c04716
16. X. Cheng, J. Gao, J. Li, G. Cheng, M. Zou, H. Piao, *AAPS PharmSciTech* **2020**, *21*, 160. DOI:10.1208/s12249-020-01685-1
17. Y. Ma, Y. Yang, J. Xie, J. Xu, P. Yue, M. Yang, *Int J Nanomedicine* **2018**, *13*, 3763–3779. DOI:10.2147/IJN.S164228
18. K. Ueda, K. Higashi, K. Moribe, *Int J Pharm* **2019**, *561*, 82–92. DOI:10.1016/j.ijpharm.2019.02.034
19. S. Pattnaik, K. Swain, J.V. Rao, V. Talla, K.B. Prusty, S.K. Subudhi, *RSC Adv* **2015**, *5*, 74720–74725. DOI:10.1039/C5RA13038G
20. S. Pattnaik, K. Swain, P. Manaswini, E. Divyavani, J. V. Rao, V. Talla, S. K. Subudhi, *Journal of Drug Delivery Science and Technology* **2015**, *29*, 199–209. DOI:10.1016/j.jddst.2015.07.021
21. S. Pattnaik, K. Swain, J.V. Rao, V. Talla, K.B. Prusty, S.K. Subudhi, *RSC advances* **2015**, *5*, 91960–91965.

- DOI:10.1039/C5RA20411A
22. S. Pattnaik, Y. Surendra, J. V. Rao, K. Swain, In: Masoud Mozafari (Ed.) Woodhead Publishing Series in Biomaterials, Nanoengineered Biomaterials for Advanced Drug Delivery, Elsevier, 2020, pp. 421–445.
DOI:10.1016/B978-0-08-102985-5.00018-8
23. S. Pattnaik, K. Swain, In: Inamuddin, A. M. Asiri, A. Mohammad (Eds.) Woodhead Publishing Series in Biomaterials, Applications of Nanocomposite Materials in Drug Delivery, Woodhead Publishing, 2018, pp. 589–604.
DOI:10.1016/B978-0-12-813741-3.00025-X
24. J. Xue, T. Wu, Y. Dai, Y. Xia, *Chem Rev* 2019, 119, 5298–5415.
DOI:10.1021/acs.chemrev.8b00593
25. Y. Bai, D. Wang, Z. Zhang, J. Pan, Z. Cui, D-G. Yu, S-W. A. Bligh, *Polymer Testing* 2021, 93, 106872.
DOI:10.1016/j.polymertesting.2020.106872
26. M. L. Ohnsorg, P.C. Prendergast, L. L. Robinson, M.R. Bockman, F. S. Bates, and T. M. Reineke, *ACS Macro Letters* 2021, 10, 375–381. DOI:10.1021/acsmacrolett.0c00890
27. D. N. Karunaratne, I. R. Ariyaratna, D. Welideniya, A. Siriwardhana, D. Gunasekera and V. Karunaratne, *Current Nanomedicine* 2017, 7, 84–110.
DOI:10.2174/2468187307666161227171349
28. H. Rahim, A. Sadiq, S. Khan, F. Amin, R. Ullah, A. A. Shahat, H. M. Mahmood, *Int J Nanomedicine* 2019, 14, 6287.
DOI:10.2147/IJN.S210548
29. S. A. Fouad, F. A. Malaak, M. A. El-Nabarawi, K. Abu Zeid, A.M. Ghoneim, *PLoS ONE* 2021, 16, e0245482.
DOI:10.1371/journal.pone.0245482
30. S. Mallick, S. Pattnaik, K. Swain, P. De, A. Saha, G. Ghoshal, A. Mondal, *Eur J Pharm Biopharm* 2008, 68, 346–351.
DOI:10.1016/j.ejpb.2007.06.003
31. N. J. Babu and A. Nangia, *Crystal Growth & Design* 2011, 11, 2662–2679. DOI:10.1021/cg200492w
32. A. Ziaee, S. O’Dea, A. Howard-Hildige, L. Padrela, C. Potter, J. Iqbal, A.B. Albadarin, G. Walker, E.J. O’Reilly, *Int J Pharm* 2019, 572, 118816. DOI:10.1016/j.ijpharm.2019.118816

Povzetek

Slaba topnost zdravilnih učinkovin v vodi predstavlja velik izziv za farmacevtske tehnologe, ki pripravljajo formulacije za učinkovito peroralno dostavo. Slaba topnost je pogosto povezana z oteženim raztapljanjem in posledično nizko biološko uporabnostjo tistih učinkovin, pri katerih je črevesna absorpcija omejena s hitrostjo raztapljanja. V tej študiji so z elektrostatskim sukanjem razvili polimerna nanovlakna s ciljem izboljšanja vodotopnosti ibuprofena, zdravila II. razreda po biofarmaceutskem klasifikacijskem sistemu. Hidrofilne polimere, kot je polivinil piroolidon, ki se lahko sukajo, so uporabili kot nosilni sistem za izdelavo nanovlaken. Optimizirali so parametre elektrostatskega sukanja, kot so pretok, napetost in razdalja med šobo in zbiralnikom. Izdelana nanovlakna z vključenim ibuprofenom so ovrednotili z vrstično elektronsko mikroskopijo in diferenčno dinamično kalorimetrijo. Izvedli so tudi raziskave sproščanja učinkovine in absorpcije v ex vivo pogojih. Platforma na osnovi nanovlaken je bistveno izboljšala in vitro absorpcijo ibuprofena v primerjavi s čistimi kristali ibuprofena.



Except when otherwise noted, articles in this journal are published under the terms and conditions of the Creative Commons Attribution 4.0 International License

Scientific paper

Combined Pharmacophore Modeling, 3D-QSAR, Molecular Docking and Molecular Dynamics Study on Indolyl-aryl-sulfone Derivatives as New HIV1 Inhibitors

Mebarka Ouassaf,^{1,*} Faizan Abul Qais,² Salah Belaidi,^{1,*} Mohamed Bakhouch,³
Ahmed Said Mohamed⁴ and Samir Chtita⁵

¹ Group of Computational and Medicinal Chemistry, LMCE Laboratory, University of Biskra, BP 145 Biskra 707000, Algeria

² Department of Agricultural Microbiology, Faculty of Agricultural Sciences, Aligarh Muslim University, Aligarh, UP-202002, India

³ Laboratory of Bioorganic Chemistry, Department of Chemistry, Faculty of Sciences, Chouaib Doukkali University, El Jadida, Morocco

⁴ Institut de Recherche Médicinale, Centre d'Etude et de Recherche de Djibouti, Djibouti

⁵ Laboratory of Analytical and Molecular Chemistry, Faculty of Sciences Ben M'Sik, Hassan II University of Casablanca, B.P 7955, Casablanca, Morocco

* Corresponding author: **E-mail: s.belaidi@univ-biskra.dz

*E-Mail: nouassaf@univ-biskra.dz

Received: 02-22-2022

Abstract

The present study deals with the *in silico* of 45 indolyl-aryl-sulfones known as anti-HIV1. The data were collected from recent previously reported inhibitors and divided into a sub-set of 33 compounds as the training set and the remaining 12 compounds were kept in the test set. The selected pharmacophore-ADRRR-yielded a statistically significant 3D-QSAR model containing high confidence scores ($R^2 = 0.930$, $Q^2 = 0.848$, and $RMSE = 0.460$). The predictive power of the established pharmacophore model was validated with an external test ($r^2 = 0.848$). A systematic virtual screening workflow shows an enrichment factor and has revealed a high predictive power. Then the model was used to screen the filtered PubChem database mapping all chemical features of model pharmacophore. The recognized hits were further assessed by *in silico* ADMET studies. Molecular dynamics also used to explore the stability of obtained complexes. Finally, these selected compounds are probably to become a good lead molecule for the development of effective anti-HIV-1 drugs.

Keywords: Indolyl-aryl-sulfone, HIV-1 inhibitor, Pharmacophore, 3D-QSAR, Molecular Docking, Molecular Dynamics.

1. Introduction

AIDS is one of the most destructive of human immune system pandemic in the world, caused by human immunodeficiency virus infection (HIV).¹ It continues to be a critical global public health concern, 1.5 million people were newly infected with HIV in 2020, and around 38 million HIV-infected persons are estimated to be dealing with it to date.² Unfortunately, there is no effective treatment for HIV infection. Luckily, available antiretroviral drugs are used to control the proliferation of the virus.

Therefore, persons having HIV can lead healthy and productive lives.³

Most of the drugs designed and licensed have been classified as Nucleoside Reverse Transcriptase inhibitors (NRTI's), Non-nucleoside Reverse Transcriptase Inhibitors (NNRTI's), Protease Inhibitors (PI's), Fusion Inhibitors, HIV integrase strand transfer inhibitors and Inhibitors-CCR5 co-receptor antagonist.⁴ Protease is an important factor for viral maturation within the HIV life cycle.^{5,6} The HIV protease is a homodimeric aspartyl pro-

tease and each monomer consists of 99 amino acid residues with a catalytic Asp at position 25. At nine processing sites, the main structural component of HIV-1 is the Gag polyprotein. HIV-1 protease cleaves polyprotein precursors Gag and Gag-Pol encoded by the HIV-1 virus genome to create mature active proteins.⁷ Gag-Pol is incorporated into virions via interactions with the Gag precursor Pr55gag. The protease (PR) incorporated into Gag-Pol mediates proteolytic processing of both Pr55gag and Gag-Pol during or shortly after release of viral particles from cells. Since efficient viral incorporation of Gag-Pol depends on interaction with Pr55gag through its N-terminal Gag domain, prevention of premature Gag cleavage may attenuate Gag-Pol packaging deficiencies associated with enhancement of the PR cleavage.⁸

The vital role of HIV protease in viral maturation makes it a popular drug design target; there are 10 FDA-approved HIV protease inhibitors, namely: Saquinavir, Indinavir, Ritonavir, Nelfinavir, Amprenavir, Fosamprenavir, Lopinavir, Atazanavir, Tipranavir, and Darunavir. The FDA-approved HIV protease inhibitors have structural similarities and a similar binding pattern, which might explain some of the protease inhibitor-related adverse effects such as dyslipidaemia, hyperglycaemia, and body-fat distribution. It is possible to optimize the chemical structure of HIV protease inhibitors to avoid side effects.^{9,10}

The computer-aided drug design CADD approach has played a crucial role in the search and optimization of potential lead compounds with a substantial benefit in time and expense; it has been used during different phases of drug discovery: target identification, validation, molecular design, and interactions of drug candidates with targets of interest.^{11,12}

Pharmacophores are a set of methods related to QSAR: they produce 3-dimensional arrangements of functional group that are required for activity.^{13,14}

A well-developed pharmacophore model may be used to design novel and more active molecules, such pharmacophore models are also the starting point for 3D-QSAR analysis, and can allow quantitative predictions. In the very early stages of the drug development process, the use of 3D pharmacophore models will potentially anticipate unwanted side effects and thereby reduce the probability of late failure of drug candidates.¹⁵

Docking simulations are widely used to screen a library of compounds rapidly and to identify new drug leads employing a simple model. Docking simulations are also useful for lead enhancement using more detailed models to analyze the atomic interactions between inhibitors and target macromolecules.¹⁶

In order to take a forward step for prediction and guidance of more effective drug, we have utilized state of the art techniques in drug design for the development of a three-dimensional pharmacophore model using a dataset of indolyl-aryl-sulfone derivatives from literature. We have used also a comprehensive approach involving vir-

tual screening-based pharmacophore modeling, molecular docking and Molecular Dynamics (MD) simulations to identify potential HIV1 inhibitors. The studied compounds were consequently analyzed for ADMET properties and were found to be potential drug-like candidates that can effectively bind to the HIV protease enzyme.

Taken together the specifics of the current study could provide important insights needed for the production of next-generation of inhibitors that could theoretically reduce the function of HIV protease.

2. Materials and Methods

2.1. At a Set Preparation

In vitro biological data of a series of 45 indolyl-aryl-sulfones as anti-HIV-1 were collected from literature.¹⁷ the observed anti-HIV-1 activity was represented as EC₅₀ and converted into logarithmic scale pEC₅₀ = -logEC₅₀ (μM).

It is essential to examine the structures of the molecules in the data set before starting molecular modeling. For that, the 3D-structures of the 45 inhibitors were prepared using the builder panel in Maestro 12.0 and were generated for all ligands with LigPrep.¹⁸ Partial atomic charges were ascribed and possible ionization states were generated at a pH equal to 7.0. The OPLS3e force field was used to optimize and to produce low energy conformer of the ligand.^{19,20} Energy minimization was performed with OPLS3e force field till root mean square mean deviation (RMSD) of 0.01 Å was attained. The so-prepared ligands were used to generate pharmacophore and to build QSAR model.

2.2. Generation of Pharmacophore Model

A pharmacophore describes the arrangement of molecular or functional group's characteristics that a ligand must contain in order to produce a given biological response. Pharmacophore models are developed to identify new compounds that meet the requirements of the pharmacophore, which could have the high probability to be biologically active. Often, such pharmacophore models are the starting point for 3D-QSAR analysis.²¹

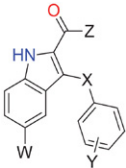
Each compound structure was represented by a set of points in 3D space that correspond to different chemical features, which help the compound to bind with the target receptor non-covalently. The data set was created by assigning pEC₅₀ > 8.6 as active and pEC₅₀ < 6.5 as inactive to the threshold. Inactive compounds can be used to screen the hypothesis because they do not provide an explanation for the activity. However, they give signals of the inactive function.

Six pharmacophore features defined the chemical features of the ligands: H-bond Acceptor (A), H-bond Donor (D), hydrophobic group (H), negatively charged group (N), positively charged group (P) and Aromatic Ring (R). The consistency of each alignment is calculated by: (1) the

vector score, the average cosine of the angles generated in the aligned structures by the corresponding pairs of vector characteristics (acceptors, donors and aromatic rings); (2) the volume score that is based on the overlap of Van der

Waals non-hydrogen atom models in each pair of structures (3); the site score which is the degree to which site points in the alignment are applicable; (4) The final score, (5) and the function-survival score.

Table 1. Various substituents attached to basic structure of indolyl-aryl-sulfones.



N°	Structural features			
	X	Y	Z	W
1	SO ₂	H	NH ₂	Cl
2	S	H	OEt	H
3	S	2-NH ₂	OEt	Cl
4	S	2-NH ₂ -5-Cl	OEt	Cl
5	SO ₂	H	OEt	H
6	SO ₂	2-NH ₂ -5-Cl	OEt	H
7	SO ₂	2-NH ₂ -5-Cl	OEt	Cl
8	S	H	NH ₂	H
9	S	2-NH ₂ -5-Cl	NH ₂	H
10	S	H	NH ₂	Cl
11	S	2-Me	NH ₂	Cl
12	S	4-F	NH ₂	Cl
13	S	4-Cl	NH ₂	Cl
14	S	4-iPr	NH ₂	Cl
15	S	4-tBu	NH ₂	Cl
16	S	3,5-Me ₂	NH ₂	Cl
17	S	2,6-Cl ₂	NH ₂	Cl
18	S	2-NH ₂ -5-Cl	NH ₂	Cl
19	SO ₂	H	NH ₂	H
20	SO ₂	2-NH ₂ -5-Cl	NH ₂	H
21	SO ₂	2-Me	NH ₂	Cl
22	SO ₂	3-Me	NH ₂	Cl
23	SO ₂	4-Me	NH ₂	Cl
24	SO ₂	4-F	NH ₂	Cl
25	SO ₂	4-Cl	NH ₂	Cl
26	SO ₂	4-iPr	NH ₂	Cl
27	SO ₂	4-tBu	NH ₂	Cl
28	SO ₂	2,4 Me ₂	NH ₂	Cl
29	SO ₂	3,5-Me ₂	NH ₂	Cl
30	SO ₂	2,6-Cl ₂	NH ₂	Cl
31	SO ₂	2-NH ₂ -5-cl	NH ₂	Cl
32	SO ₂	3,5-Me ₂	NH ₂	Br
33	SO ₂	3,5-Me ₂	NH ₂	COMe
34	SO ₂	3,5-Me ₂	NH ₂	CH(OH)Me
35	S	H	NHNH ₂	Cl
36	S	4-Me	NHNH ₂	Cl
37	S	4-F	NHNH ₂	Cl
38	S	4-Cl	NHNH ₂	Cl
39	SO ₂	H	NHNH ₂	H
40	SO ₂	H	NHNH ₂	Cl
41	SO ₂	4-Me	NHNH ₂	Cl
42	SO ₂	4-F	NHNH ₂	Cl
43	SO ₂	4-Cl	NHNH ₂	Cl
44	SO ₂	3,5-Me ₂	NHNH ₂	Cl
45	SO ₂	2-NH ₂ -5-Cl	NHNH ₂	Cl

2. 3. Building 3D-QSAR Model

QSAR modeling was performed using the selected hypothesis by dividing randomly the data set into training set (60%) and test set (40%). This phase presents two options for the alignment of the 3D-structure of molecules: pharmacophore-based alignment and atom-based alignment.

In this study, the selected 45 compounds from the chemical dataset were used to develop an atom-based 3D-QSAR model based on previously developed pharmacophoric maps as a backbone with a default grid space of 1 Å via partial least-square (PLS) regression.²²

2. 4. Model Validation

Validation is a critical aspect of pharmacophore design, particularly when the model is constructed for predicting molecular activity in external test series.²³ The intensity of the defined pharmacophore hypotheses was internally validated by statistical parameters, squared coefficient of correlation (R^2) and the ratio of variance (F). Validation on chemicals was not used in the model development, the so-called external validation, is particularly important in the context of using QSAR models for the prediction of new data in virtual screening.²⁴ The approach demonstrated by Golbraikh and Tropsha, in 2000²⁵ and Roy and al., 2008²⁶ was used to evaluate the predictive potential of the current QSAR model. Further, the best hypothesis selected was validated by enrichment

studies using the decoy test. More than 1000 decoy test set compounds retrieved from the PubChem database, were taken to evaluate the predictive power of the built model²⁷ and were taken to evaluate some parameters, such as: Enrichment Factor (EF), Robust Initial Enhancement (RIE), Receiver Operating Characteristic (ROC) and Boltzmann-Enhanced Discrimination of ROC (BEDROC). These parameters were used to benchmark the reliability of the model and for the accurate ranking of compounds.²⁸

2. 5. Virtual Screening of PubChem Database

In pharmaceutical research, computational screening of databases has become incredibly popular. Based on biological structures, virtual screening uses computer-based methods to discover new ligands.^{29,30} The aim of virtual screening, in this work, is to detect potential leads to anti-HIV with various scaffolds and high inhibitory activity. To identify inhibitors of PR HIV, we have screened the PubChem database³¹ by searching compounds having more than 80% similarity instead of compound that have the most fitness score (compound 40, Table 1). All PubChem drug-like compounds (459926) were filtered by Canvas's property filter utility to pick compounds with low-dimensional properties similar to the anti-HIV compounds. We used the following property filters: AlogP \geq 1, AlogP \leq 5, HBA \geq 2, HBA \leq 3, HBD \geq 1, HBD \leq 3, MW \geq 250, MW \leq 500, Num rings \geq 3, Num rings \leq 5, Polar \geq 45, Polar \leq 60, RB \geq 3 and RB \leq 5. As a result,

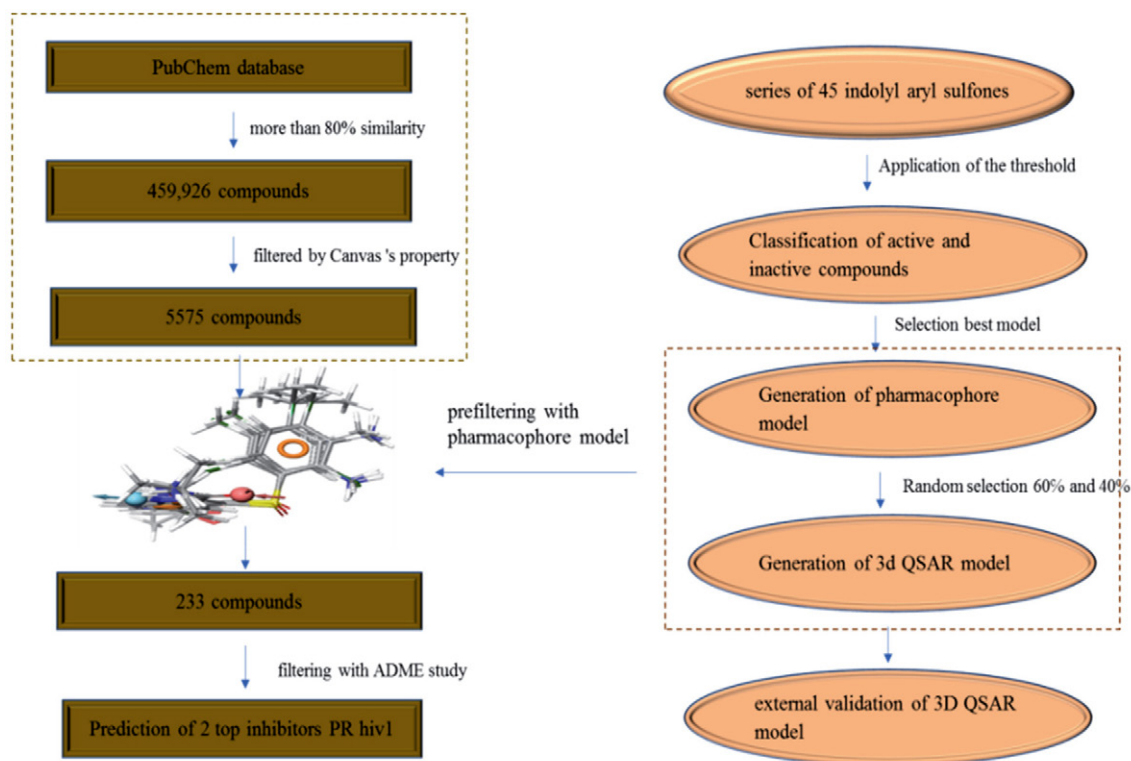


Fig. 1. Schematic representation of the methods followed in the current study.

5575 compounds were obtained and mounted as a series of decoys. Each compound must fit a minimum of four sites and a distance of 2.0 Å matching between sites. After the pharmacophore-based screening according to the fitness score, the top 230 hits were selected for molecular docking analysis. Figure 1 represents the schema of the methods followed in the current study.

2. 6. Molecular Docking Analysis

The top 230 compounds were selected for molecular docking analysis based on the pharmacophore model following virtual screening. X-ray crystal structure of wild type HIV-1 protease in complex with GRL-09510 (PDB ID: 5v4y) were obtained from the Protein Data Bank PDB.³² The protein structure was preprocessed using the Protein Preparation Wizard,³³ available in Schrödinger suite 2021-2, by eliminating crystallographic water molecules (water molecules without H-bonds), inserting all missing side chain atoms, and pH 7.0 corresponding hydrogen bonds, taking into account the necessary ionization states for the residues of both acid and basic forms of the amino acid.

Finally, energy minimization (up to 3.0 Å RMSD value) was performed using OPLS-2005 force field after the assignment of charge and protonation state. In fact, it was minimized to alleviate the steric clashes between the residues due to the addition of hydrogen atoms. The active site was defined with a radius of 10 Å around the ligand present in the crystal structure and a grid was generated at the center of gravity of the active site for docking. All studied compounds were docked into the catalytic pocket of the Protease protein (PDB-ID: 5v4y) using Grid-Based Ligand Docking with Energetics³⁴ with default parameters. Finally, the docking results were analyzed using Biovia Discovery Studio 4.5.12 (Dassault Systèmes 2018).³⁵

2. 7. Analyzing ADMET

ADMET (Absorption, Distribution, Metabolism, Elimination, Toxicity) analysis is important in drug design. These properties were calculated using the QikProp module³⁶ of Schrodinger suite for assessing the drug ability and to filter the ligand molecules at an early stage of identifying the new inhibitors.

Toxicity is the degree to which a substance can damage an organism or substructure of the organism. The predictions of toxicity of the compounds are essential to re-

duce the cost and labor of a drug's preclinical and clinical trials. The toxicity evaluation was performed also using the ProTox platform.³⁷ It gives predicted toxicity values, cytotoxicity, mutagenicity, carcinogenicity, immunotoxicity and LD50 values of selected compounds.

2. 8. Molecular Dynamics Simulations

Two compounds showing highest binding affinity towards HIV-1 protease were selected for Molecular Dynamics (MD) simulation studies. The molecular docked complexes with lowest binding energy were used as initial point for the MD simulations performed using Gromacs-2018.1 packages with amber99sb-ILDN force field.^{38,39} The protein alone and their complexes with ligands (11630770 and 55868948) were solvated in triclinic-boxed using TIP3P water model. Each structure was neutralized using counter chlorine ions. The topology of both ligands was prepared using antechamber packages in Amber Tools 19.⁴⁰ For the removal of weak Van der Waals contacts; each system was minimized using the steepest descent minimization. The systems were then equilibrated for NVT using V-rescale thermostat for 1 ns at 300 K temperature followed by NPT equilibration using Parrinello-Rahman barostat at 1.0 bar for 1 ns.^{41,42} MD simulation of each system was carried out for 100 ns and the trajectories were recorded at 10 ps intervals. Each trajectory was subjected to PBC (periodic boundary conditions) corrections before analysis. All calculations except MM-PBSA was done using Gromacs utilities. MM-PBSA calculation was performed for the calculation of various binding energies the ligands with HIV-1 protease.⁴³

3. Results and Discussions

3. 1. Pharmacophore Modeling

Our work is focused on the identification of new compounds with potential antiviral activity anti-HIV-1. To fulfill the objective, a ligand-based pharmacophore model was built using previously reported inhibitors, with a different combination of pharmacophoric features, 920 pharmacophore hypotheses have been produced.

Its vector, volume, sites survival score, and the number of matches measured the quality of each hypothesis. Table 2 represents the different scoring parameters for best hypothesis. The best fitted Model ADRRR1 with the

Table 2. Different parameter scores of the generated hypothesis ADRRR1.

	Survival score	Site	Vector	Volume	Bedroc	Matches
ADRRR1	6.067	0.944	0.977	0.917	0.843	5
ADRRR2	6.063	0.695	0.922	0.613	0.843	5
ADRRR3	6.062	0.705	0.919	0.620	0.844	5
ADRRR4	6.061	0.711	0.922	0.619	0.843	5
ADRRR5	6.061	0.681	0.932	0.622	0.844	5

highest survival score (6.067) and site score (0.944) consist five-point hypothesis one hydrogen acceptors, one hydrogen donor, and three ring group. The spatial arrangement of the best pharmacophore hypothesis, ADRRR1 with their distance between the five-pharmacophore features is shown in figure 2 and tables S1-S2.

3. 2. 3D-QSAR Model

The previously developed pharmacophore hypothesis ADRRR1 was used to build an atom-based 3D-QSAR with the phase program.⁴⁴ Based on the training set molecules for the chosen hypothesis, the pharmacophore model, that is statistically significant, was created through partial least-square (PLS) regression. The partial least-squares

factor has been raised to five, as there is a gradual improvement in the model's predictive power and statistical significance until the fifth factor.

A statistically significant 3D-QSAR model was obtained using this pharmacophore hypothesis with a strong correlation coefficient ($R^2 = 0.929$) and a high Fisher ratio ($F = 57$) for the training set. The predictive power of the developed model was also found to be important, verified by the high value of the coefficient of cross-validated correlation ($Q^2 = 0.848$) and Pearson's R (0.926) for the test set. The plots between the observed and the predicted activities were made for both the training and test sets (Figure 3). The higher values of R^2 and Q^2 in the training and test sets, respectively, are clearly indicated by the points lying extremely near to the best-fit line.

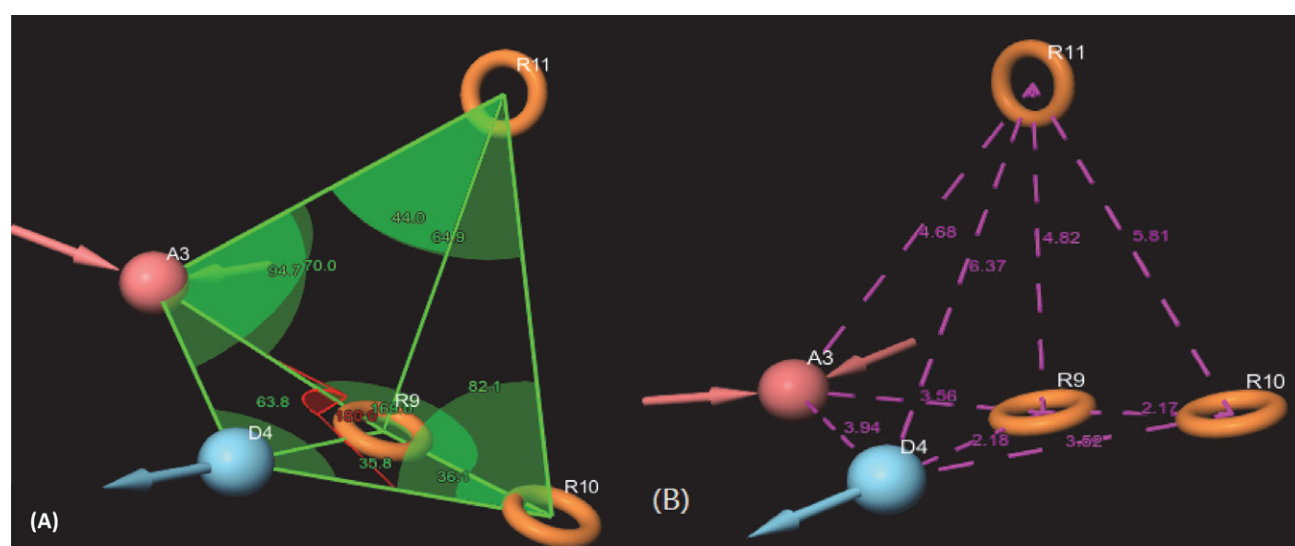


Fig. 2. (A) Pharmacophore model ADRRR1 interstice angles in ($^{\circ}$) unit between the pharmacophoric points and (B) Pharmacophore model ADRRR1 interstice distances in \AA unit.

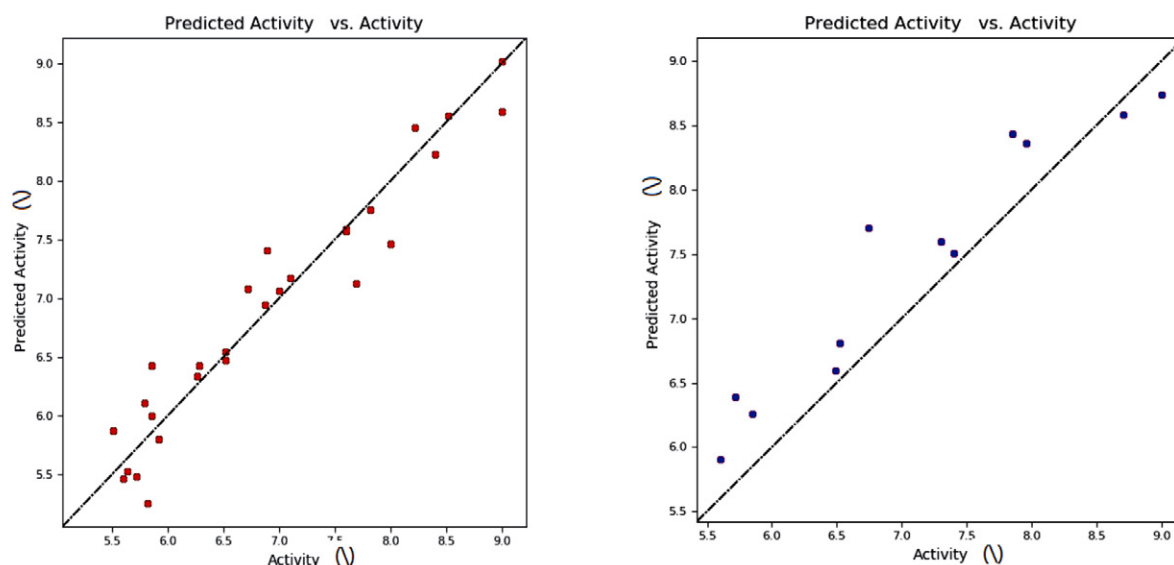


Fig. 3. The plot of the correlation between the experimental and predicted activity of based indolyl aryl sulfones inhibitors using pharmacophore-based QSAR model of training and test set.

3. 3. Model Validation

All the external validation results were above the threshold values for the various parameters presented in table S3. The squared correlation coefficient values between the observed and predicted values of the test set compounds (r^2) and (r^2_0), respectively, were observed and the model had satisfied the requirement of the term $(r^2 - r^2_0)/r^2$. This was in agreement with a previous study reported by Golbraikh and co-workers, which states that the value $(r^2 - r^2_0)/r^2$ exhibits less than 0.1. In case of good external prediction, predicted values will be very close to observed activity values. Therefore, r^2 value will be very near to r^2_0 value. In the best case r^2_m will be equal to r^2 , whereas in the worst-case r^2_m value will be zero, including values of $r^2_m < 0.6$ indicate these models are useless for external predictivity. In the present study r^2_m value of the model is acceptable (Table S3). This developed model passed all the Golbraikh and Tropsha criteria for the acceptability of the model. The screening results were evaluated by an enrichment factor at the top 1% of the ranked database (EF1) and are summarized in table S4.

reported by Golbraikh and co-workers, which states that the value $(r^2 - r^2_0)/r^2$ exhibits less than 0.1.

In case of good external prediction, predicted values will be very close to observed activity values. Therefore, R^2 value will be very near to R^2_0 value. In the best case r^2_m will be equal to r^2 , whereas in the worst-case r^2_m value will be zero, including values of $r^2_m < 0.6$ indicate these models are useless for external predictivity. In the present study r^2_m value of the model are acceptable (Table S3).

This developed model passed all the Golbraikh and Tropsha criteria for the acceptability of the model. The screening results were evaluated by an enrichment factor at the top 1% of the ranked database (EF1) and are summarized in table S4.

The enrichment factor (EF) of this screening protocol was calculated to be 13.012, which indicated that selected model has 13 times more stability to identify active molecules than inactive.

Visualization of the validation was presented in ROC analysis to show how effectively the pharmacophore mod-

Table 3. 3D-QSAR PLS statistical results of the selected Pharmacophore model ADRRR1.

ID	PLS factors	SD	R ²	F	P	RMSE	Q ²	Pearson-R
ADRRR1	1	0.650	0.722	39	4.52 10 ⁻⁹	0.600	0.742	0.869
	2	0.509	0.835	49	1.78 10 ⁻¹¹	0.620	0.724	0.865
	3	0.425	0.889	56	5.83 10 ⁻¹³	0.490	0.826	0.914
	4	0.404	0.903	50	7.10 10 ⁻¹³	0.530	0.799	0.904
	5	0.351	0.930	57	4.30 10 ⁻¹⁴	0.460	0.848	0.925

All the external validation results were above the threshold values for the various parameters presented in table S3. The squared correlation coefficient values between the observed and predicted values of the test set compounds (r^2) and (r^2_0), respectively, were observed and the model had satisfied the requirement of the term $(r^2 - r^2_0)/r^2$. This was in agreement with a previous study

els distinguished between active and inactive compounds (Figure 4). Sensitivity (in other words, true positive rate, recall, hit rate) and specificity (in other words, true negative rate) are general indices to show the predictive power of a validated model and is indicated by the area under the curve. The area under the curve (AUC) was calculated as 0.8157.

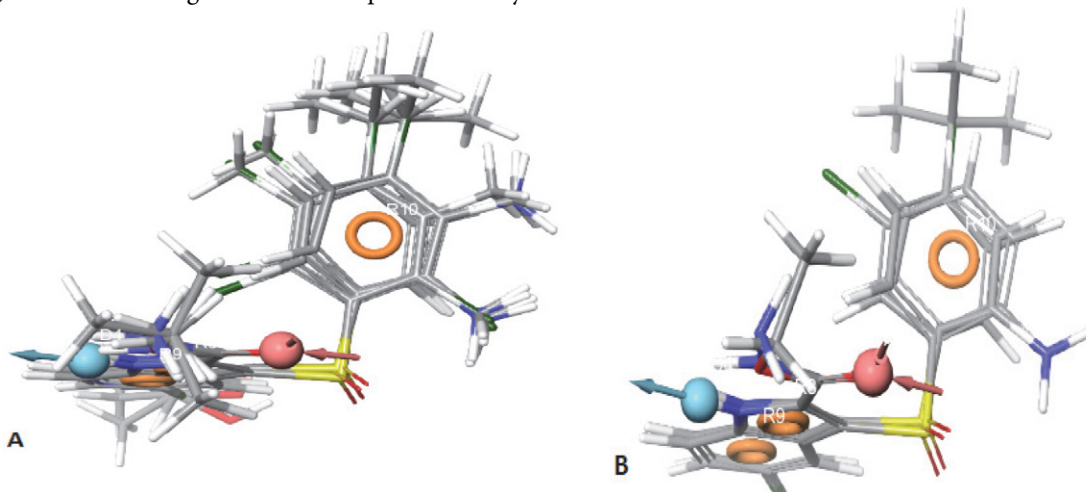


Fig. 4. (A) Mapping of the active compounds onto the pharmacophore. (B) Mapping of inactive compounds on to the pharmacophore.

Thus, we can conclude that our model is not randomly classified. Considering area under the ROC curve, it is statistically significant from those obtained by random classifier (Area = 0.5).

The result revealed that in 1% of the total database the generated model screened 28 decoys and five active compounds overall while in the top 2% it was able to get 21 decoys and 8 active compounds hits, with an enrichment factor of 19. The detailed results are given in table S5.

3. 4. Contour Plot Analysis

Contour plot analysis was conducted at spatial locations of the system to interpret and understand the distinct vital pharmacophoric criteria. Positive and negative activity coefficients of different properties are described in the map, including (a) donor hydrogen bond, (b) hydrophobic/non-polar and (c) ionizable negative properties. The blue cubes show their individual positive contribution, and the red cubes reflect the negative contribution (Figure 5).

3. 4. 1. H-Bond

Red region near and around position X and W indicates that the substitutions at these positions by groups having more hydrogen bond donor property is unfavorable to anti-HIV activity for example in compounds 3 and 5.

The blue cubes around the position Z suggests that the presence of a donor substitution (e.g N, O, P, or S) at this position may favor the formation of H bond interaction. Almost all the compounds containing Sulfur Dioxide (e, g Compound 1) were found to have better activity

profile in comparison with the ones with Sulfur atom (e, g Compound 8).

3. 4. 2. Hydrophobic

Another significant component that affects the anti-HIV activity is the hydrophobic character. In figure 5B, the contour map for hydrophobic characteristics displays blue cubes highly distributed proximal to the R9, R10 and R8 regions of indolyl-aryl-sulfones. This result reveals that the multiple rings R8, R9, and R10 of the indolyl-aryl-sulfones may enhance the hydrophobicity, and might play a major role in its higher activity. The presence of red cubes at W position of phenyl ring directly attached to the Cl group indicates that hydrophobic groups are unfavorable at this position. This assumption is supported by the low activity of Cl substituted compounds when compared to their unsubstituted derivatives. This is evident while comparing the compounds 6 with 7 and 32.

3. 4. 3. Negative

In contour plot of compound 25 (Figure 5C), the presence of red cubes at *para* position X indicates that the presence of electron withdrawing groups is undesirable at this position. This is evident while comparing the compounds 2 (X: S) with 5 (X: SO₂). On the contrary, the presence of blue cubes at *para* position of W indicated the preference of electron withdrawing groups at this position. This is explained by the significant anti-HIV activity of compounds with *para* halogen substitution (30, 35 and 40) (pEC₅₀= 8.70, 7.82 and 7.60) in the order of Br > COMe > CHOHMe.

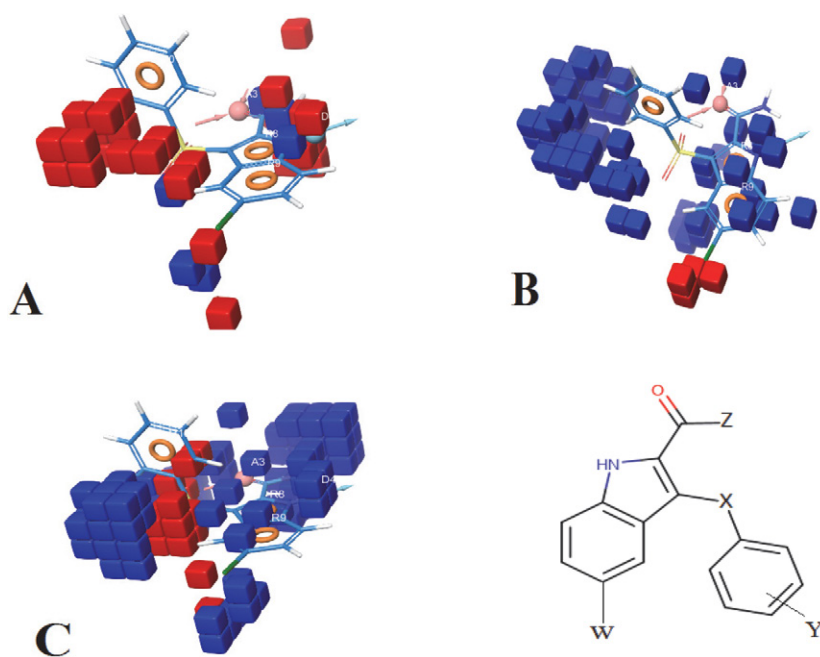


Fig. 5. QSAR model visualized in the context of favorable and unfavorable effects in compound: (A) hydrogen bond donor, (B) hydrophobic/non-polar and (C) negative ionizable properties.

3. 5. Identifying Novel Inhibitors

The created five-site pharmacophore hypothesis, ADRRR-1, was used to identify new inhibitors with a new scaffold that corresponds to the 3D-QSAR model's predicted molecular properties. Lead-like compounds from PubChem have been used to obtain new inhibitors, which could potentially target the HIV protease receptor. There was a total of 5575 hits compounds found from the PubChem datasets was similar 80% for most active compound of indolyl-aryl-sulfones composes. Pharmacophore model was used to identify the molecules that satisfy the hypothesis. Pharmacophore pre-filtering with ADRRR-1 hypothesis reduced initial 233 hits.

3. 6. Virtual Docking Screening

Molecular docking simulations for the selected set of hits were performed using the Glide (Grid-Based Ligand Docking with Energetics) program available in Schrödinger 2021. The 3D structures were prepared using the Maestro LigPrep module. This module generates possible 3D conformations for each ligand with various ionization states at pH 7.0 ± 2.0 . The docking screening process was conducted in two steps: (i) Glide/SP is performed for 230 ligands accelerated docking simulations; (ii) Glide/XP docking has chosen the top-docking ligands for more detailed analyses. The scores of docking studies Glide/SP are shown in the (Table S5).

The key residues involved in substrate binding, including Asp25 Gly27 Ala28 Asp29 Asp30 Thr31 Val32 Ile47 Gly48 Gly49 Ile50 Gly51 Gly52 Phe53 Ile54 Leu76 Thr80 Pro81 Val82 Ile84, the structural analysis using the X-ray crystallographic data of PR complexed with GRL-09510 (8FM) showed that the P2-Crwn-THF of GRL-09510 forms a strong hydrogen-bond network with the backbone atoms of Asp 29 and Asp 30.

Validation of the docking process was done by docking of the compounds Nelfinavir and co-crystallized ligand 8FM ((3S,3aR,5R,7aS,8S)-hexahydro-4H-3,5-methanofuro[2,3-b] pyran-8-yl [(2S,3R)-3-hydroxy-4-[[4-methoxyphenyl] sulfonyl] (2-methylpropyl) amino]-1-phenylbutan-2-yl) carbamate) at the active site of the target. Whereas, Nelfinavir is one of many protease inhibitors currently available, used to limit viral replication and improve immune function in people with HIV infection.⁴⁵ The docking complex and binding interactions of Nelfinavir with HIV-1 protease are given in (Figure S1) with binding affinity -5.88

kJ/mol. This interaction is favored by the formation of the H-bond and non-hydrophobic interactions. The H-bonds are supported by the amino acids, Asp29 and Asp25 with the active site of protease and salt bridge interaction with Asp25, whereas pi-alkyl stacking with Val82 and Ile54. By comparing the docked energy of all the molecules studied, it is noteworthy that six bonds have better energy scores than Nelfinavir, knowing that the energy value for the reaction of the indicated molecule is -5.88 kcal/mol (Table 4).

The top-scored hit molecule identified is PubChem 11560933 with a binding energy of -7.55 kcal/mol. The second top-scored hit molecule is PubChem 11654778 with a binding energy of -7.227 kcal/mol and the third top-scored hit molecule is PubChem 11710411 with an average binding energy of -6.655 kcal/mol. The molecular structure of top-scored compounds can be seen in table 5.

Visualization of the docking results revealed that all the ligands adopted a very similar orientation in the active site. The nitrogen atoms with amide groups are oriented to the two aspartic acids as shown in figure 6. All of them form H-bond, while their large hydrophobic groups were often orientated to the main hydrophobic site, which distinguishes the PR active site. Moreover, the literature was mentioned that the catalytic triad Asp-Thr-Gly that is where the ligand binds determines the active site of the enzyme.^{46,47}

Simplifying the docking results for the compounds, we have taken the 2D representative ligands; the binding mode of the most active compound CID 11560933 is shown in table S13. In its binding mode, the Diamino Hexanoyl amino fragment is observed to be inserted deeply in the cavity, interacting with Gly27 Asp29 Ala28 and Val32 through H-bond and pi-H contacts, respectively.

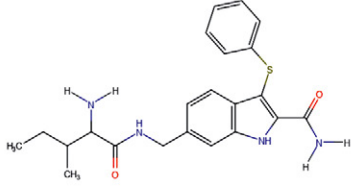
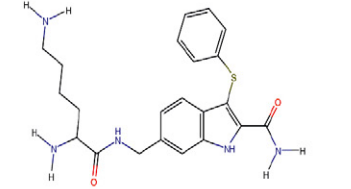
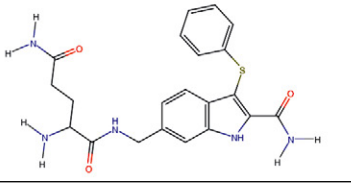
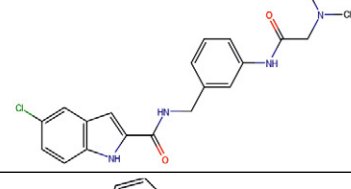
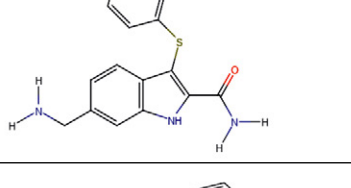
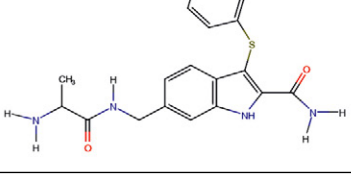
In ligand 11654778, the two oxygen of the pentane diamide have shown strong hydrogen bonding acceptor interaction with aspartate (residue number 29 and 30) was also mapped on HBA features on ADRRR1 pharmacophore model.

Whereas the nitrogen atom of the carboxamide group in all the compounds shows H-bonds with Gly27 are observed explaining why the H-donor is beneficial for activity in the pharmacophore 3D-QSAR model. It should be noted that favorable interactions of hydrophobic type are observed between the indole rings and the residues Ala28, Ile54 and Val32; we can say that the aromatic ring was important for binding and stability of ligand with the HIV-1 PR active site complex.

Table 4. Docking scores of the selected hits using GLIDE module.

Compound Names CID	Xp score	Glid E model	Compound Names	Xp score	Glid E model
CID 11560933	-7.554	-56.274	CID 55868948	-6.615	-45.144
CID 11654778	-7.227	-53.648	CID 11567743	-6.454	-45.532
CID 11710411	-6.655	-48.052	CID 11630770	-6.449	-47.750
Nelfinavir.	-5.882	-51.263	MF8	-4.851	-48.632

Table 5. Details of virtual screening compounds.

Structure	CID	Molecular formula	PubChem IUPAC name	Molecular mass (g/mol)
	11567743	C ₂₂ H ₂₆ N ₄ O ₂ S	6-[[[(2-amino-3-methylpentanoyl)amino]methyl]-3-phenylsulfanyl-1H-indole-2-carboxamide	410.5
	11560933	C ₂₂ H ₂₇ N ₅ O ₂ S	6-[(2,6-diaminohexanoylamino)methyl]-3-phenylsulfanyl-1H-indole-2-carboxamide	425.5
	11654778	C ₂₁ H ₂₃ N ₅ O ₃ S	2-amino-N-[[3-[(2-carbamoyl-3-phenylsulfanyl-1H-indol-6-yl)methyl]pentanediamide	425.5
	55868948	C ₂₀ H ₂₁ ClN ₄ O ₂	5-chloro-N-[[3-[[2-(dimethylamino)acetyl]amino]phenyl]methyl]-1H-indole-2-carboxamide	384.9
	11630770	C ₁₆ H ₁₅ N ₃ OS	6-(aminomethyl)-3-phenylsulfanyl-1H-indole-2-carboxamide	297.4
	11710411	C ₁₉ H ₂₀ N ₄ O ₂ S	6-[(2-aminopropanoylamino)methyl]-3-phenylsulfanyl-1H-indole-2-carboxamide	368.5

One of the most important characteristics of the HIV-1 protease is that all amino acids of the active site are hydrophobic except for hydrophilic aspartic acids (Asp25).⁴⁸ Due to these HIV-1 protease active site characters, the hits are considered a good inhibitor of the activity of HIV-1 protease because its hydrophobic surface provides strong Van der Waals interaction between hits and HIV-1 protease active site, which are beneficial to activity. This supports the proposed model pharmacophore ADRRR1 as it consists of three rings.

The compounds CID 11560933, CID 11654778,

CID 11710411, CID 55868948, CID 11567746, and CID 11630770 make good interaction with HIV-1 protease by forming hydrogen bonds, hydrophobic interactions and non-bonding interaction with catalytic residues such as Asp30, Thr80, Gly27, Asp29, Ile54 and Ile84 at the active site cavity of HIV protease. These interactions systems have the lowest total energies. According to this study, the type and spatial location of the hit compounds agree perfectly with the pattern of enzyme inhibitor interactions identified from Nelfinavir. In future, optimality of the compounds should be confirmed experimentally and

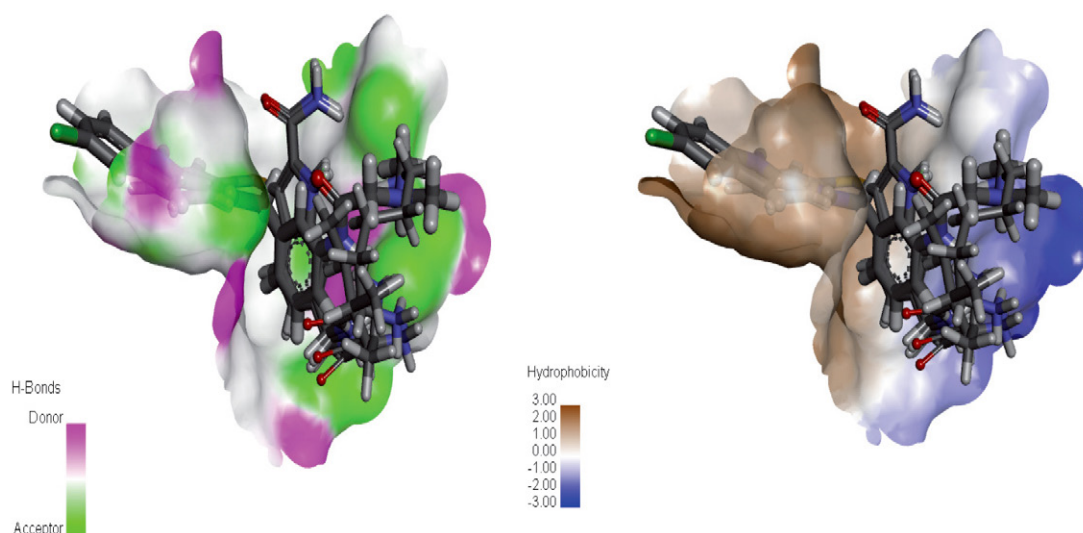


Fig. 6. The orientation of HIV 1 PR inhibitors in the active site and hydrogen and hydrophobic surface

compared its binding modes with a number of HIV-1 protease.

3. 7. Analyzing Absorption, Distribution, Metabolism and Excretion (ADME)

For additional validation purpose, The QikProp module of Schrodinger is a quick, accurate, and easy-to-use to describe absorption, distribution, metabolism and elimination results listed in table 6.

The aqueous solubility plays an essential role in the bioavailability of the candidate. The aqueous solubility parameter (QPlog S) of the test entities was assessed and the compounds were also found to be in the permissible range (< 0.5) (Table 6).

One of the essential factors to be studied concerning the absorption of the drug molecule is also intestinal absorption or permeation, which was further supported by the expected permeability of Caco-2 cells (QPpCaco). The estimation of the test compounds for Caco-2 cell permeability the compounds CID 55868948 shows excellent

results, predicting strong intestinal absorption. The other compounds have poor permeability across the gut–blood barrier. The parameters of the brain/blood partition coefficient (QPlogBB) define the drug’s ability to pass through the blood-brain barrier, which is important for ADME to investigate drug performance. The QikProp descriptor for blood/brain partition coefficient QPlogBB has shown reliable prediction for all the test compounds and reference drugs. Predictions related to skin permeability (K_p), showed that these parameters for the active analogs fall within the standard ranges normally observed for drugs (Table 6). In addition, four out of the six compounds, shown to be more than 25% human oral absorption. Human Ether-a-go-go Related Gene (hERG) parameter is used to determine the potential cardiac toxicity of the compounds. The hERG encodes a potassium ion (K^+) channel that plays a role during systolic and diastolic activities of the heart. The blockage of hERG K^+ channels can lead to cardiac arrhythmia. All the six compounds have $\log IC_{50}$ (hERG) values less than the acceptable range for the blockage of hERG K^+ channels ($\log IC_{50}$ (hERG) < -5); however,

Table 6. Estimated physicochemical and pharmacokinetic parameters by QikProp.

Compound Names CID	QPlogs	QPpCaco	QplogHEGd	Qlog BB	Percent human oral absorption	Metabolism	Logkp
11560933	-2.474	0.822	-4.316	-3.024	7.540	7	-7.518
11654778	-0.446	1.018	-3.709	-2.655	8.635	7	-7.374
11710411	-3.067	15.627	-5.325	-1.665	40.552	5	-5.837
55868948	-4.648	211.95	-7.225	-0.459	86.524	4	-4.064
11567743	-3.223	25.586	-5.525	-1.540	50.499	5	-5.302
11630770	-3.231	64.203	-5.923	-0.929	65.168	4	-5.479

QPlogS is the predicted aqueous solubility, $\log S$: S in moles/l is the concentration of the solute in a saturated solution that is in equilibrium with the crystalline solid; **QPpCaco** is the predicted apparent Caco-2 cell permeability in nm/s; Caco-2 cells are a model for the gut–blood barrier Recommended values **QPpCaco** = <25 POOR, >500 great; **QplogHEGd**: Predicted IC_{50} value for blockage of hERG K^+ channels QplogHEGd concern below -5. **QPlog BB** is the predicted brain–blood partition coefficient; **Percent Human-OralAbsorption** = <20 POOR, >80 great; **QPlogBB** = -3.0 to 1.2; *Recommended values – As per the guidelines given in Schrodinger’s Maestro software suite manual

the values are near the borderline. All the six compounds were predicted to possess non-blocker to hERG channel (Table 6). An estimated number of possible metabolic reactions has also been predicted by QikProp and used to determine whether the molecules can easily gain access to the target site after entering the blood stream. The compounds have the most elevated QPlogP values. A number of likely metabolic responses of the compounds are in the range of 4-7. The *In silico* ADMET results revealed that the top six of Mpro inhibitors are virtually safe and active.

3. 8. Prediction of Toxicity

The computational prediction of toxicities was based on 5 different targets linked to adverse drug-reactions. The hepatotoxicity, carcinogenicity, mutagenicity and cytotoxicity of the compounds were predicted. It was found that 6 compounds have shown no toxicity.

The LD50 has been also predicted, the obtained results have shown that compounds 11630770 and 5586948 present a LD50 of 650 and 1000 mg/kg, respectively, as well as class four of toxicity. The other compounds show moderate toxicity with a LD50 value of 200 mg/kg and class 3 of toxicity.

Table 7. Toxicity prediction of the selected compounds

Compound Names CID	Hepatotoxicity	Carcinogenicity	Mutagenicity	Cytotoxicity	LD50 mg/Kg
11567743	Inactive	Inactive	Inactive	Inactive	200
11560933	Inactive	Inactive	Inactive	Inactive	200
11654778	Inactive	Inactive	Inactive	Inactive	200
55868948	Inactive	Inactive	Inactive	Inactive	625
11630770	Inactive	Inactive	Inactive	Inactive	1000
11710411	Inactive	Inactive	Inactive	Inactive	200

3. 9. Molecular Dynamics Simulations

To further obtain the insights regarding the interaction of the ligands (CID 11630770 and CID 55868948) with 5v4y HIV-1 protease, Molecular Dynamics Simulation was performed. The docked complex was used as initial conformations for MD simulations.

3. 9. 1. Analysis of RMSD and RMSF

The initial analysis of MD simulation was performed by calculating the root-mean square deviations (RMSD) with respect to their respective backbone of initial structure to assess the stability of the 5v4y HIV-1 protease and complexes under physiological conditions. The RMSD of 5v4y HIV-1 protease and complexes is shown in figure 7 and listed in table 8. The RMSD of 5v4y HIV-1 protease alone showed some variations initial time till 20 ns then it became stable for entire simulation period. The average RMSD of was found to be 0.290 ± 0.047 nm. The RMSD of 5v4y HIV-1 protease CID 11630770 complex was found

to be more stable during simulation competed to 5v4y HIV-1 protease alone. However, 5v4y HIV-1 protease 55868948 complex showed more variations with some spikes in RMSD. The RMSD average of both complexes was statistically insignificant (p -value < 0.05) with respect to 5v4y HIV-1 protease alone. The RMSD analysis of CID 55868948 alone revealed that these variations were due to the fluctuations in RMSD of the ligand (CID 55868948). The fluctuation in structures was assessed by calculating the root mean square fluctuation (RMSF) of C_{α} of 5v4y HIV-1 protease in the absence and the presence of ligands (Figure 8A). As evident from data, the RMSF of most of the residues of 5v4y HIV-1 protease alone was found to be less than 0.2 nm. A similar fluctuation was recorded for 5v4y HIV-1 protease CID 55868948 complex where most of the fluctuation in most of residues was below 0.2 nm. However, there was comparatively more fluctuations in C_{α} atoms of 5v4y HIV-1 protease CID 55868948 complex. The RMSF of each atom of both ligands (CID 11630770 and CID 55868948) was also calculated (Figure 8B). The RMSF value of the atoms of both ligands varied from their respective initial values indicating that the ligands exhibited dynamical shift from its initial position in the binding region.

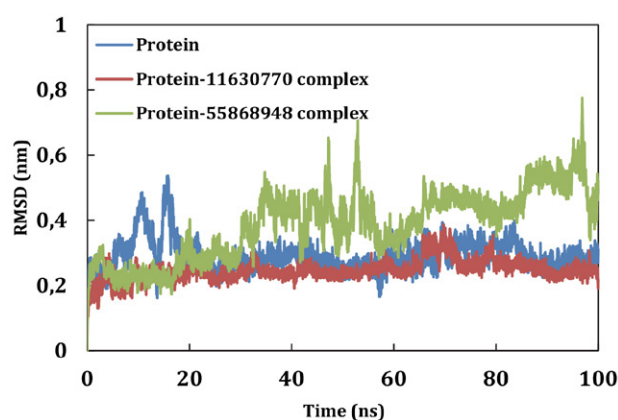


Fig. 7. Root mean square deviation (RMSD) of HIV-1 protease in the absence and presence of 11630770 and 55868948.

3. 9. 2. Assessment of Rg, SASA and Energies

The mass-weighted root mean square distance of a collection of atoms from their common center of mass is

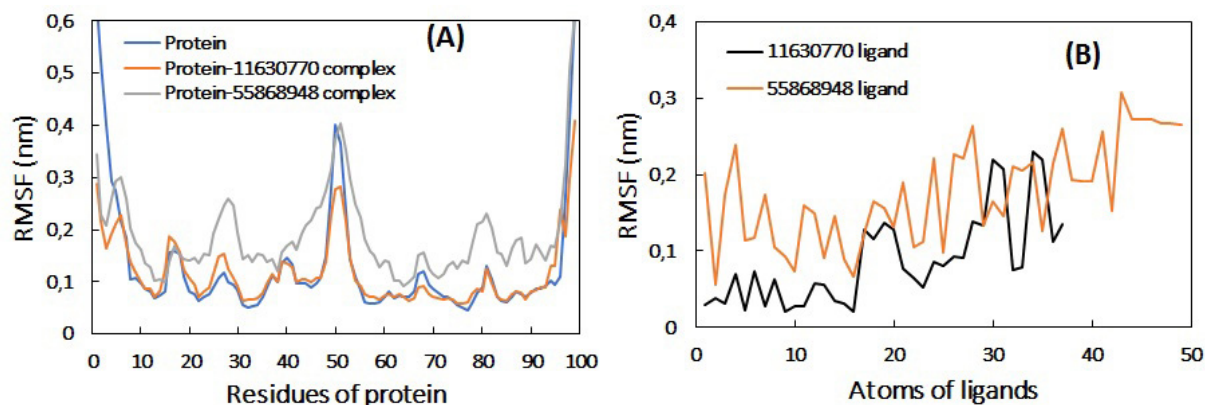


Fig. 8. Root mean square fluctuation (RMSF) of HIV-1 protease in the absence and presence of 11630770 and 55868948. (B) The average RMSF value of each atom of ligands during the MD simulation.

defined as radius of gyration (R_g). The R_g is also considered as indicator of the stability of proteins or their complexes during MD.⁴⁹ Generally, compact or globular proteins exhibit lesser variations in their R_g compared to the expanded form of proteins (5V4Y).

The changes in R_g of 5v4y HIV-1 protease alone and in complex with ligands are shown in figure 9A. The R_g of 5v4y HIV-1 protease alone and 5v4y HIV-1 protease CID 11630770 complex was found to be stable during entire simulation period with negligible variations. On contrary, the R_g of 5v4y HIV-1 protease CID 55868948 complex showed relatively more variations that may be due to the dynamic behavior of the ligand. The average RMSD of HIV-1 protease alone, 5v4y HIV-1 protease CID 11630770 complex, and 5v4y HIV-1 protease CID 55868948 complex was found to be 1.278 ± 0.021 , 1.265 ± 0.016 , and 1.301 ± 0.027 nm, respectively. These values were statistically insignificant with respect to the control (HIV-1 protease alone).

Solvent accessible surface area (SASA) of proteins is also taken into account while studying the stability of pro-

teins during MD simulation.⁵⁰ SASA of HIV-1 protease in the absence and the presence of ligands over simulation time is presented in figure 9B. The average SASA of HIV-1 protease alone, HIV-1 protease CID 11630770 complex, and HIV-1 protease CID 55868948 complex was found to be 64.318 ± 2.388 , 63.049 ± 2.194 , and 65.833 ± 1.995 nm², respectively. The negligible variations in SASA of these structures further confirm their stable nature under physiological conditions.

Further verification of the stability of HIV-1 protease and complexes was performed by calculating the physicochemical parameters such as potential energy and total energy (Figure S2). The straight line with negligible fluctuations in potential energy and total energy shows that the system reached equilibrium and remained stable during the entire simulation period.⁵¹ The RMSD, R_g and SASA values of both complexes showed statistically insignificant variations with respect to the potential and total energies HIV-1 protease alone (Table 8).

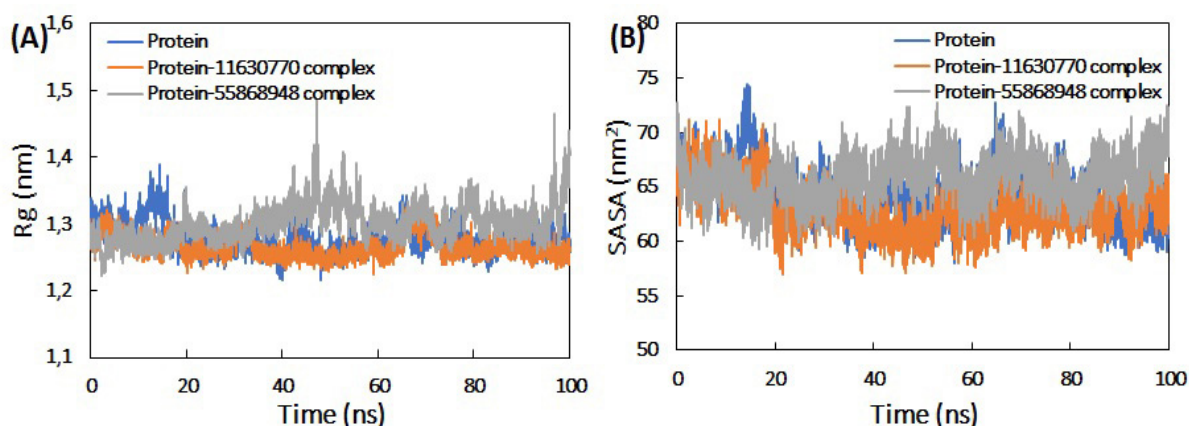


Fig. 9. (A) Radius of gyration (R_g) of 5v4y HIV-1 protease in the absence and presence of CID 11630770 and CID 55868948 as a function of simulation time. (B) Solvent accessible surface area (SASA) of HIV-1 protease in the absence and presence of CID 11630770 and CID 55868948 as a function of simulation time.

Table 8. Average RMSD, R_g and SASA of HIV-1 protease alone, and their complexes calculated over 10000 frames of 100 ns MD simulation.

Parameters	Proteins/complexes	Values
RMSD (nm)	HIV-1 protease only	0.290 ± 0.047
	HIV-1 protease 11630770 complex	0.246 ± 0.031
	HIV-1 protease 55868948 complex	0.386 ± 0.105
	11630770 only	0.096 ± 0.030
	55868948 only	0.191 ± 0.060
R_g (nm)	HIV-1 protease only	1.278 ± 0.021
	HIV-1 protease 11630770 complex	1.265 ± 0.016
	HIV-1 protease 55868948 complex	1.301 ± 0.027
	11630770 only	0.342 ± 0.003
	55868948 only	0.520 ± 0.033
SASA (nm ²)	HIV-1 protease only	64.318 ± 2.388
	HIV-1 protease 11630770 complex	63.049 ± 2.194
	HIV-1 protease 55868948 complex	65.833 ± 1.995
	11630770 only	05.227 ± 0.195
	55868948 only	06.869 ± 0.244
Potential energy (kcal/mol)	HIV-1 protease only	-6.360 ± 0.013
	HIV-1 protease 11630770 complex	-6.366 ± 0.014
	HIV-1 protease 55868948 complex	-6.358 ± 0.014
	HIV-1 protease only	-5.096 ± 0.018
Total energy (kcal/mol)	HIV-1 protease 11630770 complex	-5.101 ± 0.018
	HIV-1 protease 55868948 complex	-5.092 ± 0.018
	HIV-1 protease only	-5.092 ± 0.018

RMSD: Root-mean square deviation, R_g : Radius of gyration, SASA: Solvent accessible surface area.

3. 9. 3. Analysis of Hydrogen Bonds and Secondary Structure

The interaction of ligands with HIV-1 protease was studied by calculating the hydrogens bond profiles for 10000 frames of the MD simulation (Figure 10A). The average number of hydrogen bonds between CID 11630770 and HIV-1 protease was found to be 2.437 ± 1.050 . Lesser number of average hydrogens binds was between CID 55868948 and HIV-1 protease. The hydrogen bond existence was also calculated for both ligands. As observed, the hydrogen bond existence between CID 11630770 and HIV-1 protease was found over the entire simulation period. However, the hydro-

gen bond existence between CID 55868948 and HIV-1 protease showed some breaks as the MD simulation progressed.

The effect of binding of the ligands on the secondary structure of HIV-1 protease was studied by calculating the average secondary structure of all frames of the respective trajectories (Figure 10B). The coil, β -sheet, bends, and turns in HIV-1 protease alone was found to be 22.34, 49.03, 11.18, and 11.55% respectively. These secondary structural components were insignificantly altered in the presence of both ligands. However, there was some increment in α -helix, which increased from 4.81% to 5.27% due to binding of 55868948

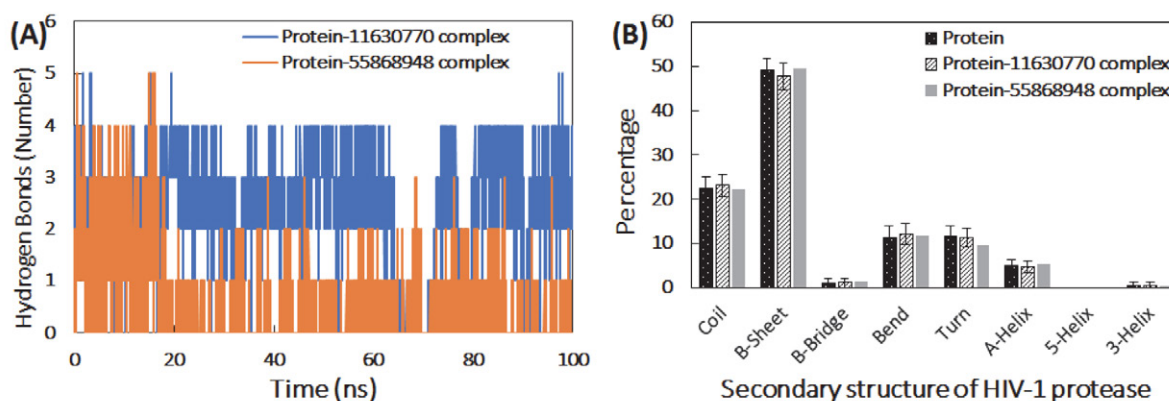


Fig. 10. (A) Number of hydrogen bonds the ligands (11630770 and 55868948) and HIV-1 protease over simulation time. (B) Percentage of secondary structure in HIV-1 protease in the absence and presence of 11630770 and 55868948.

3.9.4. Calculation of Binding Energies and Identification of Key Residues Involved in Binding

The detailed investigation of the various binding energies involved in the interaction of both ligands with HIV-1 protease was done using MM-PBSA calculation. Usually in protein-ligand interactions, non-covalent interactions are predominant. The forces include hydrophobic forces, hydrogen bonds, electrostatic interactions, Van der Waals force. Each of these forces contributes either positively or negatively to the overall binding energy.⁵² The MM-PBSA binding energies were calculated by extracting 100 frames from the entire MD simulation trajectories at uniform intervals (Table 9). In the binding of 11630770 to HIV-1 protease, electrostatic interactions were most prominent followed by Van der Waals interactions. The interaction of 55868948 with HIV-1 protease was mostly favored by Van der Waals forces. Additionally, there was also small contribution of SASA energy in the overall binding of both leads. However, polar solvation energy impaired the interaction of both ligands with HIV-1 protease. The overall binding energy for 11630770 and 55868948 were found to be -7.067 ± 0.509 and -7.218 ± 2.080 kcal/mol respectively.

From MM-PBSA calculations, the binding energies of all residues can be calculated. The polar, a polar and total binding energy contribution of the key residues of HIV-1 protease in the interaction is presented in figure 10 B. Glu-21, Asp-25, Asp-29, Asp-30, Glu-34, Glu-35, Asp-60, Glu-65, Ile-84, and Phe-99 were the major contributor to overall binding energy in interaction of 11630770 with HIV-1 protease. Similarly, Glu-21, Asp-25, Asp-29, Asp-30, Glu-34, Glu-35, Ile-50, Asp-60, Glu-65, Pro-81, Val-82, Phe-99 of HIV-1 protease contributed maximally in the binding of 55868948 to the protein. It is interesting to note that polar energy of some key residues contributed negatively towards the total binding process.

Table 9. Binding free energy (kcal mol⁻¹) for the interaction of protein with 11630770 and 55868948 ligands using MMBSA analysis.

Type of energy	Ligands	
	11630770 ligand	55868948 ligand
ΔE_{vdW}	-24.258 ± 0.533	-20.163 ± 1.340
ΔE_{ele}	-45.156 ± 1.261	-3.787 ± 1.817
ΔE_{PSE}	66.022 ± 1.583	19.443 ± 1.997
ΔE_{SASA}	-3.650 ± 0.046	-2.701 ± 0.163
ΔE_{BE}	-7.067 ± 0.509	-7.218 ± 2.080

ΔE_{vdW} : Van der Waal energy, ΔE_{ele} : Electrostatic energy, ΔE_{PSE} : Polar solvation energy, ΔE_{SASA} : Solvent accessible surface area energy and ΔE_{BE} : Binding energy.

3.9.5. Principal Component Analysis

Principal component analysis (PCA) is the standard statistical procedure used for the investigation of large-scale motion in protein, which is performed by reducing the dimensionality of data set without losing important information, which is characterized by eigenvectors.⁵³ PCA was done to assess the differences in the flexibility parameters between the HIV-1 protease alone and complexes. Using PCA analysis, a set of eigenvectors and eigenvalues were projected (Figure 12A). HIV-1 protease alone and HIV-1 protease 11630770 complex occupied larger conformational space compared to HIV-1 protease 55868948 complex. These observations denote the presence of more structural stability HIV-1 protease 11630770 complex than HIV-1 protease 55868948 complex.

Moreover, the free energy landscapes for the protein alone and both complexes were plotted to decipher the variations in the protein folding patterns (Figure 13). Variations in the projection of free energy were recorded where alone energetically favorable and relatively stable was compared to both the complexes. The observations show that the binding of ligands partly perturbed the conformation of HIV-1 protease.

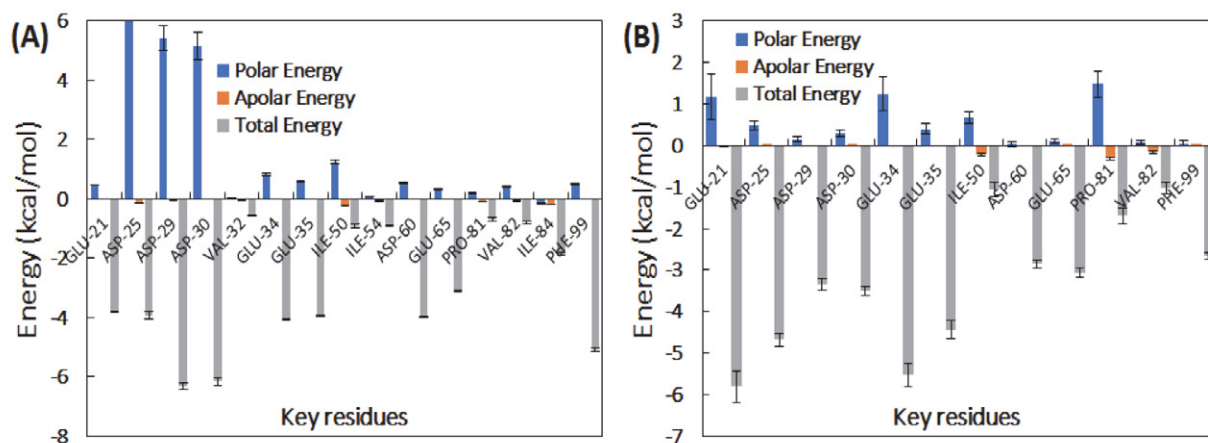


Fig. 11. (A) Polar, apolar and total energy contributions of the key residues of HIV-1 protease for binding of 11630770. (B) Polar, apolar and total energy contributions of the key residues of HIV-1 protease for binding of 55868948.

To gain further insights into the conformational transition of HIV-1 protease, the lowest energy minima structures were extracted. The Ramachandran plots were made for the energy minima structures of HIV-1 protease alone and in complex with the ligands (Figure 12B). The phi (ϕ) and psi (ψ) angles for HIV-1 protease alone were found to be -82.31 and 93.60 , respectively. The ϕ and ψ angles for HIV-1 protease 11630770 complex were obtained as -85.15 and 91.30 , respectively. Similarly, ϕ and ψ angles for HIV-1 protease CID 55868948 complex were recorded as -85.14 and 84.72 , respectively. In both the complexes, remarkable variations in the dihedral angles with respect

Donor (HBD), Hydrogen-Bond Acceptor (HBA), hydrophobic and aromatic groups, which may be responsible for the HIV1 inhibition. Both generated pharmacophore model was validated for its quality to identify new reliable chemical compounds. The validation procedure included two methods: test set validation, and decoy set validation. Based on the 3D-QSAR model ADRRR we have selected hits from the PubChem database. Initial screened compounds were passed through several criteria including the range of activity of training set, fitness score more than 2.5 and comparison of dock score and binding energy with Nelfinavir to reach the potential compounds. Docking into

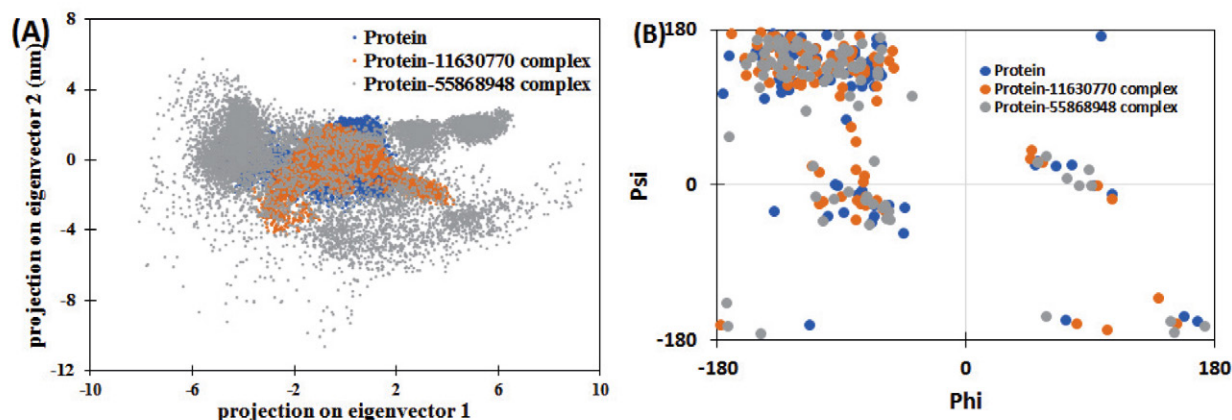


Fig. 12. (A) Principal component analysis (PCA) of HIV-1 protease in the absence and presence of 11630770 and 55868948. (B) Ramachandran plot of the energy minima of HIV-1 protease in the absence and presence of 11630770 and 55868948.

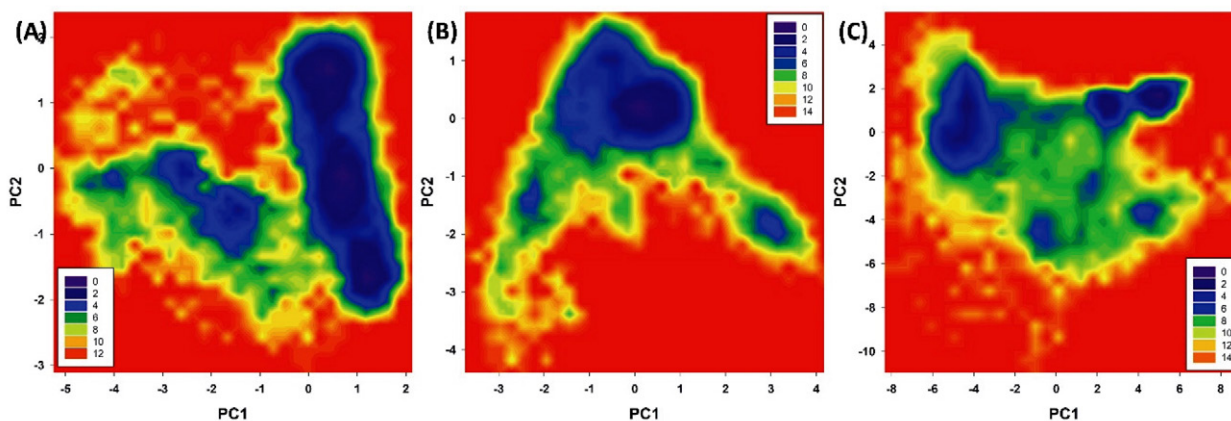


Fig. 13. Free energy landscape plot of (A) HIV-1 protease alone (B) HIV-1 protease 11630770 complex and (C) HIV-1 protease 5586894 complex.

to HIV-1 protease alone were observed, indicating the structural transition in the presence of ligands.

4. Conclusion

In this study, a five-featured (ADRRR) pharmacophore model for the HIV1 inhibitors was developed. The generated model revealed the importance of Hydrogen-Bond

predicted active site conclusively infers those hydrophobic contacts possess more dominance compared to other interactions. Subsequently, amide group play an essential role in hydrogen binding. ADME properties of the six hits were found to be in accordance with known chemically and biologically active compounds. Conclusively, the hits obtained on virtual screening of the database have provided new chemical starting points for design and development of novel HIV-1 inhibitory agents.

5. References

- B. Gazzard, J. Anderson, A. Babiker, M. Boffito, G. Brook, G. Brough, D. Churchill, B. Cromarty, S. Das, M. Fisher, A. Freedman, A. M. Geretti, M. Johnson, S. Khoo, C. Leen, D. Nair, B. Peters, A. Phillips, D. Pillay, A. Pozniak, J. Walsh, E. Wilkins, I. Williams, M. Williams, M. Youle, *HIV Med.* **2008**, *9*, 563–608. DOI:10.1111/j.1468-1293.2008.00636.x
- Global HIV & AIDS statistics-Fact sheet. **ONUSIDA**. <https://www.unaids.org/en/resources/fact-sheet>
- S. J. Pocock, D. R. Elbourne, *N. Engl. J. Med.* **2000**, *342*, 1907–1909. DOI:10.1056/NEJM200006223422511
- C. F. Gilks, S. Crowley, R. Ekpini, S. Gove, J. Perriens, Y. Souteyrand, D. Sutherland, M. Vitoria, T. Guerna, K. De Cock, *the Lancet.* **2006**, *368*, 505–510. DOI:10.1016/S0140-6736(06)69158-7
- A. B. Kleinpeter and E. O. Freed, *Viruses*, **2020**, *12*, E940. DOI:10.3390/v12090940
- E. Urano, U. Timilsina, J. A. Kaplan, S. Ablan, D. Ghimire, P. Pham, N. Kuruppu, R. Mandt, S. R. Durell, T. J. Nitz, D. E. Martin, C. T. Wild, R. Gaur, E. O. Freed, *J. Virol.* **2019**, *93*, 2017–18. DOI:10.1128/JVI.02017-18
- S. Mattei, A. Tan, B. Glass, B. Müller, H.G. Kräusslich, J. A. G. Briggs, *Proc. Natl. Acad. Sci. USA*, **2018**, *115*, 9401–9410. DOI:10.1073/pnas.1811237115
- Y. R. Lin, S. M. Chu, F. H. Yu, K.-J. Huang, C. T. Wang, *BMC Microbiol.*, **2022**, *22*, 94. DOI:10.1186/s12866-022-02503-3
- C. Voshavar, *Curr. Top. Med. Chem.*, **2019**, *19*, 1571–1598. DOI:10.2174/1568026619666190619115243
- Z. Lv, Y. Chu, Y. Wang, *HIV AIDS (Auckl.)*. **2015**, *7*, 95–104. DOI:10.2147/HIV.S79956
- A. V. Veselovsky, A.S. Ivanov, *Curr. Drug Targets Infect. Disord.* **2003**, *3*, 33–40. DOI:10.2174/1568005033342145
- C. M. Song, S. J. Lim, J. C. Tong, *Brief. Bioinform.* **2009**, *10*, 579–591. DOI:10.1093/bib/bbp023
- S. Y. Yang, *Drug Discov. Today*, **2010**, *15*, 444–450. DOI:10.1016/j.drudis.2010.03.013
- S. A. Khedkar, A. K. Malde, E. C. Coutinho, S. Srivastava, *J. Med. Chem.* **2007**, *3*, 187–197. DOI:10.2174/157340607780059521
- H. Kubinyi, *3D QSAR in Drug Design: Volume 1, Theory Methods and Applications*, Springer Science & Business Media, Berlin, Germany, **1993**.
- R. Dias, W. F. De Azevedo, *Curr. Drug Targets*, **2008**, *9*, 1040–1047. DOI:10.2174/138945008786949432
- R. Ragno, A. Coluccia, G. La Regina, G. De Martino, F. Piscitelli, A. Lavecchia, E. Novellino, A. Bergamini, C. Ciapini, A. Sinistro, G. Maga, E. Crespan, M. Artico, R. Silvestri, *J. Med. Chem.* **2006**, *49*, 3172–3184. DOI:10.1021/jm0512490
- LigPrep, Schrödinger Release 2021-4, Schrödinger, LLC, New York, NY, **2021**. <https://www.schrodinger.com/products/lig-prep>
- E. Harder, W. Damm, J. Maple, C. Wu, M. Reboul, J.Y. Xiang, L. Wang, D. Lupyan, M. K. Dahlgren, J. L. Knight, J. W. Kaus, D. S. Cerutti, G. Krilov, W. L. Jorgensen, R. Abel, R. A. Friesner, E. D. Harder, *J. Chem. Theory Comput.*, **2016**, *12*, 281–296. DOI:10.1021/acs.jctc.5b00864
- K. Roos, C. Wu, W. Damm, M. Reboul, J. M. Stevenson, C. Lu, C. Lu, M. K. Dahlgren, S. Mondal, W. Chen, L. Wang, R. Abel, R. A. Friesner, E. D. Harder, *J. Chem. Theory Comput.* **2019**, *15*, 1863–1874. DOI:10.1021/acs.jctc.8b01026
- R. Kunal, K. Supratik, N. D. Rudra, *Understanding the Basics of QSAR for Applications in Pharmaceutical Sciences and Risk Assessment*, Elsevier, Amsterdam, Pays-Bas, **2015**; DOI:10.1016/C2014-0-00286-9
- W. J. Dunn, D. Rogers, *Genetic Partial Least Squares in QSAR. Genetic Algorithms in Molecular Modeling*. Academic Press, London, **1996**. Pp. 109–130. DOI:10.1016/B978-012213810-2/50006-2
- A. R. Leach, V. J. Gillet, R. A. Lewis, R. Taylor, *J. Med. Chem.* **2010**, *53*, 539–558. DOI:10.1021/jm900817u
- P. Gramatica, *QSAR Comb. Sci.*, **2007**, *26*, 694–701. DOI:10.1002/qsar.200610151
- A. Golbraikh, A. Tropsha, *Mol. Divers.* **2000**, *5*, 231–243. DOI:10.1023/A:1021372108686
- K. Roy, *Expert. Opin. Drug Discov.*, **2007**, *2*, 1567–1577. DOI:10.1517/17460441.2.12.1567
- J. Kirchmair, P. Markt, S. Distinto, G. Wolber, T. Langer, *J. Comput. Aided Mol. Des.* **2008**, *22*, 213–228. DOI:10.1007/s10822-007-9163-6
- M. D. Mackey, J. L. Melville, *J. Chem. Inf. Model.* **2009**, *49*, 1154–1162. DOI:10.1021/ci8003978
- M. Lill, *Virtual Screening in Drug Design, Methods Mol. Biol.* **2013**, *993*, 1–12. DOI:10.1007/978-1-62703-342-8_1
- E. Lionta, G. Spyrou, D. K. Vassilatis, Z. Cournia, *Curr. Top Med. Chem.* **2014**, *14*, 1923–1938. DOI:10.2174/1568026614666140929124445
- S. Kim, P. A. Thiessen, E.E. Bolton, J. Chen, G. Fu, A. Gindulyte, *Nucleic Acids Res.* **2016**, *44*, 202–213. DOI:10.1093/nar/gkv951
- M. Amano, P. Miguel Salcedo-Gómez, R.S. Yedidi, N. S. Delino, H. Nakata, K. Venkateswara Rao, *Sci. Rep.* **2017**, *7*, 12235. DOI:10.1038/s41598-017-12052-9
- Schrödinger Suite 2021 Protein Preparation Wizard; Epik Schrödinger, LLC: New York, NY, USA, **2021**.
- R. A. Friesner, R. B. Murphy, M. P. Repasky, L. L. Frye, J. R. Greenwood, T. A. Halgren, *J. Med. Chem.*, **2006**, *49*, 6177–6196. DOI:10.1021/jm051256o
- Dassault Systèmes BIOVIA Discovery Studio Modeling Environment, Release **2017**
- L. Ioakimidis, L. Thoukydidis, A. Mirza, S. Naeem, J. Reynison, *QSAR Comb. Sci.* **2008**, *27*, 445–456. DOI:10.1002/qsar.200730051
- P. Banerjee, A. O. Eckert, A. K. Schrey, R. Preissner, *Nucleic Acids Res.* **2018**, *46*, 257–263. DOI:10.1093/nar/gky318
- H. J. C. Berendsen, D. Van der Spoel, R. van Drunen, *Comput. Phys. Commun.*, **1995**, *91*, 43–56. DOI:10.1016/0010-4655(95)00042-E
- J. A. Maier, C. Martinez, K. Kasavajhala, L. Wickstrom, K. E. Hauser, C. Simmerling, *J. Chem. Theory Comput.* **2015**, *11*, 3696–3713. DOI:10.1021/acs.jctc.5b00255
- J. Wang, W. Wang, P. A. Kollman, D. A. Case, *J. Mol. Graph.*

- Model.* **2006**, 25, 247–260. DOI:10.1016/j.jmngm.2005.12.005
41. M. Topel, A. L. Ferguson, *J. Chem. Phys.* **2020**, 153, 194–102. DOI:10.1063/5.0024732
42. M. Parrinello, A. Rahman, *J. Appl. Phys.* **1981**, 52, 7182–7190. DOI:10.1063/1.328693
43. R. Kumari, R. Kumar, A. Lynn, *J. Chem. Inf. Model.* **2014**, 54, 1951–1962. DOI:10.1021/ci500020m
44. Schrödinger Release 2021-2: phase; Schrödinger, LLC: New York, NY, USA, **2021**.
45. Bardsley-Elliott, G. L. Plosker, *Drugs.* **2000**, 59, 581–620. DOI:10.2165/00003495-200059030-00014
46. B. Jarvis, D. Faulds, *Drugs.* **1998**, 56, 147–167. DOI:10.2165/00003495-199856010-00013
47. P. P. Mager, *Med. Res. Rev.* **2001**, 21, 348–353. DOI:10.1002/med.1012
48. L. K. Nicholson, T. Yamazaki, D. A. Torchia, S. Grzesiek, A. Bax, S.J. Stahl, *Nat. Struct. Mol. Biol.* **1995**, 2, 274–280. DOI:10.1038/nsb0495-274
49. F. A. Qais, T. Sarwar, I. Ahmad, R. A. Khan, S. A. Shahzad, F. M. Husain, *Int. J. Biol. Macromol.* **2021**, 169, 143–152. DOI:10.1016/j.ijbiomac.2020.12.096
50. B. Rath, F. Abul Qais, R. Patro, S. Mohapatra, T. Sharma, *Bi-oorg. Med. Chem. Lett.* **2021**, 41, 128029. DOI:10.1016/j.bmcl.2021.128029
51. P. V. Coveney, S. Wan, *Chem. Phys.* **2016**, 18, 30236–30240. DOI:10.1039/C6CP02349E
52. S. Siddiqui, F. Ameen, T. Kausar, S. M. Nayeem, S. Ur Rehman, M. Tabish, *Spectrochim. Acta A*, **2021**, 249, 119296. DOI:10.1016/j.saa.2020.119296
53. S. Siddiqui, F. Ameen, I. Jahan, S. M. Nayeem, M. Tabish. *New J. Chem.* **2019**, 43, 4137–4151. DOI:10.1039/C8NJ05486J

Povzetek

Ta raziskava obravnava *in silico* 45 indolil-aril-sulfonov, znanih kot anti-HIV1. Podatki so bili zbrani iz nedavnih predhodno prijavljenih zaviralcev in razdeljeni na podskupino 33 spojin, namenjenih nizu preizkušanj, preostalih 12 spojin pa je bilo shranjenih v namen testnega niza. Izbrani farmakofor –ADRRR– je podal statistično pomemben model 3D-QSAR, ki vključuje visoke ocene zaupanja ($R^2 = 0,930$, $Q^2 = 0,848$ in $RMSE = 0,460$). Napovedna moč uveljavljenega modela farmakofora je bila potrjena z zunanjim testom ($r^2 = 0,848$). Sistematičen navidezni potek dela je pokazal visok faktor uporabnosti in razkril visoko moč napovedovanja. Nato je bil model uporabljen za pregled filtrirane baze podatkov PubChem in označil vse kemijske značilnosti modelne farmakofore. Ustrezni zadetki so bili dodatno ocenjeni z *in silico* ADMET študijami. Poleg tega se molekularna dinamika lahko uporablja tudi za raziskovanje stabilnosti dobljenih kompleksov. V končni fazi bodo te izbrane komponente lahko postale dobra začetna molekula za razvoj učinkovitih učinkovin proti HIV-1.



Except when otherwise noted, articles in this journal are published under the terms and conditions of the Creative Commons Attribution 4.0 International License

DRUŠTVENE VESTI IN DRUGE AKTIVNOSTI
SOCIETY NEWS, ANNOUNCEMENTS, ACTIVITIES

Vsebina

Poročilo o delu v letu 2021	S51
Koledar važnejših znanstvenih srečanj s področja kemije in kemijske tehnologije	S56
Navodila za avtorje	S60

Contents

Report for 2021	S51
Scientific meetings – Chemistry and chemical engineering.....	S56
Instructions for authors	S60

POROČILO PREDSEDNIKA SLOVENSKEGA KEMIJSKEGA DRUŠTVA O DELU DRUŠTVA V LETU 2021

Tudi v letu 2021 je bilo društvo aktivno na številnih področjih. Izvajali smo redne letne aktivnosti, pri katerih je bil glavni poudarek na rednem izdajanju društvene revije *Acta Chimica Slovenica* (ACSi) ter organizaciji največjega letnega dogodka društva, konference »Slovenski kemijski dnevi 2021«.

Rednim aktivnostim so se pridružile tudi aktivnosti ob 70. letnici društva. Tako smo 15. februarja organizirali online slovesnost ob 70. letnici društva, kjer so lahko člani in drugi vabljeni ter zainteresirani poslušalci prisostvovali dvema vabljenima predavanj. Prvo predavanje z naslovom *Z živim srebrom do srebra – Od alkimije do kemije* in slovenski prispevek k postopku, ki je spremenil svet, je izvedel prof. dr. Alojz Demšar, drugo, z naslovom *Računalnik in kemija – Zaveznika v boju proti raku* pa prof. dr. Urban Bren. Dogodek smo popestrili s prikazom voščil, ki so nam jih namenila sorodna društva po svetu ter slovenske partnerske inštitucije. Ob tej priložnosti se zahvaljujem prof. dr. Zorki Novak Pintarič za odlično vodenje dogodka, hkrati pa zahvala tudi podjetjem Krka d.d., Novo mesto, Kemomed, Aquafil, Primalab in Mettler Toledo za sponzorsko podporo pri organizaciji slovesnosti. Za 23. september načrtovana slavnostna akademija ob 70. letnici društva in podelitev častnih ter zaslužnih članstev ter priznanj društva je bila zaradi Covid-19 razmer preložena na leto 2022.

Za namen 70. letnice je bila oblikovana tudi nova grafična podoba, ki smo jo prikazali na plaketi »70 let«, roll-upih, power point predlogah in vabilih.

23. junija 2021 smo izvedli redni občni zbor društva, kjer smo izvolili nove vodstvene organe društva, častne, zaslužne člane ter prejemnike priznanj, glasovali pa smo tudi o spremembah in dopolnitvah statuta ter združitvi Sekcije za analizo kemije in Spektroskopsko sekcijo v skupno sekcijo.

Slovenski kemijski dnevi 2021 so bili organizirani v Portorožu, v Kongresnem centru Grand hotela Bernardin, in sicer v dneh od 22. do 24. septembra 2021. Programskemu in organizacijskemu odboru je predsedoval znan. svet. dr. Albin Pintar, skupaj s člani odbora v zasedbi prof. dr. Romana Cerc-Korošec, prof. dr. Zorka Novak Pintarič, prof. dr. Darja Lisjak, doc. dr. Matic Lozinšek, prof. dr. Matjaž Valant, dr. Silvo Zupančič in Marjana Gantar Albreht.

Na konferenci je bilo predstavljenih preko 200 prispevkov v obliki predavanj in posterjev, kar je največ v zadnjih petih letih. Delo je potekalo plenarno in v treh vzporednih sekcijah. Udeleženci konference, bilo jih je 305 iz Slovenije in sedmih drugih držav, so bili zelo zadovoljni s kakovostjo znanstvenih in strokovnih prispevkov ter družabnim programom srečanja. Na konferenci je sodelovalo tudi 19 razstavljalcev laboratorijske in procesne opreme. Sponzorji dogodka so bili Kemijski inštitut, Cin-

karna, AquafilSLO, Kemomed, Kobis, Krka, Laboratorijum, Merck, Mettler Toledo, Optik Instruments, Primalab in Vigor. Objavili smo zbornik povzetkov konference, ki je dostopen na USB ključku ter na voljo v NUK-u in strokovnih knjižnicah po Sloveniji.

Plenarni predavatelji na konferenci so bili prof. dr. Barbara Malič (Institut »Jožef Stefan«, Ljubljana), dr. Ute Resch-Genger (Federal Institute for Materials Research and Testing, Berlin, Nemčija) in dr. Lukas Palatinus (Institute of Physics of the Czech Academy of Sciences, Praga, Češka). Poleg treh plenarnih predavanj so udeleženci poslušali šest »keynote« vabljenih predavanj, ki so jih izvedli izr. prof. dr. Kristina Žužek Rožman (Institut »Jožef Stefan«, Ljubljana), izr. prof. dr. Griša Močnik (Univerza v Novi Gorici in Institut »Jožef Stefan«, Ljubljana), prof. dr. Irena Kralj Cigić (Fakulteta za kemijo in kemijsko tehnologijo, Univerza v Ljubljani), dr. Sebastijan Kovačič (Kemijski inštitut, Ljubljana), prof. dr. Maja Leitgeb (Fakulteta za kemijo in kemijsko tehnologijo, Univerza v Mariboru) in dr. Igor Mihelič (Melamin d.d., Kočevje).

Ob zaključku konference smo že tradicionalno podelili nagrade doktorskim študentom za najboljša predavanja in posterske predstavitve. Finančni del podeljenih nagrad je sponzoriral Kemijski inštitut.

V letu 2021 smo v reviji **Acta Chimica Slovenica** (ACSi) izdali 4 številke revije, v katerih je bilo skupaj objavljenih 94 originalnih znanstvenih člankov na skupno 1026 straneh z dvokolonskim tiskom. Članki pokrivajo vsa področja kemije, kemije materialov in kemijskega in biokemijskega inženirstva. Od objavljenih člankov so bili štirje tako imenovani »Feature Articles« (FA) in eden »Review Articles« (RA). Vsi članki so objavljeni na spletu in so prosto dostopni. Poleg tega so objavljeni tudi v več podatkovnih bazah. Vseh člankov, ki so bili leta 2020 oddani v uredniški sistem, je bilo 705, kar pomeni, da jih je bilo na koncu sprejetih okoli 13%. Člani Slovenskega kemijskega društva in avtorji člankov prejmejo elektronsko obvestilo o izidu nove številke. Reviji ACSi se vztrajno viša faktor vpliva. Za leto 2020 je faktor vpliva zrastel na 1,735 (iz 1,1,223 v letu 2019). Tako je revija napredovala iz četrtega v tretji kvartil. Sprememb uredniške politike in s tem vsebine revije ni bilo, zato v letu 2022 nadaljujemo po isti poti. V društvenih vesteh smo objavili seznam diplomskih, magistrskih in doktorskih del FKKT UL, FKKT UM, podiplomskega študijskega programa »Znanosti o okolju« in Fakultete za znanosti okolju, UNG v letu 2020. Objavili smo tudi letna poročila sekcij. V letu 2021 so društvene vesti obsegale 122 strani. Na društvenih straneh sta bila poleg ostalih novic objavljena zanimiv strokovni članek avtorja dr. M. Dolinarja in predstavitev nove znanstvene monografije avtorjev dr. J. Faganelija ter dr. A. Maleja.

Zahvaljujem se tudi vsem inštitucijam, ki so v letu 2021 finančno podprle izdajanje revije Acta Chimica Slovenica. Te so Fakulteta za kemijo in kemijsko tehnologijo Univerze v Ljubljani, Fakulteta za kemijo in kemijsko tehnologijo Univerze v Mariboru, Kemijski inštitut in Inštitut »Jožef Stefan«. Sponzorji revije so bili z objavo oglasa Krka d.d., Novo mesto, Donau Lab d.o.o. Ljubljana, Helios Domžale, d.o.o. in Sandoz.

V letu 2021 smo nadaljevali z aktivnostmi za pridobivanje novih članov. Medse smo jih privabili 22, od tega 19 študentov. Za komunikacijo s člani smo pogosteje uporabljali Facebook in Twitter omrežje ter jih obveščali o dogodkih po elektronski pošti.

Člani Slovenskega kemijskega društva so bili aktivni tudi na področju mednarodnega sodelovanja. Predvsem je potrebno omejiti članstvo društva v mednarodnih zdru-

ženjih IUPAC, ECTN, IUCr, EURACHEM, EuChemS, EFCE, EPF, ECA in EFCATS.

Izpostaviti gre tudi sodelovanje pri organizaciji konference 9th European variety in university chemistry education conference (EUROVARIETY 2021), ki je je organizirala Pedagoška fakulteta UL, pod okriljem organizacije EuChemS in Komisije za izobraževanje pri Slovenskem kemijskem društvu

Društvo se je v letu 2021 uspešno prijavilo na Javni razpis ARRS za sofinanciranje delovanja v mednarodnih znanstvenih združenjih v letu 2021, kjer smo bili uspešni pri vseh oddanih vlogah.

*prof. dr. Ksenija Kogej, glavna urednica ACSi
dr. Albin Pintar, predsednik organizacijskega odbora
konference Slovenski kemijski dnevi
dr. Peter Venturini, predsednik društva*

Poročilo o delovanju in aktivnostih Mariborske podružnice v letu 2021

Mariborska podružnica se je v letu 2021 usmerila v izpolnitev ciljev, ki si jih je zastavila v preteklem letu.

V Portorožu smo se udeležili konference Slovenski kemijski dnevi, kjer smo predsedovali pri različnih sekcijah, sodelovali smo kot pr edavatelji in kot predstavniki prispevkov na posterjih ter v komisiji za ocenjevanje študentskih del.

Skrb Mariborske podružnice je tudi stalno izobraževanje članov. V ta namen smo organizirali strokovna predavanja in razne seminarje, na katerih so predavali priznani tuji in domači strokovnjaki. Predavanja so pokrivala pomembna področja teoretične in uporabne kemije, kemijske in procesne tehnike ter kemijskega izobraževanja.

Gostili smo Dr. Bojana Kulčarja iz Leka Lendava, ki je predstavil podjetje in svoje izkušnje prenosa znanja iz matične fakultete v industrijsko okolje. Podobno predstavitve je izvedel dr. Žan Zore iz Etola (Celje).

Na predlog Fakultete za kemijo in kemijsko tehnologijo Univerze v Mariboru je naziv častni doktor prejel prof.

dr. Rafiqul Gani za izjemne dosežke in zasluge pri razvoju in delovanju Fakultete za kemijo in kemijsko tehnologijo Univerze v Mariboru. S svojim delom je prispeval večanju ugleda naše članice.

Gostili smo prof. dr. Kathleen Aviso in prof. dr. Michael Angelo Promentilla (Univerza De La Salle, Filipini), ki sta izvedla 2-tedensko predavanje na temo optimiranja procesov.

Aktivno smo sodelovali tudi pri mednarodnih poletnih šolah. V mesecu juliju je na naši fakulteti potekala mednarodna polenta šola na temo visokotlačnih tehnologij: 'ESS-HPT 2021' *The European Summer school in High Pressure Technology*, ki jo je organiziral naš Laboratorij za separacijske procese in produktno tehniko v sodelovanju s Tehnološko fakulteto v Gradcu.

Matjaž Finsgar

Poročilo Sekcije za kristalografijo za leto 2021

V letu 2021 se je epidemija COVID-19 delno umirila, zato so bili izvedena nekatera znanstvena srečanja, na primer kongres Mednarodne kristalografske zveze (International Union of Crystallography) avgusta v Pragi. Ta kongres, kot tudi večina drugih kristalografskih srečanj je bil izveden hibridno, kar je omogočilo sodelovanje predstavnika kristalografske sekcije Slovenskega kemijskega društva, da je sodeloval na zasedanjih skupščin obeh kristalografskih združenj (Mednarodne kristalografske zveze in Evropskega kristalografskega združenja (European Crystallographic Association) v katerih smo slovenski kristalografi polnopravni člani.

Nekatera druga srečanja (na primer Evropske konferenca o praškovni difrakciji in tudi Hrvaško-slovensko kristalografsko srečanje) pa so bila ponovno preložena za eno leto v upanju, da bo mogoča normalna izvedba v živo.

Ne glede na preložitve, je bilo potrebnega nekaj dela in truda, da smo za obe srečanja obdržali plenarne pred-

vatelje, sponzorje in se dogovorili s kongresnimi centri in hoteli za nove termine pod podobno ugodnimi pogoji. Večino dela za oba dogodka so sicer opravili hrvaški kolegi, ker se bosta oba dogodka odvijala na Hrvaškem, smo pa člani sekcije, ki sodelujemo v organizacijskem odboru, pomagali kolikor je bilo potrebno.

V času pisanja tega poročila je že objavljeno, da bo letos v začetku junija v Šibeniku na klasičen način z udeležbo v živo, izpeljana Evropska konferenca o praškovni difrakciji v Šibeniku, ki se je bo udeležilo tudi nekaj slovenskih raziskovalcev. Prav tako je objavljeno, da bo Hrvaško-slovensko kristalografsko srečanje izvedeno klasično letos od 8. do 11. septembra v Poreču. Prijave se še zbirajo, vsekakor pa računamo tudi na tradicionalno dobro udeležbo slovenskih raziskovalcev.

prof. dr. Anton Meden

Poročilo Analizne sekcije za 2021 v okviru Slovenskega kemijskega društva

Osnovna dejavnost sekcije za Analizno kemijo v okviru Slovenskega kemijskega društva je organiziranje mednarodnih in domačih znanstvenih ter strokovnih srečanj, predavanj domačih in tujih strokovnjakov ter izvedba različnih delavnic, seminarjev in simpozijev. Člani sekcije pa sodelujejo tudi znotraj delovnih skupin Eurachem in drugih združenj v evropskem prostoru (DAC, FECS) in tako pomembno prispevajo k prepoznavnosti Slovenskega kemijskega društva.

Na delo sekcije za Analizno kemijo v letu 2021 je bistveno vplivala epidemija Sars-Covid 19, tako so planirane aktivnosti potekale na spletu, veliko dogodkov pa je bila odpovedanih ali prestavljenih. Takšno usodo je doletelo tudi tradicionalno mednarodno srečanje podiplomskih študentov in njihovih mentorjev YISAC (Young Investigators Seminar on Analytical Chemistry), ki bi moralo potekati junija 2021 na Univerzi v Lodzu na Poljskem. Ker

srečanja ni bilo mogoče organizirati je obveljala dokončna odpoved in izvedba v letu 2022. Med redkimi aktivnostmi sekcije, ki so bile izvedene, kot običajno, velja izpostaviti 27. jubilejno konferenco »Slovenski kemijski dnevi 2021«, ki se je odvijala septembra 2021 v Portorožu. Posebej vzpodbudna je aktivna udeležba mlajših kolegov iz različnih institucij, ki so na zavidljivem nivoju predstavili raznolike in zanimive raziskave na področju spektroskopije, kromatografije, elektrokemije, materialov in okolja.

V prihodnje želimo v sekcijo aktivno vključiti mlajše kolege in nadaljevati z organizacijo domačih ter tujih srečanj, predavanj in konferenc. Posebej želimo okrepiti povezovanje in prenos znanja iz univerzitetnih in raziskovalnih laboratorijev v industrijo.

prof. dr. Mitja Kolar

Poročilo Sekcije mladih kemikov za leto 2021

Glavni namen sekcije mladih kemikov je vzpostavitev vezi med študenti, mladimi raziskovalci, mladimi doktorji, znanstveno-raziskovalnimi inštitucijami, kemijsko in farmacevtsko industrijo ter pedagoškimi delavci v šolah in fakultetah. Sekcija mladih kemikov je članica v European Young Chemists' Network (EYCN) v okviru EuChemMS in International Young Chemists Network (IYCN) v okviru IUPAC, tako da je ena njenih pomembnejših nalog tudi povezovanje mladih kemikov in delovanje na skupnih projektih v mednarodnem merilu.

V letu 2021 smo se udeležili generalne skupščine združenja IYCN, ki je potekala v spletni obliki in na kateri se je izvolilo vodstvo v naslednjem mandatnem obdobju. Prav tako je bila v pripravah novembrska organizacija ekskurzije v Krko, kjer smo združili moči s Študentsko organizacijo Fakultete za kemijo in kemijsko tehnologijo Univerze v Ljubljani. Na žalost je bila zaradi ukrepov povezanih z epidemijo ekskurzija prestavljena v pomlad 2022.

dr. Sara Drvarič Talian

Poročilo Sekcije za keramiko za leto 2021

Evropska keramična organizacija (ECerS) je svojo osrednjo bienalno konferenco in razstavo zadnjič organizirala leta 2019 v Torinu v Italiji. Leta 2021 je bilo srečanje predvideno v Dresdnu v Nemčiji, ki pa je bilo zaradi težav s pandemijo COVID-19 prestavljeno na leto 2022, ko se bo pod imenom Ceramics in Europe združilo tri keramične konference, ECerS XVII, 9. Mednarodno konferenco o keramiki (International Ceramic Conference, ICC) in konferenco Electroceramics XVIII. Srečanje bo potekalo v Krakovu na Poljskem od 10. do 14. julija 2022, njeno organizacijo pa podpirajo Evropsko keramično združenje, Mednarodna keramična zveza (ICF), Fraunhofer IKTS in Elektrokeramična mreža društva ECerS.

Pod okriljem ECerSa in njene mreže Europe Makes Ceramics (EMC) je bilo v letu 2021 izvedeno srečanje foruma mladih keramičarjev za aditivno proizvodnjo (The young Ceramists Additive Manufacturing Forum). Srečanje je potekalo preko spleta 29. oktobra 2021 z 80 udeleženci, pokrivalo pa je tematike tehnologije, materialov in aplikacij ter oblikovanja in programske opreme.

ECerS je za leto 2021 podelil sledeče nagrade:

- Stuijts nagrada (raziskovalki / raziskovalcu, ki pripada državi članici društva, za izjemne prispevke v keramični znanosti, tehnologiji in izobraževalni dejavnosti ali proizvodnji): prof. Jérôme Chevalier, National Institute of Applied Sciences of Lyon, Francija.
- Richard Brook nagrada (raziskovalki / raziskovalcu iz države zunaj Evrope za izjemen prispevek k keramični znanosti ali tehnologiji ter za izboljšanje razumevanja in sodelovanja v mednarodni keramični skupnosti): prof. Bikramjit Basu, Indian Ceramic Society.

- Nagrada »Mlad znanstvenik / Mlada znanstvenica« (raziskovalki / raziskovalcu, mlajši od 40 let, zaradi izjemnih prispevkov k keramičnim znanostim): Izr. prof. Ondřej Jankovský, Institute of Chemical Technology, Praga, Češka republika.
- Babini nagrada (raziskovalki / raziskovalcu za izjemen tehnični prispevek k razvoju evropske keramične industrije): Franco Stefani, System Logistic SpA, System Ceramics SpA, Laminam SpA, Italija.

Hermína Hudelja, doktorandka iz Odseka za nanostrukturne materiale Instituta »Jožef Stefan«, se je udeležila tekmovanja mladih keramikov ECerS »Student Speech Contest«. Tekmovanje je bilo izpeljano v okviru 14. bienalne konference za mlade znanstvenike s področja keramike (»14th ECerS Conference for Young Scientists in Ceramics«), 20.-23. oktobra 2021, v Novem Sadu v Srbiji. Na tekmovanju svoje rezultate predstavijo mladi znanstveniki, kot predstavniki držav pridruženih članic ECerSa. Zmagal je predstavnik Avstrije, Maximilian Staudacher iz Montanuniversität Leoben, Avstrija. Drugo mesto je zasedla predstavnica iz Velike Britanije, Else Ellermann iz University of Cambridge. Tretja je bila predstavnica Belgije, Chloé Goutagny iz Belgian Ceramic Research Centre, Belgija. Tekmovalo je 18 predstavnic in predstavnikov pridruženih članic.

V letu 2021 je bila s strani Young Ceramists Network (YCN) izpeljana spletna delavnica YCN 2021 »Pitch me your idea«, v platformi Gather Town, med 15. in 17. junijem. Na delavnici je sodelovalo 77 udeležencev iz 29. držav. 24 udeležencev je sodelovalo v tekmovanju kratkih predstavitev svojih raziskovalnih idej. Zmagal je Vojtěch Nečina iz praške University of Chemistry and Technology,

Češka. Drugo mesto je zasedel Moritz Weiß iz Karlsruher Institut für Technologie, Nemčija. Tretja je bila Oana-Andreea Condurache iz Odseka za elektronsko keramiko Instituta »Jožef Stefan«.

V letu 2021 je na mestu predsednika društva ECerS dr. Francis Cambier, Belgian Ceramic Research Centre, Belgija, zamenjal prof. Jon Binnerja, University of Birmingham, Velika Britanija, ki je društvo vodil med letoma 2019 in 2021.

V okviru Divizije za elektroniko Ameriškega keramičnega društva je v letu 2021 izr. prof. Matjaž Spreitzer iz Odseka za raziskave sodobnih materialov Instituta »Jožef Stefan« postal tajnik divizije omenjenega društva.

*Izr. prof. Matjaž Spreitzer in
izr. prof. Andraž Kocjan*

KOLEDAR VAŽNEJŠIH ZNANSTVENIH SREČANJ S PODROČJA KEMIJE IN KEMIJSKE TEHNOLOGIJE

SCIENTIFIC MEETINGS – CHEMISTRY AND CHEMICAL ENGINEERING

2022

June 2022

- 6 – 10 11TH EUROPEAN CONFERENCE ON SOLAR CHEMISTRY AND PHOTOCATALYSIS:
ENVIRONMENTAL APPLICATIONS - SPEA11
Turin, Italy
Information: <https://www.spea11.unito.it/home>
- 6 – 10 10TH INTERNATIONAL CONFERENCE ON MECHANOCHEMISTRY AND MECHANICAL
ALLOYING
Cagliari, Italy
Information: <https://income2022.it/>
- 9 – 10 58TH SERBIAN CHEMICAL SOCIETY CONFERENCE
Belgrade, Serbia
Information: <https://www.shd.org.rs>
- 12 – 16 XLVI »ATTILIO CORBELLA« INTERNATIONAL SUMMER SCHOOL ON ORGANIC
SYNTHESIS
Gargnano, Italy
Information: <https://corbellasummerschool.unimi.it/>
- 13 – 15 SYMPOSIUM ON THE INTERACTIONS BETWEEN SEDIMENTS AND WATER
Piran, Slovenia
Information: <https://www.iasws2022.si/>
- 13 – 16 4TH TRAINING SCHOOL 'MECHANOCHEMICAL SYNTHESIS AND KINETICS'
Cagliari, Italy
Information: <https://www.mechsustind.eu/>
- 23 – 24 GREEN AND UNCONVENTIONAL SYNTHESIS, APPROACHES AND FUNCTIONAL
ASSESSMENT AIM 2020 (AIM 2020 ADVANCED INORGANIC MATERIALS)
Bari, Italy
Information: <http://www.unconventional-aim2020-bari.it/ž>
- 28 – July 1 26TH INTERNATIONAL SYMPOSIUM ON SEPARATION SCIENCES - ISSS 2022
Ljubljana, Slovenia
Information: <https://iss2020.si/>
- 28 – July 1 25TH INTERNATIONAL SYMPOSIUM ON HIGH-PERFORMANCE THIN-LAYER
CHROMATOGRAPHY (25TH HPTLC)
Ljubljana, Slovenia
Information: www.hptlc2020.si
- 30 – July 2 4TH INTERNATIONAL CONGRESS OF CHEMISTS AND CHEMICAL ENGINEERS OF
B&H
Sarajevo, Bosnia and Herzegovina
Information: iccebih.dktks.ba

July 2022

- 4 – 8 CHEMISTRY FOR CULTURAL HERITAGE - CHEMCH-2020
Ravenna, Italy
Information: <https://eventi.unibo.it/chemch2022>
- 11 – 13 EUROPEAN CONFERENCE OF RESEARCH IN CHEMISTRY EDUCATION (ECRICE 2020)
Rehovot, Israel
Information: <https://www.weizmann.ac.il/conferences/ECRICE2020/>
- 13 – 14 TOTAL FOOD 2022: MAXIMISING VALUE FROM THE FOOD CHAIN
Nottingham, UK
Information: <https://www.nottingham.ac.uk/conference/fac-sci/biosciences/total-food/index.aspx>
- 18 – 22 SECOND INTERNATIONAL CONFERENCE ON NONCOVALENT INTERACTIONS 2021-2022 - ICNI2021
Strasbourg, France
Information: <http://icni2021.unistra.fr/>

August 2022

- 27 – Sept 2 INTERNATIONAL MASS SPECTROMETRY CONFERENCE 2022
Maastricht, The Netherlands
Information: <https://www.imsc2022.com/>
- 28 – Sept 1 8TH EUCHEMS CHEMISTRY CONGRESS (ECC8)
Lisbon, Portugal
Information: <https://euchems2022.eu/>

September 2022

- 5 – 9 9TH IUPAC INTERNATIONAL CONFERENCE ON GREEN CHEMISTRY - ICGC-9
Athens, Greece
Information: greeniupac2020.org
- 21 – 23 19. RUŽIČKA DAYS
Vukovar, Croatia
Information: <http://www.ruzickadays.eu>
- 21 – 23 SCS ANNUAL MEETING 2022
Portorož-Portorose, Slovenia
Information: <https://skd2022.chem-soc.si/>
- 27 – 30 11TH CENTRAL EUROPEAN CONGRESS ON FOOD AND NUTRITION
Čatež ob Savi, Slovenia
Information: <https://cefood2022.si/>

October 2022

- 5 – 7 7 MS FOOD DAY
Florence, Italy
Information: <https://www.spettrometriadimassa.it/Congressi/7MS-FoodDay/index.html>
- 12 – 14 CHEMICAL RESEARCH IN FLANDERS - CHEMISTRY CONFERENCE FOR YOUNG SCIENTISTS 2022
Blankenberge, Belgium
Information: <https://crf-chemcys.be/>
- 21 – 22 XIV CONFERENCE OF CHEMISTS, TECHNOLOGISTS AND ECOLOGISTS OF THE REPUBLIC OF SRPSKA
Banja Luka, Bosnia and Herzegovina
Information: <https://savjetovanje.tf.unibl.org/>

23 – 26 31ST INTERNATIONAL SYMPOSIUM ON THE CHEMISTRY OF NATURAL PRODUCTS
AND 11TH INTERNATIONAL CONGRESS ON BIODIVERSITY (ISCNP31 & ICOB11)
Naples, Italy

Information: <https://www.iscnp31-icob11.org/index.php>

November 2022

8 – 11 SOLUTIONS IN CHEMISTRY 2022
Sveti Martin na Muri, Croatia

Information: <https://solutionsinchemistry.hkd.hr/>

December 2022

5 – 8 ENVIRONMENTAL MEETING ON ENVIRONMENTAL CHEMISTRY 2022 – EMEC22
Ljubljana, Slovenia

Information: <https://www.emec22.com/>

2023

July 2023

2 – 6 FEZA 2023 - 9TH CONFERENCE OF THE FEDERATION OF THE EUROPEAN ZEOLITE
ASSOCIATIONS

Portorož-Portorose, Slovenia

Information: <https://feza2023.org/en/>

Acta Chimica Slovenica

Author Guidelines

Submissions

Submission to ACSi is made with the implicit understanding that neither the manuscript nor the essence of its content has been published in whole or in part and that it is not being considered for publication elsewhere. All the listed authors should have agreed on the content and the corresponding (submitting) author is responsible for having ensured that this agreement has been reached. The acceptance of an article is based entirely on its scientific merit, as judged by peer review. There are no page charges for publishing articles in ACSi. The authors are asked to read the Author Guidelines carefully to gain an overview and assess if their manuscript is suitable for ACSi.

Additional information

- Citing spectral and analytical data
- Depositing X-ray data

Submission material

Typical submission consists of:

- full manuscript (PDF file, with title, authors, abstract, keywords, figures and tables embedded, and references)
- supplementary files
 - **Full manuscript** (original Word file)
 - **Statement of novelty** (Word file)
 - **List of suggested reviewers** (Word file)
 - **ZIP file containing graphics** (figures, illustrations, images, photographs)
 - **Graphical abstract** (single graphics file)
 - **Proposed cover picture** (optional, single graphics file)
 - **Appendices** (optional, Word files, graphics files)

Incomplete or not properly prepared submissions will be rejected.

Submission process

Before submission, authors should go through the checklist at the bottom of the page and prepare for submission.

Submission process consists of 5 steps.

Step 1: Starting the submission

- Choose one of the journal sections.
- Confirm all the requirements of the **checklist**.
- Additional plain text comments for the editor can be provided in the relevant text field.

Step 2: Upload submission

- Upload full manuscript in the form of a Word file (with title, authors, abstract, keywords, figures and tables embedded, and references).

Step 3: Enter metadata

- First name, last name, contact email and affiliation for all authors, in relevant order, must be provided. Corresponding author has to be selected. Full postal address and phone number of the corresponding author has to be provided.

- **Title and abstract** must be provided in plain text.
- Keywords must be provided (max. 6, separated by semicolons).
- Data about contributors and supporting agencies may be entered.
- **References** in plain text must be provided in the relevant text field.

Step 4: Upload supplementary files

- Original Word file (original of the PDF uploaded in the step 2)
- **List of suggested reviewers** with at least five reviewers with two recent references from the field of submitted manuscript must be uploaded as a Word file. At the same time, authors should declare (i) that they have no conflict of interest with suggested reviewers and (ii) that suggested reviewers are experts in the field of the submitted manuscript.
- All **graphics** have to be uploaded in a single ZIP file. Graphics should be named Figure 1.jpg, Figure 2.eps, etc.
- **Graphical abstract image** must be uploaded separately
- **Proposed cover picture** (optional) should be uploaded separately.
- Any additional **appendices** (optional) to the paper may be uploaded. Appendices may be published as a supplementary material to the paper, if accepted.
- For each uploaded file the author is asked for additional metadata which may be provided. Depending of the type of the file please provide the relevant title (Statement of novelty, List of suggested reviewers, Figures, Graphical abstract, Proposed cover picture, Appendix).

Step 5: Confirmation

- Final confirmation is required.

Article Types

Feature Articles are contributions that are written on Editor's invitation. They should be clear and concise summaries of the author's most recent work written with the broad scope of ACSi in mind. They are intended to be general overviews of the authors' subfield of research but should be written in a way that engages and informs scientists in other areas. They should contain the following (see also general guidelines for article structure below): (1) an introduction that acquaints readers with the authors' research field and outlines the important questions for which answers are being sought; (2) interesting, novel, and recent contributions of the author(s) to the field; and (3) a summary that presents possible future directions. Manuscripts should normally not exceed 40 pages of one column format (font size 12, 33 lines per page). Generally, experts who have made an important contribution to a specific field in recent years will be invited by the Editor to contribute a **Feature Article**. Individuals may, however, send a proposal (of no more than one page) for a **Feature Article** to the Editor-in-Chief for consideration.

Scientific articles should report significant and innovative achievements in chemistry and related sciences and should exhibit a high level of originality. They should have the following structure:

1. Title (max. 150 characters),
2. Authors and affiliations,
3. Abstract (max. 1000 characters),
4. Keywords (max. 6),
5. Introduction,
6. Experimental,
7. Results and Discussion,
8. Conclusions,
9. Acknowledgements,
10. References.

The sections should be arranged in the sequence generally accepted for publications in the respective fields and should be successively numbered.

Short communications generally follow the same order of sections as Scientific articles, but should be short (max. 2500 words) and report a significant aspect of research work meriting separate publication. Editors may decide that a Scientific paper is categorized as a Short Communication if its length is short.

Technical articles report applications of an already described innovation. Typically, technical articles are not based on new experiments.

Preparation of Submissions

Text of the submitted articles must be prepared with Microsoft Word. Normal style set to single column, 1.5 line spacing, and 12 pt Times New Roman font is recommended. Line numbering (continuous, for the whole document) must be enabled to simplify the reviewing process. For any other format, please consult the editor. Articles should be written in English. Correct spelling and grammar are the sole responsibility of the author(s). Papers should be written in a concise and succinct manner. The authors shall respect the ISO 80000 standard [1], and IUPAC Green Book [2] rules on the names and symbols of quantities and units. The Système International d'Unités (SI) must be used for all dimensional quantities.

Graphics (figures, graphs, illustrations, digital images, photographs) should be inserted in the text where appropriate. The captions should be self-explanatory. Lettering should be readable (suggested 8 point Arial font) with equal size in all figures. Use common programs such as MS Excel or similar to prepare figures (graphs) and ChemDraw to prepare structures in their final size. Width of graphs in the manuscript should be 8 cm. Only in special cases (in case of numerous data, visibility issues) graphs can be 17 cm wide. All graphs in the manuscript should be inserted in relevant places and **aligned left**. The same graphs should be provided separately as images of appropriate resolution (see below) and submitted together in a ZIP file (Graphics ZIP). Please do not submit figures as a Word file. In **graphs**, only the graph area determined by both axes should be in the frame, while a frame around the whole graph should be omitted. The graph area should be white. The legend should be inside the graph area. The style of all graphs should be the same. **Figures and illustrations** should be of sufficient quality for the printed version, i.e. 300 dpi minimum. **Digital images and photographs** should be of high quality (minimum

250 dpi resolution). On submission, figures should be of good enough resolution to be assessed by the referees, ideally as JPEGs. High-resolution figures (in JPEG, TIFF, or EPS format) might be required if the paper is accepted for publication.

Tables should be prepared in the Word file of the paper as usual Word tables. The captions should appear above the table and should be self-explanatory.

References should be numbered and ordered sequentially as they appear in the text, likewise methods, tables, figure captions. When cited in the text, reference numbers should be superscripted, following punctuation marks. It is the sole responsibility of authors to cite articles that have been submitted to a journal or were in print at the time of submission to ACSi. Formatting of references to published work should follow the journal style; please also consult a recent issue:

1. J. W. Smith, A. G. White, *Acta Chim. Slov.* **2008**, *55*, 1055–1059.
2. M. F. Kemmere, T. F. Keurentjes, in: S. P. Nunes, K. V. Peinemann (Ed.): *Membrane Technology in the Chemical Industry*, Wiley-VCH, Weinheim, Germany, **2008**, pp. 229–255.
3. J. Levec, Arrangement and process for oxidizing an aqueous medium, US Patent Number 5,928,521, date of patent July 27, **1999**.
4. L. A. Bursill, J. M. Thomas, in: R. Sersale, C. Collola, R. Aiello (Eds.), *Recent Progress Report and Discussions: 5th International Zeolite Conference*, Naples, Italy, 1980, Gianini, Naples, **1981**, pp. 25–30.
5. J. Szegezdi, F. Csizmadia, Prediction of dissociation constant using microconstants, http://www.chemaxon.com/conf/Prediction_of_dissociation_constant_using_microconstants.pdf, (assessed: March 31, 2008)

Titles of journals should be abbreviated according to Chemical Abstracts Service Source Index (CASSI).

Special Notes

- Complete characterization, **including crystal structure**, should be given when the synthesis of new compounds in crystal form is reported.
- Numerical **data should be reported with the number of significant digits corresponding to the magnitude** of experimental uncertainty.
- **The SI system of units and IUPAC recommendations** for nomenclature, symbols and abbreviations should be followed closely. Additionally, the authors should follow the general guidelines when citing spectral and analytical data, and depositing crystallographic data.
- **Characters** should be correctly represented throughout the manuscript: for example, 1 (one) and l (ell), 0 (zero) and O (oh), x (ex), D7 (times sign), B0 (degree sign). Use Symbol font for all Greek letters and mathematical symbols.
- The rules and recommendations of the **IUBMB** and the **International Union of Pure and Applied Chemistry (IUPAC)** should be used for abbreviation of chemical names, nomenclature of chemical compounds, enzyme nomenclature, isotopic compounds, optically active isomers, and spectroscopic data.
- **A conflict of interest** occurs when an individual (author, reviewer, editor) or its organization is in-

volved in multiple interests, one of which could possibly corrupt the motivation for an act in the other. Financial relationships are the most easily identifiable conflicts of interest, while conflicts can occur also as personal relationships, academic competition, etc. **The Editors** will make effort to ensure that conflicts of interest will not compromise the evaluation process; potential editors and reviewers will be asked to exempt themselves from review process when such conflict of interest exists. When the manuscript is submitted for publication, **the authors** are expected to disclose any relationships that might pose potential conflict of interest with respect to results reported in that manuscript. In the Acknowledgement section the source of funding support should be mentioned. The statement of disclosure must be provided as Comments to Editor during the submission process.

- **Published statement of Informed Consent.** Research described in papers submitted to ACSi must adhere to the principles of the Declaration of Helsinki (<http://www.wma.net/e/policy/b3.htm>). These studies must be approved by an appropriate institutional review board or committee, and informed consent must be obtained from subjects. The Methods section of the paper must include: 1) a statement of protocol approval from an institutional review board or committee and 2), a statement that informed consent was obtained from the human subjects or their representatives.
- **Published Statement of Human and Animal Rights.** When reporting experiments on human subjects, authors should indicate whether the procedures followed were in accordance with the ethical standards of the responsible committee on human experimentation (institutional and national) and with the Helsinki Declaration of 1975, as revised in 2008. If doubt exists whether the research was conducted in accordance with the Helsinki Declaration, the authors must explain the rationale for their approach and demonstrate that the institutional review body explicitly approved the doubtful aspects of the study. When reporting experiments on animals, authors should indicate whether the institutional and national guide for the care and use of laboratory animals was followed.
- To avoid conflict of interest between authors and referees we expect that not more than one referee is from the same country as the corresponding author(s), however, not from the same institution.
- Contributions authored by **Slovenian scientists** are evaluated by non-Slovenian referees.
- Papers describing **microwave-assisted reactions** performed in domestic microwave ovens are not considered for publication in *Acta Chimica Slovenica*.
- *Manuscripts that are **not prepared and submitted** in accord with the instructions for authors are not considered for publication.*

Appendices

Authors are encouraged to make use of supporting information for publication, which is supplementary material (appendices) that is submitted at the same time as the manuscript. It is made available on the Journal's

web site and is linked to the article in the Journal's Web edition. The use of supporting information is particularly appropriate for presenting additional graphs, spectra, tables and discussion and is more likely to be of interest to specialists than to general readers. When preparing supporting information, authors should keep in mind that the supporting information files will not be edited by the editorial staff. In addition, the files should be not too large (upper limit 10 MB) and should be provided in common widely known file formats to be accessible to readers without difficulty. All files of supplementary materials are loaded separately during the submission process as supplementary files.

Proposed Cover Picture and Graphical Abstract Image

Graphical content: an ideally full-colour illustration of resolution 300 dpi from the manuscript must be proposed with the submission. Graphical abstract pictures are printed in size 6.5 x 4 cm (hence minimal resolution of 770 x 470 pixels). Cover picture is printed in size 11 x 9.5 cm (hence minimal resolution of 1300 x 1130 pixels)

Authors are encouraged to submit illustrations as candidates for the journal Cover Picture*. The illustration must be related to the subject matter of the paper. Usually both proposed cover picture and graphical abstract are the same, but authors may provide different pictures as well.

* The authors will be asked to contribute to the costs of the cover picture production.

Statement of novelty

Statement of novelty is provided in a Word file and submitted as a supplementary file in step 4 of submission process. Authors should in no more than 100 words emphasize the scientific novelty of the presented research. Do not repeat for this purpose the content of your abstract.

List of suggested reviewers

List of suggested reviewers is a Word file submitted as a supplementary file in step 4 of submission process. Authors should propose the names, full affiliation (department, institution, city and country) and e-mail addresses of five potential referees. Field of expertise and at least two references relevant to the scientific field of the submitted manuscript must be provided for each of the suggested reviewers. The referees should be knowledgeable about the subject but have no close connection with any of the authors. In addition, referees should be from institutions other than (and countries other than) those of any of the authors. Authors declare no conflict of interest with suggested reviewers. Authors declare that suggested reviewers are experts in the field of submitted manuscript.

How to Submit

Users registered in the role of author can start submission by choosing USER HOME link on the top of the page, then choosing the role of the Author and follow the relevant link for starting the submission process.

Prior to submission we strongly recommend that you familiarize yourself with the ACSi style by browsing the journal, particularly if you have not submitted to the ACSi before or recently.

Correspondence

All correspondence with the ACSi editor regarding the paper goes through this web site and emails. Emails are sent and recorded in the web site database. In the correspondence with the editorial office please provide ID number of your manuscript. All emails you receive from the system contain relevant links. **Please do not answer the emails directly but use the embedded links in the emails for carrying out relevant actions.** Alternatively, you can carry out all the actions and correspondence through the online system by logging in and selecting relevant options.

Proofs

Proofs will be dispatched via e-mail and corrections should be returned to the editor by e-mail as quickly as possible, normally within 48 hours of receipt. Typing errors should be corrected; other changes of contents will be treated as new submissions.

Submission Preparation Checklist

As part of the submission process, authors are required to check off their submission's compliance with all of the following items, and submissions may be returned to authors that do not adhere to these guidelines.

1. The submission has not been previously published, nor is it under consideration for publication in any other journal (or an explanation has been provided in Comments to the Editor).
2. All the listed authors have agreed on the content and the corresponding (submitting) author is responsible for having ensured that this agreement has been reached.
3. The submission files are in the correct format: manuscript is created in MS Word but will be **submitted in PDF** (for reviewers) as well as in original MS Word format (as a supplementary file for technical editing); diagrams and graphs are created in Excel and saved in one of the file formats: TIFF, EPS or JPG; illustrations are also saved in one of these formats. The preferred position of graphic files in a document is to embed them close to the place where they are mentioned in the text (See **Author guidelines** for details).
4. The manuscript has been examined for spelling and grammar (spell checked).
5. The **title** (maximum 150 characters) briefly explains the contents of the manuscript.
6. Full names (first and last) of all authors together with the affiliation address are provided. Name of author(s) denoted as the corresponding author(s), together with their e-mail address, full postal address and telephone/fax numbers are given.
7. The **abstract** states the objective and conclusions of the research concisely in no more than 150 words.
8. Keywords (minimum three, maximum six) are provided.
9. **Statement of novelty** (maximum 100 words) clearly explaining new findings reported in the manuscript should be prepared as a separate Word file.
10. The text adheres to the stylistic and bibliographic requirements outlined in the **Author guidelines**.
11. Text in normal style is set to single column, 1.5 line spacing, and 12 pt. Times New Roman font is

recommended. All tables, figures and illustrations have appropriate captions and are placed within the text at the appropriate points.

12. Mathematical and chemical equations are provided in separate lines and numbered (Arabic numbers) consecutively in parenthesis at the end of the line. All equation numbers are (if necessary) appropriately included in the text. Corresponding numbers are checked.
13. Tables, Figures, illustrations, are prepared in correct format and resolution (see **Author guidelines**).
14. The lettering used in the figures and graphs do not vary greatly in size. The recommended lettering size is 8 point Arial.
15. Separate files for each figure and illustration are prepared. The names (numbers) of the separate files are the same as they appear in the text. All the figure files are packed for uploading in a single ZIP file.
16. Authors have read **special notes** and have accordingly prepared their manuscript (if necessary).
17. References in the text and in the References are correctly cited. (see **Author guidelines**). All references mentioned in the Reference list are cited in the text, and vice versa.
18. Permission has been obtained for use of copyrighted material from other sources (including the Web).
19. The names, full affiliation (department, institution, city and country), e-mail addresses and references of five potential referees from institutions other than (and countries other than) those of any of the authors are prepared in the word file. At least two relevant references (important recent papers with high impact factor, head positions of departments, labs, research groups, etc.) for each suggested reviewer must be provided. Authors declare no conflict of interest with suggested reviewers. Authors declare that suggested reviewers are experts in the field of submitted manuscript.
20. Full-colour illustration or graph from the manuscript is proposed for graphical abstract.
21. **Appendices** (if appropriate) as supplementary material are prepared and will be submitted at the same time as the manuscript.

Privacy Statement

The names and email addresses entered in this journal site will be used exclusively for the stated purposes of this journal and will not be made available for any other purpose or to any other party.

ISSN: 1580-3155

Koristni naslovi

Slovensko kemijsko društvo
Slovenian Chemical Society



Slovensko kemijsko društvo

www.chem-soc.si

e-mail: chem.soc@ki.si



Wessex Institute of Technology

www.wessex.ac.uk



SETAC

www.setac.org



European Water Association

<http://www.ewa-online.eu/>



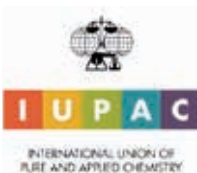
European Science Foundation

www.esf.org



European Federation of Chemical Engineering

<https://efce.info/>



International Union of Pure and Applied Chemistry

<https://iupac.org/>

Novice evropske zveze kemijskih društev EuChemS najdete na:



Brussels News Updates

<http://www.euchems.eu/newsletters/>



M BRAUN



DONAU LAB Ljubljana
Member of LPPgroup



SYSTAG



CHEMTRIX
Scalable Flow Chemistry



büchiglasuster
switzerland Pilot Plant and Reactor Systems

MAGNEZIJ Krka 300

MAGNEZIJ Krka 400



BODITE ŠE BOLJ NEUSTAVLJIVI

Magneziju Krka 300 se je pridružil **Magnezij Krka 400**,
ki vsebuje **več magnezija** in tako še bolj pripomore k:

- ✓ zmanjševanju utrujenosti in izčrpanosti,
- ✓ normalnemu delovanju mišic.

www.magnezijkrka.si

Prehransko dopolnilo ni nadomestilo za uravnoteženo in raznovrstno prehrano. Skrbite tudi za zdrav življenjski slog.



NOVO

MAGNEZIJ Krka

400

granulat za napitek

MAGNEZIJEV CITRAT 400 mg magnezija

2 mg vitamina B₂

pridružen k zmanjševanju

utrujenosti in izčrpanosti

magnezij pripomore

k normalnemu delovanju mišic

EMKORT NA DAN

2 granule

40 sachetov po 6 g granule za napitek

Mg



KRKA

Razvoj in inovacije za globalno uspešnost

Znanje, kreativnost zaposlenih in inovacije so ključnega pomena v okolju, kjer nastajajo pametni premazi skupine KANSAI HELIOS. Z rešitvami, ki zadostijo široki paleti potreb, kontinuiranim razvojem ter s kakovostnimi izdelki, Helios predstavlja evropski center za inovacije in poslovni razvoj skupine Kansai Paint.

Part of  **KANSAI
PAINT**

www.helios-group.eu

 **KANSAI
HELIOS**
Designing Excellence



Slovensko kemijsko društvo
Slovenian Chemical Society

SLOVENSKI KEMIJSKI DNEVI 2022

21-23. SEPTEMBER 2022



SKD2022.CHEM-SOC.SI

KONGRESNI CENTER
GRAND HOTELA
BERNARDIN, PORTOROŽ

ActaChimicaSlovenica

ActaChimicaSlovenica

Soft hydrophilic nano and microgels are attractive polymer constructs with several potential applications; they are deformable and, in some cases, biocompatible. Gel particles prepared of a thermoresponsive polymer either swell or collapse with changing temperature. Poly(N-vinylcaprolactam) gel particles may be synthesized through precipitation polymerization or (mini)emulsion polymerization. A new approach is the polymerization induced self-assembly (page 251).



Year 2022, Vol. 69, No. 2

